



Defense Threat Reduction Agency
8725 John J. Kingman Road, MS
6201 Fort Belvoir, VA 22060-6201



DTRA-TR-15-27

TECHNICAL REPORT

Combustion Dynamics of Biocidal Metal-Based Energetic Components in Turbulent Reactive Flows

Distribution Statement A. Approved for public release; distribution is unlimited.

November 2015

HDTRA1-10-1-0003

Nick Glumac

Prepared by:
University of Illinois at Urbana-Champaign
1206 West Green Street
Urbana, IL 61801

DESTRUCTION NOTICE:

Destroy this report when it is no longer needed.
Do not return to sender.

PLEASE NOTIFY THE DEFENSE THREAT REDUCTION
AGENCY, ATTN: DTRIAC/ J9STT, 8725 JOHN J. KINGMAN ROAD,
MS-6201, FT BELVOIR, VA 22060-6201, IF YOUR ADDRESS
IS INCORRECT, IF YOU WISH IT DELETED FROM THE
DISTRIBUTION LIST, OR IF THE ADDRESSEE IS NO
LONGER EMPLOYED BY YOUR ORGANIZATION.

REPORT DOCUMENTATION PAGE

*Form Approved
OMB No. 0704-0188*

Public reporting burden for this collection of information is estimated to average 1 hour per response, including the time for reviewing instructions, searching existing data sources, gathering and maintaining the data needed, and completing and reviewing this collection of information. Send comments regarding this burden estimate or any other aspect of this collection of information, including suggestions for reducing this burden to Department of Defense, Washington Headquarters Services, Directorate for Information Operations and Reports (0704-0188), 1215 Jefferson Davis Highway, Suite 1204, Arlington, VA 22202-4302. Respondents should be aware that notwithstanding any other provision of law, no person shall be subject to any penalty for failing to comply with a collection of information if it does not display a currently valid OMB control number. **PLEASE DO NOT RETURN YOUR FORM TO THE ABOVE ADDRESS.**

1. REPORT DATE (DD-MM-YYYY)			2. REPORT TYPE			3. DATES COVERED (From - To)	
4. TITLE AND SUBTITLE			5a. CONTRACT NUMBER				
			5b. GRANT NUMBER				
			5c. PROGRAM ELEMENT NUMBER				
6. AUTHOR(S)			5d. PROJECT NUMBER				
			5e. TASK NUMBER				
			5f. WORK UNIT NUMBER				
7. PERFORMING ORGANIZATION NAME(S) AND ADDRESS(ES)			8. PERFORMING ORGANIZATION REPORT NUMBER				
9. SPONSORING / MONITORING AGENCY NAME(S) AND ADDRESS(ES)			10. SPONSOR/MONITOR'S ACRONYM(S)				
			11. SPONSOR/MONITOR'S REPORT NUMBER(S)				
12. DISTRIBUTION / AVAILABILITY STATEMENT							
13. SUPPLEMENTARY NOTES							
14. ABSTRACT							
15. SUBJECT TERMS							
16. SECURITY CLASSIFICATION OF:			17. LIMITATION OF ABSTRACT	18. NUMBER OF PAGES	19a. NAME OF RESPONSIBLE PERSON		
a. REPORT	b. ABSTRACT	c. THIS PAGE			19b. TELEPHONE NUMBER (include area code)		

UNIT CONVERSION TABLE
U.S. customary units to and from international units of measurement*

U.S. Customary Units	Multiply by ← Divide by [†]	International Units
Length/Area/Volume		
inch (in)	2.54 $\times 10^{-2}$	meter (m)
foot (ft)	3.048 $\times 10^{-1}$	meter (m)
yard (yd)	9.144 $\times 10^{-1}$	meter (m)
mile (mi, international)	1.609 344 $\times 10^3$	meter (m)
mile (nmi, nautical, U.S.)	1.852 $\times 10^3$	meter (m)
barn (b)	1 $\times 10^{-28}$	square meter (m^2)
gallon (gal, U.S. liquid)	3.785 412 $\times 10^{-3}$	cubic meter (m^3)
cubic foot (ft^3)	2.831 685 $\times 10^{-2}$	cubic meter (m^3)
Mass/Density		
pound (lb)	4.535 924 $\times 10^{-1}$	kilogram (kg)
unified atomic mass unit (amu)	1.660 539 $\times 10^{-27}$	kilogram (kg)
pound-mass per cubic foot ($lb\ ft^{-3}$)	1.601 846 $\times 10^1$	kilogram per cubic meter ($kg\ m^{-3}$)
pound-force (lbf avoirdupois)	4.448 222	newton (N)
Energy/Work/Power		
electron volt (eV)	1.602 177 $\times 10^{-19}$	joule (J)
erg	1 $\times 10^{-7}$	joule (J)
kiloton (kt) (TNT equivalent)	4.184 $\times 10^{12}$	joule (J)
British thermal unit (Btu) (thermochemical)	1.054 350 $\times 10^3$	joule (J)
foot-pound-force (ft lbf)	1.355 818	joule (J)
calorie (cal) (thermochemical)	4.184	joule (J)
Pressure		
atmosphere (atm)	1.013 250 $\times 10^5$	pascal (Pa)
pound force per square inch (psi)	6.984 757 $\times 10^3$	pascal (Pa)
Temperature		
degree Fahrenheit ($^{\circ}\text{F}$)	$[\text{T}({}^{\circ}\text{F}) - 32]/1.8$	degree Celsius (${}^{\circ}\text{C}$)
degree Fahrenheit ($^{\circ}\text{F}$)	$[\text{T}({}^{\circ}\text{F}) + 459.67]/1.8$	kelvin (K)
Radiation		
curie (Ci) [activity of radionuclides]	3.7 $\times 10^{10}$	per second (s^{-1}) [becquerel (Bq)]
roentgen (R) [air exposure]	2.579 760 $\times 10^{-4}$	coulomb per kilogram ($C\ kg^{-1}$)
rad [absorbed dose]	1 $\times 10^{-2}$	joule per kilogram ($J\ kg^{-1}$) [gray (Gy)]
rem [equivalent and effective dose]	1 $\times 10^{-2}$	joule per kilogram ($J\ kg^{-1}$) [sievert (Sv)]

* Specific details regarding the implementation of SI units may be viewed at <http://www.bipm.org/en/si/>.

[†]Multiply the U.S. customary unit by the factor to get the international unit. Divide the international unit by the factor to get the U.S. customary unit.

Final Project Report

HDTRA1-10-1-0003

COMBUSTION DYNAMICS OF BIOCIDAL METAL-BASED ENERGETIC COMPONENTS IN TURBULENT REACTIVE FLOWS

Submitted by

Nick Glumac

**Mechanical Science & Engineering Department
University of Illinois, Urbana-Champaign
1206 West Green Street
Urbana, IL 61801**

Edward Dreizin

**Otto H. York Department of Chemical, Biological, and Pharmaceutical Engineering
New Jersey Institute of Technology
University Heights
Newark, NJ 07102**

Program Manager:

Dr. Suhithi Peiris

Date:

10/8/2014



Report Summary

This research was a collaborative study between University of Illinois, Urbana-Champaign (UIUC) and New Jersey Institute of Technology (NJIT) with the objective of analyzing and quantifying the fundamental kinetics and reaction dynamics of novel, biocidal, metal-based energetic components. A combination of techniques and facilities developed for analyzing Al-based systems, involving single particle as well as group combustion and using advanced diagnostics, was applied to novel metal systems, including W/Zr and Ti/B, to address the DTRA thrust area on the “....creation of new energetic molecules/materials that enhance the defeat of WMDs, [and] the improvement of modeling, and simulation of these materials.” The proposed approach leveraged unique capabilities at NJIT and UIUC to analyze and quantify reaction kinetics of metal-based components, providing formulators with the fundamental insight required to design new compounds with significantly enhanced performance in counter-WMD applications.

The work involved two independent research groups: Dr. Edward Dreizin’s group at NJIT and Dr. Nick Glumac’s group at UIUC. Close contact and collaboration between the groups was maintained, though most of the tasks and sub-tasks involved working towards similar goals (e.g. kinetic rate expressions) using complementary tools at UIUC and NJIT. The effort was very successful, generating a wealth of published works and information regarding kinetics and dynamics of reacting particulate materials.

This report will be presented in 22 chapters, with each chapter representing a somewhat self-contained topic. In many cases, those chapters formed the basis for individual published papers. Chapters 1-5 focus on NJIT’s efforts with aluminum combustion. A new facility for simultaneous measurement of particle size and combustion time was developed at NJIT, and this facility yielded very large datasets of kinetics information on aluminum. Chapters 1 & 2 discuss this facility and the insights that it provided for micron sized aluminum particle combustion. Chapter 3 continues the pioneering work on nanoscale aluminum, looking at theoretical underpinnings of the pyrophoricity of ultrafine Al. Chapter 4 compares Al combustion in the new facility with other metal and alloy particulates, while Chapter 5 analyses related experimental results in more detail with added emphasis on particle temperature measurements.

Chapters 6 and 7 describe efforts at NJIT on other metals and alloys, specifically mechanically milled Al/hydrocarbon particles in Chapter 6 and titanium and zirconium in Chapter 7. The work with Al/hydrocarbon particles offers a new potential route to rapid ignition and combustion of Al particles, while the Ti and Zr work offer fundamental insights into the combustion of metals that burn heterogeneously.

A common theme in the project is the effect of turbulence on the combustion rate, and both NJIT and UIUC looked at this effect with different tools. Chapter 8 highlights NJIT’s efforts of inducing turbulence in a flame, quantifying it, and then measuring the effect on combustion rate. Chapter 9 focusses on water as an oxidizer, especially at lower temperatures, and some surprising results are found whereby oxidation rates are non-negligible even at temperatures just above ambient.

Chapters 10-12 are primarily theoretical efforts on heterogeneous combustion (Chapter 10), continuing Dreizin's detailed modeling efforts in this area. Chapters 11 and 12 look at the effect of two neglected parameters: surface tension (Chapter 11) and melting point suppression (Chapter 12), and quantify the effects on fine particle aluminum combustion.

Chapters 13 – 22 represent experimental work at UIUC addressing various aspects of the particle combustion problem. Chapter 13 focusses on determining the volatilization temperature of Al_2O_3 , a hotly contested value, using shock tube measurements. Chapter 14 looks at high temperatures that may occur at high explosive detonation breakout, with implications for enhanced particle reactivity.

Since AlO emission is widely used as a diagnostic tool in flows with Al combustion, Chapter 15 takes a detailed look at this practice and discusses some limitations and issues with correlating AlO intensity to combustion rates or completeness.

Aluminum combustion in aluminized explosives is examined in highly controlled experiments in Chapter 16, looking a size and environment effects and quantifying reactivity.

Chapters 17 and 19 take a look at alternative materials for biocidal applications; W/Zr (Chapter 17) and Ti/2B (Chapter 19). The former shows that tungsten alloys can be made to burn readily using NJIT's mechanical alloying techniques, while Chapter 19 shows that the intermetallic reaction in Ti/2B alloys is not necessary to achieve large conversion efficiencies.

Chapter 18 continues our work on novel diagnostics for particulate flows, extending our broadband laser techniques to the ultraviolet and showing the first in-fireball detection of AlF and MgF in energetics systems.

Chapter 20 discussed the potentially important role of the thermal accommodation coefficient (TAC) in nano-aluminum combustion, and some evidence for a low TAC of 0.01 or smaller is presented. While clearly a controversial result, compelling evidence to support low TAC values is carefully presented.

Chapter 21 and 22 cover use of the shock tube in novel fashions. Chapter 21 discusses how it can be used to create well controlled particle thermal profiles to calibrate and validate nanothermometer work sponsored by DTRA. Chapter 22 complements NJIT's work on turbulence by generating controlled turbulence at constant temperature in the shock tube and measuring the combustion rate while comparing it to quiescent environments.

Contents

CHAPTER 1: COMBUSTION TIMES AND EMISSION PROFILES OF MICRON-SIZED ALUMINUM PARTICLES BURNING IN DIFFERENT ENVIRONMENTS ..	10
Introduction.....	10
Experimental.....	11
Results.....	15
Discussion	23
Conclusions.....	26
References.....	27
CHAPTER 2: COMBUSTION CHARACTERISTICS OF MICRON-SIZED ALUMINUM PARTICLES IN OXYGENATED ENVIRONMENTS ..	28
Introduction.....	28
Experimental.....	28
Results.....	32
Discussion	39
Conclusions.....	40
References.....	41
CHAPTER 3: PYROPHORICITY OF NANO-SIZED ALUMINUM PARTICLES ..	43
Introduction.....	43
Model Formulation	43
Results and Discussion	47
Conclusions.....	49
References.....	49
CHAPTER 4: PARTICLE COMBUSTION DYNAMICS OF METAL-BASED REACTIVE MATERIALS ..	51
Introduction.....	51
Experimental setup.....	52
Data Processing.....	54
Materials	56
Results.....	58
Discussion	67
Conclusions.....	69
References.....	69
CHAPTER 5: ON WEAK EFFECT OF PARTICLE SIZE ON ITS BURN TIME FOR MICRON-SIZED ALUMINUM POWDERS ..	73
Introduction.....	73
Technical approach	73

Results.....	77
Discussion	81
Conclusions.....	85
References.....	85
CHAPTER 6: OXIDATION, IGNITION AND COMBUSTION OF AL-HYDROCARBON COMPOSITE REACTIVE POWDERS	87
Introduction.....	87
Materials	87
Experimental.....	89
Results.....	91
Discussion.....	101
Conclusions.....	102
References.....	103
CHAPTER 7: COMBUSTION OF MICRON-SIZED PARTICLES OF TITANIUM AND ZIRCONIUM	105
Introduction.....	105
Experimental.....	105
Data processing.....	106
Results.....	108
Discussion	109
References.....	110
CHAPTER 8: ALUMINUM PARTICLE COMBUSTION IN TURBULENT FLAMES	116
Introduction.....	116
Experimental.....	117
Results.....	123
Correlation for the burn rate	126
Conclusions.....	127
References.....	128
CHAPTER 9: COMBUSTION OF FINE ALUMINUM AND MAGNESIUM POWDERS IN WATER	130
Introduction.....	130
Experimental	131
Predicted temperature, concentration, and velocity profiles.....	138
Experimental results.....	141
Discussion	145

Conclusions.....	148
References.....	149
CHAPTER 10: MODEL OF HETEROGENEOUS COMBUSTION OF SMALL PARTICLES	151
Nomenclature.....	151
Introduction.....	152
Physical Model.....	153
Equations.....	156
Parameters and Solution Procedure	159
Results and Discussions	161
Conclusions.....	166
Appendix A.....	167
References.....	169
CHAPTER 11: EFFECT OF SURFACE TENSION ON THE TEMPERATURE OF BURNING METAL DROPLETS	171
Introduction.....	171
Boiling point as a function of pressure	171
Laplace pressure as a function of temperature.....	173
Implications for metal combustion	173
References.....	177
CHAPTER 12: DEPRESSION OF MELTING POINT FOR PROTECTIVE ALUMINUM OXIDE FILMS	180
Introduction.....	180
Estimated depression of the melting point.....	180
Experimental detection of melting point of natural aluminum oxide film	182
Discussion	184
Concluding remarks	184
References.....	184

CHAPTER 13: MICRO-ALUMINA PARTICLE VOLATILIZATION TEMPERATURE MEASUREMENTS IN A HETEROGENEOUS SHOCK TUBE

Introduction.....	186
Experimental Methods.....	187
Results and Discussion.....	193
Conclusion.....	204
References.....	204

CHAPTER 14: EARLY TIME SPECTROSCOPIC MEASUREMENTS DURING HIGH EXPLOSIVE DETONATION BREAKOUT INTO AIR

Introduction.....	206
Experimental.....	207
Results and Discussion.....	207
References.....	215

CHAPTER 15: ON ALO EMISSION SPECTROSCOPY AS A DIAGNOSTIC IN ENERGETIC MATERIALS TESTING

Introduction.....	217
Experimental.....	218
Results and Analysis.....	219
Analysis and Conclusions.....	227
References.....	228

CHAPTER 16: PARTICLE SIZE AND GAS ENVIRONMENT EFFECTS ON BLAST AND OVERPRESSURE ENHANCEMENT IN ALUMINIZED EXPLOSIVES

Introduction.....	233
Experimental.....	235
Results.....	237
Conclusions.....	243
References.....	243

CHAPTER 17: TUNGSTEN COMBUSTION IN EXPLOSIVELY INITIATED W/ZR MECHANICAL ALLOYS

Introduction.....	244
Experimental.....	244
Results.....	246

Discussion.....	249
Conclusions.....	250
References.....	250
CHAPTER 18: ULTRAVIOLET (UV) ABSORPTION SPECTROSCOPY IN OPTICALLY DENSE FIREBALLS USING BROADBAND SECOND HARMONIC GENERATION OF A PULSED MODELESS DYE LASER	
Introduction.....	252
Diagnostic Setup.....	253
Results and Discussion.....	257
Summary and Conclusions.....	262
Reference.....	263
CHAPTER 19: EXPLOSIVE INITIATION OF VARIOUS FORMS OF TI/2B REACTIVE MATERIALS	
Introduction.....	265
Experimental Methods.....	265
Results and Discussion.....	269
Conclusions.....	280
Reference.....	281
CHAPTER 20: HEAT TRANSFER EFFECTS IN NANO-ALUMINUM COMBUSTION AT HIGH TEMPERATURES	
Introduction.....	282
Experimental Setup.....	283
Experimental Results.....	286
Model Description.....	289
Discussion.....	290
Conclusions.....	293
References.....	294
CHAPTER 21: CALIBRATION TOOLS FOR NANOTHERMOMETERS: USING THE SHOCK TUBE	
Introduction.....	296
Setup.....	296
Particle Collection Procedure.....	297

Analysis.....	298
Conclusions.....	300
CHAPTER 22: TURBULENT INTERACTIONS WITH NORMAL SHOCKS AND THEIR EFFECTS ON NANO AL BURN TIME	
Introduction.....	301
Setup and Procedure.....	301
Results and Discussion.....	306
Conclusion.....	312
References.....	312

CHAPTER 1: COMBUSTION TIMES AND EMISSION PROFILES OF MICRON-SIZED ALUMINUM PARTICLES BURNING IN DIFFERENT ENVIRONMENTS

Introduction

Aluminum is an important energetic component of many solid propellants, explosives, and pyrotechnic formulations [1 – 4]. One critical parameter of aluminum combustion, universally important for all applications, is the particle burn time, τ_b , as a function of the particle diameter, D . For practical purposes the burn time is commonly expressed as a power law $\tau_b \sim D^n$, with the exponent n and pre-exponent factor depending on the oxidizing environment, temperature, and pressure, e.g., [5 – 8]. Various D^n type trends were reported by different authors based on a diverse set of experiments. Generally, laboratory experiments in well-characterized environments reported in the literature can be broadly divided into two groups: experiments using individual metal particles, e.g., [9 – 14], and experiments employing aerosolized powders or clouds, e.g., [7, 15 – 19]. For individual particles, the measurements of combustion times are often direct, while indirect methods and data analyses are used to extract the information on particle burn times or burn rates from the cloud combustion experiments. It is also worth noting that single metal particle combustion experiments in general, and direct measurements of combustion times for individual aluminum droplets in particular, were restricted to relatively large particles, with sizes 50 μm or greater. However, most practical applications deal with finer aluminum powders with particle sizes on the order of, or finer than, 20 μm . It is also interesting that in many experimental configurations, aluminum particles burn in combustion products of hydrocarbon fuels. In such cases, the oxidizers are mixtures of CO_2 , H_2O , and O_2 in various proportions. While this situation imitates some practical applications, the specific oxidizer mixtures produced in laboratory burners and in practical energetic formulations differ from one another substantially. Laboratory experiments with mixed oxidizers are also not particularly useful for extracting the information about efficiency of individual oxidizing species, which is required to model the practical configurations. The information on aluminum combustion in CO_2 and H_2O is very limited [9, 20, 21], with most data coming from experiments in mixed oxidizers, where the effects of different oxidizers are somewhat difficult to uncouple.

Considering the limitations of the available data on aluminum combustion, the goal of the current work was to directly measure optical signatures and burn times of individual, micron-sized aluminum particles. The focus of these experiments was to establish a direct correlation between particle diameters and their optical signatures and burn times for particles under 20 μm . The measurements were performed in well-characterized oxidizing environments with individual oxidizers including O_2 , CO_2 , and H_2O . These measurements are expected to serve as a foundation for development of a mechanistic aluminum combustion model. The model should account for multiple processes occurring in aluminum combustion and is not expected to be limited to a quasi-steady description. At the same time, the model should be relatively simple to enable its implementation in practical calculations. The measurements reported in this paper are

expected to help to identify the most important reaction mechanisms and processes to be included into the mechanistic model of aluminum combustion.

Experimental

Apparatus

The experimental setup used in this study is schematically shown in Fig. 1. The apparatus, experimental procedure, and data processing steps have been described in detail in a recent publication [22], and only a brief summary is presented here for completeness. Metal powder, comprised of spherical particles, was fed by an electrostatic particle generator [7, 19, 22] so that a narrow, vertically rising particle jet with a low number density is produced. The particles were carried by an oxidizing gas stream. The particle jet crosses two laser beams. First, particles intercept a 785-nm laser beam. For each particle, the scattered light intensity is proportional to its area and is used to measure the particle diameter. Two millimeters above the 785 nm laser beam, the particles traverse a focused CO₂ laser beam (~0.3 mm beam waist) in approximately 0.5 ms (i.e., particle velocities ~0.6 m/s). In the CO₂ beam, particles are rapidly heated and ignited. Emission from the incandescent and burning particles was measured to determine the particle burn times. The emission was collected by a wide angle quartz fiber, passed through a 500 nm band-pass filter, detected by a photomultiplier tube, converted to a digital signal, and stored for further analysis.

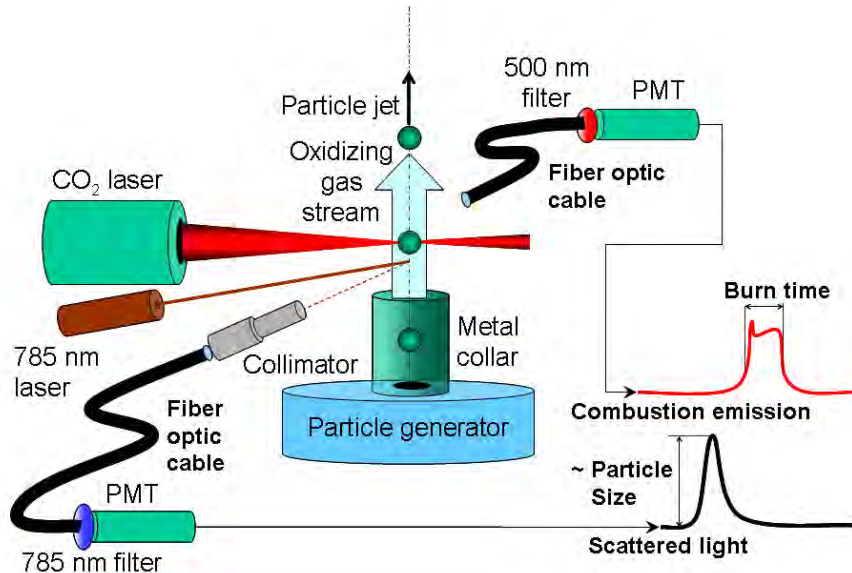


Fig. 1. Schematic diagram of the experimental setup

There are three significant modifications to the apparatus previously described in ref. [22].

First, a set of small inner diameter telescoping tubes, labeled “collimator” in Fig. 1 were attached to the fiber optic viewing the 785 nm scattered light. The field of view of the detection system was reduced to < 4.5° (full angle) and these tubes eliminated all

emission produced by incandescent or burning particles from reaching the scattered light detector.

Second, experiments were performed in various oxidizing environments. The compositions of the oxidizers included mixtures of N₂/O₂, N₂/CO₂, and N₂/H₂O (all at 1 atm.) A thin-walled aluminum collar (“metal collar” in Fig. 1) was added to the particle generator. This restricted outside air from mixing with the oxidizing gas streams. This collar is 8 mm in height and it has an outer diameter of 8.9 mm (inner diameter = 6.4 mm). High purity, dry gases were used for these experiments. Gases were metered through needle valves and flows were measured with mass flow meters (Alicat Scientific; Model M200SCCM-D) to $\pm 1\%$ accuracy. Carbon dioxide and water vapors interfere with the operation of the particle generator; so for experiments with these oxidizers, particles were fed with a pure nitrogen stream, and oxidizers were supplied in a shroud jet [22, 23] not shown in detail in Fig. 1. Detailed calculations using FLUENT software, for the gas flows in this apparatus, show that the inner and outer gas streams are well-mixed at the height where the particles intercept the CO₂ laser beam. These results are presented in Ref. [23] where the same experimental configuration was employed to study ignition of aluminum particles in different oxidizers. For oxygen/nitrogen gas mixtures, both the inner gas flow passing through the particle generator and the shroud jet had the same gas composition. Individually metered oxygen and nitrogen gas streams were mixed by passing them through a 3.0 m length of plastic tubing (1/4” od). To generate water vapor, a calibrated peristaltic pump (Control Company; Model 3384-CC) fed liquid water (3.3 mg/s) into a tube furnace held at a temperature of 200–250°C. The gas transfer lines and a top flange of the particle generator were maintained at 120°C to prevent condensation.

Specific environments used in experiments, gas flows, and calculated flow velocities are shown in Table 1. Particle flow velocities along the centerline were measured using square-wave modulated (500Hz; 50% duty cycle) green laser sheet illumination. This yielded particle velocities of about 0.6 m/s at 5 mm above the collar rim (13 mm above the particle generator outlet) and these velocities agree with those estimated from the offset time found when correlating the scattering peaks with the corresponding ignition peaks (see below for details).

Table 1. Gas Environments and Flow Rates for Ignition Experiments. Jet Velocities are Calculated at the Exit Plane of the Respective Orifice.

Inner Jet Gas	Outer Jet Gas	Collar ?	Flow Rate, cc/min		Jet Velocity, m/s	
			Inner	Outer	Inner	Outer
Air	Air	No	73.0	158	1.61	0.09
O ₂ :N ₂ 1:9	O ₂ :N ₂ 1:9	Yes	62.3	141	1.38	0.08
O ₂ :N ₂ 2:3	O ₂ :N ₂ 2:3	Yes	64.9	125	1.43	0.07
N ₂	CO ₂	Yes	73.6	165	1.63	0.09
N ₂	H ₂ O:N ₂ 9:1	Yes	67.5	386	1.49	0.21

Lastly, a 14-bit data acquisition board (DAC, National Instruments, Model PCI-6133) replaced the 12-bit, sequential DAC used in prior work. The new DAC has eight independent D/A converters and a maximum sampling rate of 3.0 MS/s (0.33 μ s per sampling event). In the current experiments, the sampling rate was 100 kS/s; or 10 μ s

per data point; except for the experiments with air, where the sampling rate was increased to 500 kS/s. For each scan, the time during which sequences of pulses of both scattered light and light produced by incandescent particles were continuously collected, was 10 s. Typically, 50-150 scans were collected for a set of experiments with a selected oxidizing gas mixture.

Materials

Spherically shaped micron sized aluminum particles were used for these experiments (Alfa Aesar, 10-14 μm nominal particle size). Prior to experiments, the powder was dried in a glass vial at 65-85°C under vacuum for more than 2 hours. The vial was quickly capped after opening the vacuum oven and after a cooling period, the sample vial was roll-milled (i.e., milled with an aluminum or Teflon solid rod, 1cm diam.) for approximately 20 min. This procedure reduced the number of agglomerated particles, but did not deform the shape of the particles - as confirmed by electron microscopy.

Measurements, processing, and interpretations

Prior to each combustion experiment, the particle sizing system was calibrated, as described elsewhere [22]. In these calibrations, particle size distributions measured by a commercial analyzer, LS230 by Beckman-Coulter, was matched with the size distributions determined from the scattered light pulses. Please see ref. [22] for details including the particle size distribution for the aluminum powder used in this work.

In each measurement, two separate pulse sequences were acquired simultaneously. In the first sequence, each pulse was produced by the scattered light and its amplitude was proportional to the particle surface area. In the second pulse sequence, each pulse represented an incandescent particle and its duration was equal to the time the particle remained incandescent. The two pulse sequences were correlated with each other to determine the emission duration for each individually sized particle. The details of the correlation procedure are given elsewhere [22]. It is based on matching the two sequences of pulses to each other while determining the “offset time” by which one pulse sequence needs to be shifted in time relative to another one to achieve the match. The offset time was compared to the time a particle travels between the two laser beams, which could be readily found from the average particle velocity and distance between the beams. When the two times were sufficiently close, the experimental results were further processed. A typical experiment includes collecting both pulse sequences during 50 - 150 separate 10-s intervals. There were typically 500-2000 scatter signal pulses and 50-100 particle emission pulses in each pair of the collected pulse sequences. After the overlapping peaks are removed and two sequences are correlated, approximately 20-50 pulses remain in each pulse sequence, representing the number of particles for which both sizes and burn times were determined.

Measurement of the particle size is very straightforward based on the scattered light intensity and calibration [22]. However, interpretation of the pulse durations produced by the incandescent particles is more difficult. To illustrate the problem with this interpretation and how it is addressed, consider a cartoon shown in Fig. 2. It schematically shows three particles of the same diameter crossing the laser beam at

different locations. In one possible scenario, particle 1 is not heated to ignition, particle 2 ignites and starts burning within the laser beam, and particle 3 is heated so that it ignites just when it exits the beam. In such a case, the durations of pulses produced by incandescent particles 1 and 2 would be shorter than the combustion time of interest. For particle 1, duration of emission is simply defined by the time the particle cools off. (Note that cooling times are very short for particles moving in a room temperature gas. An estimate shows that a 20 μm particle at 2793 K will cool to 933 K in about 5.8 ms, but the particle incandescence at 500 nm (spectral detection window) will drop 3 decades in light intensity (our detection limit) in about 1.5 ms. This is substantially shorter than the observed burn times discussed below). For particle 2, part of its combustion was assisted by the laser beam so that the rate of reaction is accelerated. Thus, only the longest pulse measured for particle 3 represents the burn time of interest. Because this consideration is valid for particles of any dimensions, it is concluded that for each particle size, only the longest measured pulse durations represent the burn times of interest. Considering that majority of particles do not cross the laser beam at the very specific location required to ignite, but not burn the particle while in the beam, it becomes clear that only a small fraction of the recorded emission pulses carries the useful information about the burn time of interest. In other words, many pulses need to be collected and processed so that the fraction of the pulses reflecting the burn time of interest becomes representative.

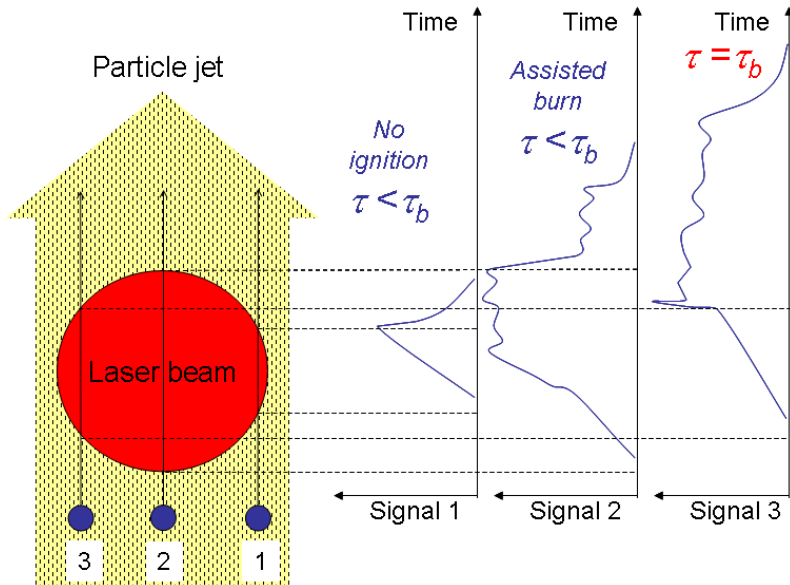


Fig. 2. Cartoon illustrating formation of pulses of different duration by particles of the same size crossing the laser beam at different locations.

A limitation on the shortest burn time that can be measured reliably is implied by the time a particle crosses the laser beam, so that it may be heated rapidly and remain incandescent while moving within the beam. Roughly, this limitation can be estimated as the ratio of the laser beam waist ($\sim 300 \mu\text{m}$) over the average particle velocity ($\sim 0.6 \text{ m/s}$) giving a heating time of about 0.5 ms.

Results

Emission Profiles

The emission intensity profiles from burning Al particles provide information about the processes and reactions occurring during combustion. Characteristic emission profiles for particles burning in different environments are shown in Figs. 3 – 7. The profiles shown are not selected to represent only the longest pulses for each particle size; instead, representative samples of profiles of different durations are shown for all environments.

The profiles measured for Al combustion in oxygen/nitrogen mixtures are collected in Figs. 3 – 5. The profiles look similar to one another and always begin with a relatively sharp initial peak. A closer examination of the peak fronts shows that for many pulses, the rate of the initial signal rise exhibits a sharp, step-wise increase, possibly indicating particle ignition within the laser beam. For particles burning in 10% O₂, Fig. 3, the first emission peak is relatively sharp and is followed by a steadily decaying emission signal. The decay is followed by a characteristic oscillatory emission pattern preceding the particle quenching. For particles burning in 21% O₂, the first emission peak becomes wider, while still being followed by a period of nearly steady decay in the emission signal. The oscillatory pattern is less clearly visible, and in many cases the oscillations are reduced to one or two spikes in the emission signal. While the burn time trends are discussed below, it is interesting to note here that the emission pulse durations in general are substantially reduced as the oxygen concentration increases from 10 to 21 %. For particles burning in 40% O₂, the first emission peak is very broad and the oscillatory emission patterns often appear nearly immediately following the peak. The oscillations continue for the entire burn time while the particle extinction is often preceded by a sharp jump in the emission intensity. No significant reduction in the measured pulse durations is noticed as compared to the pulses obtained in the 21% O₂ environment.

The emission profiles for carbon dioxide and water are presented in Figs. 6 and 7, respectively. The carbon dioxide profiles exhibit a broad first peak followed by a long, slow decay. The leading edges of the first peaks are substantially less sharp compared to those observed for oxygenated environments. Most profiles have small but identifiable oscillations in the tail of the profile. The oscillations are overlapped with a decay in the overall emission intensity.

Inspecting the water profiles shown in Fig. 7, it appears that the initial peaks are substantially greater in intensity than the rest of the emission signal. The leading edges of the initial peaks are sharper than in CO₂. The overall duration of the initial peaks is comparable to the estimated time the particles are crossing the laser beam. Thus, it appears that immediately after the laser source is removed, the emission drops rapidly to a very low level, which is substantially lower than that observed for any of the other environments. However, the emission remains reliably above the baseline level for a

while, suggesting a relatively steady exothermic reaction that is accompanied by emission that is much weaker compared to reactions in O_2 and CO_2 .

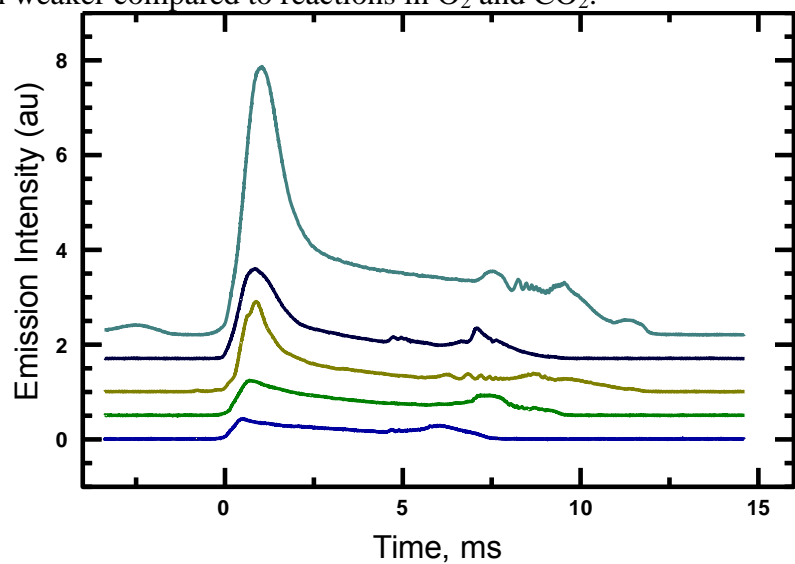


Figure 3. Emission profiles for Al particles burning in a 10/90 O_2/N_2 mixture.

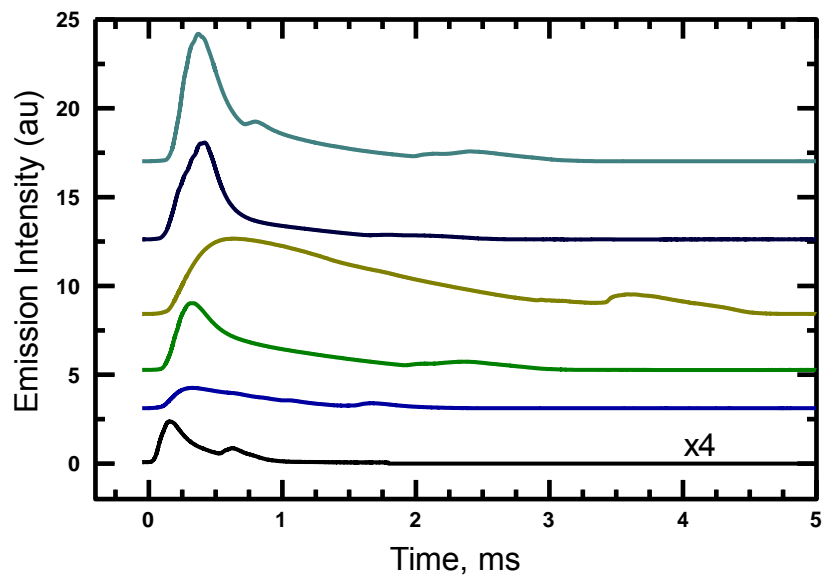


Figure 4. Emission profiles for Al particles burning in a 21/79 O_2/N_2 mixture (air).

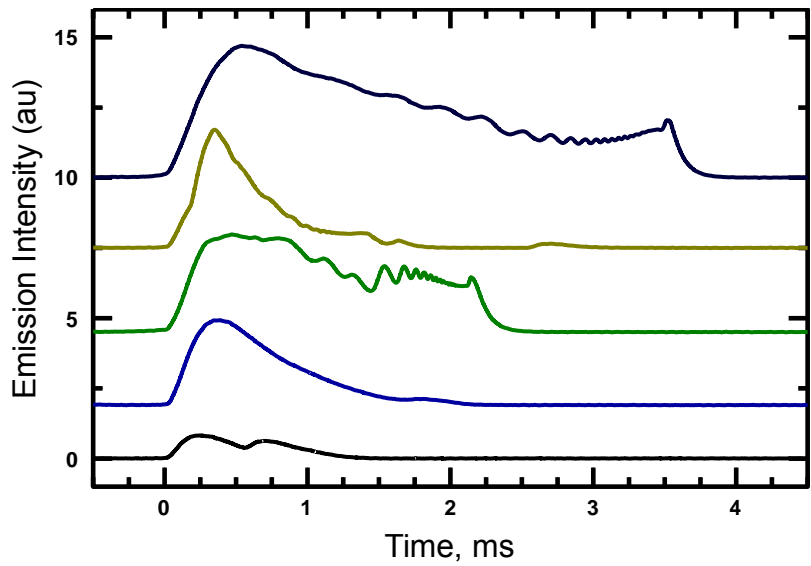


Figure 5. Emission profiles for Al particles burning in a 40/60 O₂/N₂ mixture.

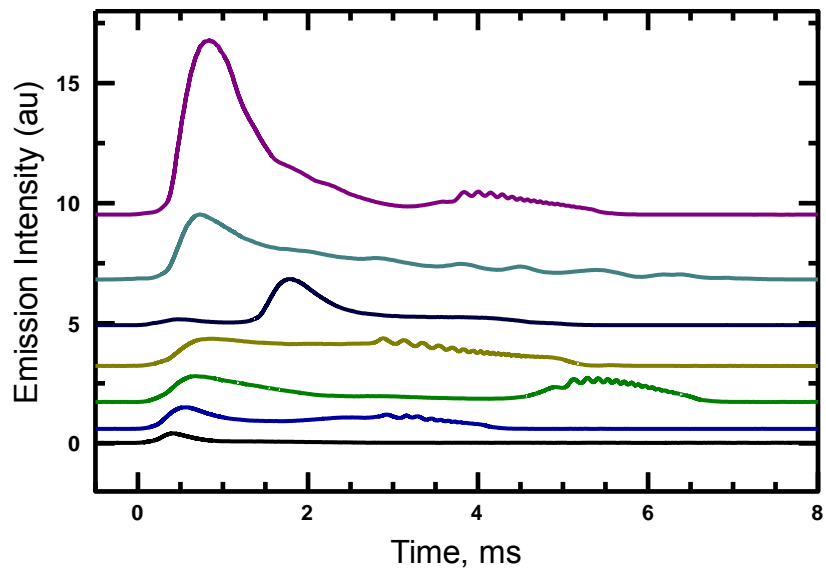


Figure 6. Emission profiles for Al particles burning in a 73/27 CO₂/N₂ mixture.

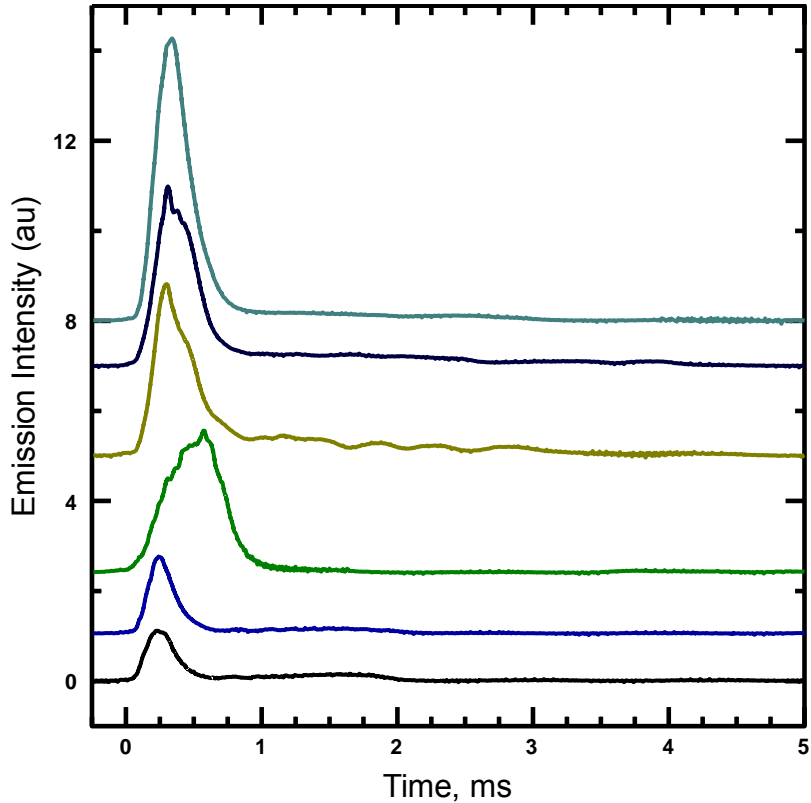


Figure 7. Emission profiles for Al particles burning in a 77/23 H₂O/N₂ mixture.

Burn Times

Burn times are presented in Figs. 8 – 12, where all experimental data points are shown. Each point represents a particle, for which the diameter is measured from the scattered pulse sequence, and the burn time is inferred from the duration of the correlated emission pulse. In other words, each point represents a pair of pulses measuring particle emission and scattered light, which are correlated in time to ensure that both pulses were produced by the same particle. As discussed above, the majority of the measured pulse durations do not represent the burn times of interest. Only the longest measured pulse durations for each particle size can be interpreted as the burn times for a self-sustained particle combustion that was not assisted by laser. For each set of experimental data points, a trendline showing the D^n fit is also shown as a solid line. The fit is obtained for data points representing the longest measured pulse durations for each particle size range. The particle size ranges and the respective longest pulse durations are selected manually and somewhat subjectively from all the measured data points. The points used to calculate the trendline are shown as filled symbols while the rest of the experimental data points are presented as open symbols. Note that each data point used in the “power-law” fits, was inspected additionally to confirm that for each such matched pair of emission and scattered light peaks both peaks were well separated from their neighbors, were clearly above the noise level, and that the emission profile was typical of aluminum combustion in the respective environment. Despite an elaborate automated peak processing routine described in ref. [22], some outlier points were still identified by this additional inspection, which were likely caused by ignition of agglomerated particles or particles

closely following each other in the jet. Such outlier points were removed from Figs. 8 – 12.

In addition to the experimental points and solid trendlines, three dashed lines are also shown for each plot. The dashed lines show particle burn times predicted for each specific environment as a function of the particle diameter using three different D^n trends reported in the literature for aluminum combustion. For all trends, the particle diameter, D , is entered in mm and the burn time, τ_b , is calculated in ms.

The first trend, given by Eq. (1), comes from a review of published experimental results, primarily for coarser Al particles, compiled by M. Beckstead [5].

$$\tau_b = \frac{7.35D^{1.8}}{(C_{O_2} + 0.6C_{H_2O} + 0.22C_{CO_2})P^{0.1}T^{0.2}} \quad (1)$$

In Eq. (1) and below, C is the concentrations of oxidizer given by the respective subscript, P is pressure, and T is the environment temperature.

The second trend is described by the set of Eqs. (2) and was proposed by N. Glumac et al. [6] based on measurements using aerosolized Al particles ignited in a shock tube. These measurements identified average combustion times of narrowly size-classified Al powders. The burn times were obtained from the widths of the optical emission peaks produced by the powders ignited in a gas heated by the shock wave.

$$\begin{aligned} \tau_b &= a_o C_{OX}^{a_1} \left(\frac{P}{P_0} \right)^{a_2} D^n \\ n &= 2 \exp(-4.3C_{OX}) \left(\frac{P}{P_0} \right)^{-0.3} \\ \tau_{b,mix} &= \left(\sum_{i=1}^n \frac{1}{\tau_{b,i}} \right)^{-1} \end{aligned} \quad (2)$$

Similarly to Eq. (1), Eqs. (2) describe effects of oxidizer concentration and ambient pressure. The reference pressure that should be used in Eqs. (2) is $P_0=8.5$ atm. The effect of the oxidizer type is given by the choice of constants a_0 , a_1 , and a_2 , as described in Table 2. Unlike Eq. (1), there is no effect of ambient temperature in Eqs. (2). However, it should be noted that the measurements used to obtain Eqs. (2) were performed in hot ambient gases.

Table 2. Selection of constants as a function of oxidizer for use in Eq. (2) [6].

Oxidizer	a_0, ms	a_1	a_2
O_2	200	0.5	-0.5
CO_2	500	0.6	0.3
H_2O	86	-1.7	0.75

Finally, the third trend used for reference calculations of the burn time is given by Eq. (3) and was taken from ref. [7] by Shoshin and Dreizin, where the particle burn times were measured using a lifted laminar flame burner. The experiments were performed in air

only, so Eq. (3) does not take into account effects of ambient pressure, temperature, oxidizer type or concentration.

$$\tau_b = 310 \cdot D \quad (3)$$

Results for burn time for aluminum in the 10% oxygen mixture are shown in Fig. 8. Both Eqs. (1) and (3) substantially underestimate the particle burn times, while Eqs. (2) predict much longer burn times than observed in experiments. Note that experimental points appear for particles greater than about 3 μm , indicating that the smaller particles were difficult to identify based on the measured scattered light pulses. This restriction is due to a smaller peak to noise ratio for the scattered signal from the small scattered light peaks produced by small particles.

A relatively weak increase in the burn time for increased particle sizes is observed and it is reasonably well described by a $D^{0.32}$ trendline.

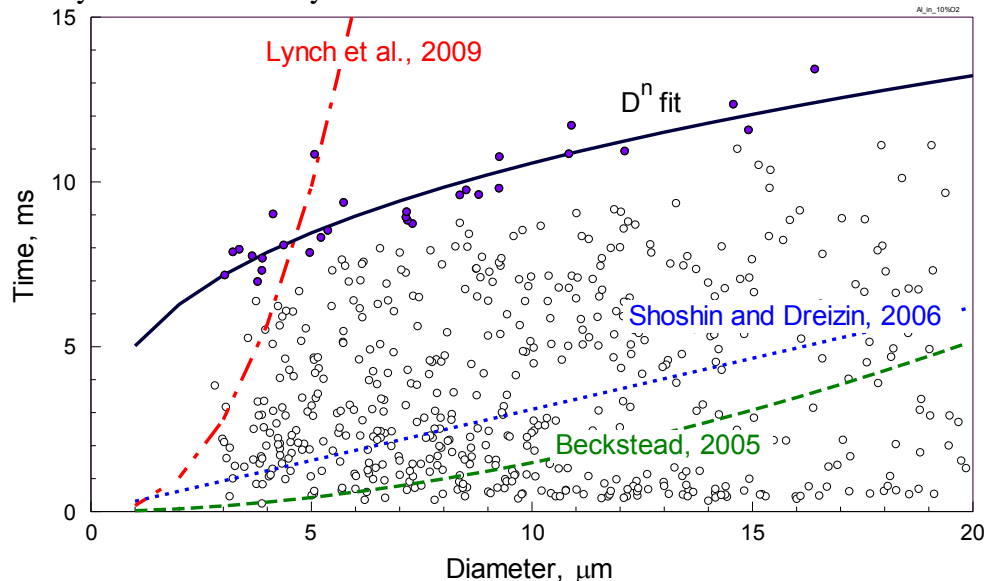


Fig. 8. Particle combustion times as a function of the particle diameters for Al burning in a 10/90 O₂/N₂ mixture. Here and in Figs. 9 – 12, open and closed symbols: experimental points; closed symbols used for the D^n fit shown by solid line ($n=0.32$). Dashed lines show D^n trends reported in the literature (see text).

As already noted from examination of individual emission traces, the burn times are substantially reduced when the concentration of oxygen is increased to 21% as shown in Fig. 9. For this case, Eq. (1) continues to under-predict the particle burn times and Eqs. (2) still predict longer burn times than observed experimentally. It is interesting that Eq. (3) appears to work rather well and for the set of data available the predicted trend nearly coincides with the directly calculated best match line.

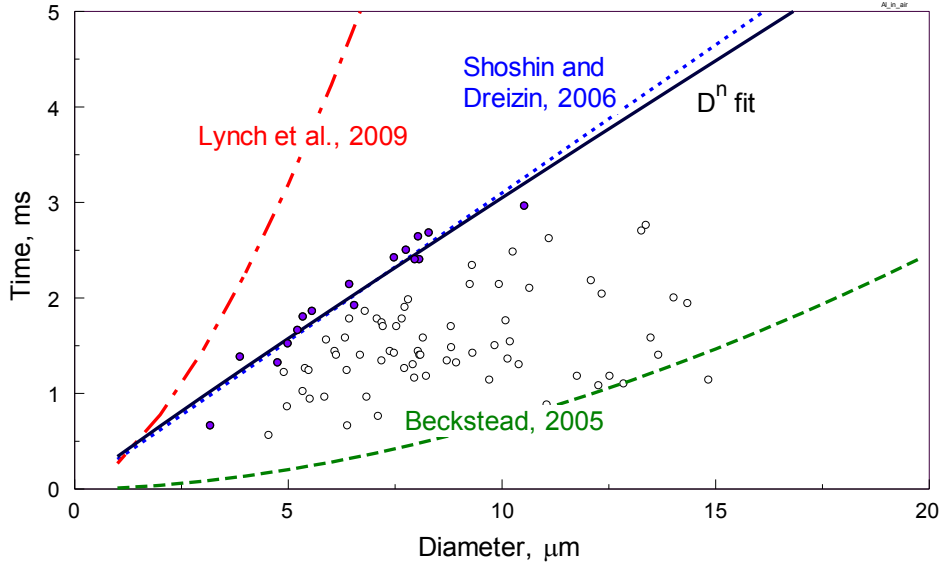


Fig. 9. Particle combustion times as a function of the particle diameters for Al burning in a 21/79 O₂/N₂ mixture (air). D^n fit is shown by a solid line ($n=0.95$).

The results for the 40% oxygen mixtures are shown in Fig. 10. It is interesting that despite substantially increased oxygen concentration, the burn times do not decrease noticeably compared to the 21% oxygen case. Calculations by both Eqs. (1) and (2) for this case predict shorter burn times than observed experimentally. Calculation by Eq. (3) somewhat over-predicts the observed burn times and the curve directly matching the experimental data is described by a $D^{0.57}$ trendline.

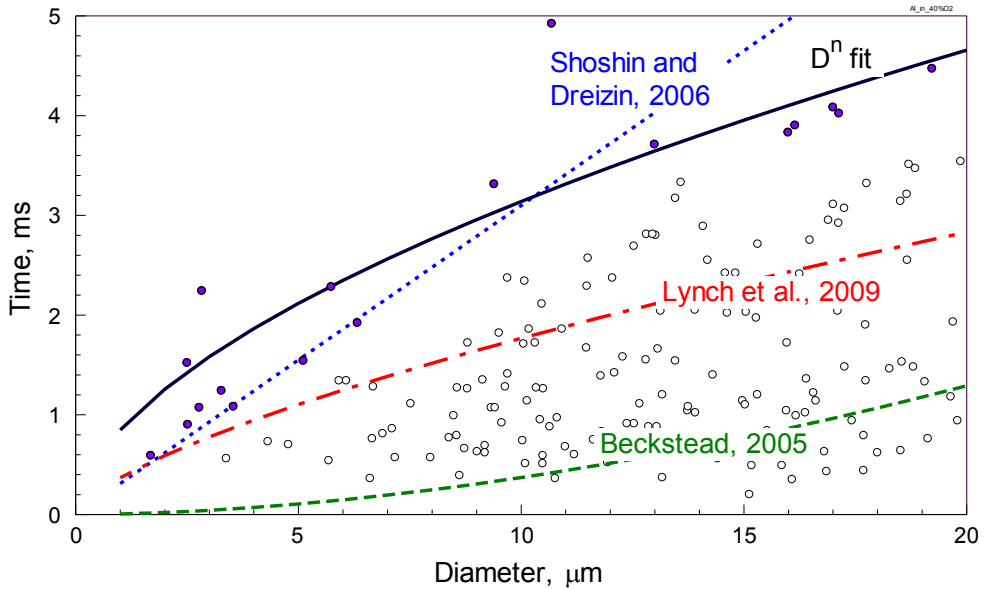


Fig. 10. Particle combustion times as a function of the particle diameters for Al burning in a 40/60 O₂/N₂ mixture. D^n fit is shown by a solid line ($n=0.57$).

Burn times for aluminum particles in 73% CO₂ mixture are shown in Fig. 11 and are quite long, despite a very high concentration of the oxidizing gas. All reported trends, Eqs. 1 – 3, substantially under-predict the combustion times as compared to the current

measurements. The experiments are described by a trendline similar to that used to describe the data for the 10% O₂ mixture.

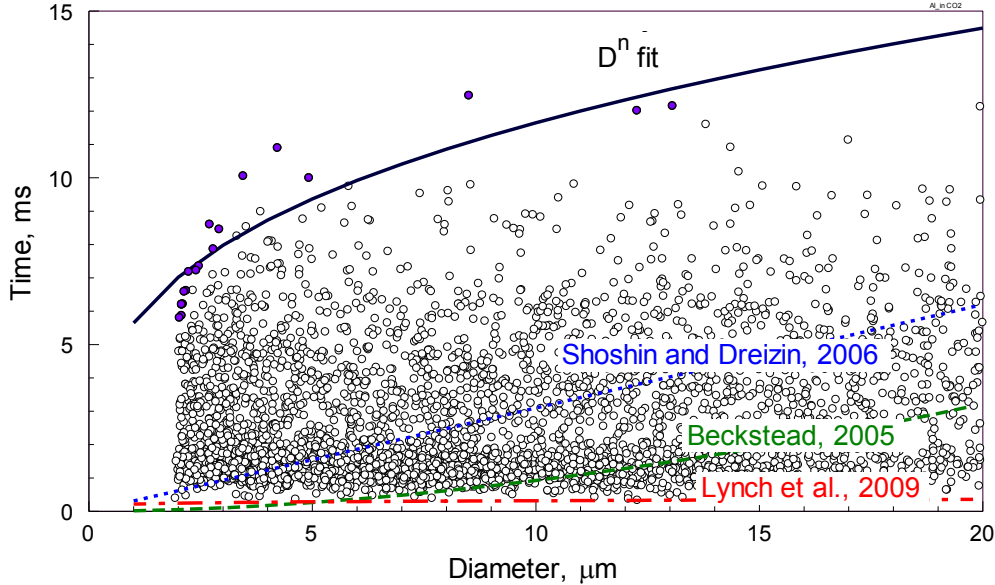


Fig. 11. Particle combustion times as a function of the particle diameters for Al burning in a 73/27 CO₂/N₂ mixture. D^n fit is shown by a solid line ($n=0.32$).

Finally, for aluminum combustion in 77% of H₂O vapor, the burn times are somewhat shorter than for CO₂, but longer than in oxygen. Once again, all reported trends significantly underestimate the combustion times.

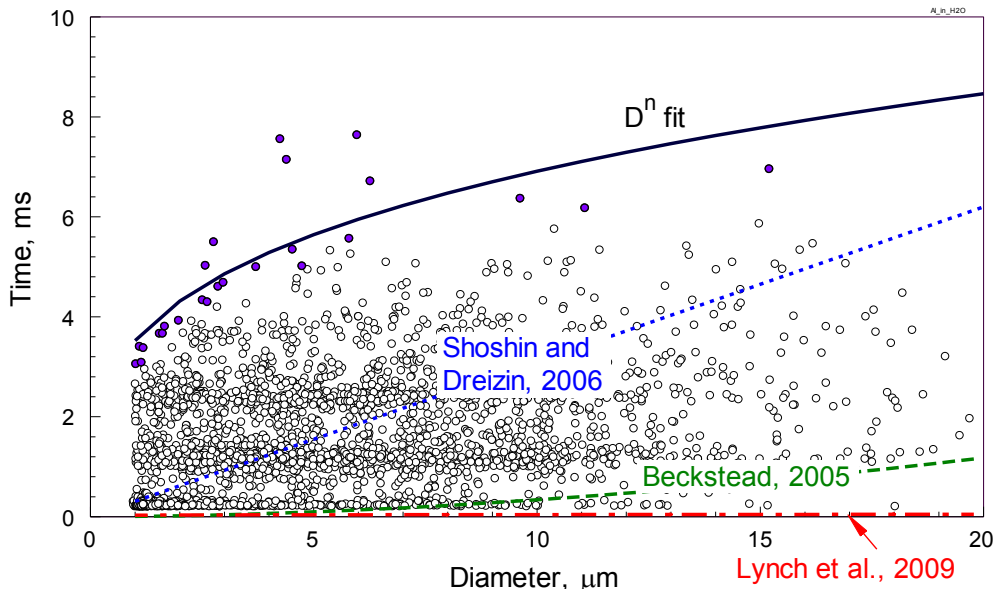


Fig. 12. Particle combustion times as a function of the particle diameters for Al burning in a 77/23 H₂O/N₂ mixture. D^n fit is shown by a solid line ($n=0.29$).

Table 3 gives the exponents and pre-exponents for all the power law fitting functions used for these experiments. It is interesting that in no case an exponent greater than 1 is

observed. At the same time, very small exponents, around 0.3, are observed for three cases: H₂O, CO₂ and 10% O₂ environments.

Discussion

This work presents, for the first time, detailed emission traces produced by individual burning aluminum particles in the size range of 3 – 20 μm . Previously, similar traces were reported for much larger particles burning in air and other environments, e.g., [12 – 14]. Previous work established that multiple peaks and oscillatory emission patterns produced by burning aluminum particles are associated with non-uniformities in the particle composition developed during combustion. Specifically, pure Al particles become saturated with the dissolved combustion products (e.g., oxidized Al species, nitrogen oxides, and more complex compounds formed in presence of CO₂ and other oxidizers) which results in separation of molten aluminum into two or more liquid solutions [12 – 14, 24]. Each solution component evaporates at a different rate resulting in an asymmetric flame and associated oscillatory emission pattern. Furthermore, continuing oxidation results in the formation of oxide caps producing yet another oscillatory emission pattern, typically observed by the end of combustion. The described above processes were identified from comparisons between the particle emission profiles and morphologies and compositions of aluminum particles rapidly quenched at different stages of their combustion [14, 24]. Such quenching experiments and analyses of the particle morphologies are extremely difficult for finer aluminum particles commonly used in practical applications. However, current results suggest that the emission profiles for finer Al particles are qualitatively identical to those observed earlier for greater size particles, suggesting that the same combustion processes occur and determine the rate of metal consumption and associated heat release. Specifically, current observations of oscillatory emission patterns occurring in a sequence similar to that reported earlier for coarse Al particles, suggest that heterogeneous processes play a substantial role in Al combustion even in environments comprising 40 % O₂.

The particle emission profiles measured in experiments performed with H₂O as an oxidizer are qualitatively different from those recorded in other environments. A very low and relatively steady level of emission suggests that the vapor phase flame is very weak or non-existent, while the particle continues to react exothermically, remaining weakly incandescent. This emission behavior suggests a surface reaction, suggesting that Al combustion in H₂O is primarily heterogeneous. Interestingly, recent estimates presented in Ref. [25] indicated that a relatively low heat release for aluminum oxidation by water is insufficient for maintaining a standoff vapor-phase flame for micron-sized particles burning in room temperature environment, as in the present experiments. Thus, present observations indicative of the surface combustion for aluminum particles in H₂O are consistent with the predictions of ref. [25].

Reviewing measured particle burn times as compared to the predictions of Eqs. (1 – 3), it becomes clear that none of the currently reported trends are suitable for practically useful and reasonably accurate prediction. In particular, the discrepancies are greatest when the experimental conditions are different from those used to establish the specific trend. In that sense, the best match fits found in this work and summarized in Table 3 are as

limited as any other proposed trends. As with other trends, they are only suitable for calculation of the particle burn times for experimental conditions similar to those used to find the respective relations.

More specifically, it is suggested that Eq. (1) based on Beckstead's analysis of multiple experimental results is heavily biased to experiments with much larger particles. Thus, estimating burn times for finer particle sizes is challenging, and, as observed here, results in substantial errors. Eqs. (2) are based on experiments performed at relatively high pressures and temperatures. It is also worth noting that Eqs. (2) are based on the measurement of the emission peak produced by a group of burning particles, so that the peak duration is dominated by larger particle sizes, even if the number of smaller particles is significant. Alternatively, only smaller particles could have ignited in selected shock tube experiments resulting in very short combustion peaks, whereas larger particle present in the system may not have ignited. Corrections for such effects and for the effect of high environment temperature are difficult, and without such corrections Eqs. (2) do not predict combustion times accurately. Finally, Eq. (3) is very simplistic and does not account for oxidizer concentration, type, or any other experimental condition. In fact it is somewhat surprising how well it described the current experimental data for mixtures with 21% O₂, for which it was initially proposed. Because Eq. (3) was obtained based on aerosol combustion experiments, it is suggested that the particle interaction effects in Al aerosol combustion are relatively weak so that the particle burn rates for single particles and particles burning in an aerosol effectively coincide with each other. Alternately, the particle number density could have been below the levels where such effects would be measureable.

Finally, to comment on the specific burn times measured in this work for different environments, it is interesting to compare these times to one another. To streamline such a comparison, all "best fit" trendlines are plotted together in Fig. 13. A small difference between the burn times measured for Al in 21% and 40% O₂ mixtures is remarkable and indicative that in these environments, the aluminum combustion may be relatively well described by a heat transfer limited droplet combustion model with a stand-off flame [26], where the rate of combustion is determined by the transfer number B , which is not affected by the oxidizer concentration and is defined as:

$$B = \frac{\Delta h_c / \nu + C_p (T - T_{boil})}{L} \quad (4)$$

where Δh is the heat of oxidation, L is the latent heat of evaporation, C_p is specific heat, ν is the stoichiometric coefficient, and T and T_{boil} are the temperatures of the hot environment (assumed here to be equal to the flame temperature) and particle surface, respectively. It is somewhat unexpected that a bit longer burn times are anticipated for the particles less than 10 μm at 40% O₂ as compared to 21% O₂. This effect may simply represent an experimental uncertainty. It is also possible that the dimensions of extinguished particles are reduced at greater oxygen concentrations, resulting in somewhat longer overall reaction times. Additional measurements and, possibly, analyses of the combustion products would be needed to address this issue in the future.

Table 3. Fitting coefficients for particle diameter power law: fitting eqn.: $\tau_{burn} = a \cdot D^n$.

Gas environment (remainder N ₂)	<i>a</i>	<i>n</i>	Correlation Coefficient, r ²
10% Oxygen	5.03	0.32	0.82
21% Oxygen (Air)	0.34	0.95	0.93
40% Oxygen	0.85	0.57	0.81
73% Carbon Dioxide	5.65	0.32	0.86
77% Water Vapor	3.52	0.29	0.68

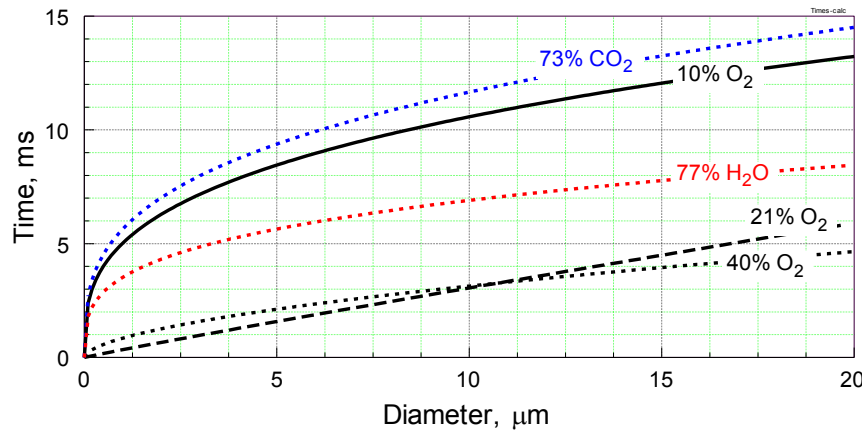


Fig. 13. Calculated burn times based on the best matches with experimental results presented in Figs. 8 – 12 for aluminum particle combustion in different oxidizing environments.

For reduced oxygen concentration, the combustion times increase substantially, suggesting that a different rate limiting process is at play. Most likely this rate-limiting process is the heterogeneous oxidation occurring on the particle surface. The overall emission level also decreased suggesting a reduction in the size of the vapor phase flame and an increasing contribution from surface reaction processes.

For CO₂ and H₂O environments, the role of surface processes is expected to be substantial for micron-sized particles, based on the heat balance estimates presented in ref. [25]. Respectively, long particle combustion times are measured despite high oxidizer concentrations in both cases. The significance of surface processes is particularly pronounced for combustion in H₂O as discussed above. Therefore, aluminum combustion models taking such processes into account need to be developed and validated by comparisons with the current and future experiments. It is interesting that the exponent close to 0.3 was found to describe the observed trends for all cases when heterogeneous reactions deem to be important. While this value of exponent indicates a very weak effect of particle size on the burn time, it can also indicate that particles of different dimensions combust in different regimes. Specifically, heterogeneous reactions, which occur at lower temperatures and generally lower rates, prevail for smaller particles, resulting in extended burn times. As the particle size increases, vapor phase reactions play an increasingly greater role, resulting in a faster burn and thus shorter burn times. Note that results summarized in Fig. 13 describe experiments performed at atmospheric pressure. In many practical systems involving

metal combustion the pressures are elevated, so that the particle dimensions for which the vapor phase reactions are important will be smaller than in this work. It is anticipated that descriptive models of metal combustion dynamics can be developed and validated based on measurements similar to those presented in this paper. These combustion dynamics should be incorporated into the models so that the effects of pressure and environment composition could be predicted with reasonable accuracy.

Conclusions

A new experimental setup enables measurements of optical emission signatures and combustion times for individually sized metal particles with diameters between 3 and 20 μm . The measurements can be carried out in various oxidizing environments, including oxygen, carbon dioxide, and water mixed with nitrogen or other inert diluent. Extending the set of environments using mixed oxidizers and, possibly, elevated pressure, are possible avenues of future work.

Optical signatures of individual micron-sized aluminum particles burning in different environments show characteristic oscillatory patterns previously observed for much larger particles. Such optical signatures highlight the importance of the heterogeneous processes in aluminum combustion. Heterogeneous reactions result in variation of surface properties of the burning droplets, which, in turn, cause formation of asymmetric flames and repeatable changes in particle emission intensities. For aluminum burning in water vapor, the optical signature of the particle is substantially weaker than in other environments, possibly indicating a primarily surface oxidation.

Results presented in this paper show that the current simplified D^n correlations for aluminum combustion time reported in the literature cannot be usefully applied for the conditions beyond the narrow ranges, for which such correlations were developed initially. It is observed that for oxygenated environments with oxygen concentrations in excess of 21%, the effect of oxygen concentration on combustion time of micron-sized aluminum particles is weak. However, combustion times increase substantially for lower oxygen concentrations. Aluminum particle combustion times are generally longer than predicted for experiments with water and carbon dioxide oxidizers. For all environments, the observed effect of particle size is relatively weak and the exponents in the descriptive D^n relations appropriate for the current experiments vary approximately from 0.3 to 1. An exponent close to 0.3 describes well the burn-times for aluminum in oxidizing environments for which heterogeneous reactions appear to dominate.

References

1. E. Price, R.K. Sigman, in: Progress in Astronautics and Aeronautics (2000), Combustion of Aluminized Solid Propellants, Georgia Inst. Technol., Atlanta, GA, 2000, pp. 663–687.
2. B. Palaszewski, L.S. Ianovski, P. Carrick, J. Prop. Power, 14 (1998) 641-648.
3. R. H. W. Waesche, J. Prop. Power, 15 (1999) 919-922.
4. F. Zhang, S.B. Murray, K.B. Gerrard, Shock Waves 15 (2006) 313-324.
5. M.W. Beckstead, Combust. Explos. Shock+ 41 (2005) 533–546.
6. P. Lynch, H. Krier, N. Glumac, Proc. Combust. Inst. 32 (2009) 1887–1893.
7. Y.L. Shoshin, E.L. Dreizin, Combust. Flame 145 (2006) 714–722.
8. Y. Huang, G.A. Risha, V. Yang, R.A. Yetter, Combust. Flame 156 (2009) 5-13.
9. P. Bucher, R.A. Yetter, F.L. Dryer, E.P. Vicenzi, T.P. Parr, D.M. Hanson-Parr Combust. Flame 117 (1999) 351-361.
10. M. Marion, C. Chauveau, I. Gökalp Combust. Sci. Technol. 115 (1996) 369 – 390
11. S.E. Olsen, M.W. Beckstead, J. Prop. Power 12 (1996) 662-671.
12. E.L. Dreizin, Combust. Flame 117 (1999) 841-850.
13. E.L. Dreizin, Combust. Flame, 116 (1999) 323-333.
14. E.L. Dreizin, Combust. Flame, 105 (1996) 541-556.
15. Y. Huang, G.A. Risha, V. Yang, R.A. Yetter, Proc. Combust. Inst. 31 II (2007) 2001-2009.
16. N.I. Poletaev, A.V. Florko, Combust. Explos. Shock+ 44 (2008) 437-443.
17. S. Goroshin, M. Kolbe, J.H.S. Lee, Proc. Combust. Inst. 28 (2000) 2811-2817.
18. S. Goroshin, J. Mamen, A. Higgins, T. Bazyn, N. Glumac, H. Krier, Proc. Combust. Inst. 31 II (2007) 2011-2019.
19. Y. Shoshin, E. Dreizin, Combust. Flame, 133 (2003) 275-287.
20. S. Rossi, E.L. Dreizin, C.K. Law, Combust. Sci. Technol. 164 (2001) 209 – 237.
21. J. Servaites, H. Krier, J.C. Melcher, R.L. Burton, Combust. Flame 125 (2001), 1040-1054.
22. R.J. Gill, S. Mohan, E.L. Dreizin Rev. Sci. Instrum. 80 (2009) 064101-1 – 064101-7.
23. S. Mohan, L. Furet, E.L. Dreizin, Combust. Flame (2010), article in press doi:10.1016/j.combustflame.2009.11.010
24. E.L. Dreizin, Prog. Energ. Combust. 26 (2000) 57-78.
25. S. Mohan, M.A. Trunov, E.L. Dreizin, Combust. Flame 156 (2009) 2213-2216.
26. I. Glassman, R.A. Yetter, Combustion. Fourth Edition. Academic Press, Burlington MA, 2008.

CHAPTER 2: COMBUSTION CHARACTERISTICS OF MICRON-SIZED ALUMINUM PARTICLES IN OXYGENATED ENVIRONMENTS

Introduction

Aluminum powder is a widely used fuel additive in solid propellants, explosives, and pyrotechnics [1-3]. Efforts to understand the combustion reactions for aluminum, to describe quantitatively and, ultimately, optimize its combustion dynamics for specific applications have been active for several decades. One parameter of practical interest is the particle burn time, τ_b . Stemming from studies of liquid droplet combustion [4], the semi-phenomenological expression of burn time is typically presented as a power law $\tau_b = a \cdot D_p^n$ with a functional dependence on the particle diameter, D_p . Commonly, the coefficient a and exponent n are determined empirically. Several authors presented expressions for these parameters for different oxidizing environments and external temperatures and pressures [4-8]. All such descriptions effectively reduce particle combustion to a steady state process neglecting changes occurring in the burn rate and corresponding heat release as a function of time.

Most of the experimental data used to develop empirical correlations for particle burn times were based on experiments with aerosolized Al powder clouds or jets [5, 6, 9-12] or with coarse, 100 μm or greater single Al particles [7, 13-15]. For particles less than 20 μm employed in many practical formulations, data on single particle combustion are limited. This size range is particularly interesting because the combustion mode is expected to transition from the gas-phase diffusion limited combustion for coarser particles to the combustion regime limited by the surface reaction kinetics for finer particles [7, 9, 11, 16].

Different mathematical descriptions for aluminum particle combustion processes have been developed recently [3, 16-18]; however, all current models assume combustion to occur steadily, neglecting substantial changes known to occur in the reaction mechanisms while the particle is burning out [15]. Comparisons between predictions and experiments continue to use overall combustion times, which could be misleading considering the substantial changes that can occur in the aluminum particle burn rate when its size is decreasing and when the size of the growing oxide cap becomes larger.

This study continues an effort presented in ref. [7] aimed at developing an experimental method for direct characterization of combustion behavior of individual, micron-sized metal particles. Initial experiments were limited to finding the total particle burn times as a function of their size, so that results could be compared to existing empirical correlations. In this effort, the diagnostics are extended to include time-resolved optical pyrometry and monitoring molecular AlO emission for burning particles. The data processing is streamlined and results for Al combustion in oxygenated environments with different oxygen concentrations are presented and discussed.

Experimental

Apparatus

Individual metal particles are fed by a gas flow into a CO₂ laser beam where they are ignited. Before particles cross the CO₂ laser beam, they cross a beam of a 785 nm, 30

mW laser and the scattered light pulses are used to measure particle sizes. Particle velocities are measured using an additional modulated laser sheet [8]. Previous publications [7, 8] described the apparatus used for this experiment. In this project, the setup was modified to enable optical temperature measurements, as shown in Fig. 1.

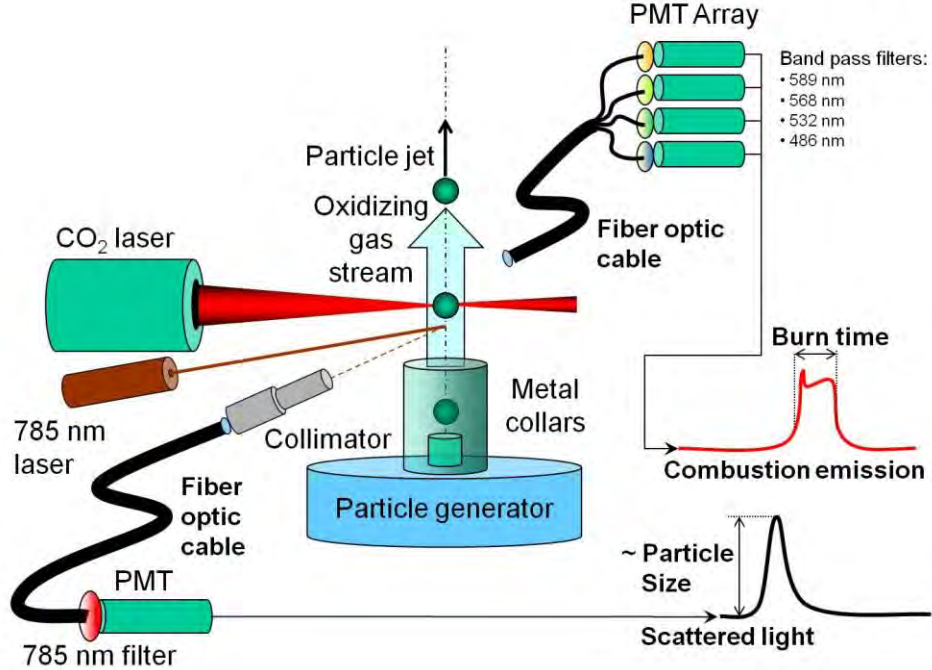


Figure 1. Experimental apparatus and diagnostics to obtain particle size and emission pulse correlation.

Light emitted by ignited particles passes through a quad-furcated fiber optic bundle leading to an array of four photomultiplier tubes (PMT, Hamamatsu H3164-10), each equipped with an interference filter. A 486 nm filter is used to detect AlO molecular emission. 532, 568, and 589 nm filters are used for optical pyrometry.

Each of the four PMTs were calibrated using a current-stabilized tungsten lamp and an irradiance calibrated spectrometer (StellarNet EPP2000). The spectrometer manufacturer provided the calibration of the CCD array, with a quartz fiber optic and a cosine filter installed. For PMT calibration, a spectrum of the current-stabilized tungsten lamp was measured. Therefore, the true lamp emission intensity for each wavelength was obtained without the need to know the emissivity of the ribbon. Then, the spectrometer fiber optic cable was replaced with that transmitting light to the filtered PMT's, so that the location of the inlet window facing the lamp did not change. The signal measured by each of the filtered PMT was then related to the respective true light intensities, so that the sensitivity factor for each PMT was obtained. The fiber optic transmission curve was not used assuming it be the identical for each fiber bundle of the quad-furcated cable. For temperature measurements, measured light intensity ratios were used and the emitters were assumed to be gray bodies. This assumption is expected to work well for the closely spaced wavelengths selected for pyrometry in this project.

For extended calibration, the tungsten lamp was operated at a few fixed current levels so that gain curves for each filtered PMT were obtained. The PMT gain curves were obtained measuring the variation of the PMT signal as a function of the applied PMT voltage at a fixed irradiance. To cross-check the accuracy of the gain functions, a set of neutral density filters was used to measure the response of each PMT under a wide range

of light intensities (>3 decades). The gain curves accurately predicted (to within a few percent) the PMT output voltages. This calibration allowed us to measure the aluminum emission over a wide dynamic range of light intensities.

Spherical aluminum powder used in this project was by from Alfa Aesar, nominal size 10 – 14 μm . The powder is fed into the laser beam using an electro-static aerosol generator [6, 8]. Experiments are conducted at 1 atm in three different room-temperature O_2/N_2 gas flows with oxygen concentrations of 10, 15 and 21 % (Air).

Data Processing

The first processing step is to compare the powder particle size distribution measured by a commercial device based on the low-angle laser light scattering, Beckman-Coulter LS230, with that implied from the amplitudes of the scattered 785 nm light pulses measured in this experiment. The best match between the two size distributions is obtained by varying a single scaling factor of the scattered light peak heights. An adjustment in the scaling factor is required for each powder, which can be explained by differences in the particle shapes and surface morphologies affecting the intensity of the scattered light. The comparison between the two size distributions for the Al powder used in this project is shown in Fig. 2. The match is imperfect but salient features of the powder size distributions are represented well.

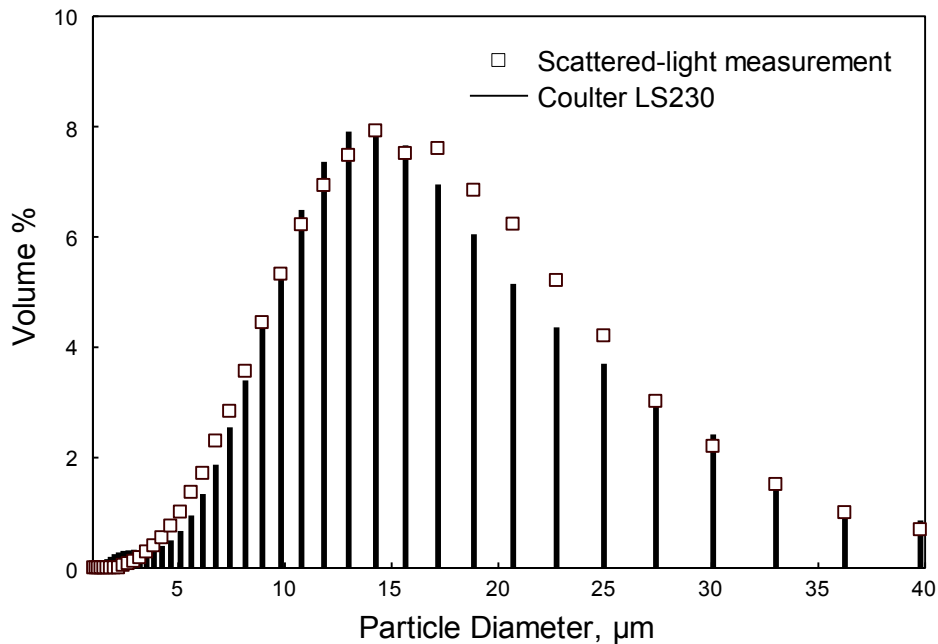


Figure 2. Particle size distribution measured in the commercial device (Coulter LS230) and the scattered-light measurement for aluminum.

The second processing step is to correlate the two measured pulse sequences: a sequence of scattered light pulses and a sequence of pulses produced by heated and ignited incandescent particles. For each particle, the scattered light pulse and its emission pulse are separated by the period required for the particle to travel between the two laser beams. This time is known approximately based on the measured particle velocities. For different particles, this time can vary in a certain range, depending on the individual particle velocities. In the signal processing procedure, the time shift between the two measured pulse sequences is varied to achieve the maximum number of matches between

pulses. The time shift must be close to that anticipated from the measured particle velocities. The pairs of pulses shifted relative to each other with that time shift (within a selected narrow time window accounting for the variation in individual particle velocities) are identified for further processing and are assumed to represent individual particles.

In the next processing step, pairs of pulses that overlap in time or immediately follow one another, and thus could represent interacting particles, are removed from further processing.

For each particle, its size is correlated with the measured emission time and combustion temperatures are determined. As described in detail elsewhere [7], only the longest emission times measured for each range of particle sizes are representative of burn times of interest. Shorter emission light pulses are produced by particles that are heated but not ignited in the laser beam and by particles that ignite well before exiting the laser beam. In the latter case, a portion of particle combustion occurred within the laser beam and thus the reaction was assisted by laser heating. The longest emission pulses are produced by particles that ignite just before exiting from the laser beam, so that their combustion is not affected by additional laser heating. Previously, the longest emission pulses were selected manually, which could have resulted in a somewhat subjective choice [7, 8]. In this project, the longest emission times are selected following a consistent procedure. First, the range of particle sizes for which the measured emission times were available was broken down into 4 size bins. For each particle size bin, cumulative distributions for measured emission times are plotted. Only the particles for which the emission times are in the top several percent for that bin are finally selected for further processing. In these experiments, the particles with burn times in the range of 97.5 - 100 % were selected. For these selected particles, burn times as a function of their size are found, particle combustion temperatures are calculated, and AlO emission traces are extracted from the sets of emission traces.

Results

A representative photograph of burning aluminum particle streaks in air is shown in Fig. 3. The flow settings are selected so that the measured average particle velocities are close to 0.5 m/s. Multiple short streaks are observed, likely produced by particles that are heated but not ignited or heated and partially burnt in the laser beam and were discounted from the data processing. Some of the long streaks correspond to particles moving in random directions after exiting the laser beam. Those particles are likely ignited and partially burned in the laser beam; they also should not be included in the data processing. Finally, the longest streaks with initially vertical particle velocities are likely to represent particles ignited when exiting from the CO₂ laser beam; these particles are included into the present analysis. Initial portions of the trajectories for the particles are straight and bright followed by weaker streaks with sharp changes in the particle direction.

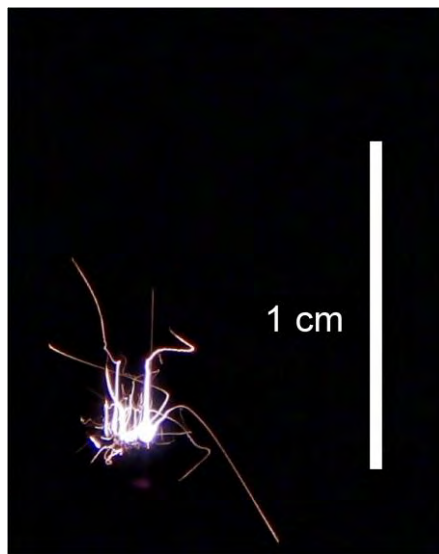


Figure 3. Photograph of burning aluminum particle streaks in air.

Selection of particles with the longest measured emission times representing meaningful burn times, not assisted by laser heating, is illustrated in Fig. 4 for an experiment with Al particles burning in air. For this specific example, the entire range of particle sizes, for which matching pairs of emission and light scattering pulses were identified, was 2 – 30 µm. This range was divided into four bins, 2 – 6, 6 – 10, 10 – 14, and 14 – 30 µm. For each size bin, normalized cumulative distributions of the particle emission durations were obtained, these distributions are shown in Fig. 4.

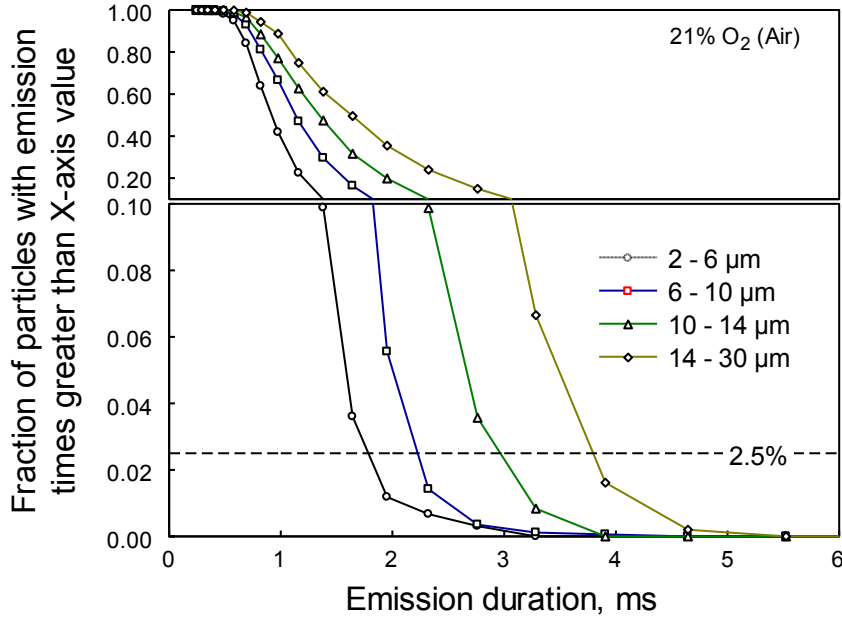


Figure 4. Normalized cumulative distributions of emission durations for Al particles burning in air.

As the distributions show, no particles emitted light longer than 6 ms and almost no emission pulses were shorter than 1 ms. For clarity, the vertical scale in Fig. 4 is expanded for the fractions less than 0.1, i.e., for the particles with the emission durations in the top 10 %. As expected, particles with larger sizes generally exhibit longer emission durations. The cutoff of 2.5 % was selected, somewhat arbitrarily, as shown by the horizontal dashed line in Fig. 4, so that the cumulative distributions are meaningfully separated from one another while a reasonable numbers of particles are available in each size bin. Greater cutoff thresholds lead to shorter inferred burn times for the same particle sizes; for example an increase in the threshold up to 10 % for a typical data set results in an almost 20% reduction in the emission time for a specified particle size range. However, the effect of particle size on the emission time remains essentially unchanged.

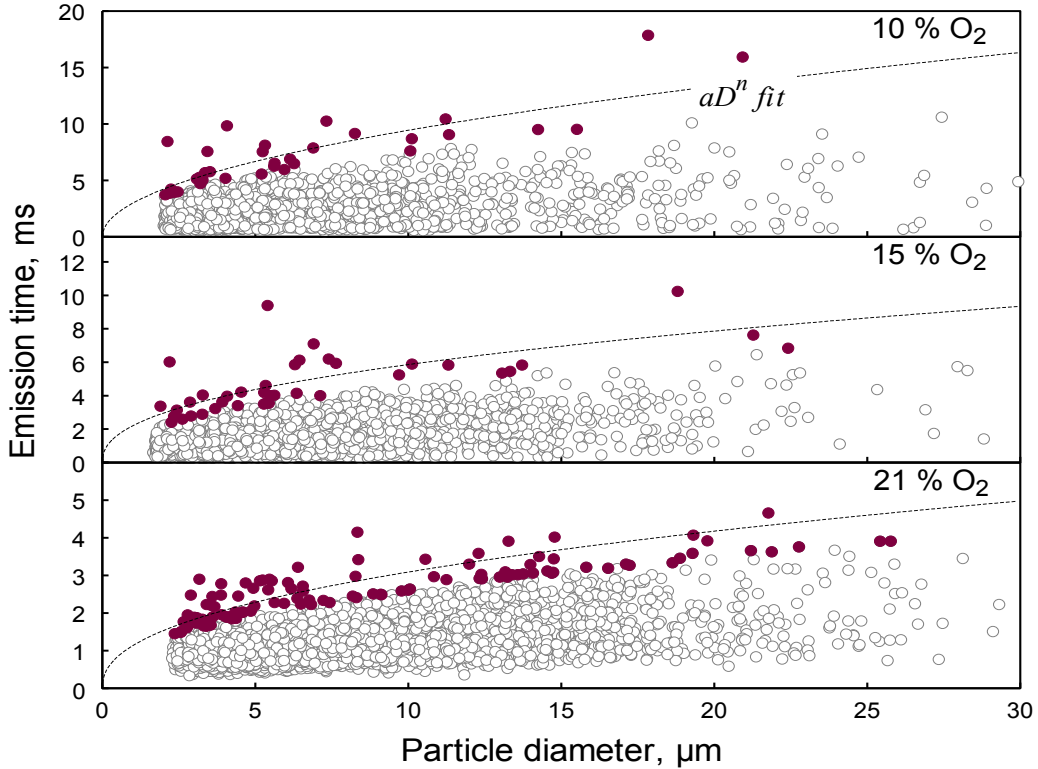


Figure 5. Burn times as a function of particle size for aluminum particles ignited in different O₂/N₂ gas mixtures.

Scatter plots shown in Fig. 5 present the matching pairs of the emission and light scattered pulses, identified as described above, for aluminum powder in three environments with different oxygen concentrations. No data points are available for particles less than 2 μm as the light scattered pulses were comparable to the signal noise. Filled symbols in Fig. 5 represent the subsets of all data points with emission times within the top 2.5 %, identified as illustrated in Fig. 4. These are the points used to determine the effect of particle size on its burn time and to analyze the particle combustion temperatures and AlO emission signatures.

Following earlier work, a trend for the burn time as a function of the particle size was obtained for each environment in the form of $\tau_b=a\cdot D^n$. The parameters a and n corresponding to the best fit for each environment are shown in Table 1. The fitting curves are also shown in Fig. 5. The exponent values in the range of 0.4 – 0.5 for pure aluminum are consistent with empirical exponents reported in some of the earlier work [11]. Note that the D^n fits presented here do not coincide with those reported in our previous paper [8] in which the same experimental setup was used. While the trends suggested based on the previously reported data sets [7] describe the present data reasonably well, the present experimental data sets are more extensive and thus offer a somewhat better assessment of the D^n trend valid in the range of particle sizes of 2 – 20 μm. Most importantly, it should be emphasized that all such descriptions imply a steady particle burn rate and effectively neglect any changes in the particle combustion regime. Thus, the significance of any D^n type trends is very limited and using such trends to describe particle combustion in practical systems is not recommended.

Table 1. Empirically-based parameters for the $\tau_b=aD^n$ fit show in Fig. 5 for the aluminum particle burn times measured in different environments

	% O ₂	a	n	Correlation, r^2
Aluminum	10	2.99	0.5	0.62
	15	2.21	0.42	0.49
	21	1.29	0.35	0.76

Figure 6 shows individual emission traces and temperature profiles for three aluminum particles burning in different O₂/N₂ gas mixtures. All three particles were selected with approximately 6 μm diameter, so the differences in the emission durations between the traces in Fig. 6 represent the effect of the oxidizing environment. The temperatures shown were calculated from the ratio of PMT signals acquired through 589 nm and 532 nm filters. This ratio was more sensitive to changes in the burning particle temperature and yielded more reliable temperature reading than the others, using the signal filtered at 568 nm.

Emission traces are qualitatively similar to those presented earlier [7]. An initial peak is followed by a decay, a plateau, which is poorly distinguished in some traces, and final intensity decay. Characteristic oscillatory patterns are observed, most clearly for the experiments in the gas mixture with 10 % O₂.

Strong temperature oscillations at the beginning and the end of each trace do not represent true temperatures and are caused by the reduced amplitude of the emission signals, so that their ratios vary dramatically. For all temperature traces, the temperature continues to increase even after the emission traces pass over their peak values. Following this initial increase, the temperature is stabilized and then slowly decreased at longer burn times for all particles. For the particle burning in air, the maximum instantaneous temperature is close to 3200 K. As the particle is burning out, its temperature drops to and remains at about 2400 K. For the particles burning at reduced oxygen concentrations, the temperatures are respectively lower. The changes in the temperature during the burn time are also less pronounced than in air.

For each particle, the highest characteristic combustion temperature was determined. This temperature was found as an average of the temperatures measured after the emission signal peaked and until the emission signal value was above one half of its peak amplitude. To illustrate this averaging routine, horizontal dashed lines in Fig. 6 cross the emission traces at the levels corresponding to one half of their peak values. The portions of the temperature traces used to obtain the averaged values are shown bold and are further highlighted by shaded panels.

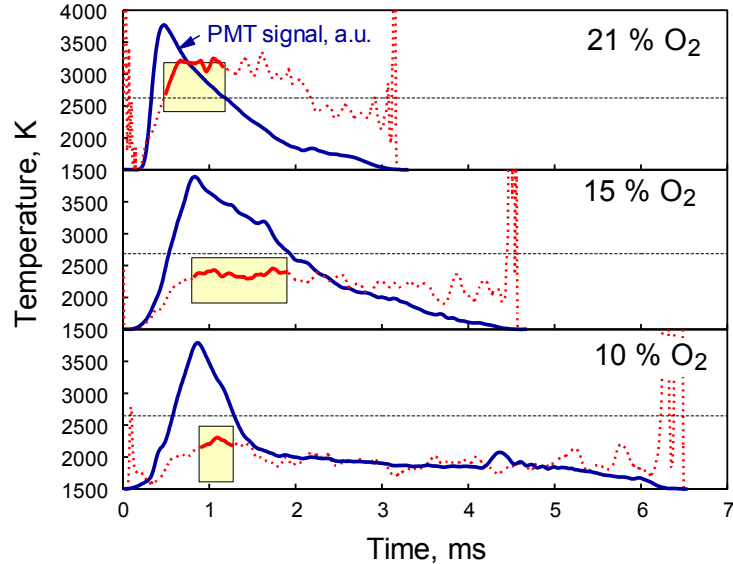


Figure 6. Emission traces measured through a 568 nm filter and temperature traces obtained from the emission intensity ratio measured at 589 and 532 nm. All results are for approximately 6 μm aluminum particles. See text for further details.

The characteristic particle temperatures obtained as described above are plotted as a function of the particle size in Fig. 7. These data represent experimental points shown as filled circles in Fig. 5. Two different approaches were used to obtain curve fits for the characteristic flame temperatures. In one approach, the data were fitted by a straight line. These fits are shown as solid lines for each gas composition in Fig. 7.

In another approach, it was assumed that the flame temperature is independent of the particle size for all particles burning in a diffusion-limited regime. Because this combustion regime is anticipated for large particles, the experimental data were described by a horizontal line for particles greater than some selected diameter, D_p^* . This selected diameter represents the smallest particle diameter, for which a diffusion-limited combustion regime is observed. For particles smaller than D_p^* , the data were described by another straight line, that had an adjustable slope representing an increase in flame temperature as a function of the particle size. Intercepts and slopes of both lines as well as the value of D_p^* , corresponding to the horizontal coordinate of their cross-section point, were treated as adjustable parameters. These lines are shown as dotted lines in Fig. 7

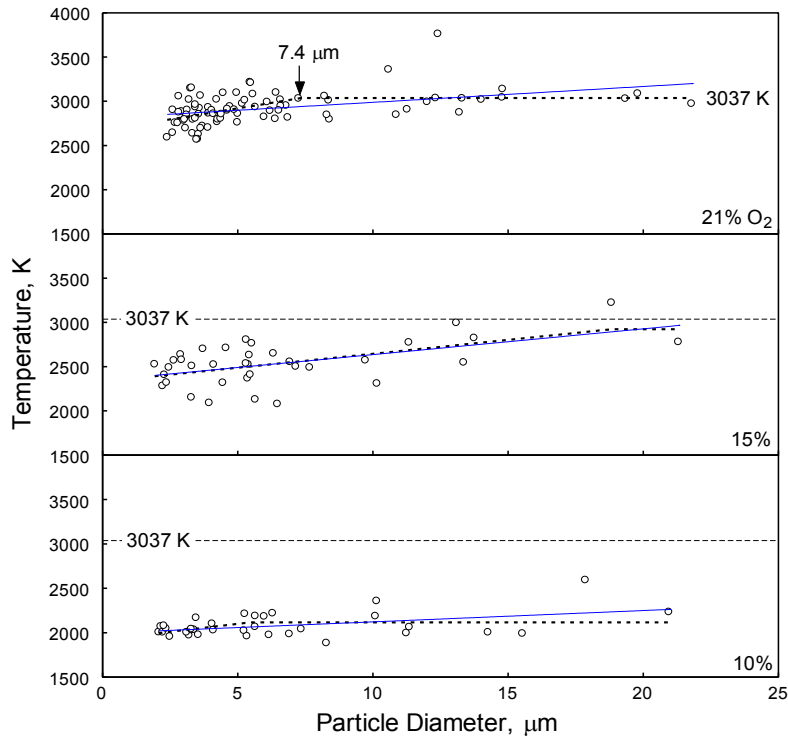


Figure 7. Average temperature distribution for Al in different atmospheres

The goodness of fits was assessed using calculated sums of squared deviations shown in Table 2.

Table 2. Sums of squared deviations for one-line and two-line fits for the temperature vs. particle size data shown in Fig. 7.

% O ₂	Sum of squared deviations	
	One line fit;	Two-line fit
10	0.45	0.32
15	0.55	0.56
21	0.42	0.47

For particles burning in air, the straight line fit is overshooting the experimental points for large particle sizes. The two-line fit describes the data rather well (and better than the single line fit, as shown in Fig. 7 and confirmed by calculated sums of squared deviations shown in Table 2). The sloped and horizontal lines cross each other at the particle size $D_p^* \approx 7.4 \mu\text{m}$. This implies that particles greater than this size burn in a gas diffusion-limited regime. For smaller aluminum particles, the temperature decreases indicating that the stand-off flame approaches the particle surface and surface reactions occurring at lower temperatures play an increasingly greater role in aluminum combustion. The steady temperature corresponding to the gas diffusion-limited combustion is 3037 K. This temperature level is also shown by dashed lines for the plots corresponding to the lower oxygen concentrations.

In agreement with the observations made for individual temperature traces shown in Fig. 6, the averaged temperatures are substantially reduced for experiments at 15 and 10 % of O₂. For the case of 15 % O₂, the single line fit effectively coincides with the two-line fit. For the two-line fit, the sloped and horizontal lines are predicted to cross at

$D_p \approx 19 \mu\text{m}$. Therefore, a slow increase in the combustion temperature occurs as a function of the particle size practically for the entire range of particle sizes considered. The temperature almost reaches the 3037 K level as the particle size increases to 20 μm . Therefore, it can be concluded that in the O₂/N₂ mixtures with 15 % of O₂, diffusion-limited combustion regime is expected for particles greater than 20 μm .

For aluminum particles burning in the gas mixture with 10 % of O₂, the temperature is fairly constant for all particle sizes considered. It is relatively low, close to 1994 K, which is likely an indication of the surface-controlled combustion.

Finally, it is interesting to assess intensity of the molecular AlO emission produced by aluminum particles burning in different environments. AlO emission is a commonly used indicator of the vapor-phase combustion processes and is known to be prominent in the spectra produced by Al flames. A PMT signal filtered at 486 nm was used to track the AlO emission in this work. To provide a quantitative measure of the AlO emission intensity that can be applied to different particles and environments, the emission measured at 486 nm, was related to that measured at 568 nm (outside of the main AlO peaks). Further, to remove the effect of particle temperature on the tracked intensity ratio, it was divided by the ratio of the calculated emission intensities $I_{486\text{nm}}/I_{568\text{nm}}$ for the black body emitter at the same temperature as the instant temperature of the burning

particle. In a confirmatory experiment, this ratio, $\frac{\left(I_{486\text{nm}}/I_{568\text{nm}} \right)_{\text{exp}}}{\left(I_{486\text{nm}}/I_{568\text{nm}} \right)_{\text{bb}}}$ was determined for a tungsten lamp and was found to be equal to one. Thus, when this ratio is greater than one, it would imply a non-negligible AlO emission.

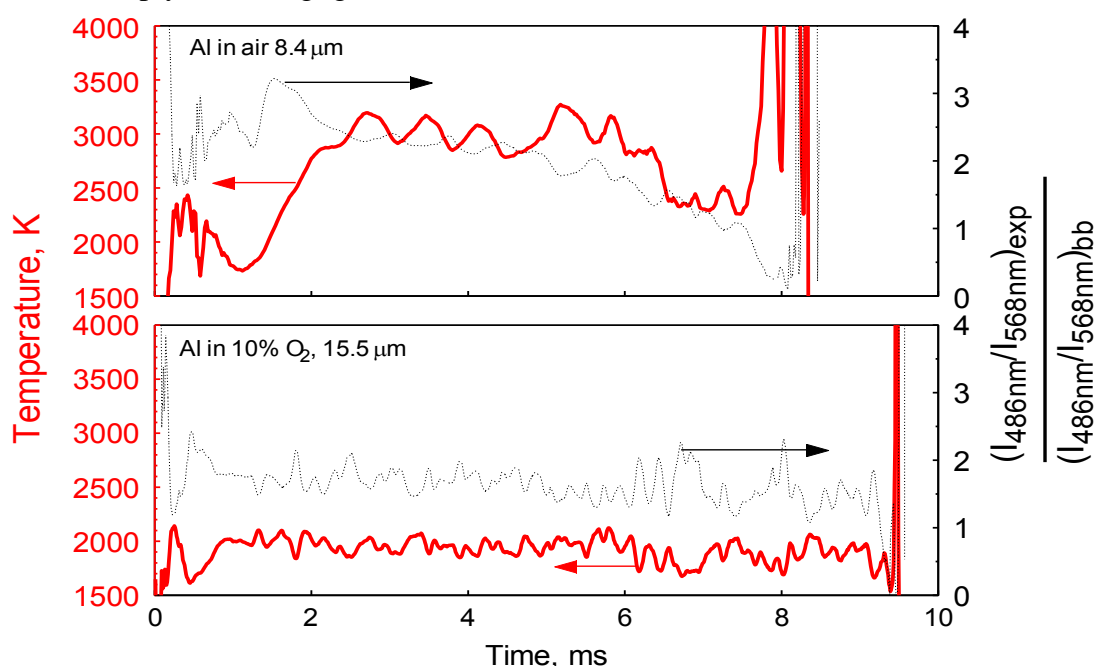


Figure 8. Traces showing particle temperatures (solid lines) and intensity ratios (dotted lines) characterizing the molecular emission of AlO for particles burning in different environments.

Characteristic intensity ratios as a function of time for the particles burning in environments with 21 and 10% of O₂ are shown as dotted lines in Fig. 8. Respective temperature traces are also shown for each particle.

For the particle burning in 21 % O₂, the AlO emission is very strong at short burn times. Interestingly, for the specific trace shown in Fig. 8 as well as for all other examined traces, the AlO emission is peaking before the maximum in the combustion temperature is reached. When the temperature reaches its steady level just above 3000 K, the AlO emission is already reduced compared to its peak value and remains relatively steady. A noticeable decrease in the AlO emission begins somewhat before the decrease in the particle temperature. The characteristic correlation between temperature and AlO emission traces described above for particles burning in air are less noticeable for particles burning at lower oxygen concentrations, for which the changes in both temperature and AlO emission as a function of time are less pronounced. However, in all cases, the maximum AlO emission is attained prior to the peak temperature. It is also worth noting that, as shown in Fig 8, even at the lowest oxygen concentration, the $\frac{\left(\frac{I_{486nm}}{I_{568nm}}\right)_{exp}}{\left(\frac{I_{486nm}}{I_{568nm}}\right)_{bb}}$ ratio is noticeably greater than 1, indicating a non-negligible presence of vapor-phase AlO.

Discussion

It is interesting to interpret changes observed in the optical signatures of the micron-sized Al particles burning in air presented in Figs. 6 and 8 in the context of the reported earlier combustion scenario for large Al particles [15]. In ref. [15], Al combustion in air was described by a three stage mechanism. In the first stage, the measured temperature was close to 3000 K; it decreased nearly stepwise to about 2750 K in the second stage. Finally, during the third stage, the temperature decreased to about 2200 K. The interpretation of that staged behavior proposed in refs. [15, 19] took into account possible dissolution of oxygen in the burning metal. Initially, formation of a saturated Al-O solution reduces the boiling point of Al and thus reduces the overall flame temperature for particles burning with a vapor phase flame. Further, the homogeneous liquid solution separates into distinct liquid phases, so that the spherical symmetry of the particle and its flame is destroyed, resulting in an oscillatory emission pattern. Sharp directional changes in particle trajectories shown in Fig. 3 provide further evidence for the asymmetric burn. Finally, as the particle burns out, the flame approaches its surface and eventually the reactions become controlled by the surface oxidation rate. The maximum temperature observed for combustion of micron-sized Al particles in air (cf. Figs. 6, 8) is remarkably close to the flame temperature reported in ref. [15] for the stage one combustion. In addition, current data for the early burn times show clearly how the particle temperature increases prior to reaching the maximum flame temperature. This temperature increase could not have been detected in ref. [15] where particles were generated by a micro-arc discharge, so that their initial temperature was near the Al boiling point. The time during which the initial temperature increase is observed in this work, can be interpreted as the time required to establish a vapor-phase flame for a self-heating Al particle. This interpretation is further supported by the observed rapid increase and peak in the AlO

emission occurring during this initial temperature ramp. Once the quasi-steady vapor phase flame is established, AlO emission becomes weaker, likely due to a more complete conversion of the evaporating Al into Al_2O_3 . As the data suggest, the duration of this transient initial process is comparable to the duration of the initial, quasi-steady combustion stage, occurring at about 3000 K. As for larger particles, the initial combustion stage is followed by a substantial reduction in the flame temperature. This temperature decrease is likely explained by transition from a nearly spherically symmetric vapor phase flame to a mixed combustion regime, when rates of heat release due to surface oxidation and reaction of the evaporated Al are comparable to each other. The reduced role of the vapor phase reaction is also supported by the reduced intensity of the AlO emission, as seen in Fig. 8. Stages 2 and 3 described earlier for large Al particles are difficult to distinguish for micron-sized particles studied here, most likely due to their significantly weaker overall emission intensity.

The discussion above applies to particles greater than about 7 μm burning in air, for which the temperature traces follow the characteristic patterns shown in Figs. 6 and 8. For finer particles burning in air, the maximum flame temperatures are lower, indicating that the full-fledged vapor phase flames were never achieved. This effect is most clearly seen in Fig. 7. It is very consistent with the predictions of ref. [17] where a maximum particle size is estimated, below which the vapor-phase flame alone cannot be self-sustaining because of the increased rate of heat losses to the cold surroundings. The critical size estimated in ref. [17] for air is 6 μm , which correlates well with the particle size of 7.4 μm , for which the flame temperature reaches its maximum quasi-steady level as shown in Fig. 7. Similarly, the vapor-phase flames are not produced in environments with reduced oxygen concentrations for any particles less than 20 μm considered in this work. However, even for particles burning at the lowest oxygen concentration, observations of both oscillatory emission patterns (Fig. 6) and greater than one factor measuring the AlO emission intensity (Fig. 8), suggest that the vapor phase reactions are not negligible. Unfortunately, this means that the reaction model describing Al particle combustion adequately cannot be readily reduced to either vapor phase or surface reaction models.

It is expected that a feasible and practically useful modeling approach can be developed if the combustion event is separated into several subsequent stages. For example, these stages can include a period while a vapor-phase flame is established, a quasi-steady, diffusion limited combustion, transition to the surface reaction, and quenching. For each stage, an expression for the burn rate can be proposed based on mechanistic understanding of the processes occurring in experiment. Data from the present experiments would serve to develop and/or validate such expressions. In particular, future models will benefit from detailed comparisons with individual particle combustion characteristics, such as overall emission times, temperature and black body and AlO emission intensity traces. Once validated, new dynamic models can replace current, steady-state models, e.g., described in ref. [4], used to predict contribution of the metal combustion processes in complex reactive systems.

Conclusions

Combustion processes for micron-sized Al particles burning in air can be separated into several stages. First, a transient process is observed during which the measured

flame temperature is increasing and molecular AlO emission peaks. It is interpreted as formation of a vapor-phase flame around a self-heating Al particle. This transient process is followed by a period when the flame temperature is stable around its maximum value just exceeding 3000 K while the AlO emission remains relatively strong. It is suggested that during this stage, the reaction is controlled by the vapor-phase combustion. In the following reaction stage, both the flame temperature and AlO emission are decreasing until the particle is extinguished. During this final stage, the vapor phase flame is suggested to approach the particle surface, and the reaction continues with an increased contribution from surface oxidation.

The characteristic maximum flame temperatures for aluminum particles burning in air are slightly higher than 3000 K for particles greater than 7.4 μm ; the temperatures are decreasing for finer particles. These observations are interpreted to suggest that particles less than 7.4 μm do not attain a full-fledged vapor phase flame, which is produced for coarser particles.

When oxygen concentration is reduced to 15 %, the maximum flame temperature of 3000 K is not attained even for the coarsest, 20 μm particles considered here. The temporal changes in the recorded particle emission signatures diminish, so that it is more difficult to distinguish between different stages in particle combustion. At 10 % oxygen concentration, combustion occurs at a nearly constant temperature close to 2000 K, indicating a surface-reaction controlled process. This temperature is not changing substantially for particles of different sizes. However, the AlO emission is substantial even for particles burning at about 2000 K, suggesting a non-negligible vapor phase reaction.

It is suggested that a useful description of the aluminum combustion dynamics must break the entire combustion process into several stages, so that different reaction mechanisms active at different burn times can be described separately. Descriptive reaction rates should be introduced for each stage, based on the experimental observations and understanding of the respective reaction mechanisms.

References

- [1] E. W. Price, Prog. Astronautics Aeronautics 90 (1984) 479-513.
- [2] E. Shafirovich, A. Varma, J. Propuls. Power 24 (2008) 385-394.
- [3] R. A. Yetter, G. A. Risha, S. F. Son, Proc. Combust. Inst. 32 (2008) 1819-1838.
- [4] M. W. Beckstead, Combust., Explosion Shock Waves 41 (2005) 533-546.
- [5] T. Bazyn, H. Krier, N. Glumac, J. Propuls. Power 21 (2005) 577-582.
- [6] Y. Shoshin, E. Dreizin, Combust. Flame 133 (2003) 275-287.
- [7] R. J. Gill, C. Badiola, E. L. Dreizin, Combust. Flame 157 (2010) 2015-2023.
- [8] R. J. Gill, S. Mohan, E. L. Dreizin, Rev. of Sci. Instrum. 80 (2009).
- [9] T. Bazyn, H. Krier, N. Glumac, Proc. Combust. Inst. 31 (2007) 2021-2028.
- [10] P. Lynch, H. Krier, N. Glumac, J. Thermophys. Heat Transfer 24 (2010) 301-308.
- [11] P. Lynch, H. Krier, N. Glumac, Proc. Combust. Inst. 32 (2009) 1887-1893.
- [12] N. I. Poletaev, A. V. Florko, Combust., Explosion Shock Waves 44 (2008) 437-443.
- [13] S. E. Olsen, M. W. Beckstead, J. of Propuls. Power 12 (1996) 662-671.
- [14] E. L. Dreizin, Combust. Flame 117 (1999) 117 841-850.
- [15] E. L. Dreizin, Combust. Flame 105 (1996) 105 541-556.

- [16] E. B. Washburn, J. N. Trivedi, L. Catoire, M. W. Beckstead, Combust. Sci. Technol. 180 (2008) 1502-1517.
- [17] S. Mohan, M. A. Trunov, E. L. Dreizin, Combust. Flame 156 (2009) 2213-2216.
- [18] E. B. Washburn, J. A. Webb, M. W. Beckstead, Combust. Flame 157 (2010) 540-545.
- [19] E. L. Dreizin, Prog. Energy Combust. Sci. 26 (2000) 57-78.

CHAPTER 3: PYROPHORICITY OF NANO-SIZED ALUMINUM PARTICLES

Introduction

Nano-sized aluminum powders have attracted considerable interest recently as potential components of energetic compositions (Gan and Qiao, 2011; Jayaraman et al., 2009; Meda et al., 2007). These powders are commonly prepared by methods involving condensation of Al vapors in inert environments (Kearns, 2004; Sarathi et al., 2007). Freshly prepared aluminum particles do not have protective surface oxide layer and must be passivated to enable their further handling. Most commonly, “natural” surface oxide layer provides the passivating effect. Often, controlled formation of such a layer is part of the powder preparation process and involves passing aerosol of just formed Al nano-particles through a chamber with a controlled oxygen concentration. As a result of this exposure to an oxidizing environment, very fine particles may self-heat substantially and oxidize fully, while the self-heating for larger size particles would be small, so that they would stabilize with a relatively thin passivating surface oxide layer. Aluminum oxidation models developed recently to describe processes leading to ignition of aluminum powders (Trunov et al., 2005; Bouillard et al., 2010) assume existence of the “natural” surface oxide layer and thus cannot be used to describe oxidation of the freshly prepared aluminum nano-particles. Instead, growth of thin oxide layers on metal surface is described by the Cabrera-Mott model (Fromhold and Cook, 1967; Zhdanov and Kasemo, 2008; Jeurgens et al., 2003), predicting higher oxidation rates compared to conventional, thermally activated diffusion. Recently, Cabrera-Mott formulation was adapted to describe oxidation of spherical nanoparticles (Ermoline and Dreizin, 2011). Using the formulation proposed by Ermoline and Dreizin (2011), in this paper pyrophoricity of aluminum nano-particles exposed to an oxidizing environment is considered; specifically, it is predicted which particles might self-heat and ignite upon such an exposure.

Model Formulation

The temperature history of a freshly prepared aluminum nano-particle inserted in an oxidizing gas environment at 300 K is predicted based on the analysis of the particle heat balance. The particle is heated by surface oxidation. Radiation and convection remove the heat from the particle. Convection is described using the transition regime heat transfer model (Mohan et al., 2008) applicable for small particles. Oxidation model is based on the Cabrera-Mott mechanism adapted for spherical nano-particles (Ermoline and Dreizin, 2011). The particle temperature history is analyzed and the particle is considered to ignite when the temperature runaway up to the alumina melting point is observed.

For an aluminum particle inserted in a gas environment at temperature T_E , the heat balance is expressed as:

$$mc \frac{dT_P}{dt} = \dot{Q}_{ch} - \dot{Q}_{conv} - \dot{Q}_r \quad (1)$$

where, m is the particle mass, c is the particle's specific heat and T_P is the particle temperature. \dot{Q}_{ch} is the chemical heat released due to aluminum oxidation, \dot{Q}_{conv} is the

heat loss due to convection, and \dot{Q}_r is the radiation heat loss. When particle reaches the Al melting point, its temperature is fixed and the left hand side of the equation (1) is

replaced by $h_m \frac{dm}{dt}$, where h_m is the latent heat of melting. Once the entire particle has melted, Eq. (1) is used again, in which specific heat is adjusted to represent molten Al.

The heat transfer analysis assumes the particle to have an initial temperature, $T_P=T_i$. In the first calculation, the minimum value of T_i leading to the particle temperature runaway is determined for different particle sizes. In the second calculation, the value of T_i for each particle size is estimated considering that particle with no oxide coverage is initially at the temperature of environment, $T_P=T_E$, and that it is heated adiabatically to T_i while the initial, monomolecular Al_2O_3 coverage is forming. Formation of that initial oxide coverage (the precursor for the forming amorphous oxide layer) occurs before the Cabrera-Mott reaction mechanism becomes valid and is expected to happen very rapidly, when a fresh aluminum surface is exposed to an oxidizing environment.

For each particle size, the value of minimum T_i leading to ignition obtained in the first calculation is compared to the value of T_i reached by the adiabatic heating of unoxidized particles due to formation of the initial monomolecular oxide coverage. This comparison enables one to determine particle sizes for which self-ignition is anticipated.

Further model details and individual terms in Eq. (1) are described below.

Radiation

The rate of radiation heat transfer from the particle to the surrounding environment is calculated using the Stefan–Boltzmann law:

$$\dot{Q}_r = \varepsilon \sigma A (T_P^4 - T_E^4) \quad (2)$$

where, ε is the emissivity of the particle surface, σ is the Stefan–Boltzmann constant, A is the particle surface area and T_P is the particle temperature. The surrounding surfaces are assumed to be at the ambient environment temperature T_E . The value of emissivity $\varepsilon=0.2$ is taken from the literature, as described for an oxidized Al surface (Lide, 2003).

Convection

Considering the small particle size and high temperature, the convection heat transfer from the particle surface to the surrounding gas is calculated using the transition regime heat transfer model based on the Fuchs analysis as described by Mohan et al. (2008). The model assumes a hypothetical Langmuir's layer around the particle. The heat transfer between the particle and the Langmuir's layer is calculated assuming the free molecular heat transfer regime:

$$\dot{q}_{\text{free molecular}} = \alpha AP \sqrt{\frac{\sigma T_\delta}{8\pi m}} \frac{\gamma+1}{\gamma-1} \left(\frac{T_P}{T_\delta} - 1 \right) \quad (3)$$

where, α is the accommodation coefficient, A is the particle surface area, P is the gas pressure, T_δ is the gas temperature at the Langmuir's layer and γ is the average adiabatic

index (averaged over T_P and T_δ , see Mohan et al. (2008)) of surrounding gas. Outside the Langmuir's layer, heat transfer is calculated using the expression for continuous medium:

$$\dot{q}_{continuum} = 4\pi \left(d / 2 + \delta(T_\delta) \right) \int_{T_\delta}^{T_P} k(T) dT \quad (4)$$

where, d is the particle diameter, δ is the Langmuir's layer thickness and k is the gas thermal conductivity. Assuming a thermally equilibrated state, $\dot{q}_{free\ molecular} = \dot{q}_{continuum} = \dot{Q}_{conv}$, so that equations 3 and 4 can be solved for T_δ . Once T_δ is found, the heat transfer rate is calculated. In calculations, the gas pressure was assumed to be one atm., and temperature-dependent air properties (Lide, 2003) were used to determine values of γ and k . The value of the accommodation coefficient used, $\alpha=0.85$ is based on the value published for Al₂O₃ for the temperature range considered (Saxena and Joshi, 1989).

Chemical Heat Release: Al Oxidation Model

The chemical heat release is calculated by an Al oxidation model based on the Cabrera-Mott formulation for spherical particles as described by Ermoline and Dreizin (2011). The model calculates the rate of growth of the oxide shell around an Al particle as,

$$\frac{dr_1}{dt} = \Omega_1 n v \exp\left(-\frac{W}{\kappa T}\right) \exp\left(-\frac{qa\phi_M}{\kappa T} \frac{r_2}{r_1 L}\right) \quad (5)$$

where, L is the oxide layer thickness, Ω_1 is the volume vacated per Al cation, v is the attempt frequency of Al cation, q is the cation charge, n is the number of cation per unit area, W is the energy barrier, κ is the Boltzmann constant, a is distance between potential minima, ϕ_M is the Mott's potential and r_1 and r_2 are the Al core and external oxide layer radii, respectively. Table 1 show all the parameters used to define the oxidation process (Jeurgens et al., 2002; Ermoline and Dreizin, 2011).

Table 1: Parameters used in the Cabrera-Mott model

ϕ_M	-1.6	V
W	2.6	eV
Ω_1	-0.0166	nm ³
v	1E12	s ⁻¹
q	3	E
n	10	nm ⁻²
a	0.12	Nm

Once the rate of growth of the oxide shell is determined, the rate of heat release is readily obtained as

$$\dot{Q}_{ch} = 4\pi\rho r_1^2 \frac{dr_1}{dt} \Delta H_{ox} \quad (6)$$

where, ρ is the Al density and ΔH_{ox} is the heat of Al oxidation. The present analysis assumes that the gas phase diffusion of oxidizer to the particle surface is not a rate-limiting process. For very low partial pressures of oxygen, this assumption may not be valid. Note, however, that a very small number of oxygen molecules are required to grow very thin oxide layers considered in these calculations (e.g., see changes in the oxide layer thickness discussed below and shown in Fig. 1). In most cases, the oxygen required is available from a gas layer adjacent to the metal surface with thickness of only 1 – 3 mean free path lengths of gas molecules. Therefore, gas phase diffusion is unlikely to be the reaction rate limiting process. In other words, the predicted reaction will be completed before concentration gradients around the particles are established.

As noted above, an initial, very thin oxide coverage must be present in order for Eq. (5) to be valid. This coverage thickness was set at 0.3 nm, a value, comparable with the dimension of d-spacing in the Al₂O₃ structure, or indicative of monomolecular oxide coverage. Formation of that initial oxide coverage is expected to occur very rapidly, with characteristic times close to those required for oxygen molecules to travel one mean free path length in the surrounding gas to reach the particle surface (on the order of 0.1 ns), so that respective particle heating is effectively adiabatic. Selection of the specific thickness for this initial oxide coverage is unimportant as long as this thickness is sufficiently small. Estimates show that when an initial coating thinner than 0.3 nm is assumed, calculations using the model described above predict its very fast, effectively adiabatic growth to about 0.3 nm, suggesting that the results of the present pyrophoricity assessment will not be affected. However, heat losses become non-negligible for thicker coatings growing according to the Cabrera-Mott kinetics. Therefore, assuming an initial oxide coverage thicker than 0.3 nm (and thus beginning to consider the Cabrera-Mott kinetics for thicker oxide layers) would imply a longer than reasonable adiabatic heating and substantial neglected heat losses, which are currently accounted for by the heat transfer model presented here. This would lead to a higher temperature at the end of initial oxide coverage period, i.e., more favorable conditions for the particle ignition.

Therefore, assuming the 0.3-nm thick oxide layer leads to a conservative estimate of a critical particle size at which ignition occurs.

In the present analysis, the temperature, T_i , required for the particle self-heating (thermal runaway) was determined in the first set of calculations using equations (1-6), in which the temperature histories for the particles with 0.3 nm oxide layer were calculated.

Particles of different sizes with the initial, 0.3 nm-thick, oxide coverage were inserted in the environment with $T_E = 300$ K, and their initial temperatures T_i were systematically increased from T_E until the particle was predicted to self-heat. Thus, the minimum ignition temperature was determined for particles of different sizes from 4 to 150 nm. It was observed that if particles reached the alumina melting point (~ 2300 K), temperature runaway always occurred. Therefore, to streamline calculations, particles self-heated up to 2300 K considered igniting in the computational code.

Results and Discussion

Figure 1 shows examples of the temperature histories and oxide thickness increase for a 20 nm particles with initial temperatures $T_i = 630$ K and 635 K inserted in air at $T_E = 300$ K. The initial temperatures are selected near the ignition threshold for 20-nm particles.

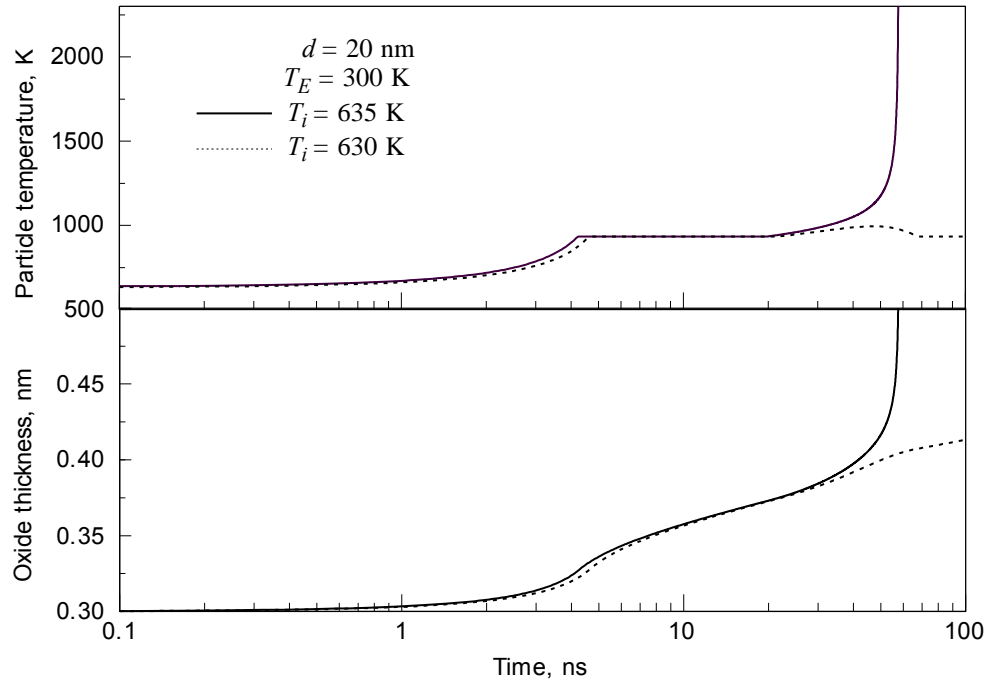


Figure 1. Temperature and oxide thickness histories for 20 nm aluminum particles inserted in air at 300 K at different initial particle temperatures.

Both particles introduced into an oxidizing environment are predicted to heat up to the melting point, melt completely, and continue self-heating after melting. For the particle that was initially at 630 K, the rate of self-heating decreases and particle begins to cool down. However, the particle that was introduced into the oxidizing medium at 635 K, continues to heat up and its temperature is predicted to run away. Note that these processes are predicted to occur quite rapidly (time scale ~ 100 ns) and the increase in the oxide thickness is relatively small, only about 0.2 nm.

The rate of reaction predicted by the Cabrera-Mott model is quite high, but it must be lower than the maximum possible reaction rate determined assuming that all oxygen molecules collide and react with the metal surface. For the example shown in Fig. 1 (a 20-nm particle) the predicted maximum possible reaction rate is close to 4000 mol/(m²·s). The rate estimated using the Cabrera-Mott model is indeed lower, i.e., 700 mol/(m²·s) immediately before the temperature runaway. Similar comparisons were made for different particle sizes confirming that the reaction rates predicted by the Cabrera-Mott reaction kinetics prior to the temperature runaway are always lower than the maximum possible reaction rates, and therefore are not unreasonable. These comparisons are also further validating the previously discussed assumption of the adiabatic particle heating during formation of the initial oxide coverage, when the reaction rate is limited by collisions of oxygen molecules and particle surface.

Calculations for the threshold ignition temperatures were performed for particles in the range of diameters from 4 to 150 nm. A solid line in Fig. 2 shows these minimum initial temperatures leading to the particle ignition as a function of the particle diameter. 4-nm diameter and finer particles have minimum ignition temperature of 301 K and lower. Larger particle are predicted to self ignite at higher temperatures.

Effectively, the curve separates ignition (above the curve) from non-ignition (below the curve) regions: if particles are entering the room temperature oxidizer at a temperature above the calculated threshold, they are expected to self-heat and ignite. A horizontal portion of the curve for particles with sizes between approximately 30 and 70 nm indicates that these particles need to be pre-heated to the melting point of Al. For larger particles in this size range, an increasingly greater fraction of the particle needs to be molten in order for the particle to become self-heated.

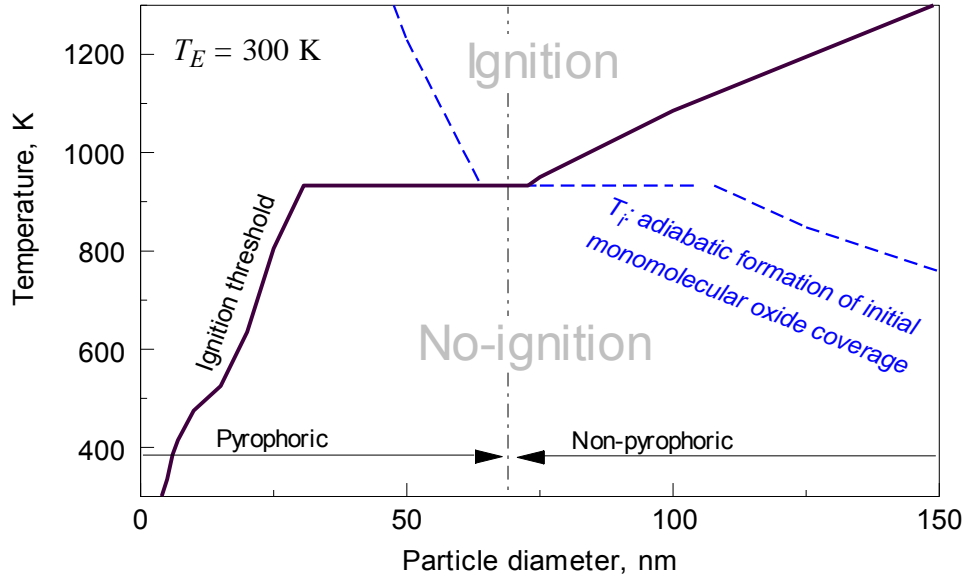


Figure 2. Solid curve: Minimum initial temperature leading to ignition for Al particles inserted in an air at 300 K. Dashed curve: Particle temperature due to its adiabatic pre-heating while a 0.3-nm oxide layer is formed. Particles less than 68.4 nm are predicted to be pre-heated to the temperature above the ignition threshold and thus are pyrophoric.

The initial temperature for a freshly prepared Al nano-particle entering an oxidizing environment is determined by the technology or method by which the powder is

prepared. It is important to realize that even if particles are cooled to room temperature in an inert environment, they will be rapidly heated immediately upon contact with an oxidizer. In a simple scenario discussed here, the initial temperature is estimated assuming an adiabatic heating of the particle from room temperature while forming the initial, 0.3-nm oxide coverage, used in the preceding calculations. This initial temperature was calculated as a function of the particle size and shown as a dashed curve in Fig. 2. Due to a small heat capacity, smaller sized particles are heated to higher temperatures as compared to larger particles. The horizontal part indicates melting, with a higher degree of melting for smaller particles. The particle size at which the dashed curve crosses the minimum ignition curve, and for which the same fraction of Al is predicted to be molten (68.4 nm) indicates the critical particle size below which the freshly prepared Al nano-particles are expected to be pyrophoric.

Some of the particle parameters used in the present calculations, such as particle emissivity or accommodation coefficient are not very well known. However, estimates showed that the predicted diameters, for which the particles become pyrophoric are relatively weak functions of these parameters because of a strong temperature effect on the Cabrera-Mott reaction kinetics, compared to relatively slow changes in emission and convection heat losses. For example, changing the accommodation coefficient from 0.85 to 0.5, changes the threshold particle diameter to 73.3 nm instead of 68.4 nm.

Conclusions

Temperature histories for nano-sized Al particles without a protective oxide film introduced into an oxidizing environment are calculated considering the transition regime heat transfer model and Cabrera-Mott reaction mechanism describing their initial oxidation. The particles are predicted to self-heat substantially, and particles below 68 nm introduced into a room-temperature oxidizing gas are predicted to be pyrophoric. The model is suitable for evaluation of early stages of oxidation of Al nanoparticles prepared using gas condensation methods.

References

- Bouillard J, Vignes A, Dufaud O, Perrin L, Thomas D (2010) Ignition and explosion risks of nanopowders. *Journal of Hazardous Materials*, 181(1-3):873-880.
- Ermoline A, Dreizin EL (2011) Equations for the Cabrera-Mott kinetics of oxidation for spherical nanoparticles. *Chemical Physics Letters*, 505(1-3):47-50.
- Fromhold Jr. AT, Cook EL (1967) Kinetics of oxide film growth on metal crystals: Electron tunneling and ionic diffusion. *Physical Review*, 158 (3):600-612.
- Gan Y, Qiao L (2011) Combustion characteristics of fuel droplets with addition of nano and micron-sized aluminum particles. *Combustion and Flame*, 158(2):354-368.
- Jayaraman K, Anand KV, Chakravarthy SR, Sarathi R (2009) Effect of nano-aluminium in plateau-burning and catalyzed composite solid propellant combustion. *Combustion and Flame*, 156(8):1662-1673.
- Jeurgens LPH, Sloof WG, Tichelaar FD, Mittemeijer EJ (2002) Growth kinetics and mechanisms of aluminum-oxide films formed by thermal oxidation of aluminum. *Journal of Applied Physics*, 92(3):1649-1656.
- Kearns M (2004) Development and applications of ultrafine aluminium powders. *Materials Science and Engineering: A*, 375-377:120-126.
- Lide DR (2003) *Handbook of Chemistry and Physics*, CRC, New York, U.S.A.

- Meda L, Marra G, Galfetti L, Severini F, De Luca L (2007) Nano-aluminum as energetic material for rocket propellants. Materials Science and Engineering: C, 27(5-8):1393-1396.
- Mohan S, Trunov MA, Dreizin EL (2008) Heating and ignition of metal particles in the transition heat transfer regime. Journal of Heat Transfer, 130(10):104505.
- Sarathi R, Sindhu TK, Chakravarthy SR (2007) Generation of nano aluminium powder through wire explosion process and its characterization. Materials Characterization, 58(2):148-155.
- Saxena SC, Joshi RK (1989) Thermal Accommodation and Adsorption Coefficients of Gases, Hemisphere, New York
- Trunov MA, Schoenitz M, Zhu X, Dreizin EL (2005) Effect of polymorphic phase transformations in Al_2O_3 film on oxidation kinetics of aluminum powders. Combustion and Flame, 140(4):310-318.
- Zhdanov VP, Kasemo B (2008) Cabrera-Mott kinetics of oxidation of nm-sized metal particles. Chemical Physics Letters, 452(4-6):285-288.

CHAPTER 4: PARTICLE COMBUSTION DYNAMICS OF METAL-BASED REACTIVE MATERIALS

Introduction

Metal powders are extensively used as additives in energetic materials for propellants, explosives, and pyrotechnics (Price 1984; Yetter et al. 2009). Aluminum, in particular, is used in many practical formulations (Dokhan et al. 2002; Frost et al. 2006; Luman et al. 2007; Meda et al. 2007; Mench et al. 1998; Sambamurthi et al. 1984). Ability to predict ignition delays and burn rates of aluminum and other metal particulates in such formulations is imperative for successful design of respective metalized energetic systems. This predictive ability must rely on accurate models describing ignition kinetics and combustion dynamics of metal particles.

Ignition kinetics is mostly concerned with heterogeneous reactions involving diffusion through or removal of protective oxide films preventing metal particles from rapid oxidation. A model describing aluminum ignition based on analysis of polymorphic phase changes in protective alumina scale was recently proposed by Trunov et al. (2006), capable of predicting ignition delays for Al particles heated at different rates. Further development of similar concepts for ignition of nanocomposite thermite powders was discussed by Ermoline et al. (2011).

Describing combustion dynamics of the ignited metal particles involves analysis of a broader range of processes, including heat and mass transfer in the gas phase surrounding the particle, kinetics of reactions occurring in the vapor phase as well as on the surface of the reacting particle, and evolution of the condensed products forming within reacting particles, often including metal-gas solutions (Dreizin 2000). Despite the relative complexity of the involved processes, or possibly, because of it, current descriptions of the combustion dynamics of metal particles are extremely simplified and often reduced to a trend suggesting that the burn time, τ , is proportional to the particle diameter, D , in the power n , $\tau \sim D^n$ (known as D^n law.) In particular, for aluminum combustion, many practical codes rely on a recent compilation of experimental data by (Beckstead 2005). However, most of the reviewed data came from experiments with relatively large particles, typically, exceeding 50 μm . Conversely, finer particles are commonly used in practical formulations, and it is unclear whether an extrapolation of the D^n trends found for coarser powders remains valid. In fact, recent research (Krier and Glumac 2009) suggests that the extrapolation becomes invalid for particles less than 20 μm . It was also suggested that the vapor-phase combustion regime common for coarse Al (and some of the other metal) particles is not sustainable when the particle size is reduced (Mohan et al. 2009) simply due to the reduced rates of heat transfer for particles with dimensions comparable to the mean free path of the gas molecules.

Development of accurate combustion dynamics models for fine metal particles requires direct experimental validation; however, such experiments are complicated. Most experimental methods involve aerosolized particle clouds (Cashdollar 2000; Dreizin et al. 2002; Goroshin et al. 1996; Huang et al. 2009; Santhanam et al. 2010; Schoenitz et al. 2003; Tang et al. 2009), where detection of individual particle burn times is difficult or impossible. Recently, an experimental technique was developed aimed to characterize individual burn times for single metal particles in the size range of 1 – 25 μm (Gill et al.

2009). A CO₂ laser was used to ignite individual particles, while a second, low-power laser was used for in-situ, scattered light-enabled size measurements for the ignited particles. This paper reviews experimental data generated using this method for several materials, including aluminum, and some of the recently developed Al-based reactive nanocomposite powders. The implications of the experimental results for development of new metal particle combustion dynamics models as well as for design of new reactive materials are also discussed.

Experimental setup

A schematic diagram of the experimental setup is shown in Fig. 1 (Badiola et al. 2011; Gill et al. 2009; Gill et al. 2010). A low number density, vertically rising aerosol jet is fed through two laser beams. First, particles cross a low-energy 785 nm laser. Light scattered by particles crossing that laser is measured by a filtered photomultiplier tube (PMT); amplitudes of pulses generated by individual particles are used to recover respective particle sizes. Particles then cross a CO₂ laser beam where they are heated to ignition. Optical emission produced by the burning particles is recorded using four filtered PMT's (Hamamatsu H3164-10.) Three of the interference filters with wavelengths at 532, 568, and 589 nm were selected to not overlap with any of the strong AlO molecular emission bands. The fourth filter, at 486 nm was selected to track one of the strongest AlO emission bands in order to gauge significance of the vapor-phase reactions.

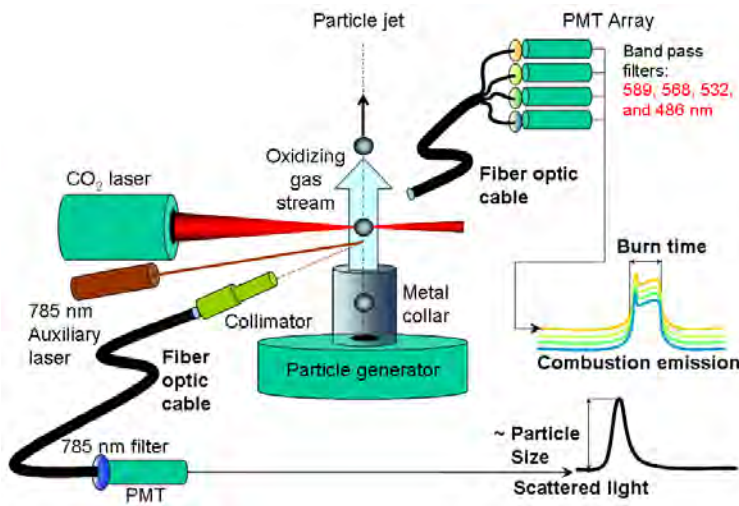


Fig. 1. Experimental apparatus

Two different designs of particle generators were used for different experiments. Pure aluminum powders and other powders with relatively low sensitivity by electrostatic discharge (ESD) ignition were fed into the aerosol jet using electrostatic aerosol generator (ESAG) (Shoshin and Dreizin 2002) schematically shown in Fig. 2.

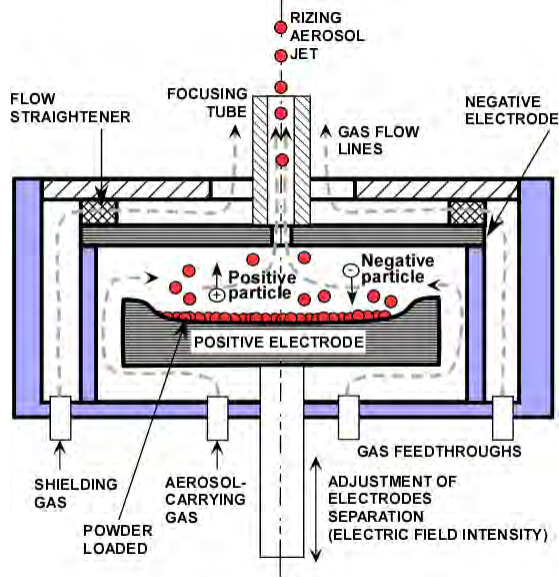


Fig. 2. Electrostatic aerosol generator (Shoshin and Dreizin 2002)

In ESAG, powder is loaded onto a bottom electrode of a plate capacitor, as shown in Fig. 2. When a DC voltage is applied, the powder is aerosolized between the capacitor's electrodes. The density of the produced aerosol is controlled by the electric field, adjusted by both applied voltage and separation between electrodes. A small opening in the top electrode serves as a nozzle. In addition, a focusing tube is used to collimate the exiting aerosol jet. A carrying gas flow controls the feed rate of aerosol. Shielding gas flow helps to maintain the shape of the produced aerosol jet and, if necessary, adjust the oxidizing gas environment.

For powders sensitive to ESD ignition, a different, vibratory particle generator was developed. It is shown schematically in Fig. 3. The powder loaded into the hopper does not fall through the opening until the entire assembly is vibrated using a speaker; the amplitude and frequency of the vibrations are adjusted to achieve a steady aerosol flow. The hopper was placed on top of a metal tube; the tube was bent and inserted into an orifice making a linear bearing with the exit plate. Thus, the final vibration of the exit tube remained one-dimensional ensuring particle flow along the vertical axis.

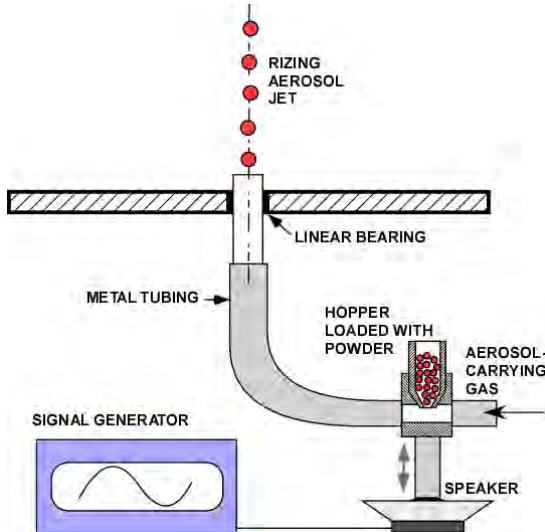


Fig. 3. Vibratory aerosol generator

All PMT's were used and calibrated in the DC mode using a current-stabilized tungsten lamp and an irradiance calibrated spectrometer (StellarNet EPP2000). For calibration, a spectrum of the current-stabilized tungsten lamp was measured with the spectrometer. The output from each of the filtered PMT's was then directly correlated with the true lamp emission intensity at the respective wavelength (Badiola et al. 2011). The PMT gain curves were obtained measuring the variation in the output as a function of the applied voltage at a fixed irradiance. To cross-check the accuracy of the gain functions, a set of neutral density filters was used to measure the response of each PMT under a wide range of light intensities. The gain curves accurately predicted (to within a few percent) the PMT output voltages.

Most experiments were conducted in room air (1 atm, 298 K). Experiments with pure aluminum were also performed at 1 atm using room-temperature O₂/N₂ gas flows with oxygen concentrations of 10 and 15 % (Badiola et al. 2011). Further, experiments were performed with pure Al powder fed through ESAG in N₂ while oxidizers CO₂ or pre-heated H₂O were flown as the shielding gases (Gill et al. 2010).

Data Processing

Data processing involves several steps (Badiola et al. 2011; Badiola and Dreizin 2012; Gill et al. 2009; Gill et al. 2010). First, the powder particle size distribution measured by a commercial Beckman-Coulter LS230 particle analyzer is compared to that obtained in-situ from the amplitudes of the scattered 785 nm light pulses. Assuming that the scattered light is described by the Mie solution, the amplitude of the recorded pulses is directly proportional to the square of the particle diameter. However, the proportionality coefficient is different for each powder because it is affected by particle surface morphology. In order to find this proportionality coefficient for each powder, the peak of the in-situ measured particle size distribution is matched with that obtained using LS230 analyzer. If the particle size distribution shapes match each other, the in-situ measurement is considered calibrated and valid.

In the next processing step, the recorded emission and scattered light pulses that overlap or follow each other closely are removed. This ensures that only individual burning particles are considered in further analysis.

The remaining two sequences of scattered light and emission pulses need to be matched with each other, so that the size for each individual incandescent particle is obtained. The two pulse sequences are shifted between themselves by the time required for the particles to travel between the two laser beams. This time is found using the particle velocity and distance between the two laser beams. The particle velocity is found using a separate measurement employing images of the aerosol jet illuminated with a modulated laser sheet (Gill et al. 2009). Note that for individual particles, the travel time between the two laser beams may vary somewhat, because of the difference in the individual particle velocities. To account for that variation, the pairs of pulses shifted relative to each other by the anticipated interval plus/minus a narrow time window accounting for the variation in individual particle velocities, were identified for further processing and assumed to represent individual particles.

In the final processing step, we identified particle signals representing the complete combustion events, as opposed to particles that were heated but unignited or ignited and partially consumed while crossing the laser beam. Indeed, some of the particles could be simply heated up but not ignited while passing through the CO₂ laser beam. Such particles could, nevertheless, be luminous enough to be detected by the present optical sensors. In addition, shorter burn times would be inferred from the recorded streaks representing particles that ignited and were partially consumed within the CO₂ laser beam, while being additionally heated by the laser. Thus, such emission pulses produced by both unignited particles and particles partially consumed within the CO₂ laser beam should be discarded.

Two methods were used to discard such pulses. One method simply removed all emission pulses except for the longest pulses identified for each particle size. This selection is based on the following reasoning. Unignited particles will cool down during a time that is much shorter compared to the combustion time for the same size particles. Similarly, particles partially consumed in the laser beam will burn out faster than similar size particles burning independently. Selection of the longest emission pulses was initially done manually (Gill et al. 2009; Gill et al. 2010), then a procedure was developed in which the particle size range was broken down into several bins and longest emission times for each bin were selected using a pre-determined threshold (Badiola et al. 2011). The second selection method was based on analysis of the shapes of the recorded emission pulses (Badiola and Dreizin 2012). Specifically, the amplitude of the emission pulse at the instant the particle was expected to exit the laser beam was compared to its maximum amplitude. For both unignited but heated particles and particles that were partially consumed in the laser beam, the emission signal when the particle exits the laser beam is expected to be relatively strong. Alternatively, for particles that are about to ignite after exiting the laser beam, the instantaneous emission signals before ignition, i.e., while exiting the laser, should be rather weak. Both selection methods were compared to each other for aluminum powder burned in air. Similar trends for burn times as a function of particle sizes were observed in both cases.

Materials

Spherically shaped micron sized aluminum particles were used for these experiments (Alfa Aesar, 10-14 μm nominal particle size). A scanning electron microscope (SEM) image of the aluminum powder is shown in Fig. 4. Prior to experiments, the powder was dried in a glass vial at 65–85°C under vacuum for more than 2 hours. The vial was sealed after its removal from the vacuum oven. After a cooling period, the vial was tumbled with an aluminum or Teflon solid rod, 1 cm diam.) for approximately 20 min. This procedure reduced the number of agglomerated particles, but did not deform their shapes - as confirmed by electron microscopy.

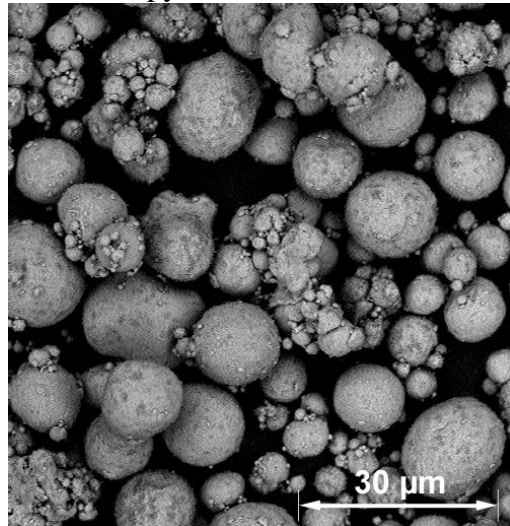


Fig. 4. Aluminum powder used in experiments

Experiments were also performed with a set of nanocomposite aluminum-based powders prepared by mechanical milling. SEM images of different materials are shown in Fig. 5.

Two of the nanocomposite powders had thermite compositions, Al·MoO₃ and Al·CuO with molar Al/oxide ratios of 5.25 and 2.67, respectively. In both cases, the compositions were metal-rich (the stoichiometric thermites of Al·MoO₃ and Al·CuO have molar Al/oxide ratios of 2 and 0.67, respectively.) Such compositions are designed to accelerate their ignition due to highly exothermic thermite reaction, while retaining the benefit of highly exothermic aluminum combustion in ambient oxidizers. These nanocomposite thermite powders were prepared by Arrested Reactive Milling (Dreizin and Schoenitz 2009). Additional details of preparation of metal-rich, Al-based thermite powders are available elsewhere (Stamatis et al. 2009; Umbrajkar et al. 2008). For both thermite powders, the particles have rugged equiaxial shapes. Particle sizes vary in a very broad range for Al·MoO₃ while Al·CuO powder is fairly coarse. It was reported that Al·CuO powder ignites when it is heated to 800 – 900 K (Stamatis et al. 2009). For Al·MoO₃, the ignition temperature was reported to be between 700 and 800 K (Umbrajkar et al. 2008).

Aluminum-iodine (Al·I₂) powder was prepared by mechanical milling of elemental aluminum and iodine at the liquid nitrogen temperature (Zhang et al. 2010a, 2010b). This material is developed to generate biocidal combustion products assisting in disabling aerosolized spores and bacteria (Grinshpun et al. 2010). Iodine concentration was 20 wt.

%. The powder comprises rock-like, equiaxial particles with relatively smooth surface. The ignition temperature for such powders was reported to vary from 900 to 1200 K, depending on milling conditions (Zhang et al. 2010a).

Another reactive material designed to produce biocidal combustion products and tested in these experiments, Al·B·I₂, included three starting components, aluminum, boron (11.1 wt. %), and iodine (20 wt. %). This material is expected to have an improved energy release compared to Al·I₂. It is also easier to prepare by mechanical milling because abrasive properties of the hard elemental boron powders accelerate embedding of both boron and iodine into aluminum matrix. This material was prepared using a SPEX Certiprep 8000 model shaker mill. Powder load was 5 g per vial, hardened steel milling vials (50 mL) and balls (9.5 mm diam.) were used. The ball to powder mass ratio was 10. The vials were additionally cooled using an air jet and milling time was 240 min. Iodine served as an effective lubricant, so no additional process control agent was required. SEM images of the prepared materials show boron inclusions distributed rather uniformly in the Al matrix. The inclusions appear as darker spots on the brighter particle surface. The particles are more rounded than in the other mechanically milled powders. The ignition temperature of this powder was measured using the same heated filament ignition setup (Ward et al. 2006) as used for testing other materials. The material was observed to ignite at 1042 – 1224 K.

Finally, two materials tested in this project comprised nanocomposite particles combining elemental aluminum with one of two hydrocarbon fuels, paraffin wax (Al-wax) and low-density polyethylene (Al-PE). The mass fractions of each wax and polyethylene were 10 wt. %. It was expected that upon ignition, the hydrocarbon fuel would evaporate resulting in the fragmentation of the prepared composite particles. It was further expected that the presence of a readily ignitable hydrocarbon fuel would assist ignition of aluminum. Both of these materials were prepared using an attritor mill (01HD model). A 1-L steel milling vial and hardened steel balls (9.5 mm diam) were used. In each milling run, 50 g of powder was loaded and the ball to powder mass ratio was 36. The milling time was 19 hours for each material. The milling vials were cooled by a flow of liquid nitrogen. Milling at the cryogenic temperature was necessary to produce the desired composite particles. At higher temperatures, the powder agglomerated and caked, while at the cryogenic temperature, hydrocarbon particles hardened and readily mixed with aluminum. SEM images of the prepared powders suggest that particle sizes vary in a broad range. The particles appear to consist of multiple agglomerated very fine flakes or smaller particles. It is suggested that the very fine particles are coated with a thin layer of hydrocarbon which serves as an adhesive promoting their agglomeration. Heated filament ignition experiments showed that Al-wax and Al-PE powders ignite at 900 – 1200 K.

For all nanocomposite powders, particles in a wide range of shapes and sizes were present, as illustrated in Fig. 5. However, these samples prepared by mechanical milling were homogeneous compositionally; in other words for each material, the bulk compositions of small and large particles were identical. In fact, large particles of the powders prepared by mechanical milling are dense agglomerates or cold welded aggregates of finer particles present in the same sample. The compositional homogeneity of such samples was reported elsewhere (Suryanarayana 2001) and confirmed to be at the

scale of 100 nm or less for reactive composite materials (Umbrajkar et al., 2008), similar to those considered in the present study.

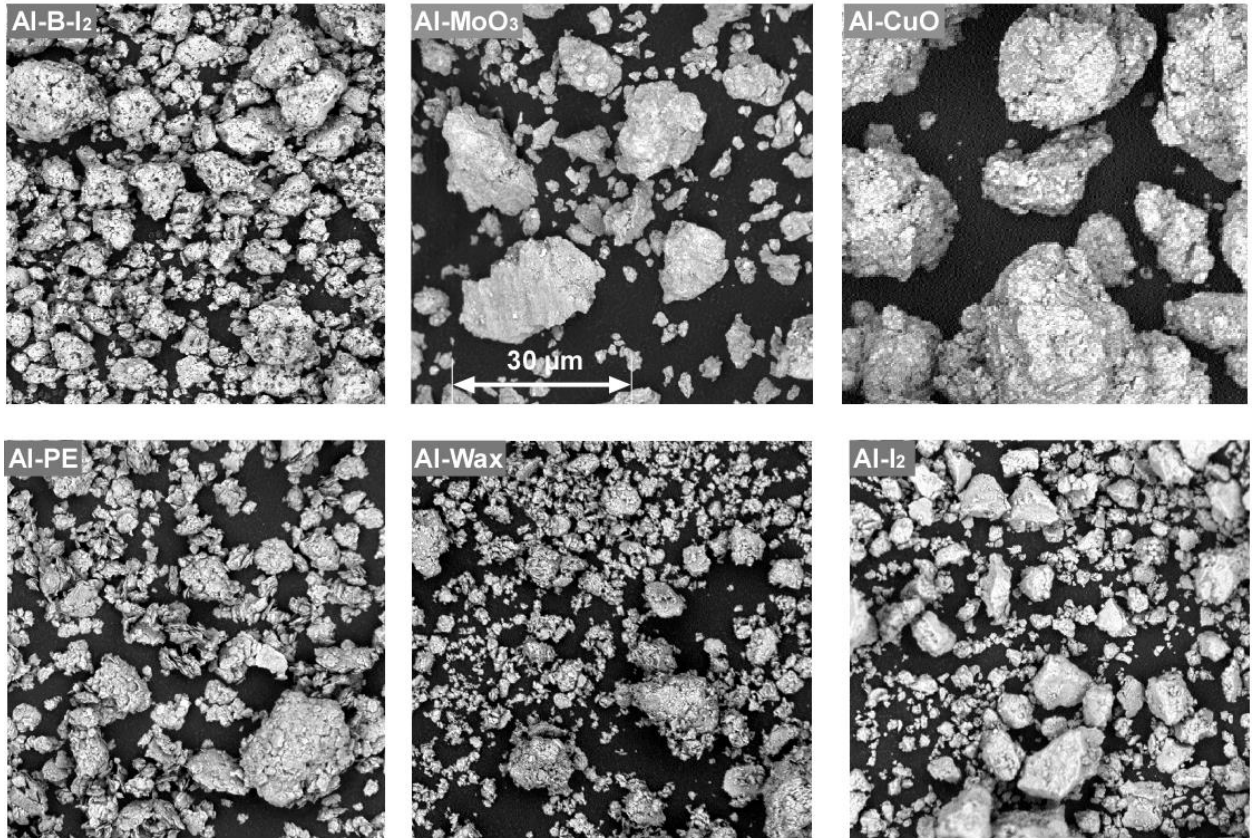


Fig. 5. SEM images of different nanocomposite materials used in experiments. The magnification is the same for all images.

Results

Particle size distributions

Particle size distributions for the spherical Al powder and composite powders prepared by mechanical milling are shown in Fig. 6. Vertical bars show the measurements obtained using a commercial Beckman-Coulter LS230 Enhanced Particle Analyzer. The symbols show the size distributions obtained using the in-situ laser light scattering. The two size distributions are matched using a single adjustable parameter depending on the scattering efficiency for each specific powder. For aluminum, two in-situ size distributions are shown (open squares and grey filled circles). The grey filled circles show result of a measurement in which the PMT sensitivity was increased to enhance detection of the finer particles, which could be discarded with the common PMT setting. Both size distributions are very close to each other and match very well the distribution obtained with the commercial instrument.

The match between the size distributions measured by the commercial particle size analyzer and using the in-situ laser light scattering is less good for mechanically milled powders, which was expected considering that the particle shapes were no longer

spherical. The discrepancies are rather significant, especially for Al·B·I₂ and Al-wax. However, it should be noted that the vibratory powder feeder used to aerosolize these powders is less effective in lifting larger particles, so that there could have been true differences between the size distributions of bulk powder samples and the powder fed into the laser beam during the experiments. In general, the in-situ particle size measurement appears to be useful.

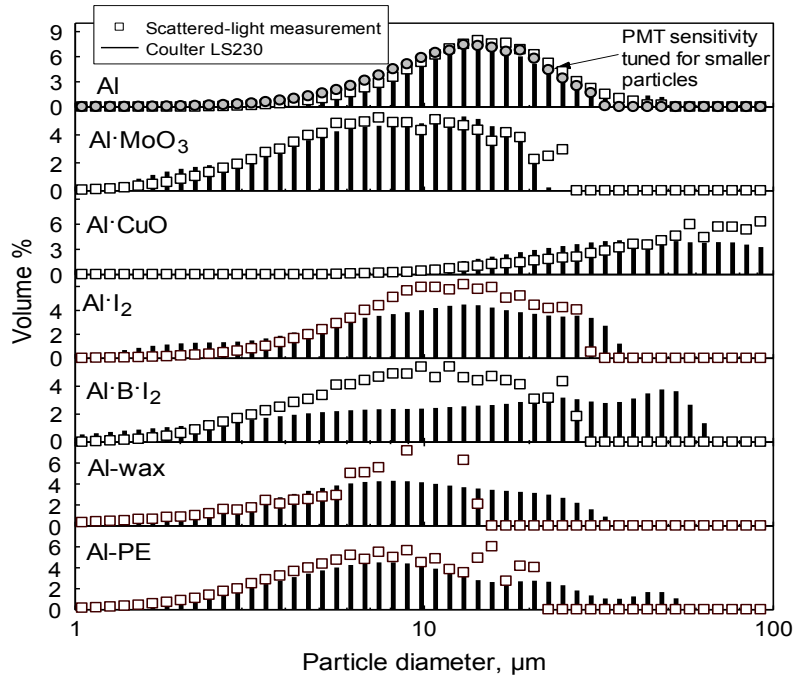


Fig. 6. Particle size distributions measured by Beckman-Coulter LS230 Enhanced Particle Analyzer (bars) and by in-situ laser light scattering (symbols).

Individual emission traces

A set of photographs showing appearance of bright streaks produced by ignited particles for different materials is shown in Fig. 7. All images are taken with a camera aperture open for 250 ms, while an approximate feed rate of powders is close to 1 particle per 10 ms, so that streaks of multiple particles ignited during the exposure time are captured. In all images, except for Al·CuO, the CO₂ laser beam was located at the bottom of the field of view and the particles are seen ignited while crossing it or soon after exiting from it. For Al·CuO particles, ignition was accompanied by a microexplosion, as shown in Fig. 7, this occurs just when the particle exits the laser beam, so that the laser beam was located approximately in the middle of the respective field of view.

Multiple streaks for Al differ in length and brightness, most likely indicating combustion of different size particles. It is also apparent that many particles burned while still in the laser beam, producing bright spots at the bottom of the image, where the laser beam was located. Burning particles are seen to change direction, as is typical for asymmetric flames described in detail for much larger Al particles (Dreizin 1999).

The streaks produced by burning Al·MoO₃ particles do not exhibit pronounced changes in direction. The streak brightness increases slower than for pure Al, a typical “spearpoint,” i.e., reduced brightness followed by a sharply increased brightness signal is consistently observed by the end of the streak. The products of fragmentation of the ignited Al·CuO particles appear to burn with oscillations in brightness, changes in the particle velocity, and spearpoints by the end of most streaks.

The streaks produced by Al·I₂ particles exhibit pronounced brightness oscillations, substantially stronger than observed for other materials. The streak brightness increases for an extended period of time after the particle ignites, somewhat similar to Al·MoO₃. Most particles explode prior to their extinction, which is also a unique feature for this material. Sudden changes in the burning particle velocity are also observed, similar to pure Al.

The streaks for Al·B·I₂ appear least bright and longest among all materials studied here. They exhibit sudden changes in velocity of burning particles, changes in the particle brightness are also observed, although not nearly as strong and periodic as for Al·I₂.

Finally, streaks of Al-wax and Al-PE are similar to each other. In both cases, the streaks widen and become brighter soon after particles exit the CO₂ laser beam. The streaks appear broader and brighter compared to all other materials. Changes in the burning particle velocities are relatively minor.

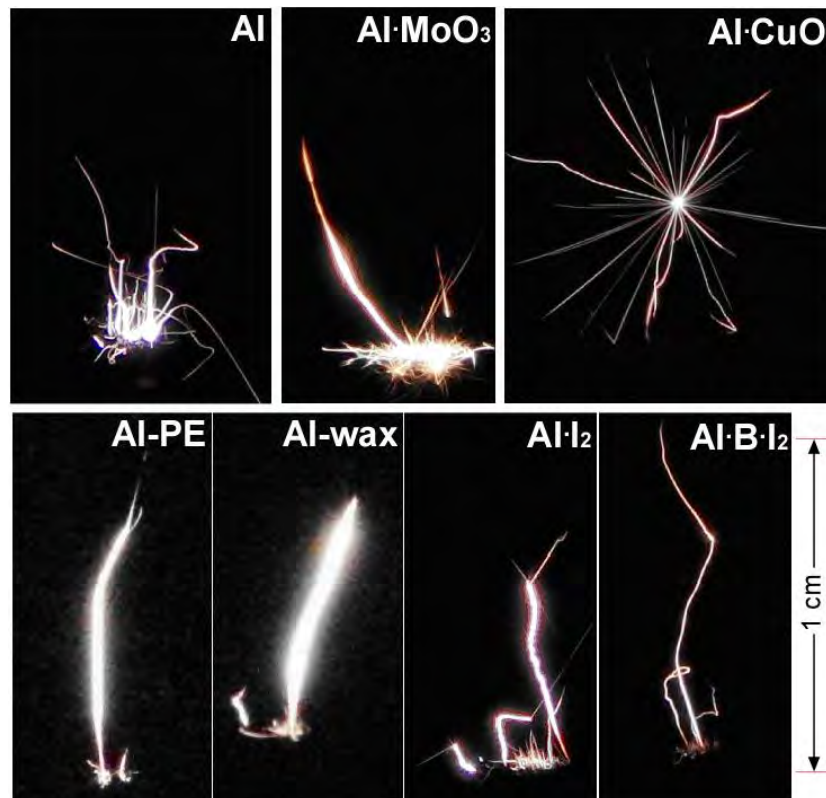


Fig. 7. Streaks of particles of different materials ignited by the CO₂ laser beam. The magnification is the same for all images.

Characteristic emission traces for all materials are shown in Fig. 8. For Al, the emission intensity increases rapidly and then decays for the most of the burn time. The rate of decay decreases after about 2/3 of the burn time.

For Al·MoO₃, the emission intensity increases relatively slowly. Small brightness oscillations are observed during this emission intensity ramp. The emission then decays rather rapidly, however, the particle does not extinguish. Instead, it remains luminous for an extended period of time. A magnified portion of the emission trace for Al·MoO₃ shows that the intensity changes noticeably, with the last sharp increase in emission most likely correlating with the spearpoints observed in the particle streaks.

The emission trace for Al·CuO begins with a very sharp intensity increase, most likely associated with the explosion of the ignited particle. The following trace is most likely dominated by the emission from the largest produced fragment. A relatively slow decay in intensity does not directly lead to extinction; similar to Al·MoO₃, the low level luminosity is preserved for a while and an increase in emission is observed before the particle extinguishes.

The emission trace for Al·I₂ shows an extended intensity ramp accompanied by strong, but decaying oscillations. After the emission intensity peaks, the particle extinguishes relatively rapidly.

For Al·B·I₂, the initial intensity ramp is relatively short, while still longer than for pure Al. It does not exhibit oscillations observed for Al·MoO₃ or Al·I₂. The emission intensity oscillates around its peak value for a while before a slow intensity decay is observed.

Finally, the traces for both Al-wax and Al-PE are similar to each other. They both show a relatively short intensity ramp followed by a slow increase in the particle emission accompanied by a decaying oscillatory pattern. These patterns are similar to that observed for Al·I₂. Also similar to Al·I₂, the Al-hydrocarbon particles extinguish relatively quickly after the peak emission intensity is achieved.

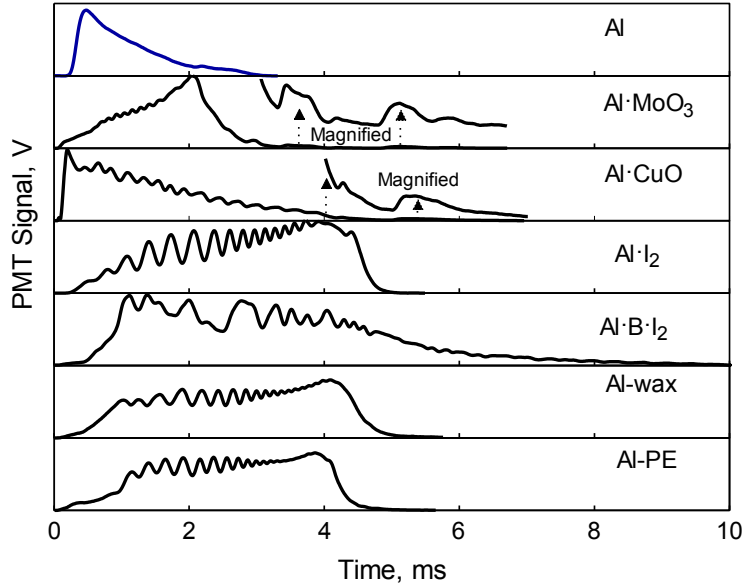


Fig. 8. Emission traces produced by individual burning particles of different materials.

Combustion times

Scatter plots showing the effect of oxidizing environment on the measured combustion times, τ , for particles of different sizes are presented in Fig. 9. These data were processed to select the longest burn times, as described in further detail by Badiola et al. (2011); Gill et al. (2009); Gill et al. (2010). Results for three different O₂/N₂ mixtures (circles) show a consistent increase in the burn time with the reduction in the oxygen concentration. The slopes of the burn times vs. diameter, $\tau(d)$, trends plotted in the log-log coordinates are not noticeably affected by the oxygen concentration. The burn times are also shown for experiments with the same aluminum powder exposed to gaseous mixtures of H₂O/N₂ and CO₂/N₂. The slopes of the respective $\tau(d)$ trends are even lower than for the O₂/N₂ environments. Burn times are the longest for CO₂/N₂. For reference, Fig. 9 also shows trendlines calculated using the $d^{1.8}$ correlation proposed by Beckstead (2005). The slope of the calculated trendlines is substantially steeper than for the experimental data. It is also interesting that the predicted trends for 73% CO₂ and 10% O₂ nearly coincide with each other, while the respective experimental data are also similar for these two environments. However, the burn times in 77% of H₂ are predicted to be the shortest, in stark contrast to the experiments, in which they are quite long and just slightly shorter than the burn times in 73% of CO₂.

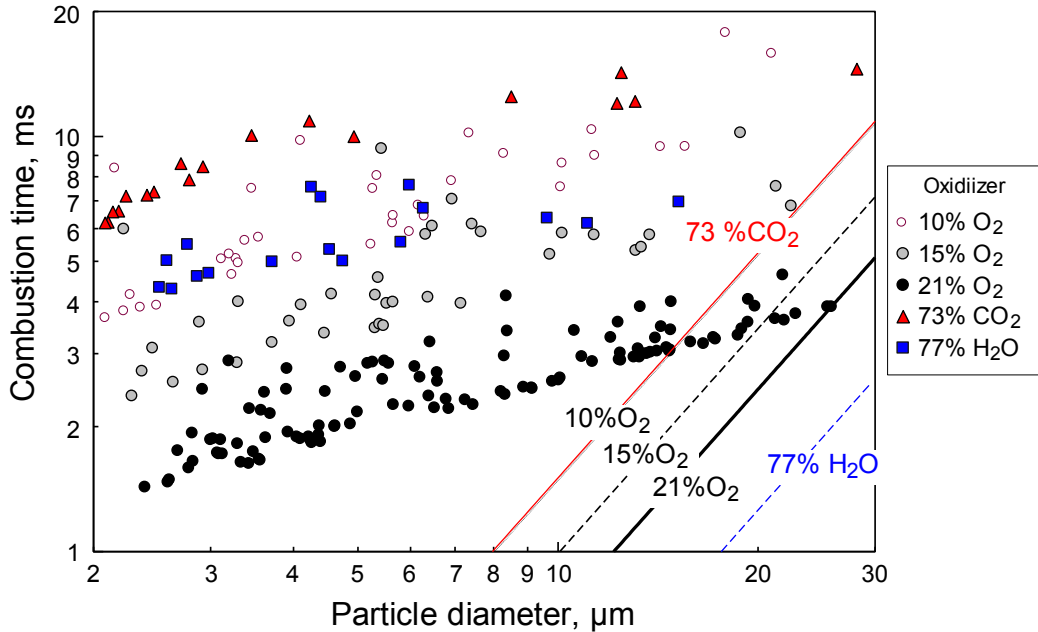


Fig. 9. Combustion times as a function of the in-situ measured particle diameters for Al powder burning in different oxidizing environments. Straight lines show respective trends calculated following $\tau \sim d^{1.8}$ law suggested by Beckstead (2005).

Combustion times as a function of the particle diameters for different materials burning in air are shown in Fig. 10. Two data sets for Al powders are shown in Figs. 10 and 11 below. Filled black circles show data for particles selected based on the shape analysis of the emission pulses, as described by Badiola and Dreizin (2012). Open grey circles show results identified based on selection of the longest emission times following the methodology presented by Badiola et al. (2011). Both data sets form trends, which are very close to each other.

The data for Al·I₂ are processed to select the longest burn times. For all other materials, the selection of data points shown in Fig. 10 (and Figs. 11 and 12) was based on the shape analyses of the respective emission pulses (Badiola and Dreizin 2012). Comparisons of the combustion times for Al and other materials are somewhat difficult because of a substantial scatter in the data presented. This scatter is most likely due to errors in measuring sizes of some of the individual particles expected chiefly due to the rugged particle shapes.

The longest combustion times are observed for Al·B·I₂, which is consistent with the longest emission streaks observed for this material, as was illustrated in Fig. 7. The burn times are close to each other and noticeably shorter for Al·I₂ and Al·MoO₃ particles. Note that for Al·MoO₃, the measured combustion times include a relatively long period of weak emission, as illustrated in Fig. 8. The interpretation of the observed combustion times for the Al·CuO particles is difficult, considering that most of these particles explode upon ignition; however, the burn times are somewhat longer than for pure Al. There is no data for pure Al particles greater than 30 μm, but the trend formed by the data points for smaller Al particles projects to the range of times observed for the respective coarser Al·CuO particles. The scatter in the measured burn times is greatest for the Al-

wax and Al-PE particles. These materials also have the greatest fractions of very fine particles. Despite scatter, it appears that the burn times for both Al-PE and Al-wax powders are similar to those of pure Al. Some of the data points indicating very long burn times for submicron particles are likely outliers produced due to an error in the size measurement for particles with significant aspect ratios (flake-like particles) present in these powders.

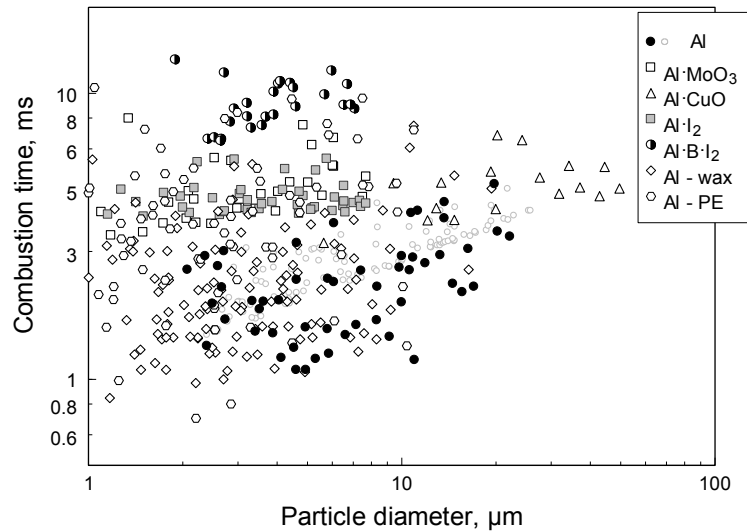


Fig. 10. Combustion times of particles of different materials in air.

Combustion temperatures and AlO emission

The color temperatures were measured based on the intensity ratio for the emission signals at 532 and 589 nm. The flame was assumed to behave as a gray body emitter, according to recent studies of emissivity of alumina at high temperatures typical of aluminum combustion (Lynch et al., 2010). Note that temperatures are not shown for Al·B·I₂, for which characteristic emission produced by boron combustion interfered with the filtered emission signals used for temperature measurements.

Characteristic combustion temperatures for powders of different materials are shown in Fig. 11. For all materials, the temperatures shown are obtained as values averaged over a period of time while the emission signal exceeded 50% of its peak value. This averaging method discards the temperatures measured during ignition and extinction, when the emission signals are weaker and thus the error of the color temperature measurement is greater. The effect of particle size on the measured temperature is noticeable for pure Al, with greater size particles burning at higher temperatures. However, this effect is hardly detectable for the mechanically milled materials. For particles less than 10 μm, the temperatures for all materials are similar to one another and close to those of pure Al. However, for coarser particles, the pure Al particle temperatures are higher than for other materials. The difference is particularly clear for Al vs. Al·CuO composite, for which a large number of coarse particles was processed.

Combustion temperature for pure Al powder was also assessed using a time-averaged spectrum collected using a EPP2000C Portable UV-Visible spectrometer (190-850 nm)

with concave holographic grating. A portion of the measured spectrum obtained integrating emission from multiple burning particles is shown in Fig. 12. This spectrum shown excludes the part heavily affected by the molecular AlO bands, which would cause a substantial error in finding the emitter's temperature by matching its spectrum with that of a grey body. The integrated spectrum is dominated by the strongest individual emitters, which are larger particles and particles burning at the highest temperatures. The grey body emission calculated to match the measured spectrum by adjusting the emitter's temperature, 3026 K, is also shown in Fig. 12. It is effectively the same as the upper-limit temperature identified by the color pyrometry for larger Al particles, as shown in Fig. 11.

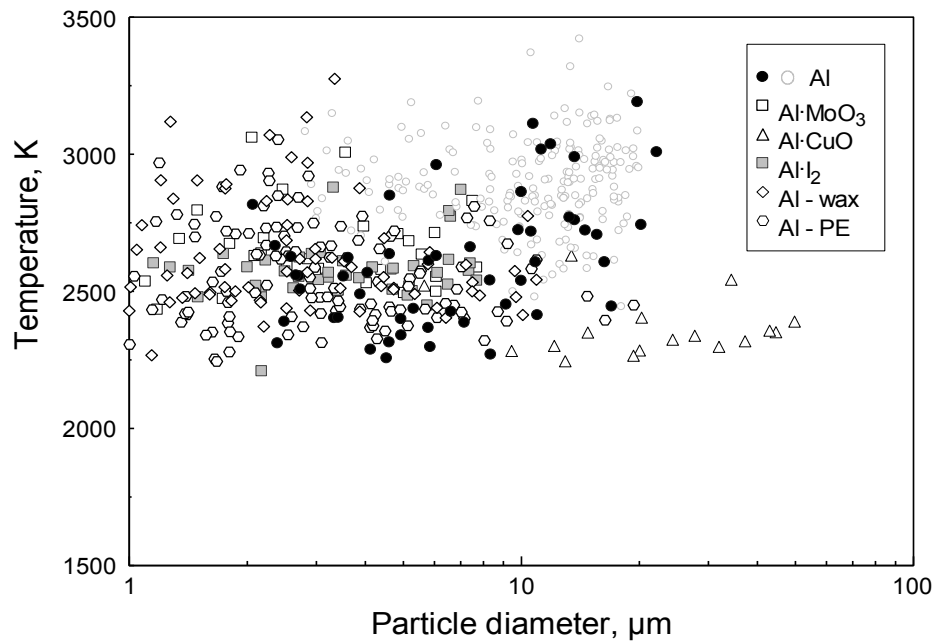


Fig. 11. Average combustion temperatures for particles of different materials burning in air.

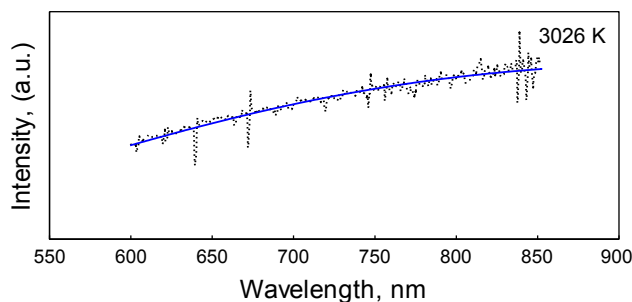


Fig. 12. Emission spectrum for pure Al powder burning in air (dashed line) fitted with a grey body emission spectrum calculated using Planck's formula (solid line) with the temperature treated as an adjustable parameter and shown in the plot.

Intensity of the characteristic molecular band emission by AlO was quantified using the following formula:

$$R_{AlO} = \frac{\left(\frac{I_{486nm}}{I_{568nm}} \right)_{exp}}{\left(\frac{I_{486nm}}{I_{568nm}} \right)_{bb}}$$

where R_{AlO} is the ratio characterizing the intensity of the molecular AlO band emission, I_x are emission intensities at the wavelength x , while the numerator values represent experimental data and denominator show theoretical intensities obtained for a black body emitter. Note that the denominator values for each data point are taken at the black body temperature equal to the respective measured instantaneous particle temperature. This ratio is equal to 1 for a black body emitter at any temperature and thus allows one to assess the intensity of AlO emission for particles reacting at different temperatures. Ratio R_{AlO} is shown in Fig. 13 for different materials; the values shown are averaged following the same procedure as used for finding the average temperatures shown in Fig. 11. The AlO emission is weakest for thermite particles, Al·MoO₃ and Al·CuO. It is somewhat stronger for Al·I₂ particles. The spread among experimental points is greatest for Al-wax and Al-PE particles; whereas the AlO emission for very fine Al-hydrocarbon composite particles is rather strong. For particles greater than several microns, AlO emission is certainly most significant for pure Al.

No data for Al·B·I₂ powders are shown in both Figs. 11 and 13, for which emission produced by B-O species interfered with the AlO emission and made it impossible to quantify the flame temperatures and AlO emission ratios.

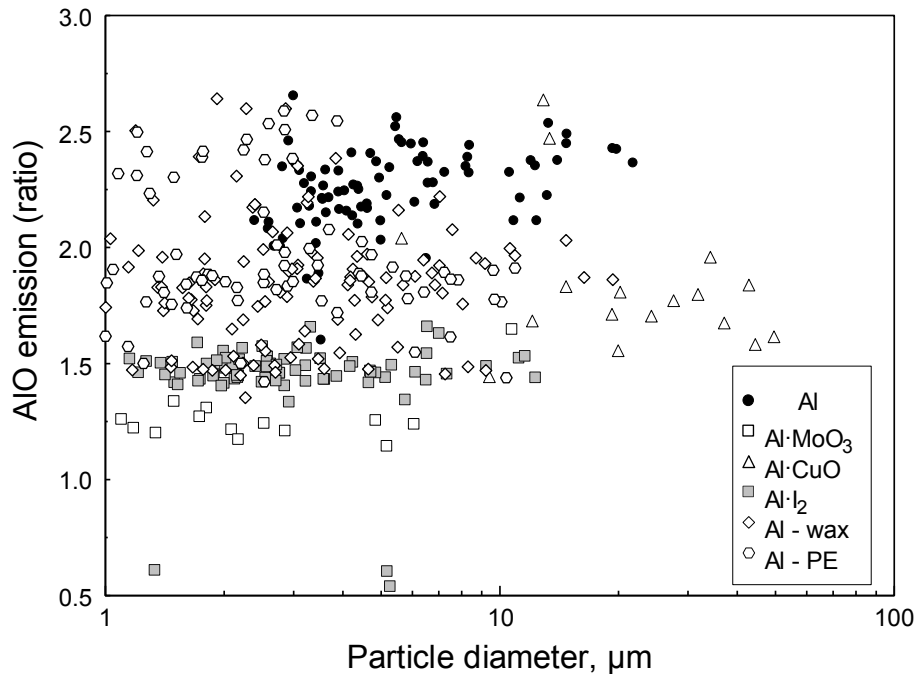


Fig. 13. Average ratios R_{Al} measuring intensity of the molecular AlO emission for particles of different materials burning in air.

Discussion

The motivation for development of many novel Al-based reactive materials is to reduce Al ignition delays. Such delays are known to result in agglomeration of molten Al particles in propellants causing an incomplete combustion and significant two-phase losses. They also reduce effectiveness of contribution from Al combustion in supporting the pressure wave generated by explosive charges. For all mechanically milled materials tested in this project, the ignition temperatures were substantially reduced compared to pure Al. However, it is observed, for some materials rather unexpectedly, that their combustion dynamics are quite different from that of pure Al.

The differences in combustion dynamics were certainly anticipated for the nanocomposite thermite powders. Combustion is expected to be altered due to the presence of difficult to oxidize Cu and Mo in the Al·CuO and Al·MoO₃, respectively. It was also reported that Al-Cu alloys and ternary Al-Cu-oxides form in combustion of clouds of aerosolized Al·CuO powders (Stamatis et al. 2009).

For Al·MoO₃, the AlO emission is rather weak, however, the measured combustion temperatures are as high or even higher compared to the pure Al particles (see Fig. 11, where most Al·MoO₃ particles are finer than 10 μm .) This suggests that the exothermic reactions occurring at the particle surface or in its interior are more significant for Al·MoO₃ than for pure Al. In other words, it appears that the thermite reaction enables a high particle temperature despite reduced rate of Al evaporation and thus reduced rate of the vapor-phase combustion. It is reasonable to suggest that the thermite reaction continues during the initial period of particle combustion, when the ramp in its emission is observed following ignition, as shown in Fig. 8. Once the thermite reaction is complete, the particle emission and temperature decrease and combustion continues mostly through surface oxidation of the formed composite particle. The observed spearpoints are most likely associated with phase changes in the produced ternary Al-Mo-O products.

For Al·CuO powders, the most distinct feature observed is the explosion of igniting particles. It is unlikely that the explosion is caused by the produced Cu vapors because it occurs immediately upon particle ignition, so that the thermite reaction producing Cu may not have been completed. It is suggested that the explosions are caused by oxygen release occurring when CuO begins to decompose leading to the nanocomposite thermite ignition as proposed by Sullivan and Zachariah (2010). Qualitatively, the fragments produced burn similarly to the pure Al particles. However, the combustion temperatures are substantially lower and AlO emission is weaker than for pure Al. This is likely due to the formation of Al-Cu alloys and ternary oxides (Stamatis et al. 2009) impeding the vapor phase Al combustion.

The difference in combustion dynamics between Al·I₂ and pure Al is quite surprising. It was expected that iodine would gasify early, before or immediately following ignition occurring at temperatures substantially higher than the volatilization temperatures for pure iodine, AlI₃, or even the temperatures at which the complete iodine loss was observed in thermo-gravimetric experiments with the mechanically milled powders (Zhang et al. 2010a, 2010b). However, emission traces of Al·I₂ particles demonstrate

sustained oscillations and an increasing emission intensity continuing for nearly the entire combustion event (cf. Fig. 8). The oscillatory behavior is produced when substantial vapor phase reaction exists while the burning particle contains inclusions, resulting in different evaporation rates from different regions of the particle surface (Dreizin 1999). The observed combustion pattern may suggest that iodine is being released rather slowly, while iodine-rich inclusions form in the molten, nearly pure Al droplet. The particle temperature and emission levels increase as it becomes closer in composition to the pure Al. The overall combustion times are extended and AlO emission levels are reduced compared to the pure Al, indicating a stronger effect of surface reactions for this material. While the mechanism of the delayed iodine release remains unclear, the observed behavior may be advantageous for the potential applications of this material as an additive generating biocidal combustion products. The delayed iodine release may help homogenizing the halogenated products over the larger volume and thus enhance potential exposure of the aerosolized spores and bacteria to such products. Following the same logic, the very long burn times observed for ternary, Al·B·I₂ composite may be similarly beneficial for the same types of applications. The low intensity of the observed Al·B·I₂ streaks suggests that these materials burn at a substantially lower temperature than Al and other composites tested in this project. The streaks shown in Fig. 7 are also thin, suggesting absence of the vapor-phase reactions.

Both Al-wax and Al-PE powders exhibit wide, bright streaks suggesting significant vapor-phase reaction continuing through the entire particle combustion event. As for Al·I₂, this effect is surprising. The evaporation of wax or polyethylene was expected to occur quite early following the particle ignition. This release of gaseous fuel was expected to cause fragmentation of the prepared particles, leading to in-situ generation of very fine Al flakes. However, this was not the combustion behavior observed in experiments. As for Al·I₂, the entire burning event appears to be affected by slow, consistent release of the volatile species, resulting in emission oscillations occurring with a decreasing amplitude and increasing overall emission intensity. The increased intensity of the vapor-phase reaction compared to other materials (visible from wide emission streaks in Fig. 7) is likely due to the combustion of the released hydrocarbon fuels, interfering with the aluminum combustion. The combustion temperatures, especially for finer composite particles, are very close to or even higher than those for pure Al. Thus, fine composite Al-hydrocarbon powders may combine the Al combustion dynamics with an enhanced ignition behavior.

Finally, it is interesting to note that the effect of particle size on the burn time was very weak for the micron-sized Al particles as well as for all other fine reactive materials particles studied in this project. If these results were attempted to be modeled using the conventional $\tau \sim D^n$ law, the exponent $n \ll 1$ would be obtained for all materials. It is hypothesized that a weak apparent effect of particle size on its burn time is associated with the changes in the heat and mass transfer for the fine particles considered in this research. More specifically, diameters of micron-sized particles approach the mean free path of the gas molecules (close to 1 μm at about 3000 K), so that the transport processes switch from continuous to free molecular regimes. Describing this change in the transport processes in the spirit of the Fuchs model (Fuchs, 1964), a thin layer is formed around the particle (referred to as Knudsen or Langmuir layer), in which the heat and mass transfer occur by free-molecular regime. In a way, this is equivalent to setting up

an insulating vacuum layer between the particle and surrounding gas. Importantly, the thickness of this “insulating” layer is close to the gas molecule mean free path and does not substantially depend on the particle size. Thus, the ratio of the Knudsen layer thickness to the particle radius will increase for smaller particles, resulting in an effective reduction in the respective heat and mass transfer rates. This change in the heat and mass transport rates is expected to cause reduction in the burn rate (and thus longer burn times) for finer particles; it can also affect the quenching conditions resulting in different reaction completeness for particles of different dimensions burning in the same environment. Further investigation of the related processes is currently in progress.

Conclusions

A recently developed experimental technique for ignition of metallic particles in the CO₂ laser beam with simultaneous measurement of particle dimensions using a scattered laser light intensity is useful for characterization of combustion dynamics of a wide range of metal-based reactive materials. For all materials tested, the effect of particle sizes on their burn times is very weak for the micron-sized particles. This weak effect is likely associated with the change from continuum to free molecular transport processes that is important for the particles in the size range of about 1 – 20 µm. New reactive materials prepared by mechanical milling and demonstrating reduced ignition delays and lowered ignition temperatures do not necessarily have burn rates higher or combustion temperatures greater than pure aluminum particles. In fact, for all composite materials explored in this study, the role of vapor-phase combustion is reduced compared to pure Al, as suggested by the reduced combustion temperatures and AlO emission intensity. Materials containing a volatile component stabilized in the metal structure by mechanical milling (iodine, wax or polyethylene, in this effort) do not release this component rapidly. Instead, the release of the volatile component occurs during the entire combustion event altering the environment near the particle surface; such composite particles burn with distinct oscillatory patterns most likely caused by formation of inclusions in the molten aluminum. For the nanocomposite thermites, the Al-metal oxide reaction can cause a continuous and relatively slow increase in the particle emission and temperature (Al·MoO₃) or disruption of the ignited particles (Al·CuO).

References

- Badiola, C. and Dreizin, E. L. (2012), 'On weak effect of particle size on its burn time for micron-sized aluminum powders', *Combustion Science and Technology*. (under review)
- Badiola, C., Gill, R. J., and Dreizin, E. L. (2011), 'Combustion characteristics of micron-sized aluminum particles in oxygenated environments', *Combustion and Flame*, 158 (10), pp. 2064-2070.
- Beckstead, M. W. (2005), 'Correlating aluminum burning times', *Combustion, Explosion and Shock Waves*, 41 (5), pp. 533-546.
- Cashdollar, K. L. (2000), 'Overview of dust explosibility characteristics', *Journal of Loss Prevention in the Process Industries*, 13 (3-5), pp. 183-199.
- Dokhan, A., Price, E.W., Seitzman, J.M., and Sigman, R.K. (2002), 'The effects of bimodal aluminum with ultrafine aluminum on the burning rates of solid

- propellants', in J. H. Chen and M. D. Colket (eds.), (2 edn., Twenty-Ninth International Symposium on Combustion Hokkaido University Sapporo Japan, 29; Sapporo), pp. 2939-2945.
- Dreizin, E. L. (1999), 'On the mechanism of asymmetric aluminum particle combustion', *Combustion and Flame*, 117 (4), pp. 841-850.
- Dreizin, E. L. (2000), 'Phase changes in metal combustion', *Progress in Energy and Combustion Science*, 26 (1), pp. 57-78.
- Dreizin, E. L., Shoshin, Y.L., Mudryy, R.S., and Hoffmann, V.K. (2002), 'Constant pressure flames of aluminum and aluminum-magnesium mechanical alloy aerosols in microgravity', *Combustion and Flame*, 130 (4), pp. 381-385.
- Dreizin, E. L. and Schoenitz, Mirko (2009), 'Nano-composite energetic powders prepared by arrested reactive milling'. US Patent 7,524,355.
- Ermoline, A., Schoenitz, M., and Dreizin, E. L. (2011), 'Reactions leading to ignition in fully dense nanocomposite Al-oxide systems', *Combustion and Flame*, 158 (6), pp. 1076-1083.
- Frost, D. L., Goroshin, S., Levine, J., Ripley, R., Zhang, F. (2006), 'Critical conditions for ignition of aluminum particles in cylindrical explosive charges', (Shock Compression of Condensed Matter - 2005: Proceedings of the Conference of the American Physical Society Topical Group on Shock Compression of Condensed Matter, 845 II; Baltimore, MD), pp. 972-975.
- Fuchs, N.A. (1964) 'The Mechanics of Aerosols'. Oxford: Pergamon Press. (Dover Publications, New York, 1989)
- Gill, R. J., Mohan, S., and Dreizin, E. L. (2009), 'Sizing and burn time measurements of micron-sized metal powders', *Review of Scientific Instruments*, 80 (6), pp. 064101-1 – 064101-7.
- Gill, R. J., Badiola, C., and Dreizin, E. L. (2010), 'Combustion times and emission profiles of micron-sized aluminum particles burning in different environments', *Combustion and Flame*, 157 (11), pp. 2015-2023.
- Goroshin, S., Fomenko, I., and Lee, J. H. S. (1996), 'Burning velocities in fuel-rich aluminum dust clouds', *Symposium (International) on Combustion*, 26 (2), pp. 1961-1967.
- Grinshpun, S. A., Li, C., Adhikari, A., Yermakov, M., Reponen, T., Schoenitz, M., Dreizin, E.L., Hoffmann, V., and Trunov, M. (2010), 'Method for studying survival of airborne viable microorganisms in combustion environments: Development and evaluation', *Aerosol and Air Quality Research*, 10 (5), pp. 414-424.
- Huang, Y., Risha, G.A., Yang, V., and Yetter, R.A. (2009), 'Effect of particle size on combustion of aluminum particle dust in air', *Combustion and Flame*, 156 (1), pp. 5-13.
- Krier, H. and Glumac, N. (2009), 'On the transition from classical diffusion-limited combustion behavior for fine and ultrafine aluminum particles', *International Journal of Energetic Materials and Chemical Propulsion*, 8 (1), pp. 71-80.
- Luman, J. R., Wehrman, B. Kuo, K. K., Yetter, R. A., Masoud, N. M., Manning, T. G., Harris, L. E., and Bruck, H. A. (2007), 'Development and characterization of high performance solid propellants containing nano-sized energetic ingredients', (31st International Symposium on Combustion, 31 II; Heidelberg), pp. 2089-2096.

- Lynch, P., Krier, H., and Glumac, N. (2010) 'Emissivity of aluminum-oxide particle clouds: Application to pyrometry of explosive fireballs' *Journal of Thermophysics and Heat Transfer* 24 (2), pp. 301-308.
- Meda, L., Marra, G., Galfetti, L., Severini, F., and De Luca, L. (2007), 'Nano-aluminum as energetic material for rocket propellants', *Materials Science and Engineering C*, 27 (5-8 SPEC. ISS.), pp. 1393-1396.
- Mench, M. M., Kuo, K. K., Yeh, C. L., and Lu, Y. C. (1998), 'Comparison of Thermal Behavior of Regular and Ultra-fine Aluminum Powders (Alex) Made from Plasma Explosion Process', *Combustion Science and Technology*, 135 (1-6), pp. 269-292.
- Mohan, S., Trunov, M. A., and Dreizin, E. L. (2009), 'On possibility of vapor-phase combustion for fine aluminum particles', *Combustion and Flame*, 156 (11), pp. 2213-2216.
- Price, E. W. (1984), *Combustion of Metalized Propellants*, 90, pp. 479-513.
- Sambamurthi, J. K., Price, E.W., and Sigman, R. K. (1984), 'Aluminum agglomeration in solid-propellant combustion', *AIAA Journal*, 22 (8), pp. 1132-1138.
- Santhanam, P. R., Hoffmann, V. K., Trunov, M. A., and Dreizin, E. L. (2010), 'Characteristics of aluminum combustion obtained from constant-volume explosion experiments', *Combustion Science and Technology*, 182 (7), pp. 904-21.
- Schoenitz, M., Dreizin, E. L., and Shtessel, E. (2003), 'Constant volume explosions of aerosols of metallic mechanical alloys and powder blends', *Journal of Propulsion and Power*, 19 (3), pp. 405-412.
- Shoshin, Y. and Dreizin, E. (2002), 'Production of well-controlled laminar aerosol jets and their application for studying aerosol combustion processes', *Aerosol Science and Technology*, 36 (9), pp. 953-962.
- Stamatis, D., Jiang Z., Hoffmann V.K., Schoenitz M., and Dreizin E.L. (2009), 'Fully dense, aluminum-rich Al-CuO nanocomposite powders for energetic formulations', *Combustion Science and Technology*, 181 (1), pp. 97-116.
- Sullivan, K. and Zachariah, M. R. (2010), 'Simultaneous pressure and optical measurements of nanoaluminum thermites: Investigating the reaction mechanism', *Journal of Propulsion and Power*, 26 (3), pp. 467-472.
- Suryanarayana, C. (2001) 'Mechanical alloying and milling', *Progress in Materials Science* 46, pp. 1-184.
- Tang, F. D., Goroshin, S., Higgins, A., and Lee, J. (2009), 'Flame propagation and quenching in iron dust clouds', (32nd International Symposium on Combustion, 32 II; Montreal, QC), pp. 1905-1912.
- Trunov, M. A., Schoenitz, M., and Dreizin, E. L. (2006), 'Effect of polymorphic phase transformations in alumina layer on ignition of aluminium particles', *Combustion Theory and Modelling*, 10 (4), pp. 603-623.
- Umbrajkar, S. M., Seshadri S., Schoenitz, M., Hoffmann, V.K., and Dreizin E.L. (2008), 'Aluminum-rich Al-MoO₃ nanocomposite powders prepared by arrested reactive milling', *Journal of Propulsion and Power*, 24 (2), pp. 192-198.
- Ward, T. S., Trunov, M.A., Schoenitz, M., and Dreizin, E.L. (2006), 'Experimental methodology and heat transfer model for identification of ignition kinetics of powdered fuels', *International Journal of Heat and Mass Transfer*, 49 (25-26), pp. 4943-4954.

- Yetter, R. A., Risha, G. A., and Son, S. F. (2009), 'Metal particle combustion and nanotechnology', (32nd International Symposium on Combustion, 32 II; Montreal, QC), pp. 1819-1838.
- Zhang, S., Schoenitz, M., and Dreizin, E. L. (2010a), 'Iodine release, oxidation, and ignition of mechanically alloyed Al-I composites', *Journal of Physical Chemistry C*, 114 (46), pp. 19653-19659.
- Zhang, S., Schoenitz, M., and Dreizin, E. L. (2010b), 'Mechanically alloyed Al-I composite materials', *Journal of Physics and Chemistry of Solids*, 71 (9), pp. 1213-1220.

CHAPTER 5: ON WEAK EFFECT OF PARTICLE SIZE ON ITS BURN TIME FOR MICRON-SIZED ALUMINUM POWDERS

Introduction

Understanding the dynamics of aluminum combustion is important to predict performance of many aluminized energetic formulations, including propellants, pyrotechnics, and explosives (Price and Sigman 2000; Dokhan et al. 2002; Yetter et al. 2008). A data compilation from multiple experiments for relatively coarse aluminum particles ($20 \mu\text{m}$ and greater) is presented in by Beckstead (2005), who organized the data to establish a trend for the particle burn time t as proportional to D^n , where D is the particle diameter. For a spherically symmetric, diffusion-limited combustion, $n=2$ (Glassman and Yetter 2008), while for aluminum particles, the values of $1.5 < n < 1.8$ are proposed based on the published experiments (Beckstead 2005).

Data compiled by Beckstead (2005) exhibit significant scatter between relatively few experiments characterizing fine ($<25 \mu\text{m}$) particles. While such fine particles are the most useful in practical configurations, experiments characterizing their burn rates directly are more difficult than for coarser particles investigated in most of the earlier studies. When the particle size becomes comparable to the molecular mean free path, the heat and mass transfer processes are no longer described in the framework of continuum formulation, suitable for coarser particles. Transition to the free-molecular transport processes as well as an increasing role of surface kinetics-controlled processes suggest that the burn rate trends established for coarser particles may not remain valid as the particle size decreases.

Indeed, in several recent studies (Shoshin and Dreizin 2003; Lynch et al. 2009; Badiola et al. 2011), combustion of fine Al powders was addressed experimentally and the values of n close to 1 or even substantially smaller than 1 were reported. The reported very small values of n indicative of a very weak effect of particle size on its burn time are somewhat surprising. The values of n close to 0.3 were determined in experiments investigating single, micron-sized aluminum particles ignited by a CO₂ laser beam and in the shock tube experiments (Shoshin and Dreizin 2003; Lynch et al. 2009; Badiola et al. 2011). In this paper, new experiments with CO₂ laser-ignited Al particles are performed, the experimental technique is further modified and refined to process new and validate previous measurements, and to generate additional data, characterizing combustion dynamics of fine aluminum particles. The results are presented and discussed in context of their compatibility with the existing trends reported for Al particle combustion.

Technical approach

The experimental apparatus described in recent papers (Gill et al. 2010; Badiola et al. 2011) was modified to better resolve sizes and burn times for finer particles ($<10 \mu\text{m}$) and to improve combustion temperature measurements. Further, data processing methodology was refined to reduce subjectivity in selecting the subset of particle emission pulses representing the complete combustion events.

Experimental apparatus and methodology

A simplified schematic diagram of the experimental setup described in detail elsewhere (Gill et al. 2009; Gill et al. 2010; Badiola et al. 2011) is shown in Fig. 1, and only a brief summary is included here for completeness.

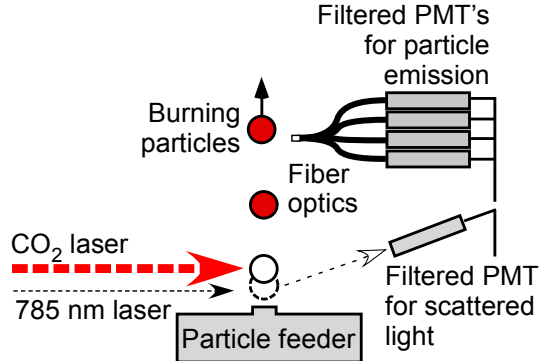


Figure 1. Experimental apparatus characterizing combustion dynamics and temperatures of micron-sized metal particles.

A vertically rising laminar gas jet issues from a nozzle of an electrostatic aerosol generator and carries particles creating a low number density, particle jet. The jet crosses two laser beams as shown in Fig. 1. Particles first pass through an auxiliary laser beam of a 785 nm, 30 mW laser generating a scattered light pulse, for which the amplitude is proportional to the square of the particle diameter. The scattered pulse amplitudes are measured using the scattered light photomultiplier tube (PMT). Particles then cross a CO₂ laser beam which heats them to ignition. A quad-furcated fiber-optics bundle collects light emission from incandescent burning particles, with each branch leading to a PMT equipped with an interference filter. The filter wavelengths were 589, 568, 532, and 486 nm. The filtered PMT's are used for color pyrometry (using emissions at 589 and 532 nm) and to track characteristic molecular emission of AlO (486 nm), commonly considered as an indicator of the vapor-phase combustion for aluminum. Calibration of the pyrometer is done using a current-stabilized tungsten lamp coupled with an irradiance-calibrated spectrometer.

Intensity of the characteristic molecular band emission by AlO is described using a ratio R_{AlO} :

$$R_{AlO} = \frac{\left(\frac{I_{486nm}}{I_{568nm}} \right)_{exp}}{\left(\frac{I_{486nm}}{I_{568nm}} \right)_{bb}}$$

where I_x are emission intensities at the wavelength x , and the numerator and denominator respectively represent experimental data and theoretical emission intensities for a black body at the temperature equal to the respective measured instantaneous particle temperature. This ratio is equal to 1 for a black body emitter at any temperature and it was observed to be equal to 1 when signals produced by a tungsten lamp were processed.

Spherical aluminum powder, nominally 10-14 μm , used in this project is from Alfa Aesar (catalog # 41001, 98% pure). The experiments are conducted in ambient air at room temperature with the average particle jet velocity close to 0.6 m/s.

In a typical experiment, a particle jet is fed through the laser beams for about 10 s; during that time, a few thousand particles cross lasers generating multiple scattered and emission light pulses. Two separate pulse sequences are captured by the data acquisition system, one representing the scattered light and another, shifted in time, representing filtered emission light pulses. The time shift between the scattered and emission pulses is equal to the time the particles travel between the two laser beams. The data processing includes:

- Removal of overlapping or close pulses produced by particles that could have affected each other during ignition and combustion,
- Matching each scattered light pulse with its respective set of the filtered emission light pulses, thus correlating particle size and emission for each particle, and finally,
- Selecting a subset of pulses among the matched scattered and emission pulses representing particles ignited just after exiting the CO₂ laser beam. Many particles could ignite and partially burn while in the CO₂ laser beam or could be heated and cooled, without any combustion; pulses produced by all such particles must be discarded from the data analysis.

Compared to the previous work (Gill et al. 2009; Gill et al. 2010; Badiola et al. 2011), modifications were made in both hardware setting and data processing as described below.

Modifications of experiment and data processing

While the volumetric particle size distribution for the used Al powder peaks at about 14 μm , most of the matched sets of emission and scattered light pulses are generated by finer particles, in the size range of 1 – 10 μm . In previous experiments, the dynamic range settings of the PMT's were adjusted to capture the broadest range of particles representing the powder used. However, the number of pulse subsets representing particles exceeding $\sim 15 \mu\text{m}$ remained small. At the same time, the broad dynamic range could have caused increased noise and errors in correctly identifying the sizes and respective burn times for the smallest particles, for which the amplitudes of scatter and emission pulses were close to the noise levels in the respective data acquisition channels. In the present experiments, the noise levels were reduced by replacing AC/DC converters powering PMT powder supplies with DC batteries. Further, the PMT dynamic range settings were changed to focus on the finest particles, while allowing saturation from the relatively few pulses generated by the coarsest particles present in the powder tested. Measurements with the dynamic range setting optimized for a wider range of particle sizes, similar to those used in earlier work were also performed to establish the sensitivity of the final results to these settings.

The second important modification was related to the data processing, specifically, to selection of the subset of matched pulses representing the complete combustion events for Al particles. Previously, this selection was made by identifying the longest emission pulses (Gill, et al. 2009; Gill et al. 2010; Badiola et al. 2011), which were assumed to represent combustion events in which reaction was not accelerated by the additional laser heating. In this work, the subset of pulses selected based on their length was compared to a subset of pulses selected based on their specific shapes. The shape analysis took into

account that for the particles heated by the CO₂ laser and cooled after exiting from the laser beam, emission pulses peak at or around the time the particles exit from the laser beam. Similarly, for particles heated and ignited while still in the laser beam, the emission signal is strong when the particles exit from the laser. Conversely, for the particles that ignite just after exiting from the laser beam, the emission intensity upon exiting the laser is expected to be weak, while it is expected to increase substantially at a later time when the particle is burning.

Based on this reasoning, a new methodology for selecting pulses of interest was proposed. The emission pulse amplitude at the instant the particle left the CO₂ laser beam, I_e , was related to the peak amplitude for the same pulse, I_{max} , as illustrated in Fig. 2.

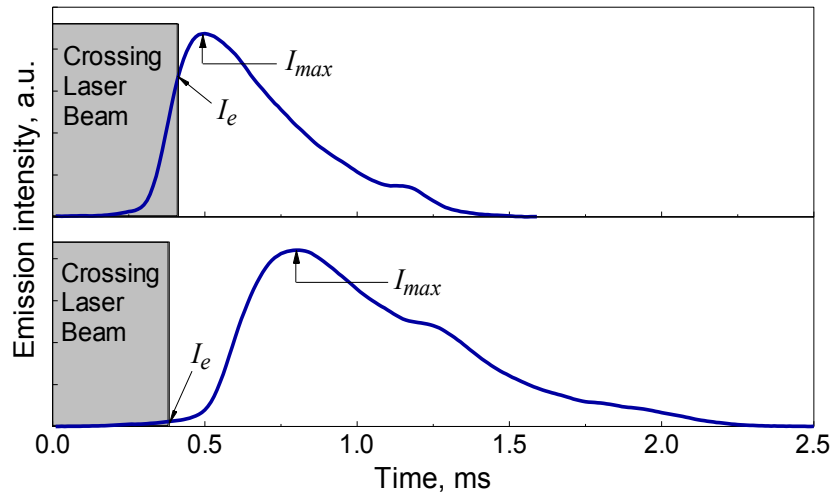


Figure 2. Selection of particle emission pulses based on their shapes. The top plot shows a pulse produced by a particle that was burned while in the laser beam, so the emission intensity at the instant it leaves the beam, I_e is comparable to the peak intensity, I_{max} . The bottom plot shows particle that ignites after exiting from the laser beam.

If the I_e/I_{max} ratio was sufficiently small (~ 0.01) the particles were considered to ignite just after exiting the laser beam, so that their respective emission pulses were treated as representing the true burn times. Other pulses were discarded. The instant when the particles exit the CO₂ laser beam was identified based on the time shift between the scattered and emission pulses, distance between the lasers (1 mm), effective heating diameter of the CO₂ beam (0.165 mm) (Mohan et al. 2008), and particle jet velocity.

Finally, the optical pyrometry employing two filtered emission pulses used previously (Gill et al. 2010; Badiola et al. 2011) was supplemented by an integrated temperature measurement from a range of burning aluminum particles. An irradiance calibrated spectrometer (StellarNet EPP2000) with an integration time of 25-30 s captured emission from multiple burning particles. The recorded spectrum was matched with that of a gray body emitter predicted using Planck's equation (Holman 2009) and treating emissivity and temperature as adjustable parameters. For these measurements, the fiber optics inlet of the spectrometer was positioned to capture emission from the brightest zone produced by multiple burning particles.

Results

Particle size distributions and individual emission traces

Figure 3 shows particle size distributions for the used Al powder; three measurements represent the output of a commercial particle size analyzer (Beckman-Coulter LS230; bars) and the in-situ measurements using old settings for the PMT dynamic ranges (squares) and new settings, emphasizing signals produced by the finest particles (circles).

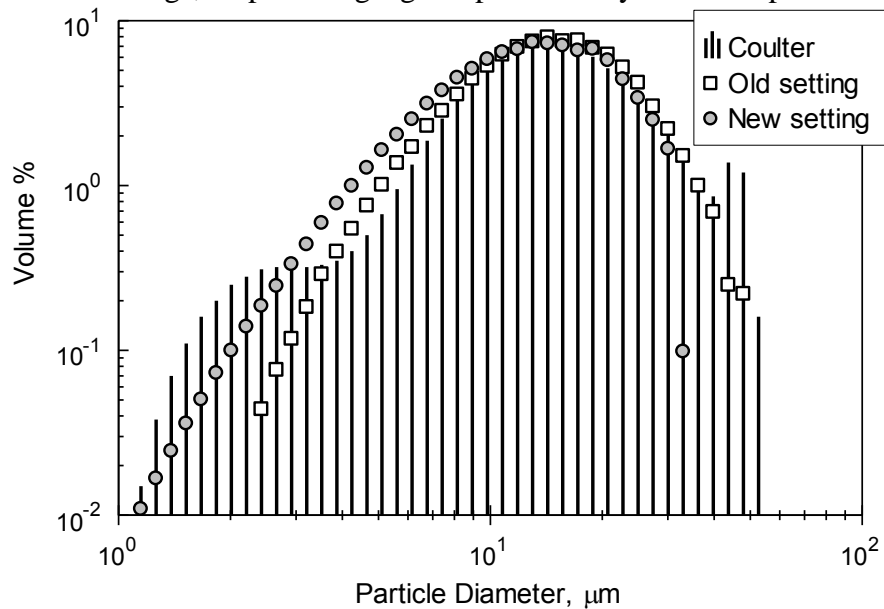


Figure 3. Particle size distribution comparison from a commercially determined device (Coulter) and two laser light scatter experiments.

The measurement with a PMT dynamic range adjusted to cover a broader range of particle sizes (“old setting” in Fig. 3) does not identify particles less than 2.5 μm and generally, appears to underestimate the number of small particles. The measurement with the PMT dynamic range adjusted to better capture fine particles (“new setting” in Fig. 3) tracks particles as small as 1.1 μm . At the same time, the “old setting” enables one to track effectively the entire size distribution (the coarsest particle of $\sim 50 \mu\text{m}$, while the measurement with “new setting” stops being accurate for particles greater than 30 μm . Despite relatively minor differences, the two size distributions measured with “old” and “new” settings were generally consistent between themselves and compared well with the particle size distribution obtained using a commercial instrument.

Individual particle emission traces, such as reported in ref. (Gill et al. 2010; Badiola et al. 2011), were analyzed for experiments with both “old” and “new” settings and were found to be qualitatively similar to each other and to those presented earlier. Features such as the initial peak, decay, and plateau of the signals were reproducible. The flame temperatures corresponding to the three phases of combustion discussed by Badiola et al. (2011) were also similar for particles of similar sizes.

Effect of particle size on its burn time, temperature, and AlO emission

Reproducing the previously used approach for selection of the longest emission pulses, the range measured particle sizes was broken into several bins. For each size bin, the emission pulses were identified with durations in the top 2.5%; these pulses were assumed to represent the complete combustion events, while all the other shorter pulses were discarded. Effect of the particular size bins on the final selection of the emission pulses was explored by choosing three different sets of bins described in Table 1. The bin sets 1 and 3 were selected to closer examine the recorded emission times for finer particles; while the bin set 2 reproduced what was used in the previous work (Badiola et al. 2011) to cover a broader particle size range.

Table 1. Size bins used to select longest emission pulses

Set #	Size Bins (μm)			
1	1.5-3	3-5	5-7	7-11
2	2-6	6-10	10-14	14-20
3	1-2.5	2.5-5	5-7.5	7.5-10

Emission times down-selected using different bin sets are shown in Fig. 4 as a function of the particle diameter. Many particles are selected using either of the bin sets. Generally, the trends produced by pulses down-selected using different bin sets are consistent with one another. In addition to the pulses selected based on the longest emission times within a particle size bin, emission pulses were down-selected based on their shape processing as discussed above. The pulses, for which the emission signal at the instant when the particle exited the CO₂ laser beam was less than 0.01 of its maximum, are shown as squares. It is noted that substantial number of squares coincides with the points representing “longest pulses”. At the same time, quite a few pulses represented by squares are characterized by somewhat shorter emission times as compared to those implied by the “longest pulse” selection. However, the overall weak trend ($n \ll 1$ in the $t \sim D^n$ expression) for the particle size effect on its burn time is confirmed for all methods used to select emission pulses representing the complete combustion events. For reference, small gray circles in Fig. 4 show the data reported previously. The previous measurements by Badiola et al. (2011) correlate well with the present data despite substantial changes in both hardware setting and data processing methodology.

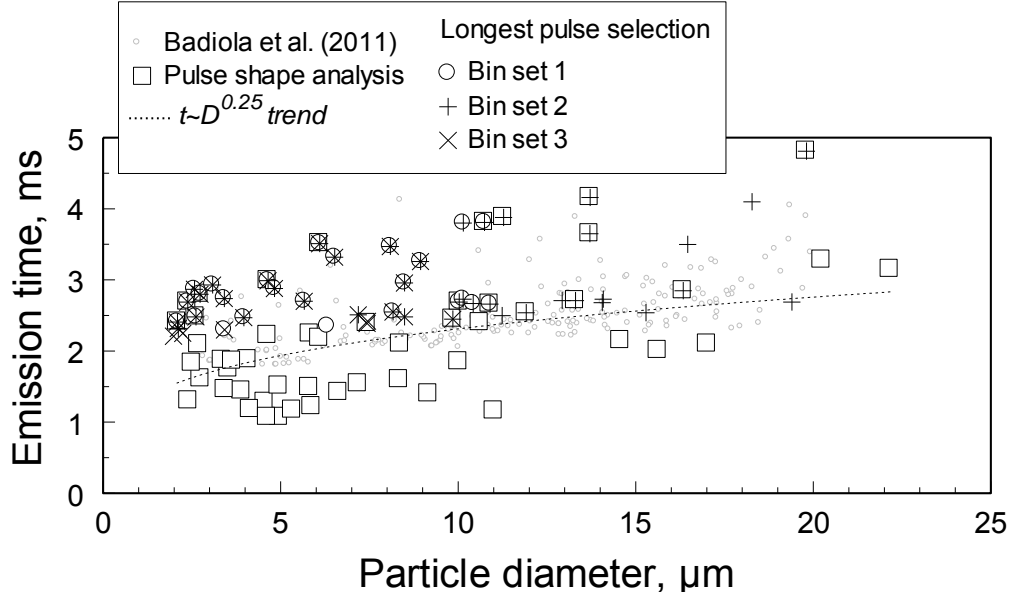


Figure 4. Emission times down-selected by different methods to represent burn times as a function of particle size for aluminum particles in air.

The processing method relying on comparison of the emission levels at the instant the particles exit from the CO₂ beam and the peak emission is suggested to be most useful, because it involves only one arbitrarily selected parameter – the ratio of the two instantaneous emission signals. It is completely independent on the particle size measurement, so that possible errors in the size cannot affect the pulse selection. For the points shown in Fig. 4 and selected using this method, the effect of particle size on burn time can be approximated by a $t \sim D^{0.25}$ trend, as shown by dotted line in Fig. 4. For clarity, further discussion and analysis only focus on the pulses down-selected use that processing technique.

Average particle temperatures obtained using down-selected emission pulses are shown in Figure 5. As in the previous work, the temperature averaging was performed when the emission signal exceeded one half of its maximum value. The results show that the average temperatures reach an upper limit of ~3000 K for coarser particles, similar to the previous report (Badiola et al. 2011). Only slightly lower temperatures are identified for finer particles, a subject of specific focus for the present experiments.

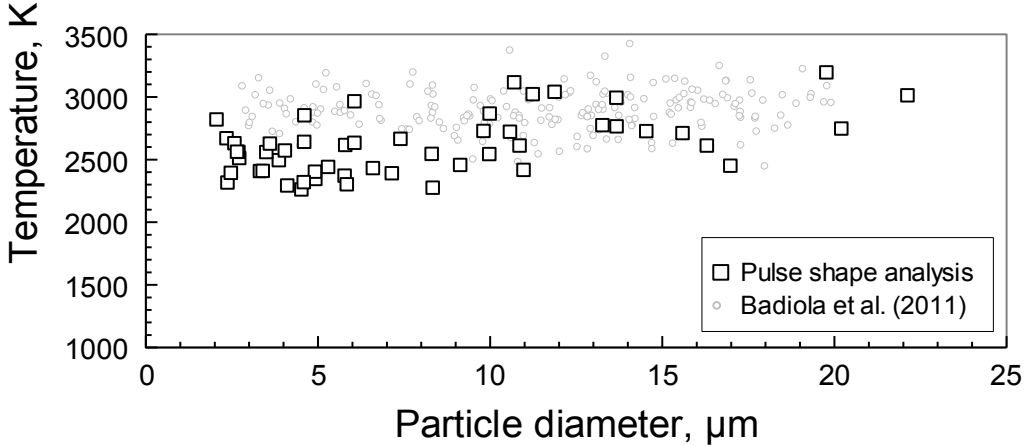


Figure 5. Average temperatures for Al particles burning in air as a function of the particle diameter.

A portion of the measured spectrum obtained integrating emission from multiple burning particles is shown in Figure 6. This portion excludes the part of the spectrum heavily affected by the molecular AlO bands, which would cause a substantial error in finding the emitter's temperature by matching its spectrum with that of a grey body. The integrated spectrum is dominated by the strongest individual emitters, which are larger particles and particles burning at the highest temperatures.

The grey body emission calculated to match the measured spectrum by adjusting the emitter's temperature, is also shown in Fig. 6. The temperature is found to be 3026 K for the calculated spectrum to match the experimental one. It is effectively the same as the upper-limit temperature identified by the color pyrometry in both previous and current experiments.

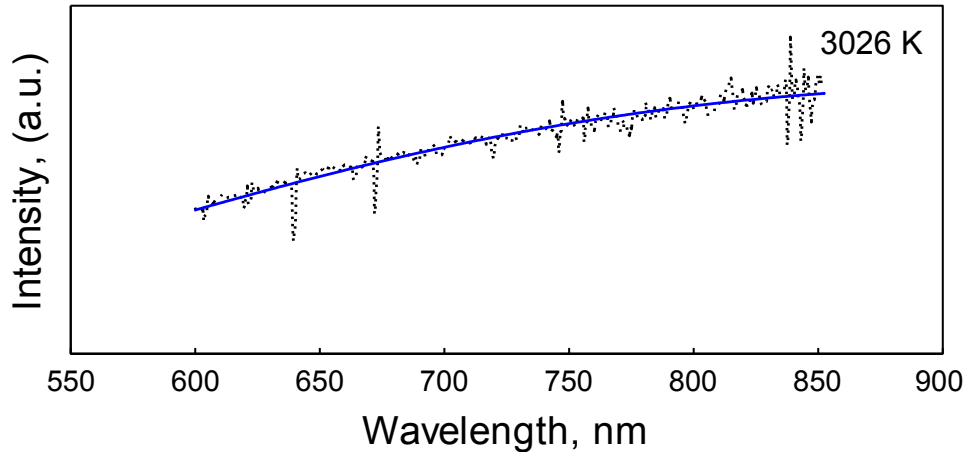


Figure 6. Multi-particle combustion spectrum (dashed line) fitted with a grey body emission spectrum calculated using Planck's formula (solid line) with the temperature treated as an adjustable parameter and shown in the plot.

Intensity of AlO emission as a function of particle size is shown in Fig. 7. Ratio R_{AlO} is shown for particles selected following both described selection algorithms: selecting longest emission pulses (using different sets of size bins, as described above, e.g., cf. Fig. 4), and selecting particles using pulse shape processing. As temperatures shown in Fig.

5, for each emission pulse, the ratios shown in Fig. 7 are averaged over the time when the measured emission exceeds one half of its maximum value. All ratios are substantially greater than 1, indicating non-negligible vapor phase reactions for particles of all sizes. For the particles selected using pulse shape analysis, a trend indicating a somewhat lower AlO emission intensity for finer particles is distinguished.

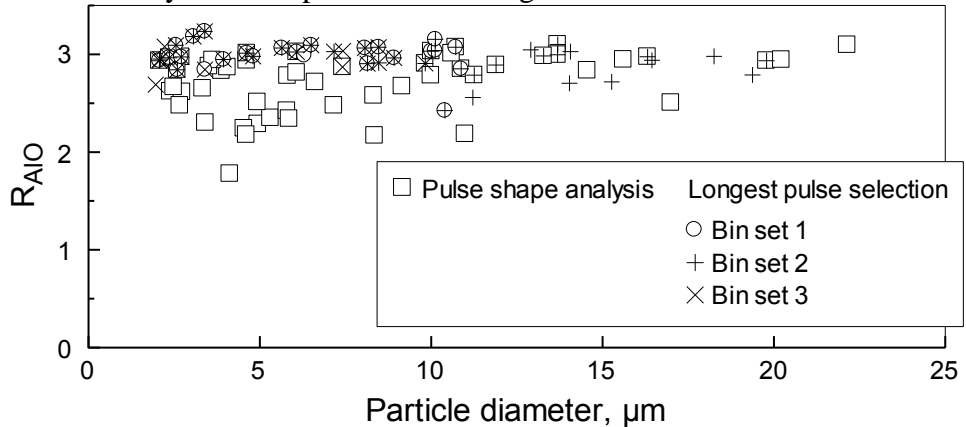


Figure 7. Average values of R_{AlO} for aluminum particles burning in air as a function of the particle diameter.

Discussion

The present experiments conducted using the modified settings and data processing methodologies have generally confirmed the previously reported trends describing burn times and temperatures of micron-sized aluminum particles as a function of their sizes. The data available from experiments also include temperature histories and relative intensity of the AlO molecular emission for the burning particles.

Results show that even the finest particles used in the present experiments burned at very high temperatures; it is further shown that the AlO molecular emission is fairly significant for particles of all sizes. These results appear to contradict the notion that as the particle size decreases, the combustion regime, rate limited by vapor-phase diffusion is replaced by a much slower surface reaction controlled by chemical kinetics of heterogeneous processes. The transition from diffusion to kinetic-controlled combustion regime is suggested to occur for particles less than 20 μm (Bazyn et al., 2007; Krier and Glumac, 2009; Tanguay et al., 2009). Tanguay et al. (2009) argue that for kinetically limited reactions, the particle temperature does not exceed the ambient temperature, effectively suggesting that such particles cannot burn in room air. Well-known theoretical considerations that support the above ideas succinctly summarized by Tanguay et al. (2009) compare the rates described by a diffusion equation with that of a chemical kinetics. However, such comparisons do not account for changes in the mass and heat transfer processes occurring when the particle size becomes comparable with the mean free path of the gas molecule. These changes result in significantly reduced rates of heat and mass transfer to the particle surface.

In other words, in addition to transition from the vapor-phase diffusion to surface kinetic-controlled reaction regime, another transition, from continuum to free molecular heat and mass transfer regime occurs when the particle size decreases. Theoretical analysis of the resulting configuration is not straightforward. Present experimental results indicating that the high-temperature combustion of fine aluminum particles in cold

ambient air is possible, and that the vapor-phase reactions for such particles are significant, should encourage respective theoretical developments. Note that the present experimental results are consistent with other recent measurements, e.g., by Lynch et al. (2010), suggesting that vapor-phase reactions are non-negligible even for nano-sized Al powders.

As a very preliminary theoretical interpretation of the present data, the measured temperature histories can be used to estimate the heat losses from particles burning in cold air; such heat losses integrated over the total combustion time can be compared to the expected heat of combustion for these particles. Thus, reaction completeness can be evaluated for particles of different sizes considered in the present experiments.

The heat losses from the burning micron-sized particles were estimated using a simplified model for the transition heat transfer regime discussed by Mohan, et al. (2009). For the purpose of this estimate, the particle is assumed to react on or in immediate vicinity of its surface, so that the measured temperature is assigned to the particle surface directly. Existence of a standoff flame with the diameter noticeably greater than the particle diameter would increase the surface from which the heat is removed and thus the rate of heat losses; thus the present estimate is valid for the smallest possible heat losses from the flame and, respectively, lower bound for the reaction completeness. The rate of heat losses \dot{Q}_E signifies the heat removal from the particle to the environment; its value is calculated using the transition model considering the free-molecular heat transfer within the Langmuir layer adjacent to the particle, and continuum thermal conductivity outside of it. For the Langmuir layer with thickness δ , the heat removal from it to the surrounding environment is expressed as:

$$\dot{Q}_E = q_{out} = 4\pi \left[\frac{d_p}{2} + \delta(T_\delta) \right] \int_{T_\delta}^{T_E} \lambda_g(T) dT \quad (1)$$

where d_p is the particle diameter, T_δ is the temperature at the Langmuir layer boundary, T_E is the temperature of the surrounding environment, and $\lambda_g(T)$ is the temperature dependent thermal conductivity of gas surrounding the burning particle.

The rate of heat transfer between the particle surface and Langmuir layer is given as:

$$\dot{Q}_E = q_{in} = \alpha \pi d_p^2 P_E \sqrt{\frac{k_B T_\delta}{8\pi m_g}} \frac{\gamma^* + 1}{\gamma^* - 1} \left(1 - \frac{T_s}{T_\delta} \right) \quad (2)$$

where α is the accommodation coefficient, P_E is the environment pressure, k_B is the Boltzmann constant, m_g is the mass of the gas molecule, γ^* is the averaged adiabatic index of gas, and T_s is the particle surface temperature (taken from experimental data). As shown in Eqs. (1) and (2), both heat transfer rates within and outside Langmuir layer are equal to each other and equal to \dot{Q}_E . Solving Eqs. (1) and (3), one finds both T_δ and \dot{Q}_E (Mohan et al. 2009).

For a heterogeneously burning particle, an additional correction, \dot{Q}_{St} , for the heat transfer rate due to Stefan flow with velocity v_{St} , directed towards the particle should be accounted for (Kalinchak and Chernenko 2009):

$$\dot{Q}_{St} = v_{St} \rho_g C_g \left(\frac{T_s + T_E}{2} \right) \quad (3)$$

where ρ_g and C_g are respectively gas density and heat capacity. The velocity, v_{St} , is defined based on the rate of aluminum mass consumption, dm_{Al}/dt , as:

$$v_{St} = \frac{1}{\pi d_p^2 \rho_g} \Omega \frac{dm_{Al}}{dt} \quad (4)$$

where Ω is the stoichiometric mass ratio for the Al-oxygen reaction.

Radiation heat losses from the burning particles were neglected.

The heat balance for the burning particle was described as:

$$\dot{Q}_{Comb} = \dot{Q}_E - \dot{Q}_{St} \quad (5)$$

where \dot{Q}_{Comb} is the rate of heat generation by the burning particle. The term \dot{Q}_{Comb} is proportional to the rate of aluminum mass consumption, so that:

$$\frac{dm_{Al}}{dt} = \frac{\dot{Q}_E - \dot{Q}_{St}}{\Delta H_{ox}} \quad (6)$$

where ΔH_{ox} is the heat of oxidation for aluminum. Solving Eqs. (1-6), one can find the instantaneous rate of aluminum consumption for each recorded data point. Integrating the instantaneous rates over the entire combustion time, τ_{comb} , and using the experimental $T_s(t)$ curve (as shown by Badiola et al., 2011) one obtains the total mass of aluminum consumed in a combustion event.

$$m_{Al} = \int_0^{\tau_{comb}} \frac{dm_{Al}}{dt} dt \quad (7)$$

For the purpose of this estimate aimed to obtain the lower bound on the aluminum consumed, the particle size, d_p , is assumed to remain constant during its combustion. In reality, for heterogeneous reaction the particle size is expected to increase while Al is transferring to Al_2O_3 . This increase in particle size would increase the rate of heat losses and thus result in a greater rate of aluminum consumption.

The values of temperature dependent gas properties, ρ_g , C_g , and λ_g , were obtained using data reported in the NIST Chemistry WebBook and citing (Laesecke et al. 1990; Span et al. 2000). The gas surrounding particles was assumed to be air and its properties were modeled as a combination of 21% of O_2 and 79% of N_2 .

The calculations were first performed for the experimental data set by Badiola et al. (2011). The results were surprising. Despite relatively conservative assumptions expected to reduce the rate of Al consumption and thus indicate an incomplete combustion, the estimates suggested that for the particles finer than $\sim 8 \mu m$, the rate of heat losses from the burning particles is very high. In fact, using Eqs. (6) and (7) yielded unrealistically large values for m_{Al} , substantially exceeding the initial mass of unburned Al particles, as shown in Fig. 8. Additional calculations were performed, in which the experimental temperatures were “corrected” so that whenever the experimental temperatures exceeded T_b , the boiling point of Al, they were superficially reduced to be equal to T_b . As shown in Fig. 8, this correction resulted in only a small difference for the calculated integrated mass of consumed Al.

The second set of calculations was performed for the experimental data set collected in this paper. The results are effectively coinciding with the estimates for the earlier data set (see Fig. 8).

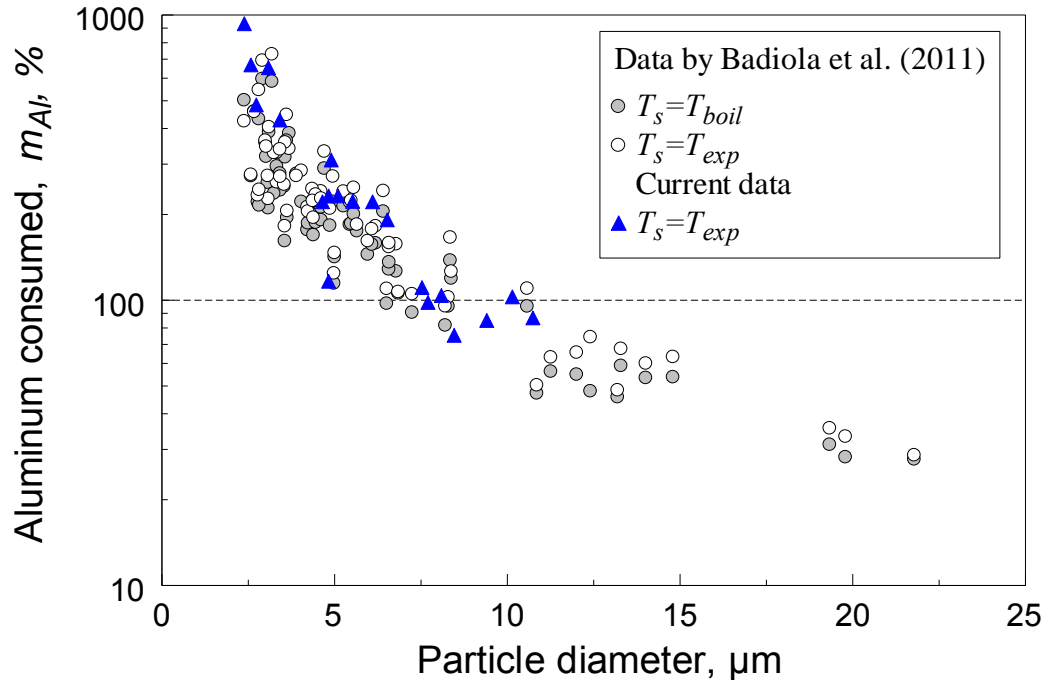


Figure 8. Normalized consumed mass of aluminum as calculated using Eq. (7). The calculated mass is normalized based on the initial particle mass calculated using the measured particle diameter.

Considering that the data describing particle burn times and temperatures were reproduced in several experiments, it is likely that the error resulting in gross overestimation of the rate of Al combustion is in the presented heat transfer model. We were unable to identify any significant omissions or grossly incorrect assumptions in the description above. However, while analyzing the results, we observed a strong sensitivity of the calculated rates of heat transfer to the temperature-dependent thermal conductivity of gas obtained using NIST Chemistry WebBook correlations for O₂ and N₂ taken from (Laesecke et al. 1990; Span et al. 2000). In the estimates discussed above, this gas was assumed to be air. Instead of or in addition to air, it is likely that the gas surrounding the burning Al particle includes substantial amount of Al vapors as well as various aluminum suboxides, such as AlO, Al₂O, and AlO₂. Thus, it is possible that the values of $\lambda_g(T)$ calculated for air are inappropriate for the present experiments. Because we were unable to find reports on thermal conductivity of gases with composition anticipated around burning Al particle, a correction of the value of $\lambda_g(T)$ by a fixed factor was considered. When this factor equals to 0.2, the points shown in Fig. 8 shift down sufficiently to suggest a complete reaction (100% of the available Al consumed) for the particles of about 3 μm . Note that the shift does not change the shape of the predicted trend, so the shifted set of points is not shown in Fig. 8. The same calculation then indicates that only about 10% of Al is consumed when the particle size approaches 15 μm . Note that a low estimated reaction completeness is indeed expected for the coarser

particles, for which a more accurate estimate should account for the stronger heat losses due to a stand-off flame with diameter greater than that of the particle.

Thus, performed estimates of the completeness of Al consumption for particles of different sizes considered in the present experiments suggest two important points. First, thermal conductivity of the gas surrounding burning Al particle is substantially smaller than that of a heated air. The effect of thermal conductivity found to be important for the present estimates must also be accounted for when the heat transfer due to Al combustion in practical systems is modeled. Second, a dramatic difference in the estimated reaction completeness for the particles with sizes changing in a relatively narrow range, e.g., from 2 to 15 μm , suggests that the same simplified heat transfer model becomes inadequate, as the particle size increases. The estimate considered here took into account only surface reaction and thus is more suitable for the finest particles. It is necessary to account for the vapor-phase reactions and standoff flames for the larger particles in order to interpret their measured combustion temperatures correctly.

Conclusions

Experiments with laser-ignited, micron-sized single Al particles burning in air were performed using an apparatus developed earlier and tuned to focus on particles less than 10 μm . In addition to the modified hardware, new methods of data processing were developed that minimized subjectivity and errors in selecting the meaningful subsets of the experimental points. The newly obtained and processed data are generally consistent with the previous results confirming a very weak effect of particle sizes on their burn time for micron-sized Al particles. Earlier temperature measurements for individual burning Al particles were reproduced and supported by spectroscopic data characterizing integrated emission from multiple burning particles. Results confirmed that Al particles finer than 10 μm burn in room temperature air achieving high combustion temperatures and producing significant molecular AlO emission. Experimental temperature histories for the particles of known sizes were processed to estimate the rates of heat losses and corresponding rates of Al consumption. It was observed that the thermal conductivity of air cannot be used in such estimates. The present experiments can only be meaningfully interpreted if the gas surrounding burning Al particles has a substantially lower thermal conductivity compared to the heated air. Further, it was observed that while a surface reaction model may be adequate for the finest particles, it must be replaced by a model including effect of standoff flame for particles exceeding $\sim 3 \mu\text{m}$.

References

- Badiola, C., Gill, R.J., and Dreizin, E.L. 2011. Combustion characteristics of micron-sized aluminum particles in oxygenated environments. *Combust. Flame*, **158**(10), 2064-2070.
- Bazyn, T., Krier, H., and Glumac, N. 2007. Evidence for the transition from the diffusion limit in aluminum particle combustion. *P. Combust. Inst.* 31, 2021-2028.
- Beckstead, M. W. (2005). Correlating aluminum burning times. *Combust. Explos. Shock+*, **41**(5), 533-546.

- Dokhan, A., Price, E.W., Seitzman, J.M., and Sigman, R.K. 2002. The effects of bimodal aluminum with ultrafine aluminum on the burning rates of solid propellants. *P. Combust. Inst.*, **29**, 2939-2945.
- Gill, R.J., Badiola, C., and Dreizin, E.L. 2010. Combustion times and emission profiles of micron-sized aluminum particles burning in different environments. *Combust. Flame*, **157**(11), 2015-2023.
- Gill, R.J., Mohan, S., and Dreizin, E.L. 2009. Sizing and burn time measurements of micron-sized metal powders. *Rev. Sci. Instrum.*, **80**(6), 064101/1-064101/7.
- Glassman, I. and Yetter, R.A. 2008. *Combustion*, 4th ed., Academic Press, Burlington.
- Holman, J. P. 2009. *Heat Transfer*. McGraw Hill, New York.
- Kalinchak, V.V. and Chernenko, A. S. 2009. High-temperature heat and mass transfer and Stefan flow on the surface of preheated metal particle in cold air. *High Temp+*, **47**(3), 415-423.
- Krier, H. Glumac, N. 2009. On the transition from classical diffusion-limited combustion behavior for fine and ultrafine aluminum particles. *Int. J. Energ. Mater. Chem. Prop.*, **8**(1) 71-80.
- Laesecke, A., Krauss, R., Sephan, K., and Wagner, W. 1990. Transport properties of fluid oxygen. *J. Phys. Chem. Ref. Data*, **19**(5), 1089-1122.
- Lynch, P., Krier, H., and Glumac, N. 2009. A correlation for burn time of aluminum particles in the transition regime. *P. Combust. Inst.*, **32**, 1887-1893.
- Lynch, P., Fiore, G., Krier, H., and Glumac, N. 2010. Gas-phase reaction in nanoaluminum combustion. *Combust. Sci. Techn.* **182**(7), 842-857.
- Mohan, S., Trunov, M.A., and Dreizin, E.L. 2008. Heating and ignition of metallic particles by a CO₂ laser. *J. Propul. Power*, **24**(2), 199-205.
- Mohan, S., Trunov, M.A. and Dreizin, E.L. 2009. On possibility of vapor-phase combustion for fine aluminum particles. *Combust. Flame*, **156**(11), 2213-2216.
- Price, E.W. and Sigman, R.K. 2000. Combustion of aluminized solid propellants. *Progr. Astronaut. Aero.*, **185**, 663-687.
- Shoshin, Y. and Dreizin, E. 2003. Particle combustion rates in premixed flames of polydisperse metal - air aerosols. *Combust. Flame*, **133**(3), 275-287.
- Span, R., Lemmon, E.W., Jacobsen, R.T., Wagner, W., and Yokozeki, A. 2000. A reference equation of state for the thermodynamic properties of nitrogen for temperatures from 63.151 to 1000 K and pressures to 2200 MPa. *J. Phys. Chem. Ref. Data*, **29**(6), 1361-1401.
- Tanguay, V., Goroshin, S., Higgins, A. J., Zhang, F. Aluminum particle combustion in high-speed detonation products. *Combust. Sci. Techn.* **181**(4), 670-693.
- Yetter, R. A., Risha, G.A., and Son, S.F. 2008. Metal particle combustion and nanotechnology. *P. Combust. Inst.*, **32**, 1819-1838.

CHAPTER 6: OXIDATION, IGNITION AND COMBUSTION OF AL-HYDROCARBON COMPOSITE REACTIVE POWDERS

Introduction

Aluminum powder is the most commonly used metal fuel additive for propellants, explosives, and pyrotechnics (Yetter et al., 2009). Its main advantages are a high combustion enthalpy, high flame temperature, and a relatively low cost. However, in many aluminized energetic formulations performance is not optimized because of relatively long ignition delays and difficulties in controlling the rate of combustion. Recent advances in materials manufacturing enable one to design Al-based reactive materials with customized combustion characteristics. Of specific interest are reduced ignition delays and ability to adjust the burn rate, e.g., by producing gaseous reaction products enhancing mixing and combustion efficiency in complex reactive flows. Materials with different burn rates are of interest for different applications; e.g., higher burn rates are desired for pressure generation and impulse, and reduced burn rates (while still complete reaction) are desired for enhanced heat distribution necessary for effective inactivation of aerosolized spores and bacteria. Finally, adjusted flame temperature and emission are often desired for pyrotechnic formulations.

This study is aimed to prepare and characterize novel Al-based alloys and composite materials using mechanical milling: a versatile technique enabling one to combine aluminum with many different components and achieve unprecedented control over the particle structure and morphology. Often materials that can be made by mechanical milling cannot be prepared otherwise. This project builds on our previous work dealing with Al-based alloys, nanocomposite thermite materials, and Al-I composites (Dreizin, 2009; Zhang et al., 2010a; Zhang et al., 2010b). In this effort, aluminum is being combined with volatile hydrocarbons producing metastable composite powders. Specifically, paraffin wax and polyethylene are used to create unique composite structures with an aluminum metal matrix. It was initially anticipated that the volatile gaseous fuel may cause fragmentation of the prepared particles during combustion, leading to generation of very finely divided Al, which may enhance combustion dynamics. Such materials were also expected to have reduced ignition temperatures compared to pure Al. It is of interest whether the materials “remember” their metastable nature and structure after their ignition and after melting of their metal matrix. The paper describes preparation and characterization of these materials.

Materials

Reactive composite powders were prepared by ball-milling aluminum and a hydrocarbon additive using a model 01HD attritor mill by Union Process. Aluminum powder, -325 mesh (< 45 µm), 99.5%, was provided by Atlantic Equipment Engineers. The additives were paraffin wax, mp: 70-80 °C, provided by Sigma Aldrich, and polyethylene powder, low density, 500 µm, provided by Alfa Aesar. 1.8 kg of 10-mm diameter hardened steel balls served as milling media. Liquid nitrogen was flushed through the cooling jacket of the mill and gaseous nitrogen was fed into a 750-ml steel milling vial. In all experiments, the ball-to-powder mass ratio was 36 and the impeller rotation rate was set to 400 rpm. Al-wax and Al-polyethylene (Al-PE) sample were milled for 19 hours each with a nominal hydrocarbon load of 10 wt. %. Milling at room temperature was found to result in strong caking, which prevented further refinement of

the material. Additional details describing preparation of reactive materials by mechanical milling and cryomilling are given elsewhere (Zhang et al., 2010a; Zhang et al., 2010b; Zhang et al., 2012).

The powders were characterized by X-ray diffraction using a Philips X'pert MRD powder diffractometer and scanning electron microscopy (SEM) using a Phenom tabletop microscope by FEI Technologies Inc. The morphologies of Al-wax and Al-PE samples are illustrated in back-scattered SEM images shown in Fig. 1. Both samples consist of micron-sized, mostly equiaxial particles. Al-wax composite powders are somewhat finer than Al-PE. A close examination of the Al-hydrocarbon particles shows that they are comprised of compacted aluminum flakes; individual flakes or flake-like agglomerates are also observed, the latter are especially abundant in the Al-PE composites. The smallest flake dimension appears to be on the scale of 10-100 nm. It is expected that such flakes adhere to one another with wax or PE coated interfaces; however the aluminum surfaces in such interfaces are formed by shear and deformation of the starting Al particles and are not expected to be coated by protective alumina.

Size distributions of the prepared powders were measured using a Beckman-Coulter LS230 Particle Size Analyzer. Figure 2 shows the particle size distribution and respective volume mean particle sizes of both samples. The shape of the size distribution is complex for Al-PE including more flake-like particles, causing possible errors in this light-scattering based measurement designed for spherical powders.

X-ray diffraction patterns showed only peaks of Al and the respective hydrocarbons. Paraffin wax showed peaks at $21\text{--}22^\circ$ and $23.5\text{--}24.5^\circ 2\Theta$, consistent with JCPDS 3-0259. Amorphous or poorly crystalline polyethylene caused a raised background in the range of $18\text{--}22^\circ 2\Theta$, where the strongest peaks for crystalline polyethylene are expected.

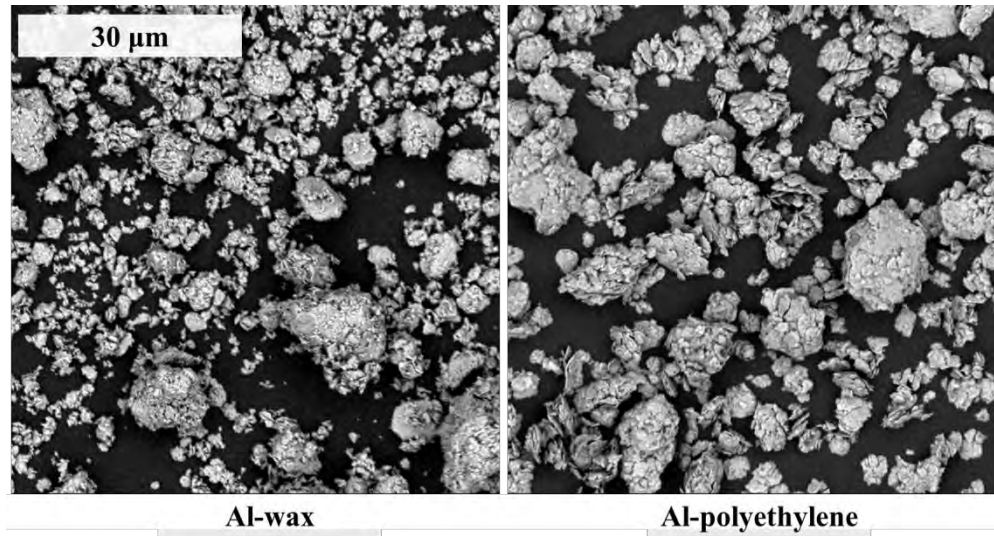


Fig. 1 SEM images of Al-wax and Al-PE composites. The scale bar is the same for both pictures.

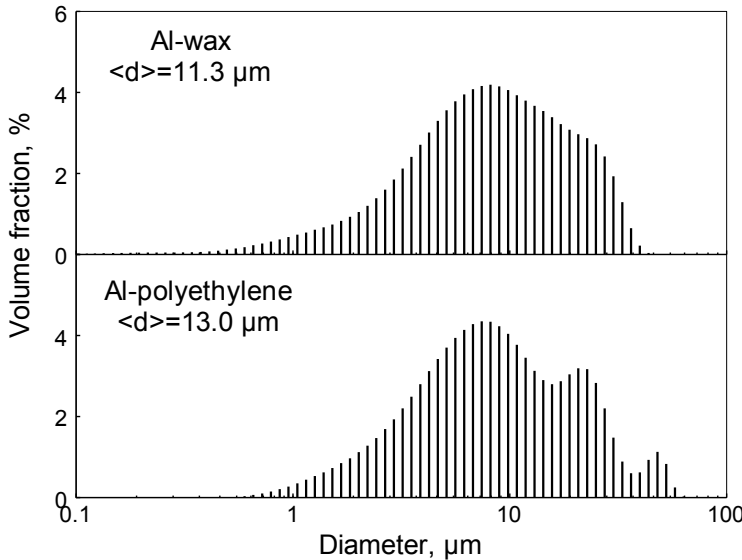


Fig. 2 Particle size distributions for Al-wax and Al-PE composites. Volume mean particle sizes are shown for both samples.

Experimental

Release of volatile species upon heating and oxidation of the prepared materials were measured by a TA Instruments model Q5000IR thermogravimetric analyzer (TGA). Alumina pans were used to hold samples for the measurements. The maximum temperature was limited to 1273 K. Experiments addressing release of volatile species in inert environment were performed at the heating rate of 10 K/min in argon. The balance and the furnace were purged with argon at 20 and 50 ml/min, respectively. The mass of sample used to measure the release of volatile component varied in the range of 10–30 mg. For oxidation measurements, experiments were performed at heating rates varied from 5 to 100 K/min to investigate the reaction kinetics. The balance and the furnace of Q5000IR were purged with argon at 10 ml/min and oxygen (purity 99.8 %) at 25 ml/min, respectively. The mass of material used in the oxidation experiments varied in the range of 0.4 – 4 mg. The TGA traces were baseline-corrected.

Ignition of the prepared materials was studied at the heating rates ranging from 2000 to 23000 K/s in air using an electrically heated filament (Ward et al., 2006), shown schematically in Fig. 3a. The heating rate of a nickel-chromium filament was adjusted by changing values of the DC voltage and resistor connected in series with the filament. A small amount of powder slurry with hexane as a liquid carrier was coated onto the filament. Hexane was dried prior to the experiment leaving a thin powder coating on the filament surface. Ignition was observed using both a silicon photodiode and a high-speed video camera. The temperature history of the heated filament was measured using a high-speed infrared pyrometer focused on the uncoated filament surface adjacent to the powder coating.

Burning characteristics of individual composite particles in air were investigated using a laser ignition apparatus (see a simplified diagram in Fig. 3b), described in detail by Gill et al. (2009); Gill et al. (2010); Badiola et al. (2011). Individual particles were fed by a laminar air flow into a CO₂ laser beam, where they were ignited. Flow settings were selected so that for all materials the measured average particle velocities were close to 0.7 m/s. Before ignition, particles crossed a beam of a 785 nm, 30 mW laser and the

scattered light pulses were used to measure particle sizes in-situ. Four photomultiplier tubes (PMT, Hamamatsu H3164-10), equipped with interference filters (486, 532, 568, and 589 nm), were used to detect the light emission from burning particles. Separate measurements using an EPP2000 High Resolution Spectrometer by StellarNet Inc were performed to verify that the particle emission did not include a parasitic sodium line at 589 nm. 532 and 589 nm filters were used for combustion temperature measurement. Considering that one of the strongest molecular bands of AlO emission is at 486 nm, while no substantial AlO emission occurs at 568 nm, the strength of the observed AlO emission was evaluated using the following ratio of the measured intensity signals:

$$R_{AlO} = \frac{(I_{486} / I_{568})_{exp}}{(I_{486} / I_{568})_{bb}} \quad (1)$$

The ratio in the numerator comes from the measurements (intensities I_{486} and I_{568} are proportional to the respective PMT voltages). The ratio in the denominator was taken for the black body emission spectrum when the black body temperature was equal to the measured particle temperature.

Some of the particles crossing the CO₂ laser beam may not have ignited; some others could have ignited and partially burned while still in the laser beam. In both cases, emission signatures should be discarded from the data analysis (Gill et al., 2009; Gill et al., 2010; Badiola et al., 2011), focusing instead on particles ignited in the laser beam and burning after exiting from it. In this project, selection of the emission pulses of interest, produced by particles that were ignited, but not partially consumed in the CO₂ beam was done considering the amplitude of the emission pulse at the instant the particles left the CO₂ beam. When this amplitude was comparable to the maximum emission signal, the particles were discarded. Conversely, emission pulses were analyzed when the signal increased substantially after the particle left the CO₂ beam. Specifically, particles were analyzed when the emission signal at the instant the particles left the CO₂ beam reached 10 % (Al-wax) or 5 % (Al-PE) of the maximum emission level for the same particle.

Combustion of the prepared composite materials was studied using a constant volume explosion (CVE) experiment (Santhanam et al., 2010). A simplified diagram of the experiment setup is shown by Fig. 3c. A 9.2-liter explosion vessel was initially evacuated. Composites were aerosolized and introduced into the vessel with an air blast delivered from a high-pressure reservoir. After a short delay, aerosolized powder was ignited by an electrically heated wire placed in the center of the vessel. The pressure trace was recorded by a pressure transducer. Samples were tested in air with a constant powder load of 4.65 g. This mass was selected to be the same as in multiple reference experiments with pure Al powders of different particle sizes (Eapen et al., 2004, Santhanam et al., 2010). For pure Al and Al-hydrocarbon in air, this mass corresponds to the equivalence ratio of 1.6 and 2.1, respectively, and was observed to be readily and reproducibly ignited in the present CVE apparatus.

The combustion products were embedded in epoxy and cross-sectioned for SEM examination. A LEO 1530 Field Emission Scanning Electron Microscope operated at 10 kV and equipped with energy-dispersive x-ray spectrum (EDX) detector was employed to analyze combustion products.

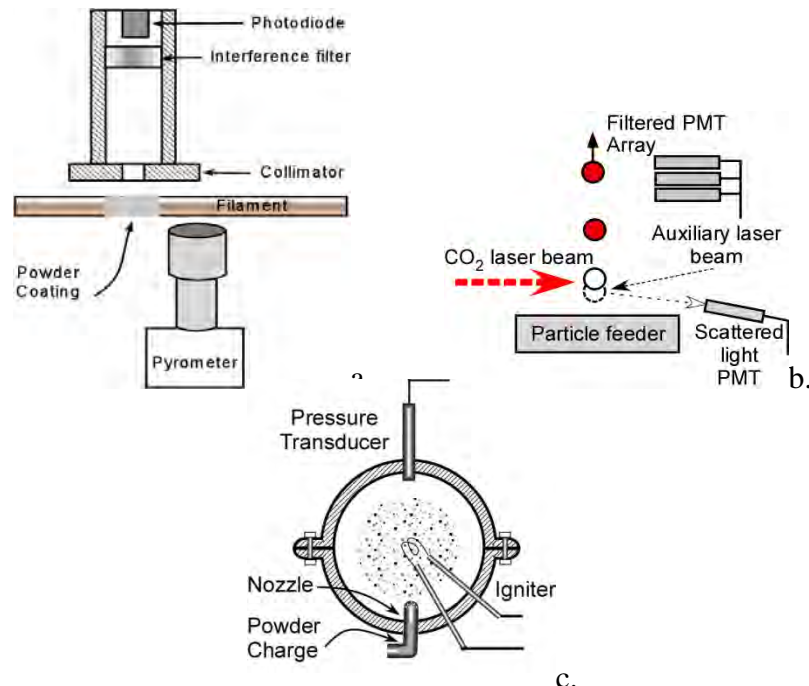


Fig. 3 Heated filament setup used for powder ignition experiment (a); Laser ignited particle combustion setup for single particle combustion experiment (b); and constant volume explosion setup for aerosol combustion experiment (c)

Results

Release of volatile species in inert environment

The TGA traces for Al-wax and Al-PE composites heated at 10 K/min in Ar are shown in Figs. 4 and 5, respectively. The mass loss traces for the starting hydrocarbons (wax and PE, respectively) are shown for reference. The gasification of pure paraffin wax starts at 430 K, and ends before the temperature reaches 740 K. The decomposition of pure PE starts at a somewhat higher temperature, ca. 580 K and ends by about 750 K. For both composite materials, the mass loss begins at lower temperatures compared to the starting hydrocarbons. This may be due to distribution of the hydrocarbons in very thin layers with developed surface areas in the composite materials, or to partial breakdown of the hydrocarbons into lighter compounds during the milling process. For wax, the decomposition of the composite and the mass loss of the starting material are rather similar to each other. For PE, the low-temperature mass loss is significantly stronger for the composite material. Furthermore, the second, stronger decomposition step occurs for the composite material noticeably earlier than for pure PE. The differences in decomposition of the initial PE vs. PE contained in the composite material can be due to a modification of PE by milling.

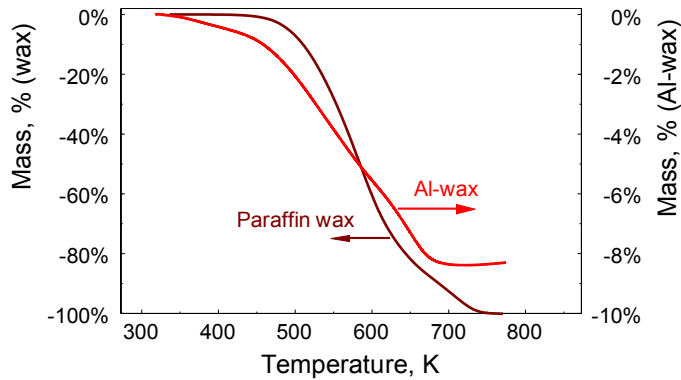


Fig. 4 TGA traces of pure paraffin wax and Al-wax composite heated at 10 K/min in argon

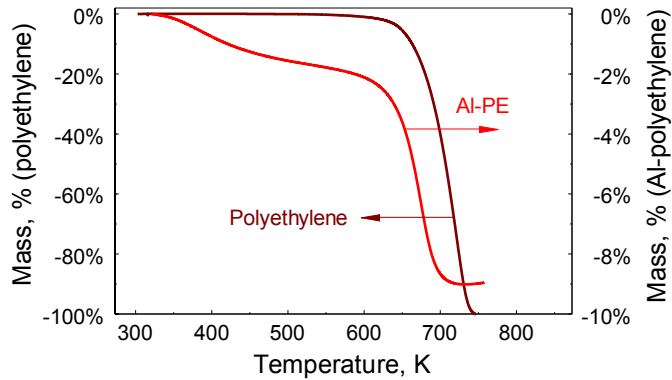


Fig. 5 TGA traces of pure PE and Al-PE composite heated at 10 K/min in argon.

Oxidation

TGA traces for oxidation of Al-wax and Al-PE composites at a heating rate of 5 K/min are shown in Fig. 6; the trace for the pure spherical aluminum with volumetric mean particle size of 9.4 μm is shown for reference. The mass changes result from the combined effects of release of volatile additives (mass loss) and oxidation (mass gain). There are two oxidation stages for pure Al in the temperature range from 273 K to 1273 K, which are associated with a phase transformation of amorphous alumina to crystalline γ - Al_2O_3 and with ensuing thermally activated growth of γ - Al_2O_3 (Trunov et al., 2005; Trunov et al., 2006).

For both, Al-wax and Al-PE composites, the oxidation traces are very similar to each other. A strong weight loss begins at about 450 K, at nearly the same temperature for both materials. The same onset of weight loss observed for both materials in an oxidizing environment is a bit surprising considering that in inert environment, rapid gasification of Al-PE composite occurs at a somewhat higher temperature than that for Al-wax (cf. Fig. 4 and Fig. 5). The weight loss trend reverses at about 560 K, and a strong oxidation stage occurs in the range of temperatures from 750 to 850 K. This oxidation stage is substantially stronger than the first oxidation stage for Al, it also occurs at a lower temperature than for Al. The oxidation rate decreases significantly before Al melts. Well after aluminum melting, at about 1070 K, another oxidation stage occurs, correlating well with the second oxidation stage observed at this same temperature range for pure Al. However, for the composite materials this second oxidation stage is much weaker than it is for the pure Al.

Kinetics of oxidation is studied by tracking the main maxima positions of dm/dT while heating Al-wax and Al-PE at different rates from 5 to 100 K/min. The data for two strong oxidation steps occurring at around 823 K and 1070K are further processed and discussed below, in the reaction kinetics section.

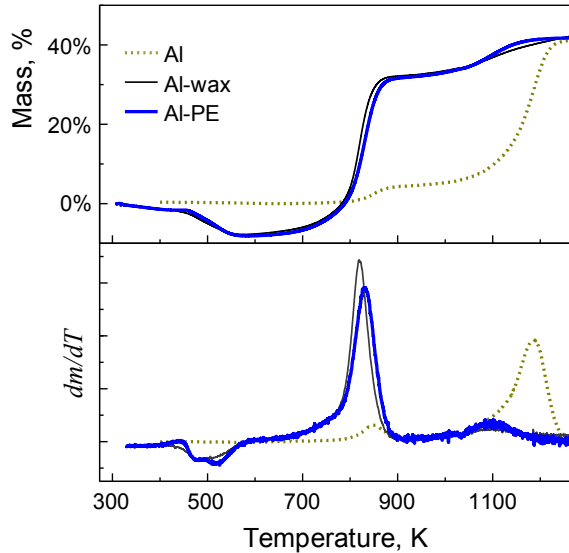


Fig. 6 TGA oxidation traces and dm/dT derivatives of Al-wax, Al-PE and reference Al (9.6 μm volumetric mean particle diameter) heated at 5 K/min in argon/oxygen flow.

Ignition

Figure 7 shows ignition temperatures of Al-wax, Al-PE composites and reference Al as a function of the heating rate. Each point represents an individual filament ignition experiment. Ignition instant is identified using recorded videos when the surface (or part of it) of the powder coating becomes brighter than the filament surface. Al-hydrocarbon composites can be easily ignited, and ignition is observed at relatively low heating rates, at which pure aluminum cannot be ignited. Ignition temperatures of Al-hydrocarbon composites fall in the range of 900 – 1200 K, which are much lower than that for pure aluminum. Generally, ignition temperatures increase slightly with increasing heating rates as is expected for a thermally activated ignition mechanism, although the observed effect is relatively weak.

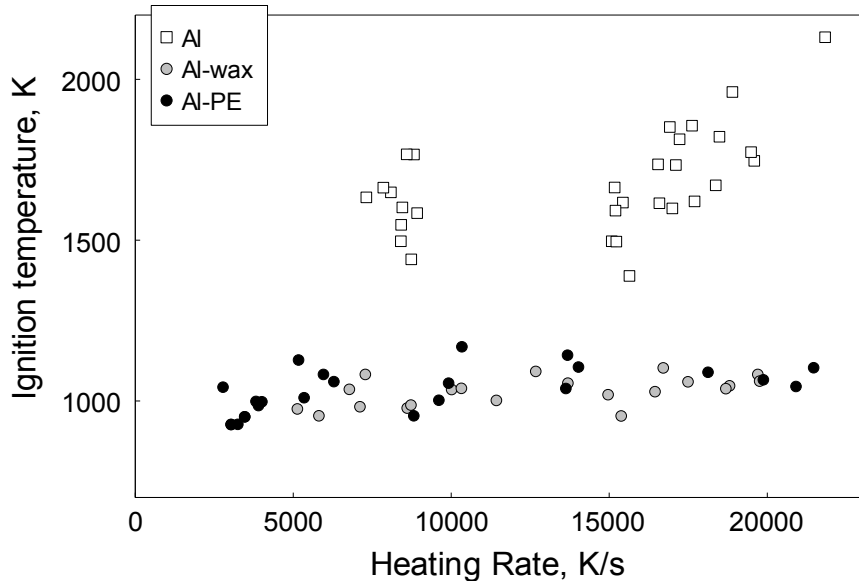


Fig. 7. Ignition temperatures for Al-wax, Al-PE and reference Al (9.6 μm volumetric mean particle diameter) measured using an electrically heated filament at different heating rates in air.

Reaction kinetics

TGA results as well as ignition results were processed using the Kissinger method, e.g., (Starink, 2003) as shown in Figs. 8 and 9. For processing, $\ln(T^2/\beta)$, where β is the heating rate, is plotted versus the reciprocal temperature for the following characteristic points identified from the TGA traces: onset of the weight loss upon heating in oxidizing environment and two maxima in the rate of oxidation, determined respectively as the first minimum and two maximum points in the dm/dT traces for oxidation experiments (cf. Fig. 6). Experimental ignition data from Fig. 7 are directly transferred into Kissinger coordinates in Figs 8 and 9, showing the results for Al-wax and Al-PE, respectively. Kinetic trends implied by the oxidation experiments (TGA) can be extrapolated as straight lines (shown as dashed lines) into the range of higher heating rates corresponding to the ignition experiments. It appears that ignition of both composites occurs at somewhat lower temperature compared to that predicted by the extrapolation of the two oxidation stages observed in TGA measurements. The extrapolation of the weight loss step points to temperatures slightly lower than the ignition temperatures. Considering that the direct extrapolation of kinetic trends observed in TGA traces into ignition experiments is only suitable for qualitative assessment of the reaction mechanisms, it is reasonable to suggest that both weight loss and oxidation contribute to processes leading to ignition of the prepared materials. Specifically, it is likely that the weight loss destroys a protective layer formed during milling and including hydrocarbon species. Removal of this protective layer accelerates oxidation and leads to powder ignition.

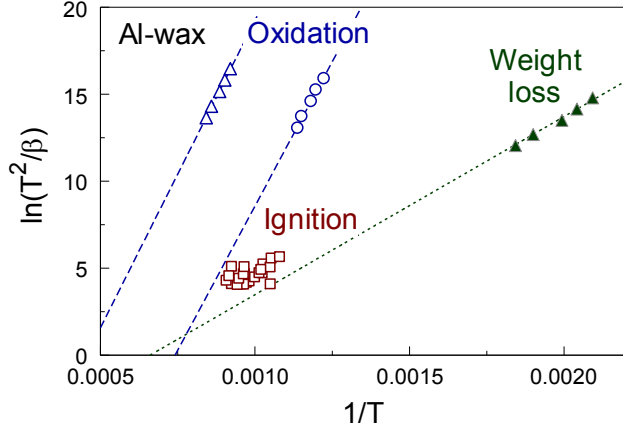


Fig. 8 Kissinger plot showing ignition temperatures measured at different heating rates (open squares) together with peak positions for oxidation stages (open triangles and circles) and the onset of weight loss (filled triangles) observed in the TGA traces for Al-wax.

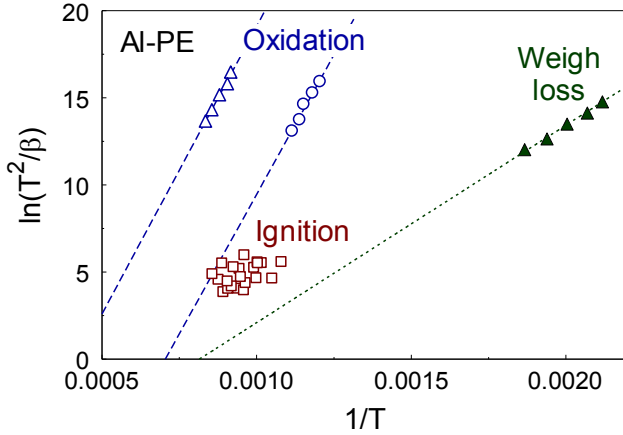


Fig. 9 Kissinger plot showing ignition temperatures measured at different heating rates (open squares) together with peak positions for oxidation stages (open triangles and circles) and the onset of weight loss (filled triangles) observed in the TGA traces for Al-PE.

Single particle combustion

Photographs of laser-ignited and burning particles of Al-wax and Al-PE composites are shown in Fig. 10; each streak represents a particle after passing through the laser beam. The camera shutter was open for 250 ms so that more than one streak could be captured in each image. In general, streaks of Al-wax and Al-PE are similar to each other. In both pictures, the streaks widen and become brighter soon after particles exit the CO_2 laser beam. The broad streaks with blurry boundaries are likely indicators of intensive vapor-phase reactions. The high overall emission intensities last relatively long, and the particles extinguish quickly after the peak emission intensity is achieved. It is also noted that Al-wax produces higher emission intensity than Al-PE.

Figure 11 shows characteristic traces for emission, temperature, and R_{AlO} (cf. Eq. 1) for both Al-wax and Al-PE. The two composites exhibit similar combustion characteristics. The overall burn time is somewhat longer than that reported for pure Al

particles (Gill et al., 2009; Gill et al., 2010; Badiola et al., 2011). The oscillatory patterns in the emission signals for both samples are much stronger, and occur over longer periods of time compared to similar signals for pure Al particles. The temperature traces are well correlated with the intensities of AlO emission, which is different from the dynamics observed for pure Al and Al-I₂, for which the temperature continued to increase after the peak in the AlO emission (Zhang et al., 2012). The combustion temperature and R_{AlO} peak after the initial increase, followed by a gradual decay throughout the rest of combustion. The combustion temperatures remain stable at around 2400 – 2800 K after pre-heating despite the strong emission oscillations. The values of R_{AlO} are substantially greater than 1 throughout combustion, indicative of substantial vapor-phase reactions.

Figure 12 shows the measured emission (burn) time as a function of the particle diameter for Al-wax, Al-PE and pure Al as a reference, taken from (Badiola et al., 2011). A strong scatter in the data for Al-hydrocarbons is due to errors in measuring particle sizes and the irregularity of the particles. The volumetric average sizes of Al used for this experiment was 15.1 μ m. Particle size distributions for composite materials include more fines compared to Al; respectively, more small particles for Al-wax and Al-PE are detected in combustion experiments compared to Al. In general, despite the scatter, Al-based composites appear to burn appreciably longer than similarly sized pure Al particles.

All emission traces were processed to determine the average flame temperature and average R_{AlO} corresponding to the relatively strong emission signal (exceeding 50% of its peak value). Average flame temperature and R_{AlO} for Al-wax, Al-PE and reference Al are shown in Fig. 13 and Fig. 14, respectively. The flame temperatures for small-sized particles for Al-wax and Al-PE fall into the similar temperature range as for Al. The trend for larger-sized particles is difficult to see because of a small number of data points available. Larger scatter and lower value of R_{AlO} is observed for both composites compared to Al particles.

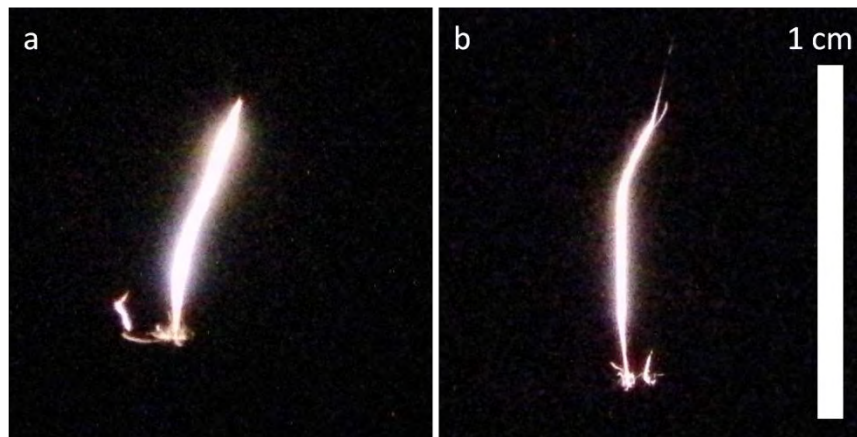


Fig. 10 Photographs of burning particle streaks for Al-wax (a) and Al-PE (b). The scale bar is the same for both pictures.

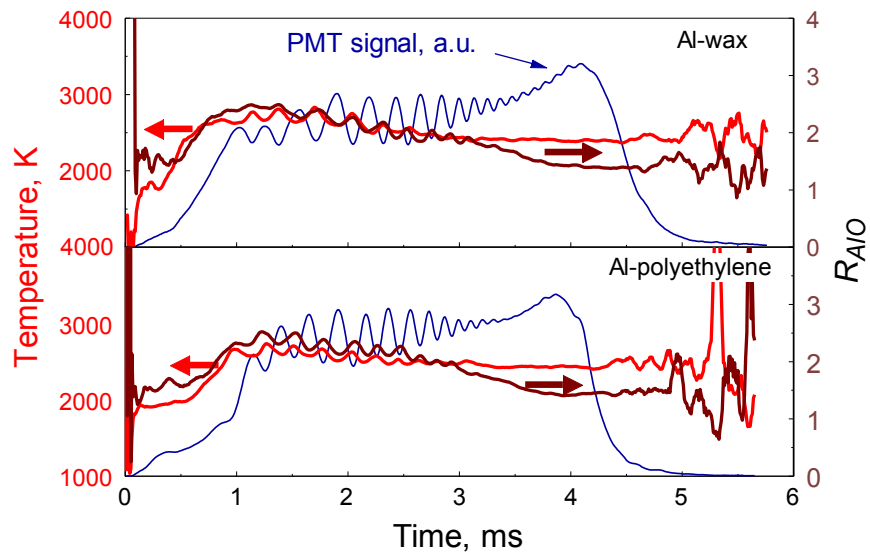


Fig. 11 Characteristic traces of emission intensity, temperature, and R_{AlO} for Al-wax and Al-PE in air. The axes for PMT signals plotted in a.u. are not shown.

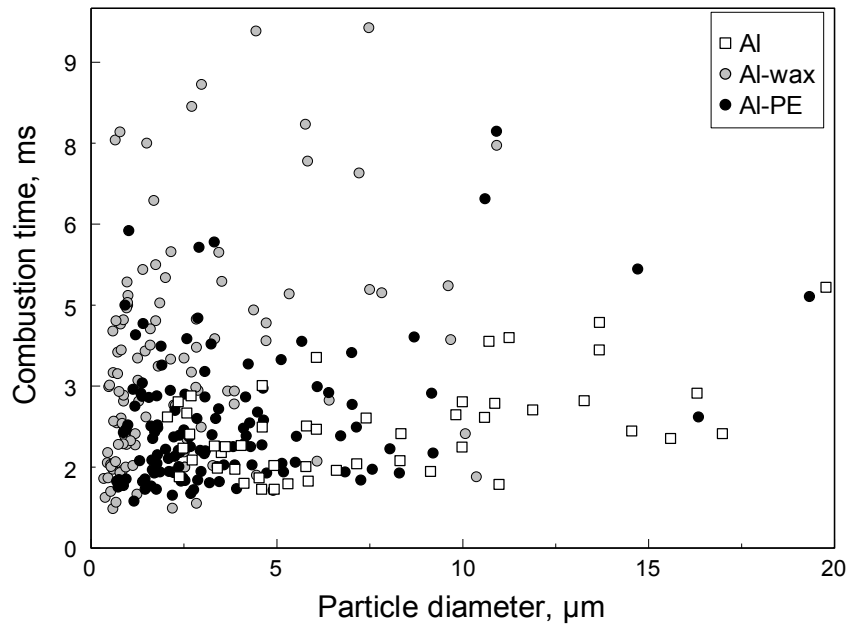


Fig. 12 Burn time for Al-wax, Al-PE, and reference Al burning in air.

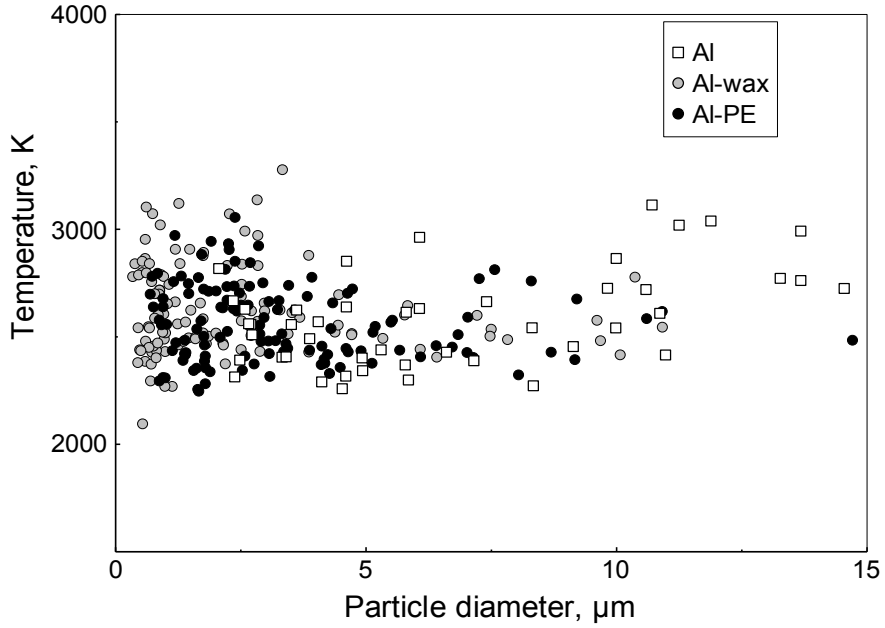


Fig. 13 Mean combustion temperatures for Al-wax, Al-PE, and reference Al burning in air.

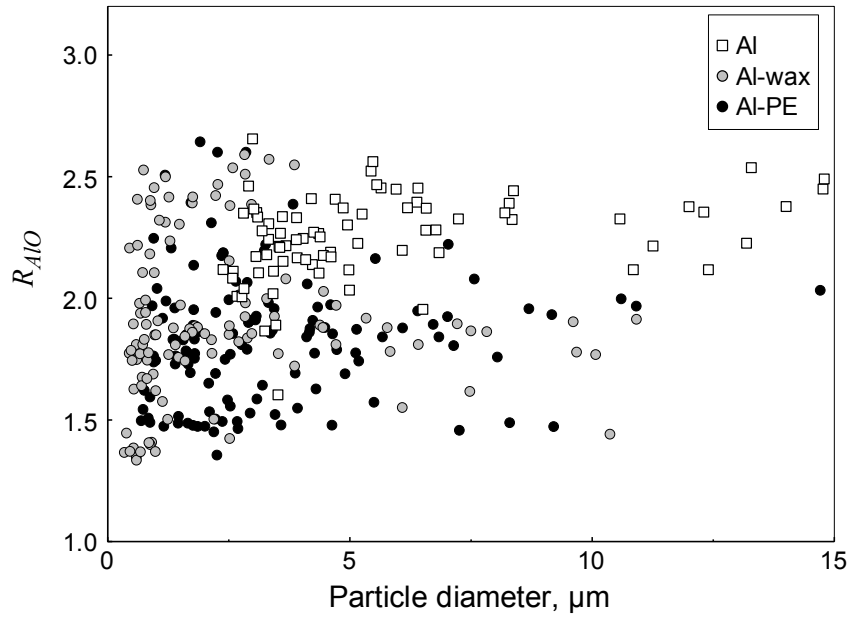


Fig. 14 AlO ratios for Al-wax, Al-PE, and reference Al burning in air.

Aerosol combustion

Figure 15 shows the pressure traces from CVE experiments for Al-wax, Al-PE composites and reference aluminum. The values of the maximum pressure and the rate of pressure rise from CVE tests are indicative of the flame temperature and combustion rate, respectively. The pressure traces for Al-wax and Al-PE are observed to fit between those shown for Al powders with average sizes 10.9 and 15.1 μm , as is expected considering their average particle sizes. Results for the measured values of maximum pressure and rate of pressure rise, respectively, P_{max} and dP/dt_{max} , are summarized in Fig.

16. The error bars for Al data indicate standard deviations from the mean values obtained from the repeated CVE experiments. Because of relatively low pressures observed, experiments for Al-wax and Al-PE composites were not repeated. For pure aluminum powder, both the maximum pressure and the rate of pressure rise increase as particle sizes decrease. Al-wax and Al-PE composites produce similar values of P_{\max} and dP/dt_{\max} , indicating comparable combustion temperatures and combustion rates compared to pure Al powder.

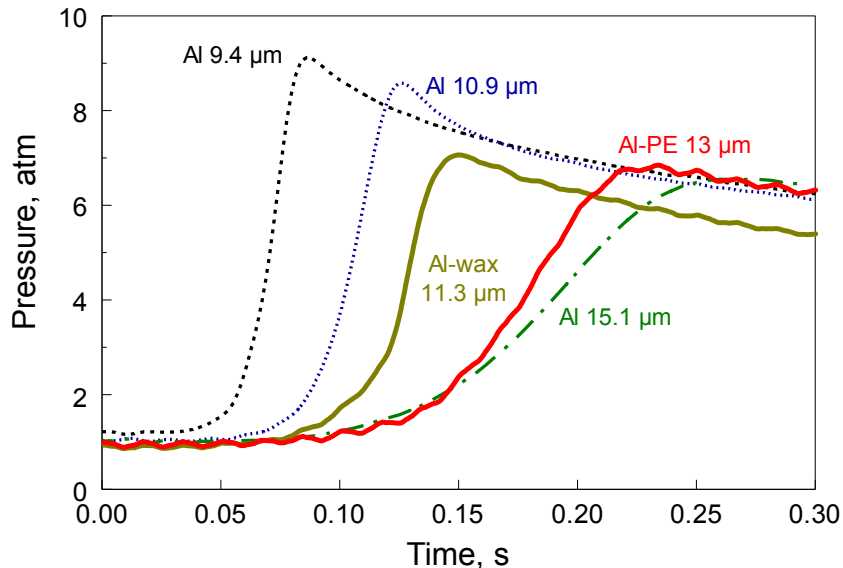


Fig. 15 Pressure traces from aerosol combustion experiments for Al-wax, Al-PE and reference Al. Dashed/dotted lines are for Al, solid lines are for composite materials. Labels show volumetric mean particle sizes for spherical Al powders.

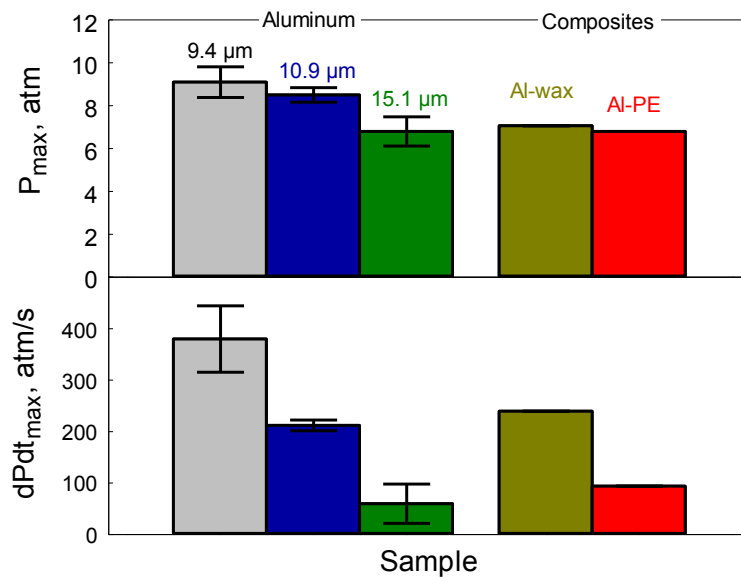


Fig. 16 Maximum pressure and maximum rate of pressure rise for Al-wax, Al-PE and reference Al measured in CVE experiments.

Combustion products

Cross-sections of combustion products from CVE experiments were examined by SEM. It is found that combustion products of Al consist of oxide particles, unreacted aluminum with oxide inclusions, and hollow structures, possibly caused by the release of gasified suboxides or boiling of Al. Strong agglomeration is observed in the products of both Al-wax and Al-PE composites, which appeared generally similar to each other. Many of the burned and partially burned particles are much coarser than the starting particles of these Al-hydrocarbon composites. Figure 17 shows back-scattered SEM images of combustion products of Al-wax composites. For brevity, additional images including those of combustion products of Al-PE composites were omitted. The image on the left of Fig. 17 shows an example of a large particle formed as a result of agglomeration. The particle consists of two main parts: the lighter phase (top, right) is less oxidized than the darker phase (bottom left). The image on the right zooms in the more oxidized portion of this particle. It shows a distinct compositional contrast produced by two phases that were likely separated during solidification. EDX spectra of the light and bright phases marked in the right image in Fig. 17 are shown in Fig. 18. Figure 18 shows the presence of Al, O, and C, with the C and O balance substantially different in the light and dark phases. The darker phase (right image in Fig. 17) contains less oxygen and more carbon compared to the lighter phase. The quantitative analysis of the phase composition of the combustion products was difficult because of substantial heterogeneity of the sample, effect of carbon coating applied to prevent charging during SEM analyses, and lack of the appropriate calibration of EDX spectra. However, EDX results for different particles and different materials could be qualitatively compared to one another. Carbon was consistently detected in the products of both Al-wax and Al-PE composites. The carbon concentration varied among different particles. Typically, more carbon was detected in the less oxidized portions of the reacted particles.

Combustion products of Al-wax and Al-PE were also characterized by X-ray diffraction analysis. X-ray diffraction shows only aluminum and alumina phases in the combustion products.

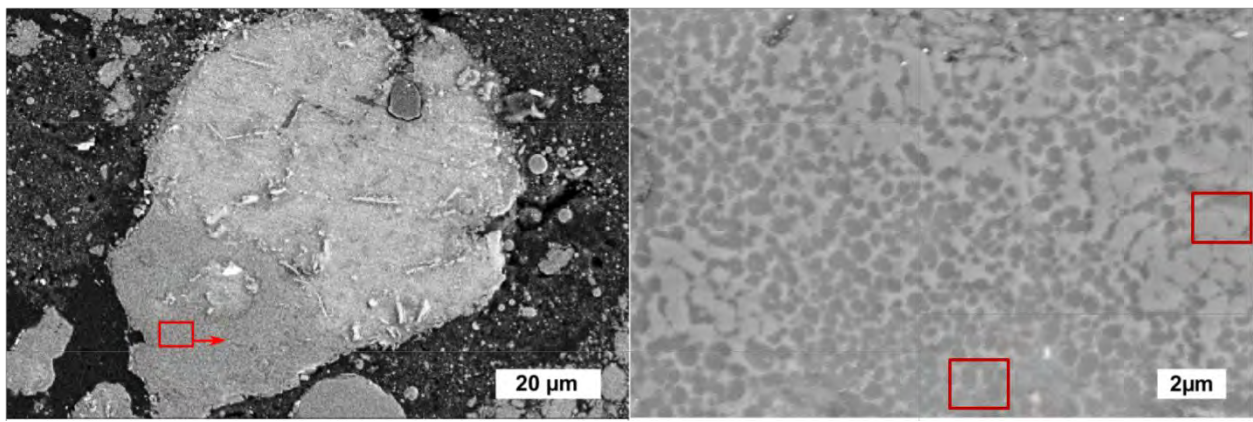


Fig. 17 SEM images of cross-sectioned combustion products of Al-wax composites. The image on the right is a magnified view of the rectangular area selected in the left image.

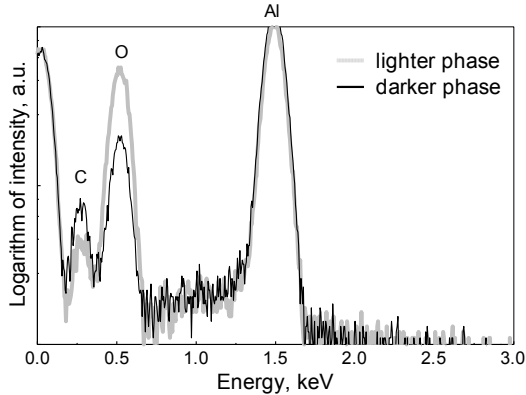


Fig. 18 EDX spectra for lighter and darker phases detected in the combustion products of Al-wax composites. The areas for which the EDX spectra were taken are marked in the right image in Fig. 17.

Discussion

Cryomilling offers a unique approach enabling one to combine aluminum with an unstable or difficult to process additive. Previous work (Zhang et al., 2010a; Zhang et al., 2010b; Zhang et al., 2012) showed that iodine is chemically bound and stabilized in the Al-I₂ composites prepared by cryomilling. Conversely, no such stabilization is observed for either wax or polyethylene. Indeed, comparing the weight loss observed upon heating with the initial amount of hydrocarbon added to the powder (cf. Figs. 4, 5), it is concluded that only 10-20 wt% of the hydrocarbon might be retained in the powder after the hydrocarbon volatilization temperatures are exceeded. This retention can be explained by formation of carbides; however, the bulk of the hydrocarbon additive is readily volatilized. Therefore, for both wax and polyethylene addressed in this work, cryomilling mostly enables their very homogeneous mixing with Al so that very fine Al flakes are covered by thin hydrocarbon layers; such covered flakes are packed to produce micron-sized particles. It appears that hydrocarbons (wax or polyethylene) behave as milling process control agents (lubricants), which do not react with Al, unlike iodine. Thus, the lubricant remains active during the entire milling time resulting in production of finer final particles compared to Al-I₂ composites, in which iodine is typically absorbed before the end of the milling run.

The unusual particle morphology for the Al-hydrocarbon composites, in which agglomerated primary particles are flake-like with the smallest dimension on the nanoscale, and for which aluminum surface is coated with hydrocarbon while there is no underlying oxide layer, is likely responsible for their unusual oxidation behavior. Indeed, a strong oxidation step following weight loss caused by volatilization of the hydrocarbon occurs at a significantly lower temperature compared to both pure Al and Al-I₂ composites made by cryomilling (Zhang et al., 2010a; Zhang et al., 2010b; Zhang et al., 2012), both of which are coated by a naturally grown amorphous alumina. The oxidation step is likely occurring at the relatively large exposed metal surface, produced when the hydrocarbon surface coating is volatilized from agglomerated flakes.

Ignition temperatures for all composite materials are substantially lower than for the pure Al. Kissinger processing of ignition and oxidation data suggests that the earliest oxidation processes are likely responsible for ignition of the prepared composite

materials. It is also speculated that volatilization and ignition of the hydrocarbon additives may aid ignition of aluminum.

In the single particle combustion experiments, substantial differences were detected in the measured emission intensity, temperature, and AlO emission traces for the prepared composite particles as compared to pure aluminum (Badiola et al., 2011). These differences are surprising. Indeed, for all materials combustion occurs at very high temperatures compared to the temperatures at which the volatile additives are expected to evaporate and aluminum is expected to melt. Thus, one might have expected that combustion would occur in a similar fashion for the pure Al and materials that are expected to consist of pure Al following the loss of readily volatile components. However, recorded optical signatures of the burning particles suggest that the additives remain in the burning material affecting aluminum combustion well after the particle ignites and melts, similar to what is observed for Al-I₂ (Zhang et al., 2012). This conclusion is further supported by SEM/EDX analyses of the combustion products, in which carbon is found in the partially oxidized particles. It is suggested that the product analysis is directly relevant to the above observations even though the products were collected from CVE rather than single particle combustion experiments. It is proposed that the evaporating hydrocarbon species change the environment around burning particles. In particular, volatile hydrocarbons may be consuming oxygen leaving the particle surface to react with products of their combustion.

Presence of oscillatory emission patterns for single particles of composite materials suggests heterogeneity of the burning particle surface. More specifically, it is suggested that oxide caps are formed early on at the surfaces of the composite particles generating asymmetric flames and associated oscillatory emission patterns. Strong periodic oscillations as well as bright trajectory, high combustion temperature and relatively high values of R_{AlO} indicate non-negligible vapor phase reactions. As stated above, is very likely that for Al-hydrocarbon composites burning in air, evaporated aluminum reacts in an atmosphere with carbon oxides and water, which are not present in similar experiments with pure Al particles. It is suggested that the presence of carbon and hydrogen reaction products in the gas composition in the immediate particle vicinity results in wider and brighter streaks, longer burn time and lower value of R_{AlO} . Because combustion temperatures for the composite materials and for pure Al are close to each other, longer combustion time observed for the composite powders may suggest that such powder particles release more heat and thus burn more completely than pure Al particles. CVE experiments suggest a similar combustion behavior for Al-hydrocarbon composites as for Al, which is consistent with the combustion temperature measurement from single particle measurements. The reason for the unattractive performance in CVE tests comes from analysis of the collected combustion products for Al-hydrocarbon composites. Specifically, formation of large numbers of very coarse agglomerates in the fuel-rich aerosols may give rise to premature quenching and low reaction completeness, causing relatively low and slowly rising pressures. It is unclear what promotes agglomeration in the aerosolized Al-hydrocarbon combustion products, but it is clear that preventing such agglomeration could substantially improve their combustion performance.

Conclusions

New aluminum-based materials are prepared by cryomilling comprised of an aluminum matrix and hydrocarbon inclusions. Hydrocarbons are not altered chemically;

Al-hydrocarbon composites consist of fine Al flakes coated with thin hydrocarbon layers (without intermediate alumina layers), and packed together into micron-sized particles. For both Al-wax and Al-PE prepared materials, their ignition temperatures are reduced substantially compared to pure aluminum. Al-hydrocarbon materials oxidize at substantially lower temperatures and noticeably faster compared to pure Al powders. Individual particle burn times are longer, the combustion temperatures are similar and values of AlO emission are lower for Al-hydrocarbon particles compared to Al. It is observed that in combustion experiments, hydrocarbon additives do not completely escape before or soon after particle ignition; instead their traces remain in the burning particles changing significantly the resulting burn rate and combustion temperature. For aerosolized powder clouds, burn rates for the Al-wax or Al-PE composite are comparable to that of pure Al. It is speculated that the combustion performance is reduced by the agglomeration observed for the partially burned particles of Al-hydrocarbon composites in the CVE configuration.

References

- Badiola, C., Gill R.J., and Dreizin E.L., (2011) Combustion characteristics of micron-sized aluminum particles in oxygenated environments, *Combustion and Flame*, 158, pp. 2064–2070
- Dreizin, E.L., (2009) Metal-based reactive nanomaterials, *Progress in Energy and Combustion Science*, 35, pp. 141 – 167
- Gill, R.J., Mohan, S., and Dreizin, E.L., (2009) Sizing and Burn Time Measurements of Micron-Sized Metal Powders, *Review of Scientific Instruments*, 80, 064101-1 – 064101-7
- Gill, R.J., Badiola, C., and Dreizin, E.L., (2010) Combustion Times and Emission Profiles of Micron-Sized Aluminum Particles Burning in Different Environments, *Combustion and Flame*, 157 (11), pp. 2015–2023
- Santhanam, P.R., Hoffmann, V.K., Trunov, M.A., and Dreizin E.L., (2010) Characteristics of aluminum combustion obtained from constant volume explosion experiments, *Combustion Science and Technology*, 182, pp. 904–921
- Starink, M.J., (2003) The determination of activation energy from linear heating rate experiments: a comparison of the accuracy of isoconversion methods, *Thermochimica Acta*, 404, pp. 163–176
- Trunov, M.A., Schoenitz, M., Zhu, X., and Dreizin, E.L., (2005) Effect of Polymorphic Phase Transformations In Al_2O_3 Film on Oxidation Kinetics of Aluminum Powders, *Combustion and Flame*, 140 (4), pp. 310–318
- Trunov, M.A., Schoenitz, M., and Dreizin, E.L., (2006) Effect of Polymorphic Phase Transformations in Alumina Layer on Ignition of Aluminum Particles, *Combustion Theory and Modeling*, 10 (4), pp. 603–624
- Ward, T.S., Trunov, M.A., Schoenitz, M., and Dreizin, E.L., (2006) Experimental Methodology and Heat Transfer Model for Identification of Ignition Kinetics of Powdered Fuels, *International Journal of Heat and Mass Transfer*, 49 (25-26), pp. 4943–4954
- Yetter, R.A., Risha, G.A., and Son, S.F., (2009) Metal particle combustion and nanotechnology, *Proceedings of the Combustion Institute* 32 II, pp. 1819-1838
- Zhang S., Schoenitz, M., and Dreizin, E.L., (2010) Mechanically alloyed Al-I composite materials. *Journal of Physics and Chemistry of Solids*, 71, pp. 1213–1220

Zhang, S., Schoenitz, M., and Dreizin, E.L., (2010) Iodine Release, Oxidation, and Ignition of Mechanically Alloyed Al–I Composites, *Journal of Physical Chemistry C*, 114 (46), pp. 19653–19659

Zhang, S., Badiola, C., Schoenitz, M., and Dreizin, E.L., (2012) Oxidation, Ignition, and Combustion of Al·I₂ Composite Powders, *Combustion and Flame*, 159(5), pp. 1980–1986

CHAPTER 7: COMBUSTION OF MICRON-SIZED PARTICLES OF TITANIUM AND ZIRCONIUM

Introduction

Combustion of zirconium and titanium powders is of interest for combustion synthesis [1-3], high density reactive materials [4, 5], pyrotechnics [6-8], and applications dealing with fire safety [9,10]. Previously, combustion was characterized for relatively coarse powders with particle sizes exceeding 20-30 μm [11-16]. Combustion times and temperatures were measured optically; a combustion mechanism was proposed [17] involving dissolution of oxygen and nitrogen in the molten metal with subsequent release of nitrogen and formation of stoichiometric oxides. The latter phase changes are accompanied by micro-explosions of the burning particles.

Recently, interest in combustion of Ti and Zr was stimulated by development of finely mixed energetic formulations involving micron size or finer particles of respective metals. It is unclear whether the trends identified experimentally for coarse Ti and Zr powders and describing effects of particle sizes on their burn times and temperatures remain valid for much finer particles, with the particle size comparable to the mean free path of the gas molecules. Experiments on combustion of individual metal particles with sizes under 20 μm became possible using an experimental setup described in refs. [18-20]. Here, the setup is adopted for experiments with Zr and Ti. The experimental objective is to establish burn rates and temperatures for such particles and compare results to those published earlier and describing combustion of coarser powders of the same metals.

Experimental

The apparatus used in this experiment employs a CO₂ laser beam to ignite individual fuel particles [18]; it was used previously to characterize combustion of aluminum in various oxidizers [19, 20]. Schematic diagram of the setup is shown in Fig. 1. Its detailed description is available elsewhere [18-20], only a brief summary is provided below.

A low number density particle jet entrained by a vertically rising laminar gas flow is generated. Particles are carried by the gas, so $Re \approx 0$. The jet crosses two laser beams as shown in Fig. 1. Particles first pass through an auxiliary laser beam of a 785-nm, 30-mW laser. Each particle crossing the beam produces a scattered light pulse. The scattered light pulse is collected at an angle of 120° selected based on Mie theory calculations; the sequence of these pulses is collected and their amplitudes are analyzed to obtain an in-situ particle size assessment.

Particles then cross a CO₂ laser beam focused to ~330 μm which heats particles to ignition. Light emission from incandescent burning particles pass through a quadrifurcated optical bundle which leads to a photomultiplier tube (PMT) array. Each PMT is equipped with an interference filter. Emission signals filtered at the wavelengths of 589 and 532 nm were used for pyrometry and a signal filtered at 568 nm served as a reference emission trace. The temperatures were obtained assuming that the particles emit as a grey body, although other spectral patterns could be considered for better accuracy [21]. The optical pyrometer was calibrated using a current-stabilized tungsten lamp with an irradiance calibrated spectrometer. In addition, the emission from a set of burning

particles is integrated (typical integration time of 25-30 s) by the spectrometer, producing an averaged emission spectrum used to recover an averaged combustion temperature.

Titanium sponge powder (99.7%, -325 mesh) used is from Atlantic Equipment Engineers and zirconium powder (99%, -325 mesh) is from Alfa Aesar. Titanium powder is fed using an electrostatic aerosol generator developed previously [18]. Due to the spark ignition sensitivity of zirconium, it could not be fed using the electrostatic aerosol generator and a separate vibratory feeder was developed and utilized. The powder was loaded into a cylindrical hopper with a 0.33 mm orifice at its bottom. The powder did not fall through the orifice until the entire assembly was vibrated. The hopper was placed above a 3-mm diameter metal tube; the assembly was attached to a 30-W speaker. A carrier gas flow was supplied to the tube; the speaker was activated and the amplitude and frequency of the vibrations were adjusted to achieve a steady aerosol flow exiting the tube. Typical operating frequencies were 100-500 Hz.

Experiments were conducted in ambient air at room temperature. The particle velocities were measured from the lengths of particle streaks photographed using a modulated laser sheet placed parallel to the aerosol jet. The average particle velocities for both metals were ~ 0.9 m/s.

In each experiment, two pulse sequences are recorded; one sequence reflects the scattered light pulses and the second one includes emission pulses. Amplitudes of the scattered light pulses depend on particle diameters and are processed to correlate the pulse peak distribution with a particle size distribution for the same powder measured using a commercial particle size analyzer [18-20]. The scattered light and emission pulse sequences are shifted in time because of the time the particles travel between the two laser beams. The data analysis includes matching the two pulse sequences, so that the particle size is determined for each individual set of recorded filtered emission pulses.

Data processing

In each experiment, thousands of matching scattered light and emission pulse sets are identified which can be assigned to individual particles passing through the laser beams. Not all such pulse sets represent combustion events of interest. As described earlier [18-20], particles may be heated but not ignited in the laser beam, still producing emission pulses. Alternatively, some particles may ignite and partially burn while in the CO₂ beam, in which case their burn rate will be accelerated due to the heat absorbed from the laser. Both unignited and partially burned particles generate shorter emission pulses compared to the same size particles that ignite just after exiting the CO₂ laser beam. Thus, considering particles producing the longest emission pulses within each narrowly chosen size range represents one approach for selecting emission signatures representing complete combustion events [18-20].

Another approach, introduced here analyzed the shapes of emission pulses. Pulses were discounted, for which the amplitude was close to its peak value when the particle was just exiting the laser beam. It was assumed that such pulses represented either unignited particles, which cooled soon after exiting the laser, or particles ignited and partially burned in the laser beam.

Both approaches are discussed in detail below.

Selection of the longest emission pulses

All particles are divided between several size bins. A threshold value in terms of pulse duration, e.g., top 99 %, is selected. For each size bin, only emission pulses with

durations exceeding this threshold value are selected. The choice of both size bins and threshold values affects the final selection of pulses assumed to represent the complete particle combustion events. To examine significance of these choices on the final result, experimental data were processed considering different sets of size bins and threshold values. The results of such processing are illustrated in Fig. 2 for titanium powder. Each combination of size bins and a threshold value represented in Fig. 2 is referred to as a set number; specific descriptions of each set number are given in Table 1.

Size bins and the threshold values for sets 1 and 2 are selected so that reasonable numbers of pulses are present and relatively evenly distributed among the bins. For sets 3 and 4, the size bins are fixed to explore the effect of different threshold values. Qualitatively, for all data sets the observed effects of particle sizes on their respective burn times are similar. Applying a conventional $\tau_b \sim D^n$ fit (where D is the particle diameter and τ_b is the burn time, or emission duration) [22], one finds the exponent values $0.22 < n < 0.25$ for groups of points selected within individual sets 1-4.

Analysis similar to that presented in Fig. 3 and Table 1 was also performed for zirconium powder; the results supported the relative insensitivity of the observed effect of particle size on its burn time to the selection of specific bin sizes and threshold values.

Selection of pulses based on the signal shape analysis

When the particle emission signal is first distinguished from the noise lever, the particle must already be crossing the CO₂ laser beam. The particle velocity, v , is known; thus, it is easy to determine when the most effective particle heating by the laser will end, assuming for simplicity that the heating occurs in the zone with the diameter equal to one-half of the beam diameter, i.e., $d=165\text{ }\mu\text{m}$ [23]. The time the particle should stop being laser-heated is estimated as $t_1=d/v$. If the particle never ignites after exiting the laser beam, its emission at t_1 will be close to its maximum value. Conversely if particle ignites after exiting the beam, its emission is expected to increase markedly. In another possible case, when particle ignites and partially burns while still crossing the laser beam, it is also expected that its emission at t_1 will be relatively strong. Thus, a criterion used in this method to select the particles with useful emission signals is to compare the amplitude of the particle emission signal at t_1 to its maximum observed emission value. This approach is illustrated in Fig. 3. The inset in Fig. 3 shows the initial portion of the recorded signal. The shaded area shows the time when the particle is being laser-heated. Signal value at the instant, t_1 , when the particle is assumed to exit the laser beam (based on the particle velocity and the beam diameter) is marked by a small open circle. Another open circle marks the maximum measured emission value observed at time t_2 . When the emission signal measured at t_1 becomes a substantial fraction of the emission measured at t_2 , the emission pulse is discounted. The only arbitrarily selected parameter for this processing assesses the difference between signals measured at t_1 and t_2 that serves as the selection threshold. Experimental points selected for both Ti and Zr using selection thresholds of 1 and 5 % are shown in Fig. 4. For both metals, the trends representing the effect of particle size on burn time are similar for both thresholds, while the scatter between points is more significant for the greater threshold values. To minimize the scatter while still retaining substantial number of experimental points, the threshold of 1 % was used below.

Results

Particle size distributions measured in-situ are compared to those obtained with a commercial Beckman-Coulter LS230 analyzer in Fig. 5. The agreement between the measured particle size distributions is very good for particles less than about 25 μm for both powders. Discrepancies are observed for coarser particles, most likely associated with difficulties of aerosolizing such particles using a relatively low velocity carrying gas flow. Additional errors could be caused by non-spherical particle shapes. The experiments are focused on combustion of finer particles, so that the possible errors in the size measurements for coarser particles were less important.

Representative burning streaks for titanium and zirconium powders are shown in Fig. 6. Images are taken under identical flow conditions and camera settings. Multiple particle streaks are captured in each image because more than one particle was fed through the laser and ignited during the time of photo-exposure (0.12 s). In both cases, particles explode by the end of combustion. Fragments produced as a result of explosion often undergo secondary micro-explosions or exhibit characteristic spear points by the end of the streaks. This behavior is qualitatively consistent with the earlier observations for the larger Ti and Zr particles [11, 12, 15, 16]. Based on close particle velocities of 0.9 m/s for both metals, a difference in the streak length can be related to the difference in the burn time between the metals. Generally, Ti particle streaks are somewhat longer indicating a longer burn time compared to Zr.

Characteristic individual emission traces and respective temperature histories for burning Ti and Zr particles are shown in Figs. 7 and 8, respectively. For both metals, an initial peak in the emission trace occurs after the initial temperature increase. There is a temperature spike at early burn times, followed by a slow temperature growth to the levels that remain nearly constant during combustion. Maximum temperatures registered by color pyrometry are close to 2900 and 3100 K for titanium and zirconium, respectively. Sharp spikes in the emission traces occur at the end of the trace correlating with the micro explosions observed in the particle streaks. The temperature does not increase when the emission spike is observed; instead, for both metals, emission spike correlates with a beginning decay in the temperature.

A summary of the burn times is given in Fig. 9. Results are presented using each of the two processing methods discussed above, emission pulses selected as longest and based on the signal ratio at times t_1 and t_2 (cf. Fig. 3). For both subsets of experimental points, the burn times increase slightly with the increase in particle size, a trend similar to that observed for fine Al particles [19, 20]. Many points selected by different processing methods coincide, while scatter is somewhat greater for the points selected using the signal ratio at times t_1 and t_2 . This scatter might represent errors in the particle size measurements; similar errors would be masked in the results selected to represent the longest emission pulses.

The increase in the burn time as a function of the particle size is clearly seen for the particles finer than 10 μm , which are well represented in the data sets shown. Only relatively few particles larger than 10 μm are present for which the data are scattered. Dashed lines represent linear trends obtained fitting the data for particles less than 10 μm selected from comparison of emission signals at the times t_1 and t_2 . The processing method used to select these points is considered to be most useful because it involves only one arbitrarily selected parameter, the threshold level for the ratio of signals measured at instants t_1 and t_2 .

The burn times for Zr are shorter than for the same size Ti particles consistently with the qualitative observation based on the lengths of particle streaks (Fig. 6). A previous experiment [24] involving space and time resolved combustion of zirconium particles in a flame cloud reported individual particle burn times of 1-5 ms for particles less than 22 μm diameter, which is in agreement with the present results.

A summary of the pyrometry data is given in Fig. 10. The data shown represent a subset of emission traces selected using the signal ratio at times t_1 and t_2 .

The recorded temperatures were processed to find the average and maximum temperature value during the time when the particle emission trace was within 20-60% of its maximum value for titanium and 30-80% for zirconium. These levels were selected for each metal to remove the effect of emission spike and account for the temperature levels observed during the plateau in the temperature traces as shown in Figs. 7 and 8. For Ti, average and maximum temperatures obtained are close to 2800 K and 2900 K, respectively. For Zr, average and maximum temperatures are around 3000 K and 3100 K, respectively. The temperatures do not change as a function of the particle size for either metal.

The results of temperature measurements using spectrometer-integrated emission are illustrated in Fig. 11. Shown are two recorded spectra and their best fits obtained using Planck's formula with adjusted temperatures [25]. Several spectra were taken for each powder and the results were consistent between themselves. Comparing Figs. 10 and 11, one observes that the temperatures obtained from the complete spectra (integrating combustion emission from multiple particles), 3343 and 3683 K for Ti and Zr, respectively, are substantially higher than the combustion temperatures obtained using individual emission traces filtered at two selected wavelengths for both metals. To analyze this discrepancy, the recorded spectra were processed to select and recover the temperature using only the signals measured at the same wavelengths as used for the pyrometry (532 and 589 nm). With that approach, the temperatures from spectrometer and pyrometer effectively coincided. Therefore, the gray body assumption used to process the filtered emission signals in the color pyrometer may not be accurate for these burning particles. In earlier experiments [26], an emission spectrum for a nitromethane-zirconium powder charge was reported to demonstrate a distinctly non-gray behavior, consistently with the present results.

Discussion

Qualitatively, emission histories, particle streaks, and micro explosions observed for both Ti and Zr particles are similar to those observed for larger size particles of the same metals [11, 12, 15-17]. Previously, micro explosions were interpreted considering dissolution of oxygen and nitrogen in the burning particles, following by formation of supersaturated solutions, release of nitrogen, and formation of stoichiometric oxides [17]. This work suggests that the same combustion scenario applies to fine Zr and Ti particles.

The measured flame temperatures were compared to the adiabatic flame temperatures calculated using CEA code [27] as well as to those presented in ref. [14, 26]. Unlike CEA code, calculations in ref. [14, 26] considered forming nitride species; however, the final adiabatic flame temperatures were close to each other and, more interestingly, close to the temperatures measured in this work using the recorded emission spectra.

The measured burn times for both Ti and Zr particles are compared to earlier data [13-16] for coarser powders in Fig. 12. In both cases, the effect of particle size on burn

time for fine particles is much weaker, while both trends appear to cross at about 25-30 μm . The reason for the weak effect of particle size on the burn time is unclear. Interestingly, a weak effect of particle size on the burn time was also observed for fine Al particles [19, 20].

The nature of heat and mass transfer processes change substantially for the particles in the size range studied, transitioning from the continuum to the free molecular regime, as the particle size decreases. This could cause substantial reduction in the reaction rate when combustion is controlled by the transport of oxidizer to metal surface. Indeed, for very fine particles, the lower rate of free molecular transport of the oxidizer molecules to the particle surface may slow down the reaction rate and thus extend the burn times. At the same time, the rate of heat removal from such fine particles to colder environment is similarly reduced for the free-molecular regime; thus the reduction in the burning particle temperature may not be significant despite the reduced burn rate.

Conclusions

Combustion times and temperatures were measured for fine particles of Zr and Ti burning in room temperature air. Particles of both Zr and Ti exhibit micro explosions, similar to those observed for larger size particles of these metals. Thus, the reaction mechanism involving formation of supersaturated metal-gas solutions and subsequent gas release leading to micro explosions remains relevant for such fine particles. For both metals, measured combustion temperatures do not depend on the particle size and are close to their respective adiabatic flame temperatures. For particles finer than ca. 25 μm , the burn times are relatively weak functions of the particle size; burn times for Zr are shorter and temperatures are higher compared to the similarly sized Ti particles. It is proposed that the weak effect of particle size on the burn time is associated with the change from continuous to free-molecular heat and mass transfer regimes occurring for the particles in the size range addressed in this study.

References

1. M. Arimondi, U. Anselmi-Tamburini, A. Gobetti, Z. A. Munir, G. Spinolo, *J.Phys.Chem.B* 101 (1997) 8059-8068.
2. J. Trambukis, Z.A. Munir, *J. Am. Ceram. Soc.* 73 (1990) 1240-1245.
3. R. Orru, G. Cao, Z.A. Munir, *Chem. Eng. Sci.* 54 (1999) 3349-3355.
4. G.S. Strohm, S.F. Son, C.J. Boucher, *48th AIAA Aerospace Sciences Meeting*, Orlando, FL, 2010.
5. M. Schoenitz, T.S. Ward, E.L. Dreizin, *Proceed. Combust. Inst.* 30 II (2005) 2071-2078.
6. U.C. Durgapal, A.S. Dixit, R.G. Sarawadekar, *Proceed. 13th Int. Pyrotechn. Sem.* Grand Junction, CO, 1988.
7. K. Miyata, N. Kubota, *Propel. Explos. Pyrotechn.* 21 (1996) 29-35.
8. J.-S. Lee, L.-K. Lin, P.-J. Huang, S.-Y., Chen, P.-J., Ch'en, C.-W., Huang, S..-S Chang, *Thermochim. Acta* 181 (1991) 329-336.
9. Y.B. Ding, J.H. Sun, X.C., He, Y. Yin, Y. Xu, X.J. Huang, *Ranshao Kexue Yu Jishu/J. Combust.Sci. Techn.* 16 (2010) 353-357.
10. K.L. Cashdollar, I.A. Zlochower, *J. Loss Prevent. Proc. Industr.* 20, (2007) 337-348.
11. R.T. Meyer, L.S. Nelson, *High Temp. Sci.* 2 (1970) 35-57.

12. L.S. Nelson, D.E. Rosner, S.C. Kurzius, H.S. Levine, *Proceed. Combust. Inst.* 12 (1969) 59-70.
13. O.G. Glotov, V.E. Zarko, V.N. Simonenko, *42nd Int. Annual Conf. ICT* Karlsruhe, Germany, 2011, 45/1-45/12.
14. E. Shafirovich, S.K. Teoh, A. Varma, *Combust., Flame* 152 (2008) 262-271.
15. I.E. Molodetsky, E.L. Dreizin, C.K. Law, *Proceed. Combust. Inst.* 26 (1996) 1919-1927.
16. I.E. Molodetsky, E.P. Vicenzi, E.L. Dreizin, C.K. Law, *Combust. Flame* 112 (1998) 522-532.
17. E.L. Dreizin, *Prog. Energ. Combust. Sci.* 26 (2000) 57-78.
18. R.J. Gill, S. Mohan, E.L. Dreizin, *Rev. Sci. Instrum.* 80 (2009) 064101-1 – 064101-7.
19. R.J. Gill, C. Badiola, E.L. Dreizin, *Combust. Flame* 157 (2010) 2015-2023.
20. C. Badiola, R.J. Gill, E.L. Dreizin, *Combust. Flame* 158 (2011) 2064-2070.
21. P. Lynch, H. Krier, N. Glumac, *J. Thermophys. Heat Tr.* 24 (2010) 301-308
22. M.W. Beckstead, *Combust. Expl. Shock Waves* 41 (2005) 533-546.
23. S. Mohan, M.A. Trunov, E.L. Dreizin, *J. Propuls. Power* 24 (2008) 199-205.
24. Y. Ding, J. Sun, X. He, Q. Wang, Y. Yin, Y. Xu, X. Chen, *Chinese Sci. Bul.* 55 (2010) 3954-3959.
25. J.P. Holman, *Heat Transfer*. New York, NY: McGraw Hill, 2009.
26. S. Goroshin, D.L. Frost, J. Levine, A. Yoshinaka, F. Zhang, *Propel. Explos. Pyrotechn.* 31 (2006) 169-181.
27. S. Gordon, B.J. McBride, *NASA Reference Publication 1311*, 1996.

Table 1. Size bins and threshold values for each data set represented in Figure 3.

Set	Size Bins (μm)				Threshold
1	1-3	3-5	5-7	7-30	98 %
2	0.5-2	2-3	3-5	5-20	99 %
3	1-2.5	2.5-5	5-7.5	7.5-10	98 %
4	1-2.5	2.5-5	5-7.5	7.5-10	95 %

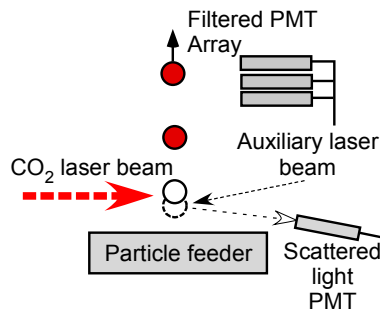


Figure 1. Experimental apparatus and diagnostics to obtain particle size and emission pulse correlation.

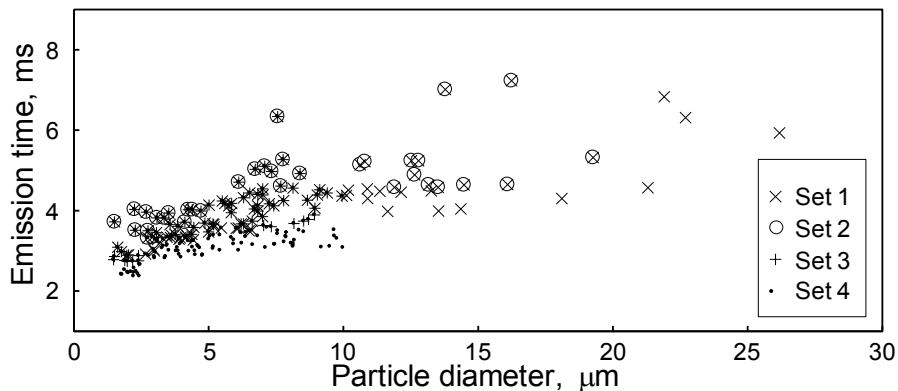


Figure 2. Longest emission times of Ti particles as a function of their diameters selected among all recorded emission pulses using size bins and threshold values shown in Table 1.

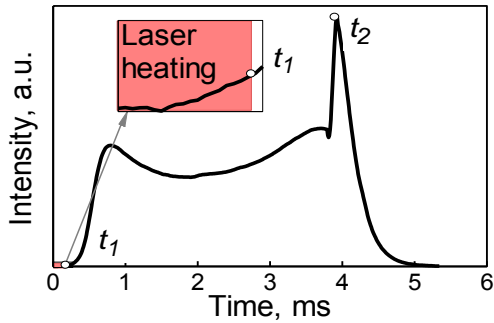


Figure 3. Characteristic emission pulse for burning Ti particle.

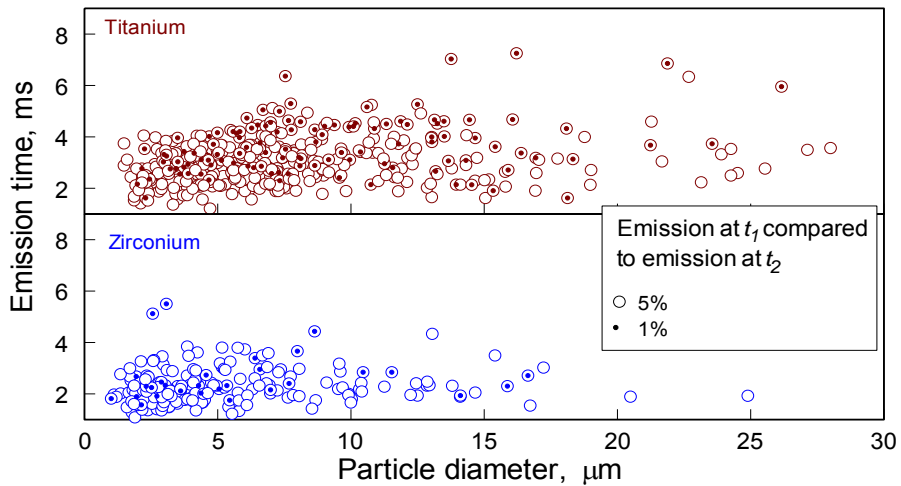


Figure 4. Emission time as a function of particle diameter for both Ti and Zr; the experimental points are selected based on the maximum fraction of emission signal at the time t_1 compared to that at t_2 (cf. Fig. 3).

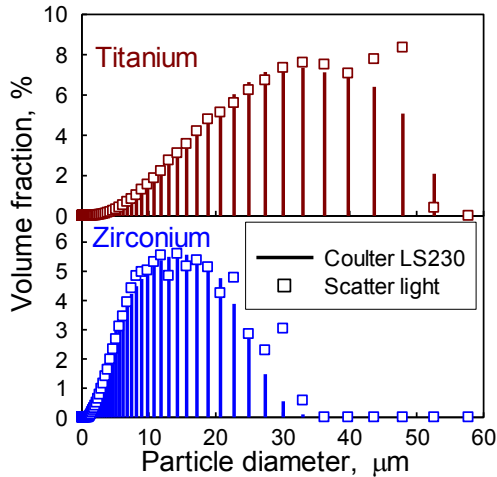


Figure 5. Particle size distributions as measured in situ and by Beckman-Coulter LS230 analyzer.

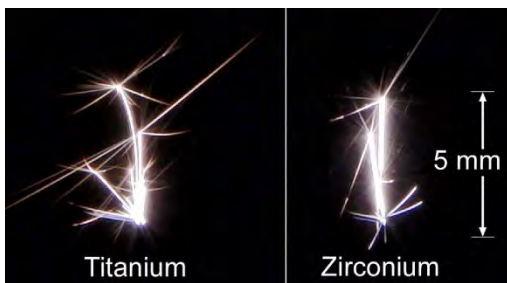


Figure 6. Streaks of laser-ignited particles of Ti and Zr.

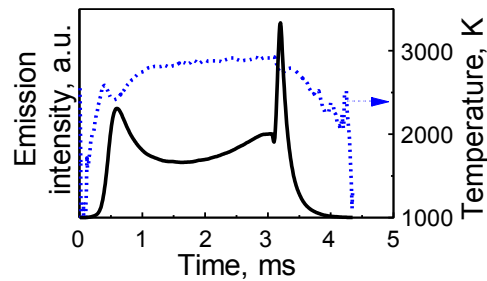


Figure 7. Emission trace and temperature history of a burning Ti particle. The particle size recovered from the respective scattered light pulse is $5.5 \mu\text{m}$.

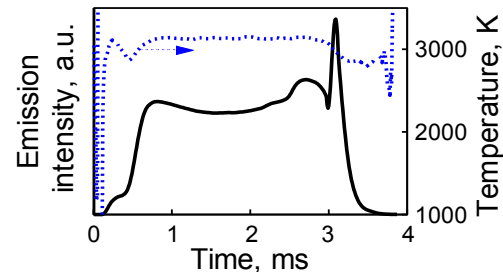


Figure 8. Emission trace and temperature history of a burning Zr particle. The particle size recovered from the respective scattered light pulse is $5.1 \mu\text{m}$.

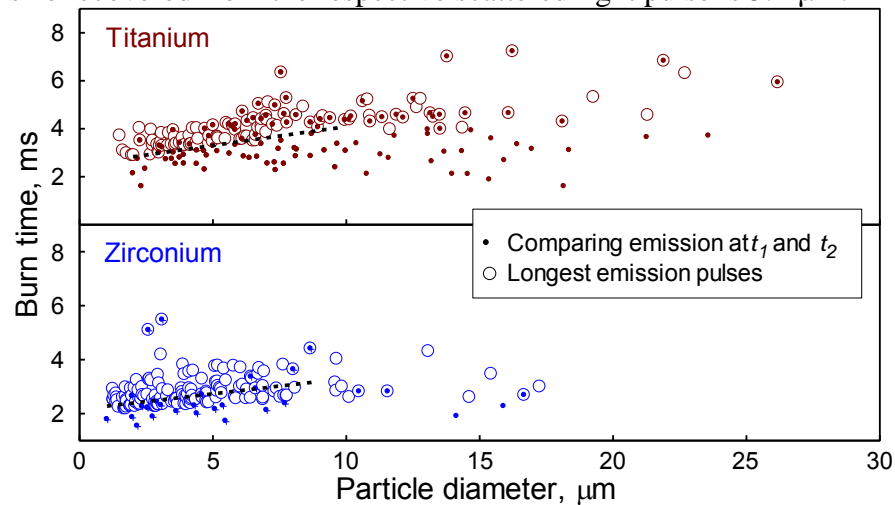


Figure 9. Burn times for Zr and Ti particles ignited in a CO_2 laser beam. Different symbols represent points selected using different data processing methods.

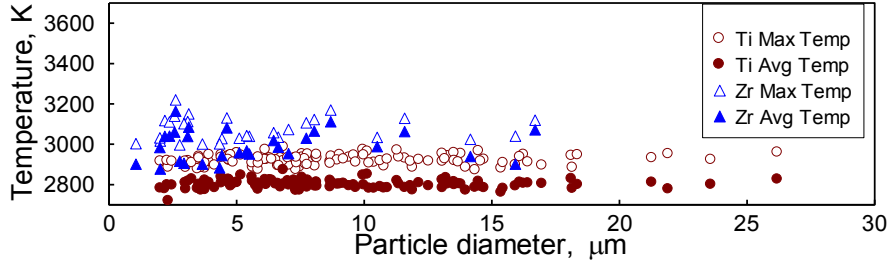


Figure 10. Averaged and maximum particle combustion temperatures obtained by color pyrometry using emission signals filtered at 532 and 589 nm for the points selected based on emission ratio at the times t_1 and t_2 (cf. Fig. 3).

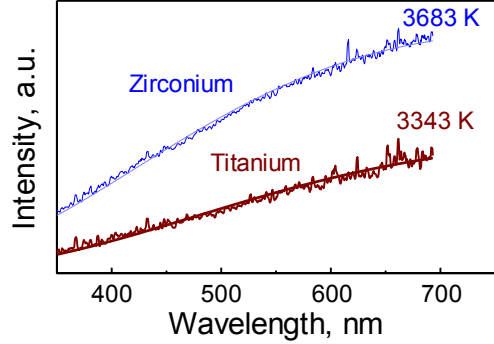


Figure 11. Recorded integrated emission spectra produced by burning Zr and Ti particles. Integration times are 25 s. The best fit lines obtained using Planck's formula are shown as well as the temperatures corresponding to each fit.

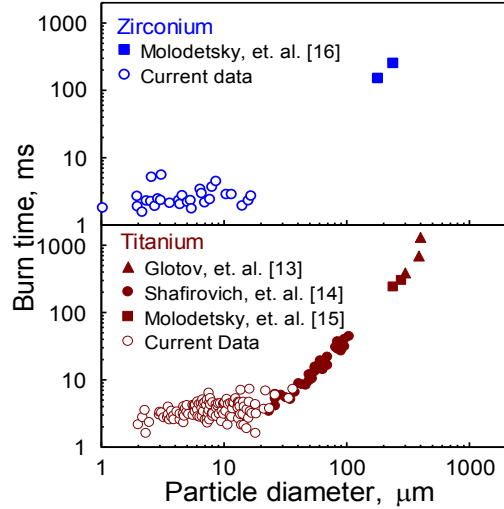


Figure 12. Burn times as a function of the particle size.

CHAPTER 8: ALUMINUM PARTICLE COMBUSTION IN TURBULENT FLAMES

Introduction

Metal powders are used as fuel additives in many energetic formulations including propellants [1-3], explosives [4-9], and pyrotechnics [10-13]. In most practical configurations, combustion of metal particles occurs in turbulent flows [14-18], commonly involving hydrocarbon combustion products mixed with surrounding atmosphere. Performance of such energetic systems is described using advanced hydrodynamic codes [19-22] which evaluate contribution of metal particle combustion using simplified submodels. The most commonly used metal additive for energetic formulations is aluminum, and many current submodels for aluminum combustion are based on experiments reviewed in ref. [23], using primarily coarse, 50 – 250 μm particles burning under well-characterized, laminar laboratory conditions. Thus, despite the advanced capabilities of contemporary hydrocodes in describing the flow and mixing patterns containing burning aluminum particles, the effect of these conditions on the burn rate remains unaccounted for. Experimental studies of the effect of turbulence on metal combustion are relatively scarce and all involve dust explosions [24-27], yielding correlations between turbulence and observed pressures and rates of pressure rise, which are difficult to interpret in terms of individual particle burn rates. On the other hand, useful correlations for the effect of turbulence on evaporation rate of liquid fuel droplet have been developed and reviewed in ref. [28]. A simple correction for the droplet vaporization rate under turbulent convective flow, K_t , is proposed as:

$$\frac{K_t}{K_l} = 1 + CI + C_{Frö} \text{Re}_d^{1/2} Sc^{1/3} \quad (1)$$

where K_l is the average vaporization rate under laminar flow conditions, C is a constant, I is turbulence intensity, and the last term on the right hand side gives Frössling's correlation for the vaporization rate in laminar flow conditions estimated based on the vaporization rate in stationary environment. It includes Frössling's coefficient $C_{Frö} \approx 0.18$ multiplied by Re_d , the Reynolds number based on the particle diameter, and by Sc , the Schmidt number. The value of turbulence intensity, I , is defined as:

$$I = \frac{u'}{U} \quad (2)$$

where U is the longitudinal mean velocity component and u' is root mean square of the fluctuating velocity component along the transversal flow direction. An expression similar to Eq. (1) which corrects the metal particle burn rate as a function of the turbulence intensity would substantially improve the predictive accuracy of hydrocodes dealing with metal combustion. However, no data necessary to obtain such an expression could be found in the literature. This paper is aimed to begin generating such experimental data and thus to begin quantifying the effect of turbulent flow conditions on the metal particle combustion.

Experimental General Approach

The experimental setup is schematically shown in Fig. 1. Aluminum powder is fed through an air-acetylene flame. The particles ignite and burn in the combustion products of the hydrocarbon flame, while surrounding air is mixed in the combustion environment providing additional oxidizer. Initial flame and particle flow are directed vertically. The turbulence is introduced by three auxiliary nozzles placed horizontally around the flame and directed tangentially within a short cylindrical enclosure. Air is fed through auxiliary nozzles at a controlled rate enabling one to adjust the level of the achieved turbulence. The generated flow pattern inducing the flame turbulence is cylindrically symmetric. This method of producing turbulence is similar to the method used in refs. [29, 30], where tangentially directed fans were installed inside an explosion vessel. In addition to the new flow pattern, this approach enhances mixing of the flame and burning particles with the surrounding air. These two effects cannot be separated from each other in the present experiment. Note, however, that the situation is analogous for a fireball produced by a metallized explosive and expanding in air: turbulent mixing of the fireball with its surroundings affects both flow pattern and gas composition to which the metal particles within the expanding fireball are subjected. The gross effect of this turbulent mixing on the particle combustion rate is of substantial interest, and this effect is explored here.

The particle burn times are measured as a function of the produced turbulence level. The burn times are obtained from the streaks produced by incandescent particles. The streaks are photographed through a rapidly spinning disk with multiple holes made along its circumference (chopper) so that the streak images appear dashed, and the number of dashes per streak can be used to determine the burn time. A statistical distribution of the burn times is correlated with the measured particle size distribution to obtain the particle burn times as a function of their diameters. Note that most particles ignite while being introduced into the laminar flame zone and continue burning passing through the turbulent regions. The measured burn times do not discriminate between these, possibly different combustion regimes. Different particles arrive into the flow regions affected by turbulent mixing at different stages of their combustion. The precise instant when each particle becomes affected by turbulent mixing depends on at least two parameters: particle size and its axial coordinate. Larger particles tend to have longer pre-heating times; particles located further away from the jet's center tend to ignite sooner because of greater oxidizer availability. Neither particle size nor its exact axial location could be measured directly, thus meaningful analysis of the respective data where the "laminar" and "turbulent" burn times are separated would be impossible. Once again, of interest is the gross effect of turbulence on the burn times of metal particles, and it is addressed in the present experiments.

Photographed particle streaks are also used to quantify the turbulence intensity. When a vertically rising particle reaches the turbulent region, its trajectory is observed to curve. From the observed trajectory curvature, acceleration is estimated. The particle mass is evaluated based on its measured burn time and the above mentioned correlation between the burn time and particle size. Finally, the drag force is estimated using the particle mass and acceleration; the force is assumed to be directly proportional to the

transversal flow velocity based on the Stokes equation. Thus, the value of the transversal component of the gas velocity curving a particle's vertical trajectory is obtained. The longitudinal component of the gas velocity is also obtained from the photographed particle streaks assuming that the particles follow the gas flow prior to entering the turbulent region.

Further details of the experimental apparatus and procedure are described below.

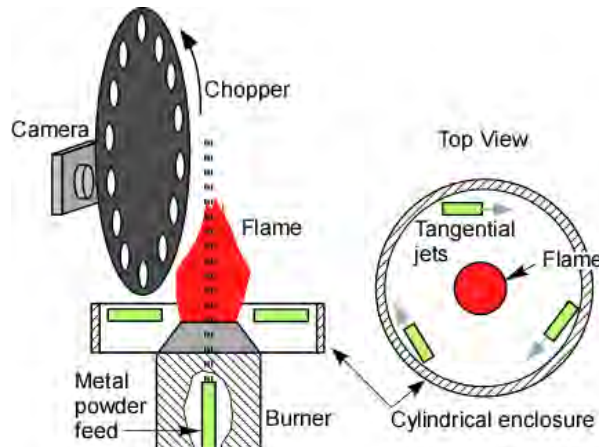


Figure 1. Schematic diagram of the experimental setup

Powder Feeder

The powder feeder was designed around the concept of creating an aerosol from directing a high velocity gas jet on a powder loaded into the threads of a screw (Fig. 2). In this design, the aerosol jet velocity is controlled by the flow rate of the carrier gas. The mass feed rate of the powder is adjusted separately by changing the thickness of the coating and rate of the screw rotation.

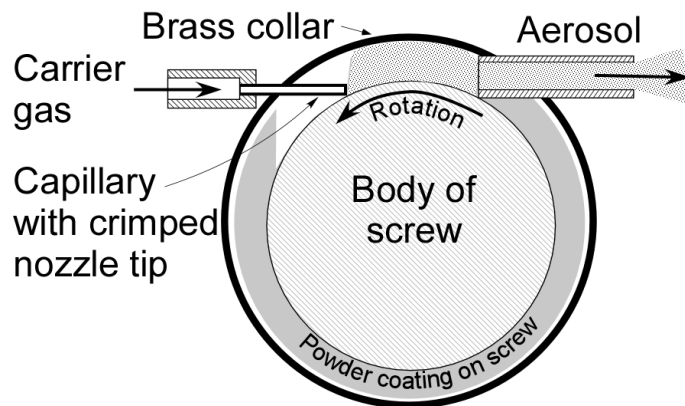


Figure 2. Schematic diagram of powder feeder

A stainless steel screw, $\frac{3}{4}''$ (19.05 mm) diameter with 16 threads per inch was used. To coat the screw with powder, the dry powder was placed in a plastic dish. The mass of powder was measured and recorded. Using a short bristle brush, the powder was deposited into the threads of the screw. After the powder had been applied, the remaining weight was recorded so that the total mass of the sample to be used in experiments was determined. The screw loaded with powder was then placed into the

feeder assembly, including a cylindrical brass collar (see Fig. 2) and a coupling connecting it with the motor.

The brass collar has feedthroughs for the carrier gas inlet and aerosol outlet. A brass capillary tube, (1/16" or 1.59 mm OD) inserted through the carrier gas inlet, was crimped to make a triangular nozzle tip (~0.62 mm on each side) that conforms to the "V" channel of the screw threads. Nitrogen was used as a carrier gas. The nozzle tip directs a high velocity nitrogen jet into the thread to efficiently remove and aerosolize the powder. The aerosol exits through an opposing small diameter brass tube on the feed screw collar (inserted into the aerosol outlet feedthrough). The brass collar together with the aerosol outlet move along the screw during the operation. The aerosol outlet is connected to the burner using flexible plastic tubing. The nitrogen feed rate is measured using a rotameter.

The rotational speed of the screw controls the amount of powder that is aerosolized and fed into the burner. The feed screw is coupled with a knuckle joint to a speed reduction gear train driven by a DC motor. Through these gears, the motor provides a nominal operating range of 0-1.9 RPM. The motor speed is controlled by a voltage regulated, 0-30 VDC power supply.

A typical powder load was 2.6 g, which was placed over about 10-cm length of the screw. In preliminary tests, various voltages and respective powder feed rates were tested. The voltage selected, 4 V, fed enough of the powder into the burner to obtain multiple particle streaks in each flame image. A higher voltage fed too many particles, so that the images became saturated. A lower voltage fed too few particles and it was difficult to identify their streaks in most flame images.

Burner

A schematic diagram of the steel burner and enclosure used to generate turbulent flow patterns is shown in Fig. 3. Acetylene and air are fed through a tube with narrowed internal diameter. Fine brass screens were installed to enhance mixing. A thin stainless steel tube placed at the axis of the burner was used to inject the particles carried by nitrogen. The flame shape is sensitive to the position of the central tube, which must be carefully centered to achieve the desired symmetric flame configuration. The produced flame is laminar. To generate turbulence, the flame needs to be disturbed or agitated. This is achieved by directing three tangential air jets around the flame. The burner is equipped with an attachment including three nozzles directed tangentially inside a hollow cylindrical enclosure. The enclosure and one of the nozzles are shown in Fig. 3. The burner is placed inside the cylinder, and the air flow is adjusted to create the desired level of turbulence. Individual rotameters are used to monitor air, acetylene, and air flow rates.

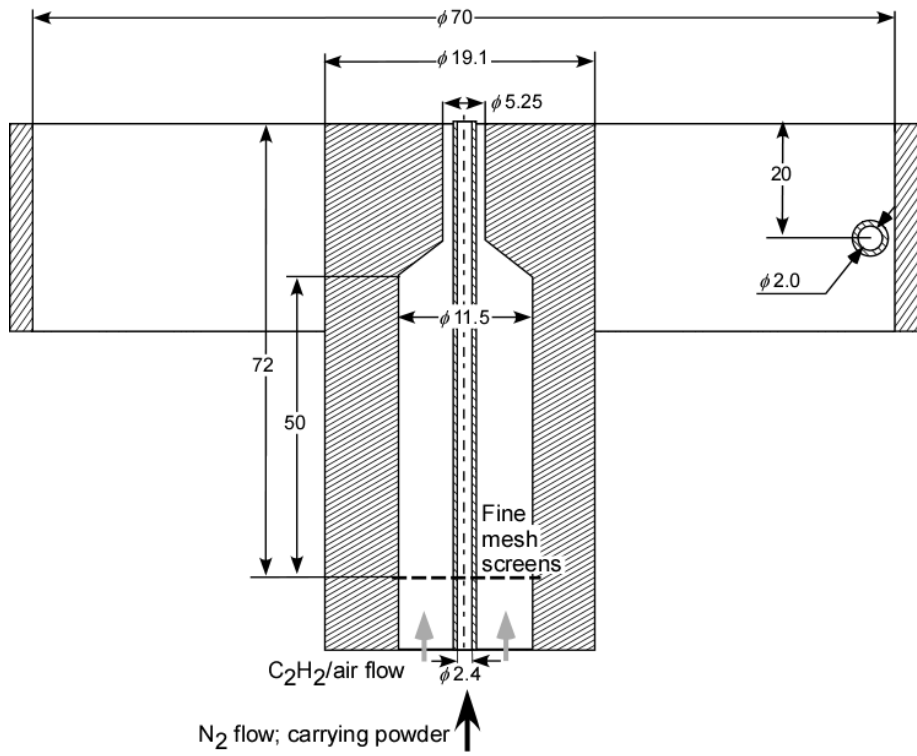


Figure 3. Schematic diagram of the burner together with enclosure and one of the turbulence-generating nozzles. All dimensions are in mm.

Material

A spherical aluminum powder designated as X-65 by the manufacturer, Alcan-Toyo America Inc., was used. The particle size distribution for this powder was measured using a Beckman-Coulter LS230 Enhanced Particle Analyzer and is shown in Fig. 4. This size distribution was used to process experimental data, as described below.

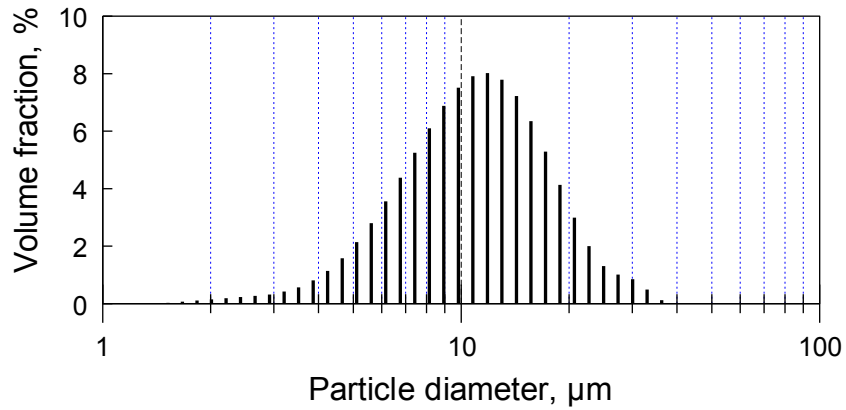


Figure 4. Particle size distribution for X-65 aluminum powder used in experiments

Images and image processing

The images were taken using a DSC-H50 camera set at a shutter speed of 1/60 s and an aperture of f/8.0. A chopper disk attached to a motor was installed in front of the

camera. The chopper was a 12-cm diameter disk with 36 holes of equal diameter made along its circumference. In preliminary tests, a light source was placed in front of the chopper and a photodiode was placed behind it to calibrate the chopping time interval adjusted by the motor speed. The chopping period, $\tau=0.21$ ms was used in experiments (corresponding to the motor speed of about 8000 rpm). Thus, each image taken during 1/60 s included 79 exposures.

A characteristic flame image with particle streaks is shown in Fig. 5. The particle streaks appear above the premixed (bright) portion of the air-acetylene flame. Initially, the particles move nearly vertically, but when they reach a turbulent zone, their trajectories curve. Several images with top views of the flame and burning particle streaks are shown in Fig. 6. The latter images were taken without the chopper disk. At different instants when different images in Fig. 6 were taken, particles move away from the flame in different directions. We observed no selected direction in which the particles would be preferentially deflected; there was also no detectable swirling pattern formed by particle streaks. Side view images of the flame, as in Fig. 5 were processed further. For each image, all clearly discernible streaks were identified, and the number of dashes per streak was calculated. The overlapping or partially visible streaks were discarded. For each flow condition, at least 200 images were taken for processing.

In order to determine the transversal flow velocity, necessary for assessing the turbulence level, a location where particle trajectories were curved was visually identified. For that location, particle coordinates for three sequential exposures (defined by the chopper positions) were measured, as illustrated in Fig. 7. Note that only particles remaining in focus during their entire observed trajectories were considered, so that the changes in their velocity component directed towards or away from the camera were negligible. The camera was focused at the center axis of the burner and the depth of the focal field was about 10 mm. The camera was about 200 mm away from the flame. A large inset in Fig. 7 shows a portion of the flame image with several streaks. A small inset shows the portion of the image where the curving of the particle trajectory began so that three sequential locations for a selected particle were identified and characterized. Both longitudinal, U , and transversal, u , particle velocities were determined before and after the trajectory started to curve (subscripts 1 and 2, respectively) as:

$$\begin{aligned} U_1 &= \frac{\Delta y_1}{\tau}; & U_2 &= \frac{\Delta y_2}{\tau}; \\ u_1 &= \frac{\Delta x_1}{\tau}; & u_2 &= \frac{\Delta x_2}{\tau} \end{aligned} \quad (3)$$

The average value between U_1 and U_2 was used as U . Note that the values of U_1 and U_2 were typically close to each other (and much greater than the slip velocity, estimated to be less than 1 mm/s for 10 μm particles). The transversal acceleration was then obtained as

$$a = \frac{u_2 - u_1}{\tau} \quad (4)$$

Finally, the transversal gas velocity u' was determined assuming that this acceleration is produced by Stokes force, so that

$$ma = 6\pi\eta ru' \quad (5)$$

where m is the particle mass and η is the gas viscosity estimated at the gas surrounding temperature (assumed to be close to 1160 K). The obtained value of u' characterizes only one of two components of the transversal gas velocity. However, it was assumed to

represent the value of u' adequately because of the cylindrical symmetry of the turbulence-generating flow. This assumption is further supported by radially expanding particle trajectories shown in Fig. 6. Note that the longitudinal particle velocities (varied around 4 m/s for individual particles) were, as expected, very close to the gas velocity estimated based on the measured gas flow rates. The ratio of u'/U_1 was taken as the turbulence intensity, I , in this work.



Figure 5. A characteristic side view image of a flame with burning Al particle streaks. The flow rates are: acetylene: 0.9 SCFH (standard cubic feet per hour), air: 10 SCFH, nitrogen: 2 SCFH. Turbulizing air flow is set at 100 SCFH.

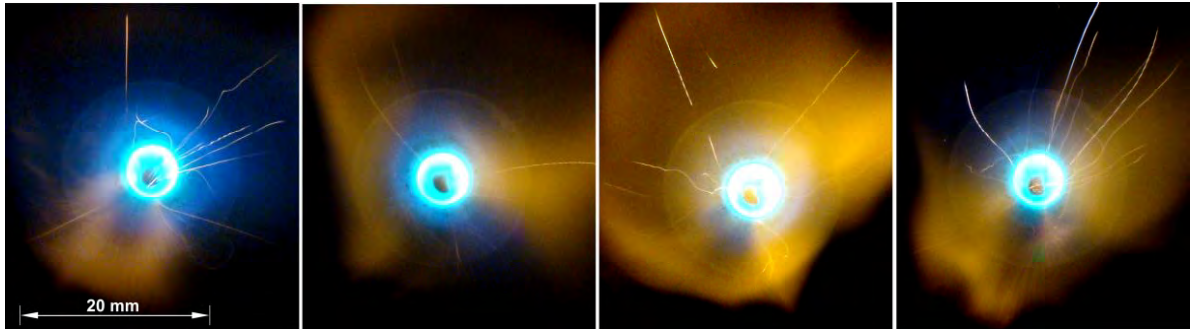


Figure 6. Characteristic top view images of a flame with burning Al particle streaks. The flow rates are: acetylene: 0.9 SCFH (standard cubic feet per hour), air: 10 SCFH, nitrogen: 2 SCFH. Turbulizing air flow is set at 100 SCFH.

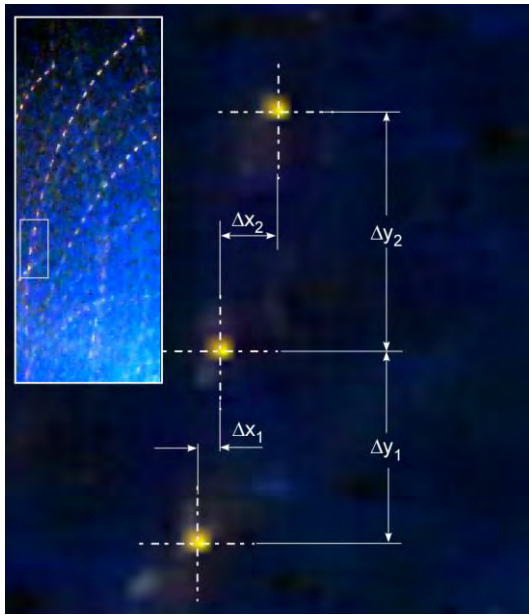


Figure 7. A fraction of the image used to determine particle longitudinal velocity and transversal acceleration used to quantify the turbulence level. A large inset shows a fragment of the flame image and the small inset shows the subregion selected to determine the particle velocities.

Results

The turbulence intensities for the turbulizing flows at 50 and 100 SCFH were respectively 0.031 and 0.080. These are values averaged over 12 particle streaks analyzed for each flow condition.

The burn time measurements are presented as histograms showing the number of particles versus their burn times broken into 18 bins. The bin times were selected in the logarithmic scale. The histograms are shown in Fig. 8 for the experiments performed at different turbulence levels. It is clear that a higher level of turbulence results in shorter burn times.

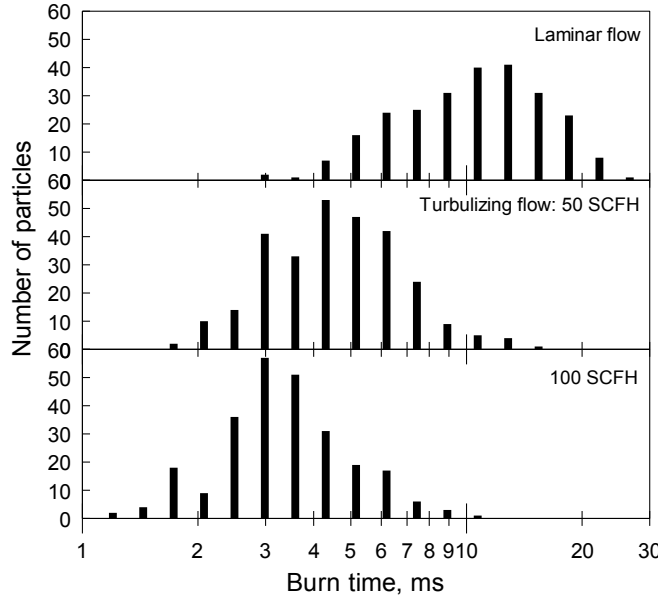


Figure 8. Histograms summarizing burn time measurements for experiments at different turbulence levels.

Using the data from Figs. 4 and 8, burn times could be directly correlated with the particle sizes. First, the volume-based particle size distributions shown in Fig. 4 were transferred into number-based distributions to be directly comparable to the data shown in Fig. 8. A plot for cumulative particle number density was obtained as shown by circles in Fig. 9. For convenience, the trend shown in Fig. 9 was fitted using a lognormal function, describing the particle diameter as a function of the cumulative particle number density, N_d :

$$N_d = \frac{1}{2} + \frac{1}{2} \operatorname{erf} \left[\frac{\ln(d) - \ln(\tilde{d})}{\sigma \sqrt{2}} \right] \quad (6)$$

where parameters σ , and \tilde{d} were found to be respectively, 0.66 and 3.75 μm . The fitting used the Levenberg-Marquardt algorithm in PSIplot software. The fitting function is also shown in Fig. 9. The identified fitting function was used to recalculate the values of particle diameters corresponding to the measured number (or number densities) of particles in each of the bins shown in Fig. 8. In other words, for each burn time bin shown in Fig. 8, corresponding cumulative particle number density was obtained. Using Fig. 8, for each such value of the cumulative particle number density, respective particle diameter was found.

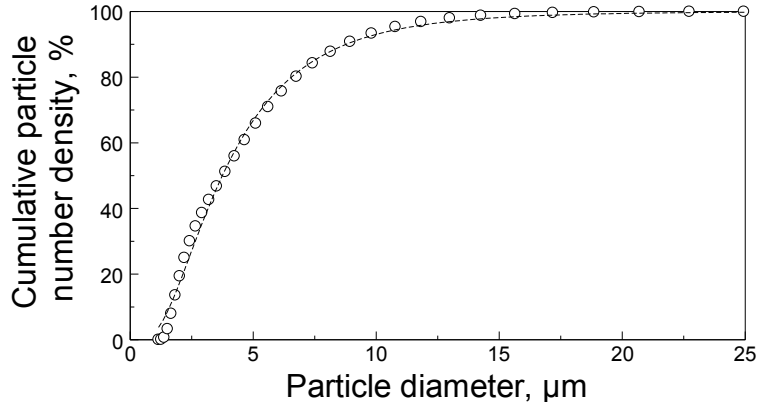


Figure 9. Cumulative percentage of particle number vs. particle diameter obtained from data in Fig. 4. Dashed line shows a fitting function.

The resulting plot is shown in Fig. 10. For comparison, the burn times from ref. [23] are also shown where an equation for particle burn time (in ms) is proposed:

$$t_b = \frac{ad^n}{X_{\text{eff}} p^{0.1} T_0^{0.2}} \quad (7)$$

where X_{eff} is effective oxidizer concentration, $p=1$ atm, is pressure, $T_0 = 298$ K is the ambient temperature, $n=1.8$ is the exponent, and $a=0.00735$ is a constant. The diameter, d , is entered in μm . The effective oxidizer concentration is calculated following ref. [23] as:

$$X_{\text{eff}} = C_{O_2} + 0.533C_{H_2O} + 0.135C_{CO_2} \quad (8)$$

where C_{O_2} , C_{H_2O} , and C_{CO_2} stand for concentrations of the respective oxidizers. Two calculations were performed using Eqs. (7) and (8) assuming that the oxidizer is oxygen in air ($X_{\text{eff}}=0.2$) or assuming that the particles burn in the combustion products of the fully reacted oxygen and acetylene:



In the latter case, the combined concentrations of H_2O and CO_2 were assumed to be equal to that of the oxygen initially contained in air and consumed by acetylene, respectively,

$$X_{\text{eff}} = 0.2 \left(0.533 \cdot \frac{1}{3} + 0.135 \cdot \frac{2}{3} \right) = 0.0535$$

As shown in Fig. 10, the correlation presented in ref. [23] substantially underestimates the particle burn times compared to the experimental data. This result is consistent with recent measurements using a shock tube experimental apparatus [31] and experiments dealing with laser-ignited individual aluminum particles [32-34]. Fitting lines for the experimental points were obtained using d^n rate law, in which the particle burn time is proportional to their diameters in power n . All sets of experimental points were described with the d^n rate law with $n \approx 0.3 \pm 0.1$.

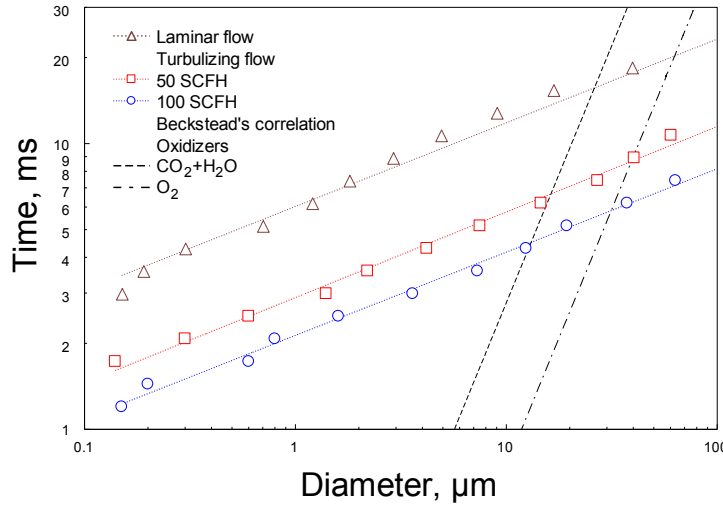


Figure 10. Particle burn times versus their size.

Correlation for the burn rate

The burn rate, \dot{m} , in g/s was roughly estimated as the mass of particle divided by its total burn time. For each particle size, the particle mass was obtained using the aluminum density of 2.7 g/m^3 . Recasting experimental data from Fig. 10 in terms of burn rates is shown in log-log scale in Fig. 11. The best fit for each of the experimental data point sets was found using a power function:

$$\dot{m} = K \cdot d^n \quad (10)$$

where K and n were adjustable parameters and particle diameter, d , was taken in μm .

The best fit lines are shown in Fig. 10. For all data sets, the value of $n=2.69$ was identified. The values of the rate coefficients K are given in Table 1 for different turbulence intensities.

Table 1. Turbulence intensities for different experimental situations and respective values of the burn rate coefficients

Turbulizing flow rate, SCFH	0	50	100
Turbulence intensity, I	0	0.036	0.080
Rate coefficient, $K, \times 10^{-10} [\text{g}/(\text{s} \cdot \mu\text{m}^{2.69})]$	2.08	3.40	5.18
K_t/K_l	1	1.63	2.49

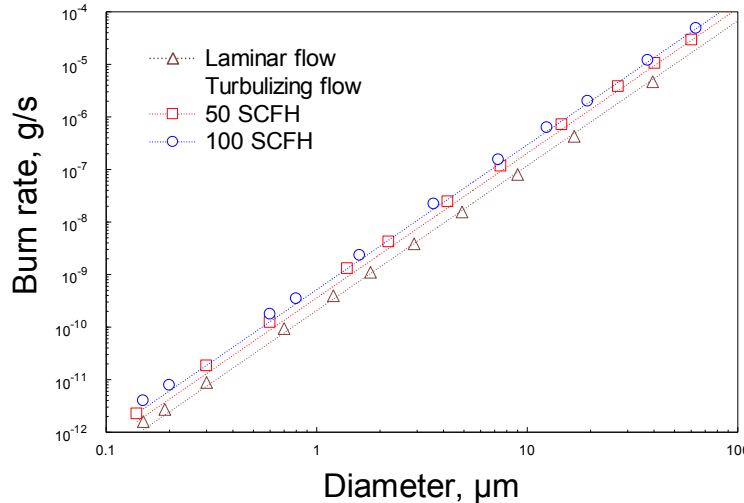


Fig. 11. Burn rates for Al particles at different turbulence levels.

For practical situations, it is useful to obtain a correction accounting for the effect of turbulence similar to Eq. (1). For the present experimental situation, the values of Re_d are very small, close to 0.041 and 0.042 for turbulence intensities of 0.036 and 0.080, respectively. The value of Schmidt number is close to 1, so that the last term in Eq. (9) becomes much smaller than 1 and can be neglected. Thus, a simplified expression for the burn rate correction is:

$$\frac{K_t}{K_l} = 1 + CI \quad (11)$$

Using Eq. (11), one can find the value of coefficient C for both turbulence intensities used in the present experiments. Based on the values from Table 1, one finds that for the turbulence intensities of 0.036 and 0.080 the values of C are 17.6 and 18.6, respectively. These values are quite close to each other suggesting that using an average of $C \approx 18.2$ in Eq. (11) provides a reasonably accurate correlation for the burn rate as a function of the turbulence intensity.

Conclusions

An experimental methodology is developed to study the effect of turbulence on combustion of fine aluminum particles. In these experiments, changes in the flow pattern are coupled with changes in mixing of the flame with external oxidizer. Both changes are affecting the particle burn rates. Experiments performed with a laminar flow and two different turbulence levels have shown a significant effect of flow conditions on the burn rates of aluminum powders. The measured burn times are longer than predicted for the micron-sized Al particles using a correlation based on survey of earlier experiments, mostly with coarser Al powders [23]. In agreement with recent studies [31-34], the burn times are proportional to $d^{0.3}$. Increased turbulence intensity results in substantial reduction of the particle burn time. The experimental bulk burn rates are well described by a $\sim d^{2.69}$ function for all flow conditions. Present data suggest that the burn rate for particle combustion in a laminar environment should be multiplied by $1 + 18.2I$, where I is the turbulence intensity, to estimate the acceleration of aluminum combustion in turbulent environments similar to those considered in the present experiments.

References

- [1] E.W. Price, Combustion of Metalized Propellants, In: K. K. Kuo and M. Summerfield (eds.) *Progr. Astronaut. Aero.* 90, Amer. Inst. of Aeronautics and Astronautics. New York (1984) 479–514.
- [2] A. Davis, *Combust. Flame*, 7 (1963) 359-367.
- [3] F. Maggi, A. Bandera, L. Galfetti, L.T. De Luca, T.L. Jackson, *Acta Astronaut.*, 66 (2010) 1563-1573.
- [4] D.L. Frost, F. Zhang, *Mater. Sci. Forum* 465-466 (2004) 421-426.
- [5] A.M. Grishkin, L.V. Dubnov, V.Y. Davydov, Y.A. Levshina, T.N. Mikhailova, *Fizika Goreniya i Vzryva*, 29 (1993) 115-117.
- [6] H.D. Jones, F.J. Zerilli, *MRS Proceedings* (1992) 296 (1993) 311-315.
- [7] P.J. Miller, R.H. Guirguis, *MRS Proceedings* (1992) 296 (1993) 299-304.
- [8] J.R. Carney, J.S. Miller, J.C. Gump, G.I. Pangilinan, *Rev. Sci. Instrum.*, 77 (2006).
- [9] C.K. Kim, J.G. Moon, J.S. Hwang, M.C. Lai, K.S. Im, Afterburning of TNT explosive products in air with aluminum particles, 46th AIAA Aerospace Sciences Meeting, Reno, NV, 2008.
- [10] A.G. Rajendran, C.B. Kartha, V.V. Babu, *Defence Sci. J.*, 50 (2000) 199-206.
- [11] P. Gillard, M. Roux, *Propell. Explos. Pyrot.*, 27 (2002) 72-79.
- [12] S.H. Ba, Q.J. Jiao, H. Ren, *Hanneng Cailiao/Chinese Journal of Energetic Materials*, 16 (2008) 219-221.
- [13] K.J. Smit, R.J. Hancox, D.J. Hatt, S.P. Murphy, L.V. De Yong, *Appl. Spectrosc.*, 51 (1997) 1400-1404.
- [14] M.F. Gogulya, M.N. Makhov, M.A. Brazhnikov, A.Y. Dolgoborodov, V.I. Arkhipov, A.N. Zhigach, I.O. Leipunskii, M.L. Kuskov, *Combust. Explos. Shock+*, 44 (2008) 198-212.
- [15] D.L. Frost, M. Cairns, S. Goroshin, F. Zhang, *AIP Conference Proceedings* 955 (2007) 781-784.
- [16] S. Goroshin, D.L. Frost, J. Levine, A. Yoshinaka, F. Zhang, *Propell. Explos. Pyrot.*, 31 (2006) 169-181.
- [17] M.F. Gogulya, M.N. Makhov, A.Y. Dolgoborodov, M.A. Brazhnikov, V.I. Arkhipov, V.G. Shchetinin, *Combust. Explos. Shock+*, 40 (2004) 445-457.
- [18] C.L. Yeh, M.M. Mench, K.K. Kuo, *Combust. Sci. Technol.*, 126 (1997) 271-289.
- [19] P.J. Miller, *MRS Proceedings* (1995), 418 (1996) 413-420.
- [20] S.K. Chidester, C.M. Tarver, L.G. Green, P.A. Urtiew, *Combust. Flame*, 110 (1997) 264-280.
- [21] J.J.I. Yoh, M.A. McClelland, J.L. Maienschein, C.M. Tarver, *P. Combust. Inst.* 31 (2007) 2353-2359.
- [22] V.W. Manner, S.J. Pemberton, J.A. Gunderson, T.J. Herrera, J.M. Lloyd, P.J. Salazar, P. Rae, B.C. Tappan, *Propell. Explos. Pyrot.*, 37 (2012) 198-206.
- [23] M.W. Beckstead, *Combust. Explos. Shock+*, 41 (2005) 533-546.
- [24] K.L. Cashdollar, *J. Loss Prevent.Proc.*, 13 (2000) 183-199.
- [25] Y.K. Pu, J. Jarosinski, V.G. Johnson, C.W. Kauffman, *P. Combust. Inst.*, 23 (1991) 843-849.
- [26] Z. Chen, B. Fan, *J. Loss Prevent.Proc.*, 18 (2005) 13-19.
- [27] A.L. Kuhl, P. Neuwald, H. Reichenbach, *Combust. Explos. Shock+*, 42 (2006) 731-734.
- [28] M. Birouk, I. Gökalp, *Prog. Energ. Combust.*, 32 (2006) 408-423.

- [29] D. Bradley, Z. Chen, J.R. Swithenbank, *P. Combust. Inst.*, 22 (1989) 1767-1775.
- [30] R.K. Kumar, E.M. Bowles, K.J. Mintz, *Combust. Flame*, 89 (1992) 320-332.
- [31] P. Lynch, H. Krier, N. Glumac, *P. Combust. Inst.*, 32 (2009) 1887-1893.
- [32] C. Badiola, R.J. Gill, E.L. Dreizin, *Combust. Flame*, 158 (2011) 2064-2070.
- [33] R.J. Gill, C. Badiola, E.L. Dreizin, *Combust. Flame*, 157 (2010) 2015-2023.
- [34] R.J. Gill, S. Mohan, E.L. Dreizin, *Rev. Sci. Instrum.*, 80 (2009) 064101-064101 – 064101-064107.

CHAPTER 9: COMBUSTION OF FINE ALUMINUM AND MAGNESIUM POWDERS IN WATER

Introduction

Metal powders have high combustion enthalpies and thus are widely used as components for pyrotechnics, explosives, and solid propellants for both air and underwater propulsion systems [1-6], where they react with such oxidizers as O₂, CO₂, and H₂O. More recently, both low- and high-temperature reactions of metals with water were explored in systems aimed at producing hydrogen and electric energy, with most studies focused on Al and Mg [5-16]. Compared with the traditional hydrogen production plants based on natural gas steam reforming, producing CO₂ with rates close to 7.5 kgCO₂/kgH₂, the systems based on metal/water combustion are theoretically free of greenhouse gas emission [8, 10, 11].

Design of both traditional energetic systems involving combustion of Al and Mg and novel hydrogen and energy generating plants requires detailed understanding and quantitative description of dynamics of respective combustion processes. However, there are relatively few studies presenting quantitative data on burn rates of Al and Mg in water. Most of the published reports present experimental data and correlations derived for coarse metal particles, e.g., particles coarser than 20 μm were used in Refs. [17, 18], and 50- μm particles were used in Refs. [18-20]. A popular correlation proposed by M. Beckstead [17] for burn times of aluminum particles in different environments is largely based on experiments with coarse powders. The correlation might not remain useful for fine particles, although fine particles will likely be employed in practical systems, where dimensions of the combustion chambers are limited, and thus shorter reaction times are desired. Reactions of fine aluminum particles in a heated steam were recently addressed using a shock tube [21, 22] and laser ignition experiments [23]. In the shock tube studies, aerosolized particle clouds reacted in high temperature water (2650 K) at elevated pressures (4 to 13 atm). The burn times were recovered for the entire clouds, based on their emission signatures. In laser ignition tests, individual particles burned in a gas composed of 77% of water and 23% of nitrogen and heated slightly above the water boiling point. Additional measurements focused on the effect of aluminum particle size on its burn rate are desired in environments with different concentrations of water. We were unable to find reports on combustion of fine magnesium particles in water.

The present research investigates the dynamics of combustion of aluminum and magnesium powders in high temperature water environment (around 2500 K), generated by a H₂/O₂ flame, at atmospheric pressure.

Experimental

Approach

Experiments were performed with fine powders of aluminum and magnesium. Particles were injected into products of a hydrogen/oxygen flame as schematically shown in Fig. 1. Particle emission signatures were recorded using an array of four photomultiplier tubes (PMT's) equipped with interference filters [23]. Assuming that larger particles burn longer the measured distribution of particle burn times was correlated with the distribution of particle sizes. A Computational Fluid Dynamics (CFD) model was developed to describe the oxidizing environment for the present experiments.

The fiber optics bundle connected to the PMT array was placed about 50 mm away from the burner and about 30 mm above its top. This placement produced optimal results for capturing emission from entire particle streaks while minimizing the noise produced by the flame. The PMT outputs were recorded and saved at a rate of 100,000 samples per second using a 16-bit PCI-6123 data acquisition board by National Instruments and Lab-view software. The data were processed using a custom Matlab code.

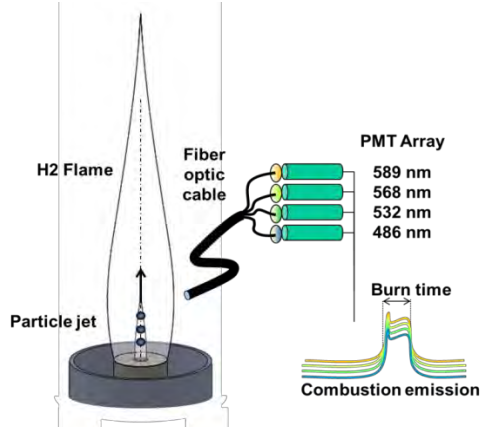


Fig. 1. Schematic of the experimental apparatus

Powder feeder

A custom screw feeder described in more detail elsewhere [24] was used to feed the metal particles into the burner. To coat the screw with powder, the dry powder was placed in a plastic dish and weighed. Using a short bristle brush, the powder was deposited into the threads of a stainless steel, $\frac{3}{4}$ " (19.05 mm) diameter screw with 16 threads per inch. A typical powder load was 0.2 g, which was placed over about 8-cm length of the screw. After the powder had been applied, the remaining weight was recorded to determine the sample mass to be used in experiments. The screw loaded with powder was then placed into a cylindrical enclosure and attached to a DC-motor. A narrow nitrogen jet blowing across a thread of a loaded screw removed powder coating

and fed it into the burner. The feed rate of powder was determined by the rotational speed of the screw. It was pre-selected in preliminary experiments to ensure production of as many particle streaks as possible during the data acquisition time while minimizing overlapping peaks produced by multiple particles burning simultaneously.

Burner

The design and dimensions of the burner are shown in Fig. 2. A thin stainless steel tube placed at the center of the burner is used to inject particles from the powder feeder carried by nitrogen flowing at 3.07 standard cubic feet per hour (SCFH) or 1.45 l/min. The nitrogen flow is surrounded by a flow of hydrogen fed through a tube with narrowed internal diameter at 9.04 SCFH (4.27 l/min). Oxygen flow is produced around the hydrogen flow to prevent the particles from reacting with oxygen directly. Oxygen is fed at 12.22 SCFH (5.77 l/min) through the outer cylinder of the burner. The outer cylinder contains several layers of 3-mm diameter steel balls (top layer shown at the bottom of Fig. 2) that help in producing a laminar oxygen flow. The flame shape is sensitive to the position of the central tube carrying the nitrogen flow, which must be carefully centered to achieve the desired symmetric flame configuration. The produced flame is laminar. Individual rotameters are used to monitor hydrogen, nitrogen, and oxygen flow rates.

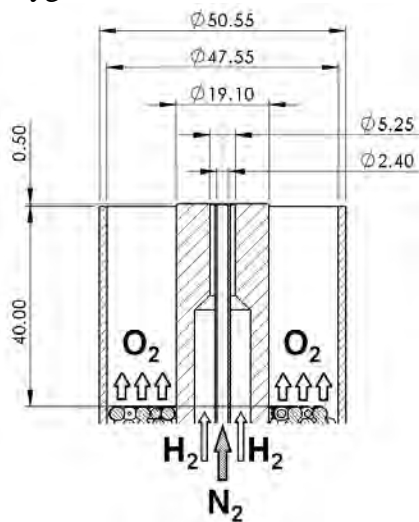


Fig. 2. Design of the burner

Materials

Commercially available powders of Al and Mg were used. Both aluminum powders were spherical, including Al 3-4.5 μm by Alfa Aesar (nominal size 3-4.5 μm) and X65 powder by Alcan-Toyo America Inc., (nominal size 6.5 μm). The magnesium powder used was 99.8% purity, -325 mesh by Alfa Aesar Stock #10233. This powder is coarser in comparison to the aluminum; particles are non-spherical but generally equiaxial. Scanning Electron Microscope (SEM) images for all three powders are shown in Fig. 3. Compared to X65 powder, the particle sizes appear to vary in a broader range for the Al 3-4.5 μm powder, including many agglomerated small particles.

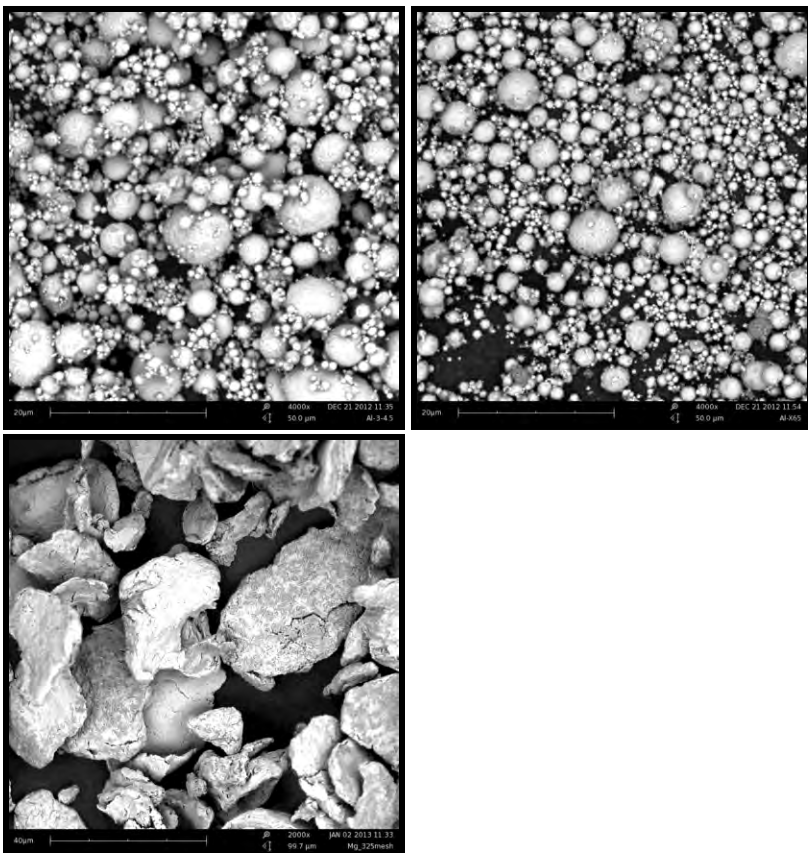


Fig. 3. SEM images of the powders used: left to right: Al 3-4.5 μm , 20- μm scale bar; Al-X65, 20- μm scale bar; Mg -325 Mesh, 40- μm scale bar.

The particle size distributions for all three powders were measured using a Beckman–Coulter LS230 Enhanced Particle Analyzer and are shown in Fig. 4. In agreement with the SEM image, the size distribution for the Al 3-4.5 μm includes a significant amount of small particles. The size distribution for the X65 powder is relatively narrow. The magnesium powder is substantially coarser than aluminum. As noted above, these measured particle size distributions are correlated with the burn time durations for each powder.

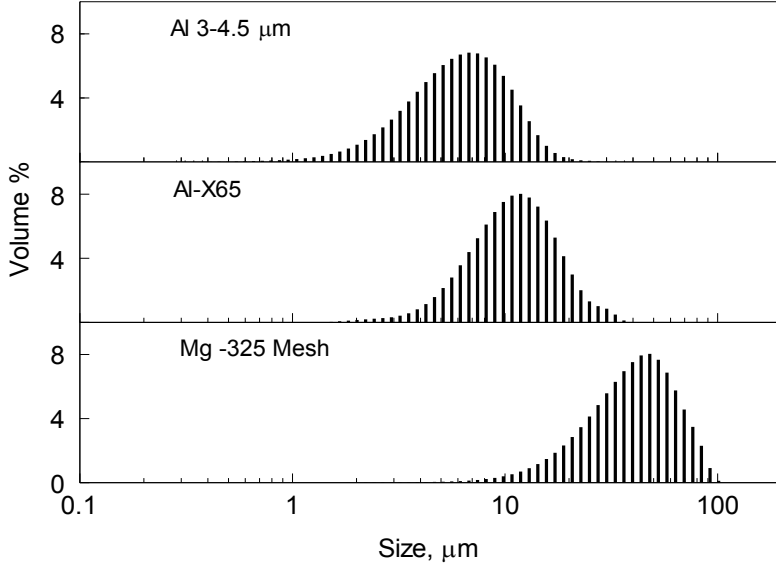


Fig. 4. Particle size distribution for three powders used in experiments.

H₂/O₂ flame computational fluid dynamics (CFD) simulation

The objective of the experiments was to characterize the burn rates of aluminum and magnesium particles in water. A CFD simulation was carried out to describe the gas composition, velocity, and temperature profiles within and around the produced flame, where particle combustion occurred. The model considered only the gas-phase flame with no particles following the Eulerian approach. The numerical simulation used a commercial CFD code STAR CCM+ 7.06, developed by CD-ADAPCO [25].

Computational domain

The computational domain is shown in Fig. 5 in relationship to the burner configuration. The fluid domain around the burner is described with a 2D axisymmetric mesh. The fluid domain represents an open environment that includes the burner; it is chosen to be 150 mm along the radial direction (approximately 6 times the radius of the burner) and 500 mm from the top of the burner (about 5 times the experimental flame height). These dimensions enabled us to describe boundary regions sufficiently far from the flame and predict stable velocity profiles in the flame vicinity. An inset in Fig. 5 shows a magnified view of the adopted mesh in the main reaction region.

The final mesh is composed by 140,000 polyhedral elements characterized by dimensions that span from 1.0 mm close to the outlet boundaries (far from the flame region) to 0.03 mm in the flame region. The grid refinement is carried out using different volume shapes enabling one to obtain a smooth grading of the cell dimension [25].

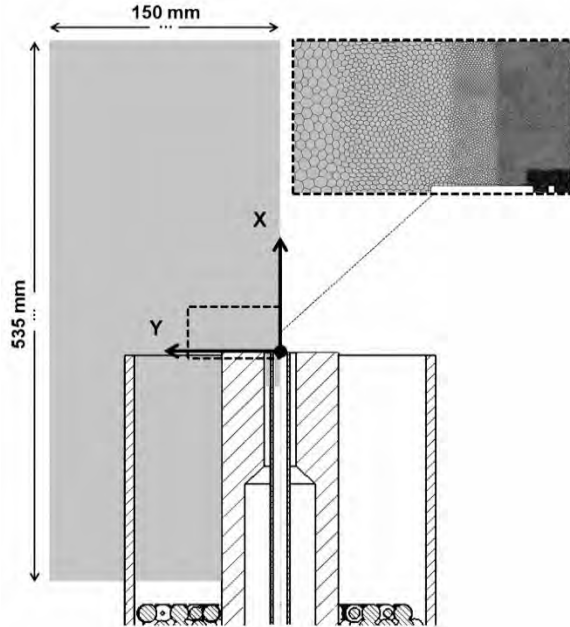


Fig. 5. Computational domain for CFD modeling

Modeling

The H₂/O₂ flame was described using a reaction model based on the adiabatic equilibrium presumed probability distribution function (PPDF) that is specific for non-premixed combustion (assuming that the reaction kinetics is fast compared to transport processes). In the adiabatic PPDF model, the atomic concentrations and the temperature determine the value of any scalar at any spatial location. Since the number of atoms in the reactor does not change because of mass conservation, the reaction state space can be characterized by a single conserved scalar: the mixture fraction. An assumption of this model is that the turbulent diffusivity is much greater than the molecular diffusivity, so that the molecular diffusivity was considered negligible. A detailed discussion of the PPDF model is available in Refs. [26] and [27]. In the reaction model, all chemical species involved in the hydrogen combustion were accounted for: H, H₂, H₂O, HO₂, H₂O₂, O, OH, and O₂. The properties of species were calculated using NASA polynomials [28].

To approach the problem, a multi component ideal gas model was selected. Due to the low flame emissivity, the flame radiation heat losses were neglected, and the burner walls were considered adiabatic. The effect of gravity is accounted for. The gas mixture dynamic viscosity, μ , was calculated using the Sutherland's law (air as a reference gas):

$$\frac{\mu}{\mu_0} = \left(\frac{T}{T_0} \right)^{3/2} \left(\frac{T_0 + S}{T + S} \right)$$

(1)

where $T_0 = 273.15$ K is a reference temperature, $\mu_0 = 1.716 \times 10^{-5}$ Pa·s is the air viscosity at T_0 , and $S = 111$ K, is the Sutherland temperature [29].

The simulations were carried out under steady state conditions. The turbulence effects were modeled using the Reynolds-Averaged Navier–Stokes k-omega shear stress transport turbulence approach [30]. Attention was paid when constructing the mesh to obtain the correct values for the non-dimensional wall distance for a wall-bounded flow, y_+ , corresponding to the turbulence model selected.

Boundary conditions

The air surrounding the burner was modeled as an ideal gas mixture composed by 76.7 mass % of N₂ and 23.3 mass % of O₂. The oxygen flow was defined by introducing a boundary condition with a constant gas velocity at the bottom of the computational domain (Fig. 5). The flows of hydrogen and nitrogen were defined at the respective burner outlets, cf. Figs. 2 and 5. Further details on the boundary conditions set according to the experimental flow rates are given in Table 2.

Table 2. Boundary conditions used to describe flows in the model

Gas	Temperature, K	Flow rate, l/min	Velocity, m/s
N ₂	293.15	1.45	5.33
O ₂	293.15	5.77	0.065
H ₂	293.15	4.27	5.23

In all simulations the convergence was achieved when residuals stabilized at values below 10^{-4} for each independent variable. The convergent velocity and temperature profiles were additionally inspected to identify any unusual patterns.

A qualitative comparison of the flame shape and the predicted concentration field of H₂O is shown in Fig. 6. The general flame shape and dimensions are reproduced reasonably well. More quantitative validations of the present model are discussed below.

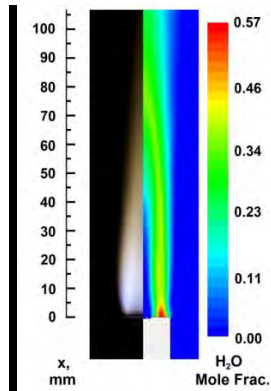


Fig. 6. A photograph of the H₂/O₂ flame (left) and a CFD-predicted water mole fraction contour plot.

Validation of the CFD results

The CFD results were validated using two different experiments. The first experiment measured the temperature profile within the flame. The second experiment quantified the gas velocity in a selected flame region.

To measure the flame temperature profile, a thin ceramic filament was inserted into the flame (with no powder fed into it), and its emission was measured using an EPP2000 High Resolution Spectrometer by StellarNet Inc. Prior to inserting the filament into the flame, the spectrum from the flame emission was recorded and treated as the baseline signal. The filament inserted into the flame was allowed to equilibrate before its emission spectrum was acquired. The measurements were performed at several filament heights, until the filament emission became weak and comparable to the background flame emission. Each recorded spectrum was approximated by a gray body emission spectrum using the emitter's temperature as an adjustable parameter. As a result, the vertical temperature profile was obtained. Because the hottest part of the heated filament produced the strongest emission signal, the measured values represent the maximum flame temperatures achieved at each height. These values were compared to the maximum temperatures predicted to exist at each height in the CFD model. The comparison is shown in Fig. 7. The experimental and computed temperature profiles are consistent with each other. Both the plateau and the decay of the temperature at increased heights are predicted well.

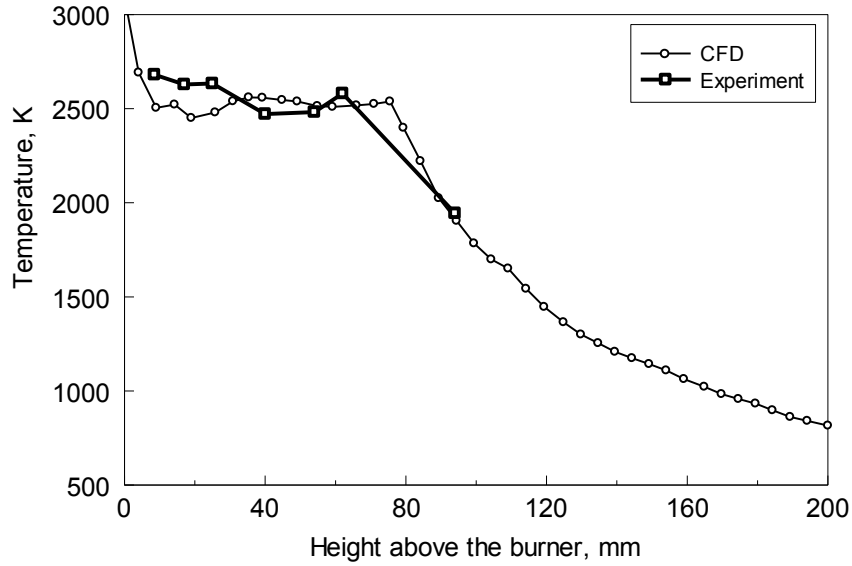


Fig. 7. Maximum temperature in the H₂/O₂ flame as a function of height above the burner

The gas velocity was measured using particle image velocimetry. A vertical, 532-nm laser sheet modulated with a frequency of 7500 Hz was placed at the flame. Streaks of aluminum-X65 particles injected into the flame and illuminated by the laser sheet were photographed. A 532-nm interference filter was placed in front of the camera lens to minimize the effect of the particle thermal emission. The dashed particle streaks were processed to recover the vertical components of their velocities. The results of measurements are shown in Fig. 8 along with the predicted velocity profiles. For most particles, their vertical velocity components agree well with the predictions. Some of the particles, however, are observed to move significantly faster, which is attributed to the effect of aluminum combustion, well known to be associated with acceleration of the burning particles.

In summary, both temperature and velocity measurements correlate well with the predictions of the present CFD model. Therefore, the CFD model-predicted concentration profiles are also likely to represent well the actual environments existing in the present experiments.

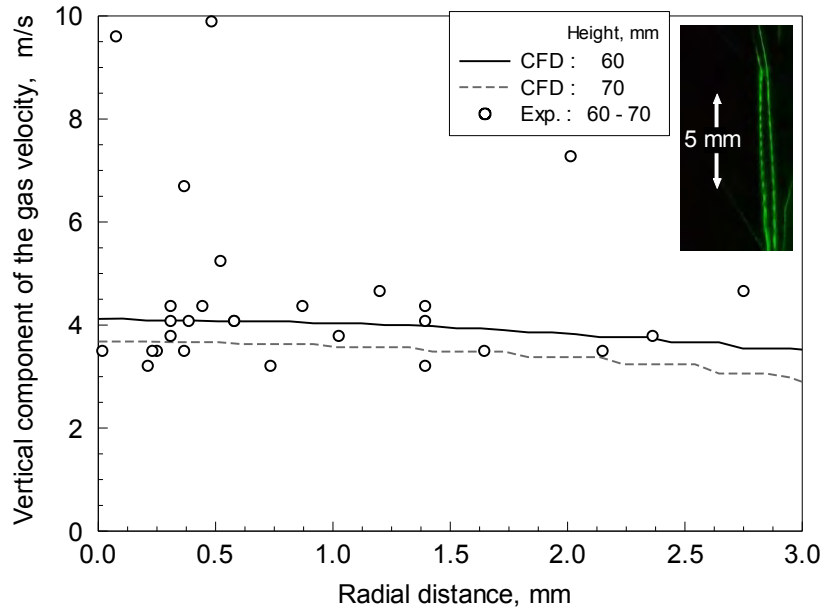


Fig. 8. Vertical component of the gas velocity as a function of the radial distance for locations 60-70 mm above the burner.

Predicted temperature, concentration, and velocity profiles

The CFD simulation results are shown in terms of temperature, velocity, and molar distributions of species involved in the reaction.

Vertical temperature profiles and concentration profiles for the main oxidizers present in the flame, H_2O and O_2 , are shown in Fig. 9 for different radial positions. Near the burner, the temperature is high at the radial distances of about 4-8 mm, quickly dropping further away from the burner's axis. For smaller radial distances, the temperature exceeds 1500 K approximately 40 mm above the burner.

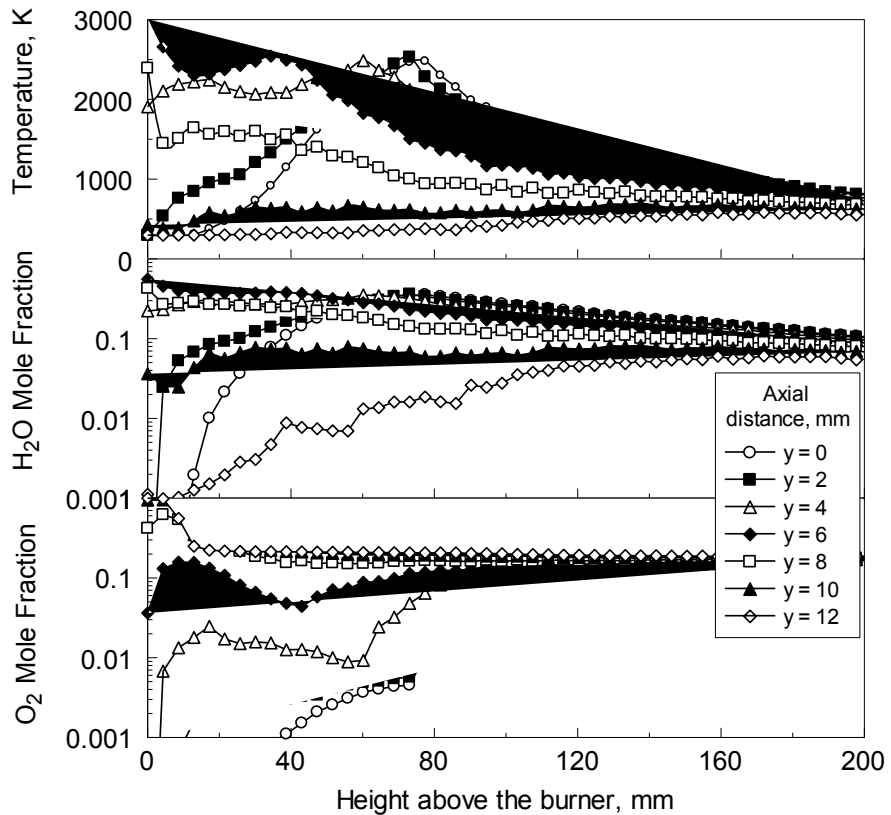


Fig. 9. Vertical profiles of temperature and main oxidizing species at different axial distances.

The water concentration is around 30 % right above the burner at the radial distances of 4-6 mm. Closer to the center of the flame, the water concentration exceeds 10-15 % at about 40 mm above the burner. At the radial distances less than 8 mm, the water concentration remains above 20% up to about 100-110 mm above the burner. Oxygen concentrations are high right above the burner at the radial distances exceeding 8 mm. Close to the center, with axial distances less than 4 mm, the oxygen concentration remains below 1-1.5 % up to 60 mm above the burner. Thus, the effect of oxygen as an oxidizer can be neglected for particles burning within 4 mm radius around the burner axis and consumed at the heights lower than 60 mm from the top of the burner.

Vertical profiles for mole fractions of all species produced in the H_2/O_2 flame along the burner's axis are shown in Fig. 10. In addition to illustrating once again that the water concentration is substantially higher than that of oxygen in the region where the particles are expected to burn, the plots also show that presence of other potential oxidizers, such as O and OH , can be neglected.

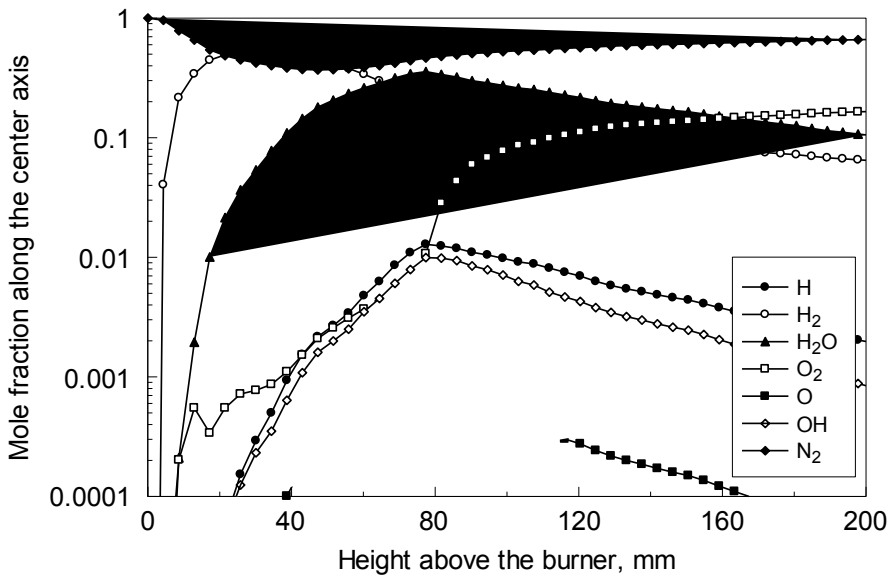


Fig. 10. Vertical profiles of the species produced in the H_2/O_2 flame along the burner's axis.

Vertical profiles for the vertical and horizontal components of the gas velocity are shown in Fig. 11. In the flame region, the vertical velocity component is about an order of magnitude greater than its horizontal component. However, the horizontal velocity component is not entirely negligible. It may cause some “focusing” of the particle jet in the region between 4 and 6 mm from the flame axis, as a result of the flows of oxygen and hydrogen towards the flame sheet. This effect was, indeed observed from close inspection of the particle trajectories. However, such effects are predicted to occur (and were observed) in a relatively narrow range of heights; for the most part, the particle trajectories are defined by the vertical component of the gas velocity.

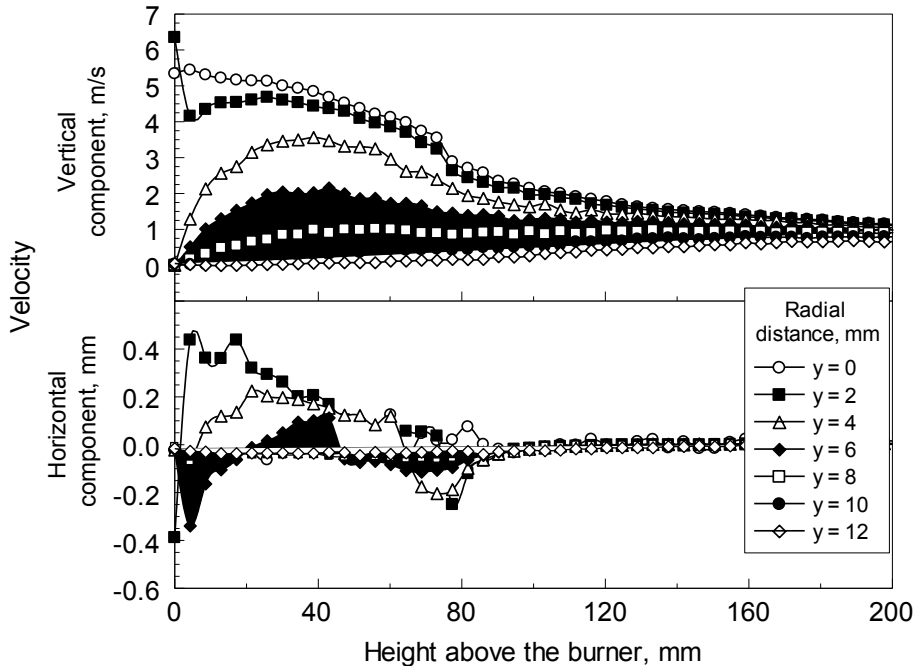


Fig. 11. Vertical profiles for the vertical and horizontal components of the gas velocity above the burner for different radial positions.

Experimental results

Multiple images of the ignited particle streaks were taken and processed to identify locations where they ignited and burned. An example of a characteristic photograph used in the processing as well as locations of particle ignition recovered from multiple similar images are shown in Fig. 12. The scales for both parts of Fig. 12 are the same, so that the particle ignition locations can be readily visualized relative to the flame region. Most particles ignite at the heights from 30 to 60 mm from the top of the burner and within ± 4 mm from its axis. Some particles ignite lower and higher than this region, very few particles are observed to ignite at the axial distances greater than 5 mm. Comparing these results with the data shown in Fig. 9, it is clear that most particles ignite and burn in water with negligible effect of oxygen on their burn rates.

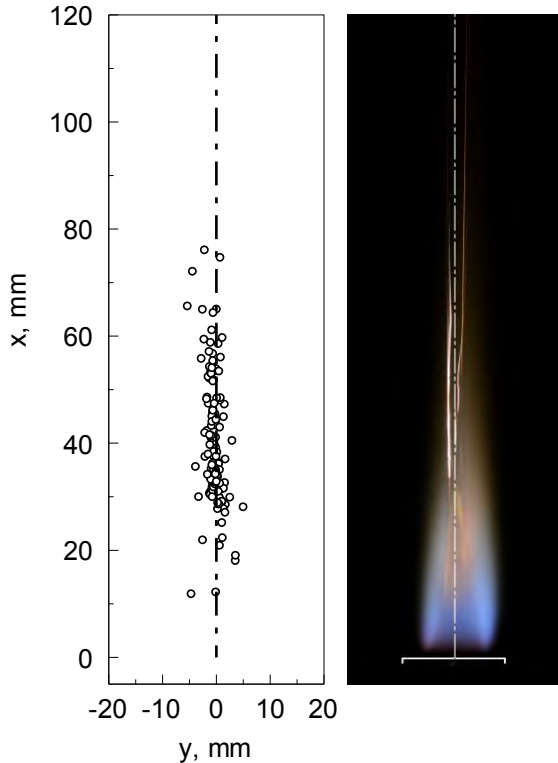


Fig. 12. Locations of particle ignition identified from processing selected flame images (height above the burner is x and axial position is y). A characteristic flame image used in the analysis is shown on the right. The scales are the same for both the image and plot.

Particle emission was measured with a substantial background emission produced by the flame. Recorded traces were processed to select peaks with sharp rise and clear decline back to the baseline level. Particle emission peaks were also observed to have characteristic shapes separating them from the flame emission fluctuations. Characteristic particle peaks are shown in Fig. 13 for all three powders tested. The peaks for 3-4.5 μm aluminum powder were relatively weak, so that the signal to noise ratio was relatively low. Aluminum-X65 powder typically produced clean, strong peaks with well-distinguished patterns corresponding to different combustion stages. An initial increase in the signal emission was accompanied by an oscillatory pattern, as shown in Fig. 13. The signal then declined and stabilized at a lower level before extinguishing, while oscillations in emission intensity continued. Qualitatively, such emission traces are similar to those observed for aluminum burning in different environments earlier [23, 31]. For magnesium, emission peaks typically showed a sharp increase in intensity followed by gradual decline. To measure burn times, the signals were processed for more than 250 individual particle peaks for each powder. The burn times were determined by the duration the signal stayed above the background flame emission level.

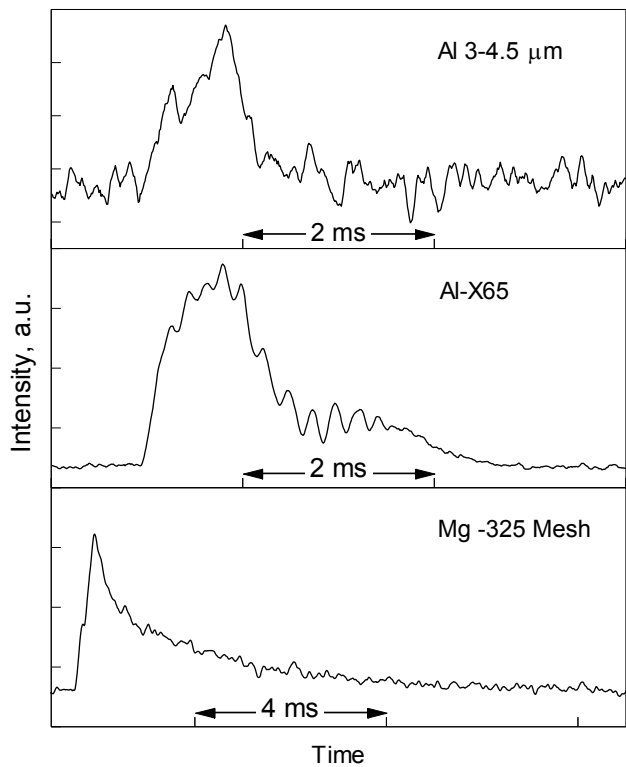


Fig. 13. Typical particle emission peaks for aluminum 3-4.5 μm , aluminum-X65, and magnesium -325 mesh.

Recorded signals were sufficiently strong to roughly evaluate color temperatures for aluminum-X65 and magnesium powders. Traces recorded at 532 and 589 nm were used. Resulting temperatures varied in broad ranges, probably illustrating that stronger signals were needed for reliable measurements. Despite the large variation, it could be concluded that the peak flame temperatures for the aluminum-X65 and for magnesium were respectively close to 2600 and 2300 K.

The burn times measured from individual particle peaks were sorted into logarithmic bins and graphed as a histogram plotting the number of particles in each time bin. The results are shown in Fig. 14. It was assumed that larger size particles burn longer, so there is a direct correlation between the particle size distributions shown in Fig. 4 (cast in terms of particle number density) and burn times shown in Fig. 14. To justify this approach, an additional correlation, between particle burn times and emission intensities was also considered. It was expected that larger particles, characterized by longer burn times, would also produce higher amplitude emission pulses. As shown in Fig. 15, this assumption works for most particles. Removal of a few outliers from the trends shown in Fig. 15 did not result in a noticeable change in the observed effect of particle size on their burn times, shown in Fig. 16.

Details of a procedure used to correlate particle size distributions (Fig. 4) and burn times (Fig. 14) are discussed elsewhere [24].

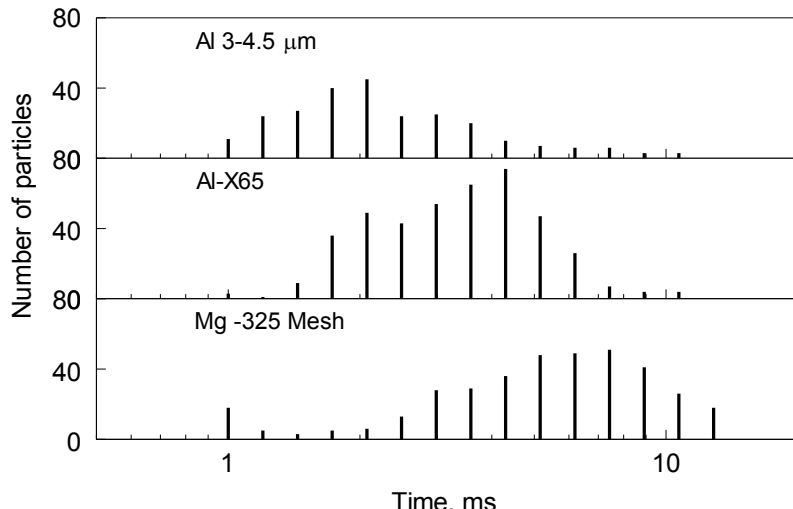


Fig. 14. Statistical distributions of the measured burn times for different powders

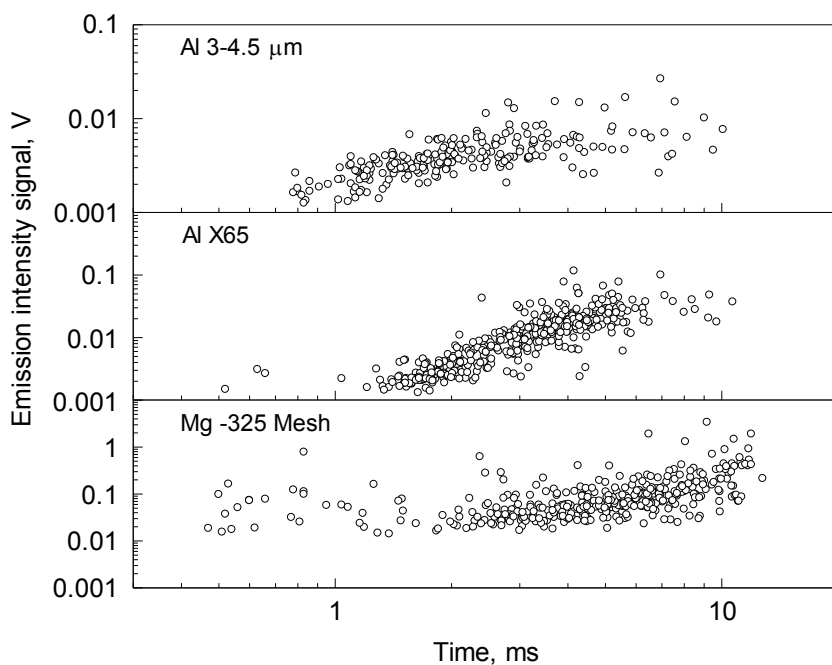


Fig. 15. Correlations between the measured burn times and maximum emission intensities for different powders

The burn times generally vary in the range of 1-10 ms. The effect of powder particle sizes on burn times is relatively weak; the straight lines shown in the log-log plot in Fig. 17 are close to $t \sim d^{0.65}$ trends for all powders. Comparing magnesium and X65 aluminum powder, it appears that Mg particles burn somewhat longer than the same size Al.

There is a discrepancy between the trends observed for two aluminum powders. It appears that particles from the 3-4.5 μm powder have longer burn times compared to the same size particles from the X65 aluminum. These longer burn times are thought to be produced by agglomerated particles, rather than indicative of true difference in combustion rates between the two aluminum powders. Indeed, the particle size distribution of the 3-4.5 μm powder shows a substantial presence of submicron particles;

at the same time, the SEM images show that such fine particles often adhere to the larger particles, as seen in Fig. 3. The agglomerates can be broken during particle size measurements, when the powder in solution is actively agitated by ultrasound; however, the agglomerate might survive passing through the powder feeder in the present combustion experiments. Particles in X65 aluminum have a narrower size distribution and fewer fines. Their SEM images show that they are less likely to agglomerate and skew the correlations between the measured burn time distribution and particle sizes. Based on the above consideration, further discussion of burn times for aluminum is focused only on the experimental trend obtained for X65 powder.

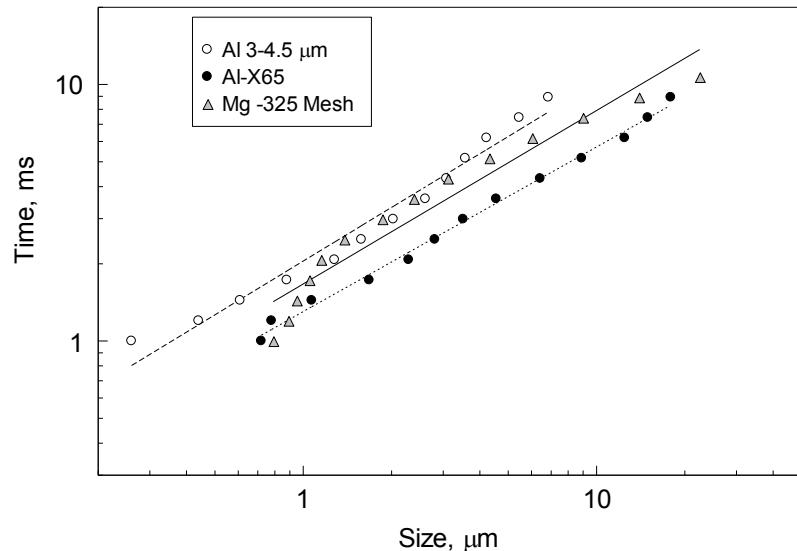


Fig. 16. Correlations of the measured burn times and particle sizes for different powders tested.

Discussion

The results are discussed separately for magnesium and aluminum powders.

Relatively few reports identified magnesium particle burn times in water [18-20]; all such reports dealt with powders that were coarser compared to those used here. Results of the present experiments are shown in Fig. 17 together with several data sets found in the literature. The experiments described here result in longer burn times and a weaker effect of powder size on the burn time compared to those expected for fine Mg particles based on the literature data. Using a conventional $t \sim D^n$ law, where t is the burn time and D is particle diameter, present experiments are described reasonably well when $n \approx 0.68$.

A recent study [20] used very large 1.5–5 mm particles ignited with a hot wire. Water vapor balanced with argon was supplied into the combustor chamber. Partial water pressure was 0.05 MPa. A high-speed camera was used to observe the flame structure and combustion process. The results produce a trend line described by $t \sim D^2$ relationship.

Interestingly, results from earlier experiments [18, 19] fit well with the $t \sim D^2$ trend line reported in ref. [20]. Prachukho et al., [19], produced water vapor using a flat flame H₂/O₂ burner with an addition of nitrogen to vary the water concentration. The flame was

placed in an enclosed environment. Water temperature was assessed to be about 1373 K. Magnesium particles were fed into the burner using a vibrating feeder and ignited within the flame. The particle sizes of the powder used varied between 1 and 250 μm ; however, the powder was size classified into six fractions: 24-40, 37-64, 66-116, 86-133, 102-152, and 144-205 μm . Burn times were recorded on a continuously moving film and measured using a rotating disk as a shutter. Ozerov et al. [18] used the same technique for igniting particles; experiments were performed at higher temperatures (up to 2073 K) and water concentration reaching 100%. Particles with sizes from 66 to 185 μm were used.

Surprisingly, the burn times measured for relatively coarse particles in Refs. [18, 19] are in the same range as the burn times measured in the present effort, although for substantially finer particles. The discrepancy may be explained considering that the entire length of the reaction chamber in experiments [18, 19] was less than 250 mm. It is suggested that larger particles, which burn longer simply did not have enough time to complete combustion while traveling through the chamber. This could significantly skew the measurement results. Other possible issues may relate to insufficiently well characterized oxidizing environment produced by the flat flame burner. The experimental details provided in refs. [18, 19] are insufficient to quantify possible presence of oxygen and other oxidizers. Finally, the size classification of the 1-250 μm powder into narrow size fractions is notoriously difficult; the actual size distributions of the obtained size fractions are not reported and could have been skewed by the presence of fine particles, which are difficult to distinguish using optical microscopy.

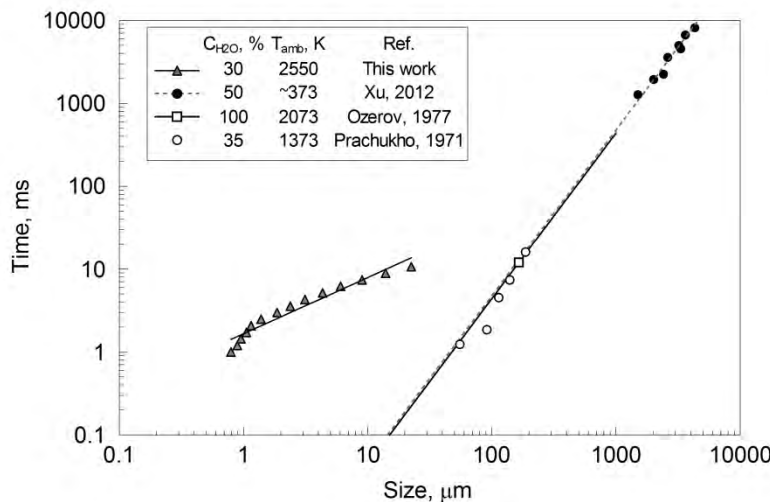


Fig. 17. Combustion time as a function of particle size for magnesium powders

The combustion behavior of aluminum particles in water has been studied in more details; both experimental data and empirical correlations are available to describe the respective burn rates. Present data as well as some of the earlier results and correlations are shown in Fig. 18. The present results are reasonably well described by a $t \sim D^{0.64}$ trend.

Using the same equipment as discussed above for Mg powders, Ozerov et al., [18] investigated combustion of aluminum particles in water vapor at 2073 K at one atmosphere. Aluminum particles with the average size of 120 μm were used. Ozerov's result and proposed correlation are shown in Fig. 18.

Recently, fine Al particles were ignited in a shock tube [21, 22]. Burn times were determined as a function of the pressure and the mole fraction of the primary oxidizers, including water, oxygen and carbon dioxide. In the reflected shock, the aerosolized aluminum particles were subjected to a high temperature (2650 K) and high pressure (8.5 atm) environment. The duration of the combustion emission pulses at 489 nm was associated with the burn times. Bazyn et al. [22] used pure spherical aluminum powders selected by sieving between 5-10 μm ; the sample mass distribution showed a strong peak around 10 μm . The water mole fraction varied approximately between 0.25 and 0.55. Lynch et al. [21] analyzed two different powders: a spherical powder with the mass distribution close to 3 μm and a sample of powder selected by sieving between 5-10 μm with a mass distribution close to 11 μm . The water mole fraction varied between 0.35 and 0.65. In Fig. 18, results of the shock tube studies are shown with large error bars accounting for the width of the size distributions for the sieved powders.

In experiments [23], that are, perhaps, most relevant to the present study, a nitrogen gas stream fed aluminum powder into a 393-K water vapor environment. The particles were ignited using a focused CO₂ laser beam. The mole fraction of water vapor produced was 0.77. The experiments used a commercial spherical powder with the nominal particle sizes of 10-14 μm and individual particle burn times were identified. The results appear to match with the present measurements for larger particles; however, the effect of particle size on the burn time is weaker and smaller particles observed in Ref. [23] to burn longer than in the present experiments. The longer burn times observed in Ref. [23] are likely associated with a much lower environment temperature.

M. Beckstead [17] proposed an empirical correlation for the aluminum particle burn times. Approximately 400 experimental data points available in literature and collected from different experiments carried out by different authors were used. These data were collected for particles with sizes spanning from 20-750 μm . This correlation defines the aluminum burning time, t [ms] as a function of the particle size, D [μm], the oxidizer mole fraction, C , the environmental pressure, p [atm], and the temperature, T [K]:

$$t_b = \frac{aD^n}{(C_{O_2} + 0.6C_{H_2O} + 0.22C_{CO_2})p^{0.1}T^{0.2}} \quad (2)$$

Beckstead [17] also suggested that the data are best correlated with coefficients $a = 0.00735$ and $n = 1.8$.

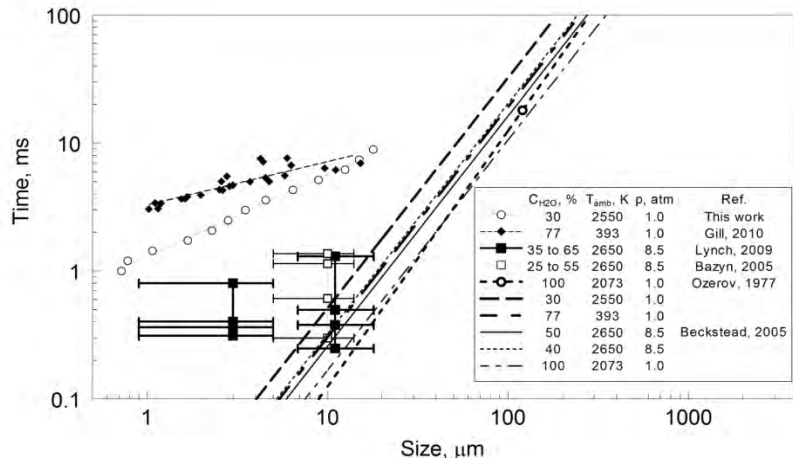


Fig. 18. Combustion time as a function of particle size for aluminum powders (results for X65 powder for present experiments are shown).

The Beckstead's correlation was used to produce trend lines shown in Fig. 18; the experimental conditions used in all other references considered were employed, resulting in several parallel lines (for all cases, $n = 1.8$).

As expected, early experiments with coarse particles are well described by the Beckstead's correlation. It is difficult to make a quantitative comparison with the shock tube data, some of which seem to correlate well within the proposed trend, while others appear to deviate from it substantially. The shorter burn times reported from the shock tube studies compared to the present experiments are likely explained by the effect of elevated pressure. This effect, proposed to be very weak by the Beckstead's correlation, may become stronger for fine particles because of two reasons:

- the heat and mass transfer processes occur in the transition regime [32, 33] and shift in pressure results in qualitative changes in the transport mechanisms;
- the pressure may also have a stronger effect for kinetically driven reactions, which are becoming more likely for fine particles [21].

The present results as well as results from Ref. [23] deviate from the Beckstead's correlation significantly. The measured burn times are about an order of magnitude longer than predicted; the effect of particle size is also much weaker than the $D^{1.8}$ trend expected based on the experiments with coarse powders. As mentioned above, changes in both transport and reaction mechanisms occurring for small particles are likely responsible for the observed combustion behavior. The weak effect of particle size on burn time observed here is consistent with our earlier experimental reports studying aluminum combustion in oxygen and other environments [23, 31, 34, 35]. A reaction model accounting for both surface reaction rates and transition transport processes is desired to interpret the present results quantitatively.

Conclusions

Combustion of fine magnesium and aluminum powders was characterized in a high temperature water vapor. For the selected experimental configuration, effect of other oxidizers on the measured particle burn rates could be neglected. The composition and temperature profiles for the gaseous environment used in experiments were validated

by detailed CFD calculations. For both metals, the particle combustion times could be approximately described by D^n law; the exponent n was close to 0.64 for aluminum and to 0.68 for magnesium. The results deviate substantially from earlier experimental data for both metals burning in water; there is also substantial discrepancy with a popular empirical correlation [17] proposed for aluminum burn times. The measured burn times are longer than implied by previous work employing coarse powders; this discrepancy is attributed to differences in both transport and chemical reaction mechanisms for fine metal particles. The present results are qualitatively consistent with recently reported trends describing burn time as a function of particle size for fine aluminum particles burning in oxygen and other oxidizers [23, 31, 34, 35].

References

- [1] T. Miller; J. Herr, in: 40th AIAA/ASME/SAE/ASEE Joint Propulsion Conference and Exhibit, American Institute of Aeronautics and Astronautics: 2004. DOI: 10.2514/6.2004-4037
- [2] T. B. R. Foote J. P. , Lineberry J. T., in: Advances in Chemical Propulsion: Science to Technology, G. D. Roy, (Ed.) 2002; Vol. 1, 133 - 147.
- [3] T. R. Sippel; T. L. Pourpoint; S. F. Son, Propell Explos Pyrot 38 (1) (2013) 56-66.
- [4] T. L. Pourpoint; T. D. Wood; M. A. Pfeil; J. Tsohas; S. F. Son, Int J Aerospace Eng 2012 (2012) 11 Art # 874076.
- [5] G. Risha; T. Connell; R. Yetter; V. Yang; T. Wood; M. Pfeil; T. Pourpoint; S. Son, in: 45th AIAA/ASME/SAE/ASEE Joint Propulsion Conference & Exhibit, American Institute of Aeronautics and Astronautics: 2009. DOI: 10.2514/6.2009-4890
- [6] M. Diwan; D. Hanna; E. Shafirovich; A. Varma, Chem Eng Sci 65 (1) (2010) 80-87.
- [7] J. Petrovic; G. Thomas, Reaction of Aluminum with Water to Produce Hydrogen. U.S. Department of Energy: 2008.
- [8] H. Z. Wang; D. Y. C. Leung; M. K. H. Leung; M. Ni, Renew Sust Energ Rev 13 (4) (2009) 845-853.
- [9] M. S. Vlaskin; E. I. Shkolnikov; A. V. Bersh; A. Z. Zhuk; A. V. Lisicyn; A. I. Sorokovikov; Y. V. Pankina, J Power Sources 196 (20) (2011) 8828-8835.
- [10] F. Franzoni; S. Mercati; M. Milani; L. Montorsi, Int J Hydrogen Energ 36 (4) (2011) 2803-2816.
- [11] S. Mercati; M. Milani; L. Montorsi; F. Paltrinieri, Appl Energ 97 (0) (2012) 686-694.
- [12] P. Dupiano; D. Stamatis; E. L. Dreizin, Int J Hydrogen Energ 36 (8) (2011) 4781-4791.
- [13] H. Nie; M. Schoenitz; E. L. Dreizin, Int J Hydrogen Energ 37 (15) (2012) 11035-11045.
- [14] W.-Z. Gai; W.-H. Liu; Z.-Y. Deng; J.-G. Zhou, Int J Hydrogen Energ 37 (17) (2012) 13132-13140.
- [15] W. Yang; Z. Han; J. Zhou; J. Liu; K. Cen, Int J Hydrogen Energ 36 (17) (2011) 10608-10613.

- [16] M. H. Grosjean; M. Zidoune; L. Roué; J. Y. Huot, Int J Hydrogen Energ 31 (1) (2006) 109-119.
- [17] M. W. Beckstead, Combust Expl Shock+ 41 (5) (2005) 533-546.
- [18] E. S. Ozerov; A. A. Yurinov, Combust Expl Shock+ 13 (6) (1977) 778-780.
- [19] V. P. Prachukho; E. S. Ozerov; A. A. Yurinov, Combust Expl Shock+ 7 (2) (1971) 195-198.
- [20] X. Huang; Z. Xia; L. Huang; J. Hu, Sci. China Technol. Sci. 55 (9) (2012) 2601-2608.
- [21] P. Lynch; H. Krier; N. Glumac, P Combust Inst 32 (2) (2009) 1887-1893.
- [22] T. Bazyn; H. Krier; N. Glumac, J Propul Power 21 (4) (2005) 577-582
- [23] R. J. Gill; C. Badiola; E. L. Dreizin, Combust Flame 157 (11) (2010) 2015-2023.
- [24] A. L. Corcoran; V. K. Hoffmann; E. L. Dreizin, Combust Flame 160 (3) (2013) 718-724.
- [25] CD-adapco, USER GUIDE Star CCM+ Version 7.06, CD-adapco, 2012, 12179.
- [26] D. Veynante; L. Vervisch, Prog Energ Combust 28 (3) (2002) 193-266
- [27] S. B. Pope, Prog Energ Combust 11 (2) (1985) 119-192
- [28] B. J. McBride; S. Gordon; M. A. Reno, in: National Aeronautics and Space Administration: Cleveland OH, 1993; Vol. NASA Technical Memorandum 4513, 1-94.
- [29] W. Sutherland, Philos Mag (S.5) 36 (1893) 507-531
- [30] F. R. Menter; M. Kuntz; R. Langtry in: *Ten Years of Industrial Experience with the SST Turbulence Model*, Turbulence, Heat and Mass Transfer 4, Antalya, Turkey, 12 - 17 October 2003, 2003; K. Hanjalic; Y. Nagano; M. Tummers, (Eds.) Antalya, Turkey, 2003.
- [31] C. Badiola; R. J. Gill; E. L. Dreizin, Combust Flame 158 (10) (2011) 2064-2070.
- [32] S. Mohan; L. Furet; E. L. Dreizin, Combust Flame 157 (7) (2010) 1356-1363.
- [33] S. Mohan; M. A. Trunov; E. L. Dreizin, Combust Flame 156 (11) (2009) 2213-2216.
- [34] C. Badiola; E. L. Dreizin, Combust Sci Technol 184 (12) (2012) 1993-2007.
- [35] E. L. Dreizin; C. Badiola; S. Zhang; Y. Aly, Int J Energetic Mater Chem Propul 10 (4) (2011) 297-319

CHAPTER 10: MODEL OF HETEROGENEOUS COMBUSTION OF SMALL PARTICLES

Nomenclature

c	Heat capacity at constant pressure, $\text{J kg}^{-1} \text{K}^{-1}$
d	Particle diameter, m
D	Diffusivity, $\text{m}^2 \text{s}^{-1}$
\dot{E}	Energy flow rate, J s^{-1}
F	A factor used to calculate reference temperature, either 1/2 or 1/3
$f(T_\delta)$	Eucken factor, $(9\gamma - 5)/4$
H	Enthalpy, J kg^{-1}
K	Thermal conductivity, $\text{W m}^{-1} \text{K}^{-1}$
k_B	Boltzmann constant, J K^{-1}
Kn	λ/r_p , Knudsen number
\dot{m}	Mass flow rate, kg s^{-1}
M	Molar mass, kg mol^{-1}
p	Pressure, Pa
q	Total heat flow rate by conduction and diffusion of enthalpy, J s^{-1}
q^c	Total heat flow rate by conduction, J s^{-1}
r	Radius, radial coordinate, m
R	Universal gas constant, $\text{J mol}^{-1} \text{K}^{-1}$
t	Time, s
T	Temperature, K
u	Stefan flow velocity, m s^{-1}
U	Internal energy per mass of a molecule, J kg^{-1}
Y	Mass fraction

Greek Symbols

γ	Specific heat ratio of gas
δ	Knudsen layer thickness, m
ϵ	Emissivity
$\epsilon_{O_2-N_2}$	Energy of intermolecular interaction of oxygen and nitrogen, J
ϵ_{O_2}	Energy of intermolecular interaction of oxygen, J
ϵ_{N_2}	Energy of intermolecular interaction of nitrogen, J
λ	Mean free path, m
ν	Stoichiometric coefficient
ρ	Density, kg m^{-3}
σ	Stefan-Boltzmann constant, $\text{W m}^{-2} \text{K}^{-4}$
$\Omega_{D/T}$	Collision integral for diffusion

Subscripts

air	Air
b	Burning
f	Fuel
i	i-th gas component

<i>in</i>	Inert gas
<i>m</i>	Metal
<i>ox</i>	Oxidizer
O_2	Oxygen
<i>p</i>	Particle
<i>pr</i>	Solid product
<i>ref</i>	Reference value
<i>Zr</i>	Zirconium
δ	Knudsen layer – continuum region interface
∞	Environment

Superscripts

<i>c</i>	Conductivity
*	Reference

Introduction

Heterogeneous particle combustion occurs in multiple practical situations, from oxidation of soot [1, 2] to combustion of coal [3, 4] to combustion of fine metal particles in propellants, explosives, and pyrotechnics [5-8]. It is commonly assumed that mass transfer controls the burn rate for coarse particles, and when the particle size decreases, the combustion becomes rate-limited by the surface reaction kinetics. The rate of mass transfer is usually assessed considering diffusion and convection in terms of conventional continuous media models. However, it is well-known that when the particle size decreases to become comparable to the gas molecule mean free path (i.e., when Knudsen number Kn increases), the heat and mass transfer processes are no longer described by the continuous model [9-11]. The transport occurs in the free-molecular regime for very small particles (typically less than 0.1 μm) and so-called transition regime exists for particles in a broad range of sizes from 0.1 to $\sim 40 \mu\text{m}$ (the relevant particle size range shifts depending on pressure). The effect of an increased value of Kn has been extensively investigated for heat and mass transport processes individually; however, few treatments are available for the situations when both heat and mass transport occur simultaneously and when temperature and concentrations gradients are not small, which are typical for particle combustion.

The effect of change in the Knudsen number is considered in detail in explicit models of diesel fuel evaporation [12, 13]. The transition mass transport regime at increasing Knudsen numbers has also been considered when analyzing the gas reaction kinetics for aerosol chemistry [14]. However, for carbon-based solid fuels and metals, all current combustion models use continuous heat and mass transfer descriptions, e.g., [2, 15-18]. These descriptions remain in use to interpret experiments for fine particles, when combustion is expected to be governed by the reaction kinetics. For a broad range of conditions when both transport and kinetic rates are comparable to each other, kinetic trends implied by the experimental data may be skewed because corrections for the heat and mass transfer rates are not accounted for. The present study is aimed to develop an approach to account for both heat and mass transport rates, so that the kinetic trends can be identified properly from the experimental data available.

An extensive review of different methods used to analyze the heat transfer in the transition regime is given in ref. [9] where different methods are classified into three main approaches: approximate analytical techniques of solving the Boltzmann equation, interpolational approach leading to simple equations applicable in the conditions close to isothermal (or small concentration differences), and limiting-sphere or two-layer model, which is sometimes also referred as Fuchs' model [19]. Based on comparison with direct Monte-Carlo simulations [9, 20], it was concluded that the latter approach is preferable over any existing interpolation formulae.

The two-layer Fuchs' approach is used here to model heterogeneous combustion of a metal particle burning in a transition regime. Specific calculations are performed for combustion of zirconium particles. This particular case is selected because of its relative simplicity since the reactions may be assumed to be limited to formation of non-volatile products. The results are compared with the experimental data published in the literature. Other cases, including combustion of carbon particles as well as combustion of other metal fuels, such as aluminum, can be considered in the future, when the theoretical description is expanded to account for the volatile species produced by surface reactions and for the effect of vapor-phase flame on the heat and mass transfer processes.

Physical Model

A steady-state model of heterogeneous combustion of a spherical fuel particle is considered as schematically illustrated in Fig. 1. The particle with radius r_p is placed in a gaseous environment consisting of an inert gas and an oxidizer. The oxidizer diffuses towards the particle where it reacts on its surface with the formation of a condensed product. Both fuel and product remain condensed, i.e., the model is limited to systems with nonvolatile metals and oxides. The product is assumed to be dissolved in the molten metal, so that there is no growing oxide film that could have impeded the surface reaction. This is consistent with the earlier reports describing dynamics of combustion for zirconium and other metals [21].

The focus of the present study is on the effect of heat and mass transport processes; the reaction occurring at the surface is assumed to be rapid, so that all the oxidizer reaching the particle surface is consumed. To simplify the analysis, only a single gas phase oxidizer and a single condensed product are considered. In the future, the model can be readily extended to describe multicomponent systems as well as systems with volatile fuels and products.

The particle surrounding is separated into two distinct regions: inside and outside of the Knudsen (or Langmuir) layer with radius r_δ and thickness $\delta = r_\delta - r_p$ of the order of one molecular mean free path [20]. Within the Knudsen layer, $r_p < r < r_\delta$, there is no collision between molecules and transport is described by molecular kinetics; outside of it, $r > r_\delta$, transport phenomena are described by the heat and mass transfer equations of continuum mechanics. The mass and energy fluxes in the two regions are matched at $r = r_\delta$. The

environment temperature is assumed to be lower than the particle surface temperature, where the reaction occurs.

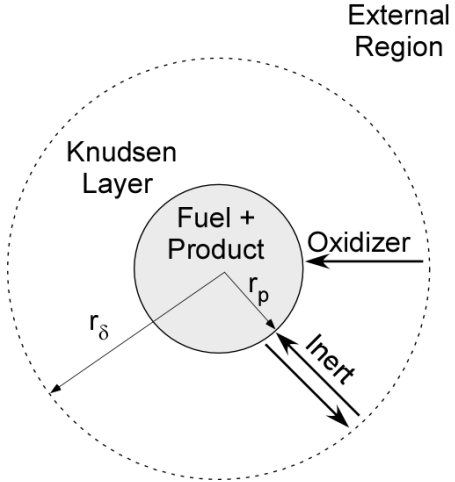


Figure 1. A particle within the Knudsen layer considered in the present model.

A direct effect of introduction of the Knudsen layer is a reduction of both heat and mass flows towards and from the particle surface. This reduction occurs when the particle dimension becomes comparable to the molecular mean free path, so that the probability of particle/molecule collision is reduced.

A number of simplifying assumptions were used, as listed below.

- a. The particle burns in a quiescent, infinite spherically symmetric gaseous environment. Influence of convection or thermophoretic effects is not considered.
- b. The combustion is treated as a steady-state process. The particle size and spatial distributions of temperature and concentrations of gaseous species remain constant.
- c. The particle temperature is uniform.
- d. The gas surrounding particle contains two components: oxidizer that reacts with the particle and an inert component.
- e. The transport of the oxidizer towards the particle is the rate-controlling process; the concentration of the oxidizer at the particle surface is zero.
- f. Values of gas mass diffusivity ρD , thermal conductivity, k , and heat capacity, c are fixed outside of the Knudsen layer. The effect of temperature on these values is accounted for by adjusting their values depending on the calculated temperature profiles. This adjustment is done using computational iterations as described below.
- g. The thermal accommodation coefficients for the gas molecules interacting with the particle surface are assumed to be equal to 1. In other words, each collision results in the complete energy transfer from gas to particle.

- h. If an oxidizer molecule impacts upon the particle surface, it always bonds to the particle chemically (reacts); in other words, the sticking coefficient is also assumed to be equal to 1.

The Fuchs' model as described above was applied mostly for single-component gas media in evaporation-condensation and heat transfer problems. Whereas the Knudsen layer thickness, δ , is known to be comparable to the mean free path of gas molecules, λ , different specific values of δ were used by different authors. Fuchs considered a mass transfer problem of droplet evaporation and argued that δ should be slightly larger than λ [22]. Young compared non-equilibrium heat transfer coefficients found from his model of droplet condensation/evaporation with the ones obtained from the solution of the Boltzmann equation and found the best match at $\delta = 0.75\lambda$ [23, 24]. Wright [25] proposed a relation between δ and Knudsen number Kn . As pointed out in Ref. [26], Wright's expression effectively gives $\delta \approx \lambda$ for a broad range of Kn . The effect of the selected value of δ was considered previously in Refs. [23, 24] for droplet evaporation – condensation problems and in Ref. [9] for high-temperature heat transfer, and was found to be negligible for a wide range of Knudsen numbers corresponding to the transition transport regime. Thus, in this work the Knudsen layer is simply assumed to be given by $\delta = \lambda$, or:

$$r_\delta = r_p + \lambda \quad (1)$$

Strictly speaking, for multicomponent systems, individual Knudsen layers must be considered for diffusion and heat transfer of each component. The question was discussed in detail in Ref. [26] for multicomponent vapor mixtures diluted in a bath gas. It was shown that for multicomponent transfer problems, the mean free path defined by collision of different molecules needs to be corrected compared to the mean free path in a single component gas; however, the correction is significant only when the mass ratio of colliding molecules is either much smaller or much greater than one [26]. Specifically, it was shown in Ref. [26], that for a broad range of molecular mass ratios of 0.43 - 86, the change in λ is less than 10%. Therefore, a single Knudsen layer assumption can be used here for the multicomponent diluted systems defined by the mean free path of a carrier gas. Therefore, Eq. (1) is used for the Knudsen layer-external region interface, where the mean free path λ is taken for air at the temperature at the Knudsen layer interface, T_δ . The mean free path expression defined by McCoy and Cha [9, 27] applicable to both monatomic and polyatomic gases was used:

$$\lambda = \frac{k(T_\delta)}{f(T_\delta)p} \left[\gamma(T_\delta) - 1 \right] \sqrt{\frac{\pi T_\delta M_{air}}{2R}} \quad (2)$$

where p is the pressure, $k(T_\delta)$ - thermal conductivity, M_{air} is the molecular mass of air, γ is the specific heat ratio of gas, and $f(T_\delta) = [9\gamma(T_\delta) - 5]/4$ is the Eucken factor. All parameters in Eq. (2) are taken at the Knudsen layer interface.

Equations

4.1 External Region; $r \geq r_\delta$

For a spherically symmetric steady flow, the radial component of the total mass flow rate \dot{m} is constant:

$$\frac{d\dot{m}}{dr} = 0 \quad (3)$$

where the mass flow rate can be expressed using the Stefan flow velocity, u , and gas density, ρ , as:

$$\dot{m} = 4\pi r^2 \rho u \quad (4)$$

The mass continuity is also valid for mass flow rates of individual gas species: oxidizer and inert components. Since the inert component is not absorbed by the particle surface, the total mass flow rate \dot{m} is just the mass flow rate of the oxidizer.

$$\dot{m} = \dot{m} Y_{ox} - 4\pi r^2 \rho D_{ox} \frac{dY_{ox}}{dr} \quad (5)$$

where Y_{ox} and D_{ox} are respectively mass fraction and the diffusion coefficient of the oxidizer molecules in the gas mixture. The energy conservation equation is:

$$\frac{d\dot{E}}{dr} = 0 \quad (6)$$

where \dot{E} is the energy flow rate, that can be expressed using the enthalpy of an oxidizer, h_{ox} as:

$$\dot{E} = \dot{m} h_{ox}(T) - 4\pi r^2 k \frac{dT}{dr} \quad (7)$$

The boundary conditions are defined at infinity and at the Knudsen layer:

$$r \rightarrow r_\infty : Y_{ox} = Y_{ox,\infty}; T = T_\infty, \quad (8)$$

$$r = r_\delta : Y_{ox} = Y_{ox,\delta}; \dot{E} = \dot{m} h_{ox}(T_\delta) - 4\pi r_\delta^2 k \left. \frac{dT}{dr} \right|_\delta; T = T_\delta \quad (9)$$

where T_∞ and $Y_{ox,\infty}$ are respectively temperature and mass fraction of oxygen in the environment, T_δ and $Y_{ox,\delta}$ are respectively temperature and mass fraction of oxygen at the Knudsen layer boundary (unknown at the moment), and h_{ox} is the specific enthalpy of formation of the oxidizer.

Assuming a constant specific heat of oxidizer, c_{ox} , its enthalpy can be calculated as a function of temperature as:

$$h_{ox}(T) = h_{ox}(T_\delta) + c_{ox}(T - T_\delta) \quad (10)$$

The solution of Eqs. (3)-(7) with the boundary conditions (8), (9) is:

$$Y_{ox} = 1 - (1 - Y_{ox,\infty}) \exp\left(-\frac{\dot{m}}{4\pi\rho D_{ox} r}\right) \quad (11)$$

$$T = T_\infty + \frac{q^c}{\dot{m}c_{ox}} \left\{ \exp\left(\frac{\dot{m}c_{ox}}{4\pi k r}\right) - \exp\left[\frac{\dot{m}c_{ox}}{4\pi k} \left(\frac{1}{r_\delta} - \frac{1}{r}\right)\right] \right\} \quad (12)$$

where the conductive heat flow through the Knudsen layer boundary is defined as

$$q^c \equiv -4\pi r_\delta^2 k \frac{dT}{dr} \Big|_{\delta}.$$

Equations (11) and (12) suggest that the mass flow rate and temperature at the Knudsen layer interface are:

$$\dot{m} = 4\pi\rho D_{ox} r_\delta \ln\left(\frac{1 - Y_{ox,\infty}}{1 - Y_{ox,\delta}}\right) \quad (13)$$

$$T_\delta = T_\infty + \frac{q^c}{\dot{m}c_{ox}} \left\{ \exp\left(\frac{\dot{m}c_{ox}}{4\pi k r_\delta}\right) - 1 \right\} \quad (14)$$

4.2 Knudsen layer; $r_p \leq r \leq r_\delta$

Energy and mass fluxes in the Knudsen layer are calculated based on velocity distribution at the particle surface and Knudsen layer interface. One of the major difficulties in the problems with the bulk flow of masses and energies is the non-Maxwellian velocity distribution of molecules. Strictly speaking, accounting for Stefan flow requires solution of the Boltzmann equation. Previously, for similar evaporation-condensation problems, Stefan flow was often neglected, and Maxwell distribution was used. In ref. [28], Maxwell distribution with a superposed bulk flow component was utilized. Young introduced a model with the Grad distribution at the Knudsen layer interface [23, 24]. Later, Young's model was used in multi-component droplet evaporation-condensation problem [29]. Here, the Young's approach is followed: half-Maxwellian and Grad velocity distributions are assumed at the particle surface and at the Knudsen layer interface, respectively. The model and respective assumptions are discussed in detail elsewhere [23]. The derivation of the equations is similar to that reported earlier [24, 29];

however, some changes are made to make the derivation suitable for the present problem (cf. Appendix A). The mass transfer of the oxidizer from the Knudsen layer towards the particle is:

$$\dot{m} = -\frac{p Y_{ox,\delta} M_\delta}{\left(\frac{1}{r_p^2} - \frac{1}{2r_\delta^2}\right)} \sqrt{\frac{8\pi}{RT_\delta M_{ox}}} \quad (15)$$

where p is pressure and M_δ is the equivalent molecular mass for a gas mixture at the Knudsen layer interface:

$$M_\delta = \frac{M_{ox} M_{in}}{(M_{in} - M_{ox}) Y_{ox,\delta} + M_{ox}} \quad (16)$$

The energy flow rate from the particle to the Knudsen layer is

$$\begin{aligned} \dot{E} = & \sqrt{\frac{8\pi}{RT_\delta}} r_p^2 p M_\delta \sum_i \frac{Y_{i,\delta}}{\sqrt{M_i}} \left(\Delta h_i - \frac{R(T_p - T_\delta)}{2M_i} \right) + \left(1 - \frac{r_p^2}{2r_\delta^2} \right) \dot{m} \left(\Delta h_{ox} - \frac{RT_p}{2M_{ox}} \right) \\ & + \frac{r_p^2}{2r_\delta^2} \left\{ q^c + \dot{m} (1 - Y_{ox,\delta}) \left[h_{ox}(T_\delta) - h_{in}(T_\delta) - \frac{5}{2} \left(\frac{R}{M_{ox}} - \frac{R}{M_{in}} \right) T_\delta \right] \right\} + \dot{m} h_{ox}(T_\delta) \end{aligned} \quad (17)$$

where h_i is the specific enthalpy of a gas component i ($i=\text{inert, oxidizer}$), summation is performed over both gas components, and $\Delta h_i = h_i(T_p) - h_i(T_\delta)$.

Boundary conditions at the particle surface:

$$r = r_p : Y_{ox} = 0; \dot{E} = \dot{m} [h_{pr}(T_p) - h_f(T_p)] - 4\pi r_p^2 \varepsilon \sigma (T_p^4 - T_\infty^4) \quad (18)$$

where h_{pr} is the enthalpy of product, ε is emissivity, and σ is the Stefan-Boltzmann constant. Note that h_{pr} is calculated for the mass of product generated when 1 kg of oxidizer is consumed. One can introduce the heat of reaction, Q (normalized per kg of oxidizer) as

$$Q(T) = -h_{pr}(T) + h_f(T) + h_{ox}(T) \quad (19)$$

where h_f is the enthalpy of fuel calculated for the mass of fuel consumed by 1 kg of oxidizer. Considering conservation of energy, the conductive heat flow over the Knudsen layer interface used in Eq. (12) is expressed as:

$$q^c = -\dot{m} Q(T_p) - \dot{m} [h_{ox}(T_p) - h_{ox}(T_\delta)] - 4\pi r_p^2 \varepsilon \sigma (T_p^4 - T_\infty^4) \quad (20)$$

Note that Eq. (20) contains the difference of the oxidizer enthalpies at the particle surface and Knudsen layer temperatures. This is because the oxidizer molecules crossing the

Knudsen layer are assumed to not experience any collisions until they strike the particle surface.

Parameters and Solution Procedure

Calculations were performed for combustion of zirconium particles in air at a temperature $T_\infty = 298\text{ K}$ and pressure 1 atm, with the air modeled as a mixture of oxygen, $Y_{ox,\infty} = 0.23$, and nitrogen that was treated as inert.

The equations in external region above assume constant gas properties. Variability of these properties with composition is neglected. The effect of temperature on thermal conductivity, heat capacity and mass diffusion ρD_{ox} is accounted for by using their values at a reference temperature T_{ref} , calculated as:

$$T_{ref} = T_\delta + F(T_\infty - T_\delta) \quad (21)$$

Eq. (21) is referred to as 1/3 rule [30, 31] or 1/2 rule [32] depending on whether $F = \frac{1}{3}$ or $F = \frac{1}{2}$. The value of $F = \frac{1}{3}$ was selected here based on a better match of the calculated burn time with the reported experimental data for large particles [33], which burn in a continuous regime. Selecting $F = \frac{1}{2}$ results in an about 5% reduction in the calculated particle temperature and in about 25% reduction in the burn rate.

Values of γ and thermal conductivity in the air were calculated using polynomial temperature dependence (in the range from 300K to 4000K) reported in [9]. The diffusion coefficient of oxygen was calculated using Chapman-Enskog kinetic theory [34]:

$$D(T) = D(T^*) \left(\frac{T}{T_{ref}} \right)^{3/2} \frac{\Omega_{D/T_{ref}}}{\Omega_{D/T}} \quad (22)$$

where $D(T^*)$ is the known value of the diffusion coefficient at a specific temperature T^* , $\Omega_{D/T}$ is the collision integral for diffusion which depends on dimensionless temperature $k_B T / \varepsilon_{O_2-N_2}$ (k_B is the Boltzmann constant, and $\varepsilon_{O_2-N_2}$ is the energy of intermolecular interaction of oxygen and nitrogen pairs). Parameter $\varepsilon_{O_2-N_2}$ was estimated through oxygen and nitrogen molecule interaction using the formula

$$\varepsilon_{O_2-N_2} = (\varepsilon_{O_2} \varepsilon_{N_2})^{1/2} \quad (23)$$

with $\varepsilon_{O_2}/k_B = 113\text{ K}$ and $\varepsilon_{N_2}/k_B = 99.8\text{ K}$ [36]. The value of diffusion coefficient of oxygen in nitrogen $D(T^*)=0.208 \cdot 10^{-4}\text{ m}^2/\text{s}$ for $T^*=298\text{ K}$ was used in Eq. (22) [35].

Values of heat capacities and enthalpies of each component were calculated using Shomate equations according to the NIST database [36].

The enthalpy of formation of products, h_{pr} in Eq. (19) affects the heat release in reaction and the resulting solution substantially. It was reported that liquid solution of oxygen in zirconium is produced when Zr particles burn in air [33, 37]. In calculations, two cases were considered: enthalpy of formation of products was assumed to be equal to the heat of oxygen dissolution in one case, and to the enthalpy of formation of ZrO_2 (standard enthalpy of formation of 1097 kJ/mol varied as a function of temperature as reported in ref. [38]) in the other case. The heat of dissolution of oxygen in liquid zirconium was estimated to be in the range 700-830 kJ/mol of zirconium [37]. A constant value of 700 kJ/mol was used here.

The final set of nonlinear algebraic equations contains four unknowns: \dot{m} , $Y_{ox,\delta}$, T_δ , T_p . It was solved using an iteration procedure provided by the MATLAB[®] standard function *fsolve* (with the default ‘trust – region dogleg’ algorithm).

The values of unknown variables change in a wide range (e.g., the order of 10^{-9} kg/s and less for mass flow rate, and 10^3 K for temperatures), leading to different variations for different quantities in each iteration, making the solution difficult. To avoid this problem, all equations were solved in a normalized form. For example, the normalized form of Eq. (14) is:

$$\left[T_\delta - f(\dot{m}, Y_{ox,\delta}, T_\delta, T_p) \right] / T_\delta = 0. \quad (14n)$$

To estimate the direction of gradient in each iteration, the analytical Jacobian of these equations was used, including the derivatives of all thermophysical properties with respect to unknowns.

Together with the solution of the current model, the equations were solved for the fully continuous case obtained assuming $r_\delta = r_p$ in Eqs. (13) and (14).

The numerical solution procedure can be summarized as follows:

1. The initial particle size is taken greater than 100 μm and a problem without Knudsen layer (i.e., the continuous problem) is solved. This problem is simple and its resulting values are used to arrive at the initial approximation for the Knudsen layer problem, which should yield very similar values for large particles. The found values of \dot{m} and T_p serve as the initial approximation of the current model with the Knudsen layer. For the initial approximation, the value of T_δ was taken equal to T_p and the value of $Y_{ox,\infty}$ was set to be a small number approaching zero (e.g., 10^{-4}).

2. The problem with Knudsen layer is solved iteratively for the same particle size as the continuous problem.

3. The particle size is reduced in small steps. For each reduced particle size, the problem is solved using solutions obtained for the previous larger particle size as the initial approximation. The specific rate by which the particle sizes can be reduced depends on the convergence of the numerical method. Generally, reducing particle sizes by 1 μm was observed to always result in converging solutions.

4. Steps 2 and 3 were repeated until the desired minimum particle size.

The relative errors of the final solution for each particle size and each unknown variable were monitored to ensure that they were less than 10^{-6} (typical values were in the range from 10^{-7} to 10^{-12}).

Once the steady-state solution was obtained, the model was expanded to account for a change in the burning particle diameter during its combustion. Because evaporation processes were neglected, the particle diameter increased as more and more metal oxidized. For each time step, the steady-state solution was obtained as described above. Between the time steps, the particle diameter was adjusted based on the calculated reaction rate.

Results and Discussions

Figure 2 represents particle temperatures calculated using different energetics of combustion process:

- a) Heat release due to formation of ZrO_2 and
- b) Heat release as a result of dissolution of oxygen in zirconium.

High reaction heat in case of formation of ZrO_2 (case a) leads to temperatures that are much higher than the boiling point of ZrO_2 , 4573 K for fine particles. The boiling of products was not considered in the model, allowing the calculated temperatures to exceed the boiling point. However, even for coarse particles, e.g., 200 μm diameter, the calculated temperatures exceed substantially the measured values reported in ref. [33]. The calculation using case b) gives temperatures below the boiling point of ZrO_2 for all particle sizes. It matches well the experimental data for coarse particles, for which the temperatures were reported to vary from 2000 to 2400 K [33], as illustrated in Fig. 2.

Figure 3 shows computed temperatures and oxygen fraction at the Knudsen layer interface as a function of the particle diameter for the reaction forming a Zr-O solution. For the diameters decreasing below approximately 40 μm , the reduced rates of heat and mass transfer in the Knudsen layer become noticeable and the oxygen fraction at the Knudsen layer interface increases, leading to a lower particle temperature. For reference, temperature calculated as a function of the particle size for a continuous model is also shown. The difference between the temperatures calculated from the continuous and transition regime transfer models becomes greater than 1000 K for particles less than 5 μm .

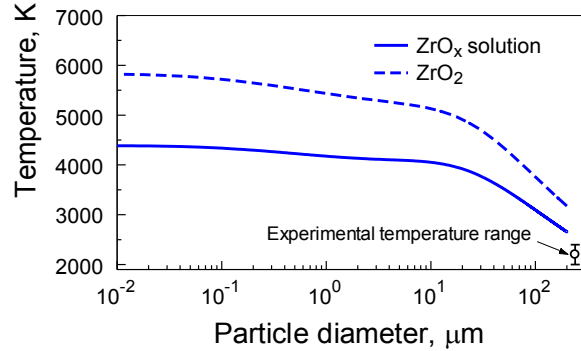


Figure 2. Temperatures for particles of different diameters calculated using transition heat transfer model with two different energetics of combustion: formation of ZrO_2 and dissolution of oxygen in Zr. The experimental temperature range for 240- μm particles [33] is also shown.

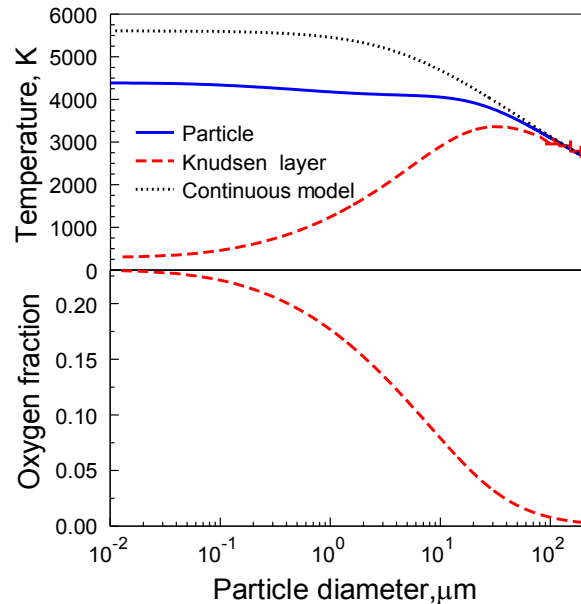


Figure 3. Temperature at the particle surface and Knudsen layer interface (a) and oxygen mass fraction (b) for various particle diameters. Continuous asymptotic solution valid for large particle diameters ($\text{Kn} \ll 1$) is shown with the dashed line.

Figure 4 illustrates the calculated spatial temperature and oxygen fraction profiles for a 1- μm diameter Zr particle in the air. As for the calculations shown in Fig. 3, the heat release is defined by dissolution of oxygen in zirconium. For comparison, results of calculations using the continuous model are also shown. The oxygen fraction at the distance r_δ (equal to one free molecular path) from the particle is significantly higher, while particle temperature about 1000 K lower than the value obtained in a continuous model. It is interesting to note how much lower both temperature and concentration gradients are for the current model compared to the continuous model at the Knudsen

layer boundary. This clearly implies lower reaction and heat transfer rates, indicating that the particle is effectively isolated from the environment by the introduced Knudsen layer.

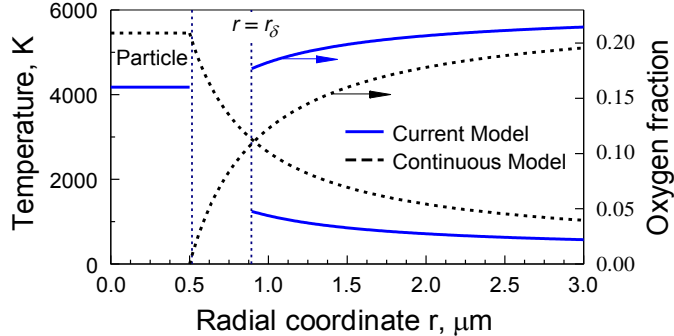


Figure 4. Spatial profiles of temperature and oxygen concentration for a particle of 1 μm diameter ($\text{Kn} = 0.8$).

The variation of oxygen mass flow rate with particle diameter is represented in Fig. 5 (once again assuming that the reaction leads to the formation of the Zr-O solution). The asymptotic trends for both continuous and free molecular regimes can be obtained from Eqs. (13) and (15), respectively. The continuous case corresponds to $\text{Kn} \rightarrow 0$, when $r_\delta/r_p \rightarrow 1$, as follows from Eq. (1), and $Y_\delta \rightarrow 0$. Substituting these limits into Eq. (13), we obtain the continuous mass flow rate:

$$\dot{m} = 4\pi\rho D_{\text{ox}} r_p \ln(1 - Y_{\text{ox},\infty}) \quad (24)$$

Similarly, in a free-molecular regime $\text{Kn} \rightarrow \infty$, $r_\delta/r_p \rightarrow \infty$, $T_\delta \rightarrow T_\infty$, and $Y_\delta \rightarrow Y_\infty$. Then, the free-molecular mass flow rate follows from Eq. (15) as

$$\dot{m} = -r_p^2 p Y_{\text{ox},\infty} M_\infty \sqrt{\frac{8\pi}{RT_\infty M_{\text{ox}}}} \quad (25)$$

The mass flow rate in a continuous regime is proportional to particle diameter radius (or diameter, d), while in the free molecular regime, it becomes proportional to r_p^2 or d^2 . These asymptotic trends for both continuous and free-molecular regimes are shown for comparison in Fig. 5. It is clear from Fig. 5 that neither continuous nor free molecular regime can describe adequately the burn rates for particles from approximately 100 nm to 30 μm diameter, covering the range of particle sizes used in combustion applications most commonly.

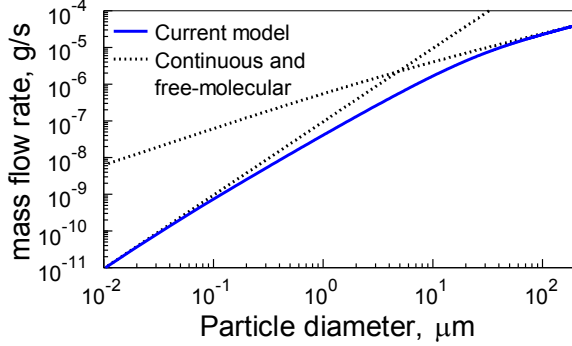


Figure 5. Mass flow rate of oxygen for various particle diameters. The dashed lines show the solutions for continuous ($\text{Kn} \ll 1$) and free-molecular ($\text{Kn} \gg 1$) regimes

Predicted steady burn rates, \dot{m} , can be directly used to approximately predict the burn times of Zr particles:

$$t_b = \frac{\pi d^3 \rho_m}{6\nu\dot{m}} \quad (26)$$

where ρ_m is density of zirconium, and ν is the stoichiometric coefficient. In calculations, the particle was assumed to be completely consumed when it absorbed enough oxygen to convert into ZrO_2 , so $\nu = \frac{M_{\text{Zr}}}{M_{\text{O}_2}}$, where M_{O_2} and M_{Zr} are respectively molecular weights of oxygen and zirconium.

This approach is expected to slightly under-estimate the burn times for the combustion scenario including formation of a saturated Zr-O solution with slightly less oxygen than in the stoichiometric ZrO_2 (followed by a fast transformation of the solution into ZrO_2 in an additional combustion step after a micro-explosion, as observed in respective particle combustion experiments [33, 39 - 42]).

Experiments on combustion of 2-25 μm diameter Zr particles ignited by a CO_2 laser were reported in Ref. [41]. The results of these experiments are shown in Fig. 6 along with earlier experimental data [33] for larger size particles (all data taken at 1 atm). For fine particles, a very weak dependence of the burn time vs. particle diameter was observed.

Figure 6 also shows the burn times for particles of different sizes estimated using both transition transfer and continuous models. Both models result in the same burn times for coarse particles, which match nicely the experimental data. The difference between the two calculated burn time trends becomes noticeable for 20- μm particles and becomes significant for particles finer than 10 μm . The effect of particle size on burn time for fine particles is predicted to become weaker by the transition transfer model; however, the predicted burn times are still shorter than the experimental ones. The effect of particle size in experiments is also weaker than for the calculated curve.

Quasi-steady calculations, in which the reaction rate was used to account for the particle size increasing during combustion, did not result in a substantially changed dynamics. The total increase in the particle size approaches 30 % of the initial size. The changes in the particle temperature are small and the predicted burn times become just a little shorter than those shown for the steady-state model in Fig. 6; the difference is indistinguishable

in the logarithmic scale used in Fig. 6. Thus, a substantial discrepancy between the calculated and experimental data remains.

The observed discrepancy may indicate the importance of the surface reaction kinetics in addition to the heat and mass transfer rates in defining the particle burn rate. Indeed, if the reaction kinetics is comparable to the rate of oxygen transfer to the particle surface, the concentration of oxidizer at the particle surface may be greater than zero, affecting the entire obtained solution. Another indication of importance of the chemical reaction might be the fact that the maximum temperatures reported in Ref. [41] for fine powders were in the range 3100 – 3683 K independent on the particle size, while the model for the diffusion limited process predicts higher temperatures, up to 4000 K for particles of 2 μm . The kinetics of surface reaction of zirconium with air is unknown. However, the present model can be readily modified to include an expression for the reaction kinetics with adjustable parameters. These parameters can be found by matching the predictions with experiments; thus unknown reaction kinetics for heterogeneously burning fuels can be established.

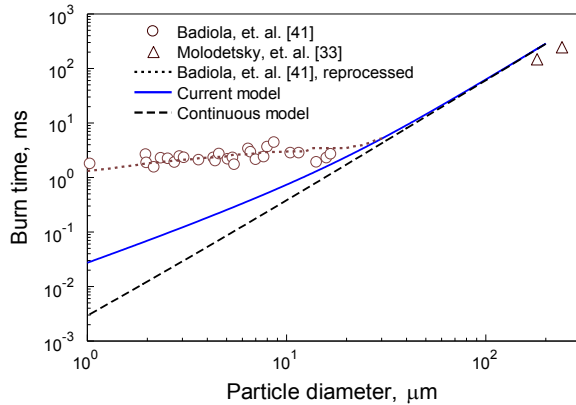


Figure 6. Burn time of Zr particles of various diameters. Experimental data [33, 41] and results of modeling. For comparison, results of both continuous solution (without Knudsen layer) and using the Knudsen layer approximation are shown.

Note that prior to developing the kinetic model, another important assumption used in the present analysis must be tested. Specifically, it was assumed here that the thermal accommodation coefficient was equal to one; however, some studies suggest that at high temperatures, this value may be reduced substantially. For example, thermal accommodation of NO on graphite was found to have values of 0.18 – 0.19 for a gas temperature of 1900 K and surface temperature of 3500 K [42]. In Ref. [43], the upper limit of thermal accommodation coefficient of gas on a silica nanoparticle at high particle (2000-2250 K) and gas (2000 K) temperatures was estimated to be equal to 0.005. In the current model, using smaller than one thermal accommodation coefficient would slow down the heat exchange between the particle and gas. Without taking into account a finite rate of surface reaction, the reduced thermal accommodation coefficient would lead us to predict even higher particle temperatures. Preliminary estimates suggest that both thermal accommodation coefficient and sticking coefficient, showing the percentage of collisions between oxidizer molecules and particle surface that result in a chemical reaction, must be reduced substantially to match the calculated and experimental data.

Furthermore, both coefficients may change with the reaction progress, while particle becomes partially oxidized and its surface properties change during combustion. Future work should, therefore, focus on quantifying the thermal accommodation coefficients for both oxidized and not oxidized fuel particles using, for example, inert gas environments to heat and cool particles of interest. Such separately measured thermal accommodation coefficients should be implemented in modeling the combustion experiments in order to recover the appropriate values of sticking coefficients and thus, respective reaction kinetics models.

Finally, the present calculations can also be compared with a different set of experiments, involving Zr-based alloys as reported in ref. [44]. Particles were ejected from a Zr_3Hf foil. Combustion was recorded with a high-speed camera and velocities of ejected particles were measured by laser velocimetry. Two types of experiments were conducted using different methods of particle ejection: by mechanical impact of a steel bead on the foil, and by the laser ablation. The mass flow rates were calculated assuming the same heat release rate as in case of combustion of pure zirconium. To calculate burn times according to Eq. (24), the particle was assumed to have density and molar mass of a mixture of Zr and Hf in the molar ratio 3:1. Figure 7 shows comparison of the present calculated burn times with the experimental data. It is interesting that the calculated burn times match well with the burn times measured for the particles generated by the laser ablation.

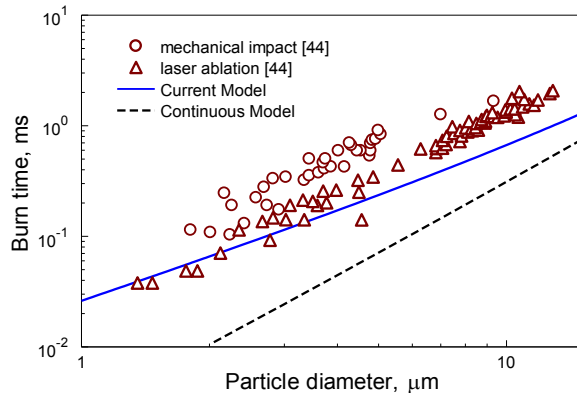


Figure 7. Comparison of computations with experimental data on burn times of Zr/Hf alloys [44].

Conclusions

A model describing heat and mass transfer for heterogeneously burning particles was developed capable of describing reaction rates for small particles, when their dimensions become comparable to the mean free path of the gas molecules. The model assumed that the combustion was rate limited by transport of oxidizer to the particle surface. The model was applied to establish combustion characteristics of Zr particles in air, assuming that the reaction products remain condensed. The predictions were compared with available experimental data. For coarse particles, both predicted combustion temperatures and burn rates match respective experimental data when the reaction is assumed to produce zirconium-oxygen solution rather than stoichiometric

ZrO_2 . This is consistent with the Zr combustion mechanism proposed earlier based on the analyses of the compositions of particles quenched at different burn times [21, 33, 37]. A reduced effect of particle size on their burn time is predicted for small particles, in qualitative agreement with recent experiments [41]. However, the model underestimates the burn times and overestimates the combustion temperatures for small particles. This discrepancy is likely associated with the finite reaction kinetics at the particle surface. It appears that values for both thermal accommodation coefficient and sticking coefficient accounting for the rate of surface reaction must be reduced substantially to obtain an adequate model. Separate measurements are desired to determine the thermal accommodation coefficients for oxidized and pure fuel particles in order to use the combustion experiments to obtain the reaction kinetics.

Appendix A

An expression for the mass flow rate with the Grad distribution at the Knudsen layer interface obtained in refs. [23, 24] was used without changes. The expression was obtained in the assumption of a small dimensionless heat flow, the condition which for the case considered here, can be written as:

$$\left| \frac{\sqrt{2\pi}q_{ox}M_{ox}}{4\pi r_\delta^2 \sqrt{RT_\delta} p Y_{ox,\delta} M_\delta} \right| \ll 1 \quad (\text{A1})$$

where q_{ox} is the heat flow rate at the Knudsen layer interface transferred by oxygen molecules due to conduction q_{ox}^c and diffusion of enthalpy which, taking into account Eq.(5), is:

$$q_{ox} = q_{ox}^c + \dot{m}(1 - Y_{ox,\delta})h_{ox}(T_\delta) \quad (\text{A2})$$

Additional work may be necessary to relax the requirement (A1) and derive a new, more complex expression for the mass flow rate for cases of strong dimensionless heat flows, which could be relevant to some of the interesting particle combustion scenarios. The energy exchange rate between the particle surface and Knudsen layer interface was deduced in refs. [23, 24, 31] using two major assumptions: a) translational energy of molecules is uncorrelated to the internal energy (i.e. rotational and vibrational energies); b) the mass flow rate is sufficiently small so that

$$\left| \frac{\dot{m}}{4\pi r^2 \sqrt{2} p} \sqrt{\frac{RT}{M_i}} \right| \ll 1 \quad (\text{A3})$$

Then, in a general case of multi-component gas, the rate of energy transfer by the component i can be written as

$$\dot{E}_i = \sqrt{\frac{8\pi}{RT_\delta}} r_p^2 p M_\delta \frac{Y_{i,\delta}}{\sqrt{M_i}} \left[(U_{i,p} - U_{i,\delta}) + \frac{2R}{M_i} (T_p - T_\delta) \right] \\ + \left(1 - \frac{r_p^2}{2r_\delta^2} \right) \dot{m}_i \left(U_{i,p} + \frac{2RT_p}{M_i} \right) + \frac{r_p^2}{2r_\delta^2} \left\{ \frac{5RT_\delta}{2M_i} \dot{m} Y_{i,\delta} + q_i \right\} \quad (\text{A4})$$

where $U_{i,p}$ and $U_{i,\delta}$ are the internal energies per mass (i.e. rotational and vibrational energy) of molecules of the i -th component at the particle surface and Knudsen layer interface, respectively, and q_i is the heat flux of the i -th component at the Knudsen layer interface, similar to Eq. (A2), which in general case is

$$q_i = q_i^c + (\dot{m}_i - m Y_{i,\delta}) h_i(T_\delta) \quad (\text{A5})$$

The internal energy per mass of molecules of the i -th component can be written as

$$U_i(T) = h_i(T) - \frac{5}{2} \frac{RT}{M_i} \quad (\text{A6})$$

Substituting Eqs. (A5), (A6) into Eq. (A4), and performing summation over all gas components, the total energy flow rate can be obtained:

$$\dot{E} = - \sqrt{\frac{8\pi}{RT_\delta}} r_p^2 p M_\delta \sum_i \frac{Y_{i,\delta}}{\sqrt{M_i}} \left[(h_i(T_p) - h_i(T_\delta)) - \frac{R}{2M_i} (T_p - T_\delta) \right] \\ + \left(1 - \frac{r_p^2}{2r_\delta^2} \right) \sum_i \dot{m}_i \left((h_i(T_p) - h_i(T_\delta)) - \frac{RT_p}{2M_i} \right) \\ + \frac{r_p^2}{2r_\delta^2} \sum_i \left\{ (\dot{m}_i - \dot{m} Y_{i,\delta}) \left(h_i(T_\delta) - \frac{5RT_\delta}{2M_i} \right) + q_i^c \right\} + \sum_i \dot{m}_i h_i(T_\delta) \quad (\text{A7})$$

References

- [1] B. R. Stanmore, Combust. Flame 136 (3) (2004) 398-427.
- [2] B. R. Stanmore; J. F. Brilhac; P. Gilot, Carbon 39 (15) (2001) 2247-2268.
- [3] K. Annamalai; W. Ryan, Prog. Energ. Combust. Sci. 19 (5) (1993) 383-446.
- [4] R. H. Hurt; J. R. Gibbins, Fuel 74 (4) (1995) 471-480
- [5] A. Pivkina; P. Ulyanova; Y. Frolov; S. Zavyalov; J. Schoonman, Propel.Expl. Pyrotech. 29 (1) (2004) 39-49
- [6] E. L. Dreizin, Prog. Energ. Combust. Sci. 35 (2) (2009) 141-167.
- [7] A. V. Fedorova, Combust. Expl. Shock+ 48 (3) (2012) 294-301.
- [8] Z. Zarei; D. L. Frost, Shock Waves 21 (5) (2011) 425-438.
- [9] F. Liu; K. J. Daun; D. R. Snelling; G. J. Smallwood, Appl. Phys.B: Lasers and Optics 83 (3) (2006) 355-382
- [10] X. Qu; E. J. Davis; B. D. Swanson, J. Aerosol Sci. 32 (11) (2001) 1315-1339.
- [11] W. Li; E. J. Davis, Aerosol Sci. Technol. 25 (1) (1996) 11-21.
- [12] E. M. Sazhina; S. S. Sazhin; M. R. Heikal; V. I. Babushok; R. J. R. Johns, Combust. Sci. Technol. 160 (1-6) (2000) 317-344
- [13] S. S. Sazhin, Prog. Energ. Combust. Sci. 32 (2) (2006) 162-214.
- [14] P. Pokkunuri; P. Nissenson; D. Dabdub, Atmospheric Environment 44 (2) (2010) 153-163.
- [15] F. D. Tang; S. Goroshin; A. J. Higgins in: *Modes of particle combustion in iron dust flames*, 2011; 2011; pp 1975-1982.
- [16] H. Krier; N. Glumac, Int. J. Energetic Mater. Chem. Propul. 8 (1) (2009) 71-80.
- [17] A. Ulas; K. K. Kuo; C. Gotzmer, Combust. Flame 127 (1-2) (2001) 1935-1957.
- [18] V. K. Bind; S. Roy; C. Rajagopal, Chem. Eng. J. 207-208 (2012) 625-634.
- [19] N. A. Fuchs, The Mechanics of Aerosols, Pergamon Press, London, 1964, 408 pp.
- [20] A. V. Filippov; D. E. Rosner, Int. J. Heat Mass Tran. 43 (1) (2001) 127-138.
- [21] E. L. Dreizin, Prog. Energ. Combust. Sci. 26 (1) (2000) 57-78.
- [22] N. A. Fuchs; Evaporation and droplet growth in gaseous media, Pergamon, London, 1959, 72 pp.
- [23] J. Young, Int. J. Heat Mass Tran. 34 (1991) 1649-1661.
- [24] J. Young, Int. J. Heat Mass Tran. 36 (1993) 2941-2956.
- [25] P. G. Wright, Discussions of the Faraday Society 30 (1960) 100-112
- [26] P. Peeters; C. Luijten, Int. J. Heat Mass Tran. 44 (2001) 181-193
- [27] B. McCoy; C. Y. Cha, Chem. Eng. Sci. 29 (1974) 381-388.
- [28] R. W. Schrage. A theoretical study of interphase mass transfer. Thesis, Columbia University Press., New York, 1953, 103 pp.
- [29] P. Peeters; G. Pieterse; M. E. H. van Dongen, Phys. Fluid. 16 (2004) 2575-2586.
- [30] G. L. Hubbard; V. E. Denny; A. F. Mills, Int. J. Heat Mass Tran. 18 (9) (1975) 1003-1008.
- [31] M. C. Yuen; L. W. Chen, Combust. Sci. Technol. 14 (1976) 147-154.

- [32] M. Renksizbulut; M. C. Yuen, J. Heat Tran. 105 (2) (1983) 384-388
- [33] I. E. Molodetsky; E. L. Dreizin; C. K. Law, Proc. Combust. Inst. 26 (2) (1996) 1919-1927.
- [34] R. B. Bird; W. E. Stewart; E. N. Lightfoot, Transport phenomena, John Wiley & Sons Inc., New York, NY, 2002, 897 pp.
- [35] T. R. Marrero; E. A. Mason, J. Phys. Chem. Ref. Data 1 (1972) 3
- [36] P. J. Linstrom; W. G. Mallard NIST Chemistry WebBook, NIST Standard Reference Database Number 69, National Institute of Standards and Technology, Gaithersburg MD, 20899. <http://webbook.nist.gov> (retrieved September 20, 2012)
- [37] I. E. Molodetsky; E. L. Dreizin, MRS Online Proceedings Library 418 (1995) 195-200.
- [38] M. W. Chase, J. Phys. Chem. Ref. Data, Monograph 9 (1998) 1-1951
- [39] L. S. Nelson; D. E. Rosner; S. C. Kurzus; H. S. Levine, Proc. Comb. Inst. 12 (1) (1969) 59-70.
- [40] L. S. Nelson, Nature 207 (4998) (1965) 741-742.
- [41] C. Badiola; E. L. Dreizin, Proc. Combust. Inst. 34 (2012) 2237-2243.
- [42] H. A. Michelsen, Appl. Phys. B 94 (1) (2008) 103-117.
- [43] I. Altman; D. Lee; J. Song; M. Choi, Phys. Rev. E 64 (5) (2001) 052202/1-052202/4.
- [44] H. Wei; C.-S. Yoo, J.Appl. Phys. 111 (2012) 023506

CHAPTER 11: EFFECT OF SURFACE TENSION ON THE TEMPERATURE OF BURNING METAL DROPLETS

Introduction

Vapor phase combustion of fuel droplets is ubiquitous in various practical systems. The droplet temperature is commonly accepted to be at the boiling point of the respective fuel [1, 2]. This assumption is used equally for hydrocarbon and metal fuel droplets. It is also commonly recognized that as the droplet size decreases, the vapor phase flame becomes more and more difficult to maintain because of accelerated rates of heat and mass transfer from the droplet surface. Respectively, at some point, combustion reactions begin primarily occurring at the surface of the burning droplet [3-5]. Predicting the droplet size and conditions for which the transition from the vapor phase to surface controlled reaction will occur is very important for designing respective combustion systems. Recently, this issue was closely looked at for aluminum particle combustion [6-8]. This was prompted by the availability of and combustion test results for fine, submicron and nano-sized Al powders. The identification of the range of particle sizes, which can burn in the vapor phase, focused on detailed analysis of heat and mass transfer for burning particles. Specifically, heat transfer in the transition regime was considered [8, 9] and further work coupling both heat and mass transfer analyses for that regime was proposed. Clearly, an accurate assessment of the surface temperature of the burning particle is critical for such analysis. A possible correction for this temperature, that is commonly assumed to be the metal's boiling point, is the subject of this letter.

In the studies of Al combustion cited above, as well as elsewhere, the effect of the droplet surface tension on the pressure inside it and, respectively, on the fuel's boiling point, was neglected. The effect was considered briefly in an early Russian paper [10], however, specific corrections for the burning particle temperatures were not discussed. For large droplets and for fuels with weak surface tension, such as common hydrocarbons, this effect may be negligible. It needs to be accounted for when fine droplets with high surface tension are dealt with. In particular, combustion of fine fuel particles with small sizes becomes increasingly important for metal fuels, for which the surface tension is quite significant. This letter describes the expected effect considering specific examples of combustion of aluminum and magnesium droplets.

Boiling point as a function of pressure

The effect of pressure on the boiling point is readily obtained from Clausius-Clapeyron equation, written with an assumption that the vapor behaves as an ideal gas:

$$\frac{dp}{p} = \frac{\Delta H_{vap}}{RT^2} dT \quad (1)$$

where p is pressure, ΔH_{vap} is the heat of formation of the metal vapor, R is the universal gas constant, and T is temperature. Based on data from NIST chemistry webbook [11], the effect of temperature on ΔH_{vap} is given as:

$$\Delta H_{vap} = \Delta_f H_{gas}^o + A \frac{T}{1000} + \frac{B}{2} \left(\frac{T}{1000} \right)^2 + \frac{C}{3} \left(\frac{T}{1000} \right)^3 + \frac{D}{4} \left(\frac{T}{1000} \right)^4 - \frac{1000E}{RT} + F - H \quad (2)$$

where $\Delta_f H_{\text{gas}}^o$ is the standard heat of formation of the metal vapor and A, B, C, D, E, F , and H are constants. Plugging Eq. (2) in Eq. (1) and integrating the result from 1 bar and boiling temperature at 1 bar, T_{boil}^o , to the pressure p and respective boiling temperature T , we obtain

$$\begin{aligned} \ln(p) = & -\left(\frac{\Delta_f H_{\text{gas}}^o + F - H}{R}\right)\left(\frac{1}{T} - \frac{1}{T_{\text{boil}}^o}\right) + \frac{A}{1000R} \ln\left(\frac{T}{T_{\text{boil}}^o}\right) + \frac{B}{2R \cdot 10^6} (T - T_{\text{boil}}^o) \\ & + \frac{C}{6R \cdot 10^9} \left[T^2 - (T_{\text{boil}}^o)^2 \right] + \frac{D}{12R \cdot 10^{12}} \left[T^3 - (T_{\text{boil}}^o)^3 \right] + \frac{1000E}{3R} \left[\frac{1}{T^3} - \frac{1}{(T_{\text{boil}}^o)^3} \right] \end{aligned} \quad (3)$$

Eq. (3) gives the correlation between the pressure and boiling temperature. Specific correlations for Al and Mg calculated using the constants A, B, C, D, E, F , and H as well as respective values of $\Delta_f H_{\text{gas}}^o$ for each metal [11] are shown as bold lines in Figs. 1 and 2, respectively. All constants used in Eq. 3 are given in Table 1.

Note that Kelvin effect resulting in an increase of the vapor pressure above the surface of a small droplet is quite small for relatively high-density metals for elevated temperatures characteristic of metal combustion; for 100-nm radius droplets the effect is causing only $\sim 1\%$ correction for the pressure. Because of the relatively insignificant correction, this effect is neglected here.

Table 1. Constants used in Eq. (3) taken from ref. [11].

Constant	Al	Mg
A	20.37692	20.77306
B	0.660817	0.035592
C	-0.313631	-0.031917
D	0.045106	0.009109
E	0.078173	0.000461
F	323.8575	140.9071
H	329.6992	147.1002
T_{boil}, K	2793	1363
$\Delta_f H_{\text{gas}}^o, \text{ kJ/mol}$	329.7	147.1
$R, \text{ J/(mol}\cdot\text{K)}$	8.31	

Laplace pressure as a function of temperature

For a spherical droplet, Laplace pressure, p_L is inversely proportional to its radius, r :

$$p_L = 2 \frac{\sigma}{r} \quad (4)$$

where σ is the surface tension. It is commonly accepted that a linear trend describes the effect of temperature on surface tension for metal melts. For aluminum in an oxidizing environment, the following equation was proposed [12]:

$$\sigma_{Al} \left[\frac{mN}{m} \right] = 875 - 0.18(T - 933) \quad (5)$$

where temperature is in K. Similarly, for magnesium, the effect of temperature on the surface tension was described as [12]:

$$\sigma_{Mg} \left[\frac{mN}{m} \right] = 577 - 0.26(T - 923) \quad (6)$$

With the above information, the Laplace pressure can be easily estimated for metal droplets of different sizes for both Al and Mg. Thin lines in Figs. 1 and 2 represent such pressures added to an assumed surrounding pressure of 1 bar for particles of different sizes for Al and Mg, respectively.

The intersections of the bold and thin lines indicate the boiling temperatures expected for the respectively sized particles burning in an oxidizing environment at 1 bar.

Implications for metal combustion

The effect of Laplace pressure on temperature of the burning Al particles is quite strong. The temperature that a particle can reach increases substantially for finer particles, possibly exceeding the boiling point of Al_2O_3 , which is commonly considered to be a practical upper limit for the flame temperature for Al [13]. The precise determination of the boiling temperature of Al_2O_3 is difficult. A considerable disagreement exists between different sources reporting it to be in the range from 3253 K [14, 15] to 3800 K [16]. It may be more rational to consider whether fine Al particles can burn in the vapor phase by comparing the predicted boiling temperatures with the reported measured temperatures for the vapor-phase aluminum flames. These temperatures are consistently reported to be in the range of 3000 - 3300 [17-20] and are likely affected by formation of metastable gaseous products, such as AlO , Al_2O , and AlO_2 and by radiation heat losses. From Fig. 1, it is apparent that particles with radii close to 1 μm and finer can be heated up to such temperatures and thus reach thermal equilibrium with the vapor phase flame. The present estimates should not be interpreted as predicting the particle sizes for which transition from the vapor phase flame to surface reaction occurs. Instead, they should be used to properly evaluate the particle temperature when different possible reaction rate limiting processes are assessed quantitatively and compared to each other.

If the surface reaction is significant, it is possible for the particle temperature to exceed the temperature of the vapor phase flame. The latter point might help interpret observations in ref. [7], where both color pyrometry and AlO emission spectra were used to measure the aluminum combustion temperature. Both temperature measurements were compared for the particles of different sizes burning in 50% O_2 and 50% Ar.

Interestingly, for the particles with average diameters between 20 and 50 μm , the temperatures inferred from the AlO spectra were higher than those obtained by pyrometry. However, the trend reversed for finer particles, and the temperatures measured by pyrometry became higher than those obtained from the AlO spectra. Because emissivity of the particle surface is greater than that of a vapor-phase flame, the pyrometric measurement is more biased to the particle surface temperature compared to the AlO spectra biased to the vapor phase emission. Thus, an increase in the pyrometric temperature compared to that implied from the AlO spectra may indeed show that the particle surface was hotter than the vapor phase flame for fine particles.

Because fine particles and nanoparticles can burn at elevated surface temperatures, they may exhibit a higher surface reaction rates than coarser particles. However, the reaction products may also change, favoring high-temperature gas species forming with a relatively weak heat effect compared to the condensed Al_2O_3 . Thus, both the reaction rate and the reaction products are predicted to depend on the particle radius. When combined, these effects might be able to explain the long burn times reported for fine Al particles recently [6, 21-25]. In addition, one should account for the decrease in the evaporation rates and increase in heat losses from the burning particle surface (including radiation). These effects, together with the altered regime of heat and mass transfer for the particles with dimensions comparable to the gas molecule mean free path, should be accounted for while developing a combustion model.

For particles coarser than ca. 10 μm , the effect of surface tension on the boiling temperature is reduced; this is also the range of particle sizes for which the vapor phase combustion is predicted to be feasible [8].

The effect of surface tension on the boiling point and thus on the rate of evaporation of the burning aluminum particles discussed here is consistent with recent experimental observations on heating different size Al powders in a shock tube [26]. The presence of vapor-phase Al was detected optically. It was observed that the concentration of Al vapors was much higher for micron-sized powders compared to nano-powders heated to the same temperature. This effect might have been surprising considering a much greater specific surface available for the nanopowders, implying a stronger flow of evaporating aluminum. However, the observation is readily understood considering estimates shown in Fig. 1. Indeed, the nanosized particles were much further from the boiling point than their coarser counterparts. Respectively, a much lower Al vapor pressure could be generated by their heating in the reflected shock.

The effect of Al_2O_3 coverage or inclusions was neglected in the above discussion. At the temperatures considered, Al_2O_3 is molten and immiscible with molten Al [27]. Thus, inclusions of Al_2O_3 (or oxide caps widely reported in the literature [28-33]) form, causing local changes in the surface tension. This is consistent with the observed asymmetric flames and jetting observed by many authors for burning Al droplets, e.g., [34-36]. Formation of oxide caps rather than continuous oxide coating is also expected for individual aluminum nano-particles reacting heterogeneously because, based on the present estimates, their temperature is expected to be substantially higher than the melting point of Al_2O_3 (2324 K [37, 38]). Note, however, that the reaction may be substantially different for aggregated nanoparticles [39, 40]. Discussion of processes

caused by agglomeration and merger of agglomerated nanoparticles is beyond the scope of this letter.

For Mg particles, the absolute increase in the boiling point for fine particles is less dramatic than for Al; however, the effect is not negligible. The vapor phase surrounding burning Mg droplets is at a much higher temperature (~ 2600 K, [19, 41]) than the metal particle itself, which is usually assumed to be at its boiling temperature, although it was observed that large burning Mg particles can be heated by 300 – 400 K above it [42]. The superheating effect was attributed to the formation of porous MgO shell. The effect is comparable to that predicted here for fine Mg particles. At any rate, the thermal gradient between the vapor-phase flame and particle surface remains strong, causing intense vapor phase combustion. Emission-based optical temperature measurements for coarse particles with distinct vapor phase flames are expected to be completely dominated by the bright flame, resulting in very high combustion temperatures. The particle inside the flame zone will be essentially invisible to the optical diagnostics.

For small particles, a reduction in the flame size is expected due to increased heat losses accompanied by a transition to the surface reaction, similar to Al. In that case, the increased particle surface temperature may become important for sustaining significant surface reaction. Unlike for aluminum, there are no known gas phase magnesium suboxides, which could noticeably reduce the heat effect of combustion, and the MgO forming on the particle surface must be solid. Formation of solid MgO directly on the particle surface would result in production of non-spherical combustion products while burning fine spherical Mg powders.

Optical measurements of temperature for fine an ultrafine burning Mg particles may be representative of their surface temperatures, which would be much lower than the temperatures of the vapor-phase flames but noticeably higher than the regular Mg boiling point. Unfortunately such measurements could not be found in the literature.

Finally, the effect of the initial MgO layer on Mg combustion may be interesting to consider. Unlike Al_2O_3 , MgO melts at about 3000 K [43], and thus it is expected to be solid at the combustion temperatures. Fragments of MgO formed upon break-up of the original oxide shell may be covered by liquid Mg. Thus, non-spherical product particles may be formed even for coarser particles, without the direct growth of solid MgO on the particle surface that can occur for fine particles, as discussed above. The non-spherical particle shapes have, indeed, been observed in the Mg combustion products [44].

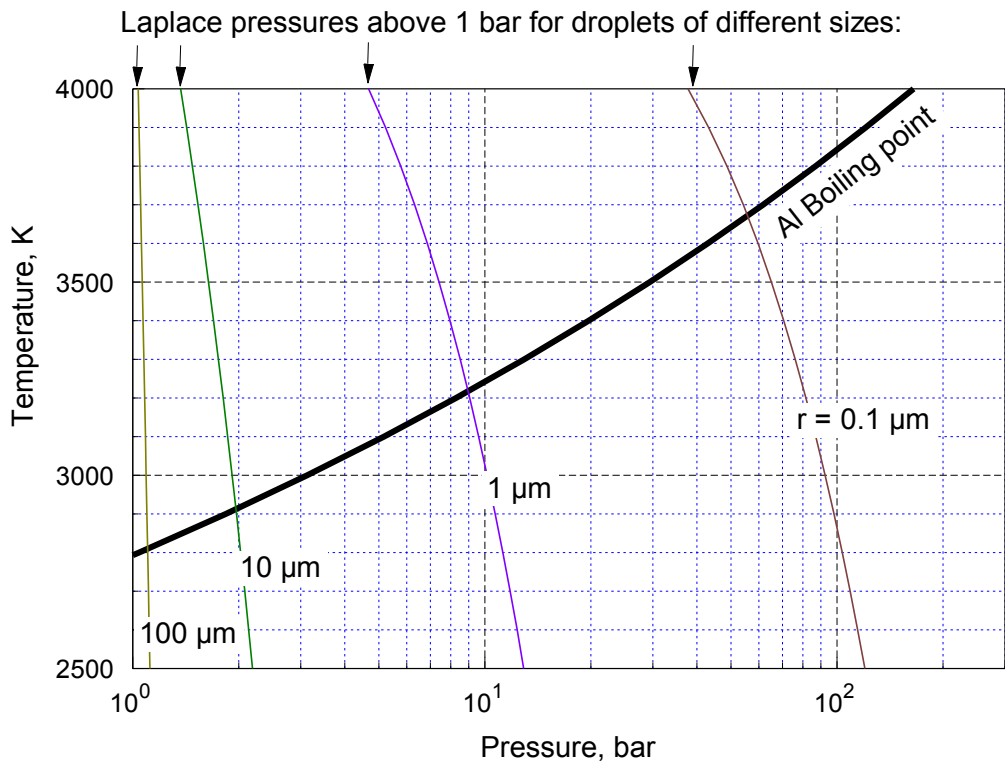


Fig. 1. Elevated boiling point of aluminum as a function of pressure (bold line) and Laplace pressures in aluminum droplets of different radii at varied temperatures (thin lines). A dashed line shows the boiling point for aluminum oxide.

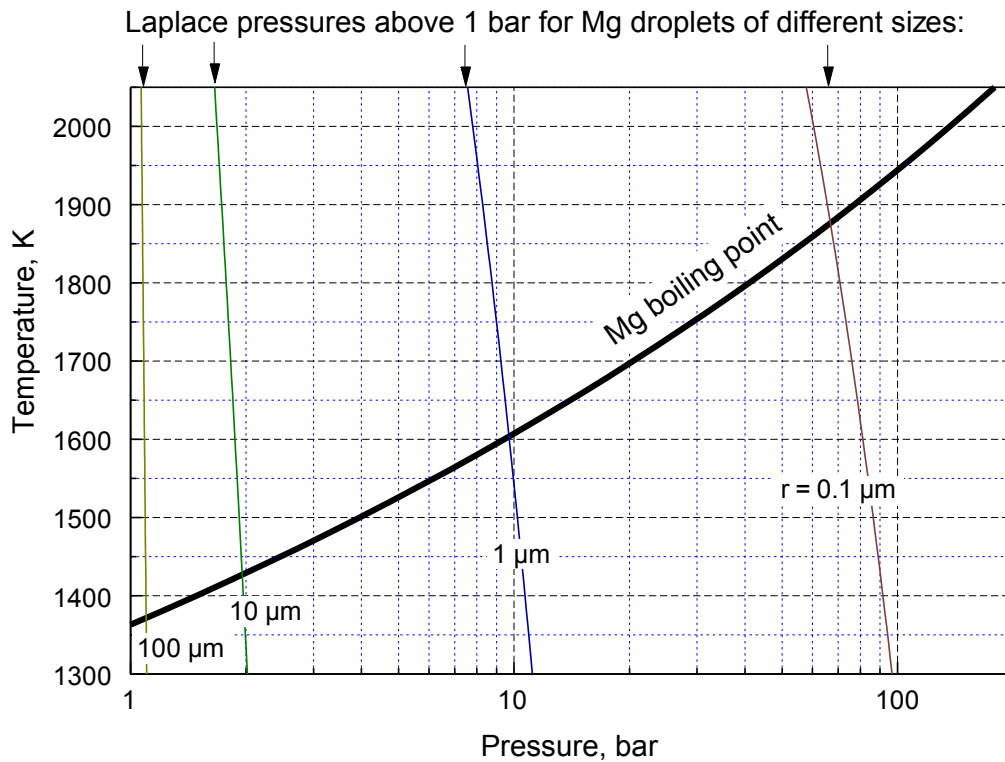


Fig. 2. Elevated boiling point of magnesium as a function of pressure (bold line) and Laplace pressures in magnesium droplets of different radii at varied temperatures (thin lines).

References

- [1] J. Warnatz, U. Maas, R.W. Dibble, Combustion: Physical and Chemical Fundamentals, Modeling and Simulation, Experiments, Pollutant Formation, 2 edition ed., Springer-Verlag, Berlin, Germany, 2006.
- [2] M. S., J.-Y. Chen, A.C. Fernandez-Pello, Fundamentals of Combustion Processes, Springer, New York, 2011.
- [3] V.E. Zarko, L.K. Gusachenko, A.D. Rychkov, Modeling of transient combustion regimes of energetic materials with surface evaporation, in: Challenges in Propellants and Combustion: 100 Years after Nobel, International Symposium on Special Topics in Chemical Propulsion Begell House, Stockholm, 1997, pp. 1014-1025.
- [4] M.W. Beckstead, Y. Liang, K.V. Pudduppakkam, Combustion, Explosion and Shock Waves, 41 (2005) 622-638.
- [5] J.C. Lee, R.A. Yetter, F.L. Dryer, Combustion and Flame, 101 (1995) 387-398.
- [6] P. Lynch, H. Krier, N. Glumac, Proceedings of the Combustion Institute, 32 (2009) 1887-1893.
- [7] T. Bazyn, H. Krier, N. Glumac, Evidence for the transition from the diffusion-limit in aluminum particle combustion, in, Heidelberg, 2007, pp. 2021-2028.
- [8] S. Mohan, M.A. Trunov, E.L. Dreizin, Combustion and Flame, 156 (2009) 2213-2216.

- [9] A. Ermoline, D. Yildiz, E.L. Dreizin, Combustion and Flame, (2013).
- [10] V.I. Shevtsov, V.P. Fursov, E.I. Gusachenko, Fiz. Aerodispersn. Sistem., (Kiev), (1982) 33-39.
- [11] M.W. Chase, J. Phys. Chem. Ref. Data, Monograph 9, (1998) 1-1951.
- [12] K.C. Mills, Y.C. Su, International Materials Reviews, 51 (2006) 329-351.
- [13] I. Glassman, R.A. Yetter, Combustion, 4th ed., Academic Press, Amsterdam ; Boston, 2008.
- [14] D.L. Perry, Handbook of Inorganic Compounds, 2 ed., CRC Press, Boca Raton, FL, 2011.
- [15] R.L. Myers, The 100 Most Important Chemical Compounds: a Reference Guide, Greenwood Press, Westport, CT, 2007.
- [16] L.S. Nelson, Techniques for Studying Liquids and Solids at Extreme Temperatures, in: E. Leroy (Ed.) Advances in High Temperature Chemistry, Elsevier, 1971, pp. 171-218.
- [17] N.I. Poletaev, A.V. Florko, Fiz. Gorenija Vzryva, 44 (2008) 72-79.
- [18] P. Lynch, H. Krier, N. Glumac, J. Thermophys. Heat Transfer, 24 (2010) 301-308.
- [19] S. Goroshin, D.L. Frost, J. Levine, A. Yoshinaka, F. Zhang, Propellants, Explos., Pyrotech., 31 (2006) 169-181.
- [20] E.L. Dreizin, Combustion and Flame, 105 (1996) 541-556.
- [21] C. Badiola, E.L. Dreizin, Combustion Science and Technology, 184 (2012) 1993-2007.
- [22] E.L. Dreizin, C. Badiola, S. Zhang, Y. Aly, International Journal of Energetic Materials and Chemical Propulsion, 10 (2011) 22.
- [23] C. Badiola, R.J. Gill, E.L. Dreizin, Combustion and Flame, 158 (2011) 2064-2070.
- [24] R.J. Gill, C. Badiola, E.L. Dreizin, Combustion and Flame, 157 (2010) 2015-2023.
- [25] H. Krier, N. Glumac, International Journal of Energetic Materials and Chemical Propulsion, 8 (2009) 71-80.
- [26] P. Lynch, G. Fiore, H. Krier, N. Glumac, Combustion Science and Technology, 182 (2010) 842-857.
- [27] H.A. Wriedt, Bulletin of Alloy Phase Diagrams, 6 (1985) 548-553.
- [28] M.W. Beckstead, Combustion, Explosion and Shock Waves, 41 (2005) 533-546.
- [29] K.P. Brooks, M.W. Beckstead, Journal of Propulsion and Power, 11 (1995) 769-780.
- [30] M.K. King, Proceedings of the Combustion Institute, 32 II (2009) 2107-2114.
- [31] V. Sarou-Kanian, J.C. Rifflet, F. Millot, I. Gökalp, Combustion and Flame, 145 (2006) 220-230.
- [32] O.G. Glotov, V.A. Zhukov, Combustion, Explosion and Shock Waves, 44 (2008) 671-680.
- [33] E.L. Dreizin, Combustion and Flame, 117 (1999) 841-850.
- [34] J. Sun, R. Dobashi, T. Hirano, Journal of Loss Prevention in the Process Industries, 19 (2006) 769-773.
- [35] P. Bucher, R.A. Yetter, F.L. Dryer, E.P. Vicenzi, T.P. Parr, D.M. Hanson-Parr, Combustion and Flame, 117 (1999) 351-361.
- [36] P. Bucher, R.A. Yetter, F.L. Dryer, T.P. Parr, D.M. Hanson-Parr, E.P. Vicenzi, Symp. (Int.) Combust., [Proc.], 26th (1996) 1899-1908.
- [37] W. Gorski, A. Dietzel, Revue Internationale Des Hautes Temperatures Et Des Refractaires, 6 (1969) 105-110.
- [38] S.J. Schneider, C.L. McDaniel, Revue Internationale Des Hautes Temperatures Et Des Refractaires, 3 (1966) 351-361.

- [39] G.C. Egan, K.T. Sullivan, T. Lagrange, B.W. Reed, M.R. Zachariah, *Journal of Applied Physics*, 115 (2014).
- [40] P. Chakraborty, M.R. Zachariah, *Combustion and Flame*, 161 (2014) 1408-1416.
- [41] A.V. Florko, V.V. Golovko, *Combustion, Explosion, and Shock Waves*, 29 (1994) 562-567.
- [42] E.Y. Shafirovich, U.I. Goldshleger, *Combustion and Flame*, 88 (1992) 425-432.
- [43] Y. Yoshimoto, *J. Phys. Soc. Jpn.*, 79 (2010) 034602/034601-034602/034612.
- [44] E.L. Dreizin, C.H. Berman, E.P. Vicenzi, *Combustion and Flame*, 122 (2000) 30-42.

CHAPTER 12: DEPRESSION OF MELTING POINT FOR PROTECTIVE ALUMINUM OXIDE FILMS

Introduction

Multiple models of aluminum ignition discussed in the literature rely on the melting of aluminum oxide as a demarcation event separating ignition processes from the reaction regime associated with combustion [1]. The focus has been on describing the transport rate of reagents including ions of Al and O, across the aluminum oxide layer, which is being analyzed up to its melting point, 2327 K, according to NIST Chemistry Webbook [2]. However, a small thickness of the aluminum oxide layer may be affecting its melting point. Indeed, the melting point depression has been extensively discussed in the literature for nano-materials, see for example a review in ref. [3] and, in particular, for nano-aluminum particles [4, 5]. The effects become significant when the characteristic material dimension becomes close to or less than approximately 10 nm. Most nano-aluminum powders are substantially greater than this dimension, so that the effect of the particle size on the Al melting point is small. However, the thickness of the “natural” aluminum oxide film is commonly in the range of 3 – 5 nm, e.g., [6, 7]; thus, the depression of its melting point can be substantial. This letter evaluates the anticipated effect theoretically and offers an experimental validation of the depressed melting point for natural aluminum oxide layers on surface of fine aluminum powders. The effect must be accounted for in detailed models of aluminum ignition assuming a step-wise change in the protective properties of aluminum oxide upon its melting. It may also need to be considered in other high-temperature processes, such as sintering of structural components, involving aluminum powders [8].

Estimated depression of the melting point

The effect can be roughly evaluated considering available theoretical models describing the depression of melting point for nano-materials. A simplified expression for the melting point of a nano-sized material is given in ref. [9]:

$$T_m = T_b \exp \left[-\frac{\alpha - 1}{\frac{D}{D_0} - 1} \right] \quad (1)$$

where D is the film thickness, α is a ratio of mean square displacements of surface atoms and interior atoms, and D_0 is a critical diameter, for which all atoms are located on the surface. For low-dimensional crystals, D_0 depends on the dimension d . For thin films, $d=2$.

The relationship for D_0 and atomic diameter h is (for films)

$$D_0 = 2(3-d)h = 2h \quad (2)$$

For surface melting, one can find

$$\alpha = \left[\frac{2C_{pm}}{3R} + 1 \right] \quad (3)$$

Where C_{pm} is heat capacity difference between liquid and solid phases at T_m .

An estimate for D_0 can be obtained as the average Al-O bond length in transition alumina: $h=1.9 \text{ \AA}$ [10].

To calculate C_{pm} , one can use data from NIST Chemistry webbook [2]; bulk alumina melts at 2327 K.

For all alumina phases, specific heat is given by Shomate equation:

$$C_p = A + B \cdot \frac{T}{1000} + C \cdot \left(\frac{T}{1000} \right)^2 + D \cdot \left(\frac{T}{1000} \right)^3 + E \cdot \left(\frac{1000}{T} \right)^2 \quad (4)$$

Where

Coefficient	A	B	C	D	E
Gamma	108.6830	37.22630	-14.20650	-14.20650	-3.209881
Liquid	192.464	$9.819856 \cdot 10^{-8}$	-2.858928×10^{-8}	2.929147×10^{-9}	5.599405×10^{-8}

Plugging in the numbers, gives $\alpha=4.773$

Finally, substituting the value of α in Eq. (1), one obtains the result shown in Fig. 1. For practical range of natural alumina thickness, from ca. 3 to 5 nm, the melting point is predicted to be depressed by 400 – 200 K.

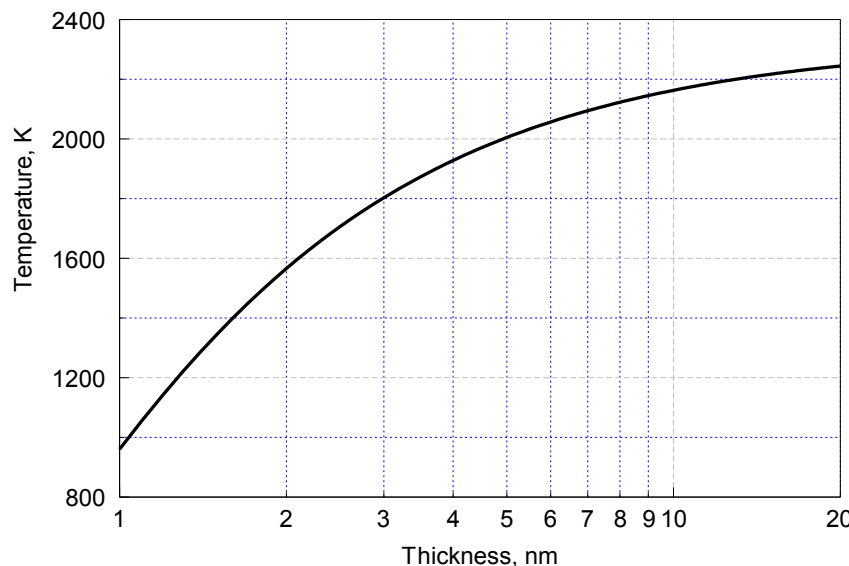


Fig. 1. Estimated melting point as a function of thickness of aluminum oxide.

Experimental detection of melting point of natural aluminum oxide film

The detection of the alumina melting point is based on an assumed change in the surface emissivity of aluminum particles covered with the naturally grown oxide film when the film is melting. To detect this change in emissivity, the following experiment was performed.

Micron sized aluminum particles in the 3-4.5 μm diameter range obtained from Alfa-Aesar were injected, aerosolized, and rapidly heated to a well characterized temperature and pressure behind the reflected shock in a heterogeneous shock tube described in full in previous publications [11, 12]. The reflected shock conditions are calculated by measuring the shock velocity and the initial temperature and pressure of the argon used as the ambient test gas. In the experimentally inert environment all particles thermally equilibrate to the known gas temperature rapidly ($<5\mu\text{s}$) relative to the overall test time of 1.6 ms and remain at the gas temperature for the remainder of the test duration.

The incandescence of the heated particles was collected using a Triax 190 spectrometer coupled to a Hamamatsu back-thinned CCD with 128x1044 pixels each 25 μm square. The resolution of the system was approximately 1.4 nm. Spectra of the thermal emission were obtained from 650-900 nm as shown in Fig. 2 and were integrated over the entire duration of the test. The wavelengths from 720-770 nm were not used to fit an emissivity trend due to strong atomic interferences from the potassium doublet near 765 nm that was present in all tests. The relative emissivity is measured by comparing the experimental emission curve to the predicted blackbody emission at the temperature determined by the shock velocity. The experimental emission curve is first calibrated to account for the instrument's spectral response prior to comparison with the black body curve. Figure 2 shows an example power law fit ($\varepsilon \sim \lambda^{2.94}$) for the relative wavelength dependence of the particles at 1521 K.

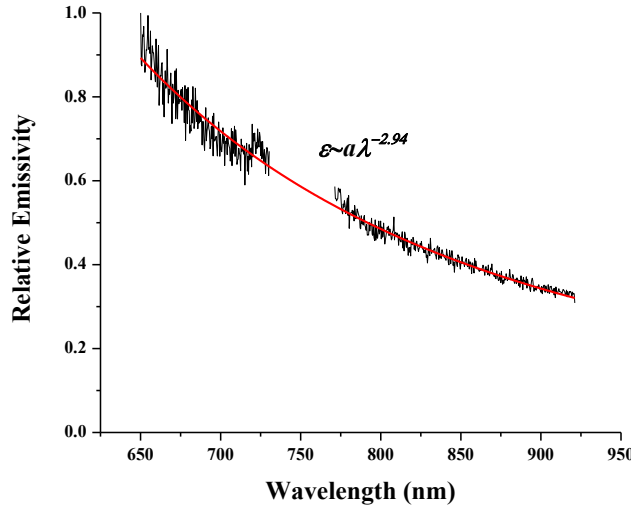


Fig. 2 Thermal emission spectra of 1-5 micron aluminum particles heated in argon at 1521 K and 7.5 bar. The power law fit shows a wavelength dependence of $\lambda^{-2.94}$

It was previously shown that the wavelength dependence of the emissivity properties of nano-alumina particles is affected by the phase of the material [13]. A similar effect is expected for micron sized aluminum particles with nanometer thin oxide layers. In the present experiments, the shift in the emissivity wavelength dependence at different temperatures is used to infer melting of the oxide layer. Figure 3 is a plot of the power law fit at different ambient temperatures. A shift in the power law coefficient between 2000 K and 2200 K suggests that melting is occurring in this temperature range. This result is consistent with an oxide thickness in the 5-8 nm range.

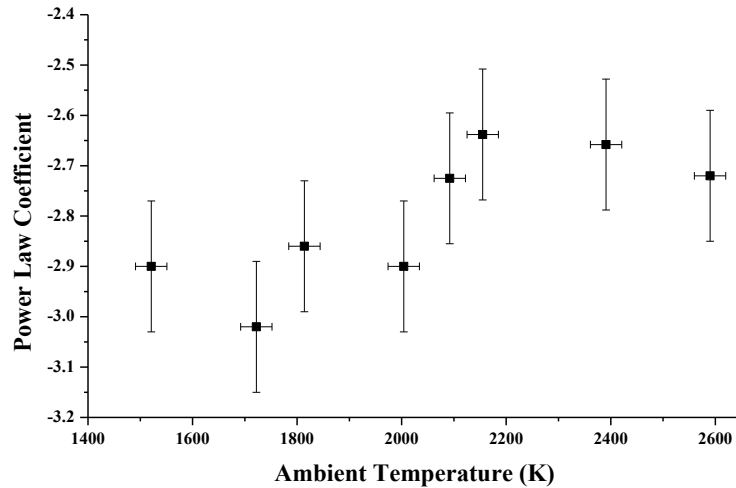


Fig. 3 Measured power law coefficient at various ambient temperatures

Discussion

The experimental data support the initial estimate of the depressed melting point of a thin layer of aluminum oxide. As noted above, this depression is important to be accounted for when modeling ignition of aluminum particles in practical systems [1, 14]. Upon melting, aluminum oxide film is expected to reduce its surface area forming a spherical inclusion and exposing aluminum surface directly to an oxidizing environment. For micron-sized aluminum powders used in most practical combustion system, the removal of protective oxide film leads to the onset of full-fledged vapor phase combustion. For burning aerosolized powders, this can lead to beginning of a qualitatively different flame propagation [15]. Predicting an ignition delay leading to the vapor phase combustion is important for respective reaction models; thus an accurate assessment of the alumina melting point is necessary.

Depression of the melting point for nano-sized aluminum oxide film should be also accounted for when composite materials involving aluminum powder are designed and manufactured, as for example is done for the aluminum-carbon nanotubes composite [16], consolidated by spark plasma sintering. Similarly, destruction of an aluminum oxide layer was of critical importance for sintering aluminum powders using combination of pulsed current and high pressure [17]. The melting of natural alumina may also be important to consider for applications involving brazing of aluminum [18].

Concluding remarks

Natural alumina film formed on surface of aluminum metal has thickness of about 3 – 5 nm. Based on its small thickness, a substantial depression of its melting point is predicted. An estimate shows that the melting point can be reduced by 200 – 400 K for practically common natural alumina thicknesses. Experiments detected a temperature range when a shift occurred in the emissivity wavelength dependence of naturally oxidized aluminum particles heated in an inert environment. This shift was assumed to be associated with melting of natural alumina. The shift occurred at temperatures varying from 2000 to 2200 K, implying that the alumina thickness was between 5 and 8 nm.

References

- [1] A. Ingenito, C. Bruno, Journal of Propulsion and Power, 20 (2004) 1056-1063.
- [2] M.W. Chase, J. Phys. Chem. Ref. Data, Monograph 9, (1998) 1-1951.
- [3] Q. Jiang, C.C. Yang, Current Nanoscience, 4 (2008) 179-200.
- [4] M.A. Trunov, S.M. Umbrajkar, M. Schoenitz, J.T. Mang, E.L. Dreizin, Journal of Physical Chemistry B, 110 (2006) 13094-13099.
- [5] J. Sun, M.L. Pantoya, S.L. Simon, Thermochimica Acta, 444 (2006) 117-127.
- [6] V.Y. Gertsman, Q.S.M. Kwok, Microscopy and Microanalysis, 11 (2005) 410-420.
- [7] F. Reichel, L.P.H. Jeurgens, G. Richter, E.J. Mittemeijer, J. Appl. Phys., 103 (2008) 093515/093511-093515/093510.
- [8] S.H. Huo, M. Qian, G.B. Schaffer, E. Crossin, Aluminium powder metallurgy, in, Woodhead Publishing Ltd., 2011, pp. 655-701.
- [9] M. Zhao, Q. Jiang, Solid State Communications, 130 (2004) 37-39.
- [10] R. Lizárraga, E. Holmström, S.C. Parker, C. Arrouvel, Physical Review B - Condensed Matter and Materials Physics, 83 (2011).

- [11] P. Lynch, H. Krier, N. Glumac, Journal of Thermophysics and Heat Transfer, 24 (2010) 301-308.
- [12] N. Glumac, H. Krier, T.I.M. Bazyn, R. Eyer, Combustion Science and Technology, 177 (2005) 485-511.
- [13] J. Kalman, D. Allen, N. Glumac, H. Krier, Journal of Thermophysics and Heat Transfer, Accepted for Publication (2014).
- [14] M. Mittal, Chem. Eng. World, 48 (2013) 38, 40, 42, 44, 46-47.
- [15] M. Soo, P. Julien, S. Goroshin, J.M. Bergthorson, D.L. Frost, Proc. Combust. Inst., 34 (2013) 2213-2220.
- [16] H. Kwon, M. Takamichi, A. Kawasaki, M. Leparoux, Mater. Chem. Phys., 138 (2013) 787-793.
- [17] T. Nagae, M. Yokota, M. Nose, S. Tomida, T. Kamiya, S. Saji, Nippon Kinzoku Gakkaishi, 65 (2001) 726-733.
- [18] J. Zaehr, S. Oswald, M. Tuerpe, H.J. Ullrich, U. Fuessel, Aluminium (Hannover, Ger.), (2011) 57-59.

CHAPTER 13: MICRO-ALUMINA PARTICLE VOLATILIZATION TEMPERATURE MEASUREMENTS IN A HETEROGENEOUS SHOCK TUBE

1. Introduction

The peak combustion temperature joins heat release rate rate among the most important performance metrics in energetic metals, often used as fuels in solid rocket motors and enhanced blast weapons. High combustion temperatures result in higher thrust in solid rocket motors. Additionally, in advanced thermobaric weapons, peak combustion temperatures are important (along with duration), for instance, in agent defeat. Aluminum is one of the most prevalently used energetic additives. Often in aluminum based reactions, spectra of the gas phase reaction intermediate AlO are measured [1], and the B-X $\Delta v = -1$ band sequence [2, 3] (505-525 nm) can be fit to a temperature, which is thought to closely mirror the peak temperature in the gas phase.

While the product of aluminum with oxygen containing oxidizers, alumina (Al_2O_3), does not have a stable gas phase, there is a temperature above which the alumina vaporizes and quickly volatilizes. According to Glassman [4], peak flame temperatures in aluminum combustion should approach this volatilization temperature of Al_2O_3 , and the first studies of large Al particles place the combustion temperatures at 3800 K and higher. Several other studies measure peak AlO temperatures consistently near 3200-3250 K in micro-Al combustion [5, 6, 7, 8] both from fitting AlO and by other means. In the studies of Bazyn, higher temperatures were measured by fitting AlO spectra emitted from the flame zones near larger particles (20 μm and larger) [9] as well as from the flame zones of aluminum particles ignited with the assistance of a Al/MoO_3 thermite reaction [10].

While these similar temperature measurements of 3200 -3250 K may be coincidence, the measurements, from different experimental ambient conditions (temperature, pressure, oxidizer concentration, and ignition method), and fit with different codes open the possibility that there may be a limiting process on the temperature for the smaller particle sizes. Schloffel et al. [5] suggest that the limiting process may be the volatilization temperature of alumina. Further confounding this issue is that there is significant ambiguity in the volatilization temperature in trusted references. The CRC tables [11] assign the temperature at which Al_2O_3 vapor pressure reaches 1 bar (an ill defined concept for Al_2O_3 , but acceptable for the other species reported in that Table) is 3248 K. On the other hand, the JANNAF tables [12] maintain that liquid alumina is present until 4000 K. Glassman uses 4000 K as well [4].

This difference in the literature can be traced back to the first studies of the alumina volatilization temperature at 1 atm. Both studies were extrapolations from measurements of the partial pressure of vapor species above the liquid phase at lower temperatures, i.e. effusion studies. The early measurements of Roff and Konschak [13] in 1926 likely had higher than reported uncertainty in the temperatures due to the pyrometric measurements made. The temperature reported from the Wanner pyrometer they were using at the time would likely have been outside of the range of calibration. It is unclear if there was a secondary calibration available to extend the usefulness of this instrument to higher temperatures. These measurements were cited in the review of Stull [14] and were later incorporated in the CRC tables. A later study in 1951 by Brewer and Searcy [15], which notably cited the Roff and Konschak work, obtained a boiling temperature of 3770 ± 200 K. This study was cited early by Grosse and Conway [16] and later was incorporated into the JANNAF references.

Alumina volatilization is not the only mechanism that can suppress the peak combustion temperature, but it is an interesting candidate because of this ambiguity in the literature. As the particle size decreases, the reaction rate clearly does not stay constant at the diffusion limited burning rate, as can be noted from burn time data [6, 17], but the heat loss from the particle

increases with increasing surface to volume ratio (decreasing diameter), and the well defined flame front approaches more of a volumetric reaction zone in the transition regime. Still, these processes seem like they should be continuous processes without a discrete limiting temperature around 3200-3250 K.

The highly controlled environment of the heterogeneous shock tube allows measurements of heated alumina particles in which the volatilization temperature of alumina can be measured without the need for extensive extrapolation from very low temperatures and pressures. Clouds of alumina particles at temperatures below the volatilization temperature should extinguish laser light. At temperatures beyond the alumina volatilization temperature, the transmitted light fraction should reach nearly unity within the test time of the shock tube. This temperature at which alumina particles transition from extinguishing to not extinguishing light in the test time was measured to infer the volatilization temperature.

2. Experimental Methods

The heterogeneous shock tube facility at the University of Illinois generates a high temperature, high pressure controlled environment ideal for making measurements in combustion conditions. The driven section (the test section) is 8 m long and 8.9 cm internal diameter. Other relevant dimensions and descriptions of this facility can be found in previous publications [18, 9]. Through the pressure ratio of the driver and driven sections, a strength selectable shock is sent through the driven section. As the shock wave reflects off the endwall, it produces a high temperature, high pressure, controlled combustion environment for approximately 2 ms. Various compositions of test gases can be used. Temperatures exceeding 4000 K and pressures up to 30 atm are achievable. Particles are injected upstream prior to the rupture of the diaphragms initiating the event and move towards the wall, are stagnated, and are heated under the influence of the gas behind the incident and reflected shocks.

Figure 1 shows the experimental setup and diagnostics used in experiments testing the volatilization temperature. Approximately 0.1 mg of particles were injected into the shock tube from a port either 0.38 or 0.78 m from the endwall approximately 1 s before the rupture of the double diaphragm section. Light from an 80 mW CW frequency doubled Nd:YAG laser (532 nm) was passed through the sapphire windows of the shock tube as shown in Figure 1. The initial pass of the laser occurred 6.3 cm from the endwall. The laser light was reflected back through the test section 5 cm from the endwall. This location was selected based upon particle trajectory modeling and from previous high speed imaging of the event. The laser light was then reflected approximately 2 m away and focused through a 532 nm bandpass filter onto a Thorlabs PDA36A photodiode. The combination of the long distance from the mirror as well as the focusing of the lens ensured that the solid angle collected by the photodiode was very small. Indeed the combination of the small solid angle and the 532 nm bandpass filter was almost always sufficient for the 80 mW laser to dominate any broadband emission from the solid particles at these wavelengths. The 532 nm laser also comes in between the $\Delta v = -1$ and $\Delta v = -2$ AlO B-X bands, so any molecular interference is negligible.

A cloud of suspended particles is needed in order to properly account for particle motion during the event and ensure that the diagnostics are properly focused. Two different size distributions of alumina were studied. Both were purchased from Alfa Aesar and have purities greater than 99.5%. The first size distribution, micro-alumina, had particles in the 0.9-2.2 μm range. The second powder, nano-alumina, had a size distribution between 40-50 nm and specific surface area between 32-40 m^2/g . Further characterization of the particles as well as the injector are available in a recent publication [19].

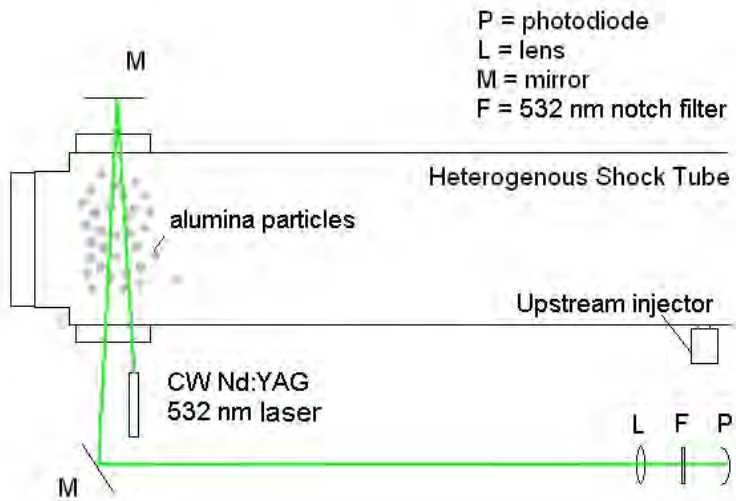


Figure 1: Schematic of Heterogeneous Shock Tube and diagnostics when making volatilization measurements.

Figure 2 shows traces from the sidewall time of arrival sensors and endwall pressure transducer during a typical experiment. Reflected shock conditions were calculated from the incident shock velocity and initial pressure and temperature. Over the experimental range studied, the incident shock velocity attenuated approximately 1.3 %/m near the endwall. Due to the very high temperature conditions not ordinarily studied in this shock tube, viscous effects were corrected for using the model of Petersen and Hanson[20]. Because of the 5 cm distance from endwall in which the reflected shock wave is entering a progressively higher pressure incident shock region, the reflected shock temperatures calculated with this attenuated shock velocity using GASEQ [21] were slightly increased by about 20 K. Changes to the reflected shock pressure were less than 0.1 atm.

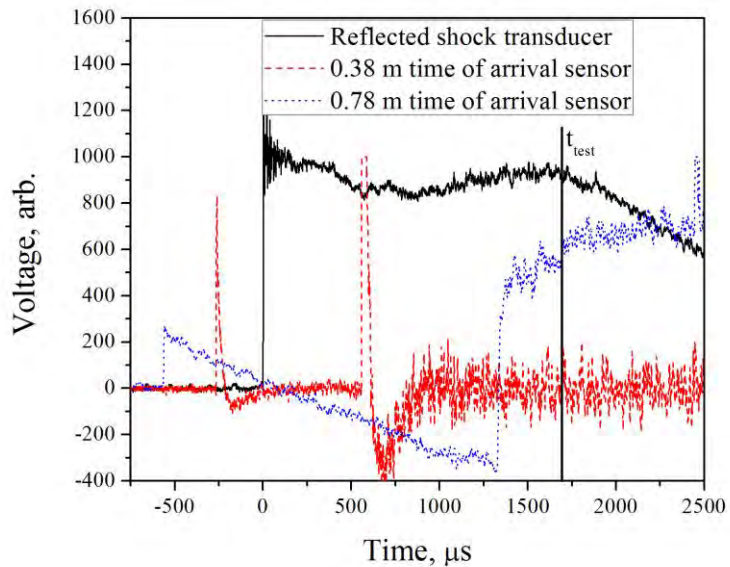


Figure 2: Pressure transducer traces of shock tube event. In this case, the reflected shock

temperature was calculated to be 3886 K and the reflected shock pressure 9.7 atm. The estimated test time of 1.7 ms agrees with the drop off of the reflected shock pressure.

In these experiments, the test time was estimated from the time between the incident shock reflection and its second reflection off the wall once it reflects off of the contact surface. The actual process must also involve weak refractions during this second approach to the endwall, because in all cases the measured endwall pressure decreases after a relatively constant period which corresponds nicely with the estimated test time. Times estimated in this way ranged from 2.2 ms at 2800 K to 1.3 ms at 4800 K. The test time at 5 cm was also decreased about 0.2 ms to account for the distance the shock traveled to the endwall.

Nano alumina particles were tested in 100% Ar, both 3 and 10 atm reflected shock pressure, and reflected shock temperatures starting at about 2800 K and increasing to 5000 K. The reflected shock temperatures were incremented until the photodiode signal showed little extinction within the shock tube test time and slightly beyond. This cutoff, as well as modeling of the evaporation rates of the particles, was used to determine a volatilization temperature at the reflected shock pressure. Additionally, micro-alumina particles were tested at 10 atm. These larger particles did not volatilize appreciably within the shock tube test times until temperatures higher than the volatilization temperature. However, the volatilization rates were predicted from the numerical scheme for evaporation and fit to a volatilization temperature lower than the test ambient temperature.

2.1. Processing

Two criteria were used to determine when a cloud of nano-alumina particles had significantly volatilized and was no longer extinguishing laser light. The first was that the transmitted light intensity, which always dropped somewhat shortly after the meeting of the reflected shock with the cloud, had to recover to 95% transmissivity within the test time (temperature dependent, but about 1.5 ms at 3900 K). At high pressures, this recovery often occurred rapidly, sometimes within 200 μ s. However, at lower pressures, this recovery required more time. The second criterion was that once the shock tube test time was reached, the average transmissivity beyond the test time was required to be within 5% of 100%. This criterion was to ensure that the cloud of particles had volatilized and not simply moved out of the test volume. The reflected shock, which reflects again off of the contact discontinuity in the shock tube, would sometimes bring the particles back into collection volume and the transmitted light intensity would subsequently drop. If the signal passed both of these criteria, it was assumed that there was limited extinction and the particles had volatilized substantially within the test time. These criteria, while not the only criteria that could be applied, were deemed satisfactory as they produced sharp cutoffs in extinction with temperature for both the low pressure and high pressure data.

This defined sharp cutoff, however, is not the volatilization temperature of the alumina. Because of the exponential nature of the vapor pressure with temperature, there can be significant evaporation of the particle at temperatures below the volatilization temperature. With such small particles, the alumina can evaporate and then dissociate within the test time at temperatures hundreds of degrees below the volatilization temperature. This particle evaporation was modeled, allowing for the calculation of a volatilization temperature for the different pressures.

2.2. Volatilization Model

The model for evaporation assumes that at each ambient temperature below the volatilization temperature, there is a rate of evaporation and dissociation of the alumina. The numerical scheme calculates this rate, which changes as the particle temperature and diameter change, and determines if, for an assumed volatilization temperature, it would be possible for a particle to evaporate during the shock tube test time. The volatilization temperature is then iterated to achieve the temperature for which particles subjected to a lower experimental ambient temperature would not evaporate.

Also, an assumption is made that there is a finite volume in which the products dissociated from alumina particles can build up into. This assumption comes from the finite spacing that the particles have, which was estimated by imaging using an acrylic section on the shock tube. Measurements of the fraction of the 0.1 ± 0.05 mg of particles injected which are actually entrained in the narrow cloud which passes the lasers (based on the ratio of the total intensity from this region to the total intensity everywhere in the tube) reveal this number to only be approximately $32 \pm 6\%$. Further, using this high speed imaging of the shock tube event, the extent of this narrow cloud of particles was measured to be 3.5 ± 0.8 cm. These observations led to an estimate of the average spacing between particles of 84 ± 28 diameters.

This spacing effectively limits the volume into which the products can diffuse and causes the buildup of dissociated products in this volume. This buildup increases the concentration of these products which slows the rate of evaporation, which is limited by the concentration gradient. As equilibrium is reached, the particle ceases to evaporate. Because there is not a stable Al_2O_3 gas phase species, the alumina was assumed to have broken down into components calculated with the Gordon McBride equilibrium solver [22] (more than 90% of which was Al, AlO , and O). These products were averaged into a single species, subscripted A, which diffused into the volume between particles.

The rate of evaporation, \dot{m} , is driven by the difference in mass fraction of the species A between the surface $y_{A,s}$ and the environment, $y_{A,amb}$:

$$\dot{m}'' = \rho D \frac{d}{2} \ln \left(1 + \frac{y_{A,amb}(t) - y_{A,s}}{y_{A,s} - 1} \right) \quad (1)$$

Where d is the particle diameter, D is the mass diffusivity of the averaged species A into the bulk gas, and ρ is the gas density. Equation (1) is the quasi-steady state, spherically symmetric mass conservation equation for high mass transfer rates. This approach assumes that the droplet is a single species, in this case species A, and the gas is a single species (almost entirely Ar) and negligibly soluble in the droplet [23]. These assumptions are reasonable for Al_2O_3 volatilization in an Ar bath gas. D was estimated using the methods described in Law's text [24], accounting for ambient temperature, pressure, and species concentration. D was calculated to be $2.08 \text{ cm}^2 \text{ s}^{-1}$ for the 10 atm studies. For

the 3 atm studies, this number increased to $7.4 \text{ cm}^2 \text{s}^{-1}$, not just because of the difference in the pressure and temperature, but also because of the slight difference in mole fractions of the dissociating species. D does not have to be recalculated with different time steps since it is dependent on the pressure and the ambient temperature, both of which do not change. The buildup of species dissociated from the particle controls the mass fraction in the environment as described above. The surface mass fraction is assumed to be equal to the vapor pressure at the particle temperature:

$$y_{A,s} = \frac{P_A M_{Al2O3}}{P M_{ave}} \quad (2)$$

where P is the ambient pressure, M_{Al2O3} is the alumina molecular weight, and M_{ave} is the average molecular weight of the environment, mostly Ar, but it does change slightly. The vapor pressure of species A is assumed to follow the Clapeyron equation with the parameters of the reactant species, $Al2O3$:

$$P_A = P \exp \left(-\frac{\Delta H_v}{R_u} \left(\frac{1}{T_p} - \frac{1}{T_{vol}} \right) \right) \quad (3)$$

where P is the pressure tested, either 3 or 10 atm, and ΔH_v is 1860 kJ/mol [4]. ΔH_v is temperature dependent. However, this temperature dependence was ignored because there would be significant uncertainty associated with fitting this value along with the volatilization temperature. Additionally, the reference value for the heat of volatilization is as uncertain as the volatilization temperature itself, so 1860 kJ/mol was assumed an acceptable value across the temperatures studied. T_{vol} is the volatilization temperature, which is iterated in the calculation.

The ambient mass fraction of the volatilizing species $y_{A,amb}$, increases as the mass of species A in the environment, $m_{A,amb}$, increases. The mass of the remaining particle m_p , decreases by this same amount.

$$m_p(t) = m_p(0) - m_{A,amb} \quad (4)$$

The numerical model accounts for three modes of heat transfer for the particle, convection/conduction (with corrections for non-continuum effects) from the ambient gas, radiation to the wall, and the vaporization of the particle.

Several initial diameters are chosen to probe the diameter effect, namely 50 nm, 500 nm, 2 μm , and 3 μm . The 50 nm particle size was chosen as representative of the nano-alumina particles. Similarly, the 2 μm particles were representative of the micro-alumina particles. While the injection strategy and the passage of the normal shocks should break up most agglomerates, any agglomeration present would increase the average particle size. At 2 μm , the agglomeration of a few particles would greatly increase the evaporation time. The particle heat up time is approximately 5 μs for the 50 nm particles and approximately 30 μs for the 2 μm particles. This heat up time is small relative to either the shock tube test time or the evaporation time of any particle tested. Although particle motion (i.e. stopping of the particles in the stagnant gas behind the reflected shock) is neglected, the particle heat up times are still very representative of the actual heat up time after the passage of the reflected shock.

This model was implemented in an explicit forward-difference time marching scheme with

the volatilization temperature as the iterant until either the diameter reached 2.5 nm or the test time was exhausted. 2.5 nm was chosen for the minimum diameter in all cases as it represented a 95% reduction of the diameter of the smallest particle size simulated. If the particle size reached $d = 2.5$ nm before the test time, then the volatilization temperature was too low relative to the ambient temperature and a higher input volatilization was the next iterant. The particulars concerning the implementation of the numerical scheme are detailed in Appendix B of [25].

Figure 3 shows the predicted decrease in the diameter of a 50 nm particle as it evaporates, for four different iterations of the volatilization temperature in a 3850 K, 10 atm ambient. For example, if the first temperature selected, (the first iterant) was a volatilization temperature of 4180 K, the evaporation rate would be too rapid and the particle would evaporate within 300 μ s. For a guess of 4260 K, the particle would evaporate within 500 μ s. As the volatilization temperature guess eventually reaches 4315 K, the evaporation rate would be insufficient to evaporate the particle within the test time; however, it would be extremely close to being completely volatilized within a few hundred microseconds. Only at even higher iterant temperatures (in this case 4335 K), would particles stop volatilizing within the test time. If the volatilization temperature were this temperature, particles subjected to the ambient temperature at the cutoff would still be present after the test time. At ambient temperatures below the cutoff, particles would continue to be present during the test time, but at temperatures just beyond the cutoff, they would evaporate within the test time. Interestingly, near the cutoff temperature, the evaporation profile with time quickly becomes more shallow with relatively small changes in temperature. This profile indicates that the actual choice of volatilization temperature in this regime between which particles stop evaporating within the test time and disappear within the test time is not particularly ambiguous, as this region of temperatures is as narrow as 25 K. Experimental uncertainty and uncertainty in the numerical scheme will certainly be higher than the uncertainty in this choice of volatilization temperature.

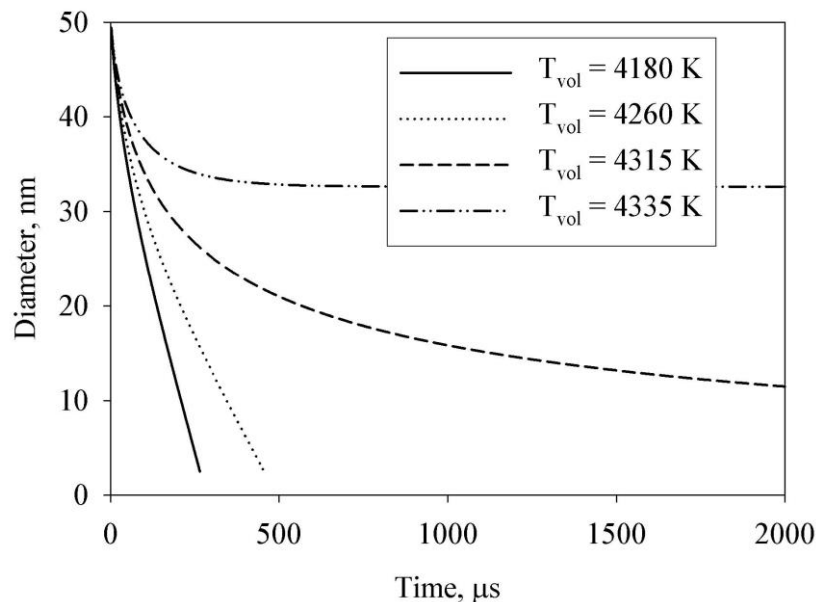


Figure 3: Predictions of the evaporation of particles for different input volatilization temperature for an ambient temperature near 3850 K. The ambient pressure is 10 atm.

Figure 4 shows the calculated evaporation time of four different particle sizes with temperature for 10 atm ambient pressure. The evaporation time was defined as the time required

for the particle to reach 2.5 nm. Approximately 450 K below the volatilization temperature at 10 atm, there was very little evaporation even for the smallest particles. The nano particles were able to evaporate well within the shock tube test time for temperatures 300 K below the volatilization temperature and even faster for higher temperatures. Predictably, the micro-particle evaporation times were longer, and, for instance, for the 3 μm particles, typically required ambient temperatures beyond the volatilization temperature in order to evaporate during the test time. The 2 μm particles would evaporate faster, but still required times comparable to the test time 100 K below the volatilization temperature.

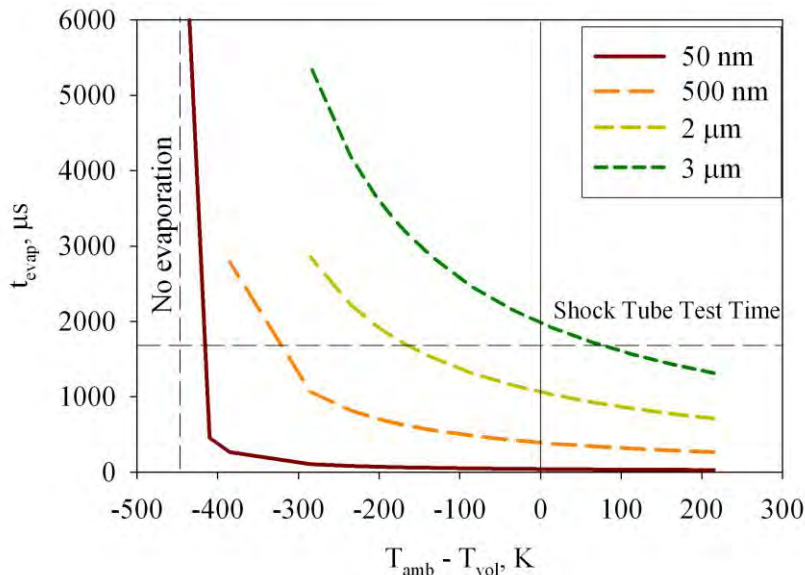


Figure 4: The evaporation time of four particle sizes vs. the temperature difference from the volatilization temperature at 10 atm. The temperature at which particles would not significantly volatilize during the shock tube test time was measured to calculate the volatilization temperature.

Results and Discussion

3.1. 10 atm volatilization experiments

Experiments conducted in 100 % Ar at 10 atm with alumina nano-particles showed a high degree of repeatability. The transmitted light intensity for similar temperatures was very similar in duration and peak extinction levels. Figure 5 shows photodiode traces through nano-alumina clouds at 10 atm for various temperatures tested. In almost all cases, there were two brief deviations (approximately 5 μs in duration) from the background signal around $t = 0$. These deviations, most often a drop in intensity, but sometimes a slight increase in intensity, were attributed to the schlieren effect from the large density gradients in the incident and reflected shocks as they pass the laser beams [26]. After $t = 0$, the reflected shock, as it passes through, stagnates the test gas. The stagnant test gas decelerates most particles, which drift into the test section, heat up, and volatilize.

The photodiode data are by no means monotonic. The fluctuations in transmitted light intensity are real and cannot be attributed either to photodiode noise or instability in the laser. Before the passage of the reflected shock, the noise level is small and the intensity is relatively flat, and the photodiode was calibrated to be linear. After the passage of the reflected shock, variations in the transmitted light intensity can be attributed to the turbulent nature of the particles within the cloud, the rich flow structure of the cloud observed in the shock tube, as well as

some beam steering. The high speed imaging in the acrylic test section show that even though the bulk gas has stagnated after the passage of the reflected shock, there is still significant particle movement. Particles move in and out of the test volume of the two passes of the laser beam. In all cases, the bulk of the cloud is very near the center of the two passes of the laser beam.

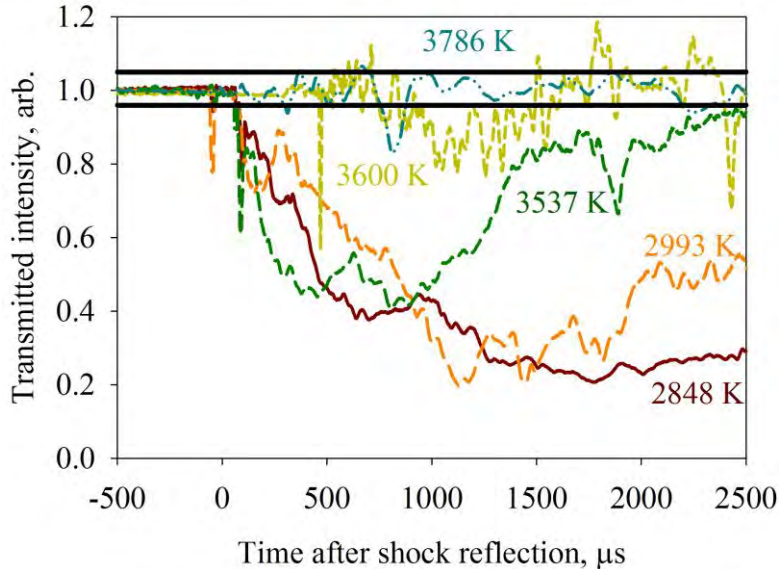


Figure 5: The transmitted light intensity through clouds of nano-alumina particles at example ambient temperatures in which there was significant extinction for 10 atm pressure.

Figure 5 also shows some of the predicted trends of the experiments. At low temperatures, for example the lowest temperature shown here of 2848 K, the transmitted intensity dropped sharply to transmissivities on the order of 0.2, and did not recover within the test time. However, as temperature increased, for example to around 3600 K, not only did the peak drop in transmitted intensity decrease (i.e. the minimum transmitted light intensity was closer to 1), the recovery in intensity began during the test time. Eventually, as temperature was increased around 3800 K, reduction in transmitted intensity was small and the transmissivity appeared to recover within the test time. Here it was more difficult to assign qualitatively if there was extinction within the test time or not. However, often there were secondary drops in transmitted light intensity just beyond the shock tube test time. These intensity reductions were likely particles which were entrained in the test section by the reflected shock after it had again reflected off of the contact discontinuity. The second extinction criterion of limited deviations in average transmissivity outside of the test time was an important distinction and used to ensure that, when extinction of the cloud was no longer observed, it was because the particles were volatilizing and not simply moving out of the test volume.

Figure 6 shows examples of the transmitted light intensity for clouds at higher temperatures. At temperatures beyond 3853 K, the transmitted light intensity was high and any peaks seen, particularly those right after shock reflection, returned to transmitted intensity approaching 1 within the test time, and indeed often within 200 μ s. While these photodiode traces qualitatively look similar to those at 3800 K, as in Fig. 5, the distinction often appeared if there was any extinction beyond the test time. The photodiode traces looked very similar for temperatures beyond 4500 K.

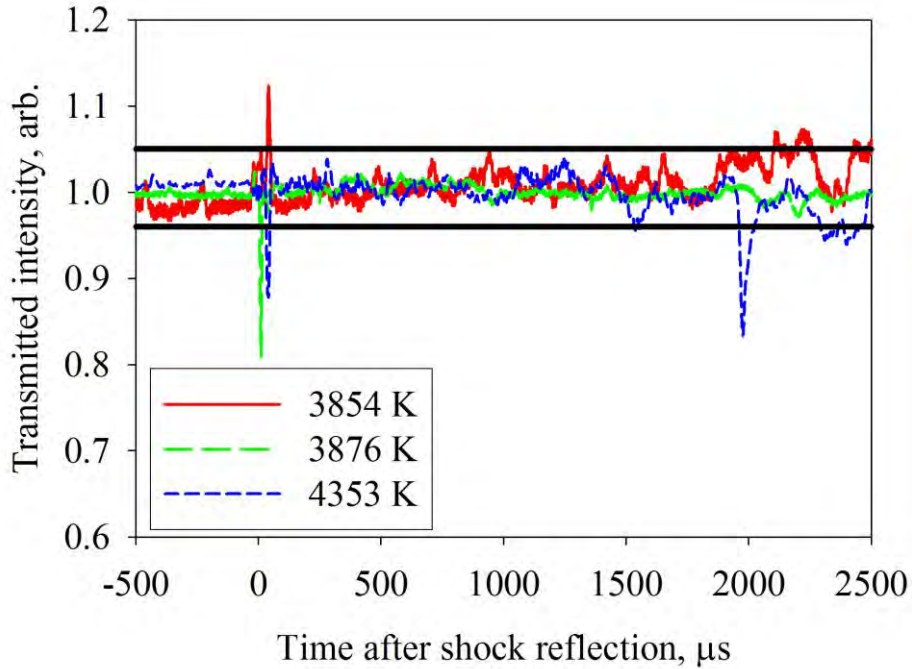


Figure 6: The transmitted light intensity through clouds of nano-alumina particles at example ambient temperatures in which there was not significant extinction for 10 atm pressure.

The quantitative extinction criteria were applied to all tests at the different temperatures and the results are shown in Table 1. The extinction criteria produced a sharp cutoff at 3860 K for 10 atm. This cutoff temperature was then inserted into the evaporation model as described in Sec. 2.2 in order to model the volatilization temperature. The volatilization temperature at 10 atm was calculated to be 4340 K.

The nearly 400 K difference between the experimentally observed cutoff temperature and the calculated volatilization temperature from the numerical model suggested tests were needed to confirm this large offset. According to the evaporation modeling, conditions which predict steeper trends for evaporation time with temperature include larger particle sizes and lower pressure. Therefore tests were also conducted in these conditions.

Classically, a strong pressure dependence on evaporation time is not predicted because the product of diffusivity and density is pressure independent. There is a very small effect of applied pressure on the vapor pressure [27], however despite the increased pressure to 10 atm from 1 atm, this effect would only account for a 0.03% difference in the vapor pressure, well within the uncertainty. The evaporation model, however, indirectly allows for pressure dependence because it allows the accumulation of volatilized species in the finite volume assumed by the modeling, which will have a different quantity of Ar initially present in the same volume with different pressures, leading to different ambient mass fractions with pressure. The finite volume into which alumina can freely evaporate and diffuse is calculated from measurements of the average particle spacing relative to the average size. This average spacing was calculated to be 84 particle diameters. This spacing may be weakly pressure dependent as the entrainment of particles into the free stream (one of the measured quantities in this calculation) is not solely dominated by the settling time of particles but also weakly on the test gas initial pressure, and other pressure effects. All those measurements were conducted in 6 atm pressure, intermediate to the 3 atm and

10 atm conditions simulated. This limited volume causes the buildup of dissociated products to slow the rate of evaporation due to the concentration gradient between the surface and the environment. As equilibrium is reached, the particle ceases to evaporate. At lower pressure, the mass fraction in the environment can more quickly equilibrate with the mass fraction at the surface. Thus at each temperature, for lower pressure, the evaporation rate is lower, and temperatures closer to the volatilization temperature are needed to completely evaporate a particle in the test time.

Table 1: The extinction of the light through the particle cloud at different ambient temperatures at 10 atm. The extinction criteria produced a sharp cutoff at 3860 K for 10 atm pressure. This cutoff was then modeled to be the result of a volatilization temperature of 4340 K at 10 atm.

Temperature, K	Extinguishing laser light after test time
2848	Yes
2993	Yes
3324	Yes
3479	Yes
3599	Yes
3786	Yes
3848	Yes
3876	No
3980	No
4274	No
4353	No

Table 1

Figure 7 shows selected photodiode traces of the transmitted light intensity through clouds of 2 μm micro-alumina particles at various temperatures for reflected shock pressures near 10 atm. As expected, significant extinction during the test time was present at temperatures 3815 K and higher. The data were noisier than for the nano-alumina particles. This higher noise level was attributed to two factors. First the size distribution of the micro-alumina particles undoubtedly lent itself to some larger particles. Because of the strong diameter dependence on particle evaporation time, for the nano-particles, evaporation time differences between 40 nm and 60 nm particles are relatively small compared to the difference between 1 μm and 3 μm particles. Any agglomerates that are present, even after the passage of two shocks, will therefore have an even greater effect. Additionally, since the mass inserted into the injector was the same for nano-alumina and micro-alumina particles, the number of particles in the free stream was smaller by several orders of magnitude. Smaller numbers of particles should enhance variability of the particle clouds, by making the environment even less uniform.

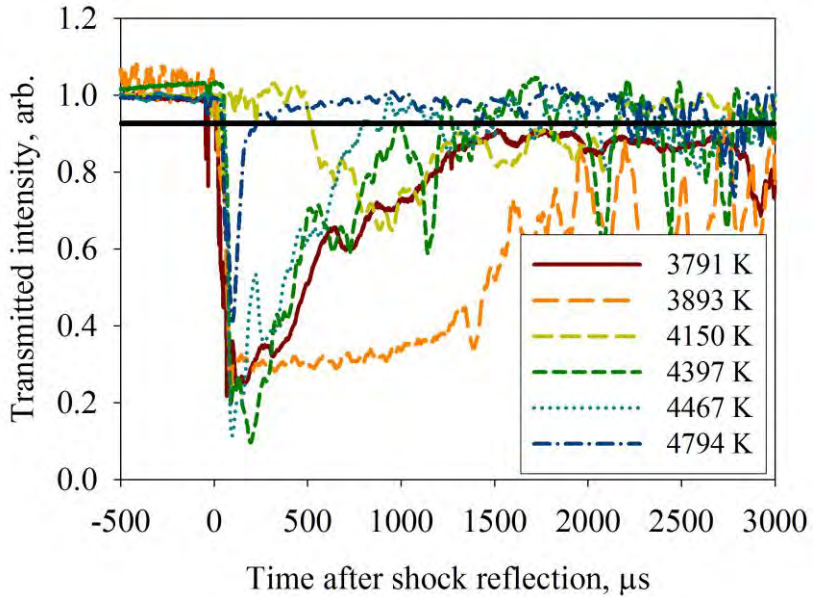


Figure 7: The transmitted light intensity through clouds of micro-alumina particles at example ambient temperatures for 10 atm pressure.

Because temperatures tested were above the volatilization temperature so that they may properly evaporate within the shock tube test time, the evaporation time was fit to the curve predicted by the evaporation code for micro sized particles at the volatilization temperature calculated with the nano-alumina particles. Because of the increased noise level, the evaporation time was relaxed to be the first time in which the transmitted light intensity recovered to 95 % and the average transmitted intensity beyond that point had to be above 90 %.

Figure 8 is the plot of these evaporation times versus temperature at 10 atm reflected shock pressure. There is some variability at similar temperatures, but, in general, the data fit reasonably well to 2 μm particles with a volatilization temperature of 4340 K, that which was calculated from the nano-alumina data. Because of the significant uncertainty in the particle distribution, there was no attempt to fit the volatilization temperature and particle size simultaneously, however, as the measurements of the particle size suggest, the surface area average of the particle size is likely larger than 2 μm , which would suggest that the volatilization temperature of 4340 K could be slightly high on the order of 100 K but not significantly higher. However, this small difference is likely within the uncertainty already present in the 4340 K calculation.

3.2. 3 atm volatilization experiments

Experiments at lower pressures were required because they resulted in smaller offsets between the volatilization temperature and the observed temperature at which particles stop extinguishing light within the test time. The 3 atm nanoalumina transmitted intensity photodiode traces were by far the noisiest that were collected. The reason for this is unclear, however it has been observed that at very high temperatures and particularly as pressure decreases, the dynamics behind the reflected shock are less ideal, particularly due to increased thickness of the turbulent boundary layer at lower pressure [20]. This could affect the clouds of particles at low pressures. Figure 9 shows example transmissivity traces for several temperatures at 3 atm. The 3 atm data did not follow clear qualitative trends like were seen in the 10 atm data for both the nano-alumina and

micro-alumina data. The peak drop in transmitted light intensity changed unpredictably, and the time at which the peak drop happened was not always consistent. Often there were sharp drops in transmissivity which slowly recovered, not always within the test time, like those seen in the micro-alumina data, for instance like at 3831 K. There were however, also experiments that showed a modest, late drop in transmissivity which never recovered. This phenomenon was exhibited, for instance in the 3164 K data. Even at higher temperatures, like in the photodiode traces seen in Fig. 10, it was difficult to qualitatively assign an extinction cutoff.

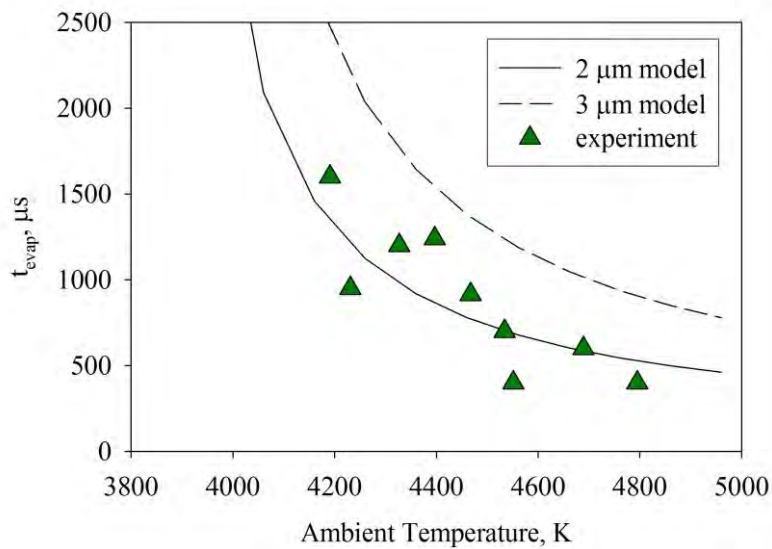


Figure 8: A fit of the evaporation time of micro-alumina particles at 10 atm for different ambient temperatures. The data fit reasonably well to a 4340 K volatilization temperature and a 2 μm particle size.

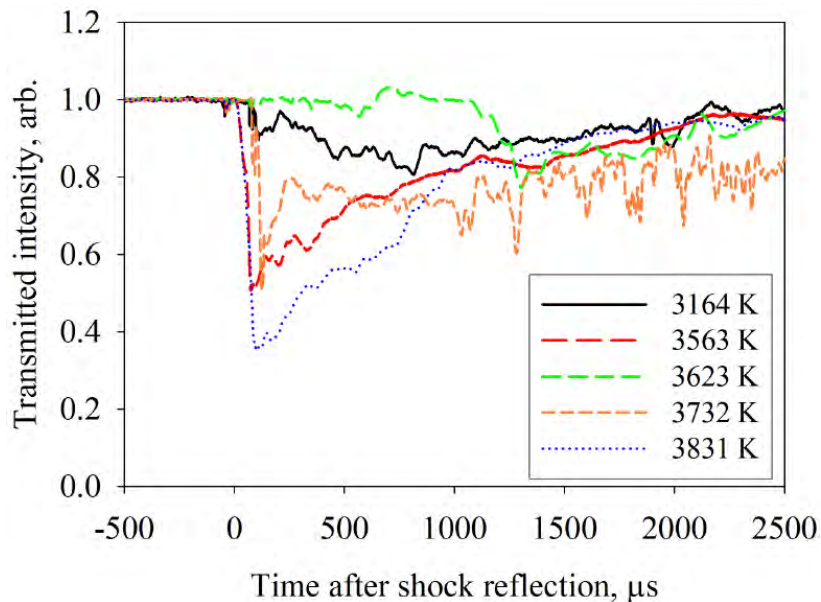


Figure 9: Example transmitted light intensity through clouds of nano-alumina particles at ambient temperatures below 4050 K and at 3 atm pressure. These clouds extinguish laser light after the shock tube test time.

Table 2: The extinction of the light through the particle cloud at different ambient temperatures at 3 atm. The extinction criteria produced a sharp cutoff at 4050 K for 3 atm pressure. This cutoff was then modeled to be the result of a volatilization temperature of 4260 K at 3 atm.

Temperature, K	Extinguishing laser light after test time
3164	Yes
3482	Yes
3563	Yes
3623	Yes
3736	Yes
3787	Yes
3831	Yes
3991	Yes
4118	No
4138	No
4160	No
4177	No
4250	No
4503	No
4551	No

However, using the quantitative criteria, the results of which are shown in Table 2, an extinction cutoff was assigned for the 3 atm data, which was 4050 K. The photodiode signals for which the nano-alumina particles volatilized within the test time are shown in Fig. 10. When the evaporation model was used in order to assign a volatilization temperature to this extinction cutoff, the temperature at 3 atm was 4260 K. Again, while the extinction cutoff temperature was almost 200 K higher than at 10 atm, because of the comparative steepness of the evaporation curve, the volatilization temperature at 3 atm was lower than at 10 atm, as expected.

3.3. Error analysis of evaporation model

Even though intuitive trends result from the calculation of the volatilization temperature, and fits of larger particles to the model's evaporation rates seem reasonable, there is still significant uncertainty associated with the volatilization temperature at these two pressures, and it must be accounted for if those points are to be used to extrapolate a volatilization temperature at 1 atm. A detailed error analysis was conducted on four possible sources of error.

The first source was an uncertainty in ambient temperature at which the particles stopped volatilizing within the test time. While it is clear that there was some arbitrariness in the criteria that were chosen to implement the cutoff in extinction as defined previously, it was consistent, repeatable and produced a sharp well defined cutoff, especially for the 10 atm data. Even so, there were three sources of uncertainty in the ambient temperature calculation.

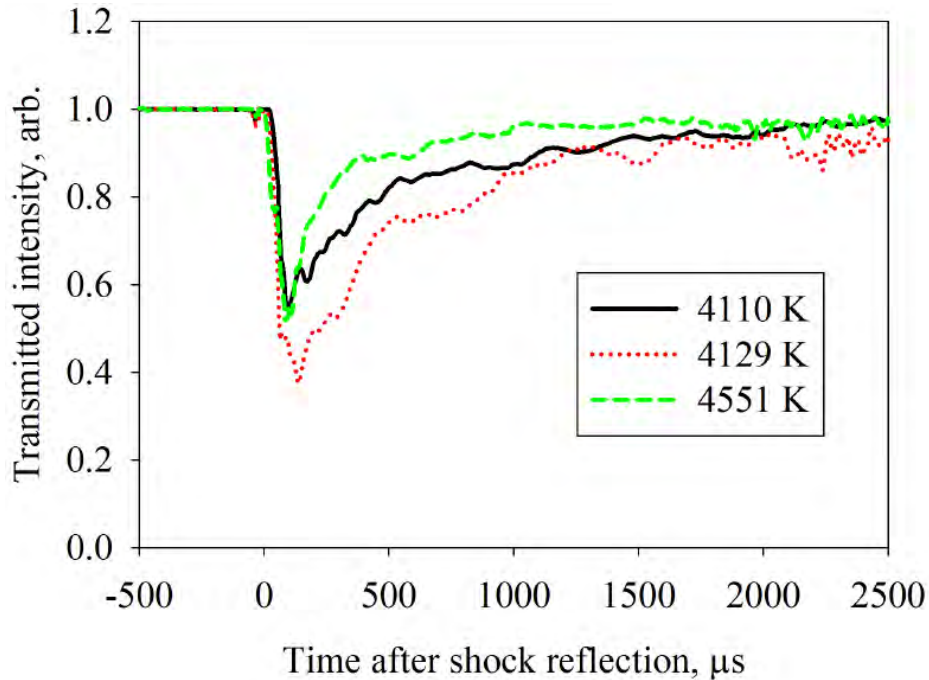


Figure 10: Example transmitted light intensity through clouds of nano-alumina particles at ambient temperatures above 4050 K and at 3 atm pressure. These clouds do not extinguish laser light after the shock tube test time.

The first source was the uncertainty from calculation of the reflected shock conditions from measurement of the incident shock velocity. This uncertainty is as low as 1% of the reflected shock temperature, or about 40 K. The second was the uncertainty in the adjustment of the reflected shock temperature at a distance of 5 cm. This was taken as the full value of the adjustment, or 20 K. The third uncertainty comes from the effect of temperature rise in the entire reflected shock region with time. This was estimated using Petersen and Hanson's method [20]. Using the endwall pressure transducer traces as well as the photodiode extinction traces, a characteristic time in which to run this calculation was 0.5 ms after shock reflection. Using this characteristic time, temperature dependent temperature rises in the reflected shock region of approximately 75 K were obtained. Adding these three sources in quadrature, the uncertainty in ambient temperature was taken to be 87 K.

The next source of error is the measurement of the spacing of the particles which defines the region into which products can volatilize. Based on a large number of imaging studies performed with the acrylic test section, this spacing was calculated to be about 84 particle diameters. Statistical uncertainty in this calculation was 33% from the propagation of one standard deviation in the quantities entering into the calculation, i.e. mass injected, percentage of the total intensity in the cloud, and the cloud extent. However, if the model is sensitive to spacing much larger than 33% higher, it could be observed in the fixed mass fraction error analysis which follows. Upon the onset of the error analysis, it was thought that this assumption and number, upon which the evaporation model depends, would very strongly affect the evaporation/volatilization rate. The sensitivity is quite low though. Furthermore, the measurement error appears much smaller than the statistical uncertainty. The extent of the cloud is clearly observable by imaging with the acrylic section and uncertainties in the mass of particles in the cloud are raised to the 1/3 power.

Mass diffusivity directly enters into the volatilization rate in Eq. (1) and could be a source of error as the calculation for each species is only known approximately. Additionally, it is unclear if the assumption that the vapor phase alumina decomposes (to its equilibrium concentration no less) immediately upon vaporization and diffuses away is valid. It is true that there is no stable gas phase of Al₂O₃, but the exact composition of the gas which diffuses from the particle is unknown. To test this effect, the calculated mass diffusivity was increased and decreased by 25%.

Finally, as a check of the assumption that the buildup of products of the dissociation of alumina in the environment eventually stop the particle from evaporating further, different fixed environment mass fractions were assumed. This test also serves as a test of the assumption of the uniform distribution. Fixing the mass fraction of the environment also affects the gradient of the mass fraction, which truly controls the evaporation rate. The fastest particle evaporation would occur if the mass fraction of dissociated species remained zero throughout. This mass fraction represents the extremely unlikely event that the particle spacing was severely under predicted (unlikely as described above, but possible). In the second test, the mass fraction of the environment was fixed at the value at which one half of the mass (or 1/8 of the diameter) had evaporated. This fixed mass fraction in the environment initially slows the evaporation of the particle and is representative of what would happen if gradient of the mass fraction was overpredicted and the vaporization and especially diffusion away into a uniform distribution was slower. The third fixed mass fraction was calculated to be the slowest the particles could volatilize with a uniform mass fraction, i.e. with a mass fraction equal to the value at which the entire mass of the particle had evaporated. This simulation represents a severe over-prediction of the mass fraction gradient.

These four modifications were applied to the numerical scheme, and the volatilization temperature was recalculated. Table 3 shows the error analysis for the conditions at 10 atm, the results were similar for the error analysis for the conditions at 3 atm. Uncertainty in the ambient temperature introduced an error of 3.5% for the 10 atm conditions and about another 3.5% comes from particle spacing calculation. On the other hand, surprisingly the mass diffusivity calculation did not strongly affect the volatilization temperature measurement. This result is likely because of the overall assumption that any volatilized species diffuse out in a uniform distribution around the particle. Any increase in the rate of the volatilization is balanced by quicker accumulation of product species slowing the rate.

For both the 10 atm and 3 atm data, when the ambient mass fraction was fixed to an intermediate value, the percent change in the recalculated volatilization temperature was small (always < 2%). However, when the ambient mass fraction was fixed at zero, very large volatilization temperatures (relative to the ambient particle temperature) were needed in order to prevent the particles from volatilizing within the test time. These values are unrealistic; however, they confirm that the volatilization temperature at its minimum, must be larger than the temperature at which particles stop extinguishing within the shock tube.

Overall, uncertainty was added in quadrature, resulting in 5% for both data points. Table 4 shows the summary of the data and error analysis.

Table 3: Error analysis for conditions of nano-particles in 10 atm. The temperature at which the particles ceased extinguishing laser light during the test time was $T_{amb} = 3860$ K, and nominally produces a volatilization temperature of 4340 K.

Error source	Error introduced	%	Vol. Temp., K	% change
<i>Ambient mass fraction, T_{amb}</i>				
3860 K	+87 K	+2%	4470	3.5 %
3860 K	-87 K	-2%	4225	3 %
<i>Particle spacing, S</i>				
84 diameters	+28 diameters	+33 %	4360	<1 %
84 diameters	-28 diameters	-33 %	4210	3.5 %
<i>Mass diffusivity, D</i>				
2.1 cm ² /s	+0.52 cm ² /s	+25 %	4340	<1 %
2.1 cm ² /s	-0.52 cm ² /s	-25 %	4340	<1 %
<i>Ambient mass fraction, $y_{A,amb}$</i>				
$y_{A,amb}$ variable	$y_{A,amb} = 0$	—	5050	16 %
$y_{A,amb}$ variable	$y_{A,amb} = 0.008$	—	4290	1 %
$y_{A,amb}$ variable	$y_{A,amb} = 0.017$	—	4290	1 %

Table 4: Results and uncertainty analysis.

Pressure, atm	Volatilization Temperature, K	Uncertainty, K
10	4340	217
3	4260	213

3.4. Extrapolation to 1 atm volatilization temperature

Three atm was the low pressure limit for the experiments. At 1 atm, for instance, the evaporation times would exceed the test time for the smallest particles for temperatures of interest. Additionally, as the data became noisier at low pressure conditions, this trend should render unusable data. Two data points as shown in Table 4 are available to extrapolate the volatilization temperature to 1 atm, though.

Using these two points and (3), a volatilization temperature of 4189 K at 1 atm was calculated as shown in Table 5. The heat of dissociation between these two points was 2313 kJ/mol. Additionally, a least squares fit can obtain the volatilization temperature at 1 atm using Eq. (3) if a heat of volatilization is assumed. Using the reference value of 1860 kJ/mol [4], this least squares fit was performed and yielded a temperature of 4163 K. This fit is plotted in Fig. 11. Both extrapolations carry uncertainties of at least 200 K. These values are high compared to the reference literature, but the data fall within the range of the uncertainty for the JANNAF reference numbers. The values are significantly larger than the value in the CRC tables [11] and also significantly larger than 3200 K. This result lends credence to the values in the JANNAF tables and strongly suggests that a lower alumina volatilization temperature is not the limiting temperature in AlO temperature measurements of burning aluminum micro-particles.

Table 5: Extrapolation of the volatilization results to 1 atm.

Calculation	Vol. Temp., K	Uncertainty, K	Heat of diss., kJ/mol
Best est.	4189	200	2313
Using ref. ΔH_v	4163	200	1860

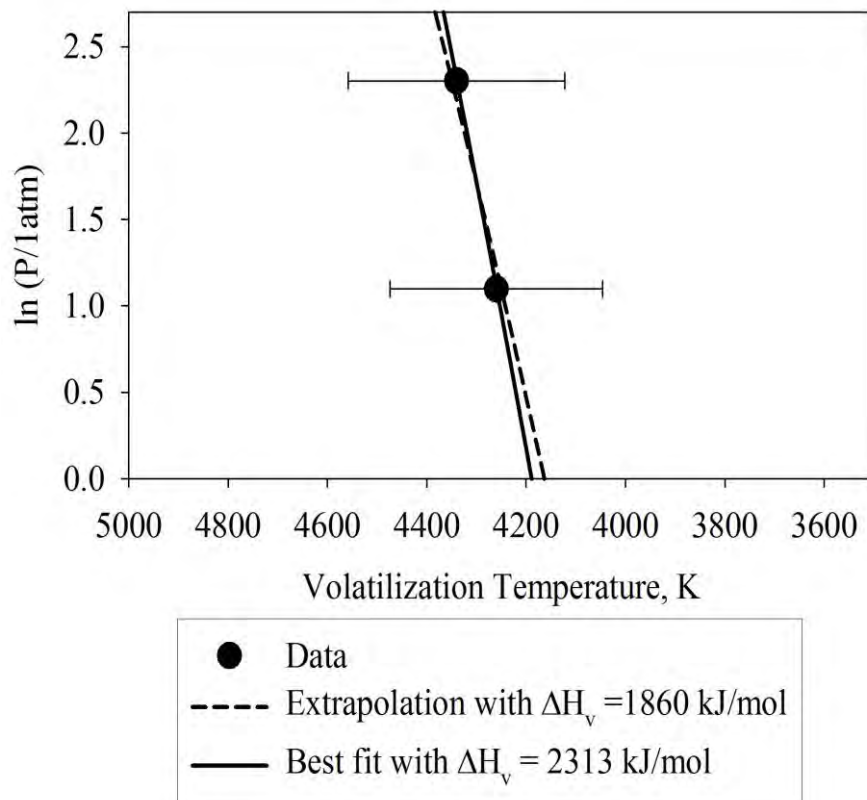


Figure 11: Extrapolation of the volatilization results to 1 atm.

4. Conclusion

An experimental study of the volatilization temperature of alumina particles was conducted in a shock tube for slightly elevated pressures by examining the extinction from a cloud of particles at a non-resonant wavelength (532 nm). The volatilization temperature was then modeled from this temperature at which clouds stop extinguishing:

1 In nano-alumina particles, at 10 atm, there is a sharp cutoff at 3860 K at which particles volatilize and stop extinguishing within the shock tube test time. This result corresponds to a modeled volatilization temperature of 4340 K at 10 atm.

2 In micro-alumina particles at 10 atm tested at higher temperatures, the evaporation time of the particles as measured from the transmitted light intensity nicely follows the trends of 2 μm particles with a volatilization temperature of 4340 K at 10 atm.

3 In nano-alumina particles at 3 atm, there is a sharp cutoff at 4050 K at which particles volatilize and stop extinguishing within the shock tube test time. This result corresponds to a volatilization temperature of 4260 K at 3 atm.

4 Extrapolating from these pressures, the best estimate for the volatilization temperature at 1 atm from experimental data was 4189 K with a heat of dissociation of 2313 kJ/mol. Using reference values for the heat of dissociation (1860 kJ/mol) gives a 1 atm temperature of 4163 +/- 200 K, certainly far higher than 3200 K, reported in the CRC handbook.

5 Alumina volatilization is therefore not the temperature limiting process during micro-aluminum combustion.

References

- [1] N. Glumac, H. Krier, T. Bazyn, R. Eyer, Combustion Science and Technology 177 (2005) 485–511.
- [2] C. Linton, R. Nicholls, Journal of Quantitative Spectroscopy and Radiative Transfer 9 (1969) 1–11.
- [3] H. Partidge, S. Langhoff, B. Lengsfeld, B. Liu, Journal of Quantitative Spectroscopy and Radiative Transfer 30 (1983) 449–462.
- [4] I. Glassman, Combustion, Academic Press, San Diego, CA, 3rd edition, 1996.
- [5] G. Schlöffel, A. Eichhorn, H. Albers, C. Mundt, F. Seiler, F. Zhang, Combustion and Flame 157 (2010) 446–454.
- [6] T. Bazyn, H. Krier, N. Glumac, Proceedings of the Combustion Institute 31 (2007) 2021–2028.
- [7] N. Poletaev, A. Florko, Combustion Explosion and Shock Waves 44 (2008) 437.
- [8] E. L. Dreizin, Combustion and Flame 105 (1996) 541–556.
- [9] T. Bazyn, Spectroscopic Measurements of the Combustion of Aluminum and Aluminum-Based Energetic Material Particles Using a Heterogeneous Shock Tube, Ph.D. thesis, University of Illinois at Urbana-Champaign, Urbana, IL, 2006.
- [10] T. Bazyn, P. Lynch, H. Krier, N. Glumac, Propellants, Explosives, and Pyrotechnics 35 (2010) 93–99.
- [11] e. D. Linne, CRC Handbook of Chemistry and Physics, 88th ed, CRC Press, Cleveland, OH, 2007/8.
- [12] e. M. Chase, NIST-JANAF Thermochemical Tables, 4th ed, American Chemical Society Press, New York, NY, 1998. [13] O. Ruff, M. Konschak, Z. Elektrochemie 32 (1926) 515–525.
- [14] D. Stull, Industrial and Engineering Chemistry 39 (1947) 540–550.

- [15] L. Brewer, A. Searcy, *Journal of the American Chemical Society* 73 (1951) 5308–5314.
- [16] A. V. Grosse, J. B. Conway, *Industrial and Engineering Chemistry* 50 (1958) 664–672.
- [17] P. Lynch, H. Krier, N. Glumac, *Proceedings of the Combustion Institute* (2009).
- [18] T. Bazyn, N. Glumac, H. Krier, T. Ward, M. Schoenitz, E. Dreizin, *Combustion Science and Technology* 179 (2007) 457–476.
- [19] P. Lynch, H. Krier, N. Glumac, *AIAA Journal of Thermophysics and Heat Transfer* 24 (2010) 301–308.
- [20] E. Petersen, R. Hanson, *Shock Waves* 10 (2001) 405–420.
- [21] C. Morley, Gaseq: A chemical equilibrium program for windows, <http://www.gaseq.co.uk>, 2005.
- [22] B. McBride, S. Gordon, Computer Program for Calculation of Complex Chemical Equilibrium Compositions and Applications I, Analysis, Technical Report RP-1311 Part I, NASA, <http://www.grc.nasa.gov/WWW/CEAWeb/ceaHome.htm>, 1994.
- [23] A. F. Mills, *Mass Transfer*, Prentice Hall, New Jersey, 2nd edition, 2001.
- [24] C. K. Law, *Combustion Physics*, Cambridge, New York, NY, 2006.
- [25] P. Lynch, High Temperature Spectroscopic Measurements of Aluminum Combustion in a Heterogeneous Shock Tube, Ph.D. thesis, University of Illinois at Urbana-Champaign, Urbana, IL, 2010.
- [26] J. Kiefer, M. Al-Alami, J.-C. Hajduk, *Applied Optics* 20 (1981) 221–230.
- [27] P. Atkins, J. dePaula, *Physical Chemistry*, Oxford University Press, New York, NY, 7th edition, 2002.

CHAPTER 14: EARLY TIME SPECTROSCOPIC MEASUREMENTS DURING HIGH EXPLOSIVE DETONATION BREAKOUT INTO AIR

Introduction

Upon reaching the air-explosive interface at the outer edge of a bare charge, a strong air shock is transmitted to maintain pressure and velocity continuity in the flow. The required downstream pressure (approximately the C-J pressure of the explosive) and velocity (of the order of a few km/s) behind the air shock imply that temperatures generated will be very high – likely in the plasma regime. This phenomenon is exploited in the ‘argon candle’ devices [1] where a high explosive in an argon atmosphere generates an extremely bright burst of broadband light for imaging or absorption spectroscopy. Though high temperatures may be reached very early during breakout, the shock attenuates rapidly with distance, causing the post-shock temperature to decrease.

The magnitude of the early time breakout temperatures has been measured in a few studies. In particular, Taylor and Kane [2] noted that in argon, spectral continua corresponding to greybody temperatures of 20000 - 30000 K were achieved for Composition B exploding in an argon atmosphere. The authors also used time-resolved absolute emission intensities at two wavelengths (405 nm and 545 nm) to infer temperatures assuming blackbody behavior. Peak temperatures in the 14000 to 26000 K range occurred right at breakout, and the decay in temperature was monitored over the first five microseconds. Significant decay was observed, though, in all shots, temperatures greater than 15000 K persisted past 4 us. There was also significant variation in inferred temperature depending on which wavelength band was used, suggesting a non-thermal radiation distribution.

Little work in the open literature is available on early time breakout in air environments, which represent the most common practical system. Koch et al. [3] discuss possible high temperatures that might be observed during PETN breakout in air. The authors make a rough estimate of breakout temperatures in the 10,000 – 15,000 K range for air. Possible implications of high temperature at breakout have received almost no attention, though the effect on non-ideal systems is likely to be significant. In some non-ideal systems, for example aluminized explosives, post-detonation reaction is important, and often additives such as boron or aluminum have high ignition temperatures. High temperature transients may enhance ignition of the particulates on the outer edge of the fireball, leading to more complete conversion than might be expected from models that ignore such transient. Of critical importance here is the fraction of explosive products that are affected by such a transient, and there has been no work, to our knowledge, on quantifying such a fraction. A second possible implication of such a transient is on interpretation of emission signals from early time emission of second phase intermediates such as AlO. While AlO has generally been used as an indicator of combustion, significant AlO emission arises from dissociated Al_2O_3 at high temperatures [4,5], and thus temporal emission traces of AlO may not be directly linked to aluminum reaction at early times in explosives testing.

In this study, we look at an RDX-based explosive using time-resolved spectroscopy to track the conditions in the first 15 microseconds after detonation breakout. Temperature and species information are derived, and implications are discussed.

Experimental

The charges used in this work consist of the Teledyne RISI RP-2 detonator which is an exploding bridgewire initiated system where the booster is a 32 mg charge of PETN, and the main charge is 18 mg of PBX-9407, which is primarily RDX. The end of the charge is uncased so that the explosive/air interface is visible. A small containment vessel was constructed to allow optical access to the end of the charge through two 6 mm thick quartz windows, the first of which is approximately 35 mm from the end of the charge, and is expendable, though it typically lasts two shots before cracking. The chamber provides sufficient protection and sound deadening so that the reactor can be mounted directly next to the spectrometer on the optical table. During firing, the blast is barely audible.

Detonators were triggered using a custom fireset consisting of a 1 uF capacitor charged to 5kV and discharged across a triggered spark gap. Timing was monitored using an oscilloscope and fast photodiode to monitor first light with respect to the trigger signal. All timing in this paper is referenced to the first-light time, which occurred approximately 5 us after capacitor discharge.

Emission was collected with three spectrometer systems. The first system is a low resolution, fast, UV-based spectrograph consisting of the Jobin Yvon CP-140 spectrograph (f/2, 200-550 nm range, 1 nm resolution) coupled to the Andor 420UV-FK Fast Kinetics CCD system that can obtain up to 128 spectra with as little as 1 μ s between spectra. The second system is the visible analogue of the UV-spectrograph, but has considerably higher efficiency and larger dispersion. The spectrometer is a custom build using camera lenses as collimator and focuser and a high efficiency 1800 gr/mm volume holographic grating as the dispersing element. In this fashion, we achieve very high throughput (f1.4) at 0.5 nm resolution over the 450-700 nm range, and the FK CCD is again used as the detector. The final system is a conventional SPEX 270M imaging spectrograph used with a Princeton Instruments PI-MAX intensified CCD detector with Super-Blue Photocathode providing up to 25% quantum efficiency in the ultraviolet. This system operates at f/4 and obtains a single spectrum per test, but the emission can be spatially integrated leading to increased signal levels so that we can achieve resolutions of 0.1 nm with sufficient signal to noise ratio (SNR) on 1-2 microsecond exposures. Standard wavelength and intensity calibrations were performed using mercury lamps, hollow cathode lamps, and NIST-traceable tungsten lamps.

Results and Discussion

UV Spectroscopy

Figure 1 shows the sequence of fast kinetics spectra from a single test for the 200 to 550 nm range using a 2 us shift time. Some temporal smearing is typically observed since the registers are shifting during exposures, so that the effective temporal resolution is probably closer to 4 us, though the interframe spacing remains 2 μ s. Spectral emission from Ca, Ca⁺, OH, and CN are readily identified, and these high temperature features last at least through 12 us after breakout. Due to the low spectral resolution and temporal smearing, little can be gained quantitatively from these spectra, but they do serve to identify key emitters and spectral regions of interest, and they provide an estimate of the temporal regions over which certain signatures appear.

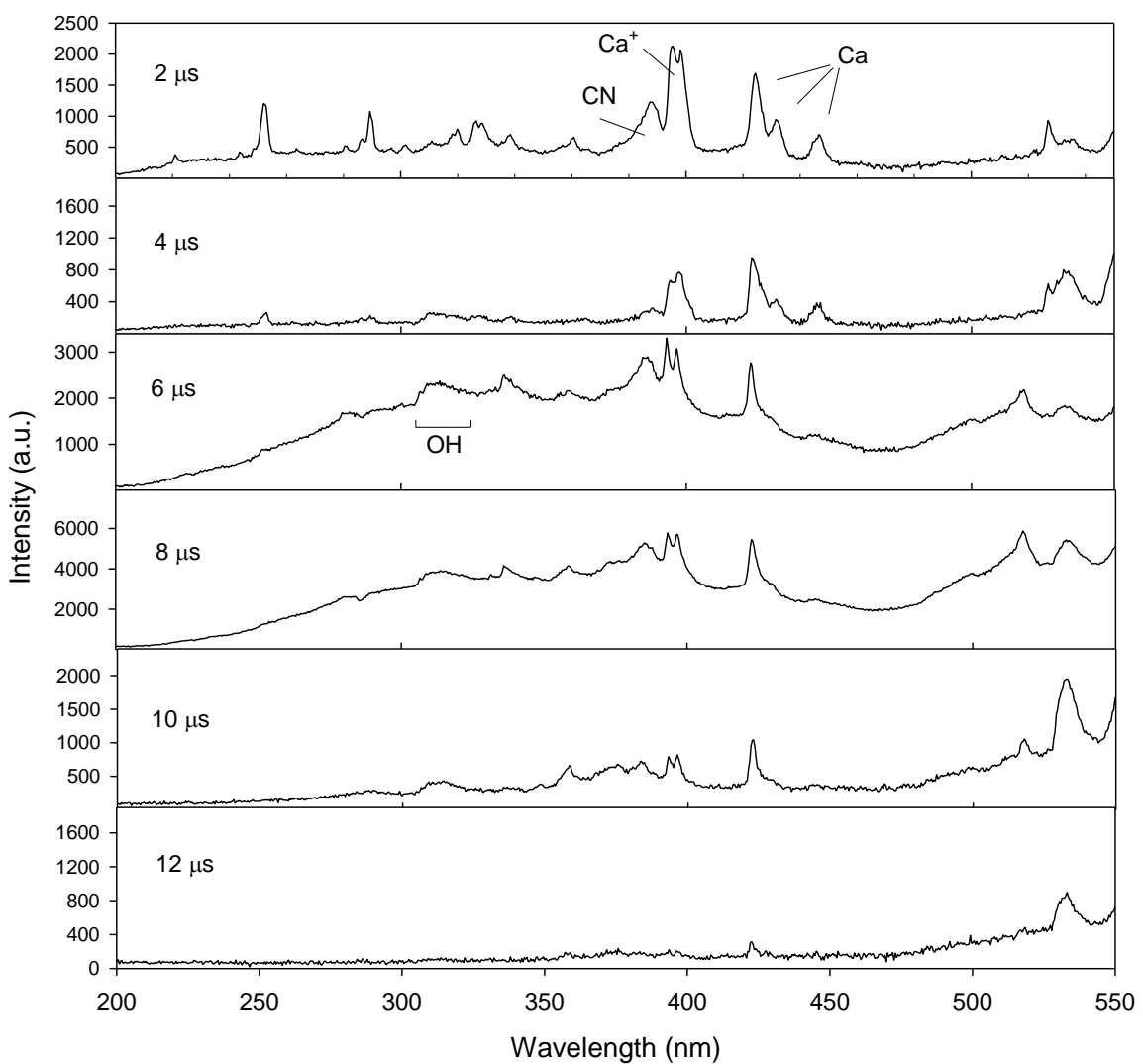


Figure 1: A fast kinetics spectral sequence of the breakout of PBX-9407 into air with a 2 μs interframe time. Approximate delay times are listed in the upper left corner of each spectrum.

Based on the low resolution spectra, higher resolution spectra in the ultraviolet were taken using the 0.25 meter spectrograph system, focusing on the first microsecond of breakout. Spectra in the 275 to 350 nm region were taken at 0.2 nm resolution in imaging mode. These breakout spectra captured emission from the central core region of the high explosive, as well as the edge regions near the brass casing. Spectra from each region were quite different, as shown in Figure 2. A list of observed peaks is shown in Table 1.

Explosive		Case Interface	
Wavelength (nm)	Tentative Assignment	Wavelength (nm)	Tentative Assignment
337.31	?	327.56	Cu I
336.22	?	324.92	Cu I
318.24	Ca II	309.44	Cu I
316.10	Ca II	308.40	?
300.84	Ca I (?)	288.47	O I
288.45	O I	285.51	?
285.53	?	280.65	O I
280.63	O I	279.90	O I
279.90	O I		

Table 1: A list of spectral peak centers for the plots shown in Figure 2 of the ultraviolet region of the breakout spectrum.

Spectra in the core high explosive region exhibited strong, broadened peaks at several wavelengths. Tentative identifications suggest calcium lines (which are commonly observed in such explosions) and possibly atomic oxygen lines are most prominent. Several lines and bands remain unidentified in these high SNR spectra. Spectra in the vicinity of the case interface show additional lines, most likely due to copper from the brass casing material. Another line around 308.4 nm remains unidentified. The observation of atomic metal lines from the casing at such an early time is somewhat surprising, though the degree to which the metal surface is atomized may still be small since atomic emission at these temperatures is strong even from trace elements such as calcium.

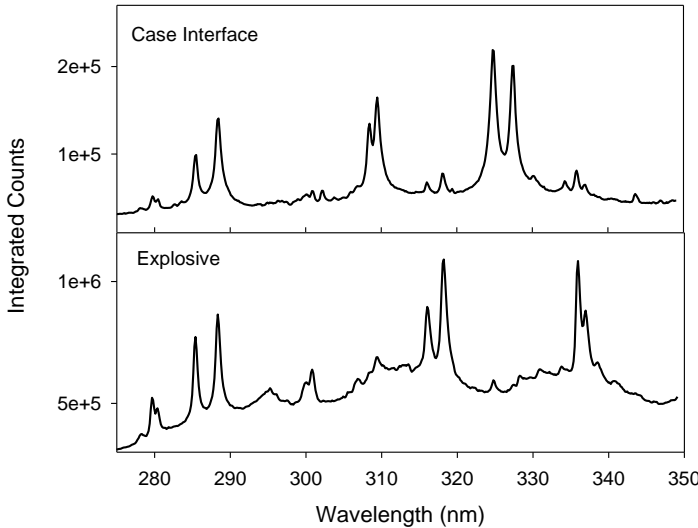


Figure 2: A 1 us duration spectrum covering the first microsecond after breakout at 0.2 nm resolution. Top spectrum: near the HE/case interface. Bottom: directly over the explosive.

Spectra in the Visible Region

Figure 3 shows several samples from the sequence of spectra from the visible FK system on a single shot. Due to the enhanced efficiency of the spectrograph, a 1 us exposure could be used, though temporal smearing of at least one frame is likely present. These spectra show several key features. Overall intensity decays by more than an order of magnitude within the first 10 us after breakout, and then fades more slowly over the next 10 us. Atomic lines appear in the first 3 us, then mostly fade (with the notable exception of the persistent Na D lines), leaving several prominent band structures around 535, 555, 605, and 620 nm. These bands persist out to at least 15 us.

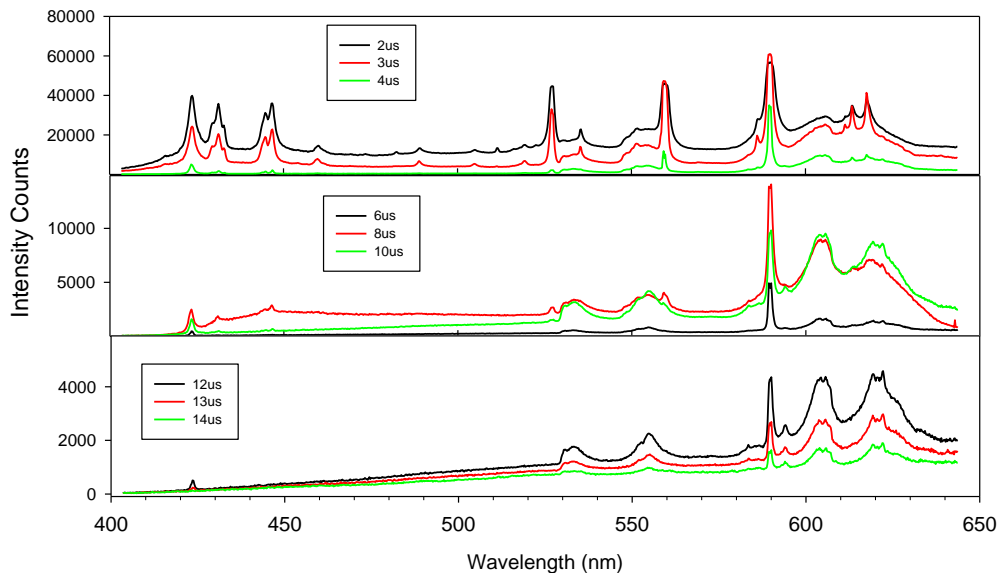


Figure 3: Spectra from the visible region taken with 1 us exposure times. Approximate delays from breakout are given in the insets.

The visible spectra in the region of 530 – 650 nm show several interesting features. For the time period from 5 – 15 μ s, the spectrum is dominated by four broad structures at 535, 550, 605, and 625 nm, which resemble molecular bands or closely grouped clusters of broadened atomic lines. Both of the green features were examined at higher resolution. Figure 4 (upper right) shows a spectrum at sub-Angstrom resolution of the feature taken in the time period from 5 to 10 μ s. The feature strongly resembles a red-degraded band with a head at 530 nm. Previous work on strong shock waves in air, nitrogen and oxygen [6] showed emission in the green only when pure oxygen was run. Spectra from that paper were digitized and compared to our results, as shown in Figure 4 (left panels). Keck et al. [6] identified the green emission as originating from neutral oxygen atoms. There is some qualitative resemblance to our spectra, but quantitatively, there is little correlation. The spectra from Keck et al do correspond to strong O I emission lines, and they demonstrate how groupings of atomic lines behind shock waves can resemble a molecular band (e.g. the 620 feature, which is a grouping of several lines originating from the $^5D^o$ state of O I). However, the bands in our spectra do not correspond well to the O I lines seen by Keck et al. The 530 nm band we observe is to the blue of the three-line grouping near 532.9 nm observed by Keck, and they observe the grouping of lines near 543.5 nm, which should be of similar intensity. We do not observe the latter group, even as a shoulder to the band. There is no evidence of the 555 nm band in the Keck et al. spectra, and this band is as strong in our spectra as the 530 nm band. This latter band is also the only band that persists after 30 μ s, as shown in Figure 4 (lower right). Though the band narrows somewhat, it remains the only prominent feature in the visible spectrum until about 50 μ s

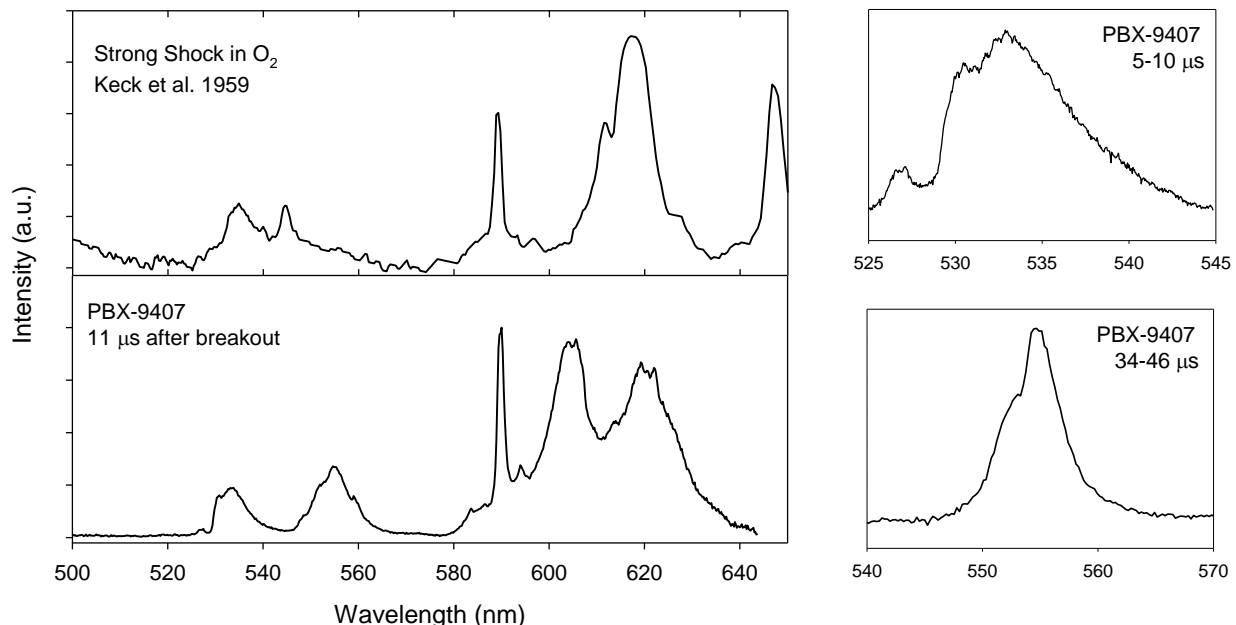


Figure 4: Upper left: A digitized portion of the spectrum from Keck et al [6] of the emission spectrum from a strong shock in oxygen. Our spectrum from 11 μ s after breakout is shown at bottom left for comparison. Top right: A high resolution spectrum of the 535 nm feature. Bottom right: The only remaining spectral feature in the visible region after 30 μ s.

Spectral features at 605 and 620 nm have no counterpart in the Keck et al. spectra for any of the environments they tested. The observed bands do not appear to be hot bands of H₂O or CO₂, nor do they correspond to groupings of atomic emission lines of O, N, Ca, Na, or K. No common bands of the molecules NO, N₂O, NO₂, N₂, O₂, CO, or CaO match these emission features. The Gaydon-Herman bands of N₂, which appear in high pressure N₂ discharges [7-9], have a main feature near 555 nm, and extensive efforts were undertaken to model these bands and match them to the observed spectra. While there is some fair correlation with the main feature, including the shoulder on the blue side, there are quantitative differences, and none of the other weaker Gaydon-Herman bands appear in any of the spectra.

Identification of these bands could be useful in providing further diagnostics for conditions that occur soon after detonation breakout. The emission is well resolved, and the band structure may be usable as a temperature diagnostic [10], even at low resolution. However, at present, the bands cannot be definitively identified.

Temperature Measurements

Temperatures were estimated from the spectra using three methods. At early times, atomic Ca lines were well resolved, and the lines in the 410 to 450 nm range can be fit to thermal distribution in a relatively sensitive fashion for temperatures in the vicinity of 1 eV. Using the optically thin assumption, fits were obtained using standard spectroscopic constants and fitting linewidth and temperature. Results are shown in Figure 5. Since the features of the spectra all fit fairly well, it is possible that optical depth effects on the spectra are minimal. However, at early times there appears to be a significant variation in structure around 430 nm between optically thin simulation and experiment, and this effect may be due to optical depth. The spectra suggest that extreme temperatures do indeed exist at some locations immediately after breakout and that decay is fairly rapid.

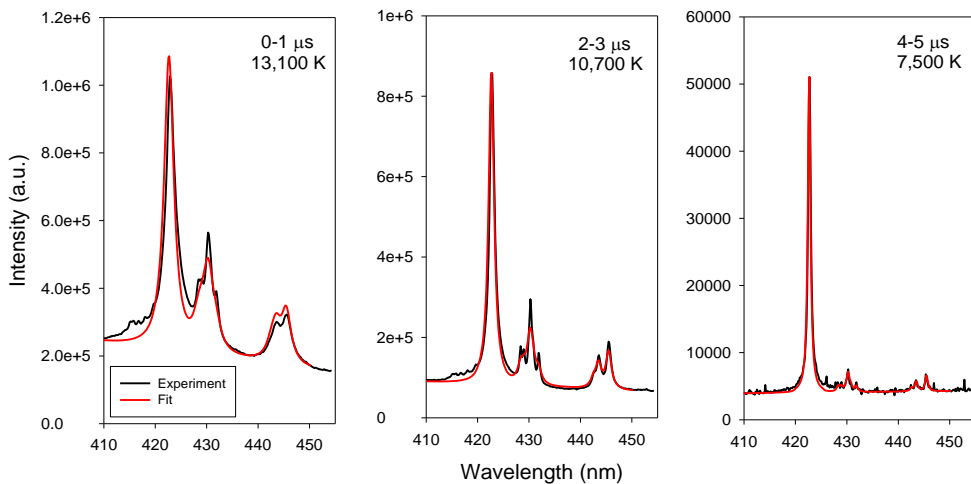


Figure 5: Spectra fit to Ca atomic emission lines for the first few us after breakout using an optically thin, thermal equilibrium model.

Beyond 5 us, the Ca atomic temperature technique is not useful due to the low intensity of the lines corresponding to higher energy levels. However, OH emission emerges at these times and can be fit using conventional codes such as LIFBASE [11]. Figure 6 shows an OH spectrum obtained at 9 us after breakout using a 2 us gate on the ICCD. The spectrum is fit to a

temperature of 8700 K. Spectra taken at 7 and 11 us after breakout were also fit, and similar temperatures resulted.

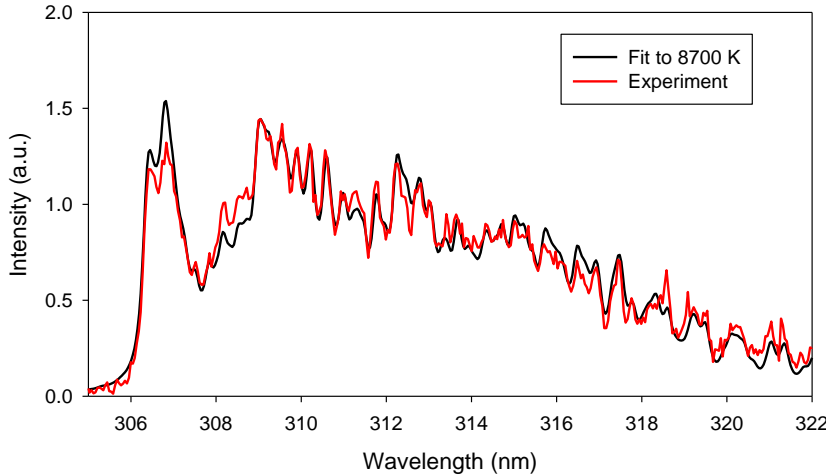


Figure 6: A spectrum taken 9 us after breakout showing OH emission, and a fit to the spectrum from the code LIFBASE [11], assuming optically thin conditions and an equilibrium rotational population distribution.

For the period of 4 to 14 us, the emission spectra in the visible FK series had a fairly featureless region from about 450 to 520 nm where only continuum radiation was observed. Assuming a greybody distribution (for lack of any information on the emissivity variation with temperature), these regions were fit to a temperature, and the results, along with those of the Ca and OH fits are displayed on Figure 7. Significantly lower temperatures were observed in the continuum fits, as compared to the molecular spectra.

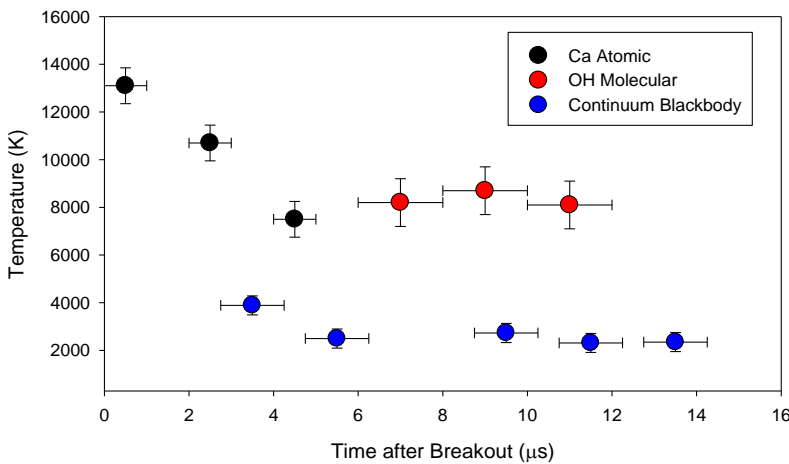


Figure 7: A summary of the temperature measurements made in this work using Ca, OH, and continuum emission.

DISCUSSION

The observed temperatures of over 1 eV are not unexpected. Brode [12] predicted 12,000 K at early times in his computational study on blast waves, and Rozhdestvenskii et al. [13] predicted nearly 10,000 K using a simple model, while Koch et al. [3] posit 10,000 – 15,000 K. The temperatures derived from the spectra are entirely consistent with past research.

Since emission is a line of sight measurement, spectra are averaged over some region, and variation in conditions (temperature and emitter concentration) along the path will affect the final profile. Thus, a “temperature” derived from an emission spectrum may not reflect any real temperature in the system. Since emitter population varies exponentially with temperature in thermally excited systems, regions of high temperature will emit much more strongly than colder regions, and thus molecular temperatures are often considered to be representative of the peak temperature in a system. Colder regions can affect the spectrum by absorption of emitted light if there is sufficient species density. Conditions in these explosions provide at least some confidence that the measured temperatures are fairly representative of the peak temperatures behind the blast wave. In the blast wave structure computed by Brode [12], there is a fairly sharp and localized temperature peak behind the blast wave, followed by a rapid falloff, suggesting that emission will come primarily from a small spatial zone, and have much cooler regions in front and behind. This structure is actually seen in high speed images from Rozhdestvenskii et al. [13] of PETN and TNT/RDX charges. For small charges such as these, the emitting zone will be a few mm at most, which may be sufficient to keep the spectra in the optically thin regime and minimize self-absorption effects. Of course, the entire spectrum is the observable quantity here, and a flow simulation complete with chemistry could, in principle, be used to generate a predicted emission spectrum, which could be compared to experiment.

Of interest is the region over which these extreme temperatures influence the chemistry in the fireball. As mentioned previously, in non-ideal systems where secondary reactions contribute significant energy release, hot zones in the fireball could potentially accelerate such reactions. The previous simulations discussed above suggest that high temperatures are primarily behind the air blast, and, in that case, little effect on the fireball might be expected. However, the fact that Ca and CN features are prominent in the spectra shows that fireball products are indeed being excited by the high temperatures. Furthermore, the time for the blast wave to separate from the fireball edge is quite long. McNesby et al. [14] showed times of several hundred us for kg scale tests, and our previous results [15] showed times of a few tens of us for 10g charges. Tests at Indian Head [16] showed that a significant fraction of the aluminum particles in an aluminized explosive were ejected out past the main blast wave, and some of our recent measurements showed that AlO temperatures derived from early time spectra of aluminized charges likely exceed 5000 K [17]. Therefore, at least some of the fireball chemistry appears affected by the early post-shock temperatures. Finally, since affected volume scales as $r^3 dr$, even small penetrations into the fireball lead to significant volumetric effects. For example a 5% penetration represents 15% of the fireball volume.

The discrepancy between molecular and continuum temperatures can likely be explained by considering the optical configuration and distribution of emitters. In our experiments, the detector is on the outside, looking into the explosive. The gaseous emitting region behind the blast wave is on the outside, and this region is relatively thin spatially and optically. The core of the fireball emits continuum radiation from condensed phase products (e.g. soot). These temperatures have been reported in many studies and typically are in the vicinity of 3000 K, as we observe here. Similar results are seen by Rozhdestvenskii et al. [13] where they used

continuum radiometric measurements to see temperatures of 2000 and 3000 K, while much higher peak temperatures were predicted.

The unidentified molecular and atomic spectral features in this work provide opportunities for further study. The band near 555 nm is particularly interesting. This band has been seen prominently in RDX, HMX [18], and PETN [19] explosions. Identification may allow use as an early time diagnostic of explosive conditions. Efforts during this work to discern structure in this band using our 1.5m spectrometer with 2400 gr/mm grating were unsuccessful. Though a cluster of broadened atomic lines cannot be ruled out as the source, no likely candidate has been uncovered.

References

- [1] Yu. N. Kiselev and B. D. Khristoforov, "Explosive High-Power Continuous Spectrum Light Source," *Fizika Goreniya i Vzryva*, Vol. 10, No. 1, pp. 116-119, 1974.
- [2] William H. Taylor, II and John W. Kane, Jr., "Radiant Properties of Strong Shock Waves in Argon, *Applied Optics*, Vol. 6, Issue 9, pp. 1493-1496 (1967)
- [3] Jon D. Koch, Scott Piecuch, James M. Lightstoner, Joel R. Carney, and Joe Hooper, Time-resolved measurements of near infrared emission spectra from explosions: Pure pentaerythritol tetranitrate and its mixtures containing silver and aluminum particles, *J. Appl. Phys.* 108, 036101 (2010)
- [4] N. Glumac, H. Krier, T. Bazyn, and R. Eyer, Temperature measurements of aluminum particles burning in carbon dioxide *Combustion Science and Technology*, 177, 485 (2005)
- [5] G. Schlöffel, A. Eichhorn, H. Albers, Ch. Mundt, F. Seiler and F. Zhang, The effect of a shock wave on the ignition behavior of aluminum particles in a shock tube, *Combustion and Flame Volume 157, Issue 3, March 2010, Pages 446-454*
- [6] J. C. Keck, J. C. Camm, B. Kivel, and T. Wentink Jr., "Radiation from Hot Air Part II. Shock Tube Study of Absolute Intensities," *Annals of Physics*, 7, 1-38 (1959).
- [7] Carroll, P. K.; Collins, C. C.; Murnaghan, J. T. Rotational studies of the Gaydon-Herman (green) bands of N₂, *Journal of Physics B: Atomic, Molecular, and Optical Physics*, Volume 5, Issue 8, pp. 1634-1654 (1972).
- [8] G. Davidson and R. O'Neil, Optical Radiation from Nitrogen and Air at High Pressure Excited by Energetic Electrons, *J. Chem. Phys.* 41, 3946 (1964)
- [9] K Aho, L -E Berg, U Hallsten, P Lindblom and O Solin, Observation of dominant emission of the Gaydon-Herman green system in dense nitrogen excited by energetic ions, *Journal of Physics B: Atomic, Molecular and Optical Physics*, Volume 27, Number 16 L525
- [10] Xu, H., Glumac, N.G., and Suslick, K.S., "Temperature Inhomogeneity during Multibubble Sonoluminescence, , *Angewandte Chemie*, 48, 1-5, 2009.
- [11] J. Luque and D.R. Crosley, "LIFBASE: Database and Spectral Program (Version 1.5)", SRI International Report MP 99-009 (1999).
- [12] Brode, H. L. "Blast Wave from a Spherical Charge," *Physics of Fluids*, 2:217 (1959).
- [13] V. B. Rozhdestvenskii, B. D. Khristoforov, and V. L. Yur'ev, "Effect of Product Composition on the Radiation Characteristics of Explosion of an Explosive in Air," *Fizika Goreniya i Vzryva*, Vol. 25, No. 5, pp. 145-148, 1989.
- [14] Kevin L. McNesby, Barrie E. Homan, John J. Ritter, Zachary Quine, Rachel Z. Ehlers, Brendan A. McAndrew, "Afterburn Ignition Delay and Shock Augmentation in Fuel Rich Solid Explosives," *Propellants, Pyrotechnics, and Explosives*, 35, 57-65, 2010.
- [15] D. Coverdill, "Explosive Initiation of Tungsten Based Reactive Materials in Air", M.S. Thesis, University of Illinois, Urbana-Champaign, 2010.

- [16] Joel R. Carney, James M. Lightstone, Thomas P. McGrath II, Richard J. Lee, "Fuel-Rich Explosive Energy Release: Oxidizer Concentration Dependence," *Propellants Explos. Pyrotech.* 2009, 34, 331 – 339
- [17] N. Glumac, J. Mott Peuker, H. Krier, and P. T. Lynch, "Optical Spectroscopy of Fireballs from Metallized Reactive Materials," 48th AIAA Aerospace Sciences Meeting, Orlando, Florida, January 2010, AIAA-2010-0695
- [18] J. R. Carney, NSWC Indian Head, Private communication.
- [19] S. Johnson, AFRL Eglin, Private communication.

CHAPTER 15: ON ALO EMISSION SPECTROSCOPY AS A DIAGNOSTIC IN ENERGETIC MATERIALS TESTING

Introduction

Aluminum combustion has been widely studied for decades, primarily because of the high specific energy of combustion when fuel and oxidizer weights are considered. This energy density has led to extensive usage of Al as an additive in propellants and explosives. Micron-sized and larger aluminum burns brightly, which has led to further use of Al in pyrotechnics, flash powders, and flash bulbs. The luminosity of aluminum combustion is derived primarily from condensed phase emission of the very hot alumina product at temperatures in the vicinity of 3000 – 4000 K[1-5]. In addition to condensed phase emission, emission from gas-phase AlO and Al are well known. AlO emits most strongly in the *B-X* band in the visible region, though several other weaker ultraviolet bands have been reported. Emission in the *B-X* band has been analyzed in hundreds of experimental studies.

AlO emission occurs as a result of gas-phase combustion of metal Al with surrounding oxidizers (which can be H₂O, CO₂, CO, NO, NO₂, as well as O₂). According to observation [6] and modeling [7], AlO is formed in the flame zone surrounding the surface of the particle, and is thus present in a region that is between the peak system temperature (at the flame zone) and the cooler surface temperature. AlO is similar in this regards to MgO, which also tends to burn in the vapor phase for micron-sized particles and larger. In contrast, species that burn at the surface (heterogeneously) such as Zr, Ta, W, Fe, and Si tend to show markedly less emission from intermediate species, except when they are present as decomposition products of desorbed oxides at very high temperature (e.g. ZrO emission is sometimes seen), due to the fact that reactant, product, and intermediate species remain in the solid phase or as surface species.

AlO is an important species in gas-phase aluminum combustion [8], but its importance can easily be overestimated because of its prominence in emission. Equilibrium analysis suggests that at combustion temperatures, AlO is often the most abundant intermediate, but not always, especially under very rich or very lean conditions. AlN is predicted to be as abundant as AlO in air combustion of aluminum, but has not been observed in emission in oxidizing environments. Al₂O and AlO₂ are equally critical intermediates, but do not have strong emission bands in the visible or ultraviolet, and so do not contribute to the emission signal. AlO is prominent in emission primarily as a result of its strong visible transition and low first and second excited electronic states. This situation is somewhat analogous to hydrocarbon flame spectra that are dominated by CH and C₂ emission, though neither species plays a central role in the gas-phase combustion mechanism of hydrocarbons. The ease of non-intrusively monitoring species in emission has led to a great amount of study of these species, with attempts being made to correlate critical thermochemical parameters to emission intensity. The consensus for many of these species is that such measurements have limited utility. CH is often used as a flame front marker either in emission or fluorescence for probing two-dimensional flame structure. However, both CH and C₂ emission result from (at least in many cases) from chemiluminescent reactions, and so the temperatures derived from fitting the molecular spectra often do not correspond to local conditions.

Similar constraints likely apply, to some extent, to any emitting species, including AlO. Despite this concern, many studies have used AlO to quantify aluminum combustion in some fashion. Emission spectroscopy is often used to identify species in aluminum combustion [9-11] such as

AlO and Al, and to detect whether aluminum is burning[12-15]. In addition to AlO emission measured from aluminum burning, AlO emission has also been measured from hot alumina (Al_2O_3), the product of aluminum combustion [16-20].

Many studies have used time resolved AlO emission to determine the burn time of aluminum particles in a shock tube [12,21-28], particles flowing in a stream[3,14,29], and Al particles in an explosive[15,30,31]. In addition, burn time models were developed using the AlO emission [30,14,23,26,27,29,32]. The combustion process, dynamics and properties have been studied for quiescent particles[2,3,28,33,34], suspended particles [5,35], compressed Al powder[36], bulk aluminum[18,37,38], and for explosives containing aluminum[15,30,39-43]. Some studies have used AlO emission to also study the ignition of aluminum [12,15,16,22,28,29, 40]. Others have studied the spatial and/or temporal evolution of the aluminum combustion [17,33,34,44-46]

By fitting continuum regions in the emission spectra in aluminized systems to Planck's black body equation, gas phase temperatures have been determined [13,14,21,22,29,44,47]. Using high resolution spectra of the AlO B-X transition, AlO vibrational temperatures have been determined by fitting the spectra to a model [4,6,18,23,46-52]. AlO emission has also been used to determine the concentration of AlO molecules [11,52].

In some experiments the AlO emission was dominated by the black body continuum emission [53-56] and in the case of nano-aluminum a weak emission signal was measured[48]. To quantify the amount of AlO during nano-aluminum combustion, absorption spectroscopy was used [57,58]. Absorption spectroscopy can also be used to validate the emission spectroscopy temperatures [23].

Recently, the use of AlO emission as a combustion diagnostic for aluminized explosives has been investigated [19,20,59]. The results indicate that the interpretation of AlO emission from explosive fireballs is not straight forward [19,20].

Experimental

We report on results from tests in the UIUC heterogeneous shock tube [21] and blast chambers[60-61]. In the shock tube, high temperature and pressure conditions can be achieved that are very similar to the environment in which Al particles burn in a propellant combustion chamber or an explosive fireball. Under these controlled conditions, AlO emission can be quantified under a variety of conditions for different particle sizes and ambient temperatures.

Explosive tests were performed using custom aluminized charges made by Teledyne/RISI and based on the RP-80 detonator, which nominally contains 80 mg of low density PETN as an initiator, and 123 mg of PBX-9407 as an output explosive. For these tests, the output pellet was mixed with 20% by weight of different aluminum powders with mean diameters of 3, 10, and 40 microns. For inert baseline tests, the pellet was mixed instead with 20% of 2 micron alumina powder.

Spectroscopic analysis of these systems was performed with two different systems. For high resolution studies, a custom 444 mm Czerny-Turner spectrograph having a 30 micron inlet slit and 2400 gr/mm holographic grating was used. Combined with a Hamamatsu 1024 x 256 pixel back-thinned CCD array, this system generated spectra covering 15 nm at 0.04 nm resolution

(FWHM). At this resolution, individual rotational lines are well resolved, and entire spectral band sequences could be captured in a single exposure. For lower resolution studies, we used a custom spectrograph consisting of two camera lenses as collimator ($f/2.8$, 100mm) and focuser ($f/1.4$, 50mm), in between which a volume holographic grating (1800 gr/mm, Edmund Scientific) served as the dispersing element. For a 50 micron slit width, the system produced a resolution of 5\AA (FWHM) with a dispersion of 10 nm/mm, allowing 250 nm to be covered on a 25 mm chip. The detector is an Andor DV420-FK Fast Kinetics camera having one row of pixels exposed, and the remainder of the chip masked. This arrangement allows for spectra to be taken at line rates of up to 1 MHz, having a total number of spectra limited to 128 (the number of rows on the chip). Using this setup, kinetic series of spectra could be obtained with as little as 1 μs between spectra.

Results and Analysis

Temperature measurements

Critical work on AlO temperature measurements in elevated temperature ambients was performed in a previous study in the heterogeneous shock tube [4]. An important conclusion of that work was that the AlO ground state was in equilibrium with the upper state, since temperatures measured in emission matched those in absorption. Furthermore, temperatures fits obtained from AlO that was dissociated from Al_2O_3 in Ar under known ambient temperature conditions, matched observed temperatures to within 100 K. However, optically thin conditions were required to achieve accurate fits. Previous work [62] showed that as optical density increased, fit temperatures from optically thin models increased, and rudimentary efforts at simultaneously fitting optical depth and temperature still led to anomalously high temperature fits.

In explosives tests, AlO spectra are often optically dense, at least for parts of the spectrum. Figure 1 shows a spectrum from a test of an aluminized charge at a resolution of 4 Angstroms. Both $\Delta v=0$ and $\Delta v=1$ band sequences show evidence for optical density, primarily as suppressed peak heights in the band heads of the bands with low v'' , especially $v''=0$, and $v''=1$.

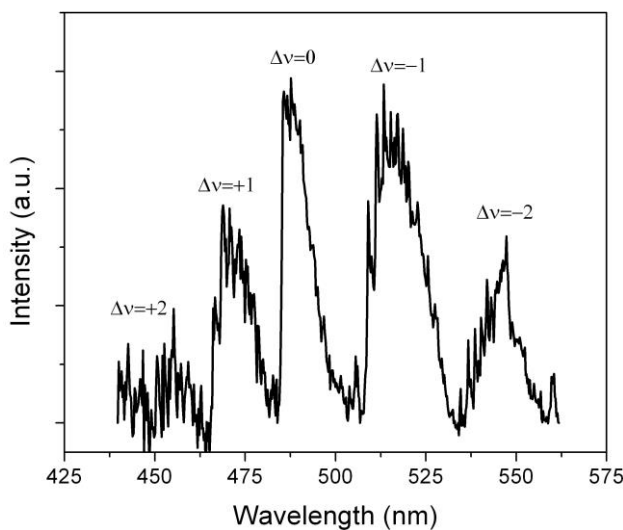


Figure 1: An AlO emission spectrum from an aluminized high explosive, obtained very soon after breakout of the detonation wave from the charge.

It should be noted that optical depth effects can be observed in isothermal environments [63], as well as environments in which a cold outer region generates edge effects. In the latter case, a temperature non-uniformity along the line of sight is inferred, but edge effects are not required for optically thin models to be invalid.

Under optically thin conditions, excellent fits between experiment and theoretical single temperature models can be obtained (see for example, our work in [4]) to a high degree of accuracy, even at low resolution (2-5 Å). In cases where there is some temperature variation in the emitting field, the temperature obtained will be much closer to the peak temperature, since the emission strength at any given location varies exponentially with temperature (i.e. as a result of the population in the upper state varying as $g_e e^{-E_i/kT}$). Thus, a fit of AlO can provide an observable linked to the peak temperature in the field of observation.

As optical density increases, it becomes more difficult to obtain quantitative AlO temperature fits, and this problem persists in many propellant and explosives tests. One option is to exploit the weakest observable transitions, which are least susceptible to optical depth effects.

An excellent candidate for temperature measurements in denser environments is the $\Delta\nu=-2$ band sequence between 530 and 550 nm. This sequence is unique in several ways. First, the sequence starts with $v''=2$, and the Franck-Condon factors for these bands are significantly lower than those of the stronger bands in the $\Delta\nu=0$ or $\Delta\nu=-1$ sequences. Thus, these bands will be optically thin under conditions where the main sequences are strongly self-absorbed. Furthermore, Franck-Condon factors increase with v'' , unlike the $\Delta\nu=0$ and $\Delta\nu=-1$ sequences where they decrease with v'' . In the latter case, this effect tends to diminish the change in band sequence shape as population shifts to higher v'' levels with temperature. This is especially true of the $\Delta\nu=0$ sequence which is relatively insensitive to temperature changes. When Franck-Condon factors increase with v'' , however, the tail of the sequence rapidly emerges as temperatures increase, leading to a pronounced change in band shape. Figure 2 shows optically thin computed emission spectra for 3000 K and 4000 K for the $\Delta\nu = -1$ and $\Delta\nu = -2$ band sequences. As seen in the figure, the $\Delta\nu = -1$ band sequence only shows significant variation in the band structure on the red side of the sequence. In cases where there is an unknown continuous background, it is difficult to distinguish between a change in band shape as a result of temperature or a varying background when only one side of the band is strongly affected by temperature. For the $\Delta\nu = -2$ sequence, the changes are more marked on both ends of the spectrum.

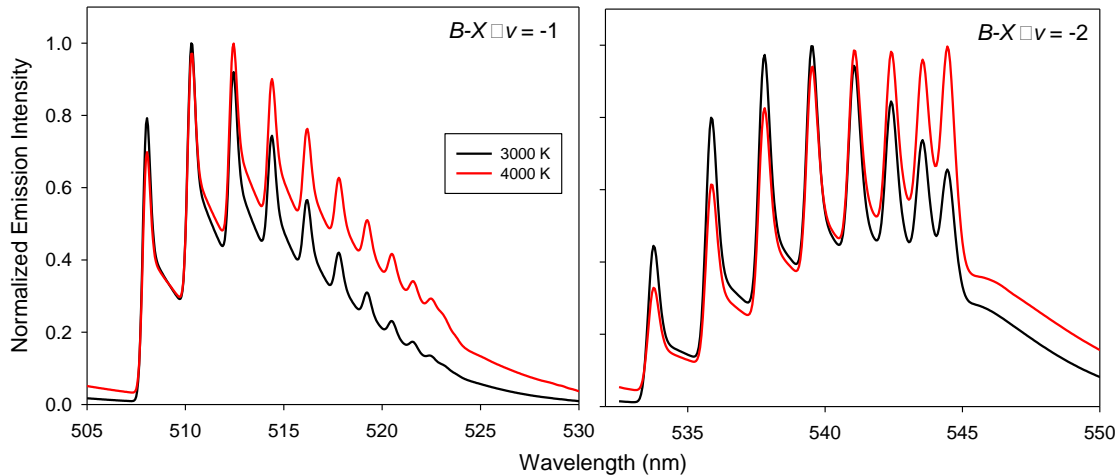


Figure 2: Optically thin emission spectra calculations for the $\Delta v=1$ and $\Delta v=-2$ sequences of the AlO $B-X$ transition for 3000 K and 4000 K.

However, the spectra shown in Figure 2 significantly understate the temperature sensitivity of the $\Delta v = -2$ sequence. In fact, the tail of the band sequence has a “head-of-heads” feature [18], where the band origins turn around from proceeding to the red to receding back to the blue at around $v'' = 10$. Current tabulated spectroscopic parameters for AlO do not allow accurate prediction of the head of heads feature, though the work in [18] provides a fine approximation. The challenge in spectral simulation arises from complications of perturbations between the low lying A state and the X state at high v'' [64]. The effect is similar to but distinct from predissociation in these levels. Nevertheless, this pileup of bands at the tail becomes experimentally apparent at higher temperatures and indeed makes the band shape change significantly with temperature over the 2000 – 4000 K range, which is the critical temperature range for most energetics tests. This combination of factors leads to a band sequence that remains optically thin under many conditions, and changes dramatically with temperature, leading to a structure that can be fit to temperature with greater precision and accuracy. To examine this band experimentally, we placed 0.1 mg of Al_2O_3 , 2 micron powder in the heterogeneous shock tube in pure argon and generated environments behind the reflected shock between 2800 K and 5000 K. The small amount of Al_2O_3 does not affect the gas temperature that is readily calculated from shock velocity measurements. In this fashion, we create a known temperature environment and can infer that the spectra originate from an isothermal optically thin cloud of known temperature [22]. AlO originates from dissociation of Al_2O_3 , even though the conditions are well below the boiling temperature [65].

Figure 3 shows the data for two temperatures of 3150 K and 3800 K. The plot shows a rapid rise in the tail bands at high temperatures, though the location of the bands is irregular. Even when degraded to 0.5 nm resolution by convolution with a 0.5 nm instrument function (comparable to common field spectral measurements), the difference between 3150 K and 3800 K is marked. Spectral models using the most current spectroscopic parameters and band intensities [66] are unable to predict the tail band structures, but using the approach in [18], an approximate spectral model can be assembled that loosely mimics the experiment. Explicit experimental data on high v'' bands in the $\Delta v = -2$ sequence would allow a truly predictive model to be assembled. Nevertheless, the $\Delta v = -2$ sequence, which is the least susceptible to optical depth effects of all the major $B-X$ bands, shows great temperature sensitivity, even at low spectral resolution.

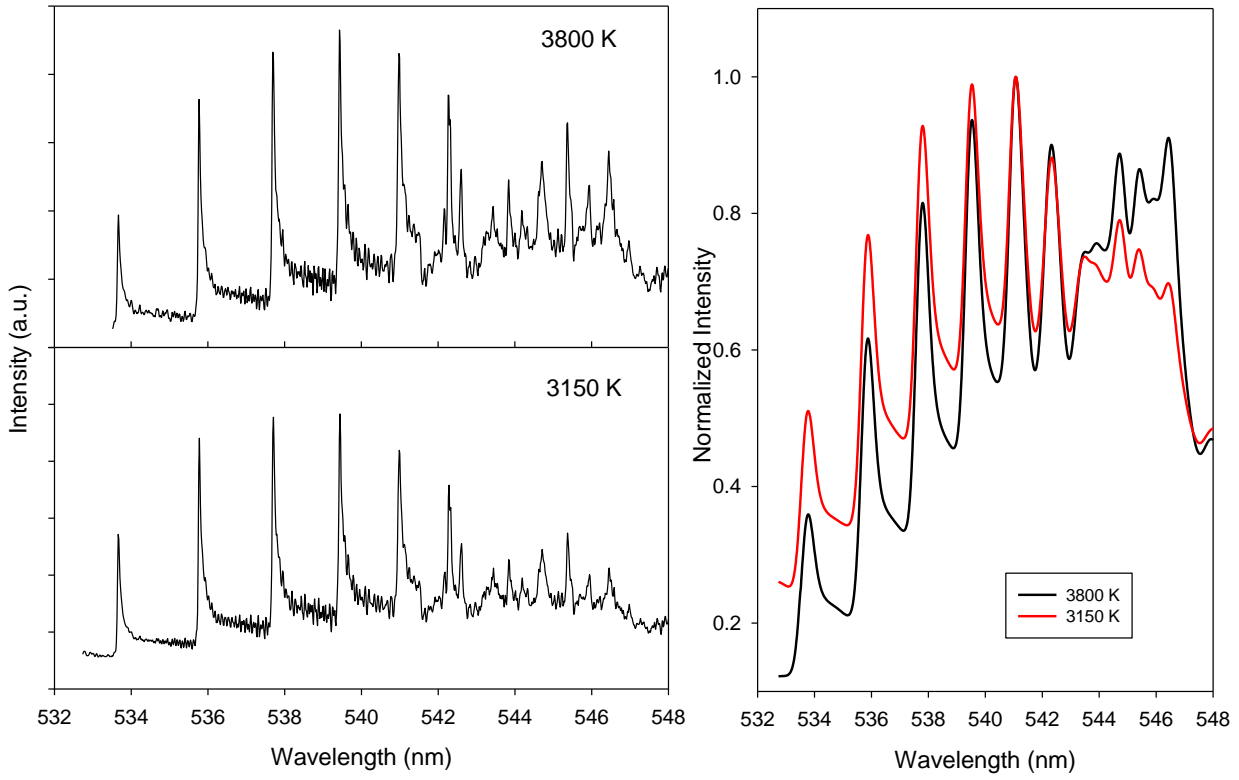


Figure 3: Experimental data from alumina placed into the heterogeneous shock tube at a known temperatures (left), and experimental spectra numerically degraded to 0.5 nm FWHM (right).

AlO as a Combustion Indicator

Emission from AlO has been widely associated with aluminum combustion. However, several studies have suggested that observation of AlO is neither a necessary nor sufficient condition for Al combustion. For particle sizes of a few microns and higher, aluminum has been found to burn, at least partially, in the vapor phase [21], resulting in emission of AlO from near the flame zone. For particles in this size range, and at elevated ambient temperatures, AlO is thus likely a good indicator of the presence of gas-phase combustion. Ignition times may be determined by the rise time of the AlO signal, and gas-phase combustion times by the duration of the signal. Indeed, these are the fundamental assumptions associated with heterogeneous shock tube measurements of Al burning time. For Al particles burning under ambient conditions, Dreizin [68] observed significant late-state Al combustion without AlO emission, and so, in those cases, AlO may only indicate the gas-phase portion of the combustion.

For nano-scale particles, most evidence suggests that the combustion most often occurs at the surface of the particle, and so little to no gas-phase AlO is formed. Indeed, Bazyn et al. [48] saw no AlO emission for most of the nano-Al combustion conditions tested, and Lynch et al. [57] saw only very small amounts of AlO in absorption during nano-Al combustion. For nano-Al combustion, AlO was observed in emission only for very high ambient temperatures (above 2500 K), where Al_2O_3 itself shows AlO emission, or for extremely high combustion rates (high pressures in oxygen). Thus, for ultrafine particles, AlO emission is not a useful diagnostic of

combustion, being neither necessary (combustion can occur without AlO emission) nor sufficient (thermal dissociation of Al_2O_3 leads to AlO emission if the temperatures are high enough).

AlO emission from aluminized explosives has been reported by several investigators [15,30,39-43]. A common observation is a strong AlO emission very early in the event (first several microseconds), followed by little or no emission at later times. Since microscale Al tends to burn on a timescale of a few hundred μs to a few ms under ambient conditions, this result is somewhat confusing. The AlO emission result in explosives can be interpreted to mean that Al combustion occurs very rapidly in aluminized explosives as a result of some activation mechanism in the violent detonation process. An alternative interpretation is that early AlO emission is not associated entirely with combustion, and that later time Al combustion (and/or AlO emission) is undetected or undersampled. Our experiments were designed to differentiate between these two cases.

Initial tests involved aluminized charges fired into air, and we compared 20% Al loaded charges with 20% Al_2O_3 loaded charges. A third case was a 20% Al loaded charge with a thin layer ($\sim 100\text{um}$) of vacuum grease spread over the exposed explosive. In each case, time-resolved spectra were recorded at low resolution (4\AA), using the collection optics focused such that the slit image produced a collimated beam that encompassed the charge, as shown in Figure 4. In this fashion, the least amount of axial spatial bias was introduced. For all cases, there was a very early peak in AlO emission, followed by a decay to undetectable levels within 20 μs . Figure 5 shows the early time spectra for the three cases.

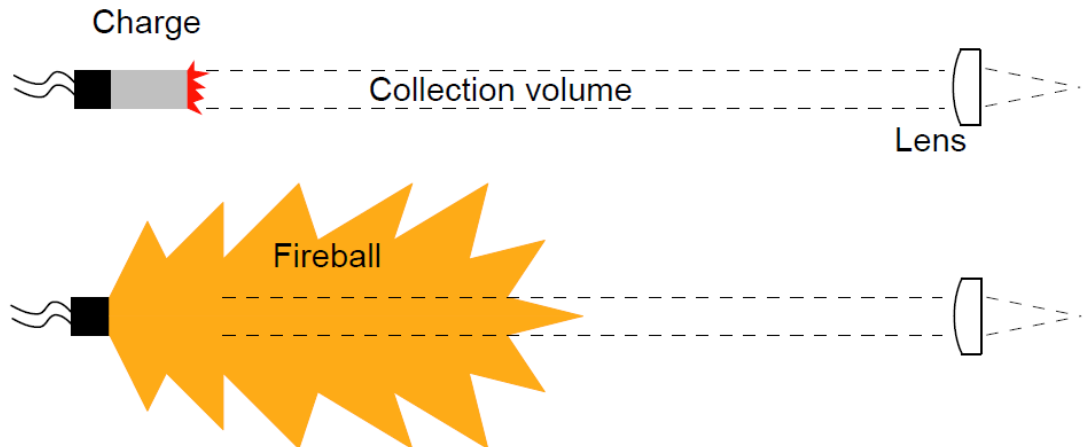


Figure 4: A schematic of the light collection configuration. Collected light is passed by fiber optic cable to the spectrograph. The collection lens is 25 mm in diameter and typically 0.5 meters from the 1 cm diameter charge.

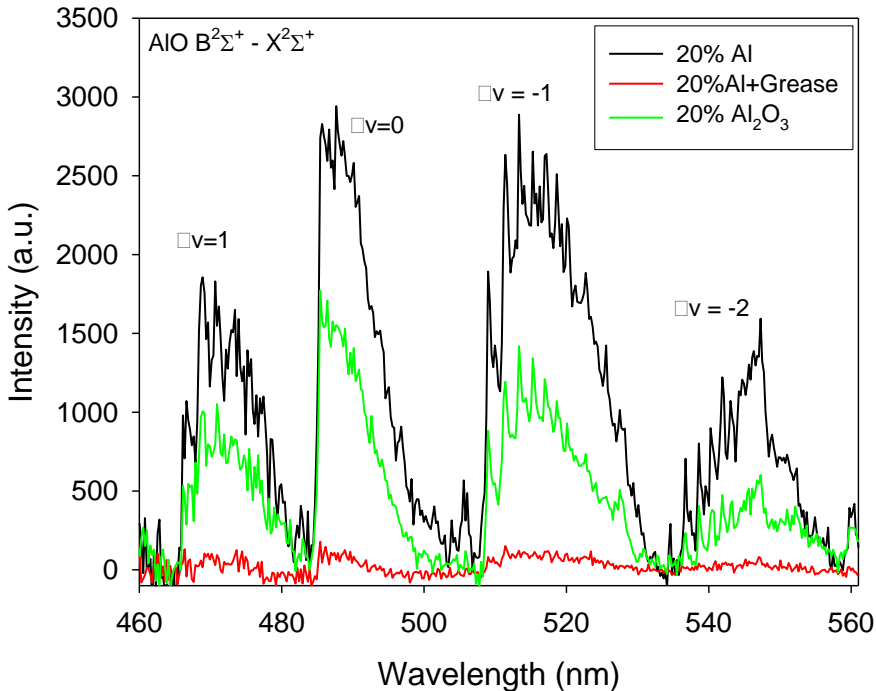


Figure 5: Early time, at 16 μ s after detonation, AlO spectra for three systems with 20% added Al or Al₂O₃.

The results shown in Figure 5 were quite unexpected. The case in which there is clearly no Al combustion (the Al₂O₃ additive) shows roughly half the AlO emission as the aluminized charge. Furthermore, a thin layer of grease on an aluminized charge almost completely eliminates the AlO signal. Thus, these results make it clear that AlO emission alone cannot be used to quantify the amount of Al combustion in these charges. There is likely some contribution from oxidation, but dissociation of the Al₂O₃ provides a non-negligible signal. The grease layer results also suggest that the emission seen by the external detector is primarily from explosive material on the outermost layer of the charge. An interpretation that is consistent with these results would be that the detonation breakout, which generates a very strong air shock [68] creates extremely high conditions soon after breakout ($T > 10000$ K) in which the outermost layer of the explosive is somewhat exposed. Under those conditions, Al will oxidize, but Al₂O₃ will also dissociate, and emission will be only weakly related to any Al reaction. A barrier coating (e.g. the grease layer) will inhibit the outer layers of explosive from seeing the high temperatures behind the air blast wave, and so emission will be greatly reduced. In this scenario, AlO is primarily a result of the breakout temperature, and not Al oxidation.

To further establish the link between AlO emission and oxidation, we tested two 20% aluminized charges (3, and 40 μ m), as well as a 50% aluminized 3 μ m charge. In each case, we obtained time-resolved AlO spectra in the configuration described above, and spectrally integrated under the AlO emission features (subtracting out a continuum background) to quantify the amount of AlO emission seen in each run.

Figure 6 tests the relationship between total AlO emission intensity and total oxidation in the particles. Total oxidation was measured by EDS in the residue, averaging over several particles and comparing oxygen content in the sample that of unoxidized aluminum (with only its

passivation layer) and fully oxidized alumina. As seen in the figure, AlO emission intensity varied significantly in these tests: the samples fired in oxygen showing three orders of magnitude more AlO emission than the identical samples fired in CO₂ and N₂. Despite this variation in AlO emission energy, there was a much smaller range of oxidation observed, between 57 and 92%, and even within that range of oxidation, total oxidation did not correlate with integrated AlO emission. For example, the two cases with the highest AlO emission had less oxidation than five other cases with at least three times less AlO emission. Significant shot-to-shot variability was observed in these tests as well. Such a result is consistent with the turbulent clustering effect of particulates in high speed flows and explosive dispersal, where particles tend to group together [69]. If groups of particles occur within the optical collection volume, then a higher signal results.

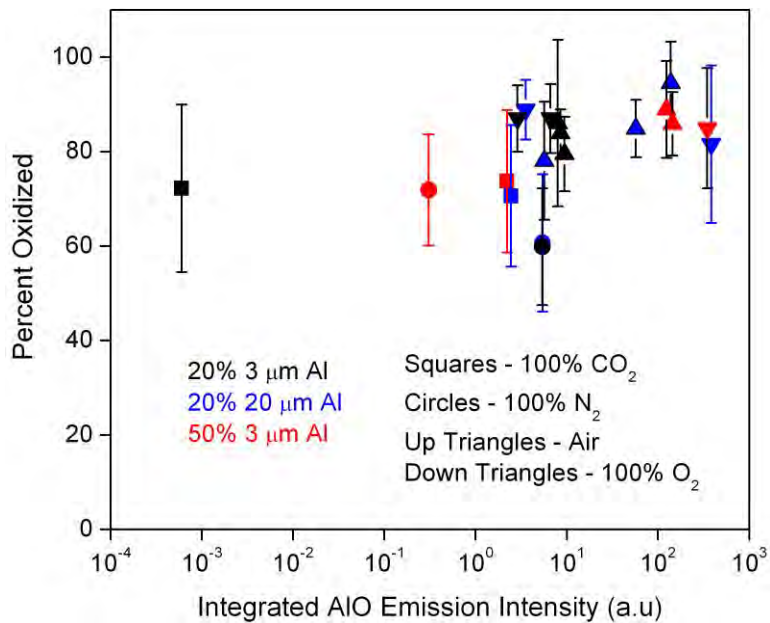


Figure 6: Integrated AlO emission intensity versus fraction of particle oxidation in the residue for three different sizes/loadings and four different ambient environments.

Explosives tests generally involve a large change in length scales for the emitting volume of gas. While the initial size of the charge is of the cm length scale in our tests, the emitting fireball expands to at least 50 cm. If the collection optics capture a cylinder 25 mm in diameter, then the fraction of the total light gathered can decrease by more than two orders of magnitude as the emitting fireball expands. Thus, light emitted early in the event (e.g. during breakout) is efficiently collected while only a much smaller fraction of the AlO emission from the larger cloud is collected. This effect was examined by taking identical charges and firing them in large chambers (1 m diameter) where the chamber diameter was much greater than the fireball diameter, and small chambers (10 cm diameter) where it was much smaller. For the 40 micron Al particles fired in air, the results are shown in Figure 7. In the larger chamber, the AlO signal decays rapidly to zero, and no AlO emission is seen after about 75 us. However, if the expansion of the fireball is restricted, forcing more of the emitting medium to be within the region of the collection optics, then a longer afterburn is detected, extending out to at least 200 μ s.

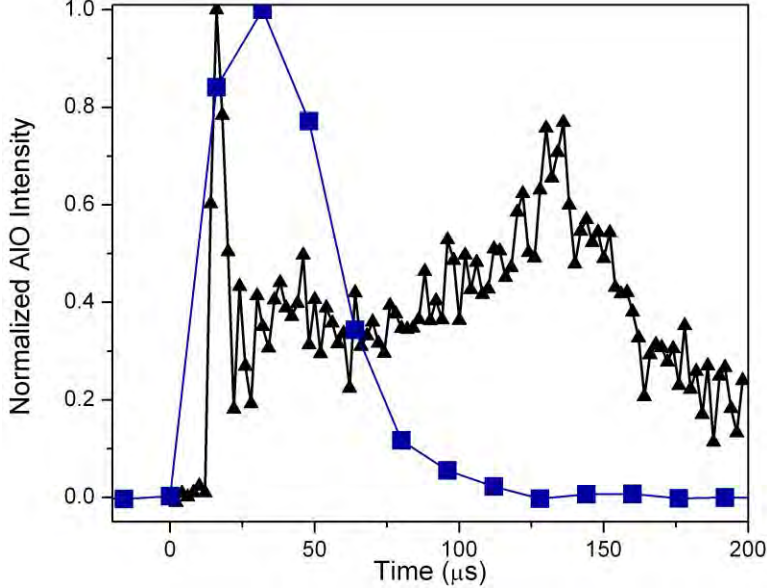


Figure 7: AlO emission intensity (normalized) for a 20% aluminized charge with 40 μm particles in a chamber where the chamber diameter is larger than the unconfined fireball (blue line) and where it is smaller than the fireball (black line).

Opacity in the fireball may also lead to biased results. Our previous work [59] suggests that aluminized explosives produce very optically thick fireballs that persist for over 100 ms after detonation. During that time period, the attenuation length is of the order of centimeters. Thus, much of the fireball from gram-scale or larger explosives is not observable to an external probe, even if the entire projected area of the fireball can be collected. To examine whether opacity is a significant effect on AlO signal, we compared 20% aluminized charges to charges having approximately half the amount of Al (~ 12 mg) placed on the external surface of the charge. While both fireballs are of similar length scales and oxidation levels are also within experimental uncertainty, more Al particles will be on the outer surface of the fireball in the latter case than in the former. The spectrally integrated AlO signal is compared for these two cases in Figure 8. A clear difference between the two cases is seen, with the case of the Al inside the explosive showing only the early peak, but the end-loaded case showing persistent AlO, even as the fireball continues to expand.

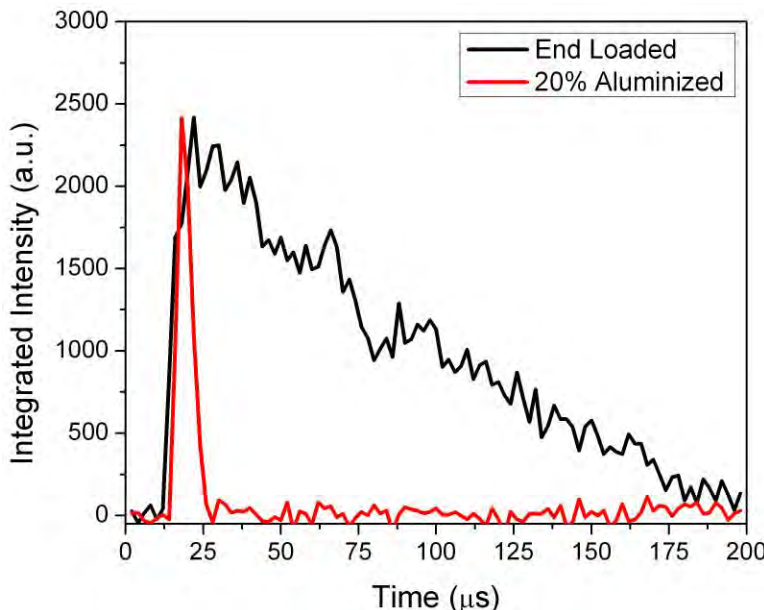


Figure 8: Two charges: one case has the aluminum (24.6 mg) premixed with the explosive (red line) and the other case has the aluminum (11.7 mg) loaded on the outside edge of the charge. When the Al burns on the outer surface of the fireball, the AlO emission intensity is greater than when most of the Al burns inside the fireball.

Analysis and Conclusions

Regarding the temperature measurements from emission measurements, interpretation of the emission “temperature” achieved from a line of sight spectrum remains a significant uncertainty. While molecular emission is strongly biased towards high temperature regions, selective absorption by colder regions of the flow can lead to errors in temperature determination. Since AlO is a short-lived intermediate that, in a standard particle diffusion flame, resides primarily in the vicinity of the flame zone, cold-zone absorption may be negligible in many standard aluminum flames. However, optical depth effects can result simply from a high number density of emitters, such as seen in dense fireballs and cloud combustion. In these cases, optical depth can interfere with temperature determination, even without a surrounding cold layer. It is precisely these conditions that are observed in many energetics tests. Under those circumstances, temperature fits to the stronger bands of AlO may not be possible with high precision, even when including a parameter for optical depth. Our results here suggest that weaker AlO $B-X$ band sequences such as the $\Delta v = -2$ sequence may provide an alternative temperature diagnostic, provided signal strengths are large enough that spectra of modest signal-to-noise ratio can be obtained. At this point, temperature can be determined empirically by extrapolation of the shock tube data from 2800 – 5000 K, but further quantification of the high v bands in the $\Delta v = -2$ may allow computational prediction of the spectrum, and associated fitting.

In terms of relating AlO emission to ignition and combustion time, several critical parameters must be considered. First, for nanoscale particles, AlO is a poor indicator since it is rarely observed, even during vigorous combustion. Second, AlO emission intensity is linearly dependent upon AlO number density (which may correlate well with combustion rate), but the emission intensity depends exponentially on temperature. Thus, when there is a significant

change in ambient temperature conditions (e.g. behind the strong blast wave following detonation breakout) emission intensity is strongly biased to conditions at the higher temperature, which may not (and probably will not) represent the conditions under which most of the metal combustion occurs. Third, when conditions yield a rapidly expanding volume of reactants (e.g. in explosives tests), collection bias in the optics can favor early time emission, which is within the collection volume, as opposed to later time emission which is distributed over the fireball. Light collection strategies that minimize these effects will lead to less bias and a more accurate picture of when AlO emission occurs. Finally, even when the entire fireball is subtended by the collection optics, optical depth of the fireball limits the amount of light from the fireball reaction that can reach the detector. Previous work [59] suggests that only light from a layer of a few cm thick on the edge of the fireball will escape the fireball and be available to reach the detector. Thus, even if AlO emission is occurring throughout the fireball, the signal reaching the detector will not be proportional to AlO number density (or combustion rate) because of absorption.

The effects listed above will tend to bias most emission measurements in explosive systems to produce large signals at breakout (high temperatures, small fireballs) followed by a rapid decay in signal as the temperatures decrease, the fireball grows, and only a small fraction of the fireball emission escapes the fireball. Such a case might lead one to believe that Al burns extremely rapidly in explosives tests, when that may not necessarily be the case. After breakout, and during fireball formation and growth, as long as temperature and pressure remain roughly constant, AlO emission should be proportional to AlO number density and thus the heat release rate resulting from the gas-phase aluminum combustion. However, in order to use AlO emission as a relative indicator of aluminum combustion in optically thick media, embedded probes[70] would have to be used at multiple locations, perhaps with stops placed within one attenuation length [71], and the results integrated over the fireball. External emission probes (the most commonly used) will necessarily undersample late time emission, even if the entire fireball is within the collection volume.

References

1. I. Glassman. Combustion. Academic Press, Orlando, FL, 2nd edition, 1987.
2. Sergio Rossi, Edward L. Dreizin, and Chung K. Law. Combustion of aluminum particles in carbon dioxide. *Combustion Science and Technology*, 164(1):209-237, 2001.
3. Carlo Badiola, Robert J. Gill, and Edward L. Dreizin. Combustion characteristics of micron-sized aluminum particles in oxygenated environments. *Combustion and Flame*, 158(10):2064-2070, 2011.
4. N. Glumac, H. Krier, T. Bazyn, and R. Eyer. Temperature measurements of aluminum particles burning in carbon dioxide. *Combustion Science and Technology*, 177(3):485-511, 2005.
5. W. K. Lewis, C. G. Rumchik, P. B. Broughton, and C. M. Lindsay. Time-resolved spectroscopic studies of aluminized explosives: Chemical dynamics and apparent temperatures. *Journal of Applied Physics*, 111(1):014903, 2012.
6. P. Bucher, R. A. Yetter, F. L. Dryer, T. P. Parr, and D. M. Hanson-Parr. PLIF species and ratiometric temperature measurements of aluminum particle combustion in O₂, CO₂ and N₂O oxidizers, and comparison with model calculations. *Symposium (International) on Combustion*, 27(2):2421-2429, 1998.

7. M. Beckstead, Y. Liang, and K. Pudduppakkam. Numerical simulation of single aluminum particle combustion (review). *Combustion, Explosion, and Shock Waves*, 41(6):622-638, 2005.
8. E.B. Washburn, J.N. Trivedi, L. Catoire, and M.W. Beckstead. The simulation of the combustion of micrometer sized aluminum particles with steam, *Combustion Science and Technology*, 180(8):1502-1517, 2008.
9. P. Bucher, R. A. Yetter, F. L. Dryer, E. P. Viceni, T. P. Parr, and D. M. Hanson-Parr. Observations on aluminum particles burning in various oxidizers. In *33rd JANNAF Combustion Subcommittee Meeting CPIA Pub. 653*, volume II, pages 449-458, 1996.
10. Joel R. Carney, J. M. Lightstone, Jon D. Koch, and Scott R. Piecuch. Visible and near infrared spectral signatures following the detonation of PETN-based explosives. In *14th International Detonation Symposium*, April 11-16 2010.
11. Jennifer L. Gottfried. Investigation of chemical processes involving laser-generated nanoenergetic materials. Technical Report ARL-MR-0736, Army Research Laboratory, 2010.
12. Ted A. Roberts, R. L. Burton, and Herman Krier. Ignition and combustion of aluminum/magnesium alloy particles in O₂ at high pressures. *Combust.Flame*, 92(1-2):125-143, 1993.
13. Z. X. Yan, J. H. Wu, S. Ye, D. Hu, and X. D. Yang. Shock-induced thermal behavior of aluminum nanoparticles in propylene oxide. *Journal of Applied Physics*, 101(2):024905, 2007.
14. V. Tanguay, S. Goroshin, A. J. Higgins, and F. Zhang. Aluminum particle combustion in high-speed detonation products. *Combustion Science and Technology*, 181(4):670-693, 2009.
15. Joel R. Carney and J. M. Lightstone. Post-detonation combustion of aluminum particles: Aluminum particle size dependence. In *Proceedings of the 6th U.S. National Combustion Meeting*, May 18-20 2009.
16. G. Schloeffel, A. Eichhorn, H. Albers, Ch Mundt, F. Seiler, and F. Zhang. The effect of a shock wave on the ignition behavior of aluminum particles in a shock tube. *Combustion and Flame*, 157(3):446-454, 2010.
17. Thuvan N. Piehler, Frank C. DeLucia Jr., Chase A. Munson, Barrie E. Homan, Andrzej W. Mizolek, and Kevin L. McNesby. Temporal evolution of the laser-induced breakdown spectroscopy spectrum of aluminum metal in different bath gases. *Appl.Opt.*, 44(18):3654-3660, 2005.
18. Olivier Varenne, Paul-Guy Fournier, Janine Fournier, Boujema Bellaoui, Abdel-Ilah Fak, Jolle Rostas, and Guy Taeb. Internal population distribution of the B state of AlO formed by fast ion beam bombardment or laser ablation of an Al₂O₃ (Al) surface. *Nuclear Instruments and Methods in Physics Research Section B: Beam Interactions with Materials and Atoms*, 171(3):259-276, 2000.
19. Jennifer Mott Peuker, H. Krier, and N. Glumac. AlO emission measurements from aluminized explosive fireballs. In *Proceedings of the 2010 Technical Meeting of the Central States Section of The Combustion Institute*, March 21-23 2010.
20. Jennifer Mott Peuker, H. Krier, and N. Glumac. Interpretations of emission measurements from aluminized explosive fireballs. In *14th International Detonation Symposium*, April 11-16 2010.
21. T. Bazyn, R. Eyer, H. Krier, and N. Glumac. Combustion characteristics of aluminum hydride at elevated pressure and temperature. *Journal of Propulsion and Power*, 20(3):427-431, 2004.

22. T. Bazyn, N. Glumac, H. Krier, T. S. Ward, M. Schoenitz, and E. L. Dreizin. Reflected shock ignition and combustion of aluminum and nanocomposite thermite powders. *Combustion Science and Technology*, 179(3):457-476, 2007.
23. T. Bazyn, H. Krier, and N. Glumac. Evidence for the transition from the diffusion-limit in aluminum particle combustion. *Proceedings of the Combustion Institute*, 31:2021-2028, 2007.
24. T. Bazyn, H. Krier, and N. Glumac. Oxidizer and pressure effects on the combustion of 10- μm aluminum particles. *Journal of Propulsion and Power*, 21(4):577-582, 2005.
25. Patrick Lynch, Nick Glumac, and Herman Krier. Combustion of aluminum particles in the transition between the diffusion and kinetic limits. In 44th AIAA/ASME/SAE/ASEE Joint Propulsion Conference & Exhibit, July 21-23 2008.
26. Patrick Lynch, Nick Glumac, and Herman Krier. Combustion of 5 μm aluminum particles in high temperature, high pressure, water vapor environment. In *43rd AIAA/ASME/SAE/ASEE Joint Propulsion Conference & Exhibit*. AIAA, July 8-11 2007.
27. Patrick Lynch, Herman Krier, and Nick Glumac. Size distribution effects in heterogeneous shock tube burntime experiments. In *45th AIAA/ASME/SAE/ASEE Joint Propulsion Conference & Exhibit*. AIAA, August 2-5 2009.
28. James Servaites, Herman Krier, J. C. Melcher, and R. L. Burton. Ignition and combustion of aluminum particles in shocked H₂O/O₂/Ar and CO₂/O₂/Ar mixtures. *Combustion and Flame*, 125(1-2):1040-1054, 2001.
29. V. Tanguay, S. Goroshin, A. Higgins, and F. Zhang. Aluminum particle combustion in high-speed detonation products. *Combustion Sci. Technol.*, 181(4):670-693, 2009.
30. Joel R. Carney, James M. Lightstone, Thomas P. McGrath II, and Richard J. Lee. Fuel-rich explosive energy release: Oxidizer concentration dependence. *Propellants, Explosives, Pyrotechnics*, 34(4):331-339, 2009.
31. Shufeng Wang, Yanqiang Yang, Zhaoyong Sun, and Dana D. Dlott. Fast spectroscopy of energy release in nanometric explosives. *Chemical Physics Letters*, 368:189-194, 2003.
32. Patrick Lynch, Herman Krier, and Nick Glumac. A correlation for burn time of aluminum particles in the transition regime. *Proceedings of the Combustion Institute*, 32(2):1887-1893, 2009.
33. Saburo Yuasa, Sakurako Sogo, and Hiroshi Isoda. Ignition and combustion of aluminum in carbon dioxide streams. *Symposium (International) on Combustion*, 24(1):1817-1825, 1992.
34. Saburo Yuasa, Yuxiu Zhu, and Sakurako Sogo. Ignition and combustion of aluminum in oxygen/nitrogen mixture streams. *Combustion and Flame*, 108(4):387-390, 1997.
35. J. Scott Miller and G. I. Pangilinan. Measurements of aluminum combustion in energetic formulations. volume 706, pages 867-870. AIP, 2004.
36. David S. Moore, Steven F. Son, and Blaine W. Asay. Time-resolved spectral emission of deflagrating nano-Al and nano-MoO₃ metastable interstitial composites. *Propellants, Explosives, Pyrotechnics*, 29(2):106-111, 2004.
37. G. I. Pangilinan and T. P. Russell. Role of Al₂O₃ chemistry in the laser-induced vaporization of Al films in air. *The Journal of Chemical Physics*, 111(2):445-448, 1999.
38. Y. Zhu and S. Yuasa. Effects of oxygen concentration on combustion of aluminum in oxygen/nitrogen mixture streams. *Combustion and Flame*, 115(3):327-334, 1998.
39. Joel R. Carney, J. S. Miller, J. C. Gump, and G. I. Pangilinan. Atmospheric effects on the combustion of detonating aluminized explosives. *CP845 Shock Compression of Condensed Matter*, pages 948-951, 2005.

40. Joel R. Carney and John Wilkinson. Atmospheric effects on time-resolved emission measurements of detonation and combustion products. In *13th International Detonation Symposium*, July 23-28 2006.
41. Joel R. Carney, J. Scott Miller, Jared C. Gump, and G. I. Pangilinan. Time-resolved optical measurements of the post-detonation combustion of aluminized explosives. *Review of Scientific Instruments*, 77(6), 2006.
42. Y. Song, W. Jing-He, W. Yan-Ping, W. Guo-Dong, and Y. Xiang-Dong. Optical investigation of shock produced chemical products in pseudo-aluminized explosive powders explosion. *Journal of Physics D: Applied Physics*, 40(11):3541-3544, 2007.
43. Ye Song, Wu Jing-He, Xue Mi-An, Wang Yan-Ping, and Yang Xiang Hu Dong and. Spectral investigations of the combustion of pseudo-nanoaluminized micro-cyclic-[CH₂N(NO₂)]₃ in a shock wave. *Journal of Physics D: Applied Physics*, 41(23):235501, 2008.
44. J. J. Weimer and I. L. Singer. Temperatures from spectroscopic studies of hot gas and flame fronts in a railgun. *IEEE Transactions on Plasma Science*, 39(1):174-179, 2011.
45. B. E. Homan, K. L. McNesby, J. Ritter, J. Colburn, and A. Brant. Investigations of the energy release mechanisms of aluminum-nickel reactive material system. 2008. Army Research Lab., Aberdeen Proving Ground, MD.
46. J. M. Lightstone, J. R. Carney, C. J. Boswell, and J. Wilkinson. Time-resolved spectroscopic measurements of aluminum oxidation in a laser ablation event. *AIP Conference Proceedings*, 955(1):1255-8, 2007.
47. S. Goroshin, J. Mamen, A. Higgins, T. Bazyn, N. Glumac, and H. Krier. Emission spectroscopy of flame fronts in aluminum suspensions. *Proceedings of the Combustion Institute*, 31:2011-2019, 2007.
48. T. Bazyn, H. Krier, and N. Glumac. Combustion of nanoaluminum at elevated pressure and temperature behind reflected shock waves. *Combustion and Flame*, 145(4):703-713, 2006.
49. N. G. Glumac, J. Servaites, and H. Krier. AlO vibrational temperature measurements from burning aluminum particles at elevated pressure. *Combustion Science and Technology*, 172:97-107, 2001.
50. P. Bucher, R. A. Yetter, F. L. Dryer, T. P. Parr, D. M. Hanson-Parr, and E. P. Viceni. Flames structure measurement of single, isolated aluminum particles burning in air. *Symposium (International) on Combustion*, 26(2):1899-1908, 1996.
51. P. Bucher, R. A. Yetter, F. L. Dryer, T. P. Parr, and D. M. Hanson-Parr. Aluminum particle gas-phase flame structure. In *34th JANNAF Combustion Subcommittee Meeting*, CPIA Pub 662, volume II, pages 295-305, 1997.
52. N. I. Poletaev and A. V. Florko. Spectral studies of the gas component of an aluminum dust flame. *Combustion Explosion and Shock Waves*, 44(4):437-443, 2008.
53. J. C. Melcher, H. Krier, and R. L. Burton. Burning aluminum particles inside a laboratory-scale solid rocket motor. *Journal of Propulsion and Power*, 18(3):631-640, 2002.
54. J. C. Melcher, R. L. Burton, and H. Krier. Combustion of Aluminum Particles in Solid Rocket Motor Flows, volume 185 of *Progress in Astronautics and Aeronautics*, pages 723-747. AIAA, Washington, DC, 2000.
55. P. Neuwald, H. Reichenbach, and A. Kuhl. Combustion of shock dispersed flake aluminum-high-speed visualization. In *37th International Conference of ICT*, 2006.

56. J. Hershkowitz, F. Schwartz, and J. V. R. Kaufman. Combustion in loose granular mixtures of potassium perchlorate and aluminum. *Symposium (International) on Combustion*, 8(1):720-727, 1991.
57. Patrick Lynch, Giovanni Fiore, Herman Krier, and Nick Glumac. Gas-phase reaction in nanoaluminum combustion. *Combustion Sci. Technol.*, 182:842-857, 2010.
58. Patrick Lynch, Giovanni Fiore, Herman Krier, and Nick Glumac. The presence of gas phase species in micro- and nano- aluminum combustion. In *47th AIAA Aerospace Sciences Meeting*, January 5-8 2009.
59. Jennifer Mott Peuker, Patrick Lynch, Herman Krier, and Nick Glumac. Optical depth measurements of fireballs from aluminized high explosives. *Optics and Lasers in Engineering*, 47(9):1009-1015, 2009.
60. Andrew Coverdill. Explosive initiation of tungsten based reactive materials in air. Master's thesis, Department of Mechanical Science and Engineering, University of Illinois, 2010.
61. Jennifer Mott Peuker. Using Optical Techniques to Measure Aluminum Burning in Post-Detonation Explosive Fireballs. PhD thesis, Department of Mechanical Science and Engineering, University of Illinois 2012.
62. T. Bazyn, H. Krier, N. Glumac, N. Shankar, X. Wang, and T. L. Jackson. Decomposition of aluminum hydride under solid rocket motor conditions. *Journal of Propulsion and Power*, 23(2):457-464, 2007.
63. J. O. Arnold, E. E. Whiting, and G. C. Lyle. Line by line calculation of spectra from diatomic molecules and atoms assuming a voigt line profile. *Journal of Quantitative Spectroscopy and Radiative Transfer*, 9(6):775-798, 1969.
64. O. Launila and L.-E. Berg. Spectroscopy of AlO: Combined analysis of the $A^2\square_i \rightarrow X^2\Sigma^+$ and $B^2\Sigma^+ \rightarrow X^2\Sigma^+$ transitions. *Journal of Molecular Spectroscopy*, 265:10-14, 2011.
65. P. Lynch, H. Krier, and N. Glumac. Micro-alumina particle volatilization temperature measurements in a heterogeneous shock tube. *Combustion and Flame*, 159(2):793-801, 2012.
66. H. Partridge, Stephen R. Langho, B. H. Lengs_eld, and B. Liu. Theoretical study of the AlO blue-green ($B^2\Sigma^+ \rightarrow X^2\Sigma^+$) band system. *Journal of Quantitative Spectroscopy and Radiative Transfer*, 30(5):449-462, 1983.
67. E. L. Dreizin. Experimental study of stages in aluminum particle combustion in air. *Combustion and Flame*, 105(4):541-556, 1996.
68. J. D. Koch, S. Piecuch, J.M. Lightstone, J.R. Carney, and J. Hooper. Time-resolved measurements of near infrared emission spectra from explosions: Pure pentaerythritol tetranitrate and its mixtures containing silver and aluminum particles. *Journal of Applied Physics*, 108(3):036101, 2010.
69. F. Zhang, D.L. Frost, P.A. Thibault, and S.B. Murray. Explosive dispersal of solid particles, *Shock Waves* 10(6):431-443, 2001.
70. Patrick Lynch. High Temperature Spectroscopic Measurements of Aluminum Combustion in a Heterogeneous Shock Tube. PhD thesis, Department of Mechanical Science and Engineering, University of Illinois, 2010.
71. R. J. Pahl and M. J. Kaneshige, Post-detonation aluminum particle temperature measurement for thermobaric explosives using two-color pyrometry, 31st International Pyrotechnics Seminar, July 11-16, 2004, Ft. Collins, Co.

CHAPTER 16: PARTICLE SIZE AND GAS ENVIRONMENT EFFECTS ON BLAST AND OVERPRESSURE ENHANCEMENT IN ALUMINIZED EXPLOSIVES

Introduction

Aluminum has been added to explosives for several decades in an attempt to increase energetic output and warhead performance. The oxidation of aluminum with high explosive detonation products is far more energetic than the decomposition of the high explosive itself, though reaction occurs on a much longer timescale. As a result of this timescale disparity, there is an optimal amount of aluminum (usually about 20-30%) that can be added to explosive formulations, above which performance is degraded. Development of such explosives has been largely empirical, with advancements achieved through a combination of limited fundamental modeling and extensive experimentation. Detailed understanding of the reaction mechanism and kinetics of aluminum reaction may enable design of explosives with higher aluminum content, resulting in significantly improved energy release without blast performance degradation.

The most critical question in the combustion of Al in aluminized explosives is under what conditions and time scales does the aluminum reaction occur, and on what critical parameters do these reaction kinetics depend. For the purposes of this study, we consider four phases of aluminum combustion, as determined by the effects of that combustion on the target. In principle, Al combustion can occur immediately behind the detonation wave in the solid explosive, and we assign this as Phase I combustion. Such combustion would contribute to the detonation pressure observed at the edge of the high explosive, manifesting itself in greater force on the external casing, and thus higher fragment velocities. After detonation breakout, the air blast wave forms and can be driven by any further reaction in the explosive products, such as Al combustion with detonation products or entrained oxygen. Blast-wave-driving reaction of Al after detonation breakout is assigned as Phase II reaction. Continued reaction of Al with air and/or detonation products can occur after blast wave departure. If the reaction produces measurable overpressure in the vicinity of the fireball that can generate work on the target (e.g. the thermobaric effect), we assign this as Phase III reaction. Slow oxidation of dispersed Al that does not produce overpressure or target damage is assigned a Phase IV. These assignments, which are by no means the only way to classify aluminum reactions, are listed along with their measurable effects in Table 1.

Table 1: A proposed breakdown of the reaction regimes for aluminum in an aluminized explosive. Increases are with respect to an explosive with inert additives.

Phase	I	II	III	IV
Key Characteristic	Reaction in detonation wave	Blast wave driving	Reaction in fireball	Late time oxidation
Approximate Reaction Timescale	μs	10-500 μs	1 - 100 ms	0.5 - 2 s
C-J Pressure Increase	YES	NO	NO	NO
Primary Blast Increase	YES	YES	NO	NO
Thermobaric Overpressure increase	NO	NO	YES	NO
Oxidation in Residue	YES	YES	YES	YES

Phase I reaction of Al has generally been considered insignificant. Several studies [1-3] have shown that the detonation velocity of aluminized explosives is not increased significantly over that of the bare explosive, suggesting that Al reaction is much slower than reactions occurring in the detonation wave. Such an observation is consistent with the experimental work on aluminum combustion that suggests that timescales for oxidation, even under extreme conditions, are generally orders of magnitude larger than detonation reaction times [4,5,6]. However, some recent work by Balas and Baker [7,8], suggests that under certain circumstances reactions of Al in some formulations are fast enough to show measurable increases in Chapman-Jouget (CJ) pressures resulting in enhanced ‘case pushing’ effects. The effect appears only in certain formulations which the authors denote “combined effects” explosives, and the group has proposed a theory that accounts for the effect [8].

Phase II, or blast-driving, reaction is a much more well-known effect. Previous studies have shown that primary blast wave strength, as measured by peak pressure and/or positive phase impulse, can be enhanced by addition of aluminum to explosives [1-3,9]. This effect is already applied to fielded warhead systems, though the details of the reaction remain poorly understood. For isolated Al particles at the 20 micron scale, for which enhanced blast effects are readily observed, reaction times in highly oxygenated environments are of the order of a few milliseconds, with significantly longer times for reaction in detonation products such as H₂O and CO₂. Yet blast waves in even kg-scale charges separate from the fireball at times that can be much less than 1 millisecond [10], leaving seemingly insufficient time for Al reaction. However, some physical effects exist that may enhance Al reactivity at early times. For example, the extreme pressures in the detonation wave can deform particles upon passing over them, leading to increases in surface area and possibly breakage or removal of part of the passivating oxide layer. In addition, immediately after breakout, pressures are extremely high in the detonation products (of the order of GPa), and thus, even though Beckstead suggests only a small pressure exponent on burning time ($\tau \sim P^{-0.1}$) [4], reactivity at these pressures may be up to an order of magnitude higher than at ambient pressure. Furthermore, temperatures immediately after breakout, at least in the outer regions of the emerging fireball can be extraordinarily high (>10,000 K) for at least 10 microseconds [11,12], leading to enhanced transport and chemical kinetics. Lastly, the work of Carney et al. [9] suggests that mixing of Al with ambient air at early times may be very rapid due to a highly turbulent interface and particles that are accelerated past the blast wave.

After detachment of the shock wave from the fireball, further reaction of metal additives will not enhance the primary blast, but may increase fireball temperature and lead to localized overpressure in the vicinity of the fireball. This thermobaric effect is desired in certain applications, and, in those cases, Phase III combustion is the preferred mode of oxidation. At these later timescales, mixing of the fireball with ambient air is extensive, and thus oxygen is available for rapid metal oxidation, in addition to combustion products. The signature of Phase III combustion is sustained temperature and overpressure on the few to few tens of millisecond timescale for small charges. Under these conditions, ambient pressures are of the order of 1 atm, and ambient temperatures in the vicinity of 1500 – 2500 K [13,14], and kinetics of aluminum under these conditions are very well known for larger particles [4] and micron-scale particles [5,6]. Heat release in Phase III is most likely the phase best simulated using previous studies of aluminum particle combustion.

For charges at the kg-scale or smaller, any overpressure in all but fully confined environments tends to decay on the timescale of a few hundred milliseconds. Despite the decay in pressure, fireball temperature can still exceed 1000 K out to a second or more [13,14]. At these temperatures, any aluminum that is not ignited will still oxidize fairly rapidly, but will not contribute to work on the target. Such Phase IV oxidation will show up in any residue analysis, but is obviously not a desirable characteristic of a formulation.

The relative amounts of oxidation that occur in Phase I – IV, and how these relative amounts depend on formulation, loading and particle size, are not precisely known. Furthermore, the fraction of reaction in each phase that corresponds to aerobic (i.e. reaction with ambient O₂) oxidation, anaerobic oxidation (i.e. reaction with CO₂, H₂O, and other detonation products, and nitridation - reaction with N₂ from the detonation products or ambient air) is also unknown. Some have speculated that aerobic channels dominate Phase II and III combustion, and thus that the oxidation rate may be limited by mixing. Few controlled experiments have addressed this critical issue, though Trzcinski et al. [2] showed that both aerobic and anaerobic channels are active in RDX-based aluminized compositions in quasi-static pressure measurements made in confined explosions.

While there have been over one hundred studies on aluminum combustion in aluminized explosives (see Vadhe et al. [15] for a partial review), several studies in particular have systematically addressed issues specific to Al reaction kinetics in these systems. Frost et al. [16] examined the critical conditions for ignition of Al in nitromethane charges, focusing on the effect of charge diameter. Brousseau et al. [3] looked at detonation velocity and air blast effects, comparing micron and nanometer sized Al. Carney et al. [9] examined the role of atmosphere on post-detonation reactivity by varying oxygen content from 0.2 to 100%. Gogulya et al. [17] added fine Al to HMX and looked at detonation velocity and optical emission noting evidence for Al reaction with detonation products in the immediate proximity of the reaction front. In a subsequent study [18], the same group conducted parametric studies leading to the conclusion that the type of explosive and Al particle size are most critical factors in aluminized explosive performance; Lefrancois et al. [19] compared aluminized explosives with explosives filled with LiF, which provides an excellent density match for Al but is inert. They verified improved blast for Al vs. LiF, with no change in cylinder velocity. McNesby et al. [10] fired 2kg charges of TNT/Al and carefully identified phases of reaction and the onset of afterburn, noting that the detachment of shock from the fireball represents a key event in the afterburn cycle.

In this work, we examine the relative roles of aerobic and anaerobic oxidation in small scale aluminized charges by varying aluminum particle diameter and ambient environment and making transient blast pressure measurements. These measurements provide baseline data against which detailed Al oxidation models can be validated, and they generate some fundamental understanding on the relevant oxidation pathways for aluminum in metallized explosives.

Experimental

Custom charges were manufactured for this project by Teledyne RISI using their standard RP-80 detonator as a template. The RP-80 uses an exploding bridgewire that initiates a detonation in 80 mg of low density PETN. The PETN detonation impinges upon the output pellet of 123 mg of PBX-9407, which is an RDX-based plastic explosive. For our experiments, RISI generated several variants of their RP-80 by mixing the output pellet with 20% by mass of each of three

classes of powder Al and an inert baseline of Al_2O_3 . The three classes of aluminum powder were standard Alliant H-2, with a mean diameter of 3 microns, a 5-10 micron class powder generated by sieving, and a 35-40 micron class powder also obtained from sieving. The alumina (Al_2O_3) powder was obtained from Alfa Aesar and had a 2 micron mean diameter. The standard RP-80 includes an external aluminum casing, which was removed prior to the experiment, leaving the charge open on top but radially confined by an inner brass case.

Charges were mounted in a 5 cm x 5 cm x 5 cm steel block that provided heavy confinement on the sides of the charge with the top of the charge unconfined. The charge assembly was placed at the bottom center of our 470 liter blast chamber. The chamber is roughly hemispherical with the walls roughly 70 charge diameters away. Piezoresistive pressure gauges (Kulite XT-190) were placed at 21.3 and 32.1 cm away from the charge in the side-on configuration in lollipop-style mounts. Data were processed to yield peak pressure (by fitting the decay to an exponential and extrapolating back to the peak) and positive phase impulse, in addition to calculating an integrated impulse versus time.

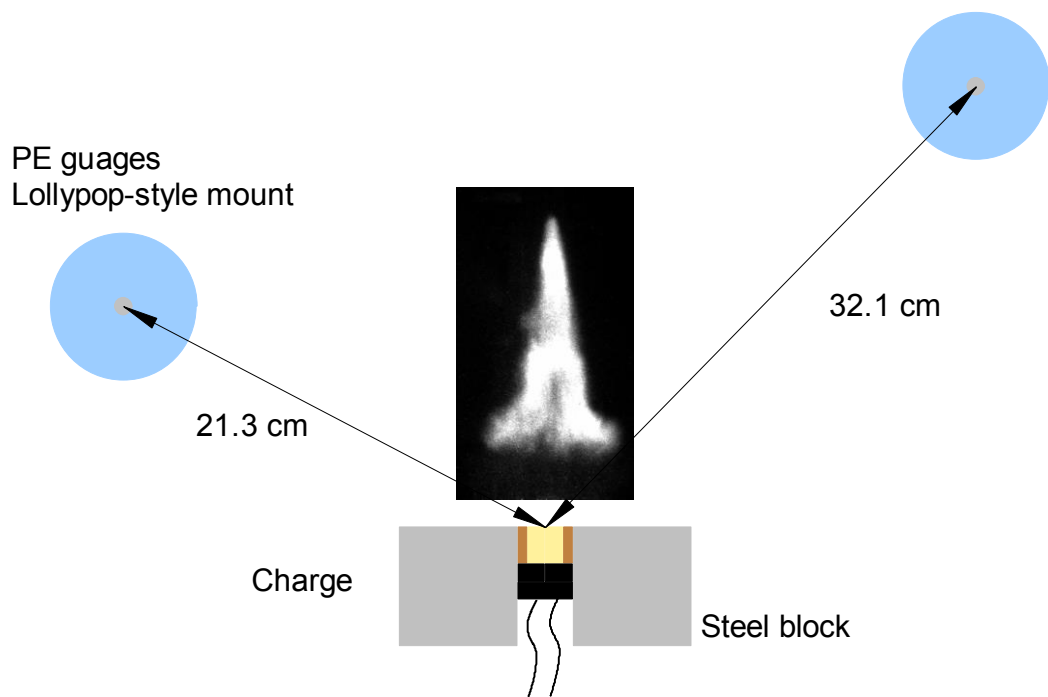


Figure 1: A schematic of the charge configuration. Piezoresistive gauges are mounted in the side-on configuration. The image in the center is taken by a high speed camera at 40 μs after initiation and shows the directionality in the explosion.

We investigated several gas phase environments, including air, oxygen-enriched air (40% O_2 in N_2), pure N_2 , and 20% CO_2 in N_2 . The latter environment was used in an attempt to distinguish between anaerobic oxidation and nitridation effects. Some tests (e.g. those in air) were repeated several times to assess repeatability and shot-to-shot variations.

Results

Blast pressure and impulse

Plots of blast pressure and impulse are shown in Figures 2a and 2b for the bare charge, inert additive, and three Al size classes. Uncertainty in impulse measurements, as estimated from repeated tests under identical conditions is approximately $\pm 5\%$ of the measurement. Peak pressure values showed similar random uncertainty, but there is also likely a further systematic uncertainty due to the finite sensor time response, and the estimation of extrapolation of the decay back to the peak pressure.

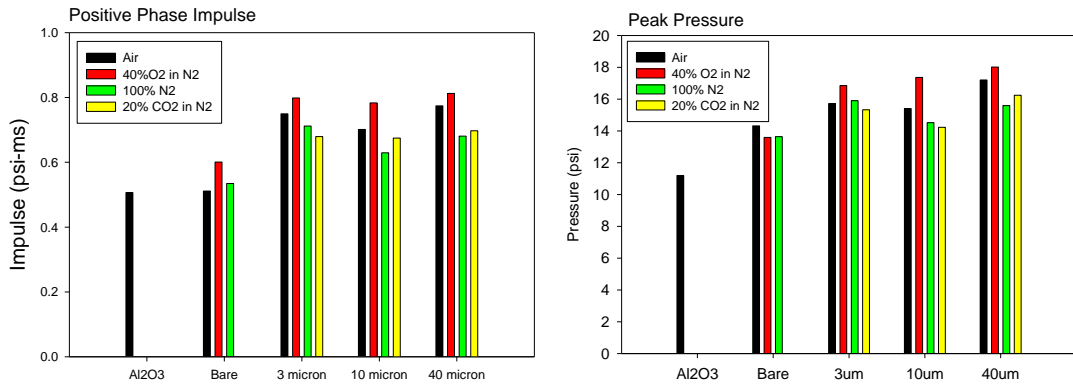


Figure 2: Sensor data from 21.3 cm from the charge surface. (a) Left: Positive phase blast impulse for five charges with different additives in four different gas phase environments. (b) Right: For the same tests as in (a), the estimated peak blast guage pressure extrapolated from the piezoresistive pressure trace. Each line represents the results of a single test.

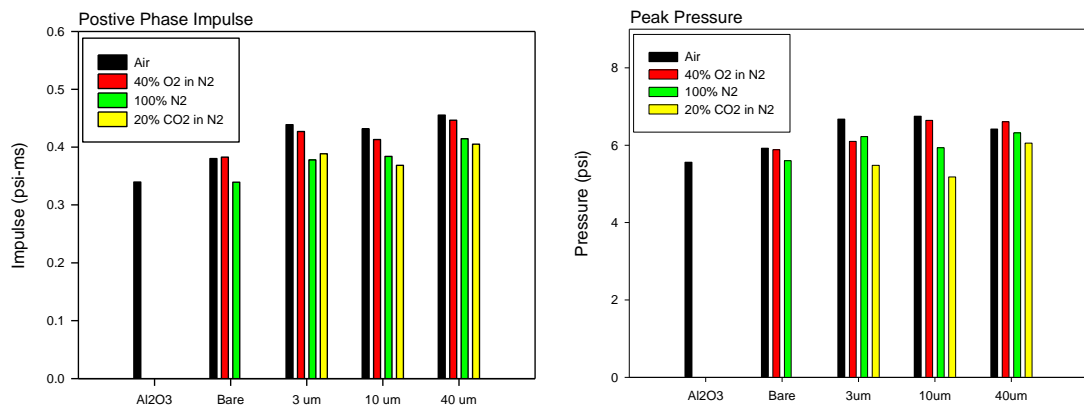


Figure 3: The same data as in Figure 2 for the farther sensor at 32.1 cm.

Several trends can be extracted from these data. In all cases, the aluminized charges produced more primary blast pressure and impulse than bare charges of the same weight and charges with inert alumina additives. Both gauge locations showed similar trends, though the magnitude of the effect was greater in the near sensor. For the most basic comparison of the (inert) alumina charge with the aluminized charges in air, the near sensor showed a positive phase impulse increase of 68% and a peak pressure increase of 30%, while the far sensor showed increases of 43 and 19%, respectively. These increases are due entirely to Phase I and/or Phase II reaction of Al with detonation products or ambient air.

To distinguish between aerobic and anaerobic contributions to the blast, one can compare the nitrogen environment cases with the air cases. Comparing the aluminized charge blast in N₂ to the alumina-based charges, the near sensor yields increases of 33% and 37% in positive phase impulse and peak pressure, while the far gauge produces 30% and 19%. Both impulse measurements were very close to half of the enhancement observed in air, suggesting an estimate for the magnitude of anaerobic effects in blast enhancement at ~50% for these cases. The peak pressures show similar relative enhancements, though somewhat higher contributions from anaerobic effects. Since impulse is an integration of several data points, and peak pressure is an extrapolation of a fit, it is likely that the impulse data are more reliable for assessing relative blast contributions.

There was no statistically significant difference between pure N₂ and 20% CO₂ cases in N₂. In four of 12 measurements the latter environment had higher blast numbers, while in the other 8, the former was stronger. It was hoped that a significant difference between these runs might suggest an estimate for the nitridation component of the anaerobic effect, but no such conclusion can be drawn from the data.

Results from tests with enhanced oxygen provided some interesting insight. If aerobic components are significant in blast enhancement, then adding additional oxygen should provide stronger blast since the increased concentration should lead to an increased aerobic oxidation rate, and this available channel may replace some reaction through the less energetic anaerobic and nitridation channels. Data from the near sensor support this assessment with small (~5%) increases in blast seen when doubling the ambient O₂ content. However, the far sensor shows negligible differences between the two environments in terms of blast, with the added-O₂ cases actually underperforming the air cases, though the difference is clearly within experimental uncertainty. However, the results are consistent across several tests and three particle classes. It is clear that doubling the O₂ concentration does not double the enhancement, suggesting that the aerobic channel may be saturated or nearly saturated. One possible explanation could be that only a certain fraction of particles are mixed enough with ambient air at early times to oxidize aerobically and that they are mostly reacted in the 20% O₂ case. In that situation, adding further O₂ would not significantly influence blast – though it may still influence overall energy release in Phases III and IV.

Particle size effects were somewhat surprising. Within the experimental uncertainty, there was no significant difference in blast enhancement over the 3 to 40 micron size range. The 40 micron sized particles would be expected to be within the d² burning law regime, and so burning times would be expected to be significantly longer than those of 10 micron particles. However, the amount of blast-driving reaction for each of these three systems is consistent in all environments. Tanguay et al. [20] have speculated that convective effects may lead to a reduction in size dependence on oxidation rate.

From these results, and some simple scaling, we can estimate the amount of aluminum reaction that drives the blast. For ideal explosives, impulse should scale as charge energy to the one-third power. Assuming a detonation energy of 6.2 kJ/kg for the PBX9407, and heat release of 31 kJ/g for the Al (the upper limit), 20% replacement of Al in the charge reacting completely would yield a blast enhancement of 21% in the far field of a spherical blast. The fact that this geometry is not entirely spherically symmetric (there is certainly a directional effect that drives the flow

preferentially upward), and that neither PBX9407 nor its aluminized variant are ideal explosives makes this calculation imperfect. However, it does suggest that an appreciable amount of the metal, quite possibly most of it, does react to drive the blast, and the fraction reacted is fairly independent of particle size in the 3-40 micron range.

Phase III effects – Impulse enhancement after primary blast

For most runs, pressure data were taken out to 10 ms. For the region from 5 – 10 ms, significant ambient fluctuations were still observed, but the fluctuations were damped and more symmetrical than early in the trace, and so by averaging the pressure in the 5 – 10 ms region, an estimate of quasi-static pressure can be obtained. Unlike blast pressure, quasi-static pressure depends linearly on the energy release, and so a more sensitive measure of reactions and reaction channels is provided.

Each run provides two measures of QSP, one from each transducer. Unlike the blast data, there is generally good agreement in magnitude of QSP from near and far sensors. Data from all runs for which late-time pressure traces are available are shown in Figure 4.

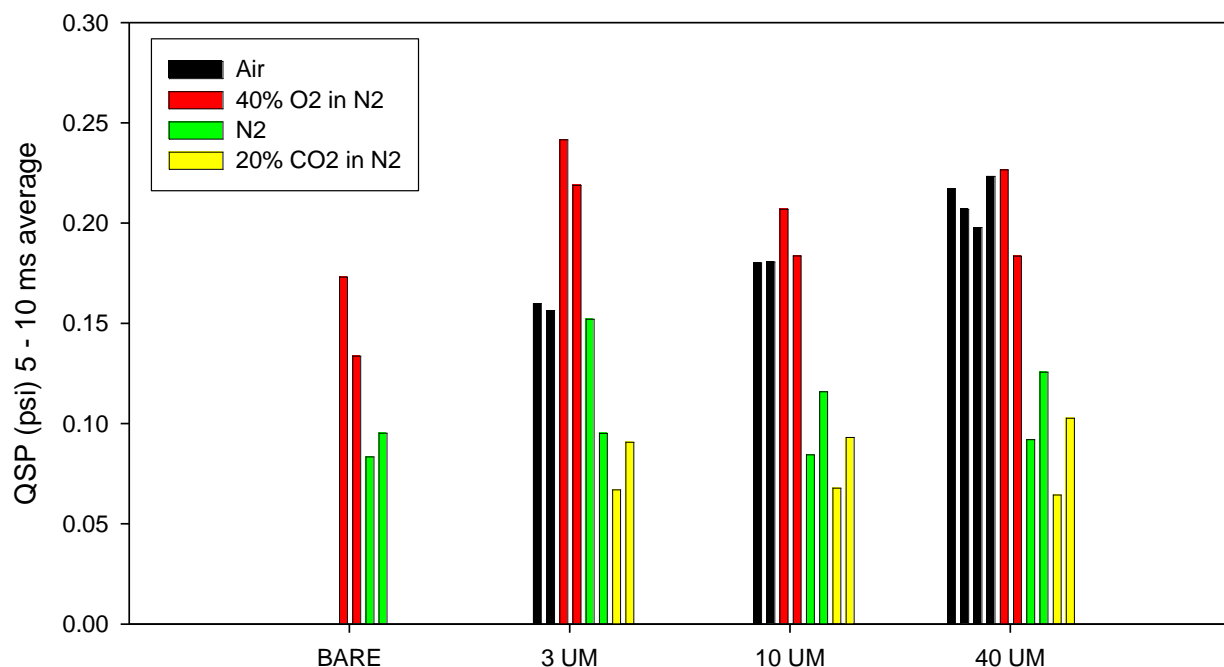


Figure 4: QSP data for 15 tests. Each test shows data from two sensors.

Bare charge data show the expected increase in QSP due to delayed reaction of the fuel-rich detonation products with air. For PBX-9407, the estimated combustion energy is 1.56 times the detonation energy, and so we expect the ratio of the QSPs for these cases to be 1.56, whereas we measure 1.72 ± 0.29 , which is well within the expected range.

Several trends are apparent. Total energy release in the aluminized charges exceeds that of the bare charge under identical conditions, though the overall effects are less pronounced than those seen in blast. Additional oxygen in the air tends to improve overall heat release by either

increasing the total amount of oxidation or shifting the aerobic/anaerobic fraction. Anaerobic enhancement of the total energy release is small, in agreement with the findings of Carney et al. [9].

To quantify these effects and provide some indication of the total amount of oxidation we can compare QSP in a relative sense to the measurements in the bare charge. We assume that the bare charge in 40% O₂ is fully oxidized by 5 ms and that its energy release is the sum of the combustion energies of the 80mg of PETN and 123mg of PBX-9407. We can then compare the relative QSP to this baseline case to estimate the amount of reaction from the aluminum additive by calculating the expected QSP for aerobic and anaerobic environments as a function of the total amount of Al reacted in each channel. The assumption that the explosive is fully oxidized in the 40% O₂ case is reasonable considering the relative QSP in the aerobic and anaerobic cases, as well as the absolute value of the QSP. For our chamber, complete oxidation of the bare charge with no energy going into case fragmentation, mount deformation, or heat losses to the mount yields a QSP of 0.22 psi, whereas the bare charge provides 0.15 ± 0.02 psi experimentally. That roughly 25% of the energy goes into deformation and heat losses is not an unrealistic estimate for such a small charge in a large (470 liter) chamber.

For the aluminized charges, the aerobic oxidation channel yields at most 31.0 kJ/g, while the anaerobic channel is about half that (17.6 kJ/g for reaction with H₂O, 15.3 with CO₂, and 11.8 for nitridation).

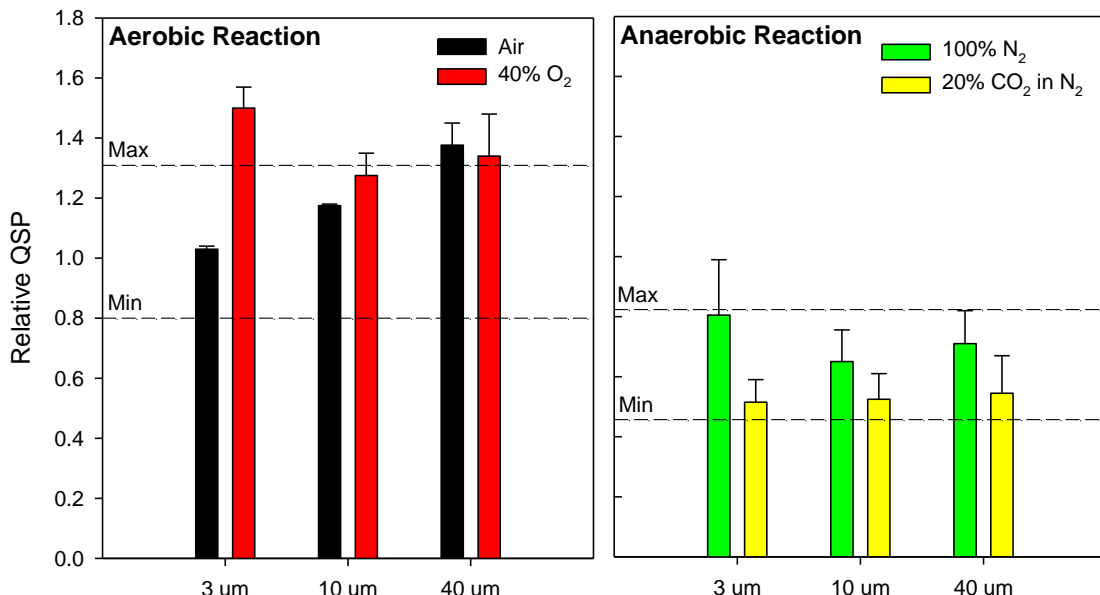


Figure 5: QSP for the runs in Figure 4, scaled to the bare charge in 40% O₂. Minimum' corresponds to no Al reaction, while 'Maximum' corresponds to complete Al reaction.

The line corresponding to “minimum” for these cases represents no aluminum reaction. This minimum QSP is the bare charge QSP corrected for the amount of displaced explosive (added aluminum displaces explosive). Thus the minimum QSP is approximately 80% of the bare charge QSP. The “maximum” is the expected QSP for full reaction of aluminum by either aerobic or anaerobic channels, and would thus be the minimum QSP plus the heat of reaction of

the aluminum in the charge times $(\gamma-1)/V$. For the air and 40% O₂ cases, the relevant comparison is shown by the aerobic limits. All results are normalized to the QSP for the 3 micron aluminized charge in air. Note that, within experimental uncertainty, the results are consistent with nearly complete Al reaction by aerobic channels. This does not mean that all reaction was with O₂, since reaction with CO₂ or H₂O leads to Al₂O₃ and products that can be further oxidized to yield identical heat release as direct aerobic oxidation.

The exception in the case of the aerobic system is the 3 micron particles, where the amount of aluminum reaction in the air case is only in the range of 50%, though the full release is attained with 40% oxygen. Anaerobic measurements in N₂ suggest that around 50% of the particles react, again with the exception being for the 3 micron case, where the anaerobic channel is pronounced. It may not be coincidental that the 3 micron particles have anomalously low aerobic oxidation in air. The results taken together suggest that the anaerobic channel for the 3 micron particles is pronounced and/or the aerobic channel suppressed. Blast data in Figures 2 and 3 show similar results, though the effect is not as apparent. A possible explanation is that smaller particles stop faster and are not thrown out into the mixing layer or even beyond the blast wave (as observed by Carney [10]), and that larger particles have a much greater chance of being propelled into oxygen rich ambient gases, leading to an enhancement of the aerobic channel.

Comparing the 20% CO₂/80% N₂ cases with pure N₂, we see that the former cases all have lower QSP than the latter, though the numbers are typically within the error limits. It is worth mentioning that while air, 40% O₂ in N₂, and 100% N₂ environments generated pressure traces that had peaks and troughs at nearly identical locations, the 20% CO₂ cases were shifted significantly at later times due to a difference in sound speeds. Thus, the relative comparison of QSP traces obtained using averages obtained over a prescribed temporal period will be least reliable for this case.

Conclusions

Charges used in this study were fairly small, and thus scaling must be considered in interpretation of these results. In general, particles in an explosive will be exposed to longer times in hot gases for larger charges, and so the oxidation levels observed here may be a lower limit on those that would be expected for larger charges. With those caveats we provide the following conclusions for 20% aluminized PBX-9407 charges:

- * Aluminum particles in the 3 – 40 micron range provide primary blast enhancement that is consistent with full reaction of the metal in the period required to drive the blast wave.
- * The blast driving reaction is approximately 50% aerobic and 50% anaerobic as determined by experiments in nitrogen environments.
- * Blast driving effects are not strongly dependent upon particle size within the 3 – 40 micron size range.
- * Quasi-static pressure measurements suggest that the oxygen in air is sufficient to fully oxidize Al within 10 ms.
- * In the absence of external oxygen, the aluminum is typically oxidized only to the 50% level, except for the smallest particle size tested (3 microns) where nearly full oxidation was observed.

Based on these experimental results, anaerobic channels cannot be neglected in simulation of aluminized charge oxidation. However, the oxygen in air plays a significant, if not dominant, role in both early and late time oxidation of added aluminum.

References

- [1] W.A. Trzciński, S. Cudziło, L. Szymańczyk, Propellants, Explosives, Pyrotechnics Volume 32, Issue 5, pp. 392–400, 2007.
- [2] W.A. Trzciński, S. Cudziło, J. Paszula, Propellants, Explosives, Pyrotechnics, Volume 32, Issue 6, pp. 502–508, 2007.
- [3] P. Brousseau, H. E. Dorsett, M. D. Cliff, and C. J. Anderson, “Detonation properties of explosives containing nanometric aluminum powder,” 2002 International Detonation Symposium, San Diego, CA.
- [4] M. Beckstead, Combustion, Explosion, and Shock Waves, Volume 41, Number 5, pp. 533-546, 2005.
- [5] T. Bazyn, H. Krier, and N. Glumac, Journal of Propulsion and Power, vol. 21, Issue 4, pp. 577-582, 2005.
- [6] P. Lynch, H. Krier, N. Glumac, Proceedings of the Combustion Institute, Volume 32, Issue 2, pp. 1887-1893, 2009.
- [7] E. L. Baker, W. Balas, C. Capellos, J. Pincay, L. Stiel, Combined Effects Aluminized Explosives, DTIC report number ADA 527993, 2008.
- [8] C. Capellos, E. L. Baker, S. Nicolich, W. Balas, J. Pincay, and L. I. Stiel, CP955, Shock Compression of Condensed Matter - 2007, edited by M. Elert, M. D. Furnish, R. Chau, N. Holmes, and J. Ngien, 2007 American Institute of Physics
- [9] J.R. Carney, J.M. Lightstone, T.P. McGrath II, R. Lee, Propellants, Explosives, Pyrotechnics, Volume 34, Issue 4, pp. 331–339, 2009
- [10] K.L. McNesby, B.E. Homan, J.J. Ritter, Z. Quine, R.Z. Ehlers, B.A. McAndrew, Propellants, Explosives, Pyrotechnics, Vol. 35, Issue 1, pp. 57–65, 2010.
- [11] N. Glumac and H. Krier, Early Time Spectroscopic Measurements during High Explosive Detonation Breakout into Air, 44th JANNAF Combustion Joint Subcommittee Meeting, Washington DC, 2010.
- [12] J.D. Koch, S. Piecuch, J.M. Lightstone, J.R. Carney, and J. Hooper, J. Appl. Phys. 108, 036101 (2010)
- [13] K. C. Gross, “Phenomenological Model for Infrared Emissions from High-Explosive Detonation Fireballs,” Doctoral Thesis, Air Force Institute of Technology, September 2007.
- [14] J. M. Gordon, “Shock Wave Dynamics of Novel Aluminized Detonations and Empirical Model for Temperature Evolution from Post-Detonation Combustion Fireballs,” Doctoral Thesis, Air Force Institute of Technology, March 2011.
- [15] P. P. Vadhe, R. B. Pawar, R. K. Sinha, S. N. Asthana and A. Subhananda Rao, Combustion, Explosion, and Shock Waves, Volume 44, Number 4, pp. 461-477, 2008.
- [16] D.L. Frost, S. Goroshin, J. Levine, R. Ripley, and F. Zhang, CP845 Shock Compression of Condensed Matter – 2005, American Institute of Physics
- [17] M. F. Gogulya, M. N. Makhov, A. Yu. Dolgorobodov, M. A. Brazhnikov, V. I. Arkhipov, and V. G. Shchetinin, Combustion, Explosion, and Shock Waves, Vol. 40, No. 4, pp. 445–457, 2004

- [18] M.F. Gogulya, A.Yu. Dolgorodov, M.N. Makhov, M.A. Brazhnikov, and V.G. Shchetinin, "Detonation performance of aluminized compositions based on BTNEN," 2002 International Detonation Symposium, San Diego, CA.
- [19] A. Lefrancois, J-Y Grouffal, P. Bouinot, S. Mencacci, "Temperature and Pressure Measurements Comparison of the Aluminized Emulsion Explosives Detonation Front and Products Expansion," 2002 International Detonation Symposium, San Diego, CA.
- [20] V. Tanguay, S. Goroshin, A. J. Higgins, and F. Zhang, Combustion Science and Technology, Vol. 181, pp. 670-693, 2009.

CHAPTER 17: TUNGSTEN COMBUSTION IN EXPLOSIVELY INITIATED W/ZR MECHANICAL ALLOYS

Introduction

Tungsten is a commonly used material for providing penetration and/or densification in warhead applications due to its very high density (S.G. = 19), strength, stiffness, and modest expense. Though it is added to some explosives (e.g. the Dense Inert Metal Explosives) as a powder, the fine metal additive does not oxidize appreciably in these applications, even though it is subject to detonation temperatures. Tungsten oxidation is moderately energetic in a thermodynamic sense. The reaction of $\text{W} + 3/2\text{O}_2 \rightarrow \text{WO}_3$ provides 4.6 kJ/g of metal, which is low compared to common energetic metals such as Al (31.1 kJ/g) and Zr (12.1 kJ/g) or even iron (7.4 kJ/g). However, 4.6 kJ/g is very close to the detonation energy of TNT, and thus tungsten metal remains a potentially energetic material, provided rapid reaction can occur. Indeed, uranium penetrators, which demonstrate pronounced behind armor blast effects due to metal combustion [1-2], generate only 4 kJ/g. Furthermore, on a volumetric basis, tungsten energy density (88.5 kJ/cm³) is surpassed only by boron and tantalum.

Though tungsten generally resists rapid oxidation, some applications have demonstrated explosive energy release. Dust explosion data for pure tungsten powders in air are available [3], and some pyrotechnics use tungsten powder for color [4], and rapid combustion is observed with as little as 3% oxidizer. Recent emphasis on dense energetic structural materials and fragments has renewed interest in tungsten, where it is often used as a densifier in alloys or composites with more reactive metals. However, if tungsten can be made to oxidize rapidly, significant potential applications may result.

Our approach is to use the mechanical alloying techniques of Dreizin [5] to make tungsten/zirconium alloys mixed mechanically at the nanoscale. Zirconium ignites rapidly and burns at high temperatures. Our hypothesis is that W, if in intimate contact with the burning Zr in an oxidizing atmosphere, may combust on a short enough timescale such that explosive work can be realized.

Experimental

Mechanical alloying (MA) was performed in a planetary ball mill which had a continuously variable planet to sun ratio, set for this work at 2.0. There were 33 stainless steel balls of 10 mm diameter used as the grinding media in each 80 ml stainless steel grinding jar. The mass ratio of the balls to the powder (charge ratio) was 10:1. Milling was conducted in 5 hour increments, with at least 1 hour pause before resuming. Milling was performed with hexane added as a process control agent. The hexane was removed after 20 hours of milling by vacuum drying.

Several different alloys and combinations of materials were tested. As a baseline, pure zirconium and pure tungsten oxide materials were used. The starting materials used for the tests were off-the-shelf powders of Zr (2-3 micron APS) and W (-325 mesh), both from Alfa Aesar. SEM micrographs of the starting materials and milled materials are shown in Figure 1. After milling, the powder morphology resembled that of flakes with very irregular shapes. Large flake dimensions were of the order of a few microns to a few tens of microns. Flake thickness was on the scale of roughly one micron.

X-ray diffraction analysis was performed on powders before milling, after milling, and after testing using a Siemens-Bruker #D5000 with a Cu X-ray tube operating at 40 kV and 30 mA. Sieved residue powders of less than 106 µm particle size were placed without compaction in a sample dish, and a locked couple scan was performed at 1.714°/min, 0.02°/data point. The

range of the scan depended on the compounds expected to be in the powder, but typically covered the range of $2\theta = 20^\circ$ to 100° . Additional high resolution scans were conducted on areas of interest; these scans were performed at a rate of $0.3^\circ/\text{min}$ and $0.01^\circ/\text{data point}$. Data were analyzed using the Jade 9 X-ray analysis software.

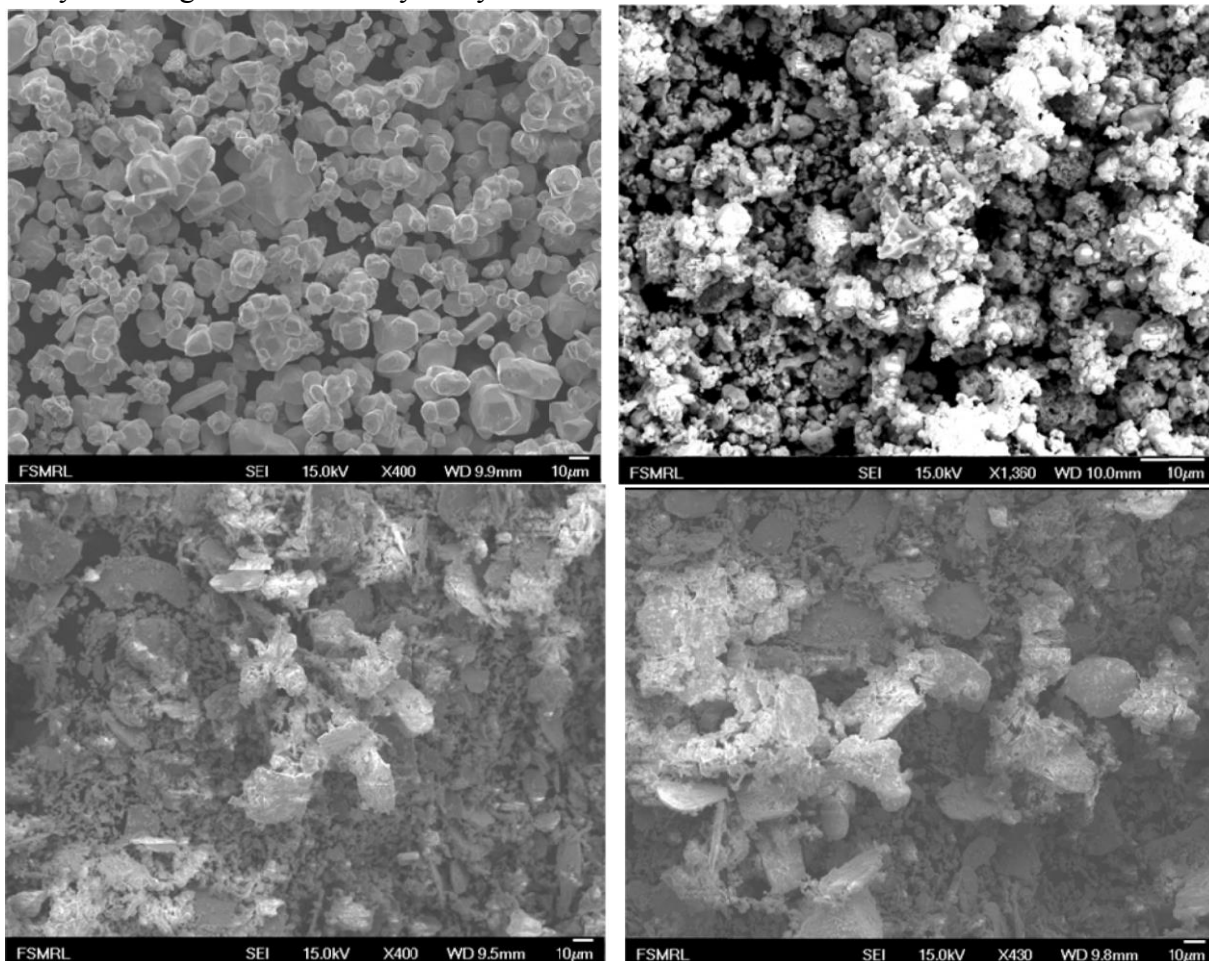


Figure 1: Starting materials before milling – W (top left) and Zr (top right). As-milled powders before compaction – 25% Zr/75% W (bottom left) and 43% Zr/57% W (bottom right).

Figure 2 shows the XRD spectra of the powders before and after milling. No new phases are shown to arise as a result of milling, and the mixture retains the elemental signature with the expected line broadening associated with a reduction in crystallite size.

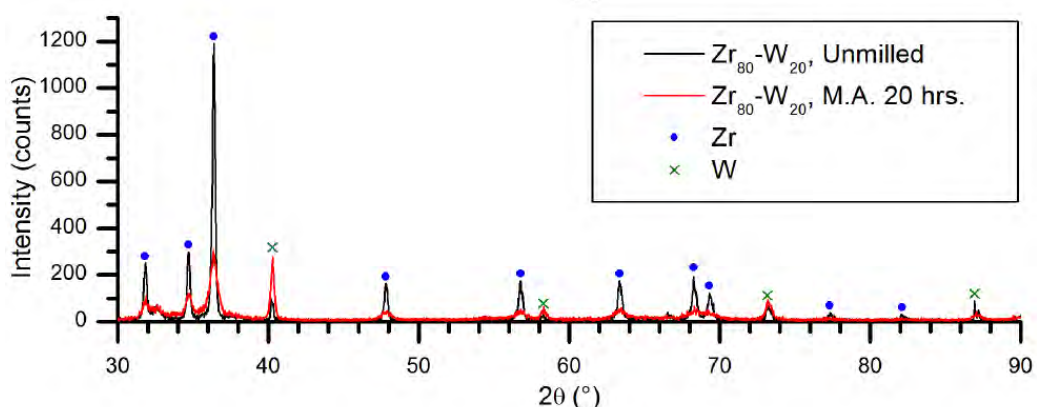


Figure 2: X-ray diffraction spectrum for powders before and after ball milling.

All materials were pressed into disk shaped pellets of 12.7 mm in diameter at 60-70% TMD using a uniaxial compressive load of 13-16 tons in a 50 ton press. For each test, 5 cm³ of material was manufactured and divided into 11 identical pellets. Pellets were arranged in a dodecahedron around a central 18g nitromethane charge, as shown in Figure 3. The sample holder was made using stereolithography from an epoxy resin, and the holder served to contain the liquid charge as well as support the reactive material pellets. The support was nominally 2.38 mm thick, except at the bottom of the recesses for the RM pellets, where the thickness was 0.5 mm. This geometry was chosen to loosely approximate a spherically symmetric charge while allowing reactive pellets to be made using simple cylindrical dies and uniaxial compression. For these experiments, the charge to RM mass ratios varied from around 1 to just over 2.



Figure 3: The explosive configuration with disk shaped RM pellets surrounding an 18g nitromethane central charge. Pellet disk diameters are 12.7 mm. The detonator is a Teledyne RISI RP-81.

Charges were detonated inside a 1.2m x 1.2m x 1.2m steel blast chamber which is fully enclosed such that the tests occur under constant volume conditions. The primary diagnostics for these measurements were transient pressure diagnostics from side-on Kulite XT-190 piezoresistive pressure transducers on lollipop-style mounts at 45.7 cm from the charge, and quasi-static chamber pressure monitored at the wall. Pressure traces were analyzed using standard methodology to yield blast parameters (peak pressure and positive phase impulse) which provide a measure of early time reactivity that drives the blast wave, as well as quasi-static pressure (QSP) that provides a measure of total energy release due to reactivity of the explosive and reactive material. Residue from each test was also collected for analysis.

Results

The critical performance results of the test series are shown in Table 1 below. Many other materials were tested, including mechanical alloys of boron, aluminum, and hafnium with tungsten, though the most striking results were seen with zirconium. The table provides quasi-static pressure, which is obtained by fitting the wall pressure trace to an exponential decay over the 20-100 ms period and extrapolating back to the instant of detonation. Pressure decay in this time period is very small. The blast pressure is the peak pressure of the primary blast wave.

Alloy	Vol (cc)	Mass % W metal	Total Mass (g)	Zr Mass (g)	Zr Energy (kJ)	Total Energy (kJ)	Blast Pressure (psi)	Blast Impulse (psi-ms)	QSP (psi)
WO ₃ inert	5	0	25.5	0	0	0	24	3.38	2.6
Zr	5	0	19.7	19.7	238	238	31	3.44	8.9
80Zr - 20W	5	33	26.8	17.8	215	255	30	3.67	8.8
60Zr - 40W	5	57	34.5	14.7	177	267	29	3.36	9.4
40Zr - 60W	5	75	40	10	121	258	27	-	9.2

Table 1: Results from the five tests examined. Blast pressure is the side-on peak pressure of the primary blast wave at 45.7 cm from the charge.

For analysis, the QSP of the WO₃ case was used as the inert baseline, and this value was subtracted from all reactive QSP cases. The QSP difference (net-QSP) was then assumed to be the contribution to QSP from the metal reaction with detonation products and/or air. For the pure Zr case, the observed QSP is consistent with 86% combustion of the Zr metal, which is a fairly typical of a very reactive material under detonation initiation without extensive ejection of unreacted metal from the fireball. Addition of the tungsten in these volume-fixed tests results in an increase in pellet mass, but a decrease in zirconium mass. Thus, if only the Zr reacted, the QSP would decrease as W replaces Zr. However, net-QSP rises slightly, closely tracking the total energy content of the pellet including contribution from tungsten combustion.

Representative pictures of the residues are shown in Figure 4 below. Pure zirconium combustion results in primarily large spherical product in the 10-50 micron size range, with some smaller non-spherical residue as well. The residue from the mechanical alloys shows similar spherical product, as well as a larger fraction of irregular shapes which, according to EDS analysis, primarily contains the tungsten residue.

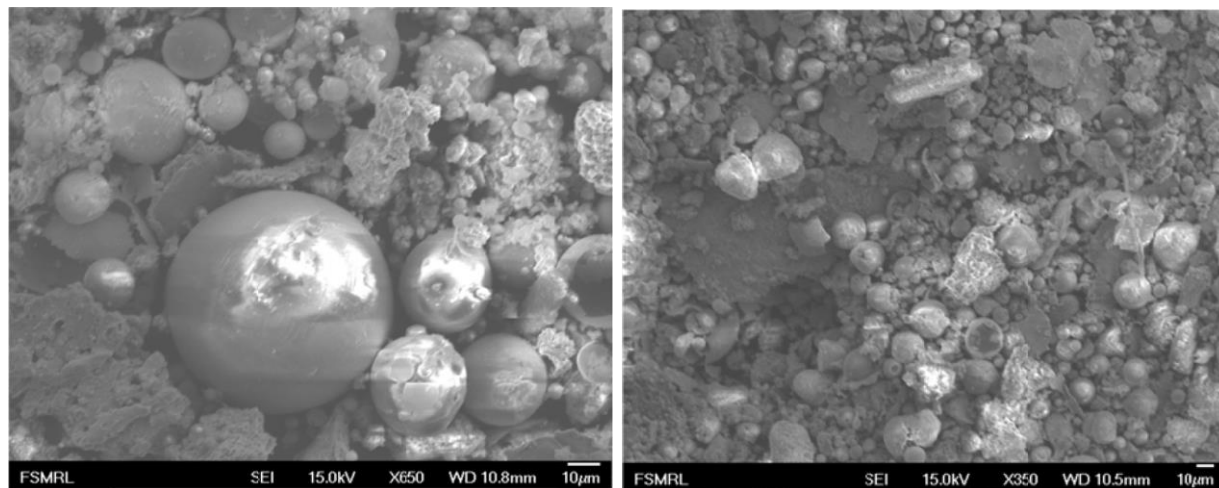


Figure 4: Residue from pure Zr combustion (left) and the 25%Zr/75%W case (right).

XRD of the collected residue showed peaks for tungsten, zirconium and both monoclinic and tetragonal ZrO₂. An XRD of the residue in the 47%Zr case is shown in Figure 5. A high resolution scan in the 22 – 25 degree range where any crystalline WO₃ would appear shows no evidence of that species. Thus, it may be concluded that any oxide of tungsten produced in this reaction is likely amorphous.

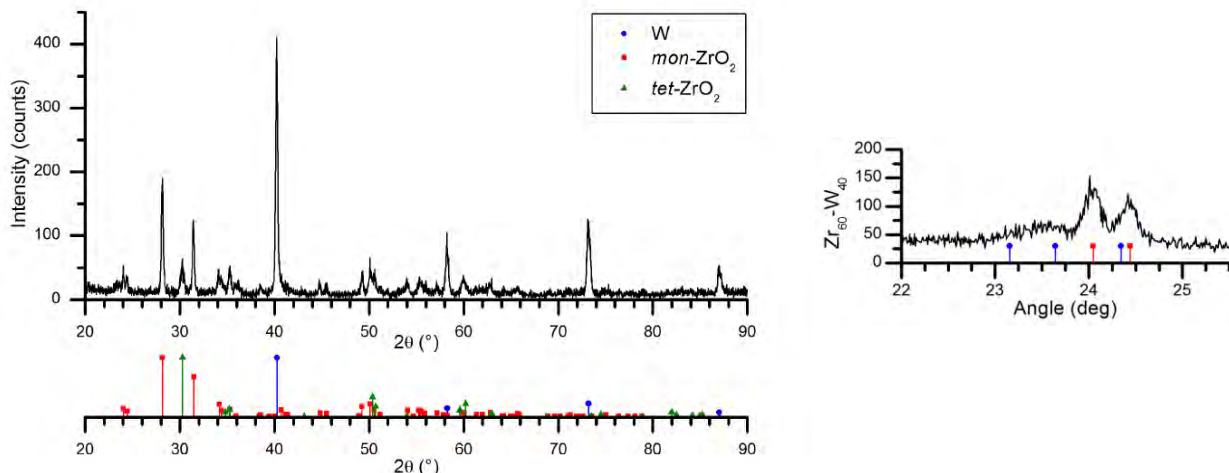


Figure 5: XRD of the residue 47%Zr/53%W test. Left: A low resolution scan showing the main contributing species. Right: A high resolution scan in the vicinity of the expected WO₃ crystalline peaks (blue lines). Only features corresponding to monoclinic ZrO₂ (red lines) are distinguishable.

Table 2 shows the quantitative data from the XRD measurements as output by the Jade-9 software. Since amorphous products are not detected by XRD, any amorphous product of Zr or W combustion will not be included in the phase analysis. Assuming that the elemental ratios are the same as the initial sample, the XRD data can be processed to estimate the amount of amorphous WO₃ (a-WO₃) in the final product and the fraction of tungsten that is combusted (%W Combustion). In addition, an estimate can be made of the expected thermal output of the reaction (Output XRD). The data in the table suggest that between 74 and 93% of the tungsten metal was fully oxidized. The expected energy outputs from the residue measurements are all between 16 and 23% high, including the case of pure Zr combustion.

Sample	Mass %	Measured XRD Mass Fractions			Processed XRD Mass Fractions			%W Combustion	Output XRD (kJ)	Output Xptl (kJ)
		Zr	W	m-ZrO ₂	t-ZrO ₂	W	ZrO ₂	a-WO ₃		
Zr	100	0	24	76	0.0	100.0	0.0	0.0	233.3	200.8
Zr/W	67	9.0	89.6	1.4	6.8	69.2	24.0	73.6	245.1	198.8
Zr/W	43	6.6	21.1	72.3	3.2	44.8	52.1	92.9	261.4	218.9
Zr/W	25	14.9	80.7	4.4	4.7	26.5	68.8	92.1	246.9	206.5

Table 2: Processed XRD data of the combustion residues, assuming the same elemental Zr/W balance as in the unreacted sample, with any tungsten that does not appear as elemental W assigned to amorphous WO₃.

Discussion

The results shown above show clearly that tungsten combustion must be occurring during the time period in which thermal output generates pressure in the chamber. If only Zr combustion was occurring, then there is enough energy to account for overpressure observed in the 67% Zr case, but not enough to account for the 43% Zr and 25% Zr cases. In the latter case, the observed energy output is 173% of the total possible Zr combustion energy output. Even in that case, an absolute minimum of 63% of the W would have to have been burned to achieve the experimental result.

Perhaps a more realistic estimate of the amount of tungsten combustion can be obtained by comparing the relative net output of the alloyed cases with that of the bare Zr metal case, where approximately 86% of the maximum possible Zr output is realized in the QSP. This analysis is shown in Figure 6. With only Zr reaction occurring, the relative output would decay monotonically with W addition. Even at 75% combustion of the W, a decay in output is expected. However, output is mostly steady for these runs, suggesting nearly complete combustion of the tungsten. While an exact fraction of tungsten combustion in these tests cannot be identified, it is clear that the vast majority of the tungsten is reacting on a rapid enough timescale to contribute to the chamber pressure rise in the 20-100 ms period.

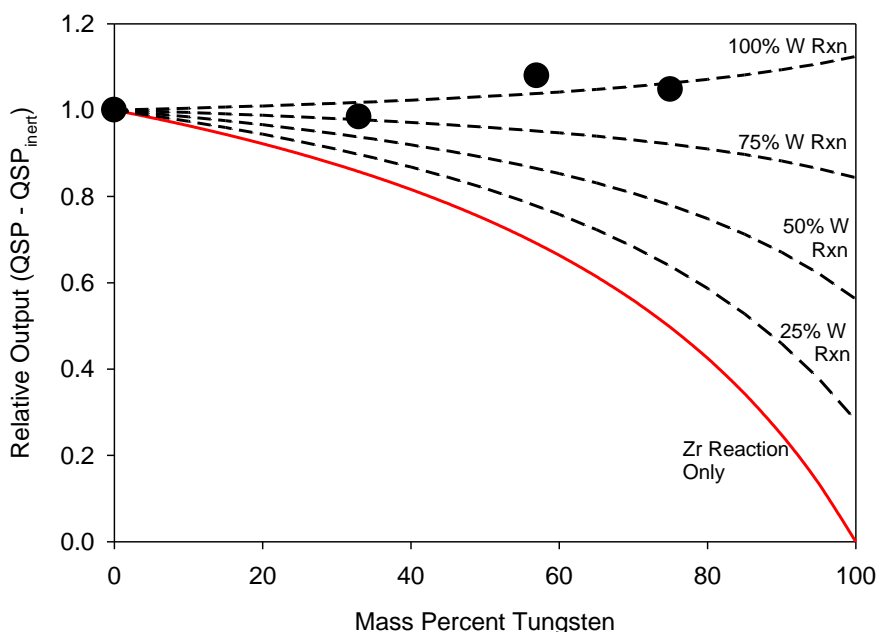


Figure 6: Relative Net-QSP, normalized to the pure Zr case, for the alloys tested here. Net-QSP is the total QSP minus that of the test with inert (WO_3) pellets. Trend lines show expected net-QSP for differing degrees of tungsten reaction.

The timescale over which tungsten reaction occurs appears to be of the same order as zirconium, or very slightly slower. Some very rapid, blast driving reaction does appear to be occurring in the Zr samples, as evidenced by the increase in blast pressure for the Zr case as compared to the WO_3 sample. As more W is added, this blast enhancement decreases, suggesting that Zr is more reactive than W. However, the positive phase impulse for the Zr cases is similar to the Zr/W cases, and the impulse traces, shown in Figure 7, show very similar behavior for the Zr and Zr/W alloys. In all reactive alloy cases, there is a marked deviation from the inert case beginning about 2 ms. By 10 ms, the slope of the impulse trace matches that expected for the measured QSP for both reactive and inert cases, suggesting that any heat release

is essentially complete by this time. These data then suggest that the reactive Zr/W alloys have a reaction timescale of less than 10 ms, and of comparable magnitude to that of pure fine Zr powder.

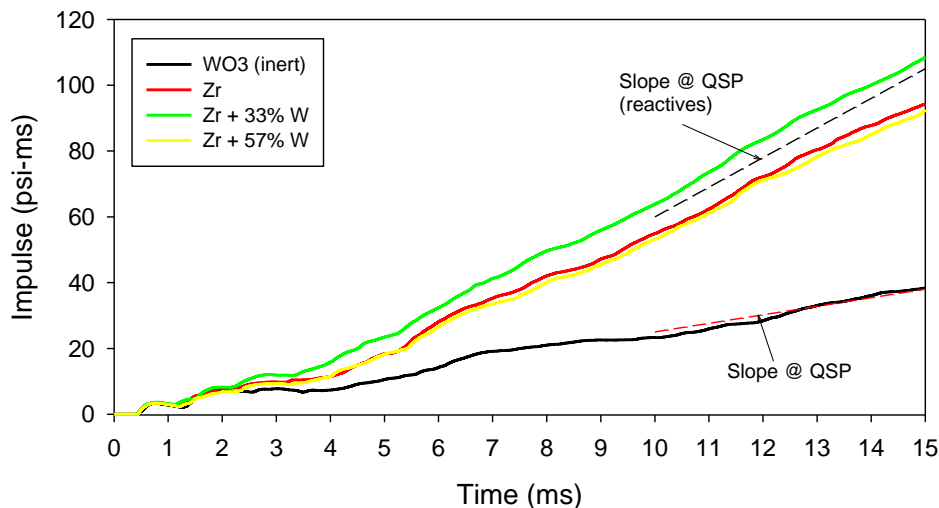


Figure 7: Time integrated, side-on impulse at 45.7 cm for four of the five tests. In the 75% W alloy, the sensor failed soon after the blast peak was observed.

While rapid and extensive tungsten oxidation is clearly observed in these experiments, the alloys tested were still relatively porous at roughly 60% TMD, which is near the maximum that can be obtained by cold pressing. A critical test of this potential of this technology for possible applications would be to test samples at near full density through manufacture by hot pressing techniques.

Conclusions

Rapid tungsten oxidation has been observed in W/Zr mechanical alloys with up to 75% tungsten by mass when explosively initiated. The timescale of reaction is at most a few 10s of milliseconds, which is slower than that of Zr, but rapid enough to contribute to overpressure in confined explosives applications. The product of combustion is most likely amorphous tungsten oxide. Quantitative analysis suggests that at least 63% of the tungsten is oxidized, though oxidation of greater than 90% is most consistent with XRD and QSP data.

References

- Bertrand,Brian P. ; Peterson,Robert L. ; Dunbar,Sterling A. ; Abrahams,Rodney R, "Blast Pressures Induced by the Impact of Kinetic Energy Penetrators on Steel Targets in an Enclosed Range," Army Ballistic Research Lab, Aberdeen Proving Groud, Final Report, Feb. 1981, ADA098039.
- Patrick, Michael A. ; Cornette, J. C., "Morphological Characteristics of Particulate Material Formed from High Velocity Impact of Depleted Uranium Projectiles with Armor Targets," Air Force Armament Lab, Eglin AFB, Final rept. Oct 77-Oct 78, ADA067121.
- M. Hertzberg, IA. Zlochower, KL. Cashdollar, Metal dust combustion: explosion limits, pressures, and temperatures, 24th Symposium (International) on Combustion, 1992.

4. G. V. Ivanov, A. A. Reshetov, A. M. Viktorenko, V. G. Surkov and L. N. Karmadonov, Powdered tungsten combustion in pyrotechnic mixtures, Combustion, Explosion, and Shock Waves, Volume 18, Number 2, 142-145.
5. X. Jianga, MA. Trunova, M. Schoenitz, RN. Davea and EL. Dreizin, Mechanical alloying and reactive milling in a high energy planetary mill, Journal of Alloys and Compounds, Volume 478, Issues 1-2, 10 June 2009, Pages 246-251

CHAPTER 18: ULTRAVIOLET (UV) ABSORPTION SPECTROSCOPY IN OPTICALLY DENSE FIREBALLS USING BROADBAND SECOND HARMONIC GENERATION OF A PULSED MODELESS DYE LASER

Introduction

Combustion measurements within the fireballs generated by explosives and other energetic materials have several diagnostic hurdles owing to the multiphase dynamics, the high temperatures, short time scales, and high optical depths of the combustion event. Explosives are often energetically enhanced by the addition of solid phase fuels like metal particles which create high temperature environments of particulate and gas phases within the fireball. The relevant diagnostic time scales within explosives systems are typically on the order of several microseconds necessitating diagnostics which can be performed with this time resolution.

One of the key diagnostic capabilities is the characterization of temperatures within the fireball and the ability to monitor chemical species that evolve during the combustion. Optical techniques are more robust within the high temperature, multiphase environments where mechanical probes methods are difficult to implement due to temperature limitations and slow response time. In fireballs containing reactive particles, it is possible that the temperatures of the solid phase and gas phase may be different due to kinetically limited and diffusion limited particle reactions. Spectroscopic diagnostics may provide the capability to analyze the possible separation of particle and gas temperatures by examining the gas phase components of the flame thereby demonstrating the regimes of particle combustion.

The high luminosities of fireballs of energetic materials lend to the prevalence of emission based diagnostics. The condensed phase temperature is often determined by using optical pyrometry or by fitting the continuum from the condensed phase to a Planck distribution, and this technique has been used as a temperature diagnostic in energetic materials in many studies.^{1, 2} There is also precedent for using metal salt tracers to introduce vaporized atomic species into flames to determine electronic excitation temperatures which can be extended to diagnostics of explosives.³ Lewis et al. have shown that by using atomic tracer elements seeded into explosives that a gas phase temperature can be measured from the relative intensities of the resulting atomic lines in the emission spectrum of the fireball.⁴ Emission from the diatomic species present in the combustion of energetic materials (e.g. AlO) can also be fit to theoretical transitions to determine temperatures and concentrations.⁵

Emission spectroscopy measurements probe upper (excited) electronic states, and, in many cases, especially when the upper state is strongly populated by exothermic reactions, the population distribution in the upper state is not representative of the more abundant ground state molecules.³ In general, a temperature derived from an emission measurement should be checked for rotational/vibrational equilibrium or by comparing to an absorption measurement. In the particular case of optically thick fireballs, it has been shown that the detonation products of gram scale and higher experiments that the attenuation lengths are on the order of a few centimeters implying that the temperatures derived from the emission measurements may be only representative of the outer edge of the fireball.⁶

The preferred measurement, in these cases, would be to probe the ground state in absorption which provides quantifiable information on species concentration and temperature, though the measurements are path averaged. However, absorption measurements in fireballs are difficult owing to the intense luminosity of the fireball and the high intensity and coherence required from a broadband source to penetrate the fireball in order to perform the measurement.

The limitations of emission spectroscopy have prompted several experiments to probe of the inside of explosive fireballs. Lewis et al. found no significant difference in apparent

temperatures measured by emission spectroscopy of the interior and the outer edge of an RDX explosive cloud revealing the possibility of temperature uniformity throughout the fireball at certain times during the combustion.⁷ Carney et al. demonstrated the use of a booster optical amplifier to measure the absorption of water vapor in the near-infrared (NIR) and obtained a line-of-sight temperature measurement in a high explosive.⁸

In previous work, Glumac was able to show proof-of-concept experiments using a modeless dye laser as a spectral source for absorption spectroscopy measurements in optically thick fireballs.⁹ Modeless dye lasers offer a widely tunable, relatively high bandwidth (~1-10 nm) coherent source and have moderate divergence and high power. In optically thick regions, there is difficulty in passing sufficient signal to detectr from other broadband sources due to the scattering of the light. The dye laser offers an intense, directional beam allowing the strong rejection of the fireball luminosity and sufficient signal at the detector even at 98% attenuation.

Dye beam wavelengths are limited to above the near-ultraviolet (UV) due to the nature of the available dyes. A great number of important diatomic and atomic transitions occur below these wavelengths necessitating broadband UV spectral sources that can access the transitions. The advantage of dye lasers is that almost any visible wavelength can be reached by the appropriate selection of dye. By utilizing broadband second harmonic generation (SHG) of the dye laser beam using a nonlinear crystal, the wavelength range can be extended into the deep UV. Absorption measurements of several more atomic and diatomic species become possible for diagnostics ranging from the transitions found in hydrocarbon flames (e.g. OH, CN, NO) to those associated with the combustion of energetic materials (e.g. Ni, Fe, BO, AlCl). In this work, energetic systems are examined, and a stationary gas of NO is used to calibrate the diagnostic. Time resolution of the diagnostic is demonstrated by probing Al atomic line absorptions in exploding bridge wires (EBW). Finally, the diagnostic is used to obtain spectra from diatomic species of metal-fluorocarbon reactions (MgF and AlF) in dispersed flash powders which are of recent interest to enhance combustion performance in energetic materials.^{10, 11} Spectra are fit to a model in order to confirm the species and yield path averaged temperatures.

Diagnostic Setup

Dye laser configuration

The schematic of the entire setup is shown in Figure 1. A frequency tripled, compact neodymium-doped yttrium aluminum garnet (Nd:YAG) laser (Quantel) at 355 nm with 5 ns pulses at 20 Hz is used as the pump for the dye laser. The maximum power available from the laser is approximately 60 mJ per pulse. The built in flash-lamp/Q-switch delay on the laser is used to adjust the power to pump the dye with 2-4 mJ per pulse which produces sufficient dye laser energy for the experimental setup.

The custom dye laser configuration is demonstrated in previous work by Glumac to produce a modeless beam with about 5% efficiency.⁹ The 355 nm Nd:YAG beam is passed through a cylindrical lens to produce a horizontally spread beam and then focused down in the vertical direction by a second cylindrical lens onto a quartz dye cuvette 40 mm in length. The cuvette is tilted at a 20 degree angle to minimize etaloning effects. A full reflecting mirror is placed at one end of the laser cavity approximately 10 cm from the cuvette, though for a modeless laser this distance may vary without much consequence. The laser has no output coupler, and the front end is empty aside from an iris to prevent stray light and an achromatic collimating lens with a focal length of 175 mm to counteract the moderate divergence of the beam.

In cases where higher power and better beam shape is desired, Glumac shows that a partially reflecting mirror may be used at the front end of the cavity as long as the cavity is

designed with very low finesse.⁹ Modeless dye lasers designed for broadband coherent anti-Stokes Raman spectroscopy (CARS) utilize Bethune dye cells and pass the initial dye beam through an amplifier to change the beam shape and divergence.¹² The power of the pump beam may be increased by using a flowing dye cell since stationary dyes tend to degrade quickly under high pump powers. The advantage of the modeless configuration is the broadband character which is found to have a much smoother spectral distribution of intensity.¹³ The power of the dye beam produced by an empty cavity front end and a stationary dye cell is found to be sufficient for the systems examined in this work. The Coumarin 450, 460, and 540 (Exciton) dye laser pulse energies are measured to be 0.1-0.2 mJ per pulse for a pump beam energy of 2-4 mJ.

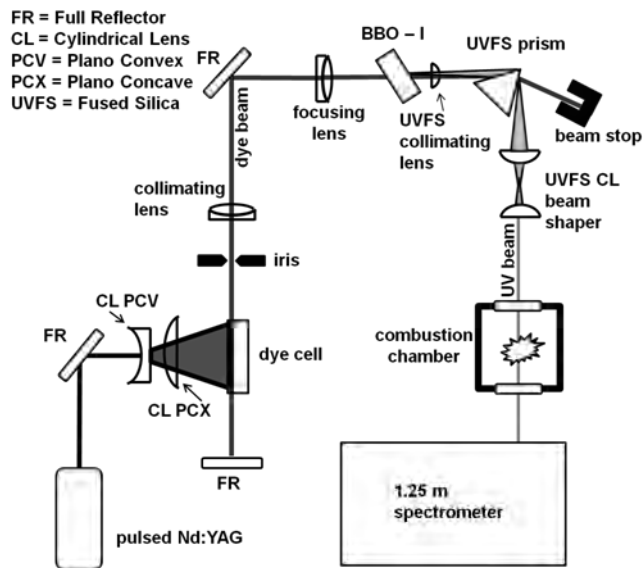


Figure 1. Schematic of the entire setup for the absorption measurement. A pulsed Nd:YAG (355 nm) pumps a dye cell in a grazing incidence configuration. The modeless dye beam is then focused onto a BBO-I crystal, and the resulting UV beam is collimated and separated from fundamental and passed through the combustion chamber.

Second harmonic generation

The wavelengths produced by dye lasers are limited to wavelengths above 330 nm for Nd:YAG pumped dyes. To extend deeper into UV spectrum to access a much greater number of species, the beam can be passed through a non-linear crystal for SHG. Critical phase matching to the non-linear crystal allows for efficient SHG of a monochromatic beam by simply rotating the crystal to the optimum angle determined by the crystal cut. Wavelengths in a broadband beam which are outside the phase-matching bandwidth, determined by the thickness of the crystal and the diameter of the beam incident on the crystal, will typically have very low SHG efficiencies. The beta barium borate (BBO) type I, 7 mm crystal with a cut-angle of 52 degrees (Radian Dyes) used in this study theoretically has less than 0.1 nm of phase matching bandwidth at the desired wavelengths for NO absorption. Shorter crystals will theoretically provide higher spectral bandwidth at the expense of conversion efficiency.

The broadband nature of ultra-short laser pulses has led to the development of several techniques for increasing the phase matching bandwidth in crystals using chromatic dispersion of the fundamental beam.¹⁴⁻¹⁷ Due to the relatively low power of the dye beam in this experimental setup, the use of any method of increasing the bandwidth which requires a significant loss in

power is generally not desired. Dispersive elements can cause significant losses due to reflections of the required polarization for SHG in the nonlinear crystal at the surfaces of the dispersive element.

Unlike the large bandwidth of ultra-short pulses (typically around 100 nm), the bandwidth of the second harmonic pulse in the present experiments is only few nanometers in wavelength since the bandwidth of the fundamental dye beam has only around 10 nm of bandwidth at maximum. Previous studies indicate that by simply creating a strong focusing condition of the fundamental beam into the crystal, a significant bandwidth in the frequency doubled beam can be achieved at a fraction of the signal loss compared to dispersive methods.^{18, 19} To demonstrate this in the current experiment, the spectral bandwidth of the SHG of a Coumarin 540 dye beam under different focusing conditions is plotted in Figure 2. The crystal is first rotated to the central phase matching angle of the dye beam, and the lenses are varied without changing the crystal angle. The tight focus decreases the effective interaction length thereby increasing the spectral bandwidth.

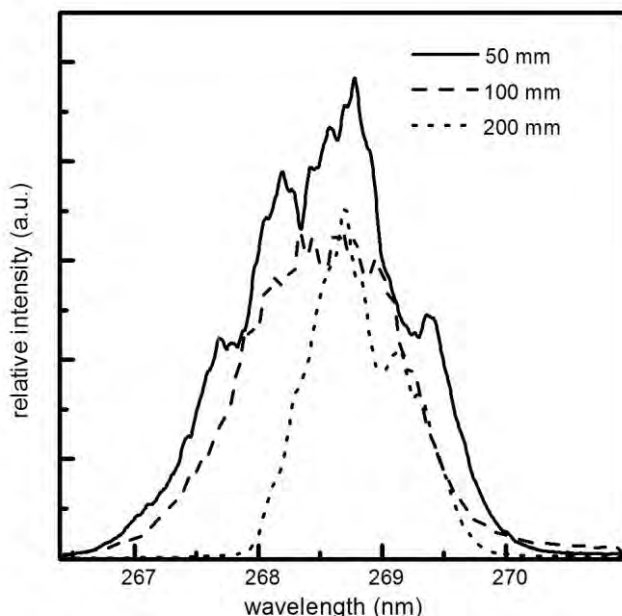


Figure 2. Spectral bandwidth of the second harmonic for different focal lengths of the lens used to focus the fundamental beam onto the nonlinear crystal.

Without spectral dispersion, the fundamental dye beam is focused onto the crystal with a 50 mm focal length achromatic lens. The crystal is then rotated until the second harmonic appears and adjusted to the desired spectral position. The combined fundamental and second harmonic beams are then re-collimated using a UV fused silica (UVFS) 25 mm focal length plano-concave lens. It is found in previous studies under strong focusing condition, the UV beam emerges nearly collimated in the horizontal direction.¹⁵ The re-collimating lens allows the collimation of the beam in the vertical direction but causes divergence in the horizontal direction necessitating cylindrical correction optics to shape the beam in the horizontal direction (see Figure 1). The combined fundamental and second harmonic emerging from the crystal are first passed through a UVFS dispersion prism with an apex angle of 60 degrees to separate the fundamental from the second harmonic and then shaped with a UVFS cylindrical inverse telescope consisting of a 75 mm and 25 mm focal length UVFS plano-convex cylindrical lens. The resulting beam is

approximately 5 mm in diameter as seen on a UV viewing card. The spectral profiles of an example dye beam (Coumarin 450 at 920 $\mu\text{mol/L}$ concentration in ethanol) and the second harmonic are shown in Figure 3. The pulse energy from the second harmonic of the Coumarin 450, 460, and 540 dye beam is determined to be 1-5 μJ per pulse.

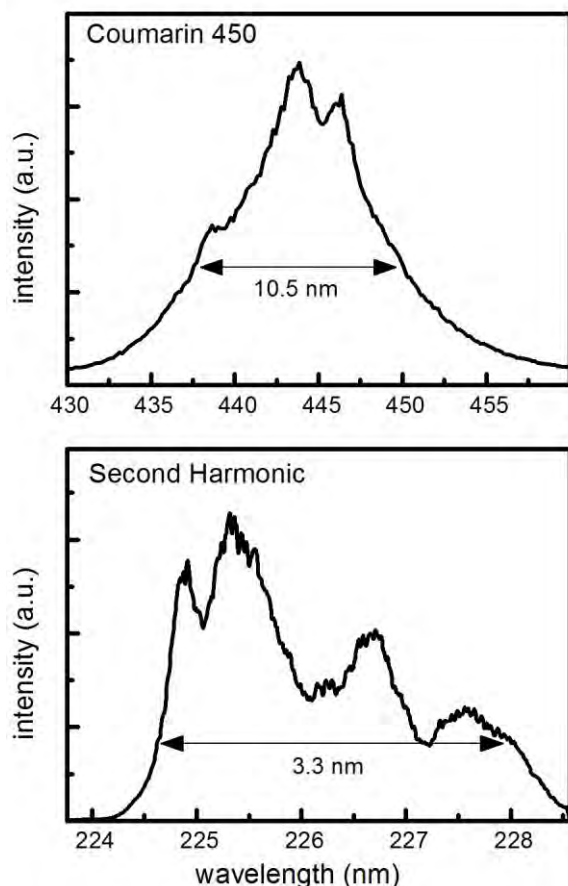


Figure 3. (top) Spectral bandwidth of modeless dye beam with Coumarin 450 as the dye averaged over several pulses. **(below)** The spectral profile of the second harmonic.

After passing through the combustion chamber, the UV beam is focused onto the 50 μm slit of a customized 1260 mm focal length Czerny-Turner SPEX 1250 spectrometer with deviation angle of 11 degrees and a 3600 grooves/mm UV holographic grating (Optometrics). The detector used for NO absorption is a GARRY 3000 which is a CCD line array of 3000 pixels each $7 \times 200 \mu\text{m}$. The approximate resolution achieved by this spectrometer is approximately 0.01 nm full-width-half-maximum (FWHM) determined by the FWHM of an elemental calibration line over a range of about 4 nm on the detector. The detector used in flash powder tests is a Hamamatsu C7041 CCD array with 1044×255 pixels each $25 \mu\text{m} \times 25 \mu\text{m}$ with an approximate resolution of 0.013 nm FWHM over about a 4 nm range. The spectrum is binned over the entire chip. Even at low dye beam powers, the generated SHG UV beam is sufficient to saturate the spectrometer detectors with a single pulse.

Results and Discussion

Stationary NO gas

The diagnostic is first calibrated with the NO $A^2\Sigma^+ \leftarrow X^2\Pi$ transition in the 226 nm to 227 nm range, the fundamental dye beam is created by pumping a solution of Coumarin 460 (Exciton) in ethanol at 0.005 mol/L. The resulting spectral bandwidth of the UV beam generated from the strong focusing of the dye beam onto the crystal is approximately 1.5 nm at FWHM. The spectral position on the detector is calibrated using a Ni-Ne hollow cathode lamp (Azzota) and checked against the position of the strong NO transitions.

A test system of NO is generated in a sealed chamber with fused silica windows using a continuous electric arc discharge in air. The electrodes are mounted within a 5 cm wide sealed chamber with quartz windows. The amount of NO produced in the chamber is correlated to the duration of the arc.

The laser is set to pulse continuously (20 Hz), and integration time is set to one second on the detector in order to obtain an averaged spectrum over the 20 pulses. A reference spectrum is first taken in the empty chamber. An optically thin spectrum of NO is obtained by producing an arc for five seconds or until only a slight absorption feature is qualitatively observed in the raw spectrum. The resulting spectrum and comparison to the LIFBASE simulation²⁰ is shown in Figure 4. Good agreement is shown between the simulation and resulting averaged spectrum from several laser shots in the optically thin limit.

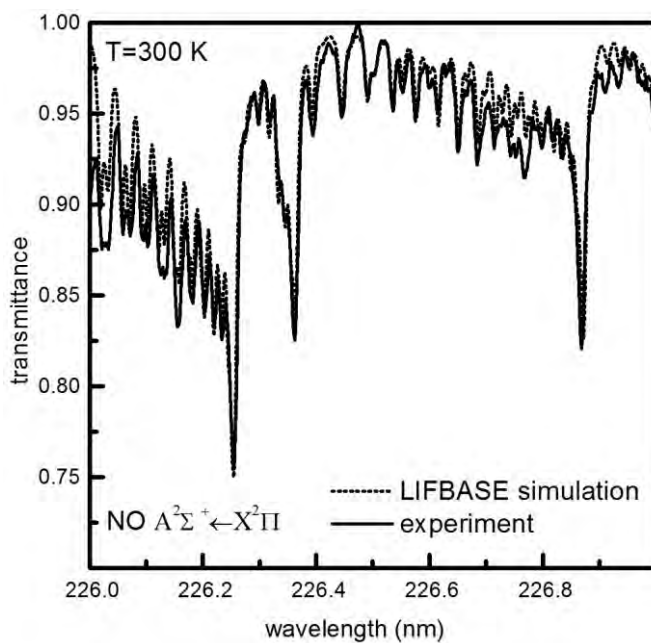


Figure 4. NO spectrum at low concentration from continuously pulsed laser (20Hz) integrated over 1 second compared to spectrum simulated by LIFBASE at T=300K.

A single pulse measurement is then taken in a high concentration of NO to simulate conditions in an optically dense fireball medium. The detector is set to a two second integration time and a reference pulse averaged over ten pulses taken in the empty chamber. An arc is then produced in the chamber for 30 seconds until the absorption signal is noticeably visible over the noise from the laser, and a second pulse is recorded. The transmittance from the single pulse measurement is plotted in Figure 5. A simulation of the NO absorption spectrum is provided by LIFBASE for comparison using the resolution of 0.013 nm obtained by spectrometer calibration and set to room temperature at 300 K. The single pulse absorption measurement produces a high

signal to noise spectrum across a 1 nm region with approximately 30 well resolved rotational lines. A comparison of the optically thick spectrum with an optically thin LIFBASE spectrum shows clearly the effects of optical depth in the spectrum, which enhance weaker lines at the expense of stronger ones.

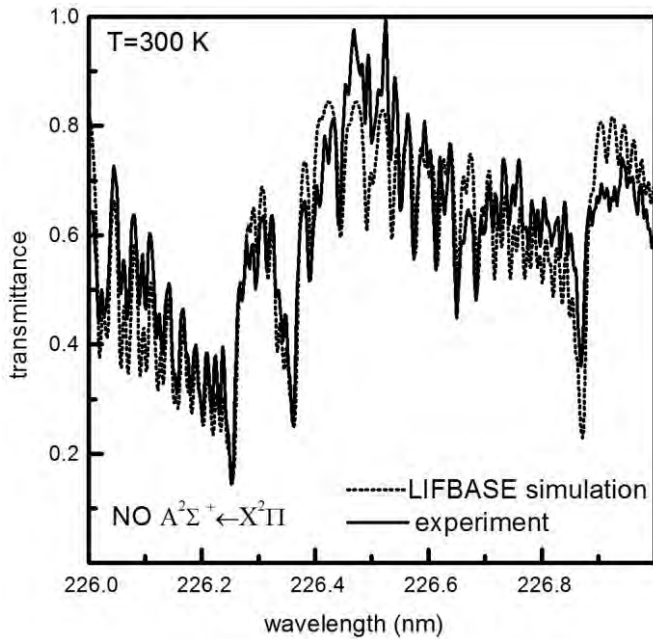


Figure 5. NO spectrum under optically thick conditions from a single pulse compared to spectrum simulated by LIFBASE at T=300K.

Time resolution in exploding bridge wires

The ability to time resolve species absorption in the UV is demonstrated in the vapor cloud produced by an aluminum EBW. Previous work⁹ showed that Al concentration in an EBW cloud varies strongly over the first millisecond after breakdown. The same dye mixture used in the stationary NO gas measurement is used to probe the spectral range from 226 nm to 227 nm. To create aluminum bridge wires, aluminum foil is cut into thin strips approximately 0.5 mm wide \times 25 μm thick. The thin strips are then clamped between two electrodes set approximately 1 cm apart. The center of the UV beam is then positioned approximately 1 cm above the bridgewire. The electrodes are then connected to a Teledyne RISI FS-43 fireset synchronized to the laser pulse output by a delay generator (Quantum) to allow for measurements at different times after the bridgewire initiation. An optical beam shutter (Thor Labs) is placed in front of the combustion chamber and connected to the pulse generator. Several single shot experiments are conducted with the absorption probe beam passing through the cloud at different times after breakdown. Before each wire is initiated, a reference pulse averaged over ten pulses is taken.

The resulting spectra for aluminum absorption lines at 200 μs increments after the initiation of the bridge wire are shown in Figure 6. Two atomic absorption lines, the Al I (${}^2\text{P}^0_{1/2} \rightarrow {}^2\text{D}_{3/2}$) transition at the lower wavelength and the Al I (${}^2\text{P}^0_{3/2} \rightarrow {}^2\text{D}_{5/2}$) transition at the upper wavelength,²¹ are apparent in the spectrum. It is seen initially that after the explosion, the absorption lines are extremely broad while gradually thinning out at later times. The broadening is attributed to the increase in equivalent width due to the optically thick spectrum. The observed linewidth far exceeds the expected pressure, Doppler, and Stark broadened linewidths in the bridgewire environment.

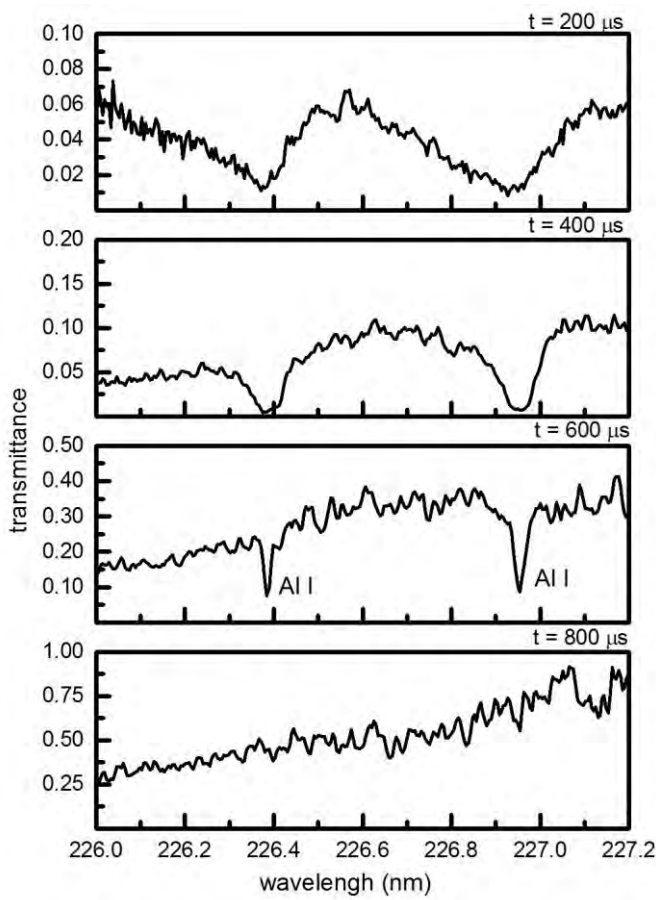


Figure 6. Al atomic line absorption in EBWs taken in a series of experiments at different times after bridge wire initiation.

Metal-Teflon Flash Powders

Flash powders mixed with PTFE powder are used to examine fluorinated metal species in absorption in a solid fuel combustion environment. The spectrum of AlF is examined in a flash powder a powder of containing $\text{KClO}_4/\text{PTFE}/\text{Al}$ (57/10/33 by wt %). The spectrum of MgF is examined in a flash powder containing $\text{KClO}_4/\text{PTFE}/\text{Mg}$ (40/10/50 by wt%). An EBW is used to disperse and ignite the powders. A tungsten bridgewire with 0.005 cm diameter (McMaster Carr) is attached between the electrodes in the combustion chamber. Testing the tungsten wire in the same manner as described in the previous section revealed no absorption features in the regions of interest at any time after the initiation of the bridgewire making it an ideal candidate for dispersing powders. A piece of non-conductive tape is placed directly under the bridgewire to support a small pile of flash powder (5 mg) that rests on top of the wire. The bridge wires are initiated and spectrum recorded in the same manner as described in the previous section.

Spectroscopic Model for AlF and MgF

The procedure for calculation of line positions and intensities used in this study is outlined in Arnold et al. utilizing the approximation to the Voigt profile provided in the reference.²² The spectroscopic constants for the aluminum AlF $\text{A}^1\Pi \leftarrow \text{X}^1\Sigma^+$ transition are taken from Rowlinson and Barrow.²³ The Franck-Condon factors for the first five vibrational levels of the $\Delta v=0$ transitions are taken from Liszt and Smith.²⁴ Due to the nearly vertical nature of the transition, factors for five subsequent vibrational levels are estimated to be unity. Spectroscopic

constants for the magnesium MgF $B^2\Sigma^+ \leftarrow X^2\Sigma^+$ transition are taken from Huber and Herzberg.²⁵ Frank-Condon Factors for the first five levels of the the $\Delta v=0$ transition were taken from Maheshwari et al..²⁶ Expressions for Hönl-London factors for both molecules are taken from Kovacs.²⁷ The calculation of the absorption coefficients is outlined by Luque.²⁰

The classical Beer's law expression is used to describe the absorption. There are five adjustable parameters for the simulation of absorption spectrum taking into account the optical thickness: the temperature, a factor of non-resonant absorption/ scattering, a factor of the amount of light that passes through the absorbers, an effective product of the number density and path length, and the effective resolution. The slit function of the spectrometer setup is approximated as a Lorentzian function. The transmittance is plotted as a function of the wavelength. The fitting parameters are the same as described in previous work in modeling the AlO absorption spectrum.²⁸ The model is meant to be primarily used to verify the species being probed. The quantitative accuracy of the temperature measurement is not assessed in this work.

MgF detection in dispersed flash powder combustion

The MgF $B^2\Sigma^+ \leftarrow X^2\Sigma^+$ $\Delta v=0$ bandhead is observed at 268.85 nm. In order to reach this transition, a Coumarin 540 dye at 0.0035 mol/L concentration is used to produce the fundamental beam. The UV pulse energy is measured to be 3 μ J. The spectral position on the detector is calibrated using the atomic lines produced by a Fe-Ne hollow cathode lamp (Analyte). The spectral bandwidth after doubling is approximately 2 nm with a profile similar to the bandwidth in Figure 2. The combustion of the dispersed magnesium flash powder provides moderate optical thickness of the MgF spectrum at times 500-600 μ s after the initiation of the tungsten EBW. The resulting spectrum is shown in Figure 7 along with the simulation at 3000 K with an effective resolution of 0.015 nm. Despite the path averaged nature of the measurement, a fair fit to the spectrum is obtained using a single temperature.

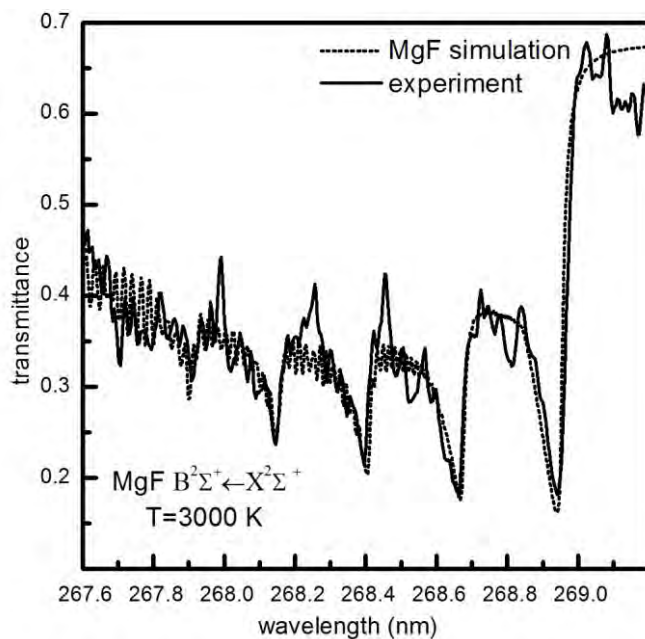


Figure 7. The absorption spectrum of MgF in flash powder combustion fit with a 3000 K simulation.

AlF detection in dispersed flash powder combustion

The AlF $A^1\Pi \leftarrow X^1\Sigma^+$ $\Delta v=0$ transition is observed with a strong absorption feature with a peak at 227.4 nm. The same Courmarin 460 dye used for the aluminum bridge wire tests is used to produce the fundamental beam. The crystal is angle adjusted to center the beam in the 227 to 228 nm region of interest for AlF. The resulting pulse energy is approximately 1 μ J. The spectral position is calibrated by the Ni-Ne hollow cathode lamp. Measurements of AlF are taken approximately 800-1000 μ s after the initiation of the EBW, and produce noticeably optically thick spectrum. There is considerable difficulty in obtaining an optically thin spectrum since the highly optically thick signal rapidly decays to negligible signal. An example spectrum of the AlF transition is shown in Figure 8 with a simulation at 2800 K with an effective resolution of 0.015 nm. There is disparity of the model in the blue-degraded absorption feature at 227.4 nm possibly due to an unaccounted source of broadening or from the relative uncertainty of the spectroscopic constants in the literature.

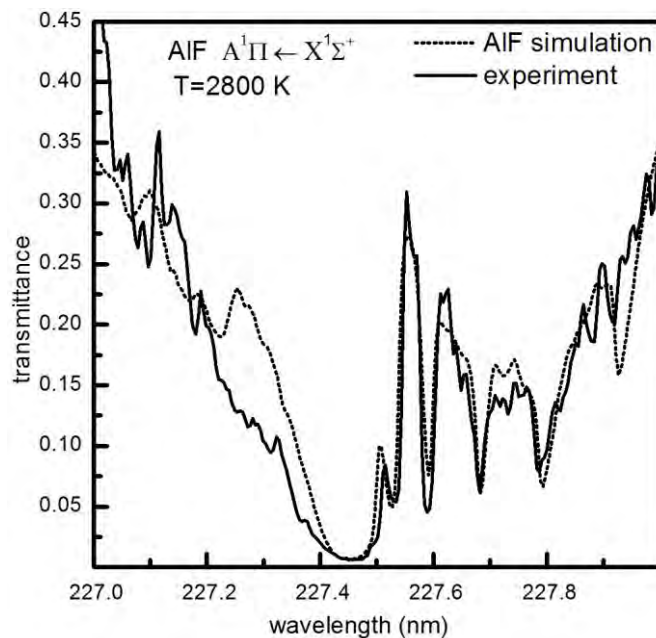


Figure 8. The absorption spectrum of AlF in flash powder combustion fit with a 2800 K simulation.

The intensity and coherence of the UV beam allows for easy alignment of the spectrometer in the second order of the grating. In the second order, the dispersion and resolution are more than doubled. The theoretical instrument resolution becomes 0.0026 nm with a range of 1.4 nm. The second order spectrum is shown in Figure 9. It is observed that pulse noise is increased. Although the majority of the rotational lines are too closely spaced to be resolved, a new feature appears in the main spectrum at about 227.5 nm which also appears in the simulated spectrum. The second order spectrum is again fit to a temperature of 2800 K.

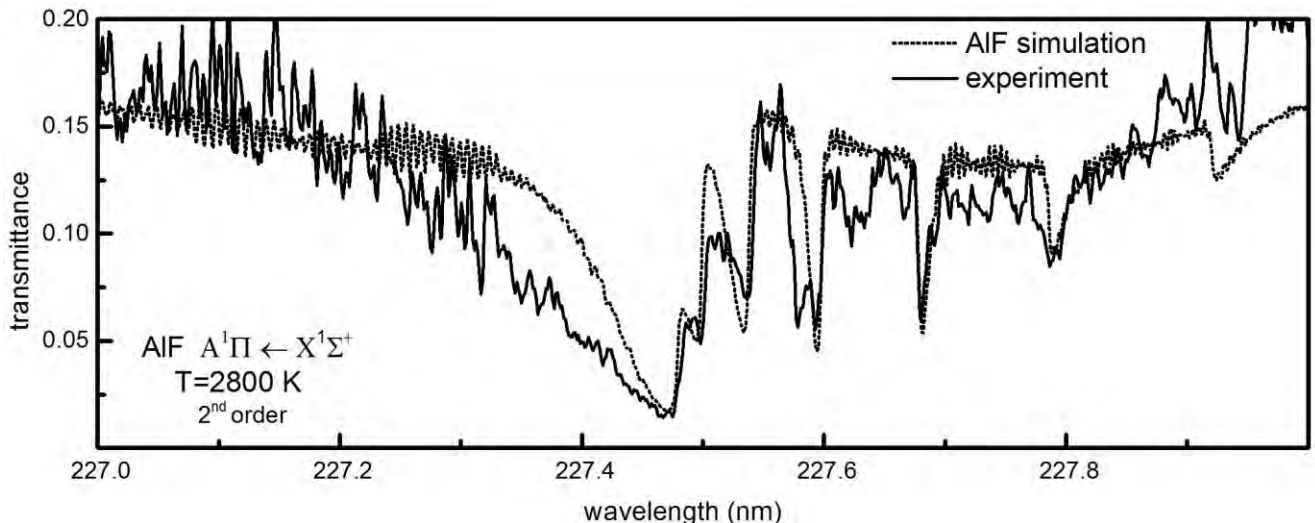


Figure 9. Second order spectrum of AlF with a simulation at 2800 K.

Absorption saturation

High pulse intensities can optically pump the absorption medium so that sufficient population in the excited state may cause non-linear absorption effects. Full saturation is considered when the excited state population is driven by the laser radiation to match the ground state. In this scenario, the medium becomes effectively transparent to the laser light and no absorption will take place.

The limiting pulse energy is determined for NO $A^2\Sigma^+ \leftarrow X^2\Pi$ absorption as an example. The spectral range of the laser is considered from 226 nm to 229 nm. A beam radius of 2.5 mm and a pulse width of 5 ns are assumed. The calculated maximum pulse energy at which the excited state population reaches 25% is found to be approximately 0.4 mJ. In cases of higher pulse energy, an increase in the beam radius can reduce the overall beam intensity allowing for greater pulse energy at a small expense of spatial resolution in the measurement.

Summary and Conclusions

The use of a modeless dye laser as a spectral source for an absorption measurement is extended into the UV beyond the limitations of pumped dye beams by using broadband SHG. Absorption measurements of the NO $A^2\Sigma^+ \leftarrow X^2\Pi$ transition and atomic lines in aluminum EBWs are used to calibrate the diagnostic showing convergence in the optically thin limit over multiple pulses and to demonstrate microsecond time resolution in a series of experiments. The diagnostic is used to probe the fireballs of flash powders dispersed by EBWs to examine the optically thick AlF $A^1\Pi \leftarrow X^1\Sigma^+$ transition, and the MgF $B^2\Sigma^+ \leftarrow X^2\Sigma^+$ transition. A single temperature is derived by fitting simulations of the diatomic transitions to the experimental data. A simple analysis of the laser intensity where saturation effects may not be negligible is given for a two level system for wavelengths near NO and AlF transitions.

It is found in this setup that the pulse noise and pulse variation do not degrade the absorption measurement significantly. The average standard deviation in amplitude over the laser pulse spectrum for a sample of ten pulses is found to be 15-20%. The noise level of a single pulse, however, is estimated to be 5-10%. Improvements in the measurement can be made by splitting the beam before the combustion chamber and acquiring a simultaneous reference measurement using an array detector as demonstrated by Glumac.⁹ Other broadband laser sources such as femtosecond lasers may offer superior noise characteristics, though currently, these tend to be more expensive than the dye based approach.

A strong focusing condition of the fundamental dye beam onto the crystal is found to be sufficient to produce approximately 1-3 nm of bandwidth. The SHG beam is able to saturate the detector in a single pulse and provides enough signal to be used for a single shot measurement in the second order of a grating. This diagnostic provides a simple tool for obtaining a path averaged measurement and overcoming the difficulties of absorption spectroscopy in explosive fireballs and other optically thick combustion systems as shown in previous studies using the visible spectrum of dyes.⁹ Several atomic and diatomic species can be accessed for measurement by careful selection of dyes and crystals. Following the assumption of approximately a 2 cm attenuation length from previous studies of optical depth in fireballs⁶ and assuming a pulse energy around 10 mJ max, the technique is estimated to be able to scale up to a 20 cm path length.

References

1. P. Lynch, H. Krier, and N. Glumac, *Emissivity of Aluminum-Oxide Particle Clouds: Application to Pyrometry of Explosive Fireballs*. J. Thermophys. Heat Transfer, 2010. **24**(2): p. 301-308.
2. S. Goroshin, D.L. Frost, J. Levine, A. Yoshinaka, and F. Zhang, *Optical Pyrometry of Fireballs of Metalized Explosives*. Propellants, Explos., Pyrotech., 2006. **31**(3): p. 169-181.
3. A.G. Gaydon, *The spectroscopy of flames*. 1974, London: Chapman and Hall.
4. W.K. Lewis and C.G. Rumchik, *Measurement of apparent temperature in post-detonation fireballs using atomic emission spectroscopy*. J. Appl. Phys., 2009. **105**(5): p. 056104.
5. J.M. Peuker, P. Lynch, H. Krier, and N. Glumac, *On AlO Emission Spectroscopy as a Diagnostic in Energetic Materials Testing*. Propellants, Explos., Pyrotech., 2013: p. 577-585.
6. J.M. Peuker, P. Lynch, H. Krier, and N. Glumac, *Optical depth measurements of fireballs from aluminized high explosives*. Opt. Lasers Eng., 2009. **47**(9): p. 1009-1015.
7. W.K. Lewis, C.G. Rumchik, and M.J. Smith, *Emission spectroscopy of the interior of optically dense post-detonation fireballs*. J. Appl. Phys., 2013. **113**(2): p. 024903.
8. J.R. Carney, J.M. Lightstone, S. Piecuch, and J.D. Koch, *Water temperature and concentration measurements within the expanding blast wave of a high explosive*. Meas. Sci. Technol., 2011. **22**(4): p. 045601.
9. N. Glumac, *Absorption Spectroscopy Measurements in Optically Dense Explosive Fireballs Using a Modeless Broadband Dye Laser*. Appl. Spectrosc., 2009. **63**(9): p. 1075-1080.
10. E.-C. Koch, *Metal-fluorocarbon based energetic materials*. 2012: John Wiley & Sons.
11. T.R. Sippel, S.F. Son, and L.J. Groven, *Altering Reactivity of Aluminum with Selective Inclusion of Polytetrafluoroethylene through Mechanical Activation*. Propellants, Explos., Pyrotech., 2013. **38**(2): p. 286-295.
12. J.W. Hahn, C.W. Park, and S.N. Park, *Broadband coherent anti-Stokes Raman spectroscopy with a modeless dye laser*. Appl. Opt., 1997. **36**(27): p. 6722-6728.
13. N. Glumac, *Absorption Spectroscopy Measurements in Optically Dense Explosive Fireballs Using a Modeless Broadband Dye Laser*. Appl. Spectrosc., 2009. **63**(9): p. 1075-1080.
14. S. Saikan, *Automatically tunable second-harmonic generation of dye lasers*. Opt. Commun., 1976. **18**(4): p. 439-443.

15. S. Saikan, D. Ouwe, and F.P. Schäfer, *Automatic phase-matched frequency-doubling system for the 240-350-nm region*. Appl. Opt., 1979. **18**(2): p. 193-196.
16. R.A. Cheville, M.T. Reiten, and N.J. Halas, *Wide-bandwidth frequency doubling with high conversion efficiency*. Opt. Lett., 1992. **17**(19): p. 1343-1345.
17. G. Szabó and Z. Bor, *Broadband frequency doubler for femtosecond pulses*. Appl. Phys. B, 1990. **50**(1): p. 51-54.
18. G.D. Boyd and D.A. Kleinman, *Parametric Interaction of Focused Gaussian Light Beams*. J. Appl. Phys., 1968. **39**(8): p. 3597-3639.
19. A.M. Weiner, A.M. Kan'an, and D.E. Leaird, *High-efficiency blue generation by frequency doubling of femtosecond pulses in a thick nonlinear crystal*. Opt. Lett., 1998. **23**(18): p. 1441-1443.
20. J. Luque and D. Crosley, *LIFBASE: Database and spectral simulation program (Version 1.5)*. SRI international report MP, 1999. **99**(009).
21. A. Kramida, Y.Ralchenko, J. Reader, and a.N.A. Team, *NIST Atomic Spectra Database*, 2012, National Institute of Standards and Technology: Gaithersburg, MD.
22. J.O. Arnold, E.E. Whiting, and G.C. Lyle, *Line by line calculation of spectra from diatomic molecules and atoms assuming a voigt line profile*. J. Quant. Spectrosc. Radiat. Transfer, 1969. **9**(6): p. 775-798.
23. H.C. Rowlinson and R.F. Barrow, *The Band-Spectrum of Aluminium Monofluoride*. Proc. Phys. Soc. London, Sect. A, 1953. **66**(5): p. 437.
24. H.S. Liszt and W.H. Smith, *RKR Franck-Condon factors for blue and ultraviolet transitions of some molecules of astrophysical interest and some comments on the interstellar abundance of CH, CH+ and SiH+*. J. Quant. Spectrosc. Radiat. Transfer, 1972. **12**(5): p. 947-958.
25. K.-P. Huber and G. Herzberg, *Constants of diatomic molecules*. Vol. 4. 1979: Van Nostrand Reinhold New York.
26. R.C. Maheshwari, I.D. Singh, and M.M. Shukla, *Franck-Condon factors and r centroids for the B-X and C-X systems of the MgF molecule*. J. Phys. B: At. Mol. Phys., 1968. **1**(5): p. 993.
27. I. Kovács and L. Nemes, *Rotational structure in the spectra of diatomic molecules*. 1969: Hilger London.
28. N. Glumac, H. Krier, T. Bazyn, and R. Eyer, *Temperature measurements of aluminum particles burning in carbon dioxide*. Combust. Sci. Technol., 2005. **177**(3): p. 485-511.

CHAPTER 19: EXPLOSIVE INITIATION OF VARIOUS FORMS OF Ti/2B REACTIVE MATERIALS

Introduction

Both titanium and boron are widely used energetic materials, though special challenges with each material inhibit even wider use. Titanium is stable and easy to ignite, though its specific energy content under oxidation is only 63% of Al and 33% of B. Boron has tremendous energy content per unit mass and volume, but suffers from difficulty in ignition, long burning times, and incomplete yields in some systems due to the formation of HOBO. In some reactive materials systems longer burning time may be advantageous, though efficient ignition and reaction completeness remain critical. The combination of titanium and boron has been proposed as a reactive material (RM) for applications of this type. It is suggested that the intermetallic reaction of $Ti + 2B \rightarrow TiB_2$, which is one of the most exothermic intermetallic reactions, may enhance the ignition of the boron and thus promote efficient oxidation over a somewhat extended time period. Indeed previous work has shown that this metal-metalloid alloy can reduce boron ignition delays and accelerate boron combustion [5].

Most previous work in the area of Ti/2B reactive materials has focused on the creation and classification of Ti/2B mechanical alloys. Jiang *et al.* experimentally investigated the creation of these mechanical alloys using an arrested reactive milling procedure [6]. Through these investigations they determined a procedure to mechanically alloy titanium and boron into a Ti/2B nanocomposite energetic material. The performance of these Ti/2B composite energetics was analyzed against a Ti/2B powder blend and aluminum in various methane/air environments by Trunov *et al.* [7]. They showed that the combustion energy and the burn rates of the Ti/2B composite were higher than the aluminum for all gas mixtures considered. It was also observed in both wet and dry gaseous environments that the Ti/2B nanocomposite alloy achieved a more rapid and efficient combustion than aluminum powder when ignited in any methane concentration.

In the proposed application, the Ti/2B system would most likely be dispersed and initiated by interaction of the RM with the detonation wave from a high explosive (HE). Under these conditions, the RM is subject to rapid acceleration, high stresses, and high temperatures. The HE imparts both kinetic and thermal energies to the RM. If the bulk of the RM is driven out of the fireball region before significant thermal activation can occur, then its chemical yield is compromised. However, since the primary oxidation of an RM will likely be aerobic (i.e. with ambient oxidizer), effective mixing of the RM at early times with the ambient air is critical as well.

Very little work has been reported on the Ti/B system under detonation interaction. In this study, we systematically vary several parameters in the structure of the alloy and the mode of initiation in order to isolate parameters that most sensitively affect yield. We compare conventional mixed powder alloys to different mechanical alloys, and we also compare these to the intermetallic TiB_2 to assess the role of the intermetallic reaction in performance. Finally, we compare the output of identical RMs under planar detonation interaction and under interaction with a merged detonation configuration.

Experimental Methods

Material Preparation

The performance of four forms of the Ti/2B combination was assessed in this experiment. The first was a TiB_2 compound (Alfa Aesar, -325 mesh), the second was a Ti/2B powder blend

prepared by hand-mixing titanium (Alfa Aesar, -325 mesh) and boron (Sigma Aldrich, -325 mesh, crystalline) powders, and the remaining forms were mechanical alloys prepared as described below.

Two mechanically alloyed Ti/2B composites were created at the University of Illinois Urbana-Champaign (UIUC), and one Ti/2B composite was mechanically alloyed at the New Jersey Institute of Technology (NJIT). The preparation of the UIUC mechanical alloys was performed in a Torrey Hills planetary ball mill using 80 mL stainless steel vials. For the first alloy, a Ti/2B molar mixture (both -325 mesh) was added to the vials with 33 stainless steel balls with a diameter of 10 mm. The mixture was milled for 45 minutes at 300 rpm while completely submerged in hexane as a process control agent. The preparation of the second UIUC Ti/2B alloy emulated the procedure implemented by NJIT for performance comparison purposes [1]. This alloy contained a Ti/2B mixture of titanium (-325 mesh, Alfa Aesar) and nano-boron (SB Boron 99, SB Boron), for a total mass of approximately 26 g. Steel balls of 10 mm diameter were added to each vial for a charge ratio of 10:1, and 50% by mass of hexane was added as a process control agent to decrease the risk of intermetallic reaction initiation. These materials were milled for 7 minutes at 350 rpm and then removed. SEM images of two of these materials are shown below in Figure 1.

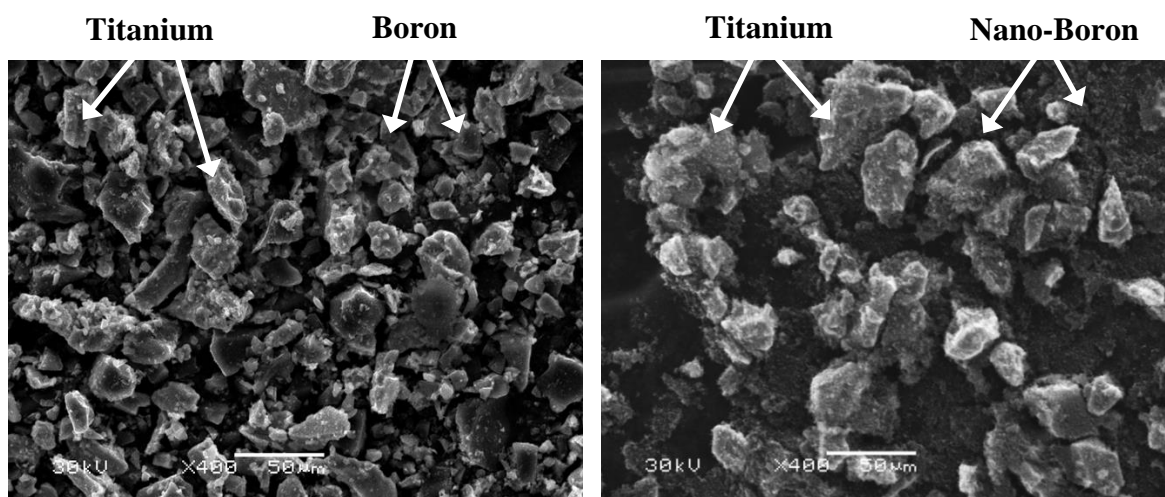


Figure 1: Pretest SEM images of (L) micron-size powder blend and (R) UIUC mechanical alloy #2. The titanium is shown with nano-boron inclusions.

Each form of the Ti/2B materials to be tested was cold-pressed into 25 mm diameter pellets with a thickness of approximately 2-3 mm. The mass of the pellets was held nearly constant throughout the tests at approximately 4.19 g, which provided a range of 63-83% of the theoretical mass density (TMD) as shown in Table 1. An inert pellet of titanium dioxide (TiO_2) was cold-pressed in an identical manner to be used as a non-reactive baseline test, and each material form was tested twice to assess the repeatability of the experiment.

Table 1: Physical Characteristics of Tested Materials

Test Material	Mass (g)	Volume (cm ³)	% Theoretical Mass Density
TiO ₂ Inert Material	4.179	1.583	63.22
UIUC Mechanical Alloy #1	4.190	1.484	80.92
UIUC Mechanical Alloy #1	4.199	1.546	76.61
Ti/2B Powder Blend	4.176	1.534	77.67
Ti/2B Powder Blend	4.190	1.583	76.81
TiB ₂ Compound	4.392	1.496	83.86
TiB ₂ Compound	4.406	1.546	81.42
NJIT Mechanical Alloy	4.064	1.830	64.28
NJIT Mechanical Alloy	4.159	1.731	68.61
UIUC Mechanical Alloy #2	4.198	1.882	64.27

Reactive Material Testing

The explosive initiation tests of the reactive material pellets were performed in air in the large blast chamber at UIUC. The cubic, steel chamber measures 1.2 m per side and contains four ports for optical access. For each single point initiation test, one RP-80 detonator from Teledyne RISI was placed beneath 10 g of PBXN-9 explosive in order to initiate the reactive material, which rested on the top surface of the high explosive. Three RP-80 detonators in a triangular pattern were used to initiate the sample in the triple point configuration tests. The reactive material test stand arrangement can be seen in Figure 2. The blast chamber was outfitted with a suite of diagnostics including transient pressure transducers, quasi-static pressure transducers, two-color infrared pyrometry, temporally- and spatially-resolved spectroscopy, and high-speed imaging. The diagnostic setup is shown in Figure 3.

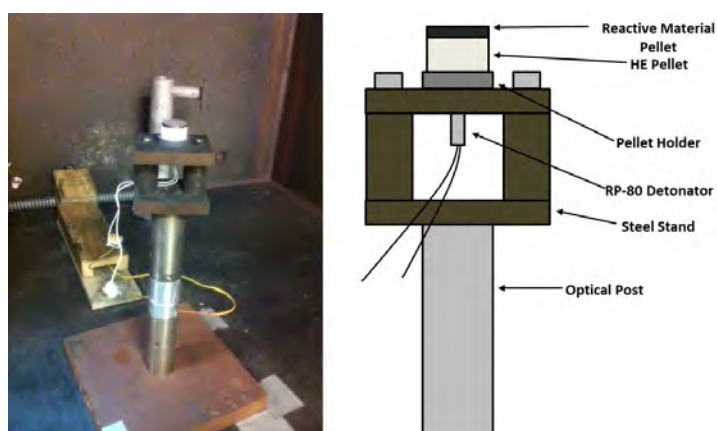
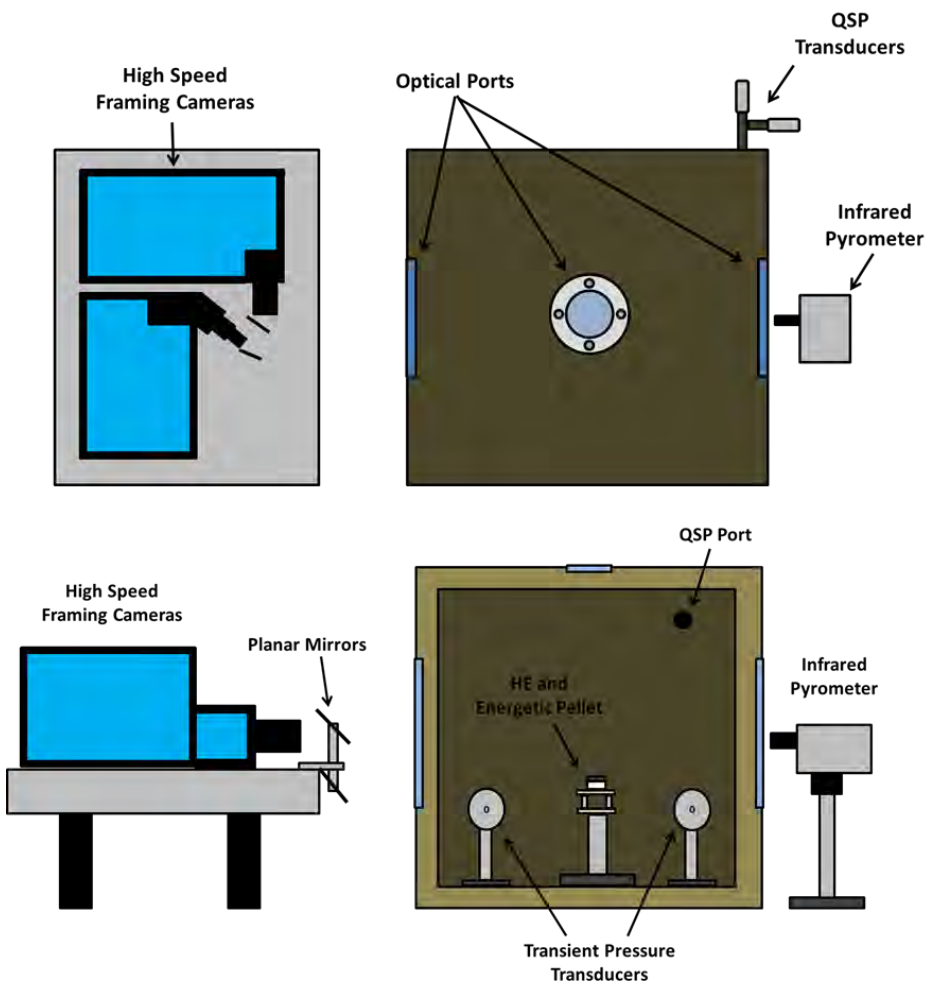


Figure 2: (L) Photograph showing reactive material and high explosive, (R) Schematic portraying close up of material arrangement



**Figure 3: Experimental blast chamber setup, Top: Overhead view,
Bottom: Front view**

The transient and quasi-static pressure measurements were recorded using two Kulite XTEL-190A piezoresistive pressure transducers and two GEMS #2200 series piezoresistive pressure transducers, respectively. Two-color, low temperature infrared pyrometry curves were obtained at wavelengths of $1 \mu\text{m}$ and $1.5 \mu\text{m}$ using a custom pyrometer. Two Cooke high speed framing cameras (HSFC) were implemented to perform high-speed imaging and spatially-resolved spectroscopy. Emission from the reaction of the pellet was directed to the HSFC imaging and spectroscopy setups using two first-surface planar mirrors. For the first two tests, the early-time progression of the reactive material breakout after detonation was recorded from an overhead view. The remaining tests employed a side-on view of the detonation in order to observe the structure developed during the material's reaction progression. The high speed images were recorded using an f/22 lens aperture and exposure settings ranging from 60 – 1000 ns.

Spatially-resolved spectroscopy was performed at the same timing intervals as the high speed imaging using an f/1.4 axial transmission spectrograph containing a volume phase holographic grating with 1800 g/mm. A collection lens was used to focus the light onto a $50 \mu\text{m}$ entrance slit, and the beam was then collimated and passed through the holographic grating. A second lens was then used to focus the dispersed light, providing a range from 413 nm to 580 nm

at 0.5 nm resolution. Figure 4 schematically illustrates the spectrograph arrangement. Wavelength calibration was performed using a mercury calibration lamp, and intensity calibration was achieved with a tungsten lamp of known temperature. Spatial calibration of the imaging diagnostic was accomplished using a grid placed in the experimental setup prior to testing.

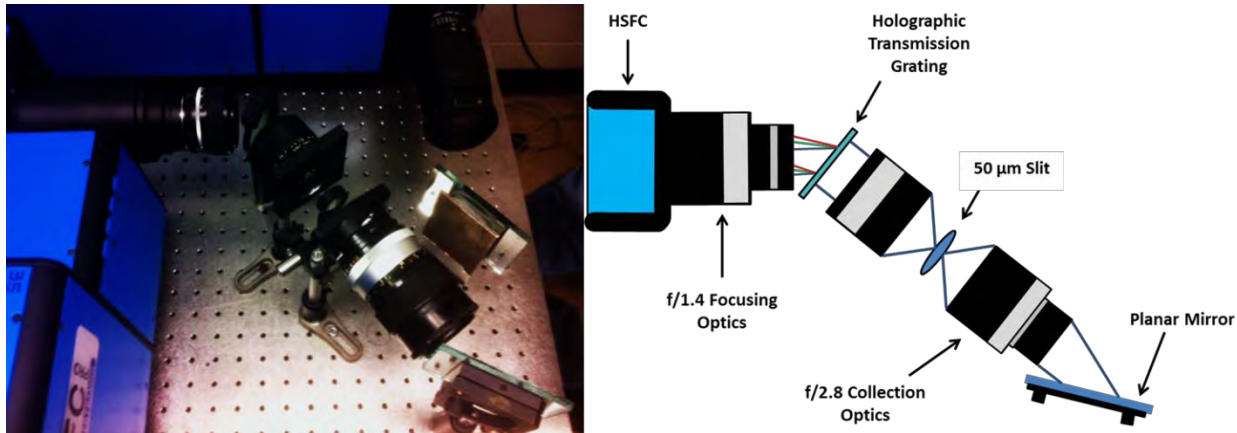


Figure 4: Photograph and schematic of framing camera spectrograph

Results and Discussion

The high speed imaging collected during the tests using the Cooke HSFC allows for an initial qualitative reactivity analysis and shows both the initial interaction between the HE and the reactive material, as well as the structure the reactive pellet forms upon detonation. The early-stage detonation of the material is shown in Figure 5 from an overhead view. The dark circle in the center is the reactive material and the surrounding halo is the detonation emission of the high explosive. As shown, the HE detonates first and the shock created due to the detonation begins to roll up on the sides and interact with the reactive material pellet. The bright outer ring at 15 μ s and 17 μ s consists of the emitting gases of the HE, while the inner bright ring represents the reaction of the energetic material on the edges of the pellet due to its interaction with the roll up of the detonation wave. There is no noticeable structural development or reaction at the center of the pellet during these time frames.

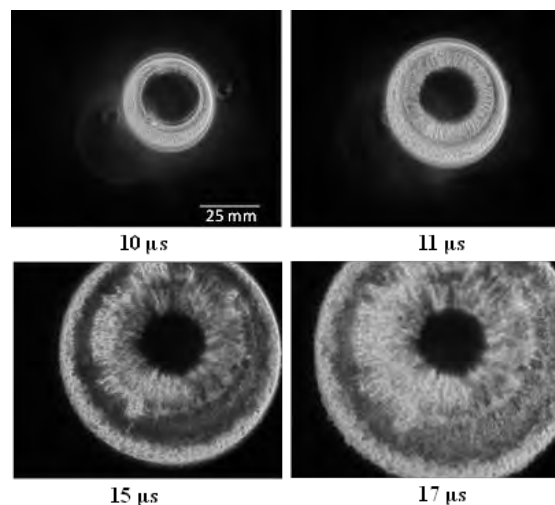


Figure 5: Overhead view of early stage single point initiation

In order to better observe the development of the pellet breakout and its reactivity at a later stage, images were also collected from a side-on view. A sequence of these images can be seen in Figure 6. The first image shows the detonation of the high explosive followed by the breakout of the energetic material as time advances. The lower portion of each of the images displays the emission of the HE, while the top portions show the energetic material reaction. In the early stages of the breakout, the detonation wave is relatively unimpeded along the circumference and the wave begins to interact with the edges of the reactive material, as was seen in the images from the overhead view. The higher density of the reactive pellet initially slows the detonation wave in the center of the pellet, making the edges of the pellet break out first. At times later than 30 μ s the pellet material begins erupting from the center, forming a conical structure as the detonation wave finally begins to displace the center material. By the end of the observed time frame, the conical structure has matured and the edge material interaction with the detonation products has formed a symmetrical, concentric structure on the edges. These detonation structures were characteristic of each Ti/2B material tested.

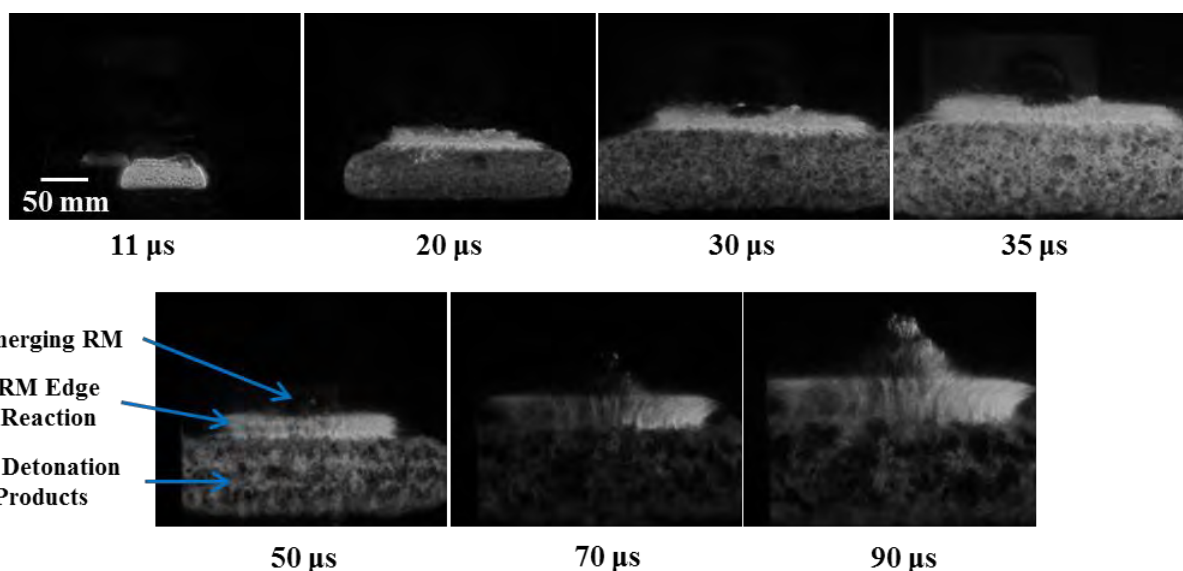


Figure 6: Progression of pellet initiation from side-on view

The high speed images gathered from the later stages of the single point detonation for the various materials can provide a first indication of the reactivity of each material form. Figure 7 shows a comparison between the UIUC mechanical alloys and the NJIT alloy. When comparing the alloy reactions using the imaging technique, the first UIUC alloy appears much less reactive than the other two alloys due to the relatively small amount of emission produced by the center material of the pellet during the reaction. This preliminary observation is useful for gaining an intuition of what to expect in terms of relative energy release between the various material forms prior to further analysis.

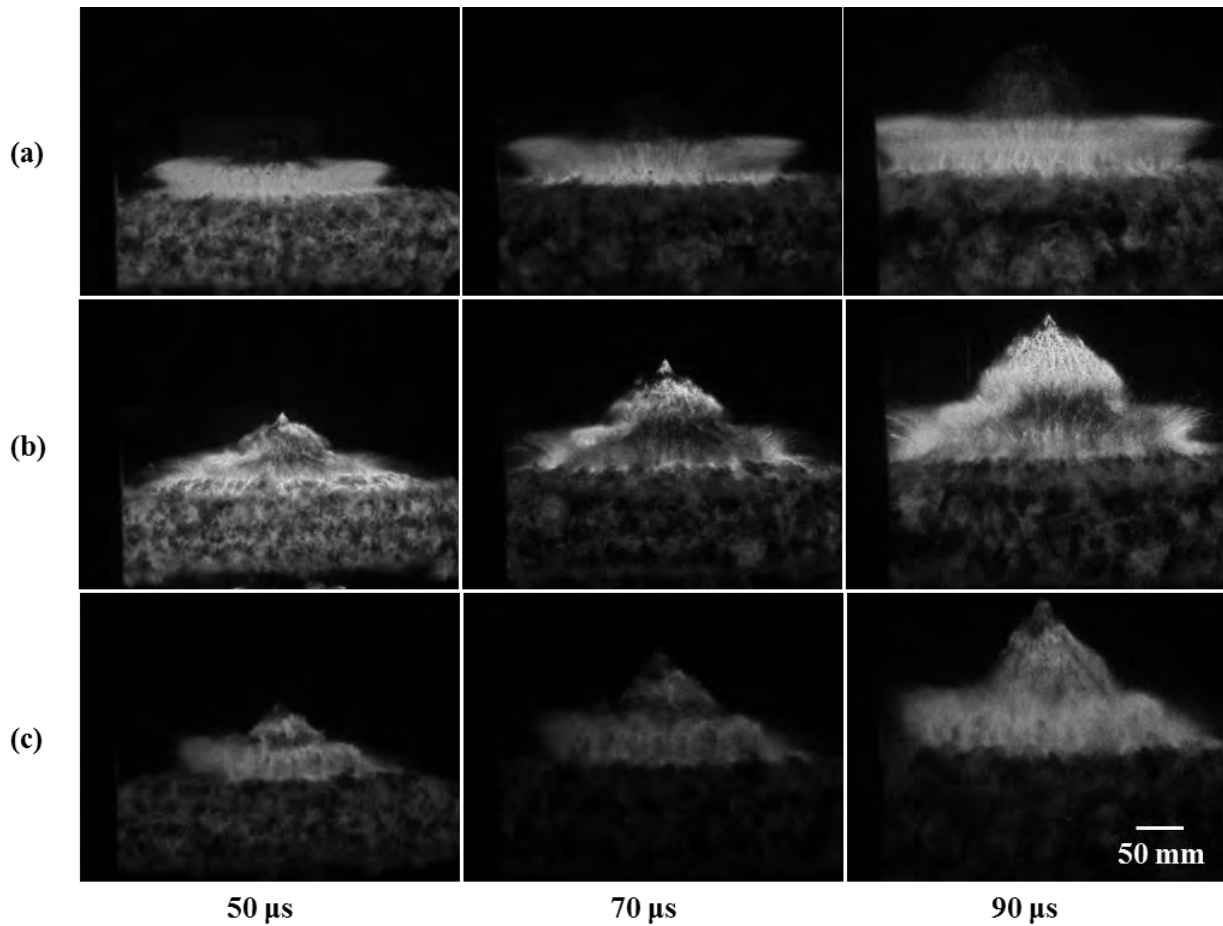


Figure 7: Qualitative comparison of mechanical alloy reactivity. (a) UIUC Mechanical Alloy #1, (b) UIUC Mechanical Alloy #2, (c) NJIT Mechanical Alloy

Similar to a single detonator, each of the detonators in the triple point configuration creates a spherical shock that moves through the explosive and reactive materials. When the detonators are initiated simultaneously, these shocks interact to create a triangular pattern directly between the detonator origins. The shock-shock interaction regions cause rapid reaction of the material and induce a structural development for the reaction. Figure 8 is an example of the shock interaction regions created due to triple point initiation (for a material not tested for this experiment) and shows the structures developed from an overhead viewpoint. The high explosive is, again, the first to breakout, followed by the reactive material located directly above each detonator. The same roll up of the blast wave can be seen on the edge of the reactive material pellet, and this structure grows as time advances. Starting with the second image, the shock interaction planes can be seen in the reactive material and continue to grow in height. These same structures are seen in the Ti/2B Mechanical Alloy #2 when tested using triple point initiation, which is also shown in Figure 8 from a side-on view. One of three shock interactions can be clearly seen in the high explosive at 11 μ s. The ridges created due to shock interaction develop more clearly in the reactive material at 25 μ s and grow in height at 45 μ s and 70 μ s. The reaction scene fills the viewing frame at 70 μ s indicating a faster reaction than the previous tests performed using single point initiation, and the emission produced from this reaction is much stronger relative to the single point initiation tests indicating more reactivity.

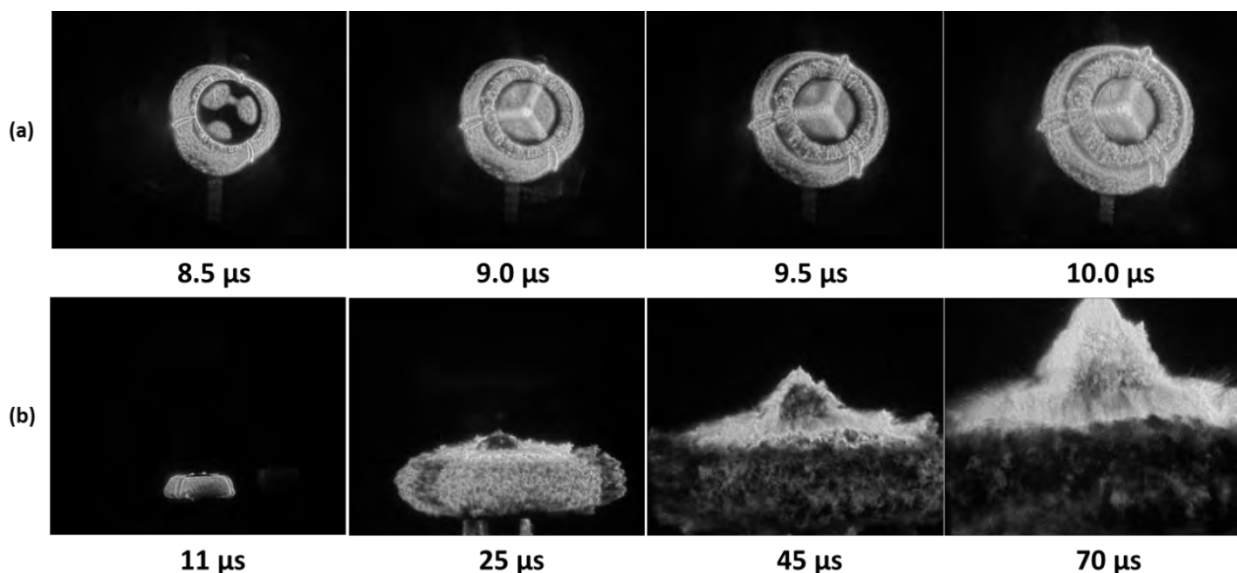


Figure 8: (a) Example of Triple Point Initiation from Overhead View, (b) Lateral View of Mechanical Alloy #2 Using Triple Point Initiation

For each image recorded during the tests, a set of corresponding, spatially-varying spectra were recorded at the same times as the high-speed images. The spectra extend from 413 nm to 580 nm, a range chosen in order to observe the vibrational band structure of boron combustion intermediates. Boron dioxide (BO_2) is a key combustion intermediate during the formation of boron trioxide (B_2O_3) and is often used as a spectral indicator of boron combustion. An example of the collected spectra is shown in Figure 9 below. Each raw spectrum is typically inverted compared to its corresponding image, and the line in the high-speed image correlates to where the spectrometer slit is focused. The spectrometer collects light from this region and then disperses it on the detector to form a spatially-resolved spectrum. The spectra in the figure below have been rotated 180 degrees to assist in understanding how the image and the spectrum correspond to one another. The first spectrum in the sequence corresponds to the emission from only the HE and the arrows in the figure show which part of the image corresponds to the spectrum. As time progresses, the BO_2 vibrational bands can be seen in the spectra, indicating a strong boron reaction in the region of the burning energetic material. Using a custom spectral analysis code, a selected region of each spectral image was calibrated and plotted to display the desired spectrum. A portion of the last spectral image in Figure 9 is shown with its corresponding region outlined in the image as an example.

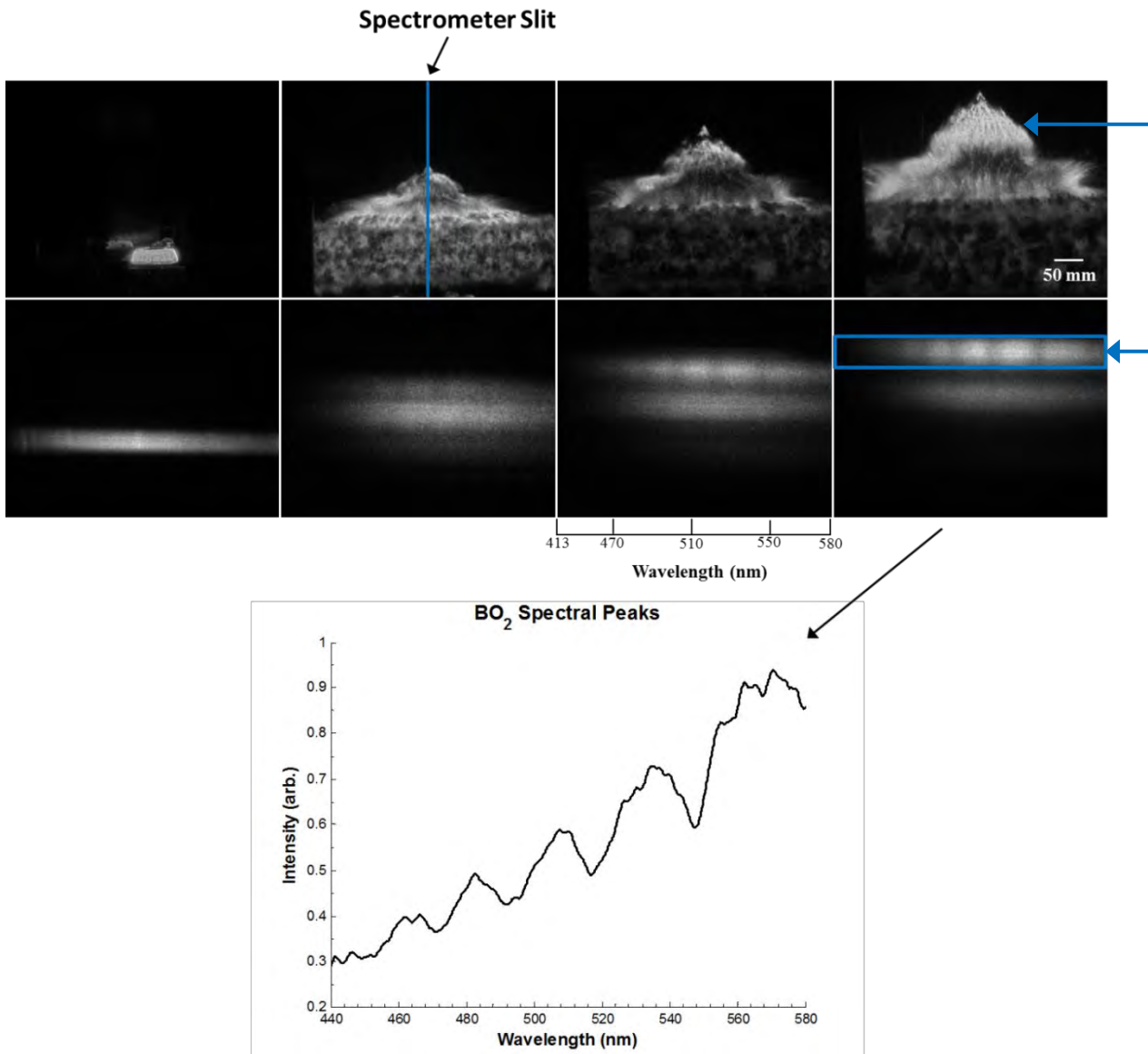


Figure 9: High speed imaging and spectroscopy of UIUC Mechanical Alloy #2 at 11, 50, 70, and 90 μ s with plotted spectrum below

A comparison of spectra produced from the reaction of each material showed the energetic material forms other than the Ti/2B reactive mechanical alloys produced spectra that showed insignificant signs of boron reaction emission. The lack of BO₂ bands seen in the spectra of the first mechanical alloy, the compound, and the powder blend reiterate the fact that the more reactive mechanical alloys are igniting a larger percentage of the boron in the material than the other forms. The emission spectra of the triple point initiation of the mechanical alloy show saturation of the BO₂ spectral peaks at later times due to intense boron combustion emission. This observation provides an initial idea of the increase in energy release when implementing a triple point configuration.

Blast temperature is also an interesting reactive material metric worth considering. The peak blast temperature achieved in these tests was measured using a custom two-color, infrared pyrometer with an uncertainty of ± 200 K. The pyrometry measurement in this experiment is spatially averaged and the measurement results for each material are given below in Table 2. One of the tests did not capture any data.

Table 2: Peak Blast Temperatures

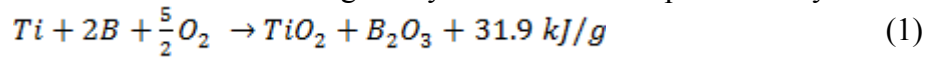
Test Material	Peak Event Temperature (K)
TiB ₂ Compound	2467
TiB ₂ Compound	2458
Ti/2B Powder Blend	2454
Ti/2B Powder Blend	2423
UIUC Mechanical Alloy #1	2456
UIUC Mechanical Alloy #1	N/A
NJIT Mechanical Alloy	2479
NJIT Mechanical Alloy	2485
UIUC Mechanical Alloy #2	2462
TiO ₂ Inert	2413

The table shows that the temperatures produced by the reaction of the tested materials are in good agreement with one another, even though the material forms are different. The temperatures seen in these experiments are also consistent with experiments performed by both Trunov and Allen. Trunov reports a temperature range of 2180 – 2370K, while Allen states a measured temperature of approximately 2500 K [7,10]. The temperatures for the more reactive alloys are very similar to the other material types, suggesting that the pyrometer is measuring similar combustion processes in each test. The melting point of boron is tabulated as approximately 2352 K, which exceeds the melting point of titanium as well as the melting point of titania and boron oxide [8]. This indicates that the boron temperature is likely dominating the reaction emission and that each of the materials is actually igniting at least a portion of the boron in the material mixture. The distinguishing factor between the reactive alloys and the other materials, then, is how much boron is being burned in each test.

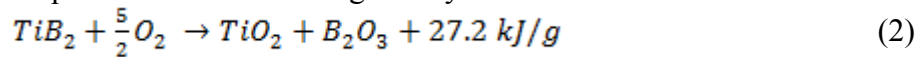
The matter of relative quantity of burned boron between material types is best answered through analysis of the pressure data and residue of the products from each test. Two quasi-static pressure (QSP) measurements were recorded by two GEMS #2200 pressure transducers for each of the materials tested, and two other separate QSP values were taken from the last 20 ms of each of the two Kulite transient pressure traces. The Kulite transducers were implemented to measure blast pressure, but also provide a long-duration QSP value. All four pressure measurements were recorded for a detonation of a totally inert pellet of titanium dioxide (TiO₂) as a baseline test. The four values, which were within 10% or better of one another, were averaged to give a mean QSP for each test conducted. The mean QSP value produced by the inert material test was 11.91 kPa, which was subtracted from the reactive mean values to yield a net QSP resulting from the reaction of the energetic material. Using an ideal gas law analysis at constant volume, an experimental value for energy release of the reactive material was determined based on the net

QSP. Table 3 gives the mass, net QSP, and the corresponding experimental energy release for each of the tested materials.

The experimental energy release can be compared to a theoretical energy release to aid in determining which materials perform best compared to the theoretical. For the mechanical alloys and the powder blend, the theoretical reaction undergone by the material is represented by



The reaction for the TiB_2 compound is similar and is given by



The formation of TiB_2 occurs through an intermetallic reaction of titanium and boron:



The theoretical energy release of the compound is lower due to the negative heat of formation of TiB_2 . The theoretical values were calculated at room temperature and a value of -323.8 kJ/mol was used as the heat of formation for titanium diboride (TiB_2) [8], [9]. When comparing theoretical and experimental energy release values in Table 3, it can be noted that the reactive materials do not achieve their full potential following the HE detonation. Higher energy output was achieved with the NJIT and UIUC #2 mechanical alloys, which release up to approximately 45.9% of the theoretical capacity with the single point detonator initiation. Comparing the measured energy release values from the two detonator configurations shows that employing a triple point configuration increases the energy release of the second Ti/2B mechanical alloy by nearly 30%, which corroborates the initial qualitative assessment based on the imaging diagnostics. The added input energy ignites more of the reactive pellet early on which enables a larger amount of boron reaction. Interestingly, the TiB_2 compound is shown to outperform the Ti/2B powder blend mixtures in terms of overpressure generation. This finding may imply that the proximity between the boron and titanium plays a large role in boron ignition and suggests that the intermetallic reaction in the powder blend plays less of a role than originally anticipated.

Table 3: Net QSP and Energy Release for Tested Materials Using Single Point and Triple Point Configurations

Test Material	Mass of Material Tested (g)	Net QSP (kPa)	Energy Release (kJ/g)	% Theoretical Energy Release
UIUC Mechanical Alloy #1	4.1900	2.71	2.93	9.18%
UIUC Mechanical Alloy #1	4.1992	4.86	5.23	16.57%
Ti/2B Powder Blend	4.1763	5.81	6.31	19.77%
Ti/2B Powder Blend	4.1900	8.14	8.81	27.59%
TiB_2 Compound	4.1719	9.07	9.36	34.41%
TiB_2 Compound	4.1418	9.34	9.62	35.36%
NJIT Mechanical Alloy	4.0635	12.01	13.41	42.02%

NJIT Mechanical Alloy	4.1587	13.38	14.59	45.71%
UIUC Mechanical Alloy #2	4.1984	13.56	14.69	45.89%
UIUC Mech. Alloy #2 Triple Point Configuration	4.144	21.68	23.73	74.35%

The total energy release of this reactive system can be assessed in terms of the energy release of its individual components. The burning of titanium to produce titania (TiO_2) contributes 13.6 J/g to the overall energy release, while the burning of boron to produce boron trioxide (B_2O_3) supplies most of the energy with 18.3 kJ/g. These energy values for the Ti/2B system are calculated on a mass basis of fuel (Ti + 2B). As can be seen from the experimental values, the first UIUC mechanical alloy, the powder blend, and the TiB_2 compound produce energy below that provided by fully burning the titanium. The conclusion can then be drawn that neither material is being consumed entirely, and it can be speculated that the boron is likely remaining entirely unburned or only a small amount of it is being burned. This analysis will be discussed further in the sections below. The mechanical alloys, however, released energies exceeding that produced only by burning the titanium, indicating the energy output was high enough to consume the titanium as well as a fraction of the boron that was mechanically alloyed to it. These results show that the NJIT and UIUC #2 mechanical alloys outperform the other materials and provide the largest QSP and highest energy release when initiated with a high explosive, especially when implementing a triple point initiation configuration.

While energy release plays a critical role in the development of novel reactive materials, it is also useful to compare the peak blast pressure enhancement effects produced by such materials. Two transient pressure transducers, labeled A and B, were implemented to record the initial blast wave pressure and QSP in each experiment. The peak overpressure of each blast was determined without fitting of the data by taking the peak value of each initial blast wave pressure curve. The curves of the initial blast pressure were also integrated to determine the blast wave impulse for each test, including the inert material test. The results of the peak pressure and impulse data are plotted below in Figure 10:

Blast Pressure and Impulse for Tested Reactive Materials

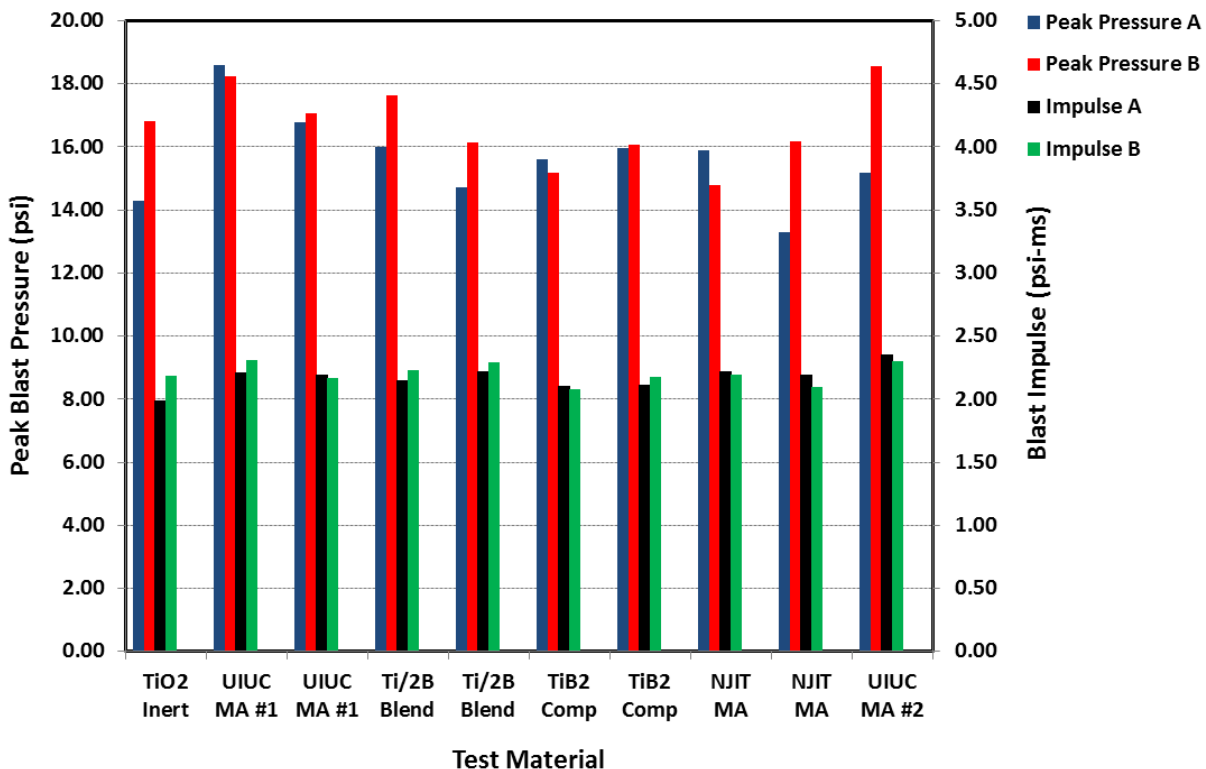


Figure 10: Graphic comparison of peak pressure and blast impulse between material forms

This chart shows the peak pressures and impulse values of the various reactive materials are similar to or only slightly higher than those produced by the inert material test, even when the triple point initiation is implemented. These results, combined with the energy release data, provide insight into the initial blast enhancement effects of the materials: while there is a definite energy release due to the reaction, the time scale over which it occurs is too long to impart any momentum to the initial blast wave. In other terms, most of the damage done by this set of energetic materials would likely be due to a longer duration overpressure rather than a higher initial blast impact.

Analysis of the reaction product residues is the final metric in comparing the performance of these material forms. The pretest SEM images of the Ti/2B powder blend and the UIUC Mechanical Alloy #2 were shown in the experimental methods section. An overview of the post-test images at the same magnification for single point and triple point initiation is shown below in Figure 11. Evidence of titanium reaction is present in all the images, represented by the spherical TiO₂ structures seen in each of the residue samples. The post-test powder blend image shows some evidence of titanium and boron reaction, though there are still amounts of unreacted material as revealed by the larger structures seen in the image. The single point initiation of mechanical alloy #2 shows more evidence of titanium reaction, but again there is some titanium

with attached nano-boron that is still unreacted near the center of the image. The triple point initiation of mechanical alloy #2 shows even more TiO_2 structures with a finer distribution and very little, if any, unreacted material in this field of view. These SEM imaging results validate the data obtained from the energy release calculations and show that the amount of titanium burned is related to the amount of boron that remains unreacted. A larger amount of TiO_2 correlates with more boron reaction in these images, implying that the titanium facilitates increased boron reaction.

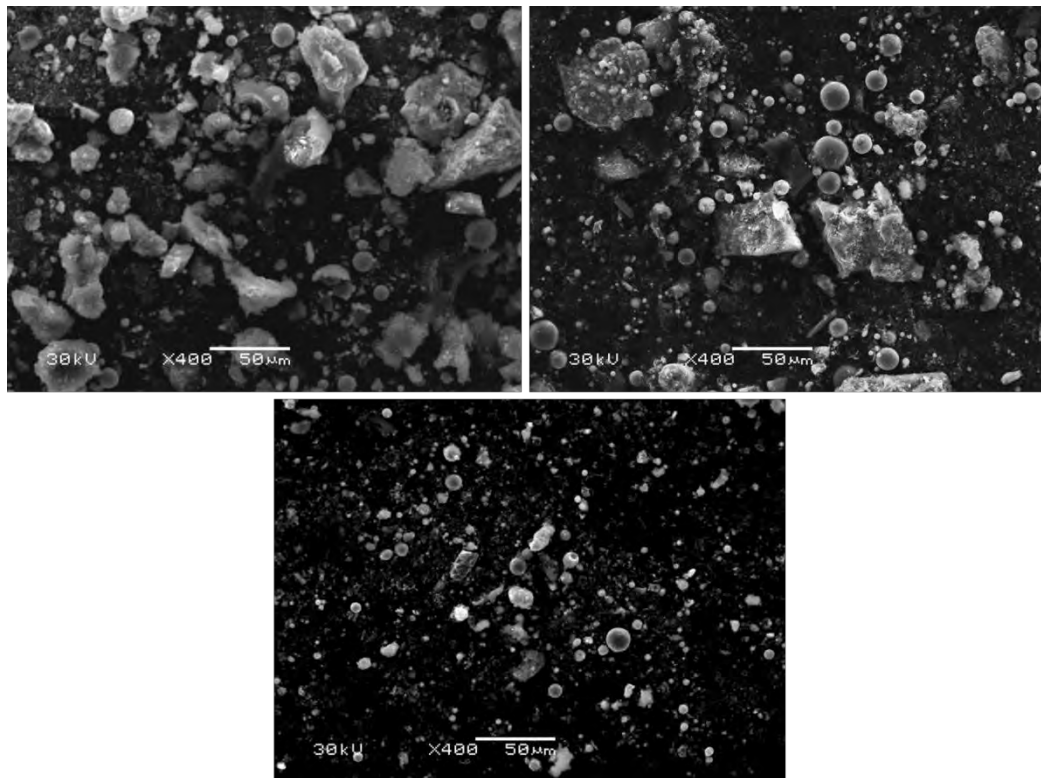


Figure 11: Post-test SEM images of (L) Ti/2B Powder Blend, (R) Mechanical Alloy #2 Single Point Initiation, and (B) Mechanical Alloy #2 Triple Point Initiation

An XRD analysis was performed on pre- and post-test powders to determine the presence of reactant and product phases in the system. Figure 12 shows the pre-test analysis of the UIUC mechanical alloy #2 and the Ti/2B powder blend. Both mixtures show a strong titanium presence, while only the powder blend shows evidence of elemental boron. This is due to the fact that the mechanical alloy contained amorphous nano-boron that has no crystalline structure and will, therefore, not be detected by x-ray diffraction.

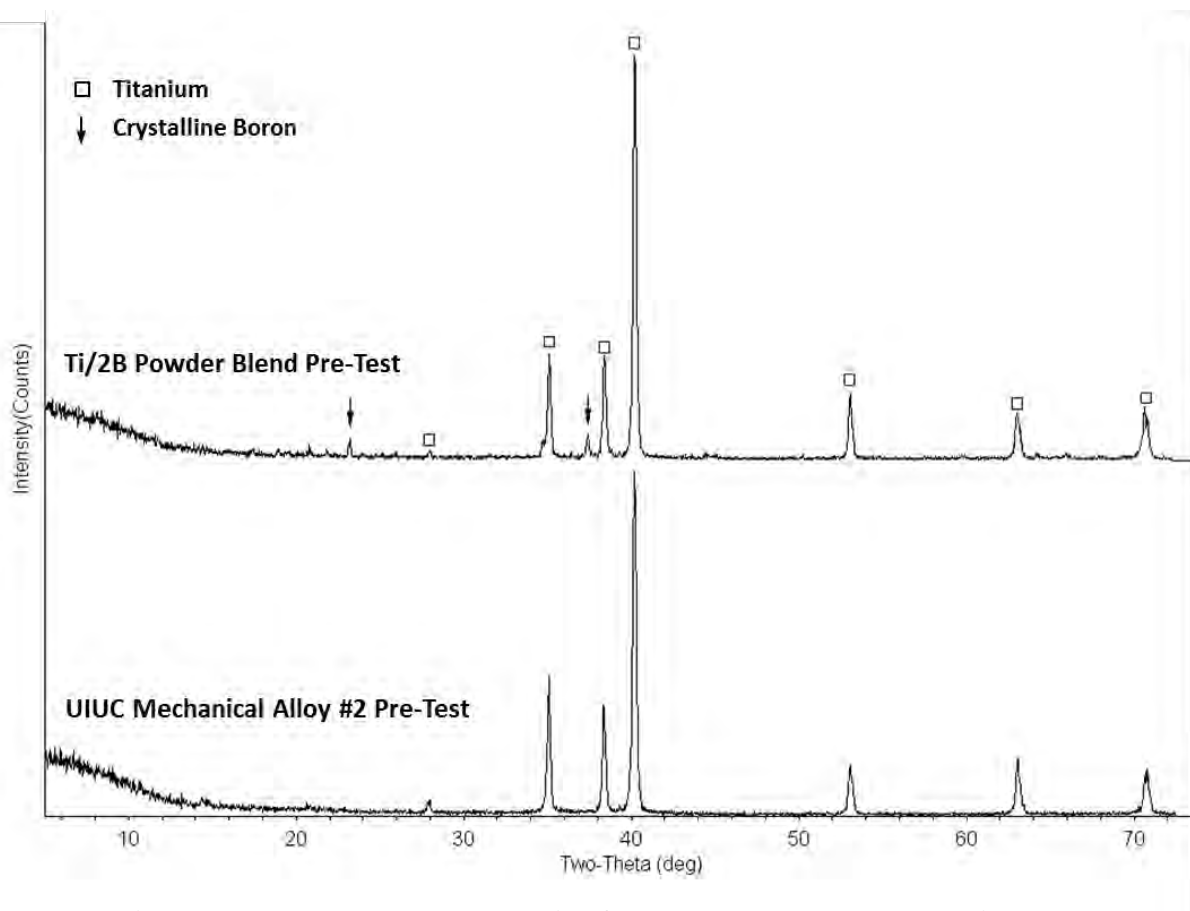


Figure 12: Pre-Test XRD analysis of powder blend and mechanical alloy

The post-combustion analysis of the residue collected from the blast chamber is shown in Figure 13 for the single point initiation of the powder blend and the mechanical alloy #2, as well as the triple point initiation of the mechanical alloy #2. The post-test x-ray spectrum of the triple point initiation of the mechanical alloy shows a much stronger presence of TiO_2 phases than either of the other collected residues. Both mechanical alloy residues confirm the presence of B_2O_3 , while there is very little, if any, boron oxide found in the residue of the powder blend. The powder blend actually shows evidence of unreacted titanium in the residue, verifying that this form of the reactive material is not fully burning the titanium and is, therefore, producing a much lower energy release and is not enhancing the boron reaction as in the case of the mechanical alloys.

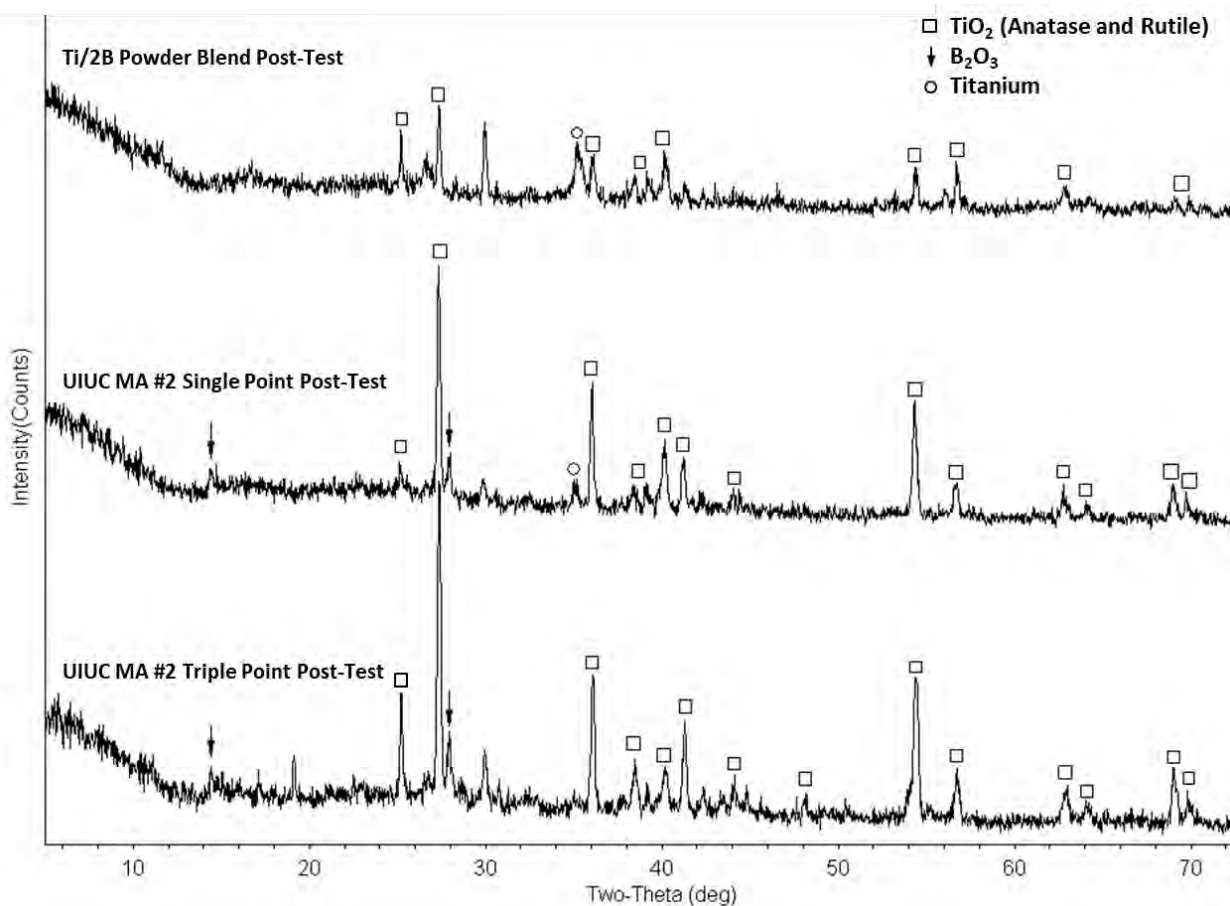


Figure 13: Post-test XRD analysis of single and triple point initiation of MA #2 with single point initiation of the Ti/2B powder blend

Conclusions

Through the detonation testing of the various forms of the Ti/2B energetic system in air, it is seen that mechanical alloys provide the best performance-enhancing effects for high explosives. Ti/2B mechanical alloys provide a larger overpressure and greater energy release than the other material forms studied, especially when implementing a triple point initiation. However, the alloying procedure and choice of constituent alloying components plays a large role in the performance of the alloy. In order to yield the highest gain from the mechanical alloys, the milling procedure must be performed properly and the constituents must reach a metastable phase without forming the TiB_2 intermetallic. The absence of boron combustion intermediates found in the spectra of the compound and powder blend validate the claim that these forms are releasing less energy upon initiation, are insufficiently burning the boron, and are providing little enhancement to the blast parameters.

Energy release calculations reveal that nanocomposite Ti/2B energetic materials produce a higher quasi-static pressure and, therefore, a higher energy yield when detonated. The nano-boron contained in these composites ignites more readily than traditional micron-sized powders, aiding in the overall energy release of the system. The other forms of the reactive material are not as efficient at igniting the larger boron particles, leading to a lower energy release. However, the TiB_2 compound outperforms the powder blend, possibly implying that the proximity of the

boron to the titanium affects the energy yield of the system. The energy output of the less reactive materials fluctuated widely, while the more reactive mixtures (including the compound) were relatively stable in the energy release. Future work on this energetic system will focus on the necessary proximity of the boron to titanium for enhanced boron ignition and its role in the differences between the compound and powder blend performances. Future studies should also explore triple point initiation more in depth to more conclusively determine its role in the reaction mechanisms of this and similar energetic systems.

References

- [1] Sheffield, O. E., Abel, J. E., LaBeur, H. E., "Development of Explosives – Metallized Explosives," Picatinny Arsenal Memorandum Report No. 44, Sept. 1953.
- [2] Vummidi, S. L., Aly, Y., Schoenitz, M., Dreizin, E. L., "Characterization of Fine Nickel-Coated Aluminum Powder as Potential Fuel Additive," Journal of Propulsion and Power, Vol. 26, May-June 2010.
- [3] Frost, D. L., Zhang, F., "Nonideal Blast Waves from Heterogeneous Explosives," Materials Science Forum, Vol. 465-466, 2004, pp. 421-426.
- [4] Gogulya, M. F., Brazhnikov, M. A., "Detonation of Metalized Composite Explosives," *Shock Wave Science and Technology Reference Library*, Vol. 4, Ch. 4, Springer, Berlin, 2009.
- [5] Schoenitz, M., Dreizin, E. L., and Shtessel, E., "Constant Volume Explosion of Aerosols of Metallic Mechanical Alloys and Powder Blends," Journal of Propulsion and Power, Vol. 19, May–June 2003, pp. 405–412.
- [6] Jiang, X., Trunov, M., Schoenitz, M., Dave, R., Dreizin, E. L., "Mechanical Alloying and Reactive Milling in a High Energy Planetary Mill," Journal of Alloys and Compounds, Vol. 478, 2009, pp. 246-251.
- [7] Trunov, M., Hoffmann, V., Schoenitz, M., Dreizin, E. L., "Combustion of Boron-Titanium Nanocomposite Powders in Different Environments," Journal of Propulsion and Power, Vol. 24, No. 2, March-April 2008.
- [8] Chase, M. W., "NIST-JANNAF Thermochemical Tables," 4th ed., 1998.
- [9] Barin, I., "Thermochemical Data of Pure Substances," VCH, Verlagsgesellschaft mbH, 1995.
- [10] Allen, D., "Optical Combustion Measurements of Novel Energetic Alloys in a Heterogeneous Shock Tube," Master's Thesis, University of Illinois Urbana-Champaign, 2012.

CHAPTER 20: HEAT TRANSFER EFFECTS IN NANO-ALUMINUM COMBUSTION AT HIGH TEMPERATURES

Introduction

Nano-aluminum combustion is an active area of research due to the potential to improve performance in propellants and explosives [1, 2]. The mechanism of nano-aluminum combustion remains poorly understood. For larger particles burning in the diffusion limit, a fair understanding of the ignition and combustion characteristics has been demonstrated [3] such that predictive simulations are possible. However, for particle sizes approaching the micron scale under most conditions, many of the trends observed in large particle combustion no longer apply. Burning rates begin to deviate from a d^2 law, with exponents curiously observed to be less than 1[4-6]. The pressure dependence of the burning rate becomes significant[7], and there is evidence that the relative oxidation efficiencies of CO₂ and H₂O change. Peak combustion temperatures begin to decrease, and ignition temperatures are also markedly lower[8]. For nano-scale Al, a significant ambient temperature dependence on the burning rate emerges[9].

Significant modeling work on n-Al combustion has occurred [8, 10, 11] and some observations have been reconciled. However, a robust model capable of simulating combustion kinetics over a wide range of conditions has not yet been achieved. A common assumption in particle combustion is that as particle size decreases, particle combustion transitions from a gas-phase diffusion limit to a mode of combustion limited by surface reaction or solid-state diffusion. In this classic latter limit, there is no gas-phase combustion, and species concentration and thermal gradients approach zero. Due to rapid heat transfer of small particles, the particle temperature does not significantly exceed that of the ambient gas. Indeed for some conditions, e.g. n-Al burning in CO₂, negligible temperature overshoots were observed in previous work. However, under other conditions with more efficient oxidizers at higher pressures, significant rises in particle temperature were measured[9].

For nano-scale particles in most environments, Knudsen number effects on heat transfer cannot be neglected since Kn ~.001 to 1. These effects are considered in laser induced incandescence (LII) experiments to determine particle size distributions of nano-particles in flows [12] and must also be considered when determining the transient thermal profile of a combusting nano-aluminum particle. However, use of non-continuum heat transfer expressions requires estimation of the energy accommodation coefficient (EAC). For LII experiments involving carbon particles, values of 0.4 have been measured[13], and thus it is common to use similar values (or even a value of 1) for other materials under similar conditions. However, theoretical and experimental work performed by Altman suggests that at high particle and gas temperatures, certain metal and metal oxide nano-particles have very small energy accommodation coefficients[14, 15]. Radiation consequently becomes a more significant pathway for heat transfer in the low accommodation coefficient regime. The experimental work by Altman et al. was performed using laser irradiation to heat up nanoparticles generated in a flame. The energy accommodation coefficient was found to be near 0.005 which agreed nicely with their theoretical upper limit[14]. Nano-aluminum particle combustion may potentially experience a similar thermal isolation effect in many applications. With such low accommodation coefficients the heat transfer from the particle via collision with gas molecules becomes inefficient, leading to particle temperatures much higher than those expected using EAC ~1.

In this work we perform experiments on nano-aluminum combustion to monitor the particle temperature, burn rate, and emission spectra. High particle temperatures and longer burn times are expected for a transition to the free molecular regime accompanied by a low energy accommodation coefficient. For ultrafine particles, classical theory predicts that rapid heat transfer results in combustion temperatures that only minimally exceed the ambient temperature, even when common Knudsen number correlations are used for Nusselt number calculation [12]. Prediction of the particle temperature requires specification of the reaction rate (i.e. heat release rate) in addition to the heat transfer coefficient. In this research the experimental data on burning time and temperature are supported by a simple model of nano-aluminum combustion that employs as few limiting assumptions as possible, focusing only on the energy balance leading to particle temperature rise. Multiple heat transfer models are considered to determine the predicted transient particle temperature and to see if the nano-aluminum particle experiences thermal isolation from the surrounding gas.

Experimental Set-up

The nano-aluminum particles were investigated using a heterogeneous shock tube described in detail in a previous publication[16]. The shock tube is capable of producing controlled high temperature and high pressure environments with various gas compositions. Temperatures greater than 4000 K and pressures above 30 atm are achievable behind the reflected shock with test times near 2 ms. Low temperatures were used for this study to test nano-aluminum combustion which has been shown to ignite at temperatures below 2000 K[9]. The combustion of the nano-aluminum particles was monitored behind the reflected shock in order to achieve the high pressures desired. The pressure was varied between 3.5-20 atm to determine the effect of the oxidizer concentration on the particle temperature and burn time.

The shock tube has an 8.4 m driven section and an 8.9 cm internal diameter. A converging duel diaphragm system separates the high pressure helium gas from the oxidizing environment. The driver to driven pressure ratio is controlled to produce the desired shock strength. The velocity of the shock is measured using four piezoelectric pressure transducers at different axial locations. The ambient temperature and pressure of the gases trailing the incident and reflected shock are calculated with the Gordon-McBride equilibrium code [17] using the known initial driven pressure, composition, and measured shock velocity. The test time of the shock tube can also be found from the pressure transducer traces and is typically near 2 ms.

A schematic of the shock tube operation with radial injection and the end section with fiber optic view ports is shown in Figure 1. This end section allows for photodiode access at multiple axial locations. The end wall has a sapphire view port for further optical access. The fiber optic section is described in further detail in a previous publication [9]. Each test was run with three photodiodes monitoring different axial locations centered at the location of aluminum particle stagnation behind the reflected shock. A nano-aluminum particle has a very small Stokes number, and therefore the particle accelerates quickly behind the incident shock and stagnates within a few microseconds behind the reflected shock. For this reason particle motion behind the reflected shock is neglected.

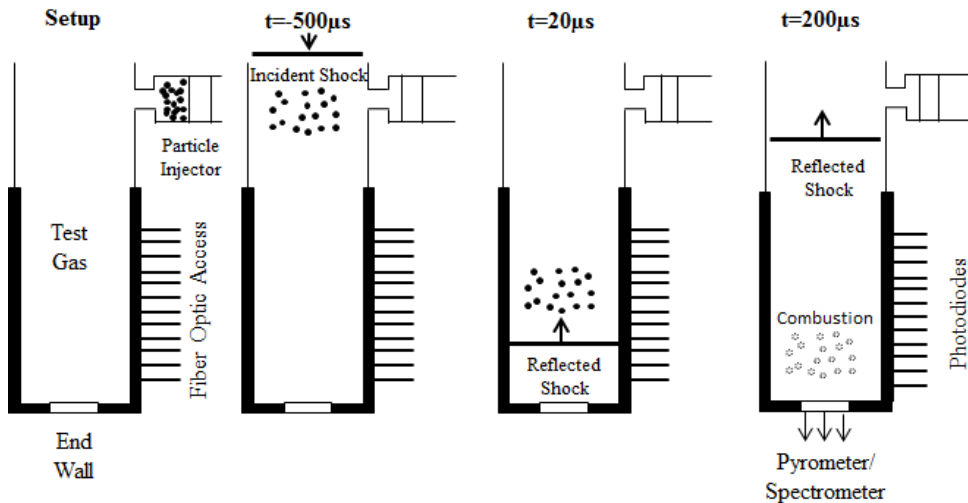


Figure 10: Schematic of shock tube test section with fiber optic access

Particles are injected radially into the test gas prior to diaphragm rupture using a pneumatically driven piston. The particles become entrained in the gas flow behind the incident shock and are swept towards the end-wall until the reflected shock stagnates them and they combust. Four particle classes were chosen to vary particle diameter while measuring burn time, temperature, and emission spectra.

A Hitachi S-4700 high resolution scanning electron microscope (SEM) was used to accurately characterize the particle size distribution of each sample. Over 100 particle diameter measurements were made from each sample in order to obtain a distribution. Table 1 shows the number average and mass average particle diameters of each nominal sample powder. The 18 nm particles were not characterized because the resolution required to characterize these particles accurately was not achievable. Any distribution obtained would have been biased towards the larger particles which were readily resolved while the smaller particles below 18 nm would not have been accounted for. The highest resolution images achieved qualitatively showed the 18 nm particle distribution to be significantly smaller than the other sample distributions even though an accurate average could not be quantified.

Table 1: Particle Classes

Particle Size (nm)	Particle Type	Number Average	Mass Average
		Particle Diameter (nm)	Particle Diameter (nm)
18	SkySpring Nanomaterials	Uncharacterized	Uncharacterized
50	SkySpring Nanomaterials	73.2	80.9
80	NovaCentrix	83.4	90.1
110	NovaCentrix	100.0	110.0

Each sample had a large distribution of particle sizes. Figure 2(a)-(c) show the histograms of the three characterized samples and Figure 2(d) shows a corresponding SEM

image for the 80 nm particles. All particles imaged were found to be highly spherical. Nano-aluminum has previously been shown to form both weak and strong agglomerates dependent on the manufacturing process. The images show the particles acquired have weak agglomeration and very little particle necking. The particles acquired from NovaCentrix are specified to be 80-90% aluminum and the oxide-coating thickness is 1.5-2.5 nm. Both samples acquired from SkySpring Nanomaterials are 99.9% pure on a trace metals basis.

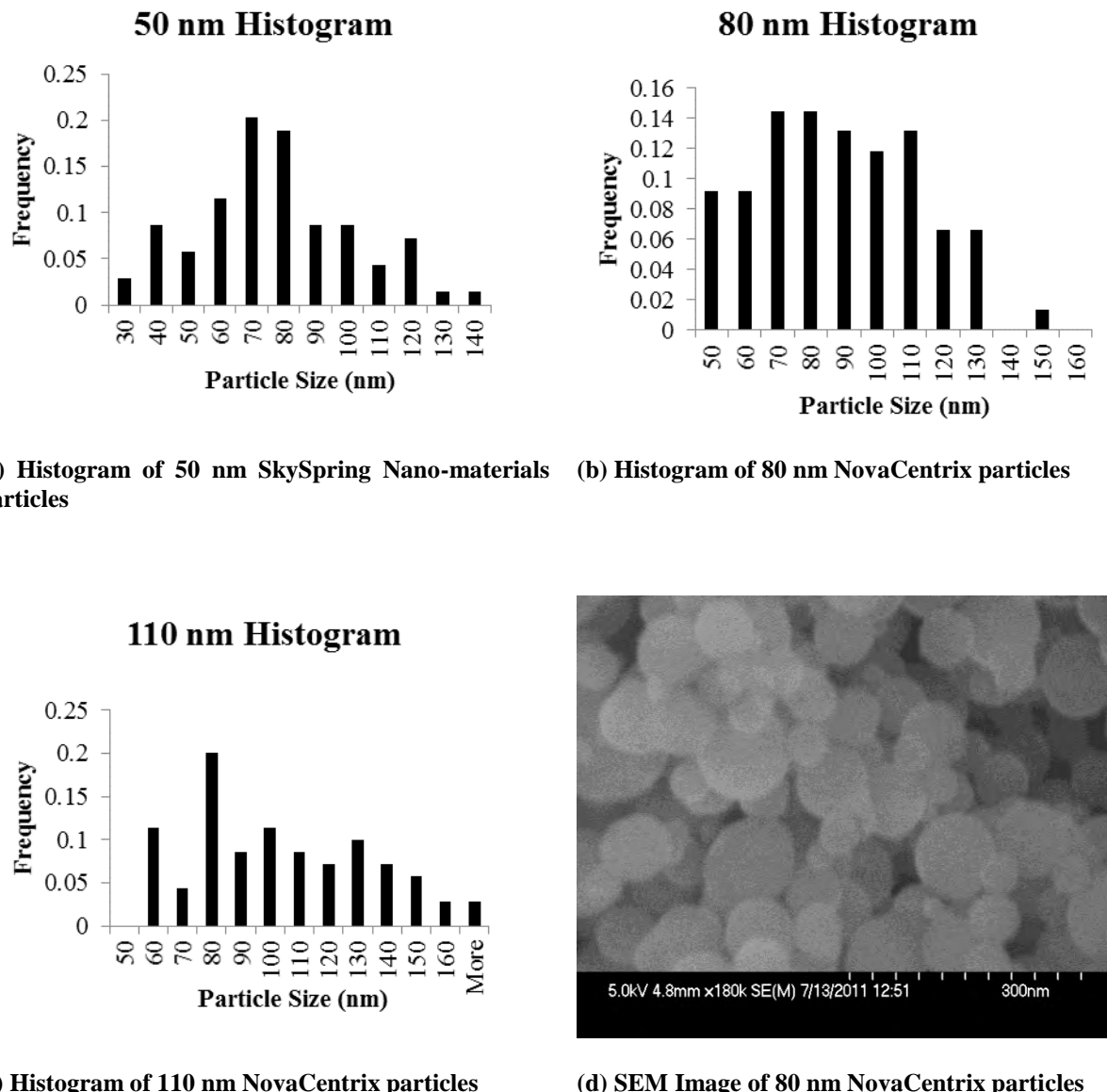


Figure 11 Particle Characterization

Emission spectra were collected using an Ocean Optics spectrometer with a 10 μm inlet slit and a 200-550 nm range. The spectral resolution of the spectrometer was approximately 1nm full-width-half-maximum (FWHM). The spectra were time integrated over the entire combustion event; a mechanical shutter was used to avoid emission from particles after the test time of the

shock tube. The spectrometer was intensity calibrated using a tungsten calibration lamp with a filament temperature of 3200 K.

Pyrometry was performed using a custom-built 3-color pyrometer. A trifurcated fiber bundle images the light from the test section through a narrow slit. The trifurcated cable splits the light collected from the test into three separate branches. Each branch passes through a collimator, interference filter, and to a photomultiplier. The interference filters have a 10 nm FWHM bandpass centered at 705, 826, and 905 nm. The shorter wavelengths are measured using Hamamatsu R928 photomultipliers; the 905 nm light is measured using a R636-10 photomultiplier with an infrared-sensitive GaAs photocathode. Outputs of the photomultipliers are amplified using a Stanford Research Systems Quad preamplifier unit with a 300 MHz bandwidth. The time response of the pyrometry system is sub-microsecond. The system is calibrated using a tungsten calibration lamp. Noise level is typically 10-20% of the signal and the measurement uncertainty has previously been estimated to be ± 150 K for micron sized particles[18].

Photometric burning time measurements were made using photodiodes coupled to different axial locations using the fiber optics in the end section shown in Figure 1. Three ThorLabs PDA36A amplified photodiodes were used to capture the luminosity from each experiment. The emission was unfiltered because the spectroscopic measurements indicated no molecular emission. The time resolution of the photodiodes is sub-microsecond.

Experimental Results

Previous measurements by Bazyn et al. have shown weak or no molecular aluminum monoxide (AlO) emission at pressures below 32 atm for nano-aluminum combustion[9]. Similar results were seen in the present experiments. Each spectrum showed only thermal radiation and no significant gas phase emission, indicating that the primary combustion mechanism involves surface reactions as hypothesized. If gaseous aluminum were present, atomic aluminum lines would likely be seen at 394.4 and 396.1 nm, and banded aluminum monoxide (AlO) emission from the *B-X* transition would likely be seen in the range from 460-530 nm. It is possible that the gas phase species are present but are not at high enough temperatures to cause detectable spontaneous emission. However, measurements by Lynch et al. showed no aluminum or aluminum monoxide absorption below 1500 K which further suggests that gas phases are not present in significant amounts[19]. The lack of gas phase emission is consistent with a reaction model in which surface processes limit the combustion rate

The average burning times can be seen in Table 2 using the 10%-90% area method to calculate the burn time. In order to calculate the 10%-90% area burn time the background intensity in the post combustion environment due to heated particles was subtracted off following the method described in a previous publication[9]. In short, a linear rise is fit from initial noise level to the background intensity level. The rise is assumed to occur from the onset of luminosity to the point of peak intensity where it then remains constant. There is some deviation from the average due to the large particle distribution and also due to the inherent uncertainty in determining the background intensity levels. More important, however, is that the luminosity traces show that as the average particle diameter increases, the photodiode trace becomes wider and the time it takes to reach peak intensity becomes longer. The burning time of the particles spans from 50-200 μ s consistently for all samples. The values for the burn time seen in Table 2 compare favorably with those seen previously by Bazyn et al. in similar conditions and are shorter than those seen in micron sized aluminum at higher temperature.

Bazyn found burn times near 170 μ s for 80 nm aluminum particles in 20% O₂ and 80% N₂ at higher pressures[9].

It is important to consider the interpretation of the luminosity traces. The emission spectrum showed no evidence of molecular emission, and therefore, the luminosity profiles being shown cannot be directly correlated to the presence of aluminum monoxide as has previously been done. When monitoring molecular emission such as AlO the assumption is that the luminosity trace corresponds to AlO presence, which indicates combustion because AlO is a key intermediate species in the gas phase combustion process. However, in this case the luminosity is due to thermal radiation evidenced by the emission spectra. Therefore, we are correlating burn time to particle temperature with a different assumption than that made when monitoring emission filtered around an aluminum monoxide band as is normally the case for micron sized particles[4].

Table 2: Summary of particle burning time in air calculated using the 10-90% area burn time method of calculation

Particle Type	Burning Time (μ s)	Deviation (μ s)
SkySpring 18nm	74.5	20.5
SkySpring 50nm	119.5	6.4
NovaCentrix 80nm	129.2	9.6
NovaCentrix 110nm	134.3	6.7

The three color pyrometry measurements indicated a rise in particle temperature above the ambient gas temperature. Multiple tests were performed for each particle size at 1500 K and 20 atm in an air-simulated environment. Table 3 shows the peak temperature calculated at the location of peak intensity tabulated for each particle class size. The temperature rise at high pressures is due to the increase in local number density of oxygen at the surface of the particle which scales linearly with pressure. The average temperature remains relatively constant for all particle sizes.

Table 3: Average peak temperature for each particle size

Particle Type	Peak Temperature (K)	Deviation (K)
SkySpring 18nm	3301	251
SkySpring 50nm	3274	338
NovaCentrix 80nm	3169	482
NovaCentrix 110nm	3472	252

The average peak temperature is between 3200-3500 K for all cases. Bazyn et al. similarly found peak temperatures for nano-aluminum combustion near 2500 K for 8.5 atm pressures and 3500K for 32 atm pressures. The values of the peak temperatures at 20 atm found in these tests range between the values found by Bazyn. These temperatures are near the boiling temperature of aluminum which varies from 3040 K at 4 atm to 3600 K at 32 atm. In a surface-process limited combustion mechanism the peak temperature increases with pressure since the reaction rate (heat release rate) is proportional to the number density of oxidizer in the vicinity of

the particle. A low pressure test performed at 3.5 atm gave a peak temperature of 2375 K, which is again consistent with the trend predicted by the surface-process limited combustion model.

The high peak temperatures and relatively long burn times observed in this work and previously by Bazyn [9] suggest that heat transfer from the particles must be relatively slow compared to that suggested by common models. In the continuum limit ($\text{Nu} \sim 2$), the nano-aluminum particle would need to fully combust in less than 0.5 μs in order for the particle to reach 3300 K in the ambient conditions of the experiment. Using a non-continuum expression valid for the transition regime ($\text{Nu} = 0.3/\text{Kn}$), the burning time is only extended to 1.5 μs . The data clearly suggests this is not the case. A more detailed heat transfer analysis is presented in the next section.

Model Description

A nano-aluminum combustion model was developed to further investigate the heat transfer of the particles. The model is an energy balance of the particle that assumes a surface-process limited combustion mechanism and heat transfer through conduction to the ambient gas and radiation to the walls of the shock tube at 300 K. Figure 3 depicts facets of the combustion model. The reaction surface is the initial surface area of the particle and does not change because diffusion of oxidizer and fuel are assumed to occur much faster than the limiting surface process (i.e. surface diffusion or chemical reaction).

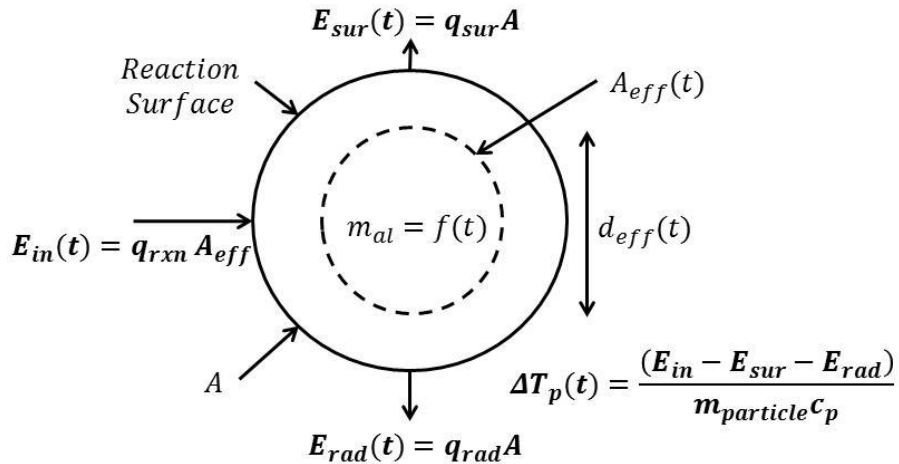
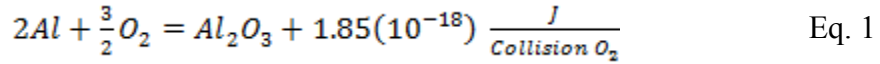


Figure 12: Depiction of the surface process nano-aluminum combustion and heat transfer model

The influx of heat to the particle is assumed to be due to the chemical reaction between the oxygen and aluminum following Equation 1, which releases $1.85(10^{-18})$ joules of energy for each collision of oxygen molecule resulting in reaction with the aluminum surface. The rate of reaction is calculated using the number density of oxygen at the particle surface (Eq. 2), thermal velocity (Eq. 3), the collision frequency (Eq. 4), and a sticking probability ϕ which is a variable parameter in the model.

The sticking probability represents the percentage of collisions that react and has a value between zero and one. A sticking probability of zero represents no reaction, and a sticking probability of one indicates each collision results in chemical reaction. The sticking probability is assumed to remain constant during the combustion of the aluminum particle. Equations 2-6

represent the calculation for the heat due to the reaction. An effective area is used for the influx of heat to model the reduction in the amount of aluminum surface area at the reaction surface during combustion. The effective area is determined by calculating the surface area of the remaining mass of aluminum at each time step as if it were a sphere. The assumption is that the reaction occurs at the outer surface of the particle, but as the particle burns the amount of reactive area decreases as a function of time following Eq. 5.



$$N_{O_2} = \frac{X_{O_2} P}{T_a K_b} \quad Eq. \ 2$$

$$c = \left(\frac{8k_b T_a}{m_{O_2} \pi} \right)^{1/2} \quad Eq. \ 3$$

$$f = (N_{O_2})^{\frac{c}{4}} \quad Eq. \ 4$$

$$A_{eff}(t) = \pi \left(\frac{m_{al}}{\rho_{al}} \frac{6}{\pi} \right)^{2/3} \quad Eq. \ 5$$

$$E_{in} = A_{eff} f q \phi \quad Eq. \ 6$$

The conduction of heat to the surrounding gas is the key effect of interest in the present study. As previously mentioned, Altman predicts a decrease in the accommodation coefficient at high temperatures. Altman puts an upper limit on the accommodation coefficient α_E following Equation 7, where Θ is the Debye temperature of the solid. For the conditions in this study Eq. 7 puts the upper limit of the accommodation coefficient at approximately 0.006. The heat transfer to the surroundings through conduction in the free molecular regime is calculated following Equation 8. Equation 9 shows the corresponding heat transfer equation assuming continuum mechanics, where k is the thermal conductivity of the gas, Nu is the Nusselt number, and d is the particle diameter. The radiation to the walls follows the Stefan-Boltzmann law using Eq. 10 with an emissivity of 0.1 for alumina[20]. The temperature of the particle changes as shown in Eq. 11.

$$\alpha_E < \frac{1}{\left(2 \frac{C_V}{R} + 1 \right) T_g T_s} \quad Eq. \ 7$$

$$E_{sur}(t) = A \frac{\alpha_e P_c}{8T_a} \left(\frac{\gamma+1}{\gamma-1} \right) (T_p - T_a) \quad Eq. \ 8$$

$$E_{sur}(t) = A (Nu) \frac{k}{d} (T_p - T_a) \quad Eq. \ 9$$

$$E_{rad}(t) = A \epsilon \sigma (T_p^4 - T_w^4) \quad Eq. \ 10$$

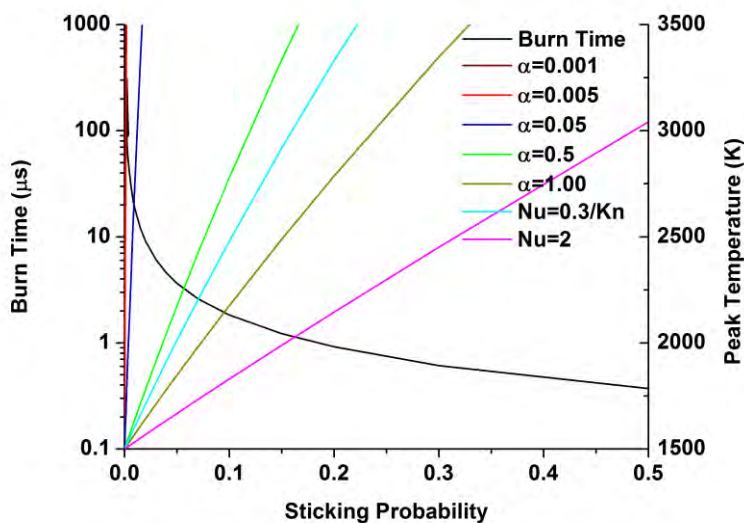
$$\Delta T(t) = \frac{(E_{in} - E_{sur} - E_{rad})}{m_{particle} c_p} \quad Eq. \ 11$$

Discussion

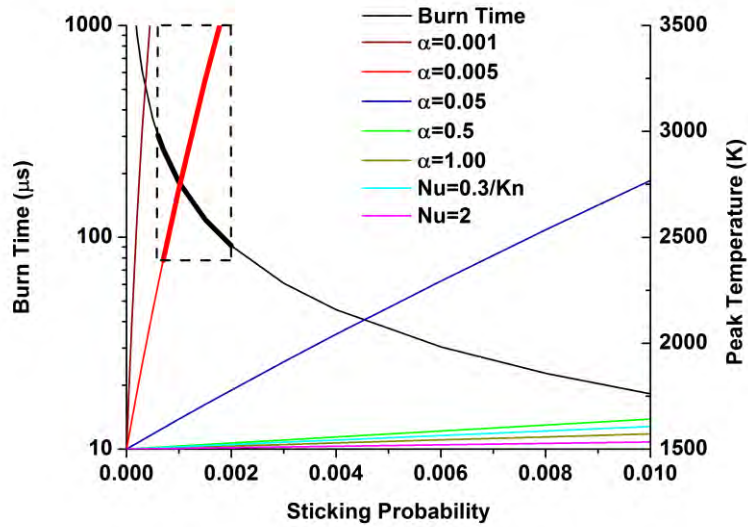
The model has two unknown parameters which must be fit to experimental data. These parameters are the sticking probability and the energy accommodation coefficient. The two unknowns are fit by comparing the model peak temperature and burning time predictions to the values obtained in the shock tube experiments. Figure 4(a) and (b) show the model predictions graphically. The burn time calculated in the model is independent of the heat transfer of the particle with the assumptions provided, and is plotted in black on the log scale. The particle is considered fully burned in the model once 90% of the original mass is reacted. A sticking probability of zero represents no reaction and therefore the burn time asymptotes towards infinity at this value. The particle temperature increases with increasing sticking probability as expected because a larger percentage of the collisions result in exothermic heat release.

Seven potential temperature profiles are plotted for comparison, each using a different accommodation coefficient or heat transfer assumption. Five accommodation coefficients, a correlation for the Nusselt number deduced from laser induced incandescence on nanoparticles[12], and a Nusselt number of 2 are considered. For a given sticking probability the burning time and particle temperature considering one of the seven heat transfer models satisfy the energy balance of the system.

It is evident that an accommodation coefficient between 0.001-0.005 is necessary in order to achieve burn times greater than 100 μ s and peak temperatures of ~3300 K as indicated by the highlighted section of Figure 4(b). The dashed box indicates the experimentally determined possible peak temperatures for sticking probabilities that give burning times also in the experimentally observed range. The best fit values for the accommodation coefficient and sticking probability are 0.0035 and 0.0009 respectively. The values obtained for the accommodation coefficient here match extremely well with the value of 0.005 found experimentally by Altman in previous work. These results clearly suggest that the nano-aluminum particles are experiencing thermal isolation from the ambient gas due to low energy accommodation coefficients.



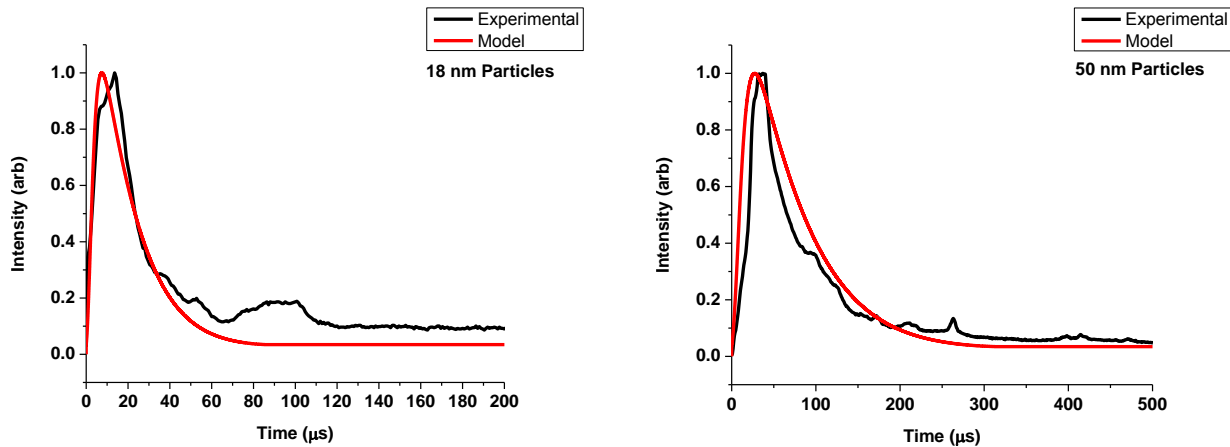
(a) Model results for an 80 nm particle comparing burn time and peak temperature at ambient conditions of 1500 K and 20 atm for sticking probabilities between 0-0.5



(b) Model results for an 80 nm particle comparing burn time and peak temperature at ambient conditions of 1500 K and 20 atm for sticking probabilities between 0-0.01

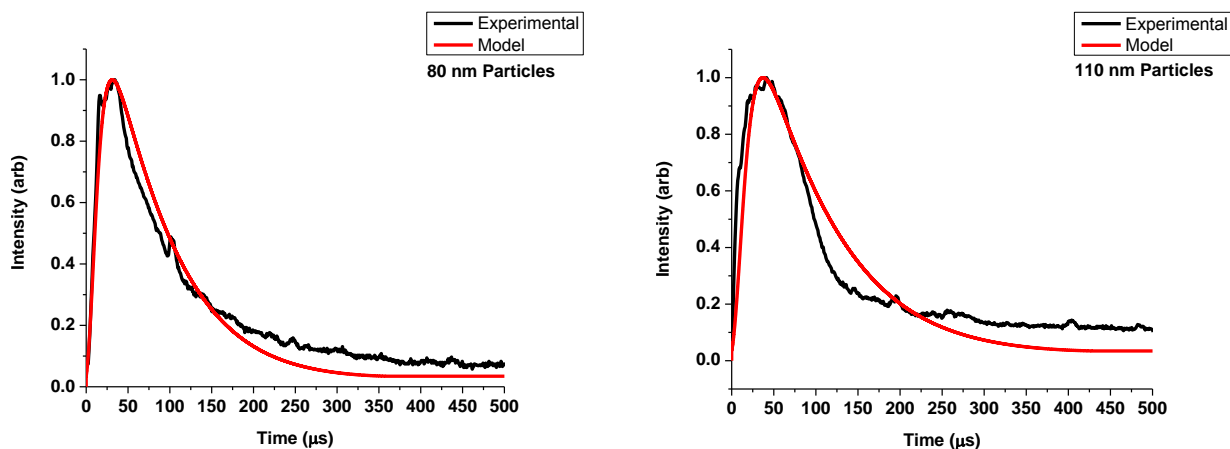
Figure 13 Comparison of burn time and peak temperature using various heat transfer models.

Further comparison of the simple model with the experiment can be made by comparing the luminosity trace to the relative model-predicted thermal radiation intensity (i.e. $\sim T^4$). Figure 5(a)-(d) shows the predicted luminosity compared to photodiode traces from the experiment at 1500 K and 20 atm in air. For these traces the best fit accommodation coefficient of 0.0035 and sticking probability of 0.0009 were chosen. The comparison between model and experiment is quite good.



(a) Model radiation for 18 nm particles at 1500 K and 20 atm in air compared to experimental data

(b) Model radiation for 50 nm particles at 1500 K and 20 atm in air compared to experimental data



(c): Model radiation for 80 nm particles at 1500 K and 20 atm in air compared to experimental data

(d) Model radiation for 110 nm particles at 1500 K and 20 atm in air compared to experimental data

Figure 14 Comparison of model radiation and experimental luminosity measurements for each particle class

The model predicts the peak temperature for each particle size to be approximately 3400 which is below the 3450 K boiling temperature of aluminum at 20 atm within uncertainty. It is likely that as the particle heats up some of the aluminum is volatilized and reacts at the surface of the particle limiting the peak temperature of the system to the boiling temperature of the aluminum at the given pressure. The peak temperature does not change significantly in the model with particle size because all modes of heat transfer scale similarly. The heat loss scales with d^2 and the heat due to chemical reaction scales with the effective area, but the peak temperature occurs near the start of the particle reaction when the effective area is very near the initial area of the particle. The transient temperature profiles change with particle size due to the effective area approximation as seen in Figure 5(a)-(d). The model prediction that the peak temperature

remains constant independent of the particle diameter agrees with the experimental data shown in Table 3 within experimental uncertainty.

The comparison extends to lower pressures as well. The model predicts a peak temperature of 2600 K at a pressure of 3.5 atm using the accommodation coefficient (0.0035) and sticking probability (0.0009) as those used to fit the data at 20 atm. Pyrometry measurements found the temperature to be 2375K at 3.5 atm. The model slightly over predicts the temperature, but the accommodation coefficient used was fit to a system with the peak particle temperature of 3100 K and an ambient gas temperature of 1500 K. In the case of lower pressure, the peak temperature is lower and following Eq. 6, a lower particle temperature implies a higher accommodation coefficient. Scaling the accommodation coefficient by this difference in expected temperature brings it to a value of approximately 0.0047. Using this value further drops the predicted temperature to 2500 K which is closer to the experimental value of 2375 ± 150 K. Clearly the accommodation coefficient may vary as the particle temperature changes during the combustion event, but here it is assumed constant.

The possible effect of particle agglomeration on the results and conclusions is worthy of consideration. If nanoparticles agglomerate rapidly or are not efficiently de-agglomerated, then large agglomerates may still readily ignite at low temperatures but will coalesce and burn as larger particles. If agglomerates contain enough primary particles, the coalesced particulate may be large enough to burn in the diffusion limit, with correspondingly high temperatures.

In our arrangement, breakup of agglomerates is strongly promoted during injection and by the shock waves. During injection, the dispersed aerosolized particles are entrained in a jet of gas, then sent through an array of fine meshes that have been shown to effectively produce a well-dispersed cloud [21]. Petersen used a much milder form of injection [22] and directly measured particle sizes in the resulting cloud, finding little agglomeration of aluminum nanoparticles within the first minute after injection. Furthermore, it has been shown that the strong shear forces of the shock waves are effective at breaking weak agglomeration in nanoparticles [23-25]. Thus, the experimental evidence to date suggests clouds formed in the shock tube are, at the least, resistant to the formation of agglomerates.

Post shock agglomeration should also be relatively slow. Calculations considering an evenly dispersed thin cloud of particles behind the incident and reflected shock using the Smoluchowski monodisperse model, which ignores electrostatic forces, suggest that each particle will conservatively collide with less than two other nano-particles during the test time. In order for a nanoparticle to increase in size from 100 nm to 500 nm, it would require an agglomerate consisting of approximately 125 primary particles assuming spherical geometry. Heat transfer analysis of a 500 nm particle using the non-continuum heat transfer approximation still shows that the agglomerate particle must combust in less than 15 μ s in order to reach 3000 K, still well below what is seen in experiment. Furthermore, the lack of significant AlO and Al emission during nano-particle combustion at 1500 K also suggests that it is not particles burning in the diffusion limit that is responsible for the measured temperature overshoot citeLynch2010CST.

Conclusions

It has been shown that in order for nano-aluminum particles to achieve the burning time and peak temperatures observed experimentally, the heat transfer from the burning particles must be significantly slower than would be expected assuming EAC values approaching 1. This effect was theoretically described by Altman and shown to be true in experiments using laser irradiation. In those experiments the energy accommodation coefficient was found to be

approximately 0.005. It has been shown here, that the best fit for the energy accommodation coefficient is 0.0035 which agrees very well both with the experiments performed by Altman and the upper estimate described previously in Eq. 6. It is therefore concluded that at the high ambient temperatures recorded in the shock tube, the particles are experiencing thermal isolation from the surrounding gas.

This effect has important consequences for modeling of nano-aluminum combustion. In particular, particle temperatures will likely be much higher than current models predict, and radiation effects may be enhanced. It is expected that similar results will arise for other metal condensed phase nano-particles combusting at high temperatures, as suggested by Altman.

References

- [1] G. A. Risha, B. J. Evans, E. Boyer, R. B. Wehrman and K. K. Kuo, "Nano-Sized Aluminum and Boron-Based Solid-Fuel Characterization in a Hybrid Rocket Engine," in *39th AIAA/ASME/SAE/ASEE Joint Propulsion Conference*, Huntsville, AL, 2003.
- [2] K. K. Kuo, "Activated aluminum as a stored energy source for propellants," in *Challenges in Propellants and Combustion, 100 Years after Nobel*, Stockholm, Begell House, 1997, pp. 636-645.
- [3] M. Beckstead, "Correlating aluminum burn times," *Combustion, Explosion and Shock Waves*, vol. 41, no. 5, pp. 533-546, 2005.
- [4] P. Lynch, H. Krier and N. Glumac, "A correlation for burn time of aluminum particles in the transition regime," *Proceedings of the Combustion Institute*, vol. 32, pp. 1887-1893, 2009.
- [5] S. Mohan, M. Trunov and E. Dreizin, "Heating and Ignition of Metal Particles in the Transition Heat Transfer Regime," *Journal of Heat Transfer*, vol. 130, 2008.
- [6] P. Bucher, R. A. Yetter, F. L. Dryer, E. P. Vincenzi, T. P. Parr and D. M. Hanson-Parr, "Observation on Aluminum Particles Burning in Various Oxidizers," in *33rd Combustion Meeting*, 1996.
- [7] T. Bazyn, H. Krier and N. Glumac, "Oxidizer and Pressure Effects on the Combustion of 10-micron Aluminum Particles," *Journal of Propulsion and Power*, vol. 21, no. 4, 2005.
- [8] M. A. Trunov, S. M. Umbrajkar, M. Schoenitz, J. T. Mang and E. L. Dreizin, "Oxidation and Melting of Aluminum Nanopowders," *Journal of Physical Chemistry*, vol. 110, no. 26, pp. 13094-13099, 2006.
- [9] T. Bazyn, H. Krier and N. Glumac, "Combustion of Nano-Aluminum at Elevated Pressure and Temperature Behind Reflected Shock Waves," *Combustion and Flame*, vol. 145, pp. 703-713, 2006.
- [10] K. Park, D. Lee, A. Rai, D. Mukherjee and M. R. Zachariah, "Size-Resolved Kinetic Measurements of Aluminum Nanoparticle Oxidation with Single Particle Mass Spectrometry," *Journal of Physical Chemistry*, vol. 109, pp. 7290-7299, 2005.
- [11] V. Levitas, "Burn time of aluminum nanoparticles: Strong effect of the heating rate and melt-dispersion mechanism," *Combustion and Flame*, pp. 543-546, 2009.
- [12] F. Liu, K. Daun, D. Snelling and G. Smallwood, "Heat conduction from a spherical nanoparticle: status of modeling heat conduction in laser-induced incandescence," *Applied Physics B*, vol. 83, pp. 355-382, 2006.
- [13] R. Starke, B. Kock and P. Roth, "Nano-particle sizing by laser-induced-incandescence (LII) in a shock wave reactor," *Shock Waves*, vol. 12, no. 5, pp. 351-360, 2003.

- [14] I. Altman, "High Temperature Estimation of Energy Accommodation Coefficient of Gas Molecules on the Surface," *Journal of Physical Studies*, vol. 3, no. 4, pp. 456-457, 1999.
- [15] I. Altman, D. Lee, J. Song and M. Choi, "Experimental estimate of energy accommodation coefficient at high temperature," *The American Physical Society*, vol. 64, no. 5, 2001.
- [16] P. Lynch, "High Temperature Spectroscopic Measurements of Aluminum Combustion in a Heterogeneous Shock Tube," *Ph.D. Dissertation, University of Illinois, Urbana-Champaign*, 2006.
- [17] B. McBride and S. Gordon, "Computer Program for Calculation of Complex Chemical Equilibrium Compositions and Applications I, Analysis," NASA RP-1311, Part I, 1994.
- [18] N. Glumac, H. Krier, T. Bazyn and R. Eyer, "Temperature Measurements of Aluminum Particles Burning in Carbon Dioxide," *Combustion Science and Technology*, vol. 177, pp. 485-511, 2005.
- [19] P. Lynch, G. Fiore, H. Krier and N. Glumac, "Gas-phase reaction in nano-aluminum combustion," *Combustion Science and Technology*, vol. 182, pp. 843-857, 2010.
- [20] P. Lynch, H. Krier and N. Glumac, "Emissivity of Aluminum Oxide Particle Clouds: Application to Pyrometry of Explosive Fireballs," *Journal of Thermophysics and Heat Transfer*, vol. 24, pp. 301-308, 2010.
- [21] J.T. Brown. "Comparison of ignition characteristics of pure and coated aluminum powder in a shock tube facility." Ph.D. Thesis 2007
- [22] D.M. Kalitjan, E.L. Petersen "Nano-aluminum aerosol characterization with application to heterogeneous shock-tube combustion." 5th US Combustion Meeting 2007
- [23] O. Brandt, A. Rajathurai, P.Roth. "First observation on break-up of particle agglomerates with shock waves." *Experimental Fluids* 1987 86-94
- [24] J.J. Strecker, P. Roth. "Particle breakup in shock waves studies by single particle light scattering" *Particle and Particle Systems Characterization* 11 1994.
- [25] L. Forney, W. McGregor. "Scaling laws for particle breakup in nozzle generated shocks" *Particulate Science and Technology* 1 1983 419-431

CHAPTER 21: CALIBRATION TOOLS FOR NANOTHERMOMETERS: USING THE SHOCK TUBE

1 Introduction

The behavior of micron or nano sized particles under detonation conditions is integral to the study of heat transfer to spores, as necessary to defeat biological weapons such as anthrax. The temperature of detonation fireballs is known to reach between 2000-4000K, and lasts for a few hundred milliseconds. However, how effectively this condition translates to local conditions on small particles in the turbulent environment surrounding an explosive post-detonation has only recently been of great interest. Altman et al. estimated the energy accommodation coefficient (EAC), which characterizes the efficiency of heat transfer between surrounding gas and nanoparticles, to be as low as 0.005. This highlights the unreliability of macro temperature measurements when applied to micro scales.

In order to sense these local conditions, methods such as thermocouples and pyrometry are currently employed, but both provide limited information about the conditions experienced by a micron sized particle. Thermocouples are intrusive and require additional instrumentation to retrieve information, and while pyrometry and other spectroscopic measurements are not intrusive, they cannot provide information about the interior of blast waves. Instead, the ideal thermometer should be of comparable size as the particles, and would move with the turbulent flow to provide a full temperature history.[2]

Using the UIUC Shock Tube Facility, tests were conducted in order to determine the effectiveness of using micron-size particles as a temperature sensing method. By varying the pressure ratio in the heterogeneous shock tube, a range of known, uniform temperature conditions can be created. The zinc test particles were then analyzed using a scanning electron microscope (SEM) to determine any changes in the structure of the particles which would be indicative of particle melting.

2 Setup

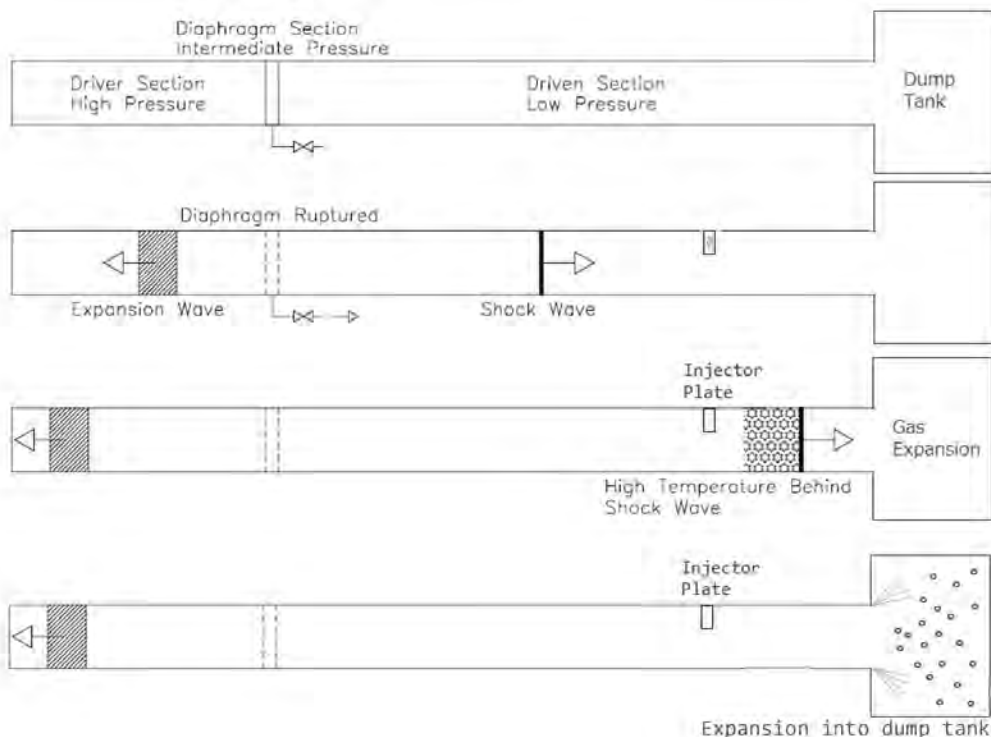
The shock tube in the UIUC Shock Tube Facility has a diameter of 5.08 cm and a length of 8.7 m. Two piezoelectric pressure transducers are placed 1.27 m apart within the wall of the driven section. By comparing the delay in response time between the two, the shock speed can be deduced, which is then input into the NASA CEA program to determine the temperature.

The particles are inserted into a port located approximately 2 m from the end of the driven section on a knife blade. As the shock passes this location, the particles are entrained into the flow by the shock and carried to the end of the driven section. Depending on the test temperature and corresponding shock velocity, the exposure time is typically between 2-5 ms. Since we are only interested in collecting the particles that have experienced the desired uniform temperature condition, those trapped in the boundary layer and therefore on the walls of the shock tube are not collected.

At the end of the driven section, a dump-tank with a volume of 40 gallons, which is approximately 50 times that of the driver section, is attached to allow for rapid expansion and quenching of the shock gas. This prevents the temperature sensing particles from experiencing any further rise in temperature due to a reflected shock.

Tests are conducted in inert argon driven gas, with pressures ranging from 200-900 torr and driver pressure at a steady 200 psi. The corresponding temperature range is approximately 500-900°K.

Figure 1: Shock tube setup



3 Particle Collection Procedure

After the shock wave propagates down the shock tube and the gas equilibrates, the pressure inside the shock tube and dump tank is raised with argon gas, if necessary, to above one atmosphere; this is necessary in order to vent the interior gas out to atmosphere. This excess pressure is vented through a valve located at the bottom of the dump tank. The gas passes through a bubbler: a 500ml beaker is filled halfway with distilled water, and the gas is piped to the bottom of the water before rising into the surrounding air. The water inside the bubbler traps any airborne particles from inside the dump tank.

Once the excess pressure is vented, the lid of the dump tank is removed and the air inside is misted with distilled water to force any remaining airborne particles to the bottom of the dump tank. Then, the lid, inside walls, and bottom of the dump tank are sprayed with water which was then allowed to flow into the bubbler. This process collects the particles attached to the inside walls of the dump tank.

A rough settling time calculation places the settling time of -325 mesh zinc in 10 cm of water to be around 4 hours. The collected particles are left inside the bubbler for approximately 12 hours in order to give them ample time to settle to the bottom. Once this time had passed, the water inside the bubbler is siphoned away, leaving approximately 100ml. Then, the particles are given another 4-6 hours to settle in case any were disturbed during the siphoning process, after which a pipet is used to remove water, leaving approximately 25ml. This remaining water is left to evaporate into the surrounding room.

After the evaporation process, the dry particles are sprayed with ethyl alcohol to remove them from the walls of the beaker and can then be transferred in the alcohol to a container for storage, or prepared for analysis at the SEM in the UIUC Center for Microanalysis of Materials.

4 Analysis

The following images were taken using the SEM facility at UIUC. After the collection of the test particles, Electron Dispersive Spectroscopy (EDS) was used in order to verify the material present in the test samples. Zn was present in each of the test samples with the addition of oxygen in all samples exposed to distilled water during the collection process. Also, evidence of carbon was found in all samples that underwent the wash down procedure due to the trapping of dust particles by the distilled water. Figure 2 compares the control samples to the tests performed above and below the melting temperature of Zn to demonstrate geometry changes.

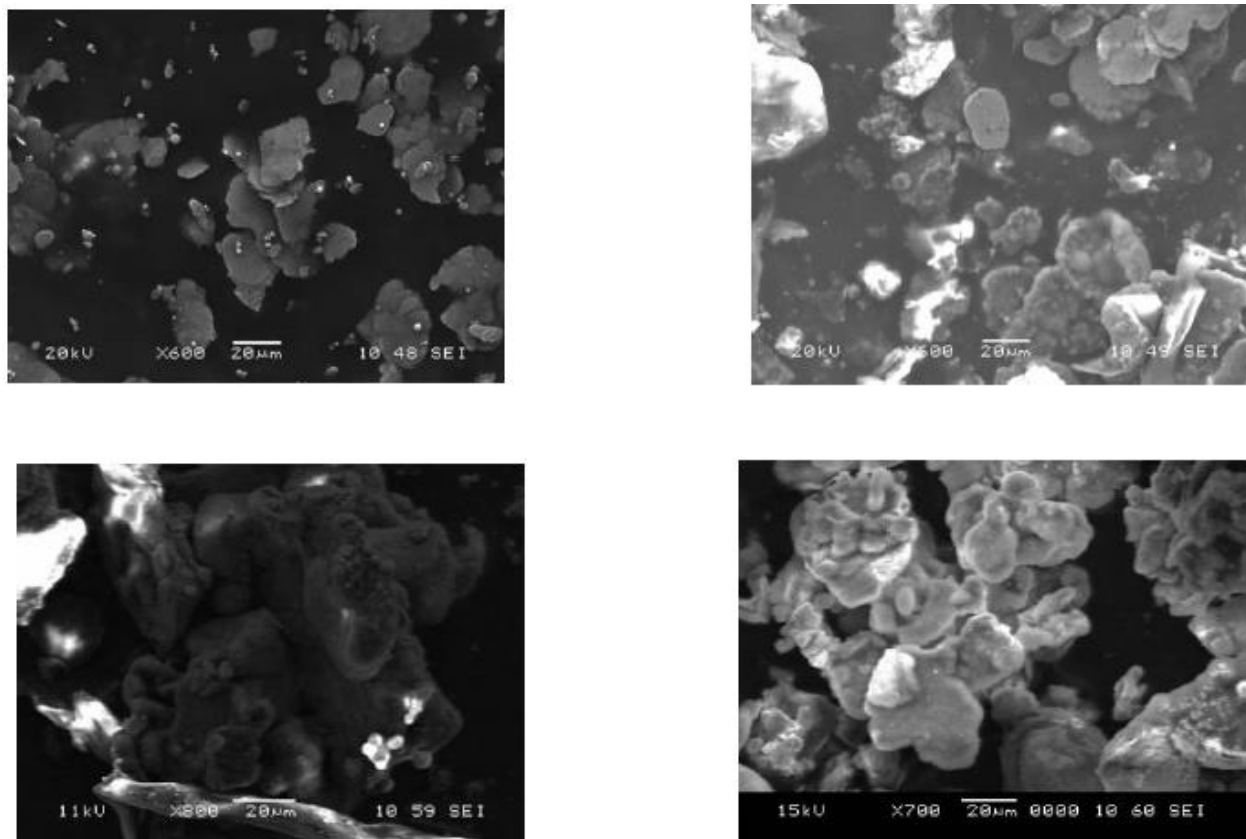


Figure 2: Overview of Zn geometry changes (a) Zn control (b) Zn at 650K (c) Zn at 731 K (d) Zn at 760K. Figure 2a shows the structure of the Zn flake before exposure in the shock tube. It is important to note that the flakes imaged in Figure 2a were not exposed to the distilled water used in the wash down procedure.

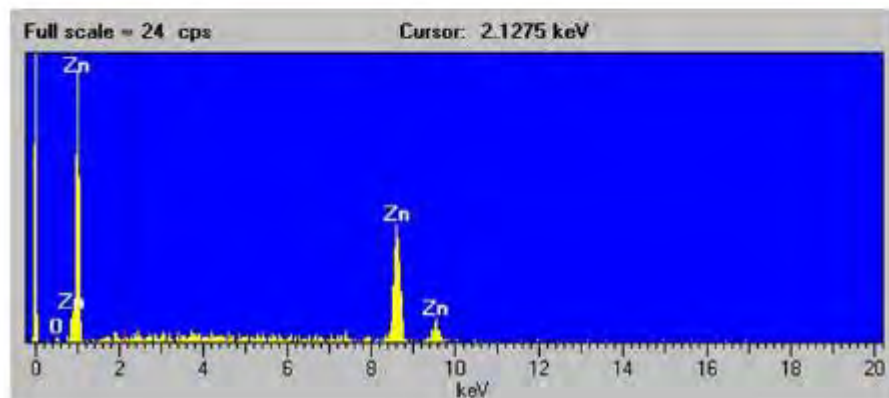
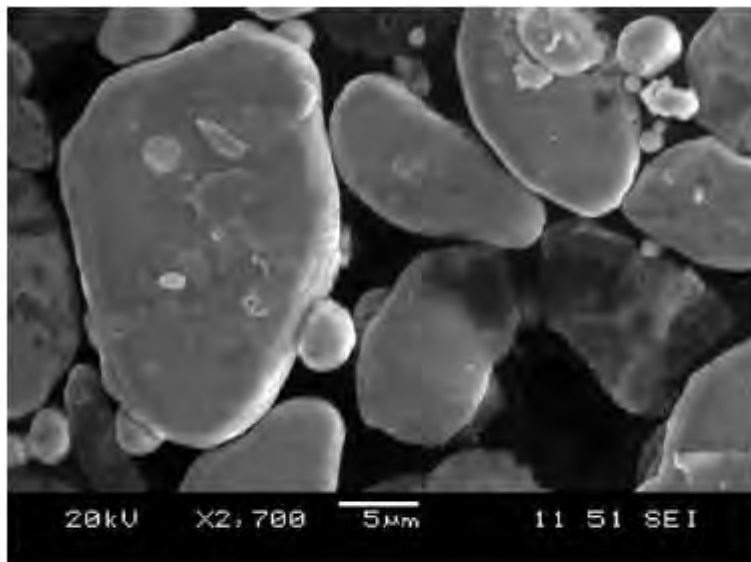


Figure 3: An SEM image (top) of flake material and the subsequent EDS spectrum (bottom).

Subsequently, in order to determine the effect of the collection process on the Zn particles, a test sample was placed in distilled water to simulate the wash down procedure. Figure 3 show Zn particles that were not exposed to a shock in the shock tube but that underwent the wash down procedure. The oxygen line in the EDS results is due to prolonged exposure to distilled water during the collection and evaporation process, which allowed an oxide layer to form on the outside surface of the Zn fake. Which this in mind, we may expect similar oxide levels to persist on all test particles, since they all undergo the wash down procedure.

Figure 2b show the results from the shock tube test below the melting point of the Zn flake. The flakes seen in Figure 2b have the same geometry as the control Zn fakes, and also show comparable oxidation to the flakes in Figure 3. Carbon appears in the EDS results from organic matter trapped by the water during the collection and evaporation process, along with possibly the carbon tape used to hold the SEM samples. The organic contaminates were minimized by covering the beakers used as bubblers and collection vessels, but could not be eliminated entirely.

Figure 4 show two features only present in temperatures above the melting point of the Zn flake. Figure 4a shows a group of Zn flakes that bonded together during testing to form a single, large particle. Figure 4b shows a region of roughness present only in higher temperature tests of

the Zn flakes. Both of these features demonstrate geometry changes that occur only during temperature tests above the melting point of Zn. The EDS results from the test above the melting point of Zn show again that oxygen is present from the exposure to distilled water during collection and evaporation. Carbon is also present from extraneous organic material trapped by the distilled water.

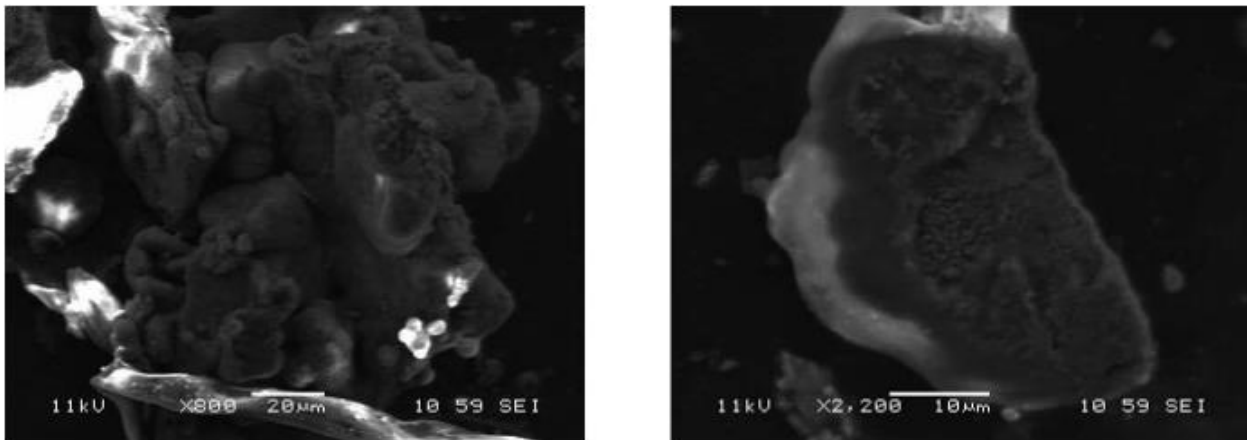


Figure 4: Zn flake expose to temperatures above the melting point.

Further testing was done to explore the oxidation of the Zn particles and examine the changes in particle geometry that would occur at temperature above the 730 K test condition.

The first of these was to flush the shock tube with Ar gas after reaching a vacuum. This was done in hopes of removing any remaining oxygen gas inside the shock tube before testing. Results from this experiment did not show a significant change from the initial test done at 730 K without the Ar flush, indicating that the oxidation present on the Zn flakes is due mostly to the wash down procedure.

The final test performed was performed to examine the effects of further raising the test temperature. Figure 2d shows the SEM results for a 760 K test. Again, globules formed indicating the melting of the Zn particles, but there was no significant geometry change when compared with the 730 K test.

Conclusions

These tests demonstrated the feasibility of using the shock tube as a means to induce a controlled temperature profile on fine particles in a flow configuration similar to that which would be observed in a blast environment. Particle temperatures in the range of 600 to 1500 K are possible, with residence times in the range of a few milliseconds.

CHAPTER 22: TURBULENT INTERACTIONS WITH NORMAL SHOCKS AND THEIR EFFECTS ON NANO AL BURN TIME

1 Introduction

Interactions between shock waves and turbulence has been a subject of increased scrutiny in the recent three decades, as its applications range from theoretical studies of boundary layers to experimental effects on mixing rate and detonation. The existence of coupling and entropy production and transport between turbulent flow and shock waves has necessitated further study as the subject has become more relevant with the advent of pulse detonation engine testing in 2008, along with similar turbulent detonation conditions in explosives testing. These interactions were also proposed to enhance fuel and oxidizer mixing rate in ramjet propulsion by Budzinski et al., as a consequence of shock waves amplifying turbulence in turbulent fields due to the nonlinear coupling of acoustic, turbulence, and entropy modes at Rankine-Hugoniot jump conditions across the shock [1].

Further, another area of interest in the propulsion and detonation fields is the topic of metal combustion-- specifically, the use of micron and nano-sized aluminum as a solid propellant option. Aluminum is a popular candidate for solid propellants due to its high energy density, along with its low hazard level and fast burning time compared to other metals with similarly high energy density. Previous work in dust explosions with micron-sized aluminum has indicated that turbulence has a direct, linear effect on the maximum burning velocity in the cloud [2]. More recent work with solid fuels has also suggested that turbulent flows cause rough surfaces on fuel particles, which increases surface area and enhances burning [3]. Due to the importance of timing alignment in applications such as blasting and solid rocket motors, particle ignition and burn time are critical factors for maximum performance. Together with the aforementioned effects caused by turbulence and shock wave interactions, we are driven to study how turbulence affects the burn time of aluminum particles.

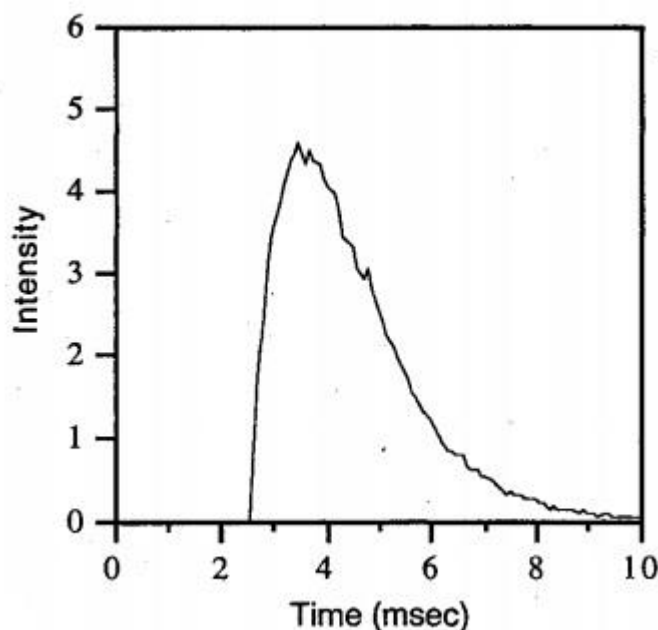


Figure 1: Sample burn time curve [4]

There are several common methods for analyzing burn time, and due to the nature of the burn time curve and plethora of said methods, resulting burn times can often vary greatly. As we can see in Fig.1, while the rising edge of the intensity curve is sharp, the trailing edge is asymptotic, and it is therefore difficult to determine a cutoff point. Analysis methods include the constant intensity cutoff method, where the cutoff is set at a constant intensity past which point the emission is believed to be insignificant; the percent peak height method, where the cutoff is a certain arbitrary percentage of the maximum peak height; and the percent total area method, where intensity is believed to be correlated with rate of energy release so a percentage of the total area is taken. Since the method selection tends to be subjective, we will use the percent total area method for consistency with previous aluminum burn time measurements conducted at UIUC in the following analysis. The burn time considered will be between 10% and 90% of the area under the intensity curve [5, 6]. The expected burn time is on the order of several hundred microseconds, with a positive correlation with particle size in the micron range.

2 Setup and Procedure

2.1 Shock tube setup

The experiments are conducted in the UIUC heterogeneous shock tube facility diagrammed in Fig.2, also called Shock Tube II in deference to a second, larger shock tube also housed in the Mechanical Engineering Department.

The shock tube consists of three major sections: the driver section, the diaphragm section, and the driven section, which includes a 0.61 m long optical section at the end made of transparent acrylic. It was constructed with an inner diameter of 5.08 cm and an outer diameter of 7.62 cm. The total length is 11 m without the optical section appendage, with 9.15 m being the driven section and 1.85 m being the driver section. Two diaphragms are clamped onto either side of the small 5 cm long diaphragm section, and high pressure is loaded into the driver section using a light gas such as helium, while the driven section is loaded with a test pressure using heavier gases such as air or argon and oxygen mixtures. The pressure ratio between the driver and driven sections determines the strength of the resulting shock.

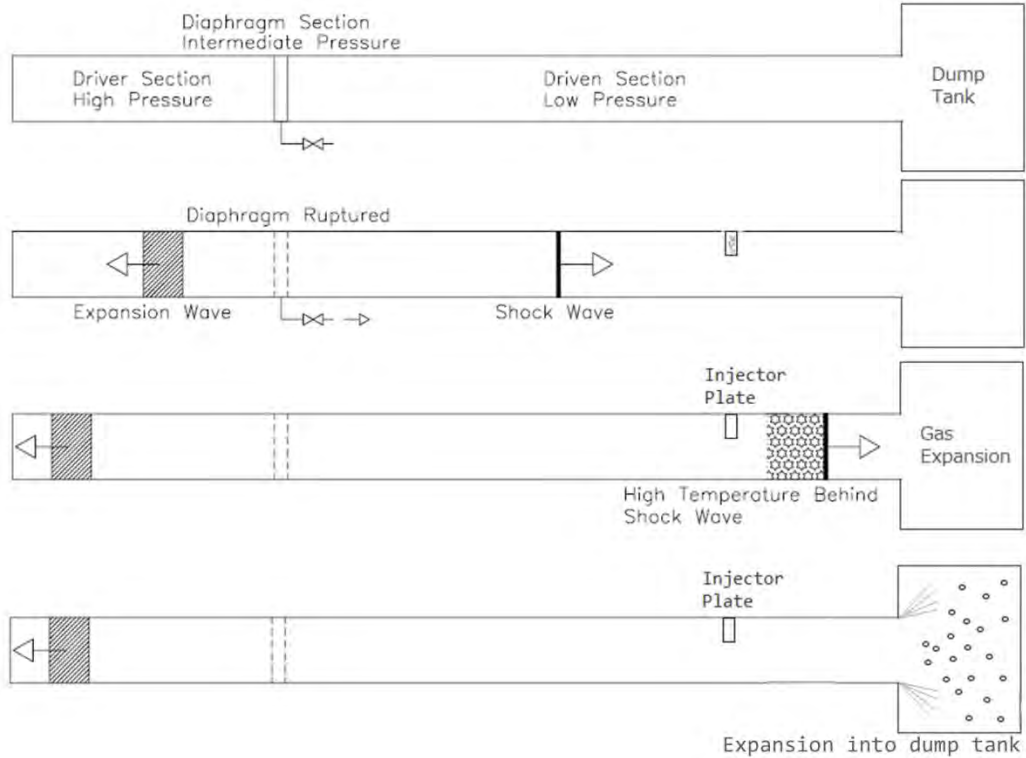
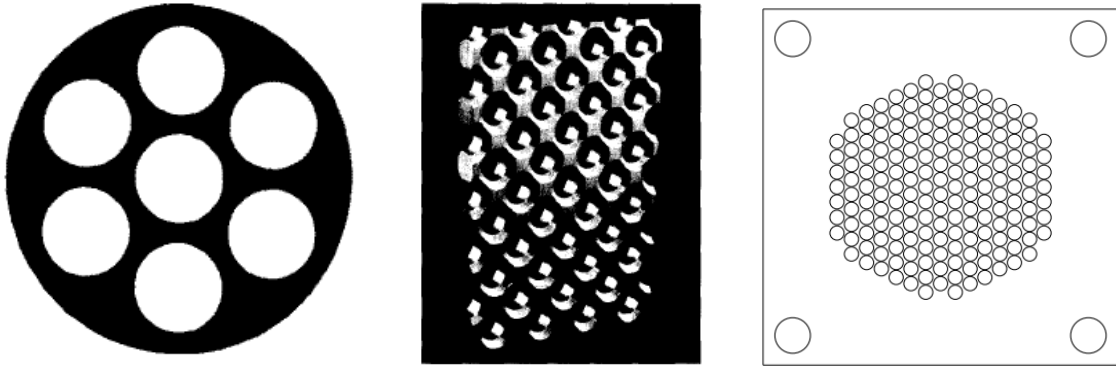


Figure 2: Shock tube diagram

The diaphragm section is loaded to an intermediate pressure to prevent the diaphragms from bursting, and is then abruptly opened to low, atmospheric pressure when the test is ready, catalyzing the bursting of both diaphragms and the propagation of a normal shock down the shock tube and a corresponding expansion wave back up into the driver section. A region of high temperature and pressure follows the initial “incident” shock, which then reflects off the endwall to create a third region of even higher temperature and pressure. Three pressure transducers are located at 0, 0.76, and 2.03 m from the endwall, whose traces allow us to calculate the shock speed and pressure. The shock speed and initial shock tube conditions can then be used to calculate temperature after the incident and reflected shock.

A perforated grid is placed in the path of the incident shock upstream of the optical section, with a pattern designed to generate a region of homogenous, isotropic turbulence in its wake. Uberoi and Kovasznay first tested a similar design in 1955, based off a “Swiss-cheese” projectile used by the Maryland Ballistics Research Laboratory [7]. Keller and Merzkirch then expanded and further tested the same design, using hot-wire anemometry to verify that the turbulence generated is in fact homogeneous and isotropic; shadowgraph imaging also proved that the turbulence front is almost planar and normal to the axis of the shock tube [8].



(a) 1955 projectile grid [7] (b) 1990 static grid [8] (c) Working grid for shock tube

Figure 3: Turbulence grid development

These factors together allow us to generate precisely characterized turbulence and temperatures, from which we can study the effects of turbulence by comparing both the visualizations of the flow and the burn times of nano and micron-sized aluminum particles.

The aluminum test particles are 40-60 nm powder produced by SkySpring Nanomaterials, which has been previously quantified by Allen et al. to have an average diameter of 73.2 nm, 110 nm diameter powder produced by NANOTECHNOLOGIES, 4 μm diameter powder, and 7.5 μm diameter H-2 powder produced by Valimet. 10 mg of test particles are loaded into the shock tube via a flat knife-blade inserted at 2.67 m from the endwall. Visualization images are taken 45 cm from the endwall, and burn time measurements are taken 20 to 40 cm from the endwall after the passage of the reflected shock. PIV images were taken 20cm from the endwall, with a viewing window of 2.5 cm wide by 2 cm tall.

2.2 Optical setup

An Optotronics green laser sheet at 260 mW was used to illuminate entrained zinc particles for preliminary image visualization. Images were taken using the Phantom 5 high speed camera at a rate of 7000 frames per second. An amplifier circuit and pulse generator track the activity of the pressure transducer located 2.03 m from the endwall, and trigger the camera to record data as soon as the incident shock passes. Burn time data was also similarly obtained using the Phantom 5 camera and trigger mechanism, with the camera additionally filtered using a 550 nm low pass filter in order to decrease higher wave length thermal emission. The filtering process allows for the AlO B-X transition emission at 486 nm to dominate the signal so we can monitor the actual burn time of the Al instead of the incandescence [5, 6]. Each image is 800 x 152 pixels, taken using a 50 mm focal lens with f/1.2.

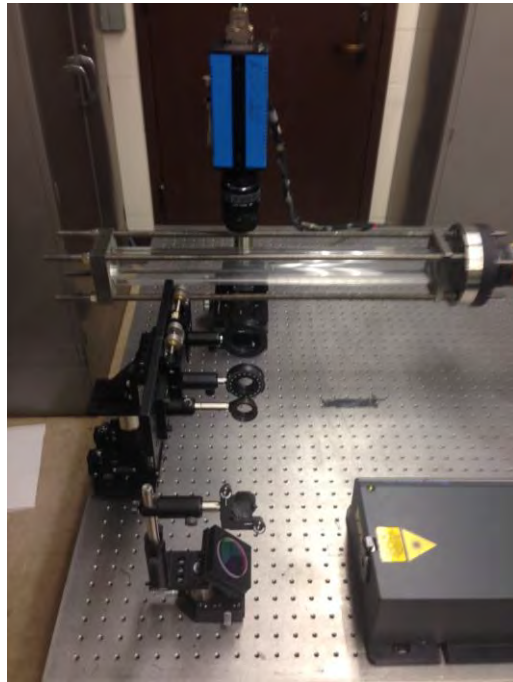


Figure 4: PIV overall setup

Additionally, PIV was used in order to quantify the turbulence generated from the perforated grid. A Solo PIV 200XT laser was pulsed twice with a delay of $0.5 \mu\text{s}$, and a PCO 1600 camera was used to record the set of images with an exposure of $0.5 \mu\text{s}$. Two 532 nm dichroic mirrors were used to direct the beam through an iris for beam shaping, then though a -50 mm cylindrical lens to spread the beam into a sheet, and finally through a 200 mm focal length spherical lens to focus down the sheet. The resulting sheet width was wider than that of the viewing window, and passed horizontally through the center of the acrylic tube. The PCO camera was installed above the tube to look down at the sheet, as indicated in Fig.4. Black board shields were erected around the setup and in front of all reflective surfaces during testing to contain the laser light.

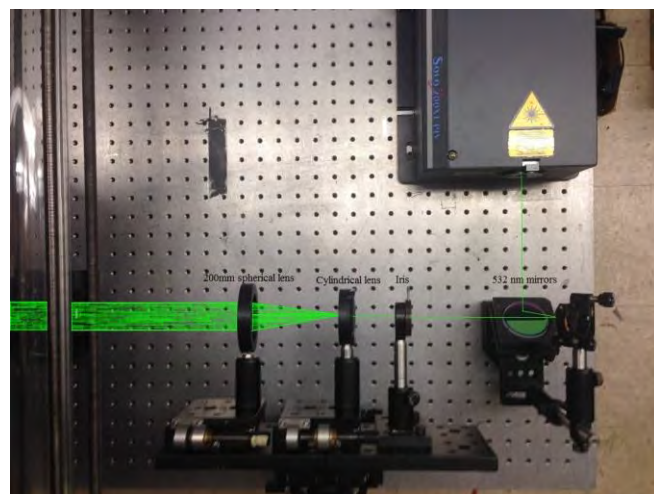


Figure 5: PIV optics setup

3 Results and Discussion

3.1 Test conditions

A preliminary set of tests were first conducted on nano-sized particles only as a proof of concept. The turbulence case was tested at 1400 K and 9.75 atm. The laminar case was tested at 1470 K and 10.7 atm. The test condition difference resulted from disturbance of the flow by the turbulence grid versus lack of a grid, despite using the same driver and driven pressure. These tests were conducted in air, and each test case was conducted once.

The second, full set of tests was conducted on the entire range of nano and micron sized particles. The driver and driven pressures were adjusted as necessary to produce the same test conditions for both cases, with a temperature of 2500 K and a pressure of 10 atm. The elevated test temperature was used to accommodate for the higher melting temperature of the larger, micron-sized aluminum. These tests were conducted in a mixture of 20% oxygen and 80% argon, whose relatively larger average molecule size allowed for use of more moderate driver pressures. Each test case was also conducted three times to access error and repeatability.

PIV data were obtained at the same conditions as the second set of tests. The error in temperature and pressure for every aforementioned test is less than 5%.

3.2 Results

3.2.1 Preliminary results

Exploratory flow visualizing images were first taken to confirm the presence of turbulence and a notable difference between flow with and without the turbulence grid. Fig.6 shows images taken first after the incident shock, and then after the reflected shock. In the incident shock case, we can clearly observe the homogeneity of the flow without turbulence, and visible gradients in the flow with turbulence. In the reflected shock case, the flow without turbulence is less uniform than the incident shock case, but is still noticeably more uniform than the turbulent case.

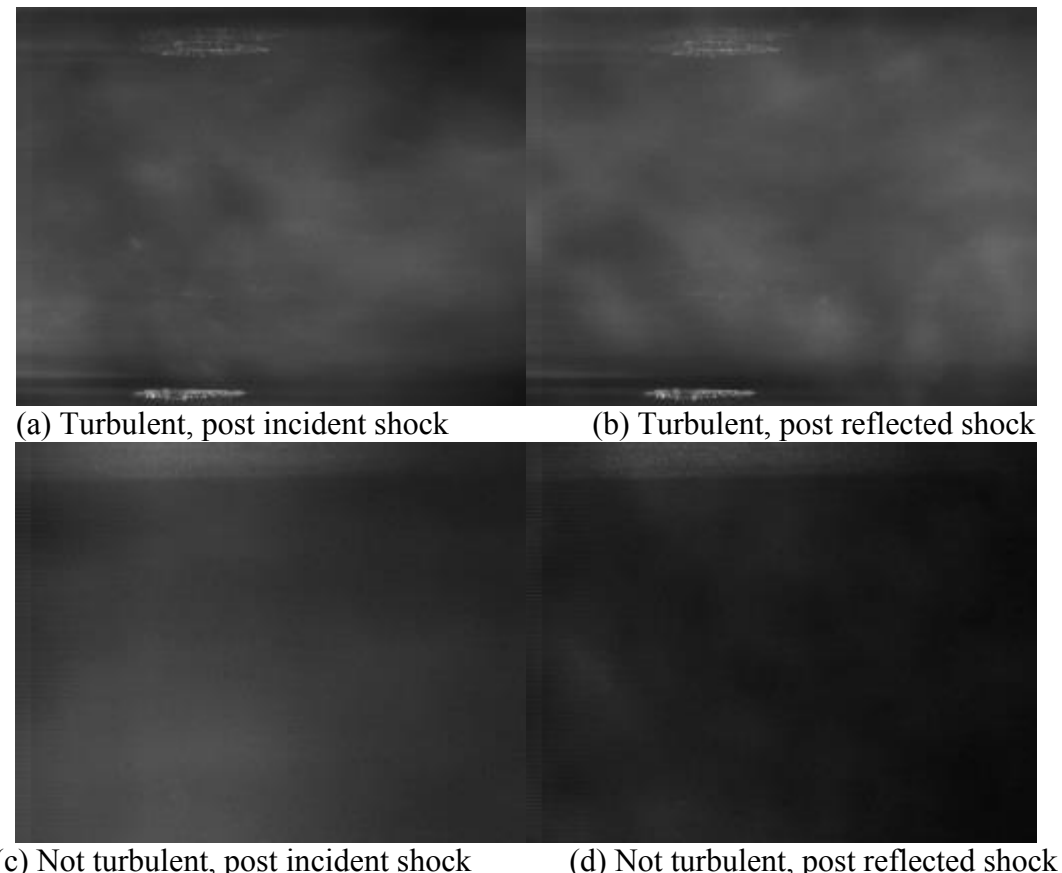


Figure 6: Flow visualization post incident and reflected shock

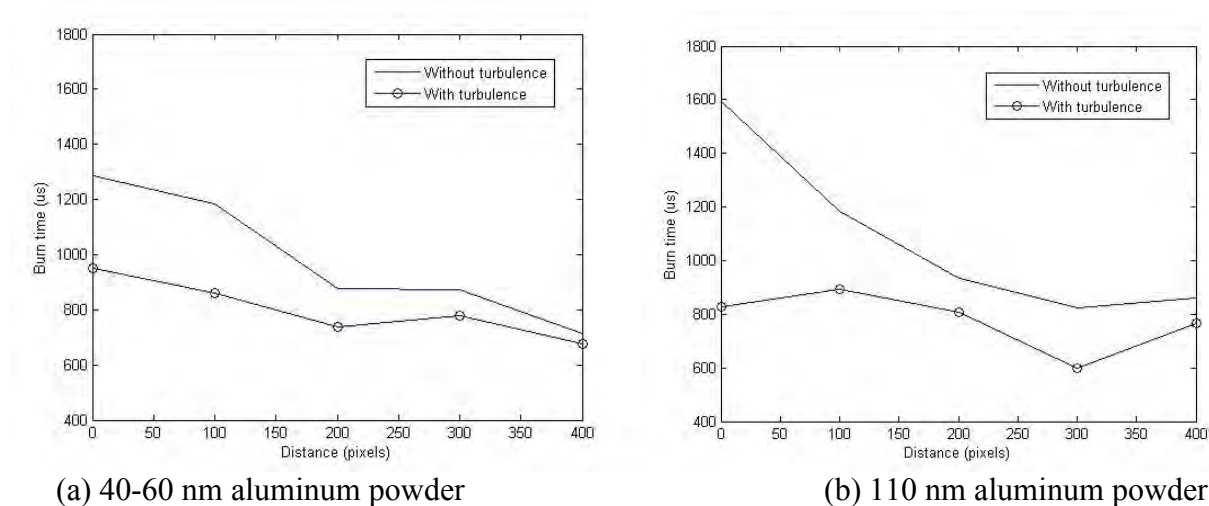


Figure 7: Burn time as function of distance from right side of frame

The test conditions presented above indicate a 5% decrease in temperature and 9% decrease in pressure for the turbulence case versus the laminar case. However, despite the lower temperature and pressure, we can observe from Fig.7 that the burn times for the turbulent cases were nevertheless consistently faster for both nanoparticle sizes. In the 40-60 nm case, turbulence shortened the burn time by about 25% and decayed down to 5% further down the shock; similar ratios exist for the 110 nm case, with the 50% time reduction at 0 pixels as an outlier most likely due to the significant analysis error margin. The axis considered for the distance spans from the right side of the frame to the left, since the reflected shock propagates from the right to the left. The burning shock front faded about 400 pixels in from the right, therefore burn times every 100 pixels were plotted for that region.

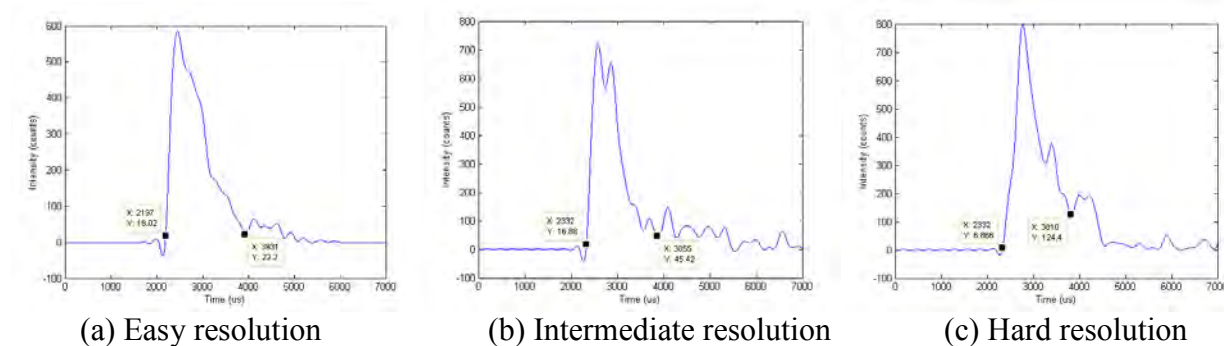


Figure 8: Range of intensity curves for calculating burn time

During application of the percent total area method for calculating burn time, it becomes clear why there are such large discrepancies in burn time reports across the literature. Fig.8 shows the variety of intensity curves extracted from photographic data. The start and end points considered for the 10% to 90% area calculation can be either very easy to pick, fairly easy to distinguish, or, as in the last case, largely subjective depending on the number of peaks included from previous curves. The error for burn time can therefore be quite large, on the order of several hundred microseconds. Previous efforts to isolate relevant data has included subtracting a linear thermal rise block from the background, or discarding portions of the signal attributed to endwall reflection or potential second afterburn of the particles [6, 5].

Previous reports of micron sized aluminum burn time has placed its value around 600-900 microseconds at 10 atm, with a positive correlation between burn time and particle diameter [5]. Extrapolating into the nano range, expected burn time should also be around several hundred microseconds. Nano sized particles have been known to burn at as low as 900K, close to the melting temperature of pure Al, but these are considered low temperature conditions and do not reliably ignite micron sized particles. Therefore, most micron and nano aluminum burn tests are conducted around 2300K, which is the melting temperature for the AlO layer formed outside of these particles. However, research has also shown a dependence between burn temperature and burn time, with the burn time at lower temperatures being significantly longer than that at higher temperatures [9]. Since our tests were conducted around 1500K instead of 2300K, it is reasonable that their burn times are significantly longer than expected from trends in literature.

3.2.2 Complete results

In order to address error and repeatability issues raised in our first set of tests, as well as expand our measurements into the micron-sized range, a second, full set of tests were conducted with 3 repeats at each condition in order to observe deviation and judge whether or not it alone contributes to the burn time difference.

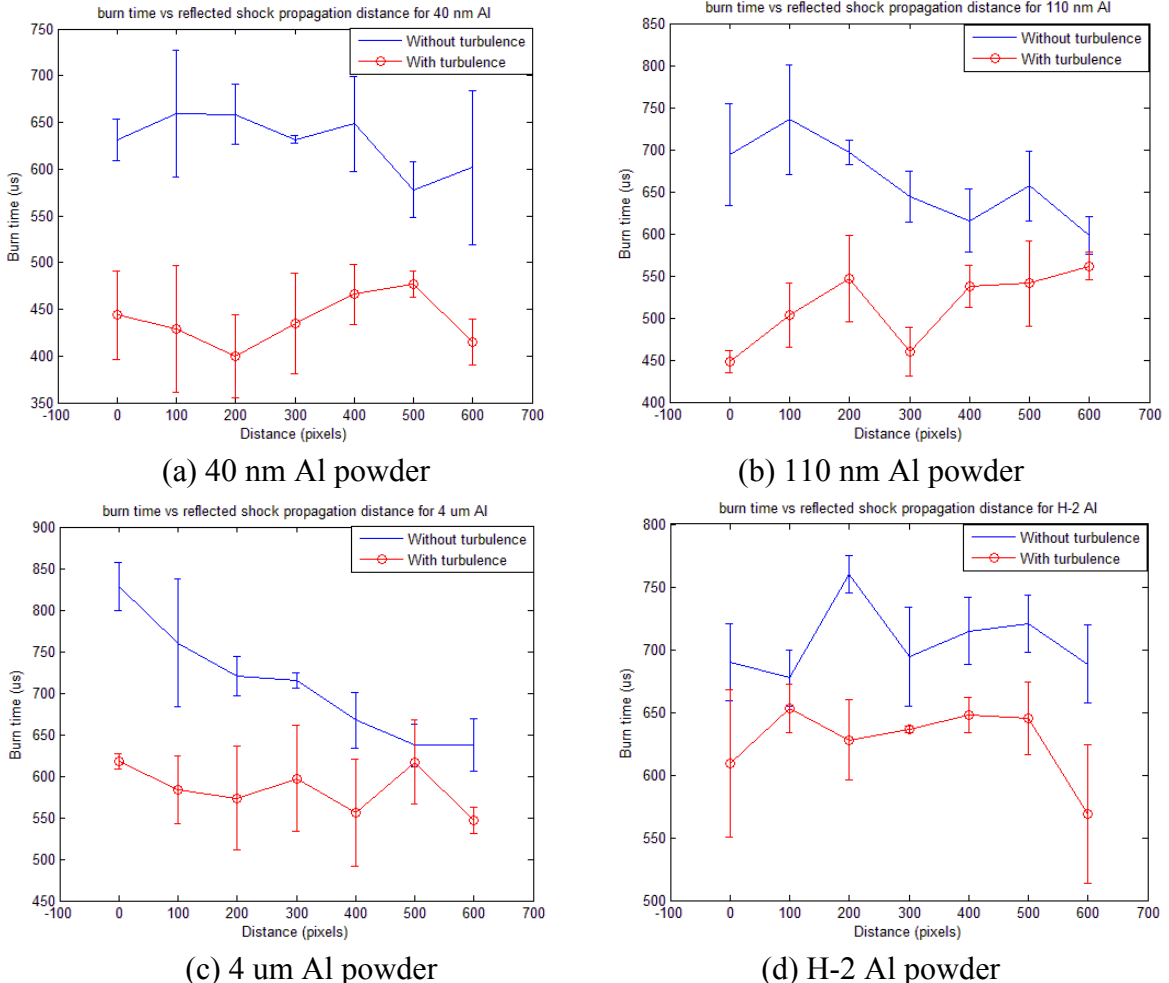


Figure 9: Burn time as function of distance

Fig. 9 summarizes the burn time data for all four particle sizes, with the error bars indicating standard error from averaging the three tests for each particle size, for each test condition. The error bars indicate that even when variation between tests is taken into consideration, the turbulent burn time is still significant shorter than the laminar burn time. The difference is slightly larger for the nano sizes than the micron sizes, with a burn time reduction percentage range of 10-25% and 5-20%, respectively. The horizontal distance over which burn time is considered has also been extended to allow for a fuller picture of the distribution. Data from either end of the viewing window tends to be less reliable than those towards the middle, since they are more likely to suffer from interference due to endwall and turbulence grid interference

effects; generally, the laminar case is less reliable on the endwall side (0 pixels), and the turbulent case is less reliable on the grid side.

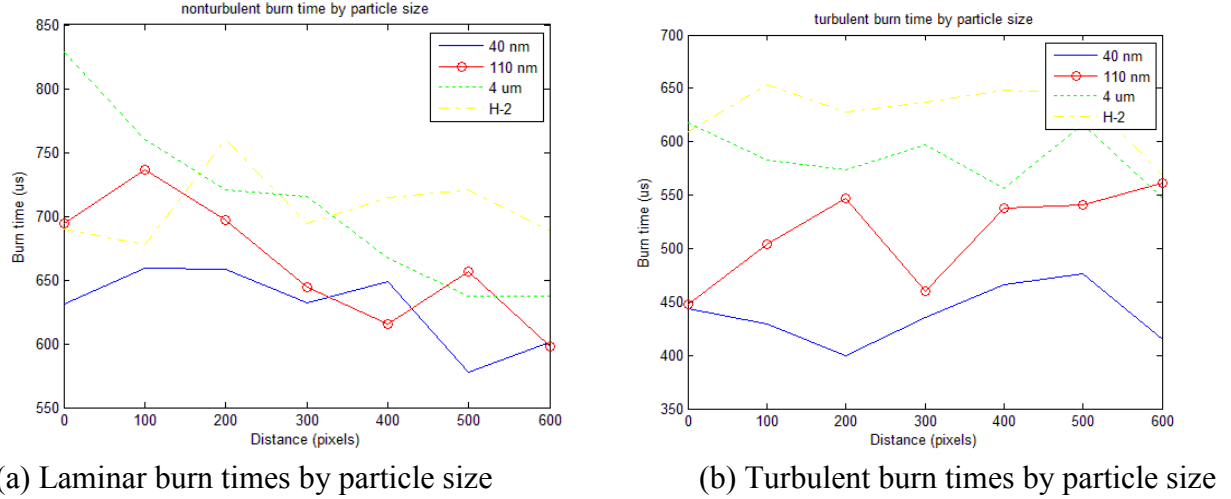
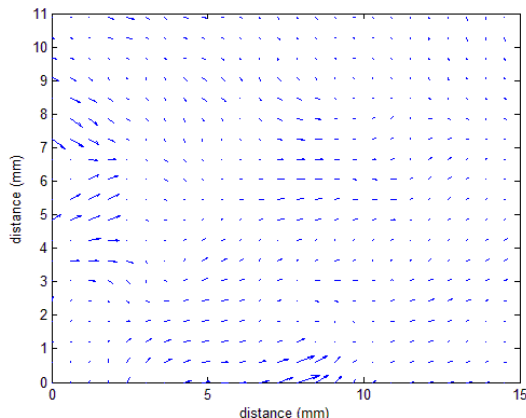


Figure 10: Burn times summarized by particle size

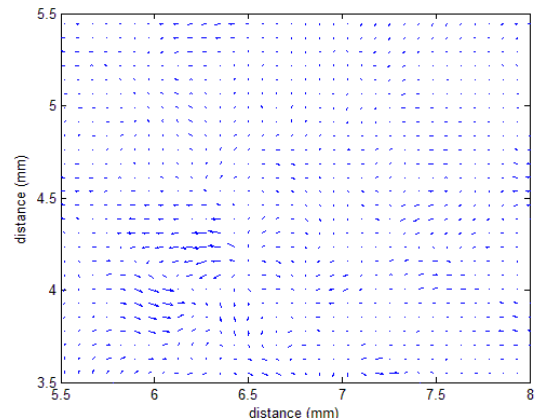
With the higher temperature and steadier pressure conditions, the burn times obtained from this set of tests also fall more in line with the expected numbers from literature mentioned in the previous section. Fig.10 summarizes the burn times for the turbulent and laminar cases by particle size, with the error bars omitted for clarity. We can see the positive trend in burn time with increasing particle size, as well as better behaved distribution further away from the endwall for the laminar case, versus the opposite for the turbulent case.

3.2.3 PIV results

Turbulence intensity data was extracted using PIV to characterize the quality of the present, with turbulence intensity defined as velocity fluctuation over mean velocity of the field. Several successful PIV shots were obtained for the turbulent case, with an average turbulence intensity of 3-4%, which is generally characterized as moderate turbulence (1% - 5%). PIV was significantly more difficult to obtain for the laminar case, possibility due to the lack of a grid aiding the particle distribution process. An average turbulence intensity of 1% or lower, however, can be estimated from data, though the resolution and therefore reliability of this number is significantly worse; turbulence intensity of under 1% is generally qualified as low turbulence.



(a) Laminar velocity field



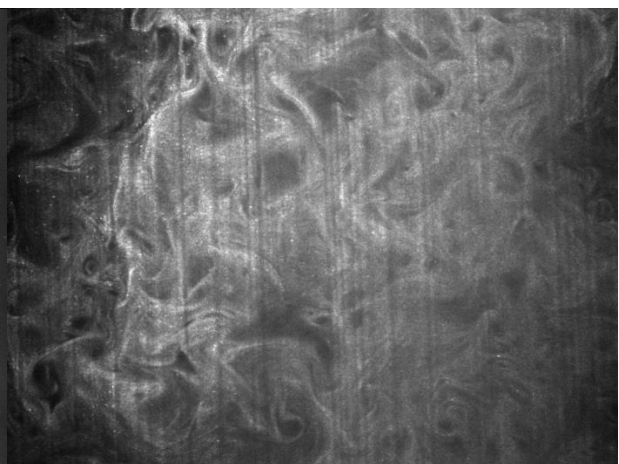
(b) Turbulent velocity field

Figure 11: Velocity fields

Fig.11 shows a sample velocity field from each condition. It is important to note that the velocity field presented includes the entire viewing window for the laminar case, but only a small part of the viewing window for the turbulent case. This is due to the lack of resolution in the laminar case, which limits it to large vectors, versus the turbulent case, where the full viewing window is saturated with tens of thousands of vectors. The seeding resolution is indicated in the raw PIV images provided in Fig.12.



(a) Laminar PIV image



(b) Turbulent PIV image

Figure 12: PIV seeding images

4 Conclusion

Our results indicate that there is indeed a notable and persistent reduction in burn time in turbulent versus laminar conditions. The reduction amount may vary from as little as 5-10% to as much as 20%, depending on various factors such as particle size, turbulence intensity, and location along the turbulent region. Tests were conducted under moderate turbulence intensity of 3-4%, with the laminar case approximating 1% ambient turbulence.

Future work should explore other options in order to address error issues, PIV seeding problems, and endwall and grid interference. A more straightforward relationship between turbulence and burn time reduction can also be drawn by evaluating and possibly eliminating confounding factors, such as the effects of increased vorticity and the reflected shock itself contributing to the turbulent environment.

References

- [1] Budzinski, J.M., Zukoski, E. E., Marble, F. E., 1992 Rayleigh scattering measurements of shock enhanced mixing, AIAA 92-3546, 28th Joint Propulsion Conference and Exhibit, 1992.
- [2] Pu, Y., Podfilipski, J., Jarosiński, J., Constant Volume Combustion of Aluminum and Cornstarch Dust in Microgravity, Combustion Science and Technology, vol. 135, no. 1-6, pp. 255-267, 1998.
- [3] Evans, B., Favorito, N.A., Kuo, K.K., Oxidizer-Type and Aluminum-Particle Addition Effects on Solid-Fuel Burning Behavior, AIAA 2006-4676, 42nd AIAA/ASME/SAE/ASEE Joint Propulsion Conference & Exhibit, 2006.
- [4] Olsen, S. E., Beckstead, M.W., Burn time measurements of single aluminum particles in steam and CO₂ mixtures, Journal of propulsion and power, vol. 12, no.4, pp. 662-671, 1996.
- [5] Lynch, P., High temperature spectroscopic measurements of aluminum combustion in a heterogeneous shock tube, Ph.D. thesis, Department of Mechanical Engineering, University of Illinois at Urbana-Champaign, 2010.
- [6] Allen, D., Optical combustion measurements of novel energetic materials in a heterogeneous shock tube, M.S. thesis, Department of Mechanical Engineering, University of Illinois at Urbana-Champaign, 2012.
- [7] Urberoi, M., Kovasznay, L., Analysis of Turbulent Density Fluctuations by the Shadow Method, J. Appl. Phys., vol. 26, no. 1, pp. 19-24, 1955.
- [8] Keller, J., Merzkirch, W., Interaction of a normal shock wave with a compressible turbulent flow, Experiments in Fluids, vol. 8, pp. 241-248, 1990.
- [9] Huang, Y., Risha, G. Al., Yang, V., Yetter, R. A., Combustion of bimodal nano/micron-sized aluminum particle dust in air, Proceedings of the Combustion Institute, vol. 31, no. 2, pp. 2001-2009, 2007.

DISTRIBUTION LIST
DTRA-TR-15-27

DEPARTMENT OF DEFENSE

DEFENSE THREAT REDUCTION
AGENCY
8725 JOHN J. KINGMAN ROAD
STOP 6201
FORT BELVOIR, VA 22060
ATTN: D. PETERSEN

DEFENSE TECHNICAL
INFORMATION CENTER
8725 JOHN J. KINGMAN ROAD,
SUITE 0944
FT. BELVOIR, VA 22060-6201
ATTN: DTIC/OCA

**DEPARTMENT OF DEFENSE
CONTRACTORS**

QUANTERION SOLUTIONS, INC.
1680 TEXAS STREET, SE
KIRTLAND AFB, NM 87117-5669
ATTN: DTRIAC